



**HAL**  
open science

# Empirical prediction of seismic strong ground motion : contributions to the nonlinear soil behavior analysis and the Empirical Green's function approach

David Alejandro Castro Cruz

## ► To cite this version:

David Alejandro Castro Cruz. Empirical prediction of seismic strong ground motion : contributions to the nonlinear soil behavior analysis and the Empirical Green's function approach. Earth Sciences. Université Côte d'Azur, 2018. English. NNT : 2018AZUR4216 . tel-02099814

**HAL Id: tel-02099814**

**<https://theses.hal.science/tel-02099814>**

Submitted on 15 Apr 2019

**HAL** is a multi-disciplinary open access archive for the deposit and dissemination of scientific research documents, whether they are published or not. The documents may come from teaching and research institutions in France or abroad, or from public or private research centers.

L'archive ouverte pluridisciplinaire **HAL**, est destinée au dépôt et à la diffusion de documents scientifiques de niveau recherche, publiés ou non, émanant des établissements d'enseignement et de recherche français ou étrangers, des laboratoires publics ou privés.



$$\rho \left( \frac{\partial v}{\partial t} + v \cdot \nabla v \right) = -\nabla p + \nabla \cdot T + f$$

$$e^{i\pi} + 1 = 0$$

# THÈSE DE DOCTORAT

Prédiction des mouvements sismiques  
forts : apport de l'analyse du comportement non-  
linéaire des sols et de l'approche des fonctions de Green  
empiriques

**David Alejandro CASTRO CRUZ**

Laboratoire Géoazur et CEREMA

Présentée en vue de l'obtention du grade  
de docteur en Sciences de la Terre  
d'Université Côte d'Azur

Dirigée par : Etienne Bertrand  
Co-dirigée par : Françoise Courboulex  
Co-encadrée par : Julie Régnier  
Soutenue le : 12 Décembre 2018

Devant le jury, composé de :

Luis Fabián Bonilla  
Hidalgo

Directeur de Recherche, IFSTTAR, Université  
Paris Est

Examineur

Cécile Cornou

Chargée de recherche, IRD, Université  
Grenoble Alpes

Rapporteur

Fabrice Cotton

Professeur, GFZ Potsdam

Rapporteur

Fernando López Caballero

Maitre de Conférence, Centrale Superlec

Examineur

“

*A farmer, whose corn always took the first prize at the State Fair, had the habit of sharing his best corn seed with all the farmers in the neighborhood.*

*When asked why, he said, “It is really a matter of self-interest. The wind picks up the pollen and carries it from field to field. So, if my neighbors grow inferior corn the cross-pollination brings down the quality of my own corn. That is why I am concerned that they plant only the very best.”*

”

**The prayer of the frog**

**Anthony de Mello**

# Résumé

L'évaluation de l'aléa sismique doit tenir compte des différents aspects qui interviennent dans le processus sismique et qui affectent le mouvement du sol en surface. Ces aspects peuvent être classés en trois grandes catégories : 1) les effets de source liés au processus de rupture et à la libération d'énergie sur la faille. 2) les effets liés à la propagation de l'énergie sismique à l'intérieur de la Terre. 3) l'influence des caractéristiques géotechniques des couches peu profondes ; appelé effet de site.

Les effets de site sont pris en compte dans la mitigation des risques par l'évaluation de la réponse sismique du sol. Lors de sollicitations cycliques, le sol présente un comportement non-linéaire, ce qui signifie que la réponse dépendra non seulement des paramètres du sol mais aussi des caractéristiques du mouvement sismique (amplitude, contenu en fréquence, durée, etc.).

Pour estimer la réponse non-linéaire du site, la pratique habituelle consiste à utiliser des simulations numériques avec une analyse linéaire équivalente ou une approche non-linéaire complète. Dans ce document, nous étudions l'influence du comportement non-linéaire du sol sur la réponse du site sismique en analysant les enregistrements sismiques des configurations des réseaux de forages. Nous utilisons les données du réseau Kiban Kyoshin (KiK-Net). Les 688 sites sont tous équipés de deux accéléromètres à trois composantes, l'un situé à la surface et l'autre en profondeur. À partir de ces données, nous calculons les amplifications du mouvement du sol depuis la surface jusqu'aux enregistrements en fond de puit à l'aide des rapports spectraux de Fourier. Une comparaison entre le rapport spectral pour le faible et le fort mouvement du sol est alors réalisée.

Le principal effet du comportement non-linéaire du sol sur la fonction de transfert du site est un déplacement de l'amplification vers les basses fréquences. Nous proposons une nouvelle méthodologie et un nouveau paramètre appelé *fsp* pour quantifier ces changements et étudier les effets non-linéaires. Ces travaux permettent d'établir une relation site-dépendante entre le paramètre *fsp* et le paramètre d'intensité du mouvement du sol. La méthode est testée sur les données accélérométriques du séisme de Kumamoto (Mw 7.1, 2016)

Nous proposons ensuite d'utiliser des corrélations entre moment seismic et la durée de la faille (Courboux et al., 2016), obtenues à partir d'une base de données globale de fonctions source et une méthode basée sur l'approche des fonctions de Green empiriques (EGF) stochastiques pour simuler les mouvements forts du sol dus à un futur séisme. Cette méthodologie est appliquée à la simulation d'un séisme de subduction en Équateur et comparée aux données réelles du séisme de Pedernales (Mw 7.8, 16 avril 2016) dans la ville de Quito.

Nous proposons enfin de combiner la méthode de simulation de mouvements forts par EGF et la prise en compte des effets non-linéaires proposée dans les premiers chapitres. La méthode est testée sur les données accélérométriques d'une réplique de le séisme de Tohoku (Mw 7.9).

**Mots clés :** Séismes, Effets de site, Comportement non-linéaire du sol, Fonctions de Green empiriques, Risque sismique, Japon, Équateur

# Abstract

Seismic hazard assessments must consider different aspects that are involved in an earthquake process and affect the surface ground motion. Those aspects can be classified into three main kinds. 1) the source effects are related to the rupture process and the release of energy. 2) the path effects related to the propagation of energy inside Earth. 3) the influence of the shallow layers geotechnical characteristics; the so-called site-effects.

The site effects are considered in risk mitigation through the evaluation of the seismic soil response. Under cyclic solicitations the soil shows a non-linear behavior, meaning that the response will not only depend on soil parameters but also on seismic motion input characteristics (amplitude, frequency content, duration, ...).

To estimate the non-linear site response, the usual practice is to use numerical simulations with equivalent linear analysis or truly non-linear time domain approach. In this document, we study the influence of the nonlinear soil behavior on the seismic site response by analyzing the earthquake recordings from borehole array configurations. We use the Kiban Kyoshin network (KiK-Net) data. All 688 sites are instrumented with two 3-components accelerometers, one located at the surface and the another at depth. From these data, we compute the ground motion amplifications from the surface to downhole recordings by the computing Fourier spectral ratios for the aim to compare between the spectral ratio for weak and strong ground motion.

The main effect of the non-linear behavior of the soil on the site transfer function is a shift of the amplification towards lower frequencies. We propose a new methodology to quantify those changes and study the nonlinear effects. This work results in a site-dependent relationship between the changes in the site response and the intensity parameter of the ground motion. The method is tested analyzing the records of the earthquake of Kumamoto (Mw 7.1, 2016).

Posteriorly, we propose to integrate a correlation between seismic moment and the duration of the fault (Couboulex et al., 2016) in the empirical Green's function method. This methodology was applied to simulate one seduction event in Ecuador, and we compare the results with the records of the Pedernales earthquake (Mw 7.8, 2016) in the city of Quito.

We attempt to take in account the nonlinear effects in the empirical Green's function method. We use the methodologies of the first part of this document based on the frequency shift parameter. The procedure could be implemented in other methodologies that can predict an earthquake at a rock reference site, such as the stochastic methods. We test the procedure using the accelerometric records for one of the aftershocks o the Tōhoku earthquake (Mw 7.9).

**Keywords:** Earthquakes, Site effects, Non-linear soil behavior, Empirical Green Functions, Seismic risk, Japan, Ecuador

# Acknowledgements

I am thankful with all the persons who were part of the process during those three years. I start with my director of the thesis, Etienne. Thanks for helping me since the beginning with all the initial problems that arriving France involved, as the security social, adapting process, between others. Also, thanks for being part of the thesis and always solving the questions and contribute ideas for developing this project. Thanks to Françoise, the co-director of the doctorate, because you explained me all the necessary to progress and to understand the seismology topic. I feel my understanding of seismology methods is one of the central learning I obtained during those years. Also, thanks Françoise for all the other aspects where your help was indispensable, as the administrative process at the end of the thesis and in my integration into the laboratory of GeoAzur. Thanks to Julie, the instructor of the thesis, for the discussions and all the knowledge you contributed to developing this thesis. I am thankful for all this group of work for the ideas, the energy, and the time you dedicated to this thesis. Equally, thank you very much for selecting me for this project and give the opportunity of research with you.

I want to thanks to the rapporteurs of this work, Cecile Corneau chargée de recherche at the laboratory of ISTerre, and the professor Fabrice Cotton of GFZ Potsdam by kindly accept to take part of your time to read and exanimate this document. Thanks for your constructive critics that made better this document.

I want to express my gratitude with the committee of the thesis, formed by Diego Mercerat of Cerema and Fernando Lopez-Caballero of Centrale Superlec, because in different opportunities they exanimated the progress of the thesis and also they gave me advice of how to improve the project. Thanks also to Fabian Bonilla-Hidalgo, and all the members of the jury for accepting come to Nice and be part of the defense of this thesis with the examination of this work.

Thanks to all the team of Cerema, the place where I developed the thesis. They always give me great talks during those three years. Thanks, to the group of risky seismic Nathalie, Philippe, Michell and the new members of the seismic risk team Ophélie and Matthieu. I want to thanks to my office mate during the thesis, Simon, who always was available to solve any question and he gave me the initial encourage and essential knowledge for learning and developing all the computations in Python. Thanks also all the members of Cerema who help me in different aspects and they had the best disposition to make my place of work very comfortable. Thanks, Marie France, Dominique, Jean-Baptiste, Yannik, and all Cerema.

Thanks to the members of GeoAzur that comment and contribute to my work, and also teach me in different opportunities, thanks Maria-Paula, Jean-Paul, Bertrand, Jenny, Anthony, Cédric. Thanks to all the persons I shared time and made better those three years. Thanks Asmae, Edward, Hector, Huyen, Louisa, Nicholas S, Reine, Sadrac, and all. Also, thanks to many persons who commented on my work in different opportunities and gave me in some cases new ways to improve the work presented herein: Jean-François Semblat, Pierre Bard.

I am especially grateful with the persons that were with me during all those years, even with the distance. Thank very much to my family and friends that always they were there to support me.

# Contents

<b>Résumé .....</b>	<b><i>i</i></b>
<b>Abstract .....</b>	<b><i>ii</i></b>
<b>Acknowledges .....</b>	<b><i>iii</i></b>
<b>Contents.....</b>	<b><i>iv</i></b>
<b>Introduction .....</b>	<b>1</b>
<b>Chapter I    <i>Theoretical verification of a new parameter to quantify the non-linear soil behavior: the frequency shift parameter Dynamic soil response model .....</i></b>	<b>5</b>
<b>I.1    Linear site response .....</b>	<b>5</b>
I.1.1    Soil response of a linear elastic soil layer on total rigid bedrock.....	5
I.1.2    Linear viscos-elastic soil on a rigid bedrock.....	9
I.1.3    Solution Multiple viscoelastic soil layers on an elastic bedrock .....	11
<b>I.2    Non-linear soil response facing a dynamic solicitation.....</b>	<b>16</b>
I.2.1    General characters of the non-linear behavior .....	16
I.2.2    Approximation with $G/G_{max}$ curves and damping curves.....	18
I.2.3    Variation of the non-linear behavior due to different parameters .....	19
I.2.4    Hyperbolic model and non-linear soil characterization.....	21
I.2.5    Characterization of the soil materials: Damping and stiffness decay curves by cyclic triaxial test	21
<b>I.3    Numerical implementation of the non-linear soil behavior.....</b>	<b>23</b>
I.3.1    Method of the equivalent linear analysis (EQL) .....	23
I.3.2    Other non-linear models .....	24
<b>I.4    Definition of a new parameter to quantify the loss of stiffness from spectral analysis .....</b>	<b>25</b>
I.4.1    The parameter $f_{sp}$ : Analysis with the equivalent linear method .....	26
<b>I.5    The parameter <math>f_{sp}</math>: Fully non-linear model .....</b>	<b>29</b>
<b>I.6    Summary and discussion .....</b>	<b>32</b>
<b>Chapter II    <i>Signal processing and Borehole arrays to study the non-linear behavior of the soil</i></b>	<b>34</b>
<b>II.1    Borehole arrays .....</b>	<b>34</b>
II.1.1    Kik-net database .....	35
II.1.2    General statistics of Kik-Net database.....	37
II.1.3    Other databases of borehole arrays .....	38

<b>II.2</b>	<b>Signal processing .....</b>	<b>39</b>
II.2.1	Selection of the window of interest .....	39
II.2.2	Removing the mean.....	40
II.2.3	Applying the Hanning's window .....	41
II.2.4	Addition of zero pad to the signal .....	43
II.2.5	Signal Process: Application of butter filter .....	43
II.2.6	Spectrum processing: Konno-Ohmachi smoothing .....	45
<b>II.3</b>	<b>Borehole spectra ratio (BSR).....</b>	<b>46</b>
<b>II.4</b>	<b>Summary .....</b>	<b>47</b>
<b>Chapter III</b>	<b><i>Impact of the soil non-linear behavior on the seismic site response.....</i></b>	<b>48</b>
<b>III.1</b>	<b>Influence of the non-linearity of the soil in <i>BSR</i>.....</b>	<b>48</b>
<b>III.2</b>	<b>RSR definition and analysis of the amplitude differences .....</b>	<b>50</b>
<b>III.3</b>	<b>Frequency shift parameter (<i>fsp</i>) from signal records .....</b>	<b>51</b>
III.3.1	Estimation of the linear site response ( <i>BSR<sub>linear</sub></i> ) .....	52
III.3.2	Computation of <i>fsp</i> parameter .....	53
III.3.3	Computation of <i>fsp</i> curves .....	55
<b>III.4</b>	<b>Comparison of <i>fsp</i> and shear modulus reduction curves.....</b>	<b>56</b>
<b>III.5</b>	<b>Prediction of strong motion 2016 Kumamoto earthquake (<i>M<sub>w</sub></i> 7.1) .....</b>	<b>57</b>
III.5.1	Methodology.....	57
III.5.2	Kumamoto earthquake and sites of analysis .....	58
III.5.3	Estimation of <i>BSR</i> .....	62
III.5.4	Prediction of the amplitude of the Fourier spectrum at surface .....	64
III.5.5	Time history prediction .....	66
III.5.6	Prediction of the response spectra .....	68
<b>III.6</b>	<b>Amplification decrease consideration.....</b>	<b>70</b>
<b>III.7</b>	<b>Predictions of the site effects using both <i>fsp</i> curves and <math>\Delta BSR_{ISA}</math>. Application to 2016 Kumamoto earthquake, <i>M<sub>w</sub></i> 7.1.....</b>	<b>76</b>
III.7.1	Methodology.....	76
III.7.2	Estimation of <i>BSR</i> .....	77
III.7.3	Prediction of the Fourier spectrum at surface .....	82
III.7.4	Time history prediction .....	83
III.7.5	Prediction of the response spectra .....	85
<b>III.8</b>	<b>Conclusion .....</b>	<b>87</b>
<b>Chapter IV</b>	<b><i>Evaluation of <i>fsp</i> on H/V spectral ratio .....</i></b>	<b>88</b>
<b>IV.1</b>	<b>Earthquake H/V spectral ratio technique .....</b>	<b>88</b>
<b>IV.2</b>	<b><math>A_{\{H/V-linear\}}</math> curve and fundamental frequency of the site, <math>f_{O\{H/V\}}</math>.....</b>	<b>88</b>
<b>IV.3</b>	<b>Effects of the non-linearity on the curve of H/V ratio .....</b>	<b>92</b>
<b>IV.4</b>	<b>Analysis of <i>fsp</i> curves for all the whole database. ....</b>	<b>94</b>
<b>IV.5</b>	<b>Summary and discussion .....</b>	<b>98</b>

<b>Chapter V</b>	<b><i>Analysis of the <math>f_{sp}</math> curves using site parameters</i></b>	<b>99</b>
<b>V.1</b>	<b>Description of the <math>f_{sp}</math> curves at the kik-net sites</b>	<b>99</b>
V.1.1	Variation of the $f_{sp}$ curves from site to another	99
V.1.2	Description of the standard deviation to quantify the variation of $f_{sp}$ curves at the kik-net sites	101
V.1.3	Selection of a sub-dataset	103
<b>V.2</b>	<b>The relationship between <math>f_{sp}</math> curves and site parameters</b>	<b>104</b>
V.2.1	Analysis of the average shear wave velocity	104
V.2.2	Influence of the impedance contrast on $f_{sp}$ curves	106
V.2.3	Influence of the downhole device on the $f_{sp}$ curves	107
V.2.4	Relationship between the fundamental frequency, determined by the H/V ratio, and $f_{sp}$ curves	108
<b>V.3</b>	<b><math>f_{sp}</math> with different intensity parameters</b>	<b>109</b>
V.3.1	Parameter: $PGA_{surface}$	109
V.3.2	$PGV_{surface}/VS_{30}$	114
<b>V.4</b>	<b>Summary and discussion</b>	<b>117</b>
<b>Chapter VI</b>	<b><i>Ground motion prediction using an Empirical Green's Function method constrained by a global database</i></b>	<b>119</b>
<b>VI.1</b>	<b>Source model (<math>\omega^2</math>-model)</b>	<b>119</b>
<b>VI.2</b>	<b>Effects of <math>M_0</math>, <math>f_c</math> and <math>\Delta\sigma</math> in the spectrum of an earthquake following the <math>\omega^2</math>-model</b>	<b>121</b>
<b>VI.3</b>	<b>Empirical Green's function method</b>	<b>124</b>
VI.3.1	Criteria to use EGF method	128
<b>VI.4</b>	<b>Relationship between corner frequency, seismic moment and stress drop</b>	<b>128</b>
<b>VI.5</b>	<b>Sensitivity analysis of EGF method facing the a stochastic duration of the fault</b>	<b>131</b>
<b>VI.6</b>	<b>Case of the Pedernales Mw 7.8 (Ecuador) Earthquake ok 16 April 2016</b>	<b>133</b>
VI.6.1	Signal processing and distance correction	136
VI.6.2	Determination of the corner frequency for each EGF	136
VI.6.3	Comparison in a blind test simulation	139
<b>VI.7</b>	<b>Simulation of a Mw8.5 earthquake in Quito</b>	<b>156</b>
<b>VI.8</b>	<b>Summary and discussion</b>	<b>163</b>
<b>Chapter VII</b>	<b><i>First attempt to the integration of non-linear site effects on the Empirical Green Function methodology using borehole arrays</i></b>	<b>165</b>
<b>VII.1</b>	<b>Methodology of integration of non-linear effects by <math>f_{sp}</math> curves and the EGF method</b>	<b>165</b>
<b>VII.1</b>	<b>Ground motion prediction of an aftershock (Mw 7.9) of the 2011 Tohoku earthquake</b>	<b>166</b>
VII.1.1	Application of the EGF method with linear site effects	166
VII.1.2	Comparison of the EGF simulation of the surface strong ground motion at FKSH10 with or without including non-linear effects	169

---

VII.2	Conclusion and discussion .....	172
	<i>Conclusions</i> .....	173
	<i>Bibliography</i> .....	176
<i>Annex A.</i>	<i>Derivation of the equation for 1D wave in a viscoelastic media</i> .....	190
<i>Annex B.</i>	<i>Results of the Kumamoto simulation</i> .....	201
<i>Annex C.</i>	<i>Fsp curves</i> .....	226
<i>Annex D.</i>	<i>Results for Quito simulation with EGF method</i> .....	242



# Introduction

Motions in the lithosphere occur at different time scales: from the very long geologic times for the plate tectonic to few seconds for fault ruptures. The fault ruptures produce earthquakes due to the sudden release of accumulated energy that is spread in the Earth in the form of seismic waves.

The number of earthquakes per year is estimated at more than one million (IRIS, 2011). About 10.000 of them reach a magnitude larger than 4 but they are unable to cause damage to the population. Strong earthquakes hopefully are less frequent, but they are able to strongly affect our societies causing several fatalities and big losses in the infrastructures. Moreover, the earthquakes can trigger landslides and tsunamis. Earthquake engineers try to anticipate and to prepare the infrastructure for mitigating the seismic risk. For this aim, the energy and the frequency of the seismic ground motions must be anticipated.

The ground motions are first related with the way the energy from the accumulated stress on a fault is released. These so-called source effects affect the ground motions and depend mainly on the moment released (that depends on the surface of the fault and the displacement of the fault), the rupture velocity, and the stress drop (difference of stress before and after an earthquake). Then, the seismic waves generated at the source are modified by their travel in the underground medium (so called path effect). Those effects cause a dissipation of the energy (geometrical and anelastic attenuation) and changes in the frequency content and waveforms, related with complex interactions between the seismic wave and the underground structure medium.

Finally, the site effects refer to the influence that superficial layers of soil have on the final surface ground motion. The Michoacan earthquake ( $M=8.5$ ) that occurred in the city of Mexico in 1985 revealed the very strong amplification in ground motions recorded on the soft unconsolidated sediment of the basin compared with the recordings outside (e.g. Anderson et al., 1986; Singh et al., 1988). The ground motion amplifications due to superficial layers caused high damages and an impact on the building of the basin. Site effects are mainly caused by the last hundred meters of soil. The area where the site effects occur is very small in comparison with the path and source effects that can involve tens or hundreds of kilometers. The high influence of the site effects in the ground motions has been detected for many other cities (e.g. Fleur et al., 2016; Laurendeau et al., 2017; LeBrun et al., 2001). The current building codes implement the site effects in different grades to manage the seismic risk of the infrastructure.

The main causes of the site effects are the strong changes in the mechanical properties of the soil close to the surface. The changes of stiffness make that the energy gets trapped in the last layers of soil, causing for some frequencies constructive interferences at the surface creating a strong amplification of the ground motion.

Furthermore, the shear modulus and the damping are dependent on the amplitude of the seismic wave that travels across the shallow soil layers. It changes the soil response of strong events with respect to weak events. This phenomenon, often called non-linear effect were first detected in seismic events comparing the modeled linear soil response with the real ones from 1957 San Francisco earthquake at several sites (Idriss and Seed, 1968). After this, using many methodologies other works have detected the soil non-linearity in seismic records. For example,

comparing the site response between strong and weak events the non-linear effects were detected in the earthquake of Mexico Mw 8.5 (Singh et al., 1988) and for the earthquake of Loma and Pieta Mw 6.9 in United States (Aki, 1993; Beresnev and Wen, 1996; Darragh and Shakal, 1991). After them, the non-linearity have been interpreted in seismograms as a reduction in the amplification at high frequencies and in some cases an increasing of the amplification at low frequencies (e.g. Bonilla et al., 2011; Régnier et al., 2016b; Sawazaki et al., 2006). Another usual way to evaluate the soil non-linearity is through proxies to estimate the stress and the strain of the soil column (e.g. Bonilla et al., 2005; Zeghal and Elgamal, 1994). In the recent years, using methods of interferometry the time that the wave takes between two points is estimated and by this the shear modulus decay is evaluated (e.g. Bonilla et al., 2017; Chandra et al., 2015; Nakata and Snieder, 2012; Sawazaki et al., 2009).

As was mentioned, the task of prediction of the seismic ground motion involves the source, path and site effects, and it is very important in the earthquake engineering. This task has been addressed by many methodologies, in some cases with numerical simulations or with empirical evaluations. For example, one empirical approach used to predict ground motion for engineering needs is the use of Ground motion prediction equation (*GMPEs*). *GMPEs* are equations build from large database of real ground motions recorded over the world (e.g. Douglas, 2011, for a review). They enable to predict a mean value and a variability of the ground motions given simple parameters like magnitude, distance and a site parameter often based on the mean shear wave velocity of the first 30 meters of soil ( $V_{S30}$ ). *GMPEs* are very powerful tools to predict ground motions parameters in general cases. The drawback of this method is the high uncertainty associated with the inclusion of different earthquakes from different regions and conditions in the analysis. It implies, for example, that important individual conditions as the site effects and the soil non-linear behavior are not taken into account.

Numerical methods are also used to attempt modeling the earthquake phenomena. These analyses employ numerical approximations that involve different complexities depending of the model. Most of them reduce the geometry to one dimension, although some of them evaluate the three components of the motions. Other kind of numerical models involve two or the three dimensions of the space. The definition of the materials in the numerical models is an essential part for the performance of the prediction of the ground motions. Often the models assume that the materials are linear. In other cases, the soil models introduce the non-linearity by relating the soil behavior with several rules that relate the soil properties with the state of the material (e.g. Iwan, 1967; Masing, 1926). These methodologies require input parameters that are complex to estimate and measure, like the geometry of deeper layers, and stiffness and damping of all the involved materials in the media. This definition of parameters brings a high cost, regarding the time and work, and also has a high uncertainty associated. Additionally, numerical models have a high uncertainty in their results due to the constitutive model and the measurement of non-linear parameters (Régnier et al., 2018).

Another alternative is the simulation by empirical methods. One of the examples is the empirical Green functions approach (*EGF*). It extrapolates weak seismic motions available in our databases to stronger motions. This method includes the source effects, path effects, and site effects. The method is also widely used because it does not require specific information as the geometry and the soil characteristics to well predict a future strong earthquake. One of the biggest complications that this methodology has is its dependence on the stress drop of the future earthquake. This dependence makes the methodology hard to be applied since it is not easy to determinate this parameter for an earthquake that has not occurred yet.

Another limitation of the EGF method is the assumption that all earthquake system is propagating in a medium characterized by linear behavior. It means that the evaluation does not consider the non-linear behavior of the shallow soil layers. This is also an important issue in most of the methodologies to simulate ground motions, not just EGF method, as stochastic methods (e.g. Boore, 2003), and GMPE formulas.

The non-linear soil effects can be a major aspect of the strong ground motion prediction. The role of the non-linear soil behavior on the seismic motion makes it important for seismic hazard assessments.

In summary the quantification and the consideration of the effects of the non-linear soil behavior is an important aspect that we study in this document.

## Objectives

In the work presented here, we aim to evaluate the non-linearity of the shallow soil layers with an empirical methodology. We search to evaluate and to quantify the effects that the non-linearity has on the seismic response of the soil. This analysis is done by studying the site response in function of the level of seismic solicitation. We use results coming from borehole spectral ratio (*BSR*) and from earthquake *H/V* spectral ratio computations.

We propose an empirical methodology to predict the non-linear soil behavior effects on site response that can be used to include the non-linearity in other methodologies of earthquake estimation, as *EGF* method. This proposition will allow to better predict strong ground motions, especially for countries with low seismicity where only weak to moderate earthquake recordings are available.

We also aim to solve the limitation of applicability for the EGF method. We will introduce in the methodology of Kohrs-Sansorny et al., (2005) a procedure to manage the variability given by the estimation of the stress drop. This procedure will be based on the analysis of the fault duration with the seismic moment (Courboux et al., 2016), transforming the fault duration regarding the stress drop.

## Outline

- Chapter I of this document presents the theoretical background to quantify and to analyze the site effects by computing the transfer function of a soil column. We present the influence of aspects as the damping, the impedance, and the bedrock by the changes that they generate on the transfer function. A new parameter called *fsp* quantifies the effect of the loss of stiffness of the soil in the transfer function. Using the equivalent linear method and a full non-linear method we test the theoretical relevancy of the *fsp* parameter under complex conditions.
- Chapter II presents the signal processing that is applied to the earthquake recordings in this work. Subsequently, Chapter II presents the borehole arrays configurations that are used to analyze the site effects.
- Chapter III presents a procedure to quantify the level of non-linearity on the sites during a strong ground motion. The procedure is based on the *fsp* parameter, using records

from vertical arrays. This parameter focuses in the measure of the stiffness degradation that the soil suffers. It shows a link between  $f_{sp}$  and the modulus reductions curve.

Using  $f_{sp}$ , we present a methodology to estimate the site response for future strong ground motions. Also, analyzing the trend of several records, a methodology that estimates the decrease of the site effects amplification is shown.

- Chapter IV presents a methodology to estimate the non-linearity influence on the site response using earthquake H/V spectral ratio technique. This methodology uses again the  $f_{sp}$  parameter, and a comparison with the estimation using borehole arrays is presented.
- Chapter V presents a statistical analysis of the results on all kik-net database. This analysis presents relationships between site parameters, as  $V_{S30}$  and fundamental resonance frequency, with the propensity of a site to develop non-linear behavior, defined by  $f_{sp}$  curves.
- Chapter VI shows a new procedure to use the EGF method estimating the stress drop of the future earthquake. This methodology also manages the variability associated with the stress drop estimation, having results comparable with the most advanced GMPE methods. However, EGF method can estimate better the site effects, producing more realistic response spectra than the general shape of the GMPE methods.
- Chapter VII presents a first attempt of the integration of the non-linear soil behavior, based on the  $f_{sp}$  parameter correction, in the EGF approach.

# Chapter I Theoretical verification of a new parameter to quantify the non-linear soil behavior: the frequency shift parameter

## Dynamic soil response model

In this chapter we introduce the analytical and numerical evaluation of seismic site response (lithological site effects) for the shear waves propagating in a unidimensional medium with a vertical incidence and the estimation of the site response. The linear elastic and visco-elastic soil behavior are first analytically analyzed and then, the non-linear soil behavior is introduced through numerical modeling. The impact of the various hypothesis on the soil behavior is observed on the site response (transfer function of the site).

With the help of this mathematical development, the theoretical relevancy of a new parameter, to quantify the impact of the non-linear soil behavior on site response, is discussed. The new parameter, called *fsp* for frequency shift parameter, quantifies one of the main effects of the soil non-linear behavior which is the decrease of the shear modulus during strong motion.

### 1.1 Linear site response

For sake of clarity, we decided to begin with the presentation of the seismic wave propagation in the simplest site configuration cases. We consider no lateral variability of the soil (one-dimension assumption) and the propagation of seismic shear waves only with a vertical incidence. In addition, the soil model used involves first a unique layer of soil underlined by a rigid rock substratum and then we will consider a multilayer of soil model with an elastic substratum.

In this section, the transfer functions between the bedrock and the surface are presented for several soil constitutive models (elastic, viscoelastic).

The 1-D assumption is not adequate for sites with complex site configurations such as a deep and narrow valleys (like Alpine valley). In the next sections, we explain briefly the 2-D and 3-D modeling. However, the vertical incidence of the wave is an assumption that is accomplished if the hypocenter of the earthquake is deep and far enough from the site investigated. It is because the direction of propagation of the waves is modified by passing from one layer of soil to another when the stiffness of soil differs. Since the stiffness of the soil decrease from the depth to the surface (especially the few hundred meters of soil) the waves will reach the surface with approximately a vertical incidence.

#### 1.1.1 Soil response of a linear elastic soil layer on rigid bedrock

This section analyzes a model that consists in one layer of soil lying on a total rigid rock with vertical shear waves propagating with vertical incidence (Figure I-1).

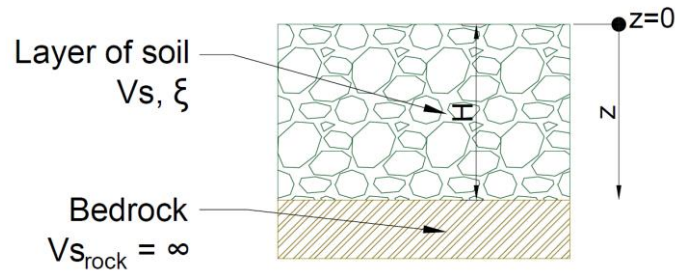


Figure I-1. Sketch of the model of soil that is overlying a bedrock.  $H$  and  $V_s$  represent the thickness and the shear velocity of the ground.

In the Figure I-1,  $H$  represents the thickness of the soil layer,  $V_s$  is the shear wave velocity, which is linked with the rigidity of the material. To analyze the propagation of a shear wave in this model, we can start from the motion equation that is required to be accomplished at any place of the model by the dynamic equilibrium (second Newton's law) express as:

$$\rho \frac{\partial^2 u}{\partial t^2} = \frac{\partial \tau}{\partial z} \quad (\text{I-1})$$

Where  $u$  represents the horizontal displacement,  $t$  is the time,  $\rho$  is the density,  $z$  is the depth, and  $\tau$  represents the shear stress. Since the model is in one dimension, the equation considers lateral displacement and shear stress traveling in the unique dimension.

If the material has no damping ( $\xi=0$ ) the relationship between the shear stress and strains ( $\gamma=\partial u/\partial z$ ) is linear. In this case, the soil can be modeled through the Hooke's law (Eq. (2)).

$$\tau = G \frac{\partial u}{\partial z} \quad (\text{I-2})$$

Where  $G$  represents the shear modulus and  $du/dz$  is the shear strain. The shear strain is a measure of the distortion of the material.

Introducing this equation (Eq. (I-2)) to the motion equation (Eq. (I-1)), the wave equation is obtained (Eq. (I-3)):

$$\frac{\partial^2 u}{\partial t^2} = V_s^2 \frac{\partial^2 u}{\partial z^2} \quad (\text{I-3})$$

Where  $V_s$  is the shear velocity defined as:

$$V_s = \sqrt{G/\rho} \quad (\text{I-4})$$

For this solution we suppose that only a mono frequential periodic wave is travelling by the media. However, from this solution the result for another kind of inputs can be also computed, as we will explain hereunder. In this case, the general solution for the Eq. (I-3) has the shape:

$$u(z, t) = A \cdot \sin(\alpha(V_s t - z) + \varphi) + B \cdot \sin(\alpha(V_s t + z) + \varphi)$$

Where  $A$ ,  $B$ ,  $\varphi$ , and  $\alpha$  are constants that will be defined with the boundaries conditions of each problem. The previous equation has two terms. Physically, the first term with amplitude  $A$  represents the upwards waves and the other the downwards waves.

In a soil column with 1D propagation, at the surface the shear stress cannot be developed. It implies that at the surface ( $z=0$ , see Figure I-1) the shear stress cannot be generated:

$$\tau(z = 0) = 0 \quad \text{then} \quad \frac{\partial u}{\partial z}(z = 0, t) = 0 \quad (\text{I-5})$$

At the bedrock, like at surface, stresses are imposed. This stress is in function of the input wave. We first consider a periodic function with a unique frequency as an input motion (Eq. (I-6)).

$$\tau(z = H) = \frac{\partial u}{\partial z} G = \tau_o \cdot \sin(2\pi f t + \varphi_l) \quad (\text{I-6})$$

Where  $\tau_o$  is the stress wave amplitude,  $\varphi_l$  is the phase of the loading wave, and  $f$  is the frequency associated with the wave. In Annex A the mathematical solution with trigonometric expressions is developed for solving the wave equation (Eq. Eq. (I-3)) under the boundary conditions previously expressed. The general solution of the problems arrives is:

$$u(z, t) = 2A \cdot \sin(2\pi f t + \varphi_l) \cos(2\pi f z / V_s) \quad (\text{I-7})$$

In the previous expression A is a constant value. In some cases, the last equation is presented in function of the angular frequency  $\omega = 2\pi f$  and the wave number  $k = \omega / V_s$ , which give the final solution:

$$u(z, t) = 2A \cdot \sin(\omega t + \varphi_l) \cos(kz)$$

The solution to the wave equation (I-7) depends on the frequency of the input wave. The transfer function between two locations, represented by the ratio between the displacements at the two locations, indicate the way the waves changes from one point to another. To study the site effects, we evaluate the displacements at the surface and at the bottom of the soil layer on the bedrock. The ratio is computed as:

$$TF_{\{0/H\}}(f) = \frac{u(0, t)}{u(H, t)} = \frac{2A \cdot \sin(2\pi f t + \varphi_l) \cos(2\pi f 0 / V_s)}{2A \cdot \sin(2\pi f t + \varphi_l) \cos(2\pi f H / V_s)}$$

$$TF_{\{0/H\}}(f) = \frac{1}{\cos(2\pi f H / V_s)} \quad (\text{I-8})$$

The formula (I-8) shows that the amplification given by the site depends on the frequency. For some frequencies the amplification tends to infinite because the denominator can be equal to zero. It occurs when the term inside the  $\cos$  function is equal to  $\pi(0.5 + n)$ , where  $n$  is any integer number.

$$f^{\{n\}} = \frac{V_s}{2H} (0.5 + n) \quad \text{for } n = 0, 1, 2, \dots \quad (\text{I-9})$$

Where  $f^{\{n\}}$  is the  $n$ th frequency peak that is amplified by the site. Those frequencies are called resonance frequencies. This phenomenon occurs because the input wave enters into constructive interference with the downwards waves that have been reflected at the free surface. This together with the hypothesis that the bedrock is rigid and that the soil is undamped, meaning that the energy cannot escape from the ground, make that the amplifications for those frequencies tend to infinite.

The first peak of the transfer function ( $f^{\{0\}}$ ) is called the fundamental resonance frequency, and is often used to characterize the soil columns (e.g. Luzi et al., 2011).

To study the amplification in other frequencies, the transfer function in Figure I-2 represents the amplification for a general case. The amplification is shown for any soil model with fixed  $H$  and  $V_s$ .

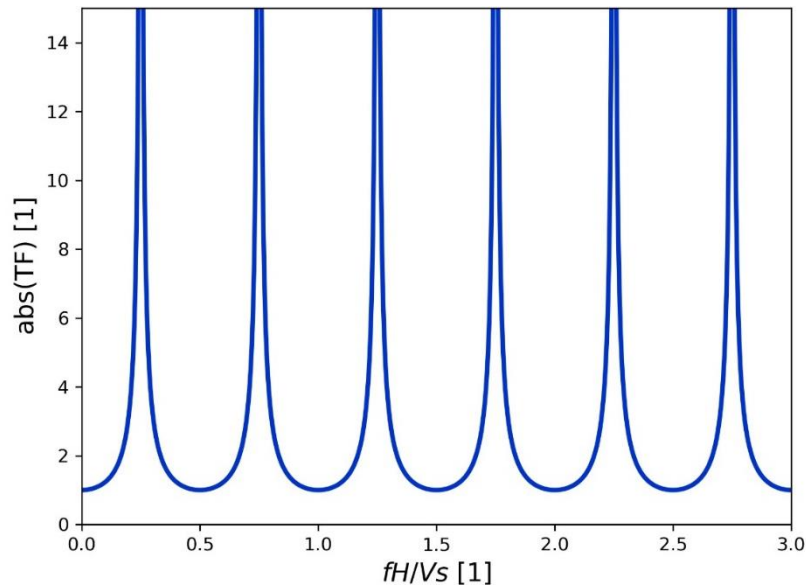


Figure I-2. Transfer for an elastic undamped layer of soil on a total rigid bedrock.

In a more realistic case, the input wave is not as simple as the Eq. (I-6). However, any function can be represented and decomposed as a summation of sinusoidal harmonic functions (Serie of Fourier, Fourier, 1822):

$$u(H, t) = \int_0^{\infty} 2|U(H, f)| \sin\left(2\pi ft + \arctan\left(\frac{-\text{Re}(U(H, f))}{\text{Im}(U(H, f))}\right)\right) df \quad (\text{I-10})$$

Where  $u(H, t)$  is the input wave,  $\text{Re}$  and  $\text{Im}$  are the functions to obtain the real and the imaginary part of a complex number respectively. The frequency depended function  $U(H, f)$  was defined by Jean-Batiste Joseph Fourier (1768-1830) as:

$$U(H, f) = \int_{-\infty}^{\infty} u(H, t) \cdot e^{-2\pi ift} dt \quad (\text{I-11})$$

Where  $U(H, f)$  is the Fourier transform of  $u(H, t)$ , also call Fourier spectrum. Note that this transform applies for any function and it could be computed at any depth  $U(z, f)$ .

The superposition principle applies for any linear system (as the Eq. (I-3)), and the solution of a composed input is equal to the summation of the solution for each part of the input. With the Fourier's methodology (Eq. (I-10)) we can decomposed the input wave into sine functions with different frequencies, each one with the shape of the Eq. (I-6). Always that the phase ( $\varphi$ ) between both points is the same, we know that the solution for each part of the input has the same formulation than the previously obtained (I-7).

Applying the superposition principle, with the transfer function and the spectrum of the input wave, the spectrum of the ground motion at the surface can be computed as follow:

$$U(0, f) = U(H, f) \cdot TF_{\{0-H\}}(f) \quad (\text{I-12})$$

Where  $TF$  is the transfer function of the system (Eq. (I-8)),  $U(H, f)$  is the spectrum of the incoming wave, and  $U(0, f)$  is the spectrum at the surface. Because Eq. (I-12) is in the frequency domain, the operation is called the convolution between  $TF$  and  $u(H, t)$ .

Finally, to compute the temporal response at the surface, the inverse transform of Fourier is applied. Already in the Eq. (I-10) was shown the formula for this transform, but usually, this transform is written in his exponential way as:

$$u(z, t) = \int_{-\infty}^{\infty} U(z, f) \cdot e^{2\pi i f t} df \quad (\text{I-13})$$

With the previous equation, we can find the solution  $u(0, t)$  with  $U(0, f)$ . It is important to note that using the Eq. (I-12) we are assuming that the phase is the same at all locations. This assumption is very well known in seismology, and many cases consider the phase even equal to zero (e.g. Brax et al., 2016; Robinson, 1967, 1957).

### I.1.2 Linear viscos-elastic soil on a elastic bedrock

All the realistic soils dissipate energy. This dissipation of energy is associated with the pore water viscosity, interparticle friction, and particles rearrangement. This phenomenon is introduced into the strain-stress relationship, making the response shear stress of the material proportional to the rate of the shear strain. This effect, called damping, is implemented in the model presented in the previous subsection. The effect of implementing the damping on the transfer function is evaluated in this subsection.

An element that produces a stress proportional to the rate of strain is known as a damper. An element that produces a stress proportional to the strain and dominated by the Hooke's law (Eq. (I-2)) is a spring. Mixing both elements, we obtain the physical representation of the viscos-elastic behavior.

In seismology, the configuration of Voigt-Kelvin is widely used. A material with this constitutive model has a hysteric behavior, with reversible strains. In this constitutive model, the stress that a material produces facing an imposed strain is dominated by the strain amplitude and rate (Eq. (I14)).

$$\tau = G \frac{\partial u}{\partial z} + \eta \frac{\partial(\frac{\partial u}{\partial z})}{\partial t} \quad (\text{I-14})$$

Where  $\eta$  and  $G$  represent the viscosity and stiffness of the material. This model cannot be used to model permanent strains under zero stress, since it tends to zero after that the load has been removed and the rate of the strain is zero. Another limitation is that in this case the failure of the material never occurs.

Introducing the constitutive model of Voigt-Kelvin (Eq. (I-14)) instead of the Hooke's law (Eq. (I-2)) in the motion equation (Eq. (I-1)), a new solution can be found, with a new differential equation that dominate the problem:

$$\rho \frac{\partial^2 u}{\partial t^2} = G \frac{\partial^2 u}{\partial z^2} + \eta \frac{\partial^3 u}{\partial z^2 \partial t} \quad (\text{I-15})$$

The Eq. (I-15) is a linear partial differential equation. The boundary conditions of this problem are the same Eq. (I-5) and (I-6). Because the new equation that dominates the problem (Eq. (I-15)) is linear, it implies that like in the elastic case, we can calculate the transfer function. The mathematical development of these equations can be found in the Annex A. The general solution for a linear partial differential equation (Eq. (I-15)) is:

$$u(z, t) = (C e^{ik^*z} + D e^{-ik^*z}) \cdot e^{i2\pi f t + \varphi_l} \quad (\text{I-16})$$

Where  $C$  and  $D$  are constants that are defined with the boundary conditions and represents the upwards and downward waves amplitude respectively. In the solution a new wave number is defined as:

$$k^{*2} = \frac{4\pi^2 f^2 \rho}{(G + 2\pi f \eta i)} \quad (I-17)$$

In the damped layer model, this number is complex. The solution of the previous equations is:

$$u(z, t) = 2C \cdot \cos(k^* z) \cdot e^{i2\pi f t + \varphi_l}$$

Where C is a constant. With the previous definition of  $u(z, t)$ , we define the displacement at  $z=0$  and  $z=H$  and the ratio gives the transfer function as:

$$TF_{\{0/H\}}(f) = \frac{u(0, t)}{u(H, t)} = \frac{2C \cdot \cos(k^* \cdot 0) \cdot e^{i2\pi f t + \varphi_l}}{2C \cdot \cos(k^* \cdot H) \cdot e^{i2\pi f t + \varphi_l}}$$

$$TF_{\{0/H\}}(f) = \frac{1}{\cos\left(2\pi f H \sqrt{\frac{\rho}{(G + 2\pi f \eta i)}}\right)}$$

Here a new term is introduced:  $\xi$  referred as the damping ratio coefficient of the material and it is defined as:

$$\xi = \frac{\pi f \eta}{V_s^2 \rho} \quad (I-18)$$

Using the damping ratio coefficient ( $\xi$ ) and introducing the definition of the stiffness in terms of shear velocity ( $G=V_s^2 \rho$ ), it reduces the transfer equation to:

$$TF_{\{0/H\}}(f) = \frac{1}{\cos\left(\frac{2\pi f H}{V_s} \sqrt{\frac{1}{(1 + 2\xi i)}}\right)} \quad (I-19)$$

The function (I-19) is the formal definition of the transfer function for a damped layer on a total rigid bedrock. However, assuming that  $\xi$  is small enough (see Annex A) the previous function can be reduced even more to:

$$|TF_{\{0/H\}}(f)| = \frac{1}{\sqrt{\cos^2\left(\frac{2\pi f H}{V_s}\right) + \sinh^2\left(\xi \frac{2\pi f H}{V_s}\right)}} \quad (I-20)$$

The transfer function with damping (I-20) makes a difference with respect to the transfer function with elastic case (I-8). The amplitude at the resonance frequencies do not go to infinite since the denominator is never equal to zero (if the term inside the hyperbolic sine is not null ( $\xi > 0$ )). However, the frequencies with maximal amplification are similar to the elastic case defined by the same Eq. (I-9).

Analyzing the amplification for all the frequencies in the damped system (Figure I-3), the transfer function does not exhibit peaks that tend to infinite in any resonance frequency. Additionally, the amplification for high frequencies are lower than the amplification for low frequencies.

Increasing the damping makes the amplification lower (Figure I-3). If the damping is high enough, at high frequencies the peaks cannot be distinguished anymore and even the transfer function can take values lower than one, meaning that the site effect is reducing the input wave amplitude.

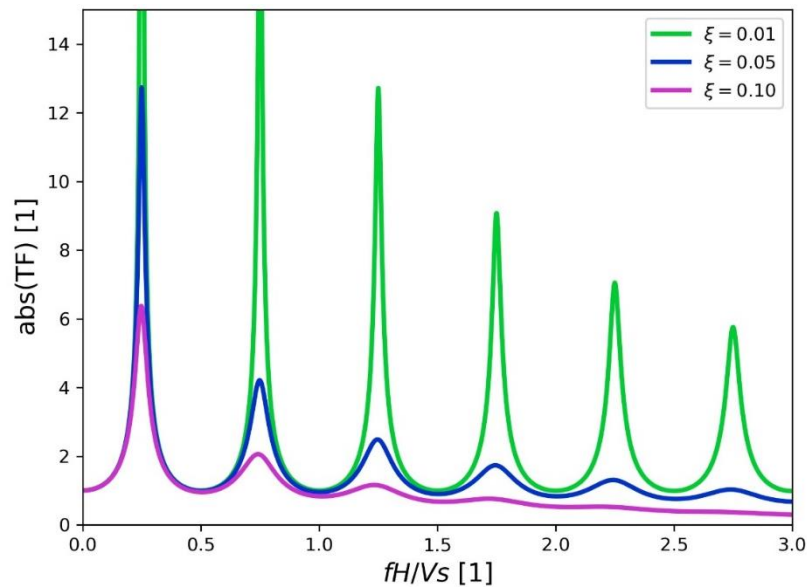


Figure I-3. Transfer function for a damped layer on a totally rigid bedrock. For example, the used layer had 5% damping.

Because the differential equation for the model (Eq. (I-14)) is a linear differential equation, the system for any input can be solved by the summation of the results for each part of the input. The procedure is the same than the one explained in the last subsection ((I-11), (I-12), Eq. (I-13)).

### I.1.3 Solution Multiple viscoelastic soil layers on an elastic bedrock

In this subsection, we analyze (1) the modifications of the wave due to the traveling from one layer of soil to another is studied and (2) that the substratum is elastic. Similar hypothesis is considered concerning the behavior of the soil, linear viscoelastic with shear waves propagating with vertical incidence.

The multiple layering and the elasticity of the bedrock creates an important effect in the transfer function that is found analytically. The bedrock in this model is not infinitely rigid, therefore, part of the energy in the downwards waves is transmitted to the bedrock, and another part is reflected in the layers of soil. This effect makes that part of the energy can leave the model.

For solving this system, we must define a new coordinate system for each layer of soil and the bedrock (Figure I-4). Zero of the local coordinate systems is the upper point of each the layer, and  $H_{(m)}$  the bottom point of each layer.

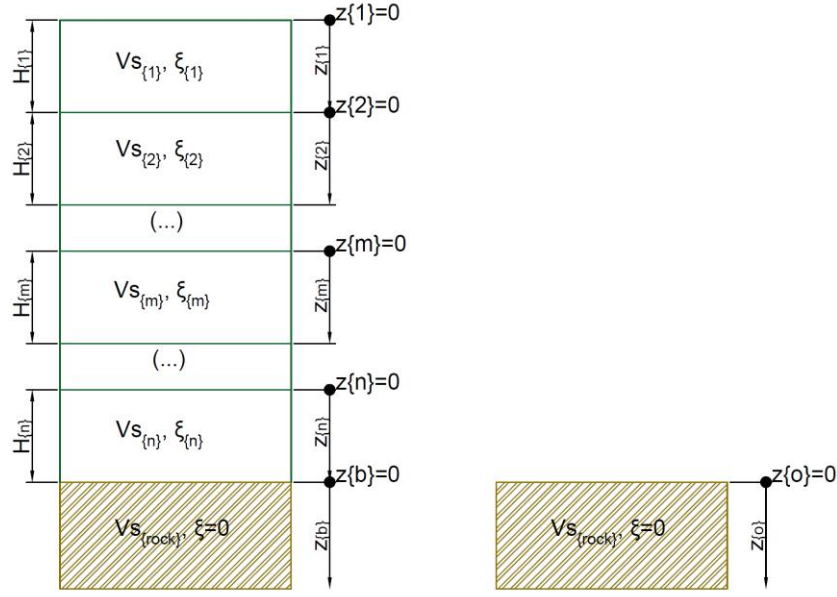


Figure I-4. Model of one damped layer lying on an elastic bedrock (left) and an outcrop (right). Each layer has a local coordinates system.

The soil layers (Figure I-4) are visco-elastic in this model and they are controlled by the Eq. (I-15). The bedrock is elastic (Eq. (I-3)). Because both equations of motion are linear, the methodology to solve this problem will follow the same procedure as the previous subsections. For each layer we define a transfer function that link the movement from one point to the other of the same layer of soil.

In this case, more solution functions must be found, one by layer. However, the general solution for all the layer has the shape of the function (I-16), because it is solved for a harmonic input:

$$\begin{aligned}
 u_{\{1\}}(z_{\{1\}}, t) &= (A_{\{1\}}e^{ik_{\{1\}}^*z_{\{1\}}} + B_{\{1\}}e^{-ik_{\{1\}}^*z_{\{1\}}}) \cdot e^{i2\pi ft} \\
 u_{\{2\}}(z_{\{2\}}, t) &= (A_{\{2\}}e^{ik_{\{2\}}^*z_{\{2\}}} + B_{\{2\}}e^{-ik_{\{2\}}^*z_{\{2\}}}) \cdot e^{i2\pi ft} \\
 &\dots \\
 u_{\{m\}}(z_{\{m\}}, t) &= (A_{\{m\}}e^{ik_{\{m\}}^*z_{\{m\}}} + B_{\{m\}}e^{-ik_{\{m\}}^*z_{\{m\}}}) \cdot e^{i2\pi ft} \\
 &\dots \\
 u_{\{b\}}(z_{\{b\}}, t) &= (A_{\{b\}}e^{ik_{\{b\}}^*z_{\{b\}}} + B_{\{b\}}e^{-ik_{\{b\}}^*z_{\{b\}}}) \cdot e^{i2\pi ft}
 \end{aligned} \tag{I-21}$$

Where  $k_{\{m\}}^*$  is the wave number (Eq. (I-17)) and  $A_{\{m\}}$  and  $B_{\{m\}}$  are constants to be defined with the boundary conditions. The other terms are explained in Figure I-4. Those solutions for each layer must accomplish the wave equation (Eq. (I-1)). The boundary conditions are the same (Eq. (I-5) and Eq. (I-6)), meaning that at the surface the shear stress is zero. In addition, the displacement and the stress must be equal at the interfaces of each layer. It guaranties the continuity of the solution in the model (Eq. (I-22)).

$$\begin{aligned}
 u_{\{m\}}(0, t) &= u_{\{m-1\}}(H_{m-1}, t) \\
 \tau_{\{m\}}(0, t) &= \tau_{\{m-1\}}(H_{m-1}, t)
 \end{aligned} \tag{I-22}$$

Solving the wave equation with the previous conditions, the constants  $A_{\{m\}}$  and  $B_{\{m\}}$  of each layer are as follow:

$$\begin{aligned}
& A_{\{m\}} \\
&= \left( A_{\{m-1\}} e^{ik_{\{m-1\}}^* H_{\{m-1\}}} (1 + \alpha_{\{m-1\}}^*) + B_{\{m-1\}} e^{-ik_{\{m-1\}}^* H_{\{m-1\}}} (1 - \alpha_{\{m-1\}}^*) \right) / 2 \\
& B_{\{m\}} \\
&= \left( A_{\{m-1\}} e^{ik_{\{m-1\}}^* H_{\{m-1\}}} (1 - \alpha_{\{m-1\}}^*) + B_{\{m-1\}} e^{-ik_{\{m-1\}}^* H_{\{m-1\}}} (1 + \alpha_{\{m-1\}}^*) \right) / 2
\end{aligned} \quad (I-23)$$

The mathematical development of the previous equation is shown in the Annex A. In the previous equation a new variable is defined to characterize the interface between two layers with the impedance ( $\alpha$ ). The impedance ( $\alpha$ ) is defined as the ratio between the apparent stiffness of the top layer and the stiffness of the lower layer.

$$\alpha_{\{m-1\}}^* = \frac{G_{\{m-1\}} (1 + 2\xi_{\{m-1\}} i) k_{\{m-1\}}^*}{G_{\{m\}} (1 + 2\xi_{\{m\}} i) k_{\{m\}}^*} \quad (I-24)$$

To find the transfer function between waves at the surface of an outcrop rock ( $z_{\{0\}}=0$ , Figure I-4), and at the top of the soil layers ( $z_{\{1\}}=0$ , Figure I-4), we obtained:

$$TF_{\{0/outcrop\}}(f) = \frac{u_{\{1\}}(0, t)}{u_{\{0\}}(0, t)} = \frac{2A_{\{1\}} \cdot e^{i2\pi f t}}{2A_{\{b\}} \cdot e^{i2\pi f t}}$$

Including the Eq. (I-23) in the previous one:

$$TF_{\{0/outcrop\}}(f) = 2 \cdot A_{\{1\}} / \left( A_{\{n\}} e^{ik_{\{n\}}^* H_{\{n\}}} (1 + \alpha_{\{n\}}^*) + B_{\{n\}} e^{-ik_{\{n\}}^* H_{\{n\}}} (1 - \alpha_{\{n\}}^*) \right) \quad (I-25)$$

Transforming the previous equation again, by replacing the coefficients  $A_{\{n\}}$  and  $B_{\{n\}}$  with Eq. (I-23):

$$TF_{\{0/outcrop\}}(f) = 4 \cdot A_{\{1\}} / \left( \begin{aligned} & A_{\{n-1\}} e^{i(k_{\{n\}}^* H_{\{n\}} + k_{\{n-1\}}^* H_{\{n-1\}})} (1 + \alpha_{\{n\}}^*) (1 + \alpha_{\{n-1\}}^*) + \\ & B_{\{n-1\}} e^{i(k_{\{n\}}^* H_{\{n\}} - k_{\{n-1\}}^* H_{\{n-1\}})} (1 + \alpha_{\{n\}}^*) (1 - \alpha_{\{n-1\}}^*) + \\ & A_{\{n-1\}} e^{i(-k_{\{n\}}^* H_{\{n\}} + k_{\{n-1\}}^* H_{\{n-1\}})} (1 - \alpha_{\{n\}}^*) (1 - \alpha_{\{n-1\}}^*) + \\ & B_{\{n-1\}} e^{i(-k_{\{n\}}^* H_{\{n\}} - k_{\{n-1\}}^* H_{\{n-1\}})} (1 - \alpha_{\{n\}}^*) (1 + \alpha_{\{n-1\}}^*) \end{aligned} \right)$$

Recurrently the terms  $A_{\{m\}}$  and  $B_{\{m\}}$  could be replaced with the Eq. (I-23) by their predecessor  $A_{\{m-1\}}$  and  $B_{\{m-1\}}$  until the first layer. The final formula is expanding, and the general solution is:

$$\left| TF_{\{0/outcrop\}}(f) \right| = 1 / \left| c(k_{\{n\}}^* H_{\{n\}}, \dots, k_{\{1\}}^* H_{\{1\}}, \alpha_{\{n\}}^*, \dots, \alpha_{\{1\}}^*) \right| \quad (I-26)$$

Where  $c$  is the combination of exponential functions obtained from recurrently replacing the coefficients (Eq. (I-23) in the Eq. (I-25)). The wave number ( $k_{\{m\}}$ ) is defined in the Eq. (I-27), the thickness of each layer ( $H_{\{m\}}$ ) depends on each case, and the impedance ( $\alpha_{\{m\}}$ ) for each layer is defined in the Eq. (I-24) (see Annex A for the mathematical developing of this formula). The wave number of each layer ( $k_{\{m\}}^*$ ) can be also defined in terms of the damping and shear velocity replacing the Eq. (I-18) and Eq. (I-4) in the Eq. (I-17):

$$k_{\{m\}}^* = \frac{2\pi f}{V_{s\{m\}}} \sqrt{\frac{1}{1 + 2\xi_{\{m\}} i}}$$

Assuming that the damping ratio is small enough (see Annex A for more details), in a first order of approximation, it allows to rewrite the square root term in the wave number as:

$$k_{\{m\}}^* \approx \frac{2\pi f}{V_{s\{m\}}} (1 - \xi_{\{m\}} i) \quad (I-27)$$

Using the same procedure, but this time involving the downwards waves, the transfer function between any layer interface and the surface (borehole transfer function) can be found as:

$$TF_{\{0/H_{\{m\}}\}}(f) = \frac{u_{\{1\}}(0, t)}{u_{\{m\}}(0, t)} = \frac{2A_{\{1\}} \cdot e^{i2\pi f t}}{(A_{\{m\}} + B_{\{m\}}) \cdot e^{i2\pi f t}}$$

Using the Eq. (I-23) in the previous equation:

$$TF_{\{0/H_{\{m\}}\}}(f) = \frac{2A_{\{1\}}}{\left( A_{\{m-1\}} e^{ik_{\{m-1\}}^* H_{\{m-1\}}} (1 + \alpha_{\{m-1\}}^*) + B_{\{m-1\}} e^{-ik_{\{m-1\}}^* H_{\{m-1\}}} (1 - \alpha_{\{m-1\}}^*) + A_{\{m-1\}} e^{ik_{\{m-1\}}^* H_{\{m-1\}}} (1 - \alpha_{\{m-1\}}^*) + B_{\{m-1\}} e^{-ik_{\{m-1\}}^* H_{\{m-1\}}} (1 + \alpha_{\{m-1\}}^*) \right)}$$

Reducing to:

$$TF_{\{0/H_{\{m\}}\}}(f) = \frac{A_{\{1\}}}{\left( A_{\{m-1\}} e^{ik_{\{m-1\}}^* H_{\{m-1\}}} + B_{\{m-1\}} e^{-ik_{\{m-1\}}^* H_{\{m-1\}}} \right)}$$

The previous equation shows that in the borehole transfer function, even if the recording device is located at interface of the layer, the impedance of deeper layers (for example  $\alpha_{\{m-1\}}^*$ ) does not affect the transfer function.

Replacing recurrently the Eq. (I-23) to move from  $A_{\{m\}}$  and  $B_{\{m\}}$  until  $A_{\{1\}}$  and  $B_{\{1\}}$ , that are equal because of the free surface conditions, the absolute value of the transfer function is:

$$|TF_{\{0/H\}}(f)| = \left| \frac{1}{d(k_{\{m\}}^* H_{\{m\}}, \dots, k_{\{1\}}^* H_{\{1\}}, \alpha_{\{m-2\}}^*, \dots, \alpha_{\{1\}}^*)} \right| \quad (I-28)$$

Where  $d$  is a combination of exponential functions, but in this case, it involves the parameters of the layers until the layer  $m$ . Additionally, it involves the downwards waves.

Using the Eq. (I-26), it is possible to find the movement at the surface due to any input wave, as was explained in the equations (I-11), (I-12) and (I-13). After, using movement at the surface, by the Eq. (I-28), the displacement for any interface point can be found, using also the inverse Fourier transform (Eq. (I-11), Eq. (I-12) and Eq. (I-13)).

To analyze the influence of the impedance contrast on the transfer function a simple case is evaluated. It consists in a monolayer model with the same characteristics of the previous subsection, but with an elastic bedrock with a finite stiffness is evaluated (Figure I-5).

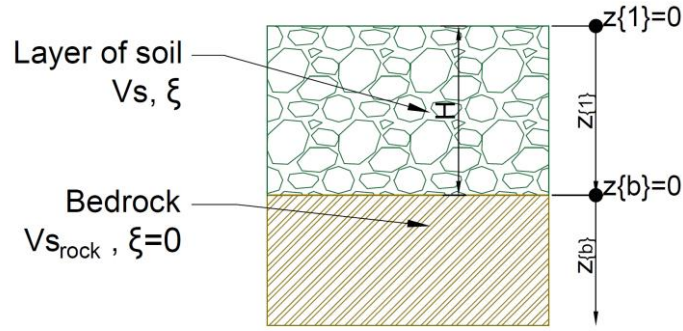


Figure I-5. Sketch of the model of soil that is overlying an elastic bedrock.  $H$ ,  $\xi$  and  $V_s$  represent the thickness, the damping, and the shear velocity of the ground.

Considering one layer of soil, using the Eq. (I-26) the transfer function would result in:

$$\left| TF_{\left\{ \begin{smallmatrix} 0 \\ outcrop \end{smallmatrix} \right\}}(f) \right| = 2 \left/ \left| e^{ik_{\{1\}}^* H_{\{1\}}} (1 + \alpha_{\{1\}}^*) + e^{-ik_{\{1\}}^* H_{\{1\}}} (1 - \alpha_{\{1\}}^*) \right| \right.$$

Reordering the previous expression and applying Euler properties and the expression of the wave number  $k^*$  in the Eq. (I-27):

$$\left| TF_{\left\{ \begin{smallmatrix} 0 \\ outcrop \end{smallmatrix} \right\}}(f) \right| = 1 \left/ \sqrt{\cos^2 \left( \frac{2\pi f}{V_{s\{1\}}} (1 - \xi_{\{1\}} i) H_{\{1\}} \right) + \alpha_{\{1\}}^{*2} \cdot \sin^2 \left( \frac{2\pi f}{V_{s\{1\}}} (1 - \xi_{\{1\}} i) H_{\{1\}} \right)} \right.$$

The previous equation shows the transfer function for a monolayer visco-elastic material. However, to isolate the effect of the impedance and in sake of simplicity the damping of this material is assumed zero ( $\xi=0$ ). It leads finally to:

$$\left| TF_{\left\{ \begin{smallmatrix} 0 \\ outcrop \end{smallmatrix} \right\}}(f) \right| = 1 \left/ \sqrt{\cos^2 \left( \frac{2\pi f}{V_{s\{1\}}} H_{\{1\}} \right) + \alpha_{\{1\}}^{*2} \cdot \sin^2 \left( \frac{2\pi f}{V_{s\{1\}}} H_{\{1\}} \right)} \right. \quad (I-29)$$

In (I-29)  $\alpha_{\{1\}}^*$  is the impedance between the soil and the bedrock (I-24),  $V_{s\{1\}}$  is the shear velocity of the soil layer and  $H$  the thickness. The impedance (I-24) for this case ( $\xi=0$ ) results in:

$$\alpha_{\{1\}}^* = \frac{G_{\{1\}} \frac{2\pi f}{V_{s\{1\}}}}{G_{\{b\}} \frac{2\pi f}{V_{s\{b\}}}} = \frac{V_{s\{1\}} \rho_{\{1\}}}{V_{s\{b\}} \rho_{\{b\}}}$$

Even when the soil layer is elastic, the amplification does not tend to infinite as it would be if the bedrock was rigid (Figure I-2).

In the Figure I-6 the impedance effect is studied. The fact that the bedrock is not totally rigid makes that the energy can be released from the system, so the amplitude is not infinite at the resonance frequencies. The resonance frequencies are the same (Eq. (I-9)) depending only of the shear modulus and the density of the upper layer; but the amplitude of the transfer function changes with the impedance between the soil and the bedrock.

If the soil layer has a higher stiffness than the bedrock, the resonance frequencies are inverted, and it would appear a deamplification as the yellow line in Figure I-6. This case is very unusual

in nature, and if it appears the impedance is not much higher than one. However, it is important to note for future analysis, that even in this case the frequency peaks keep depending in a linear way of the shear velocity of the soil layer:

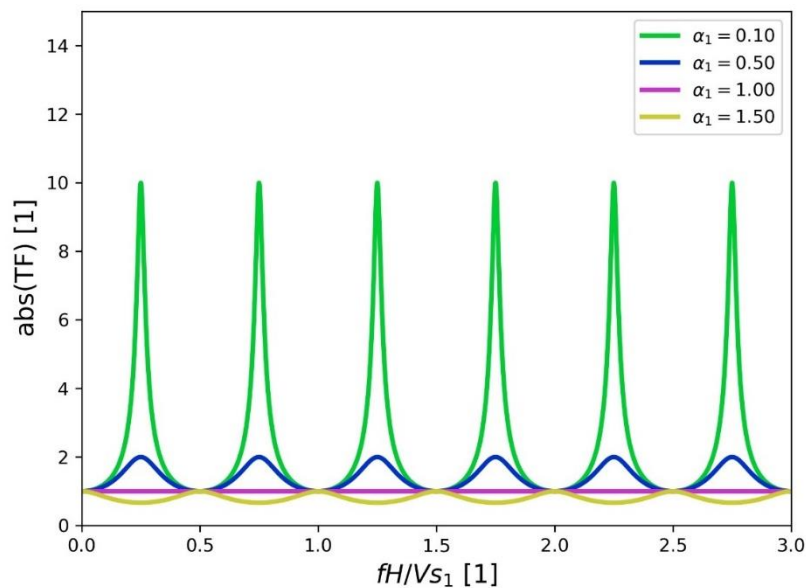


Figure I-6. Impedance effect on the transfer function for a monolayer model with no damping.

## I.2 Non-linear soil response facing a dynamic solicitation

Realistic materials present a non-linear behavior meaning that the relationships between the strain and the stress is strain dependent. The variation of the stress-strain relationship has been extensively investigated during loading and unloading processes either with laboratory tests on soil samples (cyclic triaxial tests, resonant column, cyclic torsional test, bender elements...) or directly on accelerometric data (a review of such studies is available in the chapter 3).

Considering the complexity of the soil behavior during cyclic loading several constitutive models have been proposed to reproduce those phenomena. Some of them are composed of an initial relationship between strain-stress called backbone curve, and a combination of rules that mimic the behavior of the soil during the loading and unloading process. Depending of the complexity of the model, they can model the decrease of the shear modulus and the increase of the attenuation or consider other phenomena such as pore pressure generation, (e.g. Finn et al., 1977; Pyke, 1979; Vucetic and Dobry, 1991).

### I.2.1 General characters of the non-linear behavior

The Figure I-7 shows an example of a real soil sample under a cyclic compressional test (Site KSRH10 of the KIK-net Japanese network Régnier et al., 2016a). The response of this sample clearly shows that the stress-strain ( $\tau/\gamma$ ) relationship is not linear. In this particular example we can observe that during the traction from the first cycle to the third there is a decrease of the slope. The slope represents the secant shear modulus. We also observe that there is a hysteretic behavior with an unloading path different from the loading path and with the occurrence of permanent displacement under zero stress.

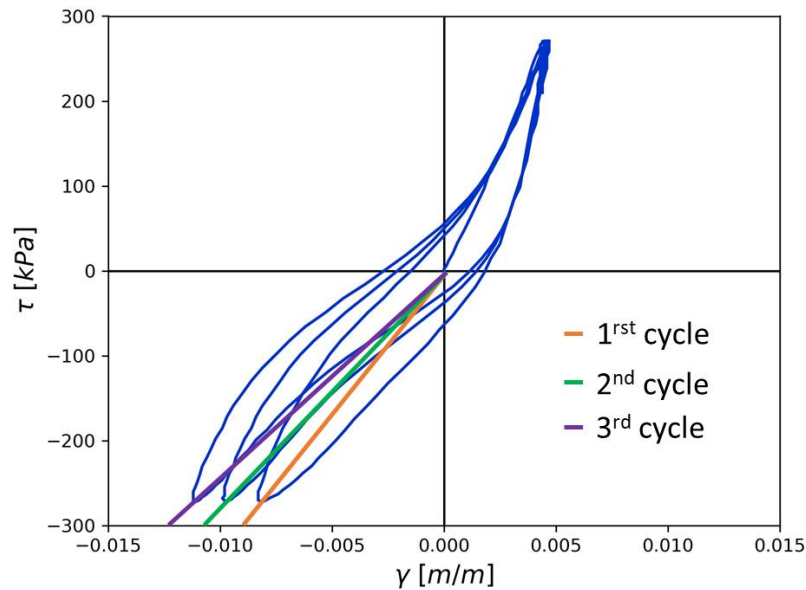


Figure I-7. Hysteric curve for a real sample under a periodic cyclic behavior stress load.

A sketch of the stress-strain relationship of a soil sample that is loaded and unloaded is shown in the Figure I-8 to explain one of the ways to generally analyze the influence of the non-linear soil behavior. First, the sample is loaded slowly from the points  $P_0$  to  $P_1$ . In this case the relationship stress-strain follows a curve that is called backbone curve (Figure I-8, top). The backbone curve for small strains is defined by a constant relationship that is the line  $G_{max}$ , where  $G_{max}$  is the slope and it represents the stiffness. After, for higher strains the backbone curve has a lower slope, representing the loss of stiffness.

From the point  $P_1$  to  $P_2$  (Figure I-8) the soil sample is unloaded. In this case, the stress-strain relationship follows a new curve that does not revert to its initial state, zero-zero point (here there is a residual deformation, the material enters the plastic behavior). Under the Masing's rules (Masing, 1926), the unloading curve is similar to the backbone curve but enlarged by 2. New cycles of loading and unloading are repeated several times from  $P_2$  to  $P_3$  (Figure I-8). The loop that is observed after one cycle illustrate the hysteretic behavior of the soil.

The point  $P_3$  (Figure I-8) shows a permanent deformation that could not be predicted by a pure linear method. After from this point ( $P_3$ ) to  $P_4$  the soil is load until a higher strain than the previous load. When the loading curve cross the backbone curve, the stress-strains relationship follows the backbone curve ( $P_1$  to  $P_4$ ). After a new cyclic load is applied from  $P_4$  to  $P_5$  defining a new hysteretic loop.

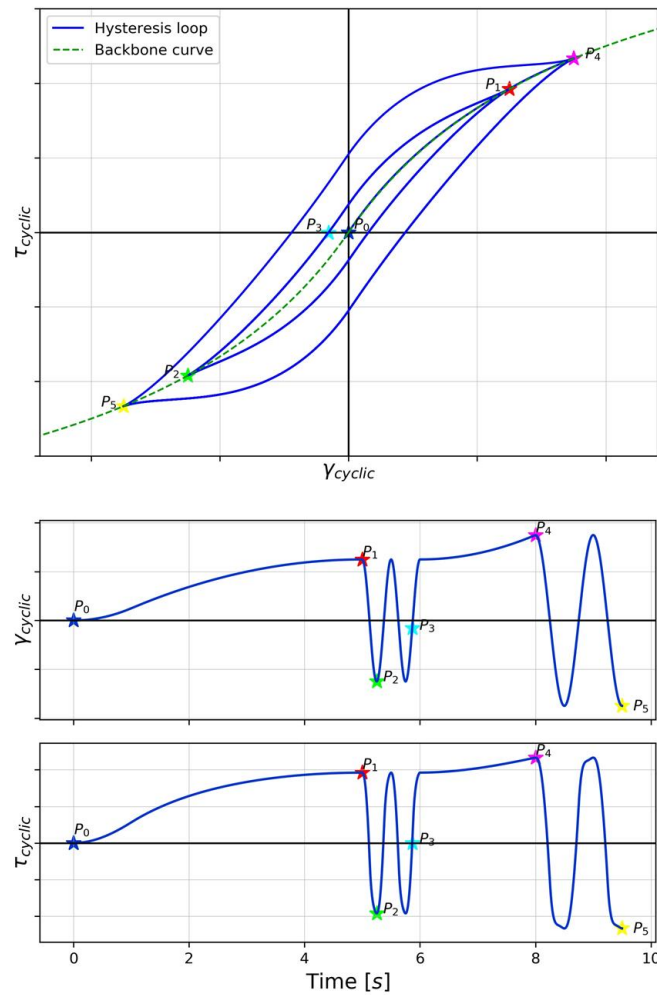


Figure I-8. Sketch of a typical variation of the stress-strain relationship facing cyclic loads (figure based in L. Kramer, 1996, Figure 6.47).

### I.2.2 Approximation with $G/G_{max}$ curves and damping curves

To represent the changes of stiffness and in the attenuation due to the non-linear soil behavior, often the modulus reduction curves and damping curves are used (Figure I-9). Those curves show the evolution of these parameters with the strain. Many constitutive models are directly based on these curves, as the hyperbolic model that will be explained on the next section. There are also other more complex models that does not use this kind of curves (e.g. Mellal and Modaressi, 1998).

When using  $G/G_{max}$  and damping curves, part of the non-linearity process is not taking in account. For example:

- Under special conditions, as for saturated loose sands, the water that is stored in the soil pores is forced to move during the shaking, creating an increase of the porewater pressure and consequently a variation in the effective stress (the effective stress is the stress that the soil particles really are supporting). During strong shakings, the porewater pressure can increase until the effective stress goes to zero and the soil losses his resistance and start to act like a fluid. This phenomenon is called liquefaction (Mogami and Kubo, 1953; Seed and Idriss, 1971) and this cannot be considered using only damping and the modulus reduction curves.

- Even before liquefaction, the pore water pressure can induce specific behavior like cyclic mobility that cannot be considered by the damping and the modulus reduction curves.
- Also, in special situations dynamic solicitations can produce changes in the consolidation of the material. It can create a hardening process on the soil (e.g. Roscoe et al., 1963) that produces plastic strains and it changes the stiffness of the material.

However, the modulus reduction and damping curves are a general and well know way to represent the non-linearity of the soil under cyclic loadings.

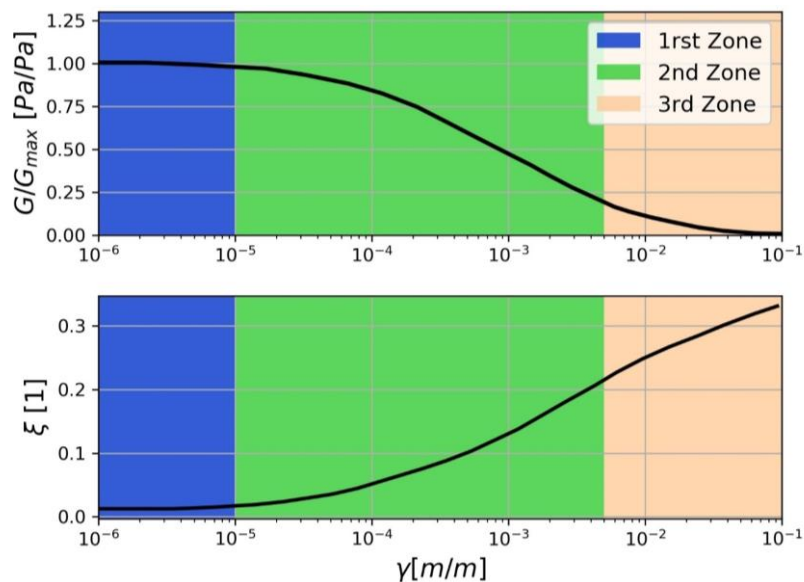


Figure I-9. General shape of the shear modulus reduction curves (top) and damping curves (bottom).  $G_{max}$  represent the shear modulus for small strains. The strain range of the zones is variable for each soil material. The values in this figure are just indicative, those have a high variability depending of each material.

The modulus reduction curve is normalized by  $G_{max}$  that is the stiffness of the material at small strains. This curve and the damping curve can be divided in three parts. The first zone (blue area in Figure I-9) is related with small strains and neither the damping nor the stiffness has a variation. In this zone, the stiffness is the highest in comparison with other zones ( $G_{max}$ ), in the other hand, the damping in this zone is the lowest ( $\xi_{min}$ ) and the behavior of the material is viscoelastic.

In the second zone (green area in Figure I-9) the soils are under moderate strains. The range is approximately between  $10^{-5}$  to  $10^{-2}$  (Ishibashi and Zhang, 1993; Seed et al., 1986) although it depends strongly on each material. In this zone the stiffness and the damping present clear changes with respect elastic response, and they are very sensitive to the changes of strains.

Finally, the third zone (orange area in Figure I-9) where the soil is under large strains (just as indicative in Figure I-9 this zone starts or  $\gamma > 10^{-2}$ , but this threshold variate depending of the soil), the stiffness and the damping are already very low and very high, respectively, in comparison with the values for small strain in the first zone. However, in those zones both parameters, especially the stiffness, starts to converge at some point with the increasing of strain.

### I.2.3 Variation of the non-linear behavior due to different parameters

The shear modulus reduction curves (Figure I-9) and the damping curves are characteristic of the material. Those curves have a high variability between materials. Additionally, the non-linear

soil behavior depends also on the soil conditions. For example, the effective stress, the plasticity index, and other factors (Vucetic and Dobry, 1991).

Kokusho, (1980) tested granular materials (sand from Toyoura sand) finding that the modulus reduction and damping curves change with different confinement effective stresses (Figure I-10). For a higher confinement the decay of the stiffness and the damping are lower. It means that the granular soils have a more linear behavior when the effective confinement stress is high.

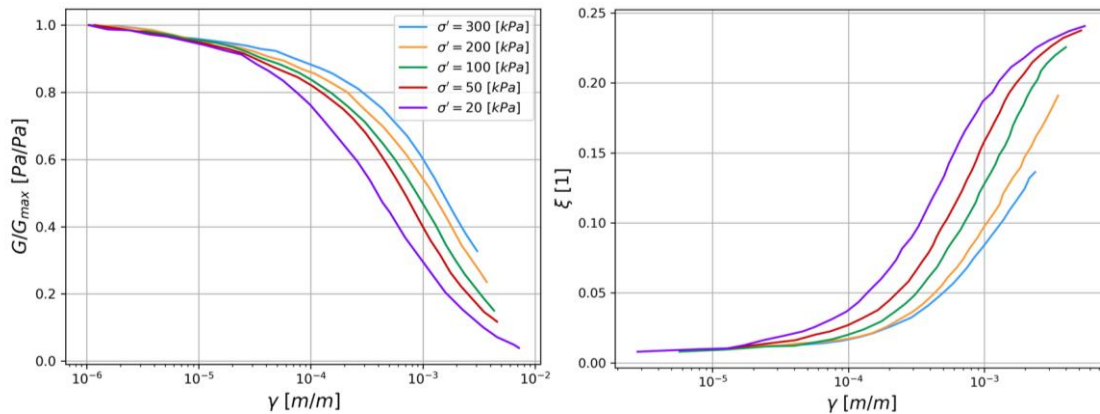


Figure I-10, Variation of the modulus reduction curve for a similar kind of sand and different confinement stresses. The figure was extracted from (Kokusho, 1980).

Additionally, for granular and sands materials the modulus reduction and damping curves depend of the granulometry of the soil (the distribution of the size particles). Menq, 2003) tested different sandy and gravelly samples, finding a lower elastic zone when the granulometry is less homogenous, (uniformly gradated). It was represented by the relationship between the coefficient of uniformity ( $C_u$ ) of the soil and the non-linear curves. Even the average size of the particles has not as higher influence as the granulometry.

For the case of the clays, the  $G/G_{max}$  and damping curves also depends of several factors. The Figure I-11 shows the variation for this kind of soil in both curves, that was obtained by several studies and summarized in Dobry and Vucetic, 1987). The figures show the influence of the proportions of voids in the soil, measured by the void index ( $e$ ), and the plastic effect of the clay, measured by the index of plasticity ( $IP$ ).

In the same study (Dobry and Vucetic, 1987) other factors that influence the modulus reduction and damping curves were analyzed. For stronger confinement stress, the damping curves are reduced (closer to zero) and the  $G/G_{max}$  curves increase (they become closer to one). It means that with high confinement stress the clays have a more linear behavior. The geologic age of the material has a similar behavior making more linear the damping and the stiffness. Additionally, since clays usually are commentated materials, the increasing of the cohesion makes also the material more linear.

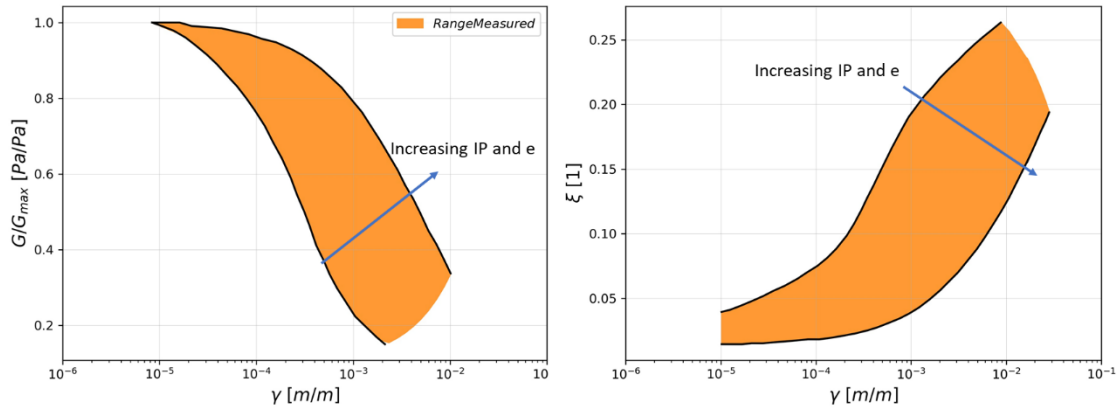


Figure I-11. Variation of the  $G/G_{max}$  curve and damping curves measured in different studies for different sites and resumed in Dobry and Vucetic, (1987). Blue lines mark the effect of the increasing of the plasticity ( $IP$ ) or the void ratio ( $e$ ). Extracted figure from Dobry and Vucetic, (1987).

Many studies have found materials that are outside of the range given by Dobry and Vucetic, (1987) (Figure I-11). However, generally the values and the influence of the parameters in the non-linear condition are accomplished (Vucetic and Dobry, 1991).

#### 1.2.4 Hyperbolic model and non-linear soil characterization

Several mathematical functions are available to model this soil behavior. One of the most used models is based on a hyperbolic function to model the backbone curve with the stiffness decay of the material (Figure I-9), from where the model takes the name: hyperbolic model.

$$G = G_{max} \cdot \frac{1}{1 + \gamma/\gamma_{ref}} \quad (I-30)$$

This model is one of the most used because of his simplicity and easiness implementation with just two parameters.  $G_{max}$  is the stiffness of the material at small strain, and  $\gamma_{ref}$  is the strain where the shear modulus of the soil is half the initial one ( $G_{max}$ ). Another way to define  $\gamma_{ref}$  is with the maximal stress that the material can suffer ( $\tau_{max}$ ). In this case  $\gamma_{ref} = \tau_{max}/G_{max}$ . This model can success in produces permanent strains.

The hyperbolic model (I-30) does not consider some phenomena that can be involved during the dynamic solicitations. Neither the pore water pressure influence nor hardening process on the soil cannot be considered either by the hyperbolic model.

#### 1.2.5 Characterization of the soil materials: Damping and stiffness decay curves by cyclic triaxial test

To calibrate any constitutive model that explains the non-linear soil behavior, the soil material must be characterized. One way is to use laboratory tests and those must be adapted to the constitutive model that will be used. As was mentioned, one of the general ways of characterizing the non-linear soil behavior is the modulus reduction and damping curves. To measure the stiffness and the damping, several laboratory procedures could be used like: cyclic compressional triaxial test , cyclic torsional test (e.g. Iwasaki et al., 1978), or cyclic direct simple shear test (e.g. Zekkos et al., 2018).

The cyclic compressional triaxial test is one of the most applied methods to define the non-linear soil parameters. In a general point of view, the cyclic triaxial test consists in a cylindrical sample subject to radial and axial stress. The pore pressure is controlled during the procedure to establish the effective stress on the sample. The difference between the radial and axial stress

is the deviator stress. In an equal way, the deviator strains are computed. From the deviator stress and strain, the shear stress and strain are computed (Ghayoomi Majid et al., 2017; Kokusho, 1980).

A cyclic load is applied as a sinusoidal signal with a frequency between 0.1 to 2 Hz. It produces a hysteric curve in the stress-strain plane. One example of a hysteric curve is presented in Figure I-12, where the variation of the stiffness and the complex stress-strain relationship is illustrated. The soil sample will be subjected to several cycles, usually the hysteretic loop used to define the non-linear parameters of the soil is from the cycles upper than 5 or 10.

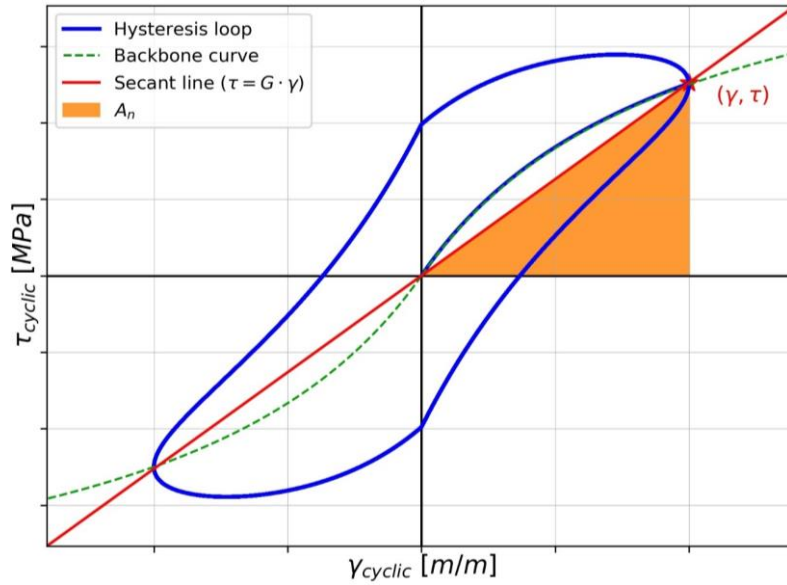


Figure I-12. Example of a hysteresis loop showing the loop of the hysteretic curve, the secant line and the area of the triangle.

The damping ( $\xi$ ) and the shear stiffness ( $G$ ) that characterize the sample can be measured (ASTM, 2003). The shear modulus is computed as the slope of the secant line (red line in Figure I-12). The damping is computed from the area of the hysteric loop and the secant curve (Eq. (I-22)). The relationships were found solving a Kevin-Voight element (Eq. (I-14)) facing an imposed cyclic strain ( $\gamma_{cyclic} = \partial u / \partial z$ ).

$$G = \tau / \gamma$$

$$\xi = 100\% \cdot A_L / 4\pi A_n \quad (I-31)$$

Where  $\tau$  and  $\gamma$  are the maximal stress and the maximal strain during the cycle, and they define the secant line (Figure I-12).  $A_L$  is the area enclosed by the hysteresis loop, and  $A_n$  is the area under the secant line until the maximal load is applied, those terms are defined in Figure I-12.

The shear modulus and the damping are computed for different level of maximal strain, or stress. Doing this, a relationship between  $G$  and  $\xi$  in terms of the maximal strain is obtained. This will result in a plot as the Figure I-9.

$G_{max}$  and  $\xi_{min}$  are characteristic of low strains, various alternative methods can be used to find those values, especially the stiffness. For example, producing a pulse and measuring the velocity of propagation in the material  $G_{max}$  can be estimated Winkler and Plona, (1982).

Semi-empirical methods to find those elastic properties from other soil characteristics were proposed. For example: using the consolidation of the material (e.g. Hardin and Blandford, 1989;

Seed and Idriss, 1970), the plasticity index (e.g. Weiler, 1988), or the Atterberg limits and the Poisson coefficient (Kurtulus et al., 2010). These relationships are not generalized, and they are proposed for specific kind of soils and will be assorted with strong uncertainties.

Generally, one of the most habitual ways for estimating  $G_{max}$  is using in-situ methods. There are many correlations between standard penetration methods (STP) with Vs and density (e.g. Dikmen, 2009), from  $G_{max}$  can be estimated. Also using correlations between the parameters obtained in the cone penetration test (CTP) and Vs30 and density allows the estimation of  $G_{max}$  (e.g. Tonni and Simonini, 2013). However, the correlations with in situ measurements are not site specific, and an estimation by these correlations brings a high uncertainty on  $G_{max}$ .

### I.3 Numerical implementation of the non-linear soil behavior

Before the 80s, in most of the analysis, the non-linear effects of the soils were neglected in the ground motions predictions (even when the non-linear effects were widely recognized by the geotechnical community). Analyzing the records from strong ground motions, as 1985 Michoacan, México (Anderson et al., 1986; Singh et al., 1988) and 1989 Loma Prieta California, United States (Beresnev and Wen, 1996), the importance of involving the non-linear effects were exposed. However, the solution for a wave equation (I-1) cannot be solved analytically for media that is non-linear (except for 1D homogeneous case with no hysteresis Chabot et al, 2018), and therefore many approximations have been developed to mimic the non-linear behavior of the soil in the wave propagation.

This section shows one of the most widely used methods to consider the non-linear soil behavior called the Equivalent Linear (EQL) method. After, we also mention other numerical approaches that use the hyperbolic constitutive model or more complex constitutive models.

#### I.3.1 Method of the equivalent linear analysis (EQL)

In this subsection The Equivalent Linear Analysis (EQL) method is explained. This method is one of the most widely used and basic approach to integrate the non-linearity of the soil. In this method, the wave propagation is solved for a soil with a viscoelastic approximation and this process is iterate with a modification of the shear modulus and damping according to the level of strain reach in the soil (subsection I.1.3). The process is as follow:

1.  $G_m^{\{i=0\}} = G_{max}$  and  $\xi_m^{\{i=0\}} = \xi_{min}$ , from the soil properties that were defined for each layer ( $m$ ). The index  $i$  symbols the number of the iteration
2. Compute the Fourier spectrum of the input motion.
3. Compute the transfer function for each layer and the input motion (Eq. (I-26) and Eq. (I-28)).
4. Convolve each transfer function to obtain the movement at each interface and at the surface.
5. Compute the effective strain at the middle of each layer  $\gamma_{\{m\}}^{\{i\}} = \chi \max(\gamma_{\{m\}}(t))$ . Where  $\chi$  is the coefficient to estimate the effective strain for the entire simulation from the maximal strain (Schnabel, 1972). The strain is defined as  $\gamma_{\{m\}} = \partial u_{\{m\}} / \partial z_{\{m\}}$ .
6. Compute new soil parameters for the next iteration from the modulus reduction and damping curves (Figure I-9) for each layer  $G_{\{m\}}^{\{i+1\}}(\gamma_{\{m\}}^{\{i\}})$  and  $\xi_{\{m\}}^{\{i+1\}}(\gamma_{\{m\}}^{\{i\}})$ .
7. If  $\left| \frac{G_{\{m\}}^{\{i+1\}} - G_{\{m\}}^{\{i\}}}{G_{\{m\}}^{\{i\}}} \right| < \theta$  for all the layers, the iteration is taken as the solution. If not, a new iteration starts from the step 3, with the new soil parameters  $G$  and  $\xi$ .

In the equivalent linear analysis, usually,  $\chi$  is taken as 0.65. The error margin to stop the simulation ( $\theta$ ) is often 0.05, but it could change depending on the condition of the simulation.

### I.3.2 Other non-linear models

The equivalent linear approach can be used for moderate level of strains (i.e., smaller than about 0.1-0.3 %), for greater strain a fully non-linear model must be used. Various constitutive models can be implemented such as:

- Iwan, (1967) model uses a modulus reduction curves like the Equivalent linear method, associating a function with the curve. In the case of the damping is obtained from a capacity of the soil to store energy and the lost energy in each cycle. Those parameters are related with the function that is assigned for modulus reduction curve. In the same way, other models like NOAHH uses more complex definitions for the modules reduction curve, as the use of a backbone curve Kondner, 1963. The details of NOAHH model can be found in Lavallee et al., 2003.
- In Chabot et al., (2018) viscoelastic materials are considered in one dimension. A Galerkin method is developed to solve the electrodynamic equations. It allows finding the solution in a multilayered media with an efficient numerical method.
- Many other models consider the effect of pore pressure and effective stiffness (for example Bonilla, 2000; Lopez-Caballero et al., 2007; Lopez-Caballero and Modaressi-Farahmand-Razavi, 2010; Mellal, 1997). Those models introduce an important effect in the constitutive model and are able to evaluate phenomena like liquefaction of soils Montoya Noguera, (2016).
- Other models consider 2D and 3D geometries, including relevant effects as the topography and anisotropy. Some models use the finite differences method to solve the equations (e.g. Cruz-Atienza, 2006; Sjögren and Petersson, 2011). Since the topography effect can have a high influence on the ground motion, in many cases a multidimensional model is necessary to be developed (Maufroy et al., 2015).
- Other multidimensional models use more detailed techniques and introduce the non-linearity of soil, for example Gatti et al., (2017). In this model, a spectral element technique was developed allowing to include complex constitutive models for non-linear behavior. Additionally, the heterogeneity of the soil properties is introduced through random fields, approximating the solution with the reality in nature. The effect of the addition of the random distribution of the soil parameters in the soil, adds several effects in the final shaking depending of the kind of soil conditions Montoya-Noguera and Lopez-Caballero, (2018).

The complexity of the models adds many new inputs to define the soil characteristics. It adds a complexity and a considerable uncertainty on the application of the models (Régnier et al., 2018, 2016a). For this reason, in many cases, the application of simpler models can result in more precise predictions of ground motions with a lower variability. For other cases, the application of the more complex model is necessary to an adequate risk evaluation. The selection of the model is an important task that depends on the conditions associated with the place where the risk is estimated.

#### I.4 Definition of a new parameter to quantify the loss of stiffness from spectral analysis

Those numerical models require a soil characterization of the non-linear properties that are not easily obtained, subjected to strong uncertainties and expensive. Besides, the variability of the results between numerical codes can be very strong (Régnier et al., 2018, 2016a).

An alternative integration of the non-linear soil behavior is the use of empirical corrections. We propose a new parameter called  $f_{sp}$  for frequency shift parameter to consider in a first approximation one of the main impacts of the decrease of the shear modulus on the site response that is the decrease of the frequency peak to a low frequency bandwidth. In this section we analyze analytically and numerically the relevancy of this parameter.

The section I.1 shows that the transfer function presents the frequencies that are amplified by the soil response. In linear domain with 1-D configuration of a mono-layer soil and considering vertical incidence of the shear waves, the resonance frequencies ( $f^{(n)}$ ) depend on the shear velocity ( $V_s$ ) and the layer thickness ( $H$ ) through  $f^{(n)} = V_s(1+2n)/(4H)$  (Eq. (I-9), section I.1). The shear velocity ( $V_s$ ) can be expressed as a function of the shear modulus as  $v_s = \sqrt{G/\rho}$  where  $G$  and  $\rho$  are the shear modulus and the density respectively.

During cyclic loading, the shear modulus ( $G$ ) decreases with the increase of strain in the soil (explained in the section I.2.2). This fact can be described by the modulus reduction curves (Figure I-9). In the equivalent linear approximation (EQL), the non-linearity of soil behavior is taken into account in an iterative process (section I.3.1).

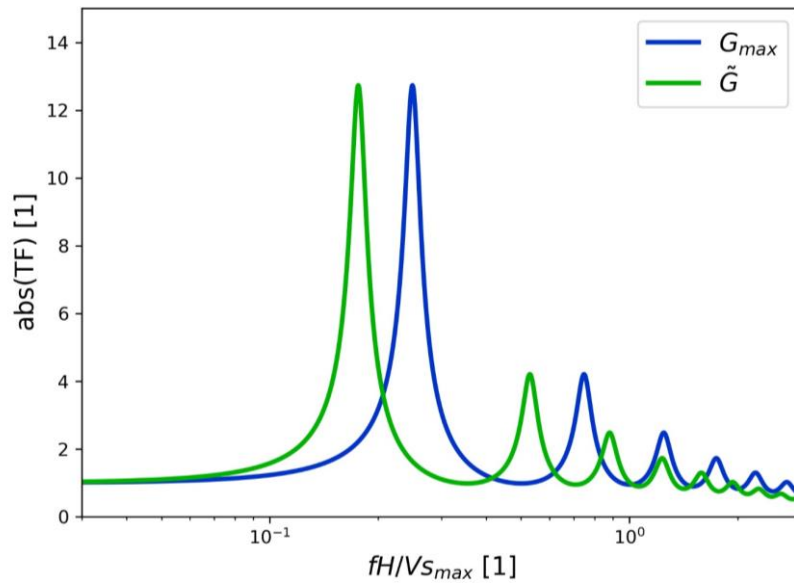


Figure I-13. Comparison between two transfer function with two states of the soil ( $G_{max}$  and  $\tilde{G}$ ). In this example  $\tilde{G} = 0.5G_{max}$  (green line).

Through the relationship between  $G$  and  $V_s$  and  $f^{(n)}$ , the frequency peaks can be expressed in function of  $G$  as:

$$f^{(n)} = \frac{\sqrt{G}}{2H\sqrt{\rho}}(0.5 + n) \quad \text{for } n = 0, 1, 2, \dots$$

Using the previous equation, the ratio between frequency peaks for the two states  $G_{max}$  and  $\tilde{G}$  is equal to:

$$f^{\{n\}}(\tilde{G}) / f^{\{n\}}(G_{max}) = \frac{\sqrt{\tilde{G}}}{2H\sqrt{\rho}}(0.5 + n) / \frac{\sqrt{G_{max}}}{2H\sqrt{\rho}}(0.5 + n)$$

Supposing that the density ( $\rho$ ) remains constant. It leads to:

$$f^{\{n\}}(\tilde{G}) / f^{\{n\}}(G_{max}) = \sqrt{\tilde{G}/G_{max}}$$

In a logarithmic scale a shift in frequency of two functions is represented by the ratio between both frequencies. The previous equation indicates that the logarithmic shift between each harmonic (Figure I-13) is equal whatever the order of the harmonic ( $n$ ) is concerned. The logarithmic shift depends just on the decay of stiffness.

We propose a parameter called frequency shift parameter ( $fsp$ ) that is the square of the logarithmic frequency shift between two estates of the soil (Eq. (I-32)).

$$fsp = \left( f^{\{n\}}(\tilde{G}) / f^{\{n\}}(G_{max}) \right)^2 \quad (I-32)$$

With the definition of  $fsp$ , for the model defined in this section it results in:

$$fsp = \tilde{G} / G_{max} \quad (I-33)$$

The Eq. (I-33) shows that the ratio of the shear modulus is proportional to the square root of the ratio between the linear resonance frequency  $f_{linear}$ , coming from  $G_{max}$ , and the ones coming from a soil with degraded soil properties (whatever the order of the harmonic).

#### I.4.1 The parameter $fsp$ : Analysis with the equivalent linear method

The Eq. (I-33) works for any monolayer case that is studied in two states, one linear and another with a degraded stiffness. This formula must work for an analysis by the Equivalent linear method (EQL). To test this assumption, a soil layer of 40 m of thickness with a shear wave velocity of 200 m/s resting on a linear substratum is studied. With these conditions, a linear model would have a fundamental resonance frequency of 1.25 Hz (Eq. (I-9)). The modulus reduction and damping curves of the soil layer were estimated as a general normal clay (Figure I-11) and they are shown in the Figure I-14.

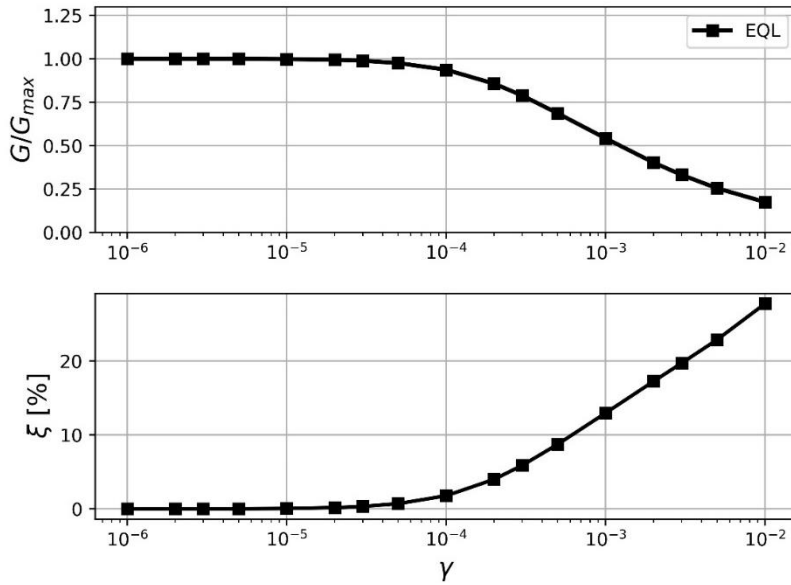


Figure I-14. Modulus reduction curve and damping curve for the soil layer that is tested.

The bedrock was modeled as an infinite monotonic and linear material with shear velocity of 1500 m/s, a density of 2000 kg/m<sup>3</sup>, and a Poisson coefficient of 0.3. A Gabor wavelet was used as an input signal. This simple wavelet makes easier the evaluation of non-linear effects since the Fourier spectrum of this function is simple and well defined. The Gabor's wavelet is defined with the Eq. (I-34).

$$g(t) = Ae^{-\left(\frac{2\pi f_m(t-t_0)}{\gamma}\right)^2} \cos(2\pi f_m(t - t_0)) \tag{I-34}$$

In the simulations,  $\gamma$  is taken as 3,  $t_0$  as 2.5s. The central frequency ( $f_m=1.25$  Hz) is chosen in agreement with the fundamental resonance frequency of the soil layer and only frequencies lower than 2 Hz are analyzed, as the energy of the input signal at higher frequencies is too small to make the ratio computation relevant (Figure I-15). A corresponds to the maximal amplitude of the signal.

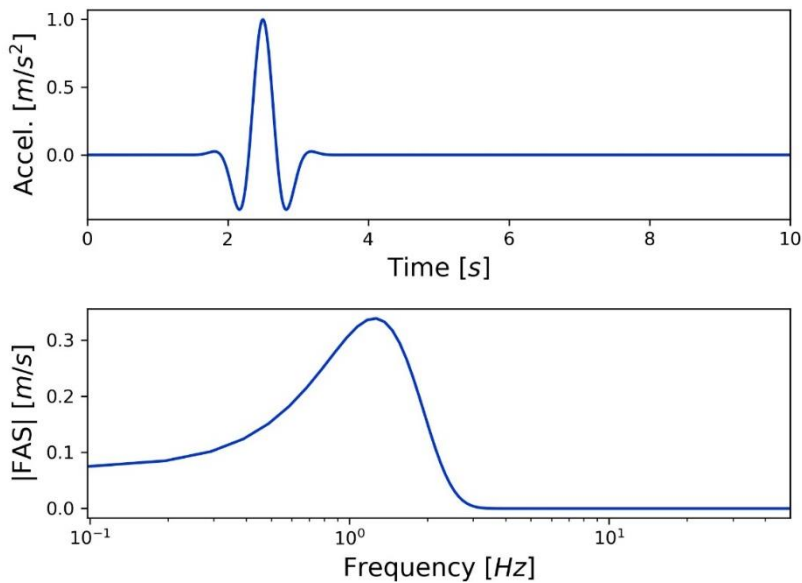


Figure I-15. Gabor wavelet that was used as input accelerogram of the model. At the top temporal wave, at the bottom the Fourier amplitude of the spectrum.  $A=1$  m/s<sup>2</sup> in this case.

Different amplitudes in the input signal ( $A$  in Eq. (I-34)) were tested to compute transfer function. The maximum amplitudes of the signals are: 0.001, 0.01, 0.05, 0.1, 0.3, 0.7 and 1  $m/s^2$ . For each case, we computed the amplitude of the ratio of the spectrum of Fourier for the surface by the interface with the bedrock (Borehole Spectral Ratio). The results are shown in Figure I-16. The results indicate that when all the parameters remain the same and only the amplitude of the signal is modified, there is a modification of the computed transfer function with a shift of the resonance frequencies that occurs. This example shows that the shift of the transfer function frequency peaks is related to the intensity of the ground motion.

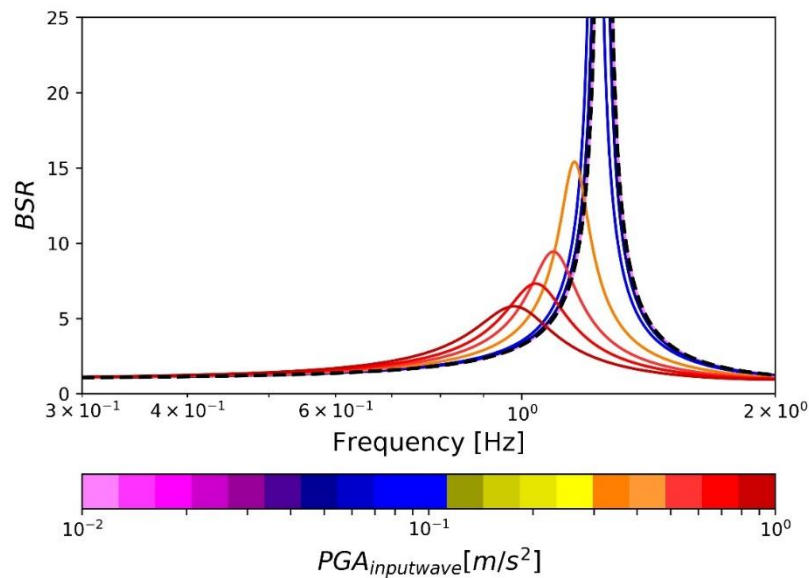


Figure I-16. Borehole spectral ratio (BSR) for inputs waves with a different amplitude and computed using EQL method. Black line BSR was developed for an amplitude of 1  $m/s^2$  but the soil layer was totally elastic with constant stiffness and no damping.

To quantify this observation, we calculate  $f_{sp}$  for each input motion level and we compare it with the decay of stiffness that is reached for each simulation (Figure I-17). In the linear equivalent approach, the effective strain ( $\gamma_{eff}$ ) is used to calculate the equivalent shear modulus and damping at each iteration (See section I.3.1). It is defined from the maximal strain as  $\gamma_{eff} = 0.65\gamma_{max}$ . Considering  $\gamma_{eff}$ , the frequency shift  $f_{sp}$  equals almost the shear modulus decay. The small error can be attributed to the iteration scheme implemented in the linear equivalent method. The good fitting between both curves shows that the  $f_{sp}$  parameter can quantify the amount of shear modulus reduction as the equivalent linear method does in mono-layer cases.

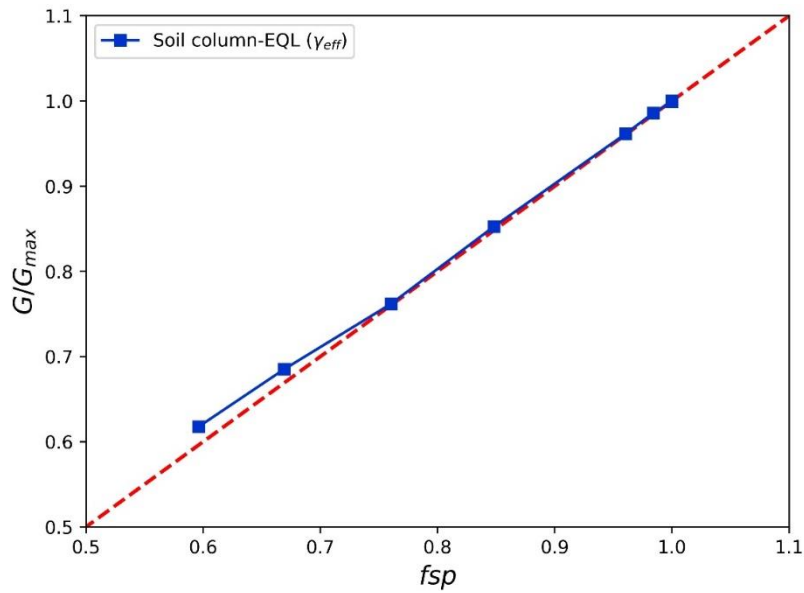


Figure I-17. Evolution of the shear decay in function of  $f_{sp}$ , Equivalent linear approach. Red dotted curve relates the line:  $G/G_{max} = f_{sp}$  (1:1 curve).

### 1.5 The parameter $f_{sp}$ : Fully non-linear model

More advanced models that integrate the non-linear soil behavior manage to consider the stiffness variable with the strain during the simulations. It is a more realistic approximation that introduces more complexity and new parameters. The Eq. (I-33) was obtained from a simple approximation. In a fully non-linear model, it is not possible to derive an analytical formulation as for equivalent linear method. Therefore, the relationship between the loss of stiffness with the increase of strain and the shift of the resonance frequencies towards lower frequency must be analyzed using numerical simulations and calculations of the numerical *transfer function*. To simulate the seismic response, we are using a 1-D fully non-linear approach implemented in CyberQuake software proposed by Modaressi and Foerster, (2000). It is based on a elastoplastic constitutive model with hardening based elastoplastic theory (Hujeux, 1985). CyberQuake derivation is explained in Mellal and Modaressi, (1998).

We are considering a model composed of a single layer of 40 m of thickness with a shear wave velocity of 200 m/s resting on a linear substratum. In the linear domain, the fundamental resonance frequency of this soil column is equal to 1.25 Hz. The bedrock was modeled as an infinite monotonic and elastic material with shear velocity of 1500 m/s, a density of 2000 kg/m<sup>3</sup>, and a Poisson coefficient of 0.3. For the fully non-linear approach, the soil mechanical parameters were chosen as they characterize a typical non-linear soil layer (Lopez-Caballero et al., 2007) The non-linear constitutive model implemented defines non-linear properties that depends on the confining pressure and consequently on depth while the  $V_s$  of the layer remains the same. All the input parameters used in the simulation are summarized in Table I-1.

Table I-1. Soil parameters for the Mellal and Modaressi, (1998) model.

$V_s^1$ (m/s)	200
$V_p^2$ (m/s)	374
$\rho^3$ (Kg/m <sup>3</sup> )	1750
$\Phi^4$ (°)	25
$\beta^5$	10
$\sigma_{ci}/\sigma_v^6$	2
$E_p^7$	20
$C^8$ (kPa)	0
$\gamma_{elastic}^9$	$1 \times 10^{-9}$
$b^{10}$	0.9
$nr^{11}$	0.4
$\psi^{12}$ (°)	20
$\alpha_\psi^{13}$	0.8

From the parameters of the constitutive model (Table I-1) the resulted modulus reduction curves and damping curves are shown in Figure I-18 for different depths.

Like in the previous section, the input signal is a Gabor wavelet and the same signal amplitudes are tested: 0.001, 0.01, 0.05, 0.1, 0.3, 0.7 and 1 m/s<sup>2</sup>. The results for the Borehole spectral ratio at each case are shown in Figure I-19. For the smallest input PGA, the computed *transfer function* is equivalent to the analytical elastic case (black dash line). For the larger input motions, the amplification peak is smaller, and it is shifted towards lower frequencies.

---

<sup>1</sup> Shear wave velocity (m/s)

<sup>2</sup> Primary wave velocity (m/s)

<sup>3</sup> Density (Kg/m<sup>3</sup>)

<sup>4</sup> Friction angle at totally mobilized plasticity (°)

<sup>5</sup> Plastic modulus

<sup>6</sup> Compaction ratio

<sup>7</sup> Plastic stiffness coefficient

<sup>8</sup> Cohesion (kPa)

<sup>9</sup> Extent of the truly elastic domain

<sup>10</sup> Shape parameter of the yield Surface

<sup>11</sup> Numerical parameter of isotropic hardening

<sup>12</sup> Slope of the characteristic line (°)

<sup>13</sup> Parameter of the magnitude of the dilatancy

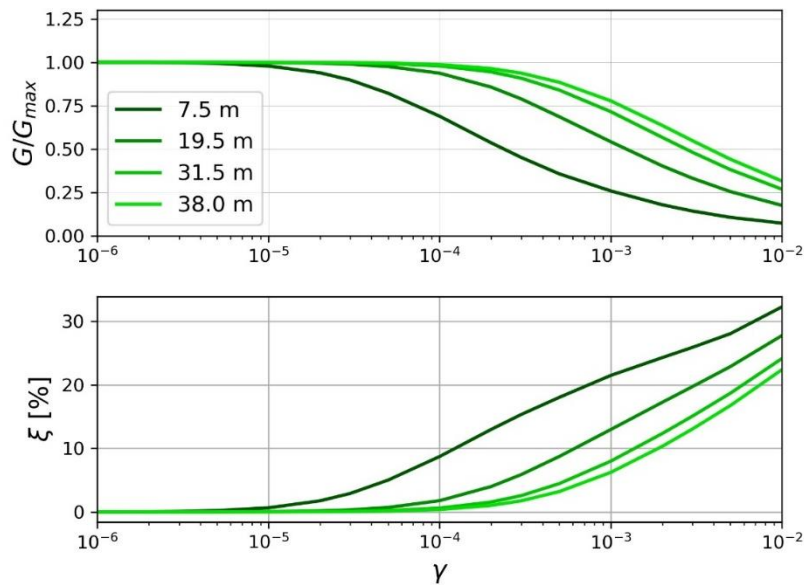


Figure I-18. Modulus reduction curves and damping curves for the soil layer at different depths. The variation with the depth is produced because the implemented soil model that change those curves in function of the confinement stress.

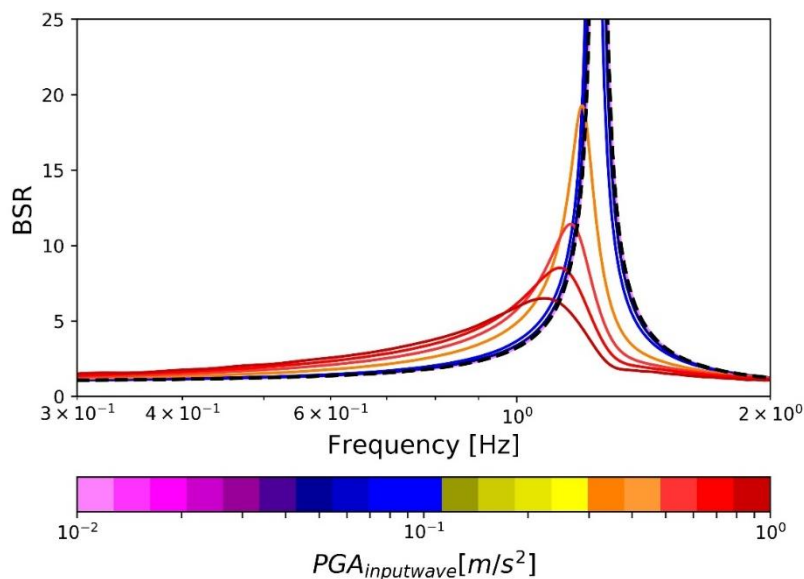


Figure I-19. BSR for inputs waves with a different amplitude and computed from a total non-linear model. Black line-BSR was developed for an amplitude of  $1 \text{ m/s}^2$  but the soil layer was totally elastic with constant stiffness and no damping.

The equivalent linear computation (Figure I-17) leads to resonance frequency shift larger than the fully non-linear approach. Indeed, besides the limitations of EQL approaches at large strain Kaklamanos et al., 2013, the non-linear soil properties differ in the two numerical approaches as mentioned above. At the soil to substratum interface, the non-linear soil properties are much more linear in the fully non-linear computation. To select one  $G/G_{max}$  that represent temporally the simulation, the effective strain ( $\gamma$ -effective, see section I.3.1) is obtained for several depths and replaced in the modulus decay curves (Figure I-19).

In the fully non-linear approach, the relationship between  $G/G_{max}$  and  $f_{sp}$  is not accomplished for all depths Figure I-20. The  $f_{sp}-G/G_{max}$  curves depend on the depth considered for the computation of the shear modulus, as both the non-linear soil properties and the maximum

shear strain rate varies with the depth. However, we notice that Eq. (I-33) still can be applied to the curve computed at 25.5 m at depth. Because the decrease in stiffness is very different between layers,  $f_{sp}$  cannot be used as a proxy for non-linear behavior for all the layers as for the EQL approach. However,  $f_{sp}$  fits the average loss of stiffness of the column layer. The reason why it's not perfectly the mean of  $G/G_{max}$  curves could be related with the definition of  $\gamma$ -effective, that is using a factor of 0.65 and this is one approximation to estimate the general shear strain during the shaking from the maximal strain.

These observations suggest that the logarithmic shift in the transfer function ( $f_{sp}$  parameter) is a good proxy parameter for the non-linear soil properties of the entire column in a generalized analysis. Although  $f_{sp}$  doesn't fit with specific layers, as 1.5m between others.

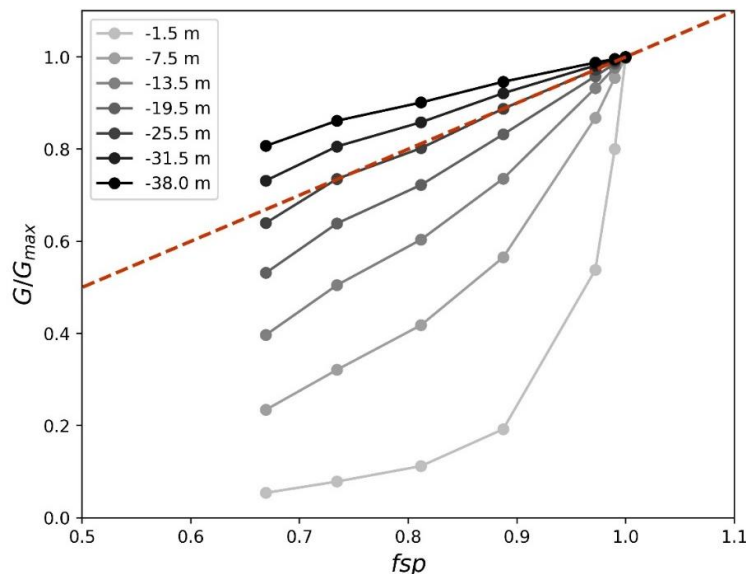


Figure I-20. Evolution of the shear decay in function of  $f_{sp}$  for a fully non-linear model. Red dotted curve relates the line:  $G/G_{max} = f_{sp}$  (1:1).

## I.6 Summary and discussion

Site effects amplify specific frequencies producing a strong motion at the surface in comparison with the motion that would be recorded at an outcrop rock (Figure I4). The resonance frequencies depend exclusively on the stiffness and the layering of the soil, if the wave is propagated in 1-D direction in a linear viscoelastic soil model.

For strong shakings, that produce large strains in the soil, the soil behavior becomes non-linear and it cannot be described by analytic solutions. Therefore, non-linear soil behavior can be introduced in numerical methods to analyze the propagation of the seismic waves during strong ground motions. For example, Equivalent linear method (EQL) approach is often used for engineering purposes because of its easiness of application. But more complex soil constitutive models can be implemented in numerical methods.

Whatever the method used, the non-linear soil parameters need to be defined. Those parameters can be defined by laboratory tests, but those tests are expensive, limited to a specific site and associated with uncertainties. Alternative characterizations involving empirical correlation with elastic properties can be also used but the uncertainties associated are even stronger because it is not site specific.

We propose a parameter to quantify the effects of non-linear soil behavior in the transfer function. This parameter is based on this equivalent linear approach method which compare the transfer function of one site characterized by different shear modulus depending on the level of deformation suffered during the shaking. We quantify the stiffness degradation of the soil by looking at the logarithmic shift produced by the non-linear soil behavior on the transfer function. Several studies have shown that this EQL approach is relevant for some analysis, but for very strong and long earthquakes it may not be adequate (e.g. Kalkan et al., 2013).

The logarithmic shift on the transfer function is called frequency shift parameter (*fsp*), and it is related directly with the non-linearity of the soil, in an EQL analysis. Using *fsp* in more complex models, this parameter fits approximately the general stiffness decay of the soil column. In the future chapter this parameter will be used to not only correct the site response from the non-linear soil behavior but also to evaluate the non-linear soil behavior during real ground motions.

## Chapter II Signal processing and Borehole arrays to study the non-linear behavior of the soil

Numerical models are based on several hypotheses that are not usually entirely accomplished, besides it will require the precise knowledge of the soil parameters including parameters that are needed to calibrate complex soil constitutive models. Alternatively, empirical methods can be used to evaluate the site effects. Among, the different methods to evaluate the site effects, the site to reference spectral ratio is one of the most used.

This method consists in selecting a site with no site effects, called reference site or outcrop. This site must be close enough to the site with sediments (relatively to the seismic source) where the site effects are evaluated to assume that both sites share the same source to site path. The site effects are evaluated by computing the spectral ratio recordings at the sediment with the one at rock outcrop (e.g. Borchardt, 1970).

The main drawback of this approach is the difficulty to find a reference station that is close to the site. The borehole arrays with an accelerometer at the surface and another at depth lying on the bedrock overcome this last issue. This chapter presents the signal processing that has been applied to the Kik-net accelerometric database. This network is composed of 688 sites with vertical arrays which allow to evaluate the borehole transfer function that will represent the site response in this work.

### II.1 Borehole arrays

The borehole arrays consist of two devices for recording the ground motion. One is at the surface and another at depth that we will call downhole (Figure II-1). This configuration has been used to study site effect many times. For example, Shearer and Orcutt (1987) uses borehole arrays to validate that 1D plane models can explain the difference in the amplification related to the site effects.

The borehole spectral ratio (*BSR*) is one of the ways to estimate the transfer function empirically. Steidl et al., 1996) compares this estimator of the transfer function (*BSR*) with surface rock references stations. The outcrop stations require to be close enough to the soil site to assume that the input motion is equivalent to both sites. Additionally, those outcrop sites must not have any site effect. However, most of them have their own response which make that borehole sites are more adequate in many cases to estimate the transfer function compare to surface rock outcrops.

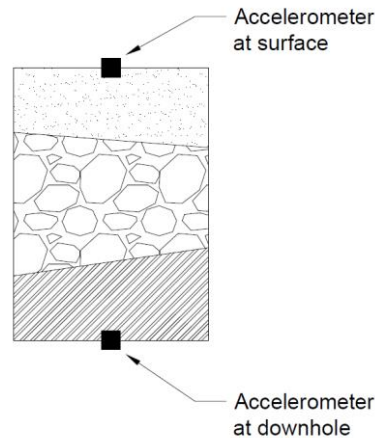


Figure II-1. Sketch of a borehole array configuration.

One main drawback of vertical arrays is that the downhole station record the whole wavefield composed of the upward and downward waves. Steidl et al., (1996) remark the importance of managing and taking care the downward waves effect for computing a *BSR*. Those downwards waves can introduce holes in the Fourier spectrum of the downhole record due to the destructive interferences between the upward and downward waves at some frequencies. When the ratio between the surface and the downhole recordings is performed, those holes create pseudo resonance peaks on the borehole transfer function. However, if the downhole site is located at the interface between the bedrock and the substratum, the frequency peaks in the *BSR* are similar to the ones calculated with a rock outcrop reference. It means that borehole arrays, can estimate the frequency peaks of the transfer function under correct conditions.

Bonilla et al., (2002) shows that the downward waves effect is reduced for stations with a downhole sensor deep. Also, that paper notes the importance of the 1D assumption in the borehole analysis. Borehole procedure has been used for many years and today is a conventional method to study site effects (e.g. Field and Jacob, 1995; Régnier et al., 2014; Shearer and Orcutt, 1987).

### II.1.1 Kik-net database

To study the empirical transfer function computed from borehole arrays, we use the KiK-net dataset in Japan. These data are available on the web page of the National Research Institute for Earth Science and Disaster Prevention (<http://www.kyoshin.bosai.go.jp>). The network is composed of 688 stations (Figure II-2) located in all Japan Okada et al., (2004). 650 sites have site characterizations  $V_s$  and  $V_p$  profiles, soil description, and information on the stations (location and information of recording devices). For each recorded earthquake, the acceleration time histories are provided, with the event origin time, the epicenter location, the depth of the hypocenter, and the magnitude of the earthquake determined by the Japanese Meteorological Agency.

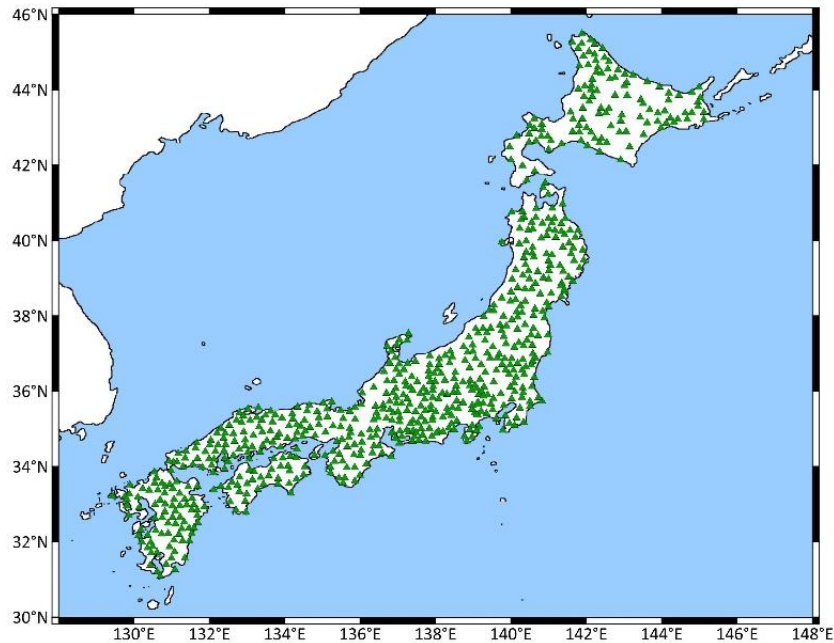


Figure II-2. The location of the stations of the Kik-net data network.

We selected recordings according to two criteria: signals from earthquakes with a magnitude higher than 2.5 and with an epicentral distance lower than 500 km. Under those two criteria, we use 319 055 signals (each one recorded in the three directions at the surface and downhole) from 12582 earthquakes, recorded between October 1997 to August 2018. Figure II-3 presents the selected records for the analysis in this paper, from 653 sites that have available data.

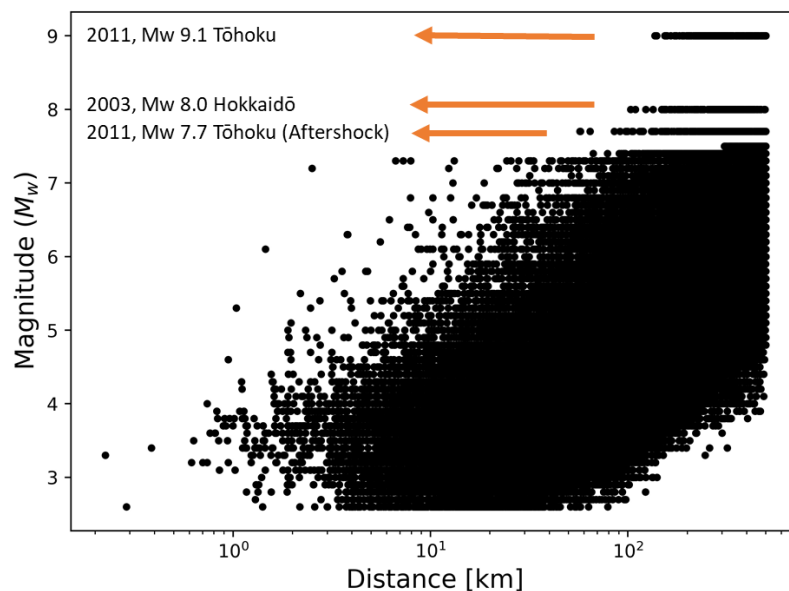


Figure II-3. Magnitude-distance distribution of earthquakes recordings used in this study.

The kik-net database stores recordings with a time window always larger than 120 s. The start and the end of the record are determined when a minimum acceleration is detected. This threshold for triggering is around  $0.002\text{--}0.004\text{ m/s}^2$ , depending on the station. Additionally, the signal always stores an additional time of recording before and after the event. The first additional time is around 15 s before the triggering, and the last is an extension of 30 s after that the signal is equal or lower than  $0.001\text{ m/s}^2$ . The previous triggers are performed on the records

at the downhole station. Aoi et al., (2004) explains the details of the thresholds and the devices in Kik-net database.

### II.1.2 General statistics of Kik-Net database

The stations of Kik-net data are located on different kind of soil, since those are spread in all Japan (Figure II-3). Figure II-4 shows the  $V_s$  profiles for all the sites. In some national codes (Eurocode 8 in Europe or in the National Earthquake Hazards Reduction Program NEHRP in the US), the site effects are evaluated by the time-average of shear velocity average over the first 30 m of soil ( $V_{s30}$ ). Figure II-5 shows that the Kik-Net database has wide range  $V_{s30}$  sites, going from 150 m/s until “rock sites” with  $V_{s30}$  upper than 2000 m/s. The database covers a wide range of sites and it is adequate to apply a general study on site effects. The depth of the downhole station is very different between stations, going from 100 m until 2000 m.

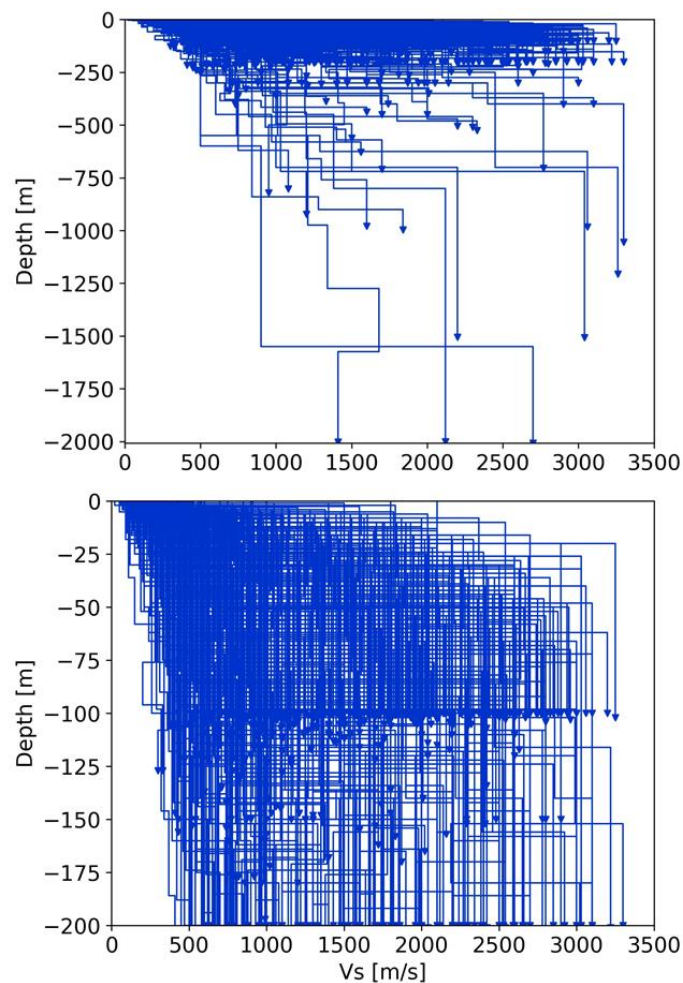


Figure II-4. Shear velocity profile ( $V_s$ ) for the sites of the Kik-Net database.

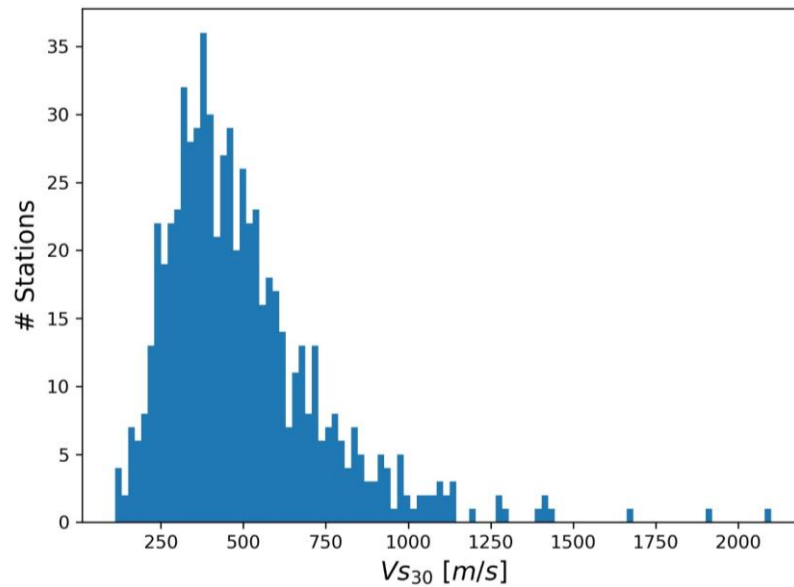


Figure II-5. Distribution of  $V_{s30}$  for the kik-Net database.

Additionally, this database has 319 055 records who presented very different intensities (Figure II-6). This wide range of shaking allows to study the effects of different shakings on the stations and be compared.

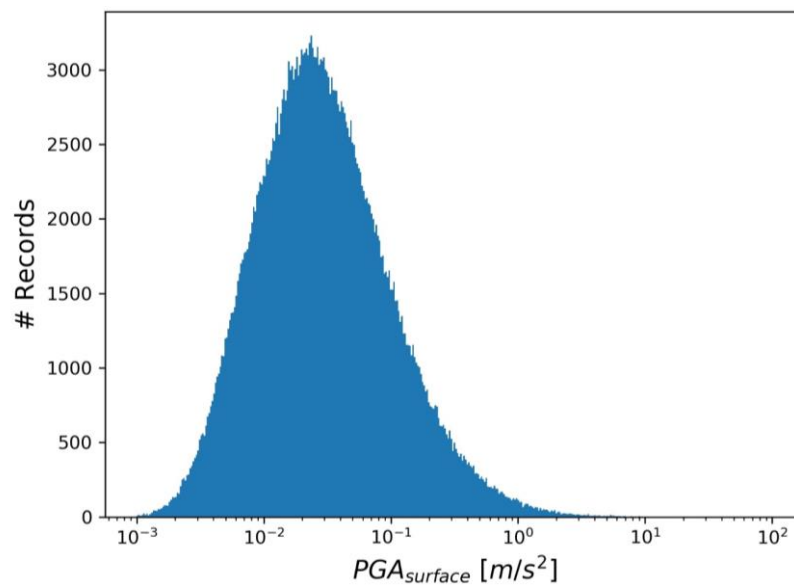


Figure II-6. Geometrical average of the horizontal components at surface of PGA for all the records that we use in this study.

### II.1.3 Other databases of borehole arrays

In this document, only the records from Kik-net database are studied. However, the borehole arrays are spread worldwide, and the same methodology could be applied to any vertical array site. For example, we can mention some of them:

- In Taiwan the network SMART II is located (Beresnev et al., 1994). It has 37 sites with borehole arrays with depths around 50, 100 and 200m. Since Taiwan is a seismologic zone and the network is working since 1992, this network has recorded many different

magnitudes including strong ground motions. Additionally, in Taiwan, new arrays have been built in the last years by the Central Weather Bureau (CWB) (Kuo et al., 2018).

- The EUROSEISTEST is an experimental site with 16 surface and six downhole devices. They are located around the valley of Mygdonia, close to Thessaloniki, Greece. The downhole devices go until 200 m deep, and they are on different kind of sites in agreement with  $V_{S30}$  classification. The database can be found in Ktenidou et al., (2018).
- Recently, in the frame of the SINAPS@ project a vertical array composed of 5 devices has been built in Argostoli (Greece) (Theodoulidis et al., 2018)
- In the United States, the Garner Valley Downhole Arrays (GVDA network) consists of 7 downhole devices with a depth between 0 to 500 m (Archuleta et al., 1992, 1992).
- In France, a borehole array with a depth of 15 m and 35 m is located in the Island Guadeloupe, France (Gueguen et al., 2011). The city of Grenoble has a borehole with a downhole sensor located at 564 m at depth (Péquegnat et al., 2008).
- Additionally, to the other databases already working, new borehole arrays are under construction. For example, in France, Dufour et al., (2018) describes the installation of a new borehole array in the Var Valley, Nice.

## II.2 Signal processing

All the selected signals were processed based on Boore, (2005) recommendations. This subsection explains briefly the procedure and their influences on the spectra of the recordings. The signal processing starts after that the recordings were corrected and scaled according to the device indications. It means that the accelerogram has the correct units (in this document  $m/s^2$ ). The same procedure is applied independently for the three directions of motion, for all the records.

### II.2.1 Selection of the window of interest

All the accelerograms must be cut to isolate the window of time that contains the event that will be studied. In KiK-net data, some recordings contain more than 1 event and have pre-event noise windows (see figure II-4). We applied a procedure to automatically select the adequate time windows for our analysis that contain the main part of the signal. The process that we applied is based on Earle and Shearer, (1994) algorithm that was modified by Oth et al., (2011) to be an adequate procedure for borehole arrays. From this last procedure, we implemented some modifications since we were not interested in picking the exact beginning of P-waves and S-waves. The modifications made the algorithm less precise in time picking, but more reliable for selecting a window large enough to include the ground motion of interest.

The procedure starts applying a butter filter order 4 with a frequency window between 0.2 Hz and 10 Hz (important to note that this filter is just applied for the procedure to find the window of analysis). After, we compute the average noise amplitude ( $A_{noise}$ ) on the absolute amplitude of the signal. To compute this average, for each case the first 0.5 s of the signal is selected, and the average amplitude for this step of time is computed. Subsequently, we apply the same calculations for the next 0.5 s step until 3.5 s. In the same way, the last 3.5 s of each signal are analyzed. We compute  $A_{noise}$  as the minimum average between all analyzed steps. Because the

kik-Net database allows for all the signals a gap of time before and after the ground motion, the beginning of the time window is adequate to evaluate the noise.

This noise amplitude is compared with the wave amplitude. The signal is divided by time steps of 0.5 s and the average amplitude is calculated ( $A_{step}$ ), the step with the highest  $A_{step}$  is selected as the maximal amplitude of the ground motion. To find the beginning of the time window, we compare the  $A_{step}$  before the maximal amplitude to the  $A_{noise}$  to select the closest one where:  $A_{noise} > k \cdot A_{step}$ .  $k$  is a value of comparison that was selected as 0.5 to find the beginning of the analysis window.

To calibrate the extension of the time windows and the  $k$  value of the procedure, we were based on the algorithms of Oth et al., (2011), where  $k$  was taken equal to 0.5. We visually analyzed a hundred of recordings to calibrate the value of the parameter  $k$ .

To ensure that the algorithm is working correctly we applied the same procedure to all the directions independently, and check that the results where similar. If it was not the case, the beginning of the ground motion was the one of the Kik-net data. We applied this procedure to all the database; in many cases, the procedure did not apply any change in the window length already selected by the kik-net system. However, as shown in the Figure II-7 , for some cases, the procedure is essential to separate the ground motion records from several events. Finally, the window of analysis is extended with 3 seconds before and after the selected points.

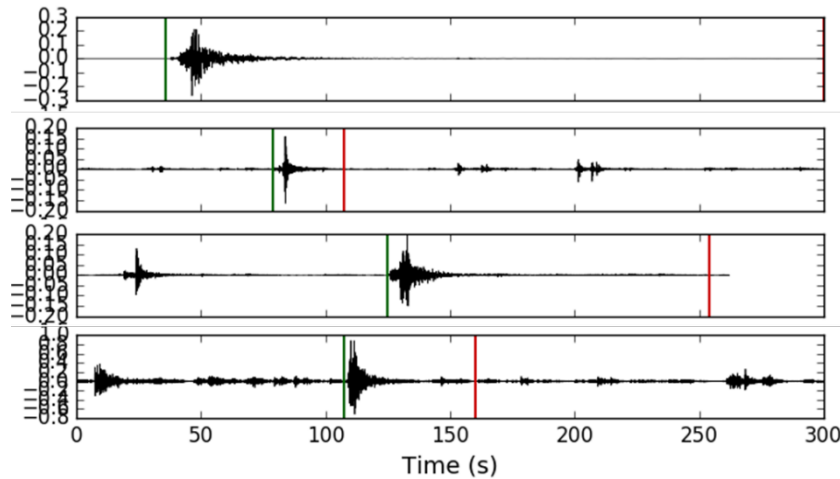


Figure II-7. Examples of the trimming algorithm application on different accelerograms. Green and red lines represent the beginning and end of the time window for the analysis.

### II.2.2 Removing the mean

The next step is to remove the mean of the signal. This procedure is applied to reduce the noise at low frequencies that can be caused by the position of the instrument. Removing the noise at low frequency is essential to integrate the acceleration time history to find the velocity or displacement time histories. This procedure it is expressed as:

$$s_1(t) = s_0(t) - \text{mean}(s_0) \quad (\text{II-1})$$

Where  $s_0$  is the row accelerogram inside the window of analysis explained just before. When we apply this correction, we suppose that the mean of the whole accelerogram should be zero which is true if in the beginning and in the end of the recorded signal the velocity of the ground is close to zero. Figure II-8 illustrates the comparison between the signal before (black curves)

and after (blue curves) applying this procedure. Removing the mean centers the accelerogram around zero and remove the low frequency content of the signal.

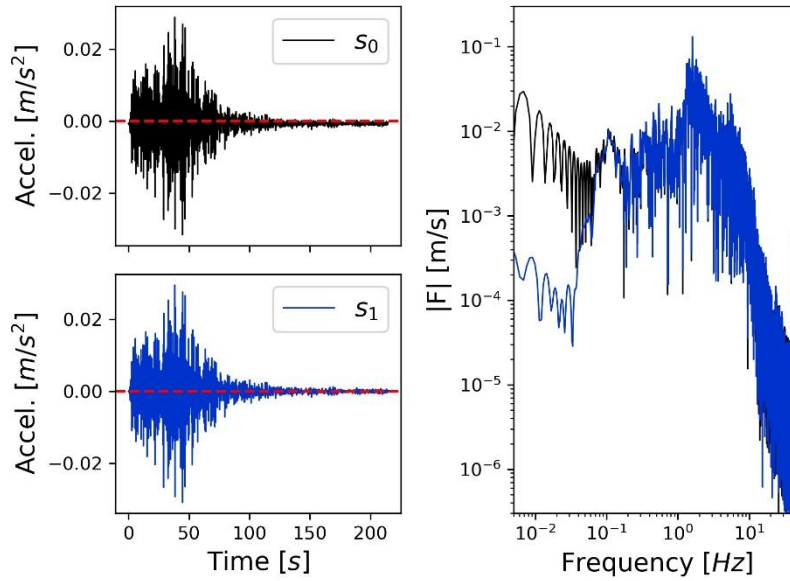


Figure II-8. Comparison with an example of a signal before (black line) and after (blue line) the mean was removed.

### II.2.3 Applying the Hanning's window

This subsection explains the procedure to cut the time window without generating an important impact on the Fourier spectrum of the signal. Different ways of cutting the window can be applied. Mathematically this cutting process is represented as:

$$s_2(t) = s_1(t) \cdot w(t) \quad (\text{II-2})$$

Where  $s_1$  is the original accelerogram,  $w$  is called the window function, and his primary objective is to put in zero all the values before and after the analysis window. Using the properties of the Fourier spectrum (Eq. (I-11)), the spectrum of the Eq. (II-2) will result in:

$$S_2(f) = F(s_1(t) \cdot w(t)) = S_1(f) * W(f)$$

$F$  means the application of the Fourier transform Eq. (I-11),  $S_1$  and  $W$  are the individual spectra for  $s_1$  and  $w$ . The symbol  $*$  indicates the operator convolution. It means that a spectrum will be affected by the window function. Expressing the previous equation with the formal definition:

$$S_2(f) = \int_{-\infty}^{\infty} S_1(\tau) \cdot W(f - \tau) d\tau \quad (\text{II-3})$$

It means, that each value of the spectrum  $S_2$  will be the weighted average of the  $S_1$  where the function of weight will be  $W$ . If  $W$  function gives much more weight when  $f-\tau=0$  than other frequencies,  $S_1$  will be equivalent to  $S_2$ . The correct window function depends on the wave that is analyzed and the range of interest. Seismological analyses usually use the Hanning window, but other functions are also valid. The most basic window function is a rectangular function, that is the done by default when the accelerograms start and stop the recording without any precaution. As illustrated in Figure II-9, the rectangular window affect more the frequency content in comparison with other window functions (cosinus and Hanning) (Figure II-9).

The cos window in the example presented in the Figure II-9, the weight decreases very fast for very low values of  $f \cdot \tau$ . The Hanning Window has an even better performance adding low weight to the frequencies far from the one of interest.

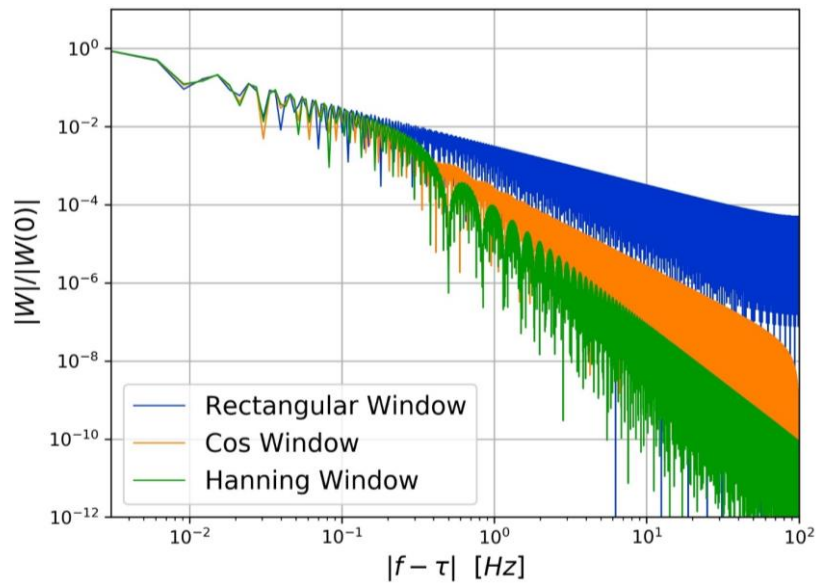


Figure II-9. Comparison of the weight that is assigned to other frequencies in the computation of the Fourier spectrum at one frequency of interest ( $f$ ) because of the application of a window to cut a signal (see Eq. (II-2) and (II-3)). In this figure, all windows were computed with a total width of 6 seconds applied for a gap of time of 100s.

In this work an Hanning window function has been used.

The Figure II-10 shows the effect on the application of an Hanning Window (blue) in comparison with the raw signal (rectangular window black line) on the Fourier spectrum. The differences are not significant, but this cutting effect is significant for signals with short windows (not shown here) or when the tails of the records already converge to zero.

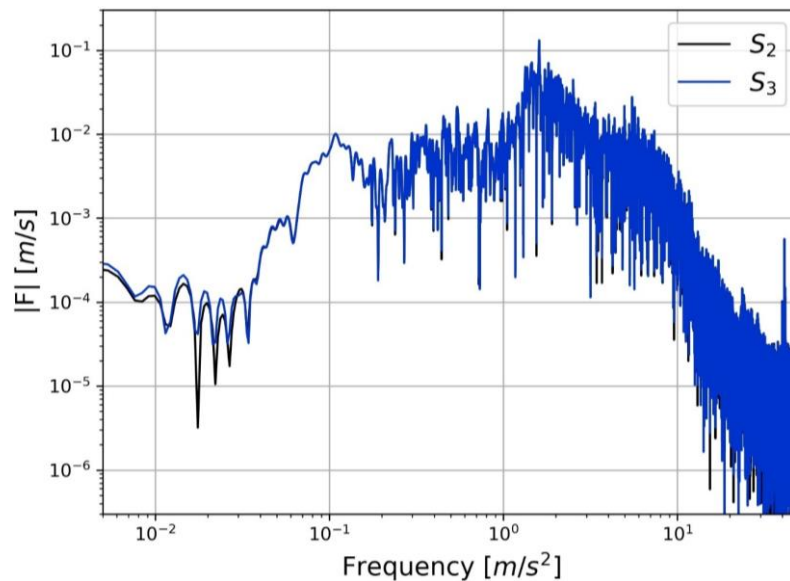


Figure II-10. Comparison of to cutting process. The black line represents the signal spectrum that is abruptly cut (rectangular window), and the blue line uses the Hanning window process that we use for the Kik-net database.

### II.2.4 Addition of zero pad to the signal

As was mentioned, when a signal has noise at low frequencies, it is imperative to apply a high pass filter. A filter of low frequencies allows to integrate the function and remove any kind of drift in the signal. This kind of filter needs that the signal is long enough to apply the correction. When the length of the wave is not long enough the application of filter could not accomplish his purpose, and for some cases even create an additional noise at low frequencies.

To avoid this problem, in Boore, (2005) is proposed to use a butter filter. It will require an addition of a pad of zeros with the length equal to:

$$T_{pad} = 1.5 n / f_c$$

Where  $T_{pad}$  is the duration of zeros that must be added,  $n$  is the grade of the butter filter, and  $f_c$  is the frequency corner of the filter that is applied.

The pad of zeros could be divided in two and apply half before and a half after the signal. Another alternative is to add it at the beginning of the signal (Eq. (II-4)). The performance of each option depends on the algorithm for applying the high pass filter.

$$s_3(t) = [0] \cup s_2 \quad (\text{II-4})$$

After applying the filter at low frequencies, the added pad will store values different than zero. They guaranty the performances of the filtered signal at low frequencies.

### II.2.5 Signal Process: Application of butter filter

In general, the filter process changes the frequency content of a spectrum. Mathematically it is expressed as:

$$S_4(f) = S_3(f) \cdot B(f) \quad (\text{II-5})$$

Where  $S_3$  is the signal spectrum before filtering,  $B$  is the filter action, and  $S_4$  is the resulted spectrum. The filter function  $B$  is a function that adapts  $S_3$  to the desired shape. This procedure is applied, for example, when specific frequencies are studied or for removing the noise on some frequencies.

The butter filter is a well-known function to manipulate seismological recordings ( $B$  in Eq. (II-2)). To apply this filter two parameters must be defined. The first parameter is the frequencies around which the filter is applied, that is called corner frequency  $f_c$ . Three kinds of filter could be applied: the low pass, the high pass and the bandpass filters. For the lowpass filter, the frequencies higher than  $f_c$  are highly modified reducing their energy. For a high pass filter; the inverse case to low pass is done, and the filter reduces the energy on the frequencies lower than  $f_c$ . When a bandpass filter is used, both cases, high-pass and low-pass filter, are applied at different  $f_c$  each one (Figure II-11); therefore, in this case, two corner frequencies are required.

Another parameter that defines the butter filter is the order of the function. This parameter determines how much smoothed will be the fall (Figure II-11). When the order is higher the fall will be faster, and the range of frequencies that are affected will be shorter. However, if the slope of the filter is too abrupt (high order) a large distortion in the waveform can be expected (Boore, 2005).

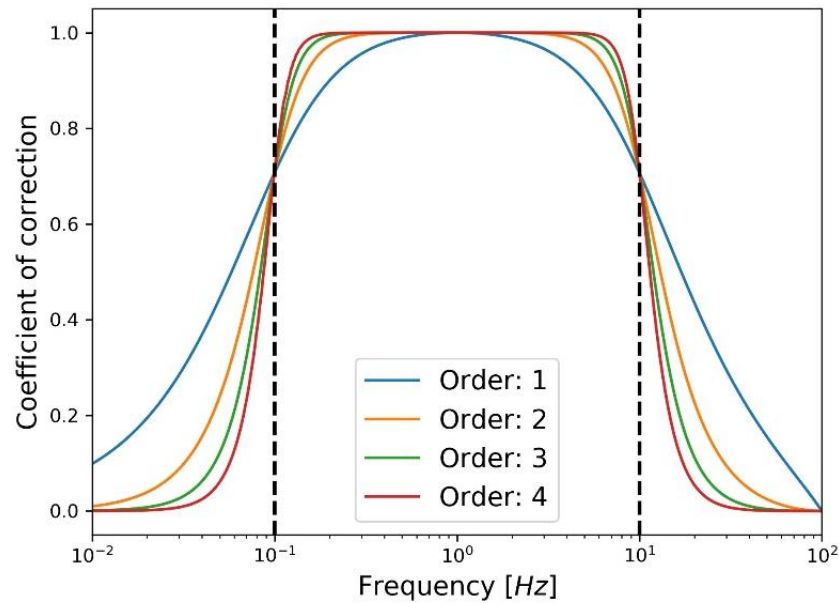


Figure II-11. Butter band-pass filter effect on different frequencies. In this example, the corner frequencies are 0.1 (high-pass) and 10 Hz (low pass). In case of changing the corner frequencies, it will just shift the fall of the filters, but the general shape of this filter is always the same.

The selection of the correct parameters depends on the quality of the records and the type of analysis. For the kik-net database, we use a high-pass filter of third order with a corner frequency of 0.1 Hz. The filter must be applied two times, one forward and another backward. Usually, the implemented algorithms in the software tools work directly on the time domain, computing  $s_4(t)$  directly by convolution instead of Eq. (II-5). In this case, the filter processing invert the phase of the signal. To solve this issue, the same filter process is applied a second time to reinvert the phase wave.

This process was implemented mainly to be able to compute in all the cases the velocity and the displacement spectrum. Figure II-12 shows an example of the application of a high pass filter in the same signal of the previous subsections. Because it is a high pass filter, the changes are produced exclusively at low frequencies

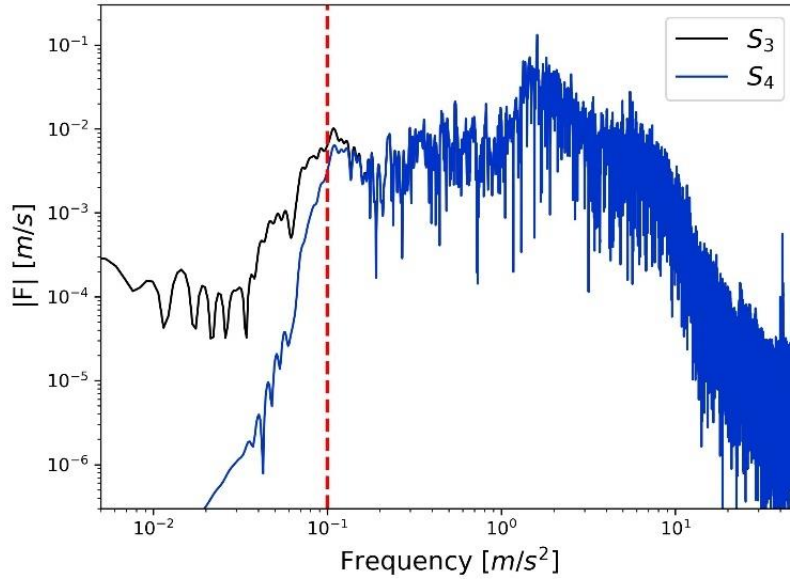


Figure II-12. Example of the general filter applied to all the database in this study. A high-pass Butter filter of order 3 with  $f_c$  equal 0.1 Hz is used and applied two times. The black line is the spectrum without any filter, and blue line the filtered spectrum.

### II.2.6 Spectrum processing: Konno-Ohmachi smoothing

The spectra that are computed with a discrete Fourier spectrum, usually present a high variability with many local peaks around a general trend (for example Figure II-12). A process of smoothing is applied to facilitate the analysis of the spectra.

The general idea of the smoothing process is to compute in a new spectrum that is the frequency-weighted average of the original spectrum. Mathematically it is written below:

$$\widehat{S}_3(f) = \sum_{\tilde{f}} [S_3(\tilde{f}) \cdot W_b(f, \tilde{f})] / \sum_{\tilde{f}} [W_b(f, \tilde{f})]$$

Where  $f$  is the frequency that is analyzed,  $\widehat{S}_3$  is the smoothed spectrum of the original one  $S_3$ .  $W_b$  is the weight function. Konno and Ohmachi, (1998) proposed a function  $W_b$  that assigns the weight in agreement to the proximity of the frequency of interest in logarithmic 10 scale. This is appropriated in seismology because the seismic spectra are illustrated in logarithmic scale. The weight function is:

$$W_b(f, \tilde{f}) = \left[ \frac{\sin(b \cdot \log_{10}(\tilde{f}/f))}{b \cdot \log_{10}(\tilde{f}/f)} \right]^4$$

The function  $W_b$  trend to 1 when  $f = \tilde{f}$ . The parameter  $b$  gives the width of the weight function and is called bandwidth. When  $b$  is lower, the far frequencies will be more relevant (Figure II-13) and therefore the final spectrum smoother (Figure II-14).

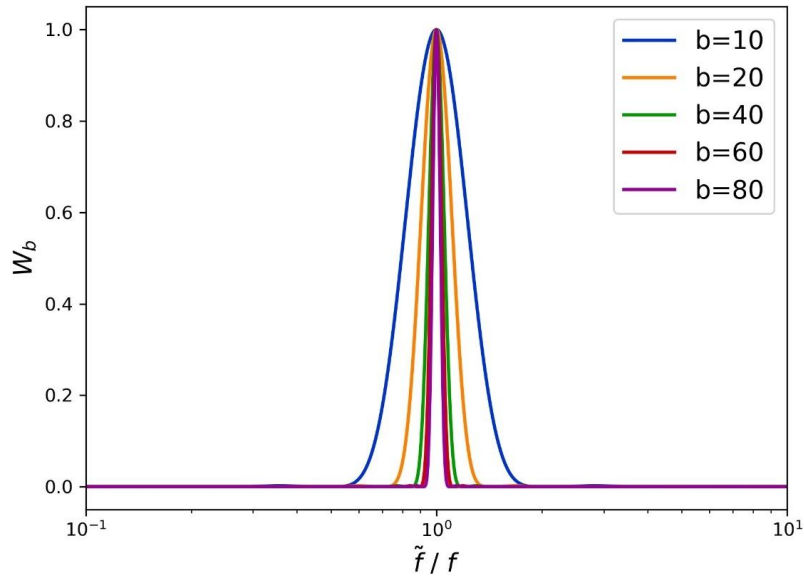


Figure II-13. Comparison of the weight for different frequencies ( $\tilde{f}$ ) in the computation of the frequency of interest ( $f$ ) when a smooth Konno-Ohmachi function is applied, with different bandwidths ( $b$ ).

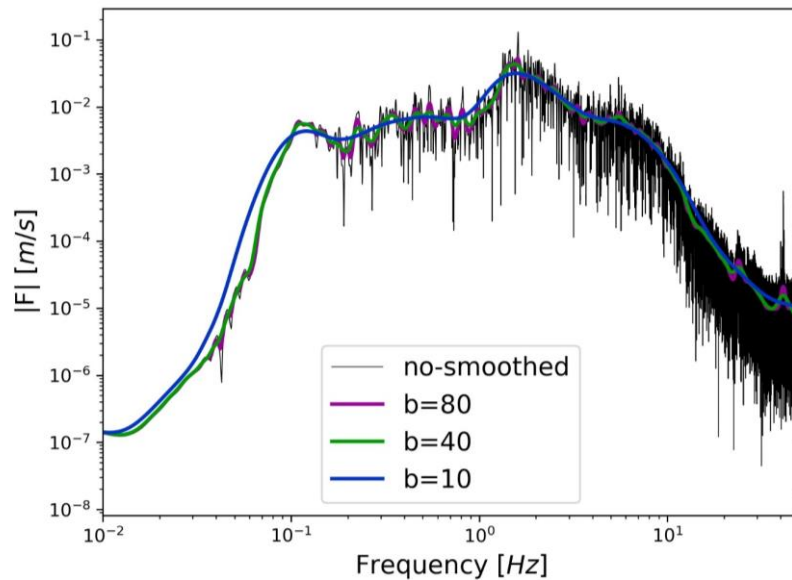


Figure II-14. Example of the effect of the smooth process in a real signal.

As was mentioned, the smoothing facilitates the analysis of the spectra and their comparisons. Additionally, the process can allow storing the data in less memory since the smoothed spectra can be interpolated (Figure II-13). In the analysis presented here, a Konno Ohmachi smoothed with a bandwidth ( $b$ ) of 40 is used for all the recordings.

### II.3 Borehole spectra ratio (BSR)

The transfer function can be estimated using the ratio of the spectra between two locations. Reordering the Eq. (I-12), the transfer function is the deconvolution between the spectrum at the surface and depth:

$$TF_{\{0-H\}}(f) = U(0, f) / U(H, f)$$

Where  $U(0, f)$  and  $U(H, f)$  is the spectrum of Fourier of the displacements at the surface and in the downhole, respectively.  $TF_{\{0-H\}}$  is the transfer function between the two points, in this case, the surface ( $z=0$ ) and the depth of the station ( $H$ ).

To pass from the displacement spectrum to the velocity spectrum or accelerogram spectrum, the displacement spectrum is integrated one and two times respectively. In frequency domain this integration results in a multiplication:

$$V = 2\pi i f U$$

$$S = -4\pi^2 f^2 U$$

Where  $V$  is the velocity spectrum and,  $S$  is the accelerogram spectrum. Replacing the previous equations in the transfer function, regarding the accelerogram, this results in:

$$TF_{\{0-H\}}(f) = S(0, f) / S(H, f)$$

The previous equations show that the transfer function is the same in terms of acceleration, displacement or velocity.

The movement is recorded in the three dimensions. The empirical site response is then assessed on the horizontal components by computing the Borehole Spectral Ratios ( $BSR$ ).  $BSR$  is defined as the ratio between the geometric average of the Fourier amplitude spectra of the horizontal components at the surface and at downhole (Eq. (II-6)).

$$BSR(f) = \sqrt{\frac{EW_{surf}^2 + NS_{surf}^2}{EW_{depth}^2 + NS_{depth}^2}} \quad (II-6)$$

$EW$  and  $NS$  are the amplitude of the discrete Fourier transform of the accelerograms for East-West, and North-South horizontal components respectively.  $BSR$  shows, in the frequency domain, how the seismic signal is modified between the downhole sensor and the one at the surface. It is important to note that the spectra in the computation of  $BSR$  use the recording with the signal processing previously presented.

#### II.4 Summary

The signal processing is essential to remove unwished effects in the recorded signals. We show that removing the mean reduces the noise at low frequencies. Also, applying an appropriated cutting function improves the estimation of the spectrum although the effect of this procedure is limited.

The impacts of the high pass Butter filter are shown on the Fourier spectra depending on the parameters chosen. The Konno-Ohmachi smoothing makes easier the comparisons and the computation of the ratio between spectra.

The borehole spectra ratio ( $BSR$ ) is a tool to estimate the site effects. Following the signal processing, it is possible to evaluate for each ground motion the site effects, especially the resonance frequencies. The evaluation of  $BSR$  and their comparisons depending on the intensity of the ground motion is the background of our methodology to evaluate the effects of the soil non-linear behavior. The Chapter I introduce the theoretical impact of the non-linear soil behavior, thanks to the database detained in this chapter the following steps is to observe the modifications of the  $BSR$  curve with the intensity of the ground motions and to check empirically the relevancy of the frequency shift parameter ( $f_{sp}$ ) that was defined in the first chapter.

## Chapter III Impact of the soil non-linear behavior on the seismic site response

In this chapter, we study the changes in the site response due to soil non-linearity. The site response is estimated by the computation of the borehole spectral ratio (*BSR*). To analyze the non-linearity, the modification of the *BSR* with the intensity of the seismic solicitations is studied.

We propose a new methodology to study the evolution of *BSR* with increasing seismic solicitation based on the evaluation of two coefficients: the frequency shift parameter (*fsp*) and  $\Delta\widehat{BSR}_{ISA}$ . The section I.4 already introduced the *fsp* parameter in numerical models to quantify the shift of the amplification peaks towards lower frequencies.  $\Delta\widehat{BSR}_{ISA}$  marks the decrease of the amplification. With both parameters we propose to study the influence of the soil non-linearity on the site effects using borehole records.

### III.1 Influence of the non-linearity of the soil in *BSR*

It has already shown that the shear-modulus reduction curve and damping curve of a given soil can be retrieved from accelerometric data. These parameters can, for instance, be estimated by finding the best fit between real accelerometric data and numerical simulations. It has been applied mainly in Taiwan and Japan (e.g. Glaser and Baise, 2000; Pavlenko and Irikura, 2003; Zeghal et al., 1995). In Goto et al., 2017 the spectral ratio of the Kumamoto earthquake (2016, Japan, Mw 7.0) is modeled with a 1-D equivalent linear site response at KMMH16 of Kik-net network. Other authors use interferometry between recordings at a different depth to derive the instantaneous wave propagation velocity in the media depending on the input motion intensity (Bonilla et al., 2017; Nakata and Snieder, 2012).

Another way to study soil non-linear behavior is to compare site-response curves computed from weak motion and strong motion. In Noguchi and Sasatani, (2008) the ratio between the Fourier spectrum of records at the surface and at downhole (*BSR*) are computed. They compared *BSR* from weak and strong ground motion by the summation of the differences at each frequency between each *BSR*, parameter that was called DNL (Degree of Non-linearity). They showed a link between the non-linear effects (defined as DNL), and an intensity parameter of the shaking (PGA). In Lussou et al., (2000) and Régnier et al., (2013) several parameters are proposed to quantify the modification of the *BSR* curves and a measurement of the frequency shift. In Field et al., (1997) ratios between spectral ratios were computed using synthetic rock reference seismograms. Similarly, in Régnier et al., 2016b the ratio of the non-linear to linear spectra are analyzed, but in this case using vertical arrays. In all cases, the authors found that the non-linear to linear site response discrepancy was related to the frequency range and increase with increasing PGA of the incident ground motion.

Following a similar approach, we compare weak motion and strong motion site responses in order to provide a methodology to correct the linear site response of the effects of non-linear soil behavior based on the analysis of recordings from vertical arrays of the Japanese Kiban Kyoshin network (KiK-Net). To illustrate our methodology, the stations IBRH11 and KSRH10 from the kik-Net database are selected. IBRH11 station has recorded 2581 earthquakes, and it is in the prefecture of Ibaraki (Figure III-1) on a soil classified as D in the Eurocode 8 (EC8) with a  $V_{S30}$  of 242 m/s. The bedrock is reached at 30m with a  $V_s$  of 2100 m/s. The downhole station is at

100m depth. The station KSRH10 has recorded 585 events and it is on a soil class D and a  $V_{s30}$  of 212 m/s.

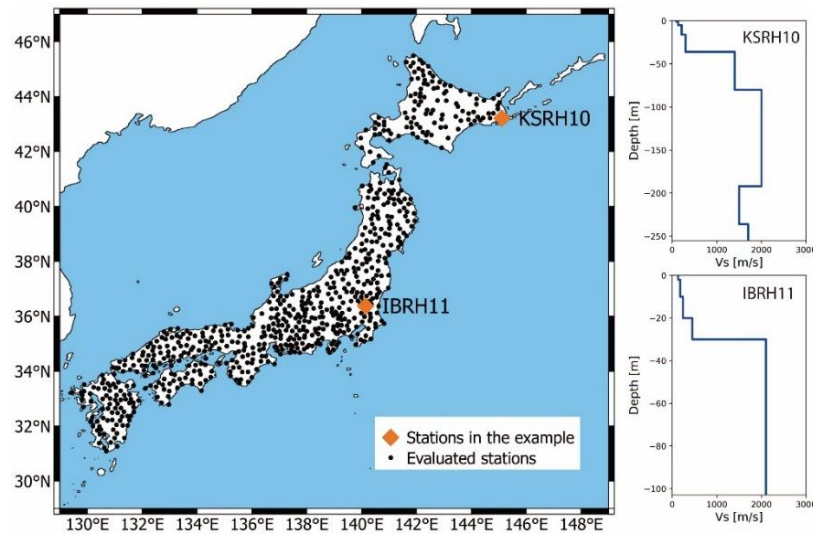


Figure III-1. Location and  $V_s$  profiles of stations IBRH11 and KSRH10 and the other stations (Japanese Kik-net network).

Figure III-2 illustrates four  $BSR$  computed from ground motions recordings at different levels ( $PGA_{surface}$ ) at IBRH11 and KSRH10 stations. We observe that weak ground motions share a similar  $BSR$ . This is because for weak ground motion the soil response is linear (Aguirre and Irikura, 1997). This is also observed in the modulus reduction and damping curves (Figure I-9), where for small strains the properties of the soil remain similar. The variability that still remain in the site response for these small seismic solicitations is mainly due to complex site geometry associated with various seismic waves sources (Thompson et al., 2009).

For stronger ground motions, the amplification peaks occur at a lower frequency bandwidth (Figure III-2). We interpret this shift as a direct effect of the soil shear modulus reduction when the seismic solicitation increases. The section I.1 shows that amplification peaks represent the resonance frequencies linked with the stiffness of the soil. This link supports the hypothesis that the frequency shift is produced by the stiffness loss for strong ground motion (section I.4).

Furthermore, the decrease in the amplitude of  $BSR$  is another effect of non-linear soil behavior linked to the increase of damping with shear strain. Both phenomena have been detected before using  $BSR$  and other methodologies (e.g. Lussou et al., 2000; Noguchi and Sasatani, 2008; Régnier et al., 2016b, 2013). The study of this changes is the essential part of the analysis of the soil response during strong ground motions.

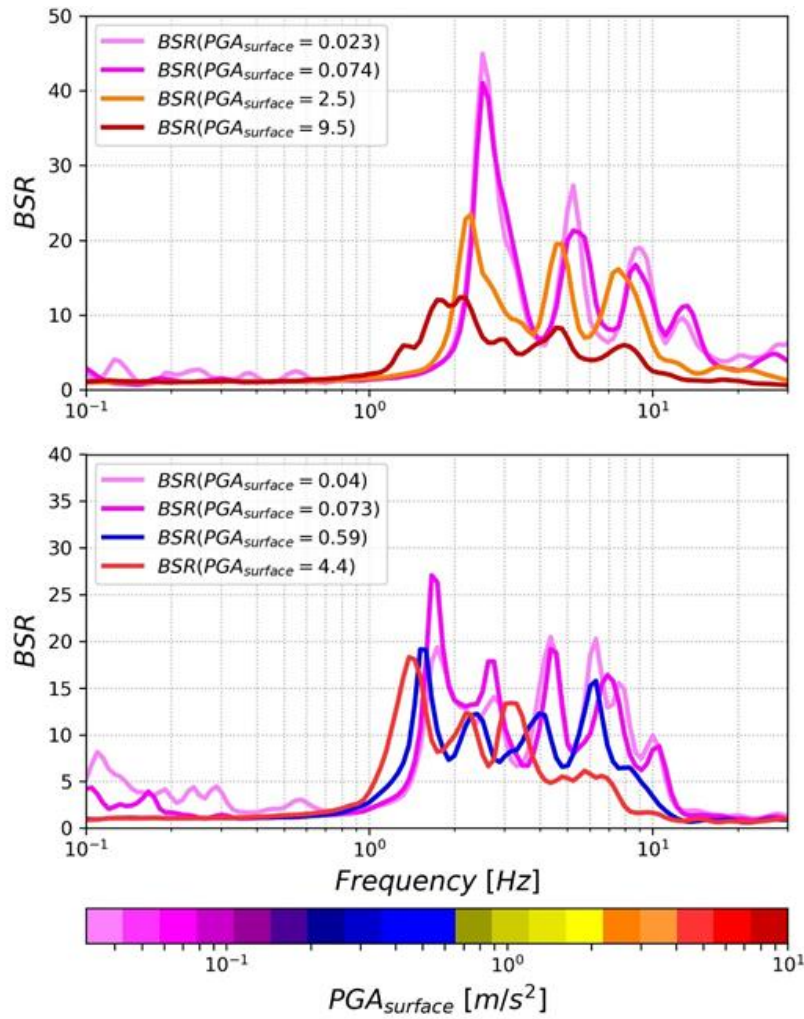


Figure III-2. BSR at IBRH11 and KSRH10 stations (KiK-net) for four earthquakes with different PGA at the downhole station.

### III.2 RSR definition and analysis of the amplitude differences

In this section, we use an approach that was proposed in Régner et al., (2016b). It consists in comparing the *BSR* from weak ground motion with the *BSR* for strong ground motion using the Ratio between both borehole Spectral Ratio (*RSR*). The Eq. (III-1) shows the definition of this new curve.

$$RSR(f) = \frac{BSR_{strong}(f)}{BSR_{weak}(f)} \quad (III-1)$$

Where  $BSR_{strong}$  is the geometric average for all the strong ground motions at a site, and  $BSR_{weak}$  is the geometric average for weak ground motions. The definitions of weak and strong ground motion are based on their intensity. In Régner et al., (2016b) was proposed the maximal peak acceleration (*PGA*) to classify the ground motions. The selection of *PGA* as a parameter to evaluate the *BSR* changes is also supported in Régner et al., (2013) that found a correlation between the changes of *BSR* and *PGA*. Using this study, the weak ground motions have a threshold between  $1 \times 10^{-3} \text{ m/s}^2$  to  $0.25 \text{ m/s}^2$ . In this work, the strong ground motions are all the earthquakes with a *PGA* between  $0.1 \text{ m/s}^2$  to  $0.3 \text{ m/s}^2$  in this analysis.

The parameter *RSR* (Eq. (III-1)) shows in which frequency the amplification increases or decreases for strong ground motions. In general, in average all sites present a decrease in the amplification at high frequencies and an increase at low frequencies (Régner et al., 2016b). This

common behavior is observed for all the ranges of  $V_{S30}$  (Figure III-3), meaning that sites considered as rock could suffer an increase in their amplification because of the non-linearity of the soil.

Sites with low  $V_{S30}$ , on average, have an increase in the amplification at lower frequency bandwidth than sites with higher  $V_{S30}$  (Figure III-3). The dispersion of the results is similar for all the  $V_{S30}$  ranges, although with small differences. Sites with low  $V_{S30}$ , develop a high dispersion at lower frequency band than sites with higher  $V_{S30}$ .

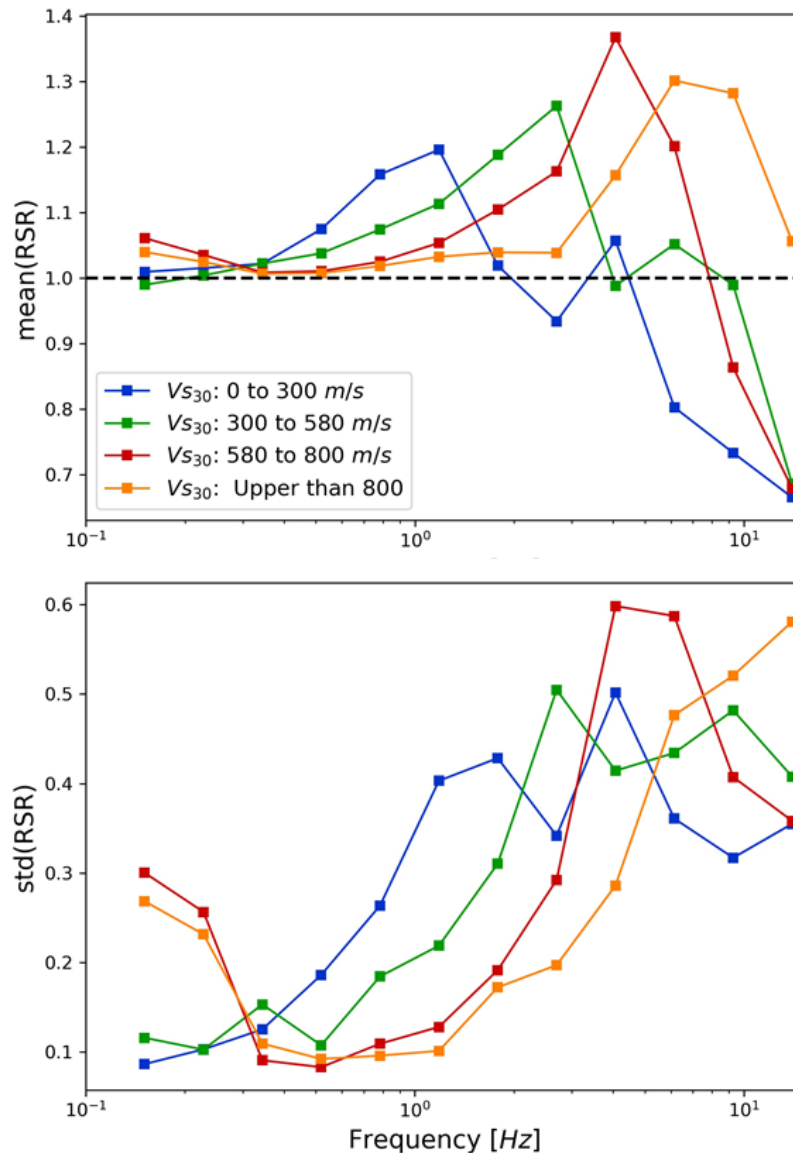


Figure III-3. Average (top) and standard deviation (bottom) of the results for  $RSR$  in all the sites. The mean and the standard deviation are presented in equally separated  $\log_{10}$  frequency bands, and the results divided by  $V_{S30}$ .

### III.3 Frequency shift parameter ( $f_{sp}$ ) from signal records

In section III.1 we showed that the effects of the soil non-linearity in the site response are mainly: A decrease in the amplitude of the amplification of the peaks, and a shift of the resonance frequencies towards lower frequencies. The combination of both effects could either reduce or amplify the site effect amplification in a given frequency band (Figure III-3). To study the non-linear phenomena, we propose a methodology that analyses each component separately. This

is different than other methodologies that studied the combination of both effects, for example *BSR* in the subsection III.2.

In this section, we propose an approach based on *fsp* parameter estimation applied to borehole records from kik-net database. Like other methodologies, we compare the linear site response with the site response derived from other recordings. To define the linear site response and the site response of each earthquake we use *BSR* by following the methodology explained here after.

### III.3.1 Estimation of the linear site response ( $BSR_{linear}$ )

Weak ground motions share a similar *BSR*, except for some variability due in particular to the non-vertical incidence of the incoming wave and the 3D geometry of sub-surface soil layers. This similarity is explained because for weak ground motion the behavior of the soil layers is almost linear, and the stiffness is constant (zone 1 in the modulus reduction curves, Figure I-9).

The weak ground motions for which the soil behaves linearly were selected based on their maximal peak accelerations (*PGA*). Our selection is based on the  $PGA_{downhole}$  since the downhole devices are less affected by the site effects, and they are less susceptible to noise effects than the surface station.

Similarly, to the previous chapter, ground motions with a  $PGA_{downhole}$  from  $10^{-4} m/s^2$  to  $6 \cdot 10^{-3} m/s^2$  were assumed to have a linear site response and equivalent *BSR* between them. To compute a borehole spectral ratio (Eq. (II-6)) that characterizes the linear site response ( $BSR_{linear}$ ), we compute the arithmetic average between all the *BSR* from weak ground motion.

$$BSR_{linear}(f) = \frac{[\sum_{i=1}^n BSR_{weak(i)}(f)]}{n} \quad (III-2)$$

$BSR_{linear}$  being the borehole spectral ratio that we suppose to be a good approximation of the linear soil response. The term  $n$  is the number of weak ground motion.

In order to illustrate the impact of the soil non-linear behavior on the *BSR*, Figure III-4 shows the results at stations IBRSH11 and KSRH10.  $BSR_{linear}$  is drawn with a black dash line, and the red line represents the *BSR* computed from a strong ground motion with  $PGA_{downhole}$  equal to 0.46 and 0.89  $m/s^2$  for IBRSH11 and KSRH10 respectively.

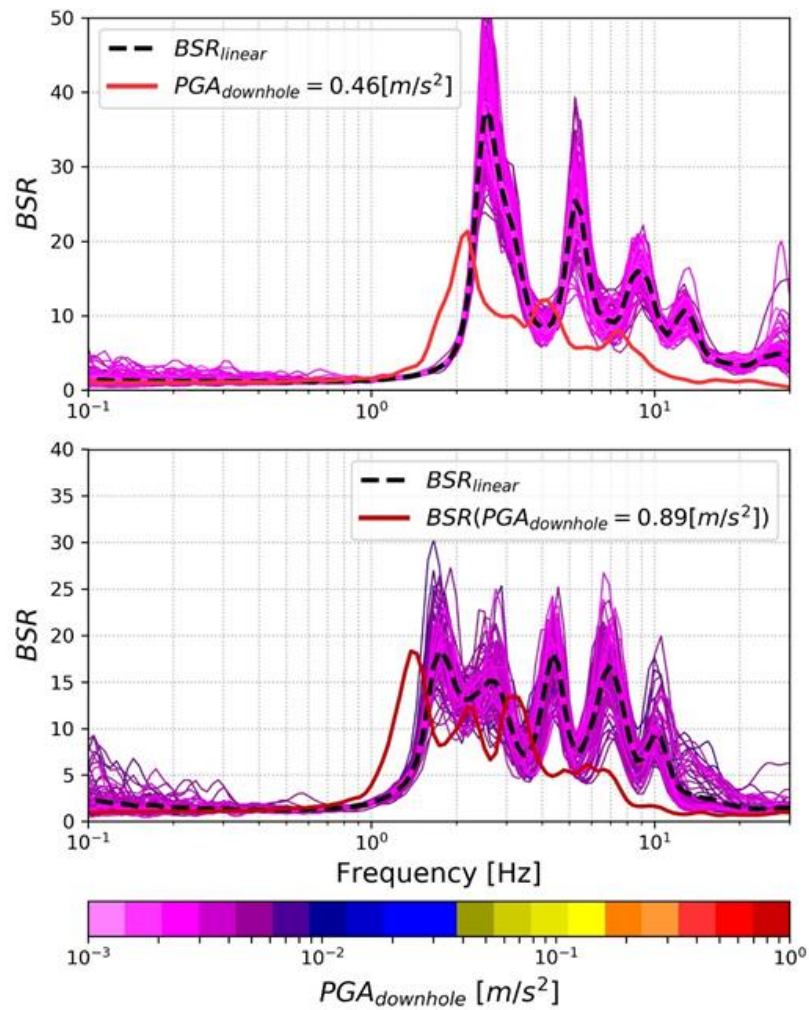


Figure III-4. Definition of  $BSR_{linear}$  as the average of all the weak ground motions (143 events IBRH11-top, 58 events for KSRH10-bottom) and comparison between  $BSR_{linear}$  with a BSR computed from one strong ground motion.

### III.3.2 Computation of $f_{sp}$ parameter

Once  $BSR_{linear}$  is computed using Eq. (III-2), we compare each  $BSR$  from all recorded ground motions for the same site with  $BSR_{linear}$ , focusing on the frequency shift between the curves. We use the same principle than the one explained in section I.4. The general idea is to find the logarithmic shift between both site response, here represented by  $BSR$ . Figure III-5 shows the meaning of  $f_{sp}$  that is the square of the gap between  $BSR$  and  $BSR_{linear}$  curves.

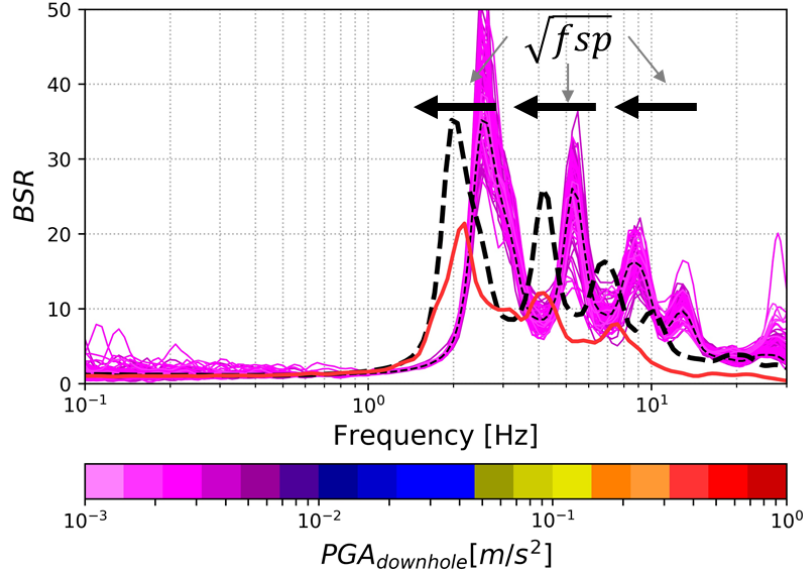


Figure III-5. Sketch of the graphical meaning of  $f_{sp}$ , highlighting that  $f_{sp}$  is the square of the logarithmic shift between resonance peaks.

For assessing the  $f_{sp}$  at all the kik-net database, we developed an algorithm. The principle is to find the logarithmic shift (III-3) that minimizes the misfit ( $\psi$ ) between  $BSR_{linear}$  and  $BSR$  (Figure III-5). Note that the misfit is weighted by the logarithmic sampling.

$$\psi = \sum_i \left| BSR_{linear} \left( \frac{\bar{f}}{L_s} \right) - BSR(\bar{f}) \right| \Delta x \quad (III-3)$$

$$\Delta x = \log_{10}(f_{i+1}/f_i) \quad \text{and} \quad \bar{f} = 0.5 \cdot (f_{i+1} + f_i)$$

In the equation (III-3)  $L_s$  is the logarithmic shift applied to  $BSR_{linear}$ .  $\psi$  is defined as a discrete approximation to compute the area between the shifted  $BSR_{linear}$  and  $BSR$ , considering a logarithmic scale as the length of the base ( $\Delta x$ ). The computation is done over a frequency window going from 0.3 Hz to 30 Hz.

Finally, we define the frequency shift parameter, so-called  $f_{sp}$ , as the square of the  $L_s$ , which produce the minimum value of misfit ( $f_{sp}=L_s^2$  when  $\psi$  is minimized). Expressing this with a mathematic formula:

$$f_{sp} = \left( \arg \min_{L_s} \psi \right)^2 \quad (III-4)$$

With  $\psi$  from Eq. (III-3). From this procedure, the influence of the soil non-linearity on every surface recording is evaluated. It means that  $\sqrt{f_{sp}}$  is a coefficient that logarithmic shift  $BSR_{linear}$  to fit  $BSR$ , for a specific ground motion. If no shift is needed to fit both curves,  $L_s$  and consequently  $f_{sp}$  are both equal to one. If  $BSR_{linear}$  needs to be logarithmically shifted to higher frequencies to fit  $BSR$ ,  $f_{sp}$  will be higher than one. On the contrary, if the needed logarithmic shift is to lower frequencies,  $f_{sp}$  will be lower than one.

Non-linear soil behavior is expected to shift the  $BSR_{linear}$  to lower frequency range and therefore induce an  $f_{sp}$  below one.

### III.3.3 Computation of $f_{sp}$ curves

$f_{sp}$  is computed for every record collected for each site. For example, for stations IBRH11 and KSRH10 the results (Figure III-6) shows the evolution of  $f_{sp}$  as a function of the ground motion intensity, in terms of  $PGA$  recorded at the downhole station.

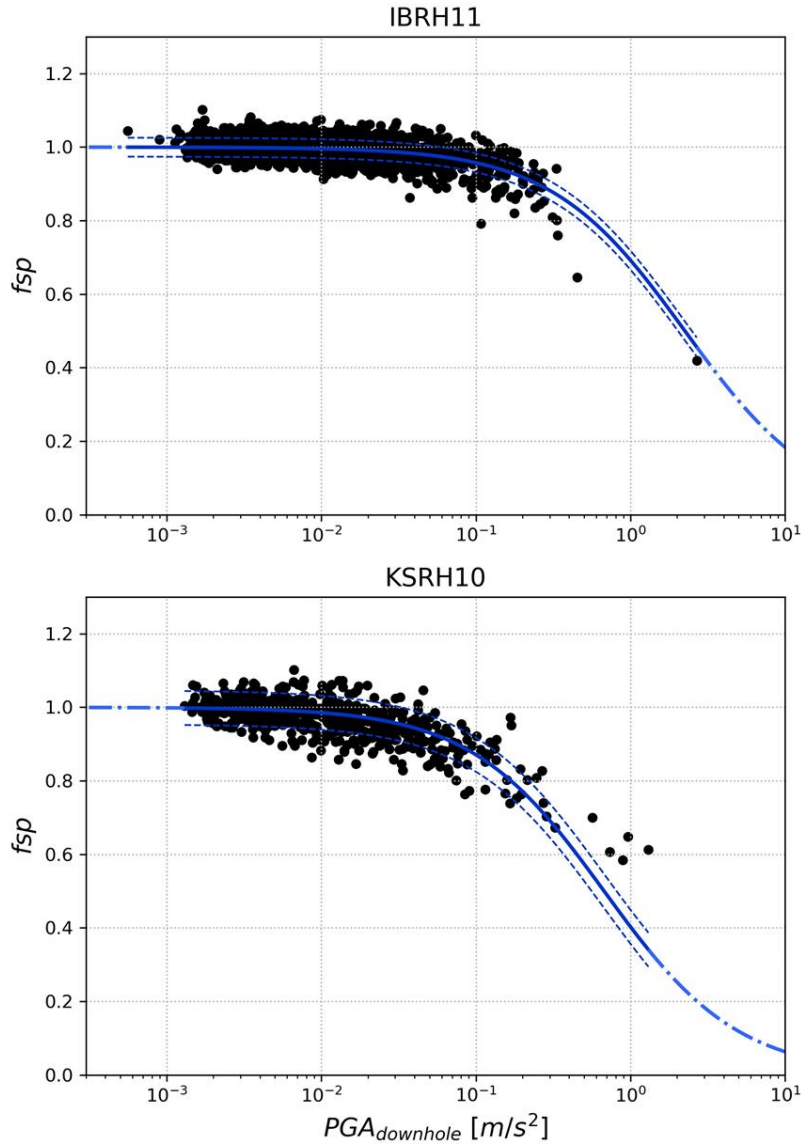


Figure III-6.  $f_{sp}$  value against  $PGA_{downhole}$ . The blue line is the best hyperbolic function that fits the data, dash blue line for the zones where the curve is extrapolated. Station IBRH11 -  $VS_{30}$ : 242 m/s

The Figure III-6 shows that for small  $PGA_{downhole}$ ,  $f_{sp}$  is close to 1 but as the solicitation level increases, the  $f_{sp}$  starts to decrease. The decay is gentle for  $PGA_{downhole}$  smaller than  $0.1 \text{ m/s}^2$  for the IBRH11 site and until  $0.03 \text{ m/s}^2$  for KSRH10. After,  $f_{sp}$  decays rapidly for larger seismic solicitations.

A hyperbolic curve was used to fit the  $f_{sp}$  points (blue line Figure III-6), with a formulation equivalent to the one used to describe the modulus reduction curves (Duncan and Chang, 1970; Ishihara, 1996). The equation for a hyperbolic curve that we call  $\widehat{f}_{sp}$  curves is defined as:

$$\widehat{f}_{sp} = \frac{1}{1 + \frac{PGA_{downhole}}{PGA_{Ref_{downhole}}}} \quad (\text{III-5})$$

Where  $PGA_{ref\ downhole}$  is a parameter that controls the hyperbolic curve for each site, and it is chosen to make the curve fit the data.  $\widehat{fsp}$  will be the estimation of  $fsp$  using the intensity of the ground motion and the trend of the  $fsp$  curve.

Graphically,  $PGA_{ref\ downhole}$  is the value of  $PGA_{downhole}$  where  $fsp$  equals to 0.5. Figure III-7 shows the meaning of this parameter schematically on the hyperbolic curve.

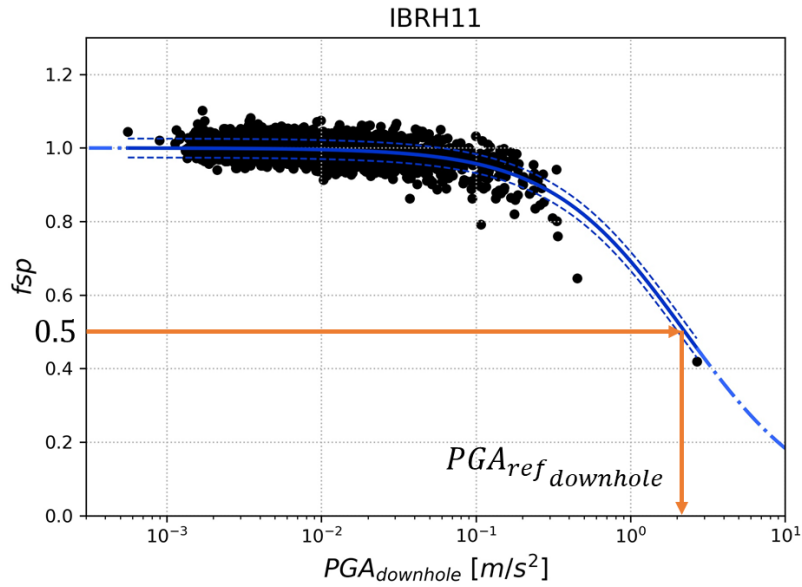


Figure III-7. Representation of  $PGA_{ref\ downhole}$  meaning in the  $fsp$  curves.

#### III.4 Comparison of $fsp$ and shear modulus reduction curves

The  $fsp$  parameter is linked to the intensity of the seismic solicitation of the soil column. In subsection I.4.1 was shown that for an EQL analysis,  $fsp$  is equal to  $G/G_{max}$ . In the case of a fully non-linear model,  $fsp$  fits, approximately, a general decay of stiffness for the entire soil column (section I.5). From those results, we propose to quantify the soil stiffness decrease, measuring the  $fsp$  parameter from real records.

We apply the process to compute  $fsp$  parameter from the earthquakes recorded at station KSRH10. This station is particularly interesting because it was characterized by in-situ and laboratory data measurements performed during the PRENOLIN project (Régnier et al., 2018).

To compare  $fsp$  with the shear modulus decay curves obtained from cyclic tri-axial tests performed at this station during the PRENOLIN project (Figure 5, Régnier et al., 2018), it is necessary to define a proxy for the strain in the soil column:

$$\gamma = \frac{\partial u}{\partial x} = \frac{\frac{\partial u}{\partial t}}{\frac{\partial x}{\partial t}} = \frac{v}{V_s}$$

Where  $v$  is the velocity of an elementary particle at a given point due to the shaking, and  $V_s$  is the shear velocity of the material. Idriss, (2011) is proposed to estimate the shear strain ( $\gamma$ ) as:

$$\gamma \approx \frac{PGV_{surface}}{VS_{30}} \quad (\text{III-6})$$

Where  $PGV_{surface}$  is the peak ground motion velocity at the surface, and  $VS_{30}$  is the average shear velocity in the first 30 m of soil. This proxy could estimate the general strain for the entire column and be linked with the stiffness decay (Chandra et al., 2016; Idriss, 2011).

Applying the same procedure described in section III.3, but in this case, using  $PGV_{surface}/V_{S30}$  as intensity measurement instead of  $PGA_{downhole}$ , we define thus a new  $f_{sp}$  curve. Looking at Figure III-8, we observe that the  $f_{sp}$  values are in the range of the shear modulus degradation values. This comparison seems to confirm that  $f_{sp}$  is a good proxy for describing the shear modulus decay with shear strain.

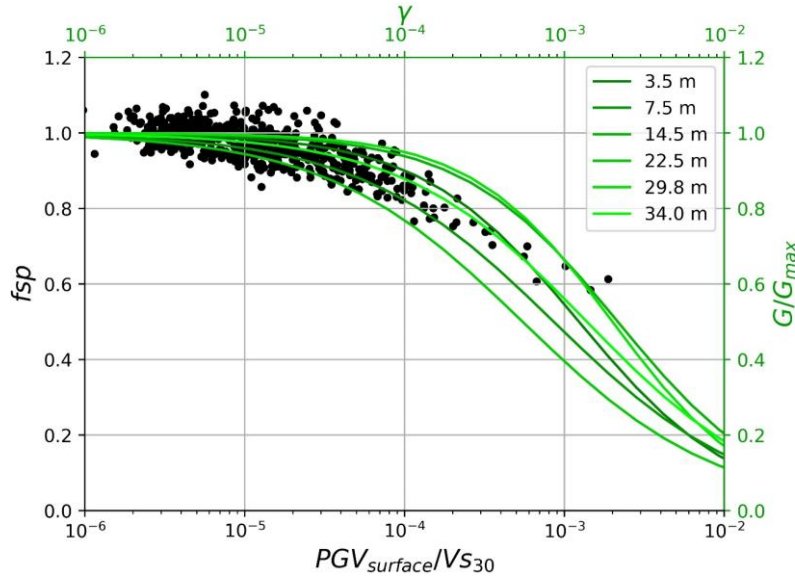


Figure III-8. Shear modulus decay curves defined in the PRENOLIN project at station KSRH10 (green lines) at different depths for cyclic triaxial tests; Figure 5 Régnier et al., (2018). Values of  $f_{sp}$  against  $PGV/V_{S30}$  calculated at the site.

### III.5 Prediction of strong motion 2016 Kumamoto earthquake ( $M_w$ 7.1)

In order to make a step further, we propose a methodology to predict the non-linear surface ground motion using the  $f_{sp}$  curves previously computed.

#### III.5.1 Methodology

For a given station, and a given input with  $PGA$  value at the downhole sensor, we can estimate  $f_{sp}$  from the non-linear regression defined in the Equation (III-5), already computed at each station.

With  $f_{sp}$  and  $BSR_{linear}$ , it is possible to estimate the  $BSR$  for the predicted ground motion. This estimation consists in applying the obtained shift (estimated  $f_{sp}$ ) to  $BSR_{linear}$  as shown in Equation (III-7).

$$\widehat{BSR}(f) = BSR_{linear} \left( f \cdot \sqrt{\widehat{f_{sp}}} \right) \quad (\text{III-7})$$

When  $\widehat{BSR}$  is the estimated borehole spectral ratio for the new ground motion.  $BSR_{linear}$  is the linear borehole spectral ratio (Eq. (III-2)),  $\widehat{f_{sp}}$  is the shift estimation following the curved in the Eq. (III-5).

The function  $\widehat{BSR}$  can be used as an approximation of the borehole transfer function for one specific earthquake. With this assumption, it is possible to compute the ground motion at the surface by the convolution between the input wave at the borehole and  $\widehat{BSR}$ . This procedure summered in Eq. (I-12) assumes, between others, 1D analysis. Here, with  $BSR$ , it transforms to:

$$S_{surface}(f) = S_{downhole}(f) \cdot \widehat{BSR}(f) \quad (\text{III-8})$$

Where  $S_{surface}$  is the spectrum of the ground motion at the surface including the non-linear effects related to the decay of stiffness,  $S_{downhole}$  is the horizontal input wave at downhole. In this section we predict directly the geometrical average of the two horizontal components, avoiding effects of bad alignment between the components of the vertical array.

### III.5.2 Kumamoto earthquake and sites of analysis

The methodology presented before is applied to the Kumamoto Earthquake recordings. The earthquake mainshock occurred on April 15th, 2016 in the south of Japan (island of Kyushu), with a moment magnitude  $M_w$  of 7.1. This earthquake initially started in a deep portion of the northern part of the Hinagu fault and then finished in the Futagawa fault (Asano and Iwata, 2016), it was the largest earthquake in Japan in 2016. In this section, the records from this earthquake are compared with predictions using the methodology described previously.

The methodology was applied to the KIK-net sites that recorded this earthquake and had a horizontal  $PGA_{surface}$  upper than  $0.5 m/s^2$ . Additionally, we removed sites with  $f_{sp}$  curves with high dispersion. The filter of stations left 26 sites (Figure III-9), but in this document eight representative sites are shown, the other can be found in Annex B.

The selected sites are all located on the island of Kyushu in Japan. The  $V_s$  profiles (Figure III-10) from the different sites cover a broad range of kind of sites. Table III-1 shows the distance to the epicenter, the  $V_{s30}$  of each site and the location for each one.

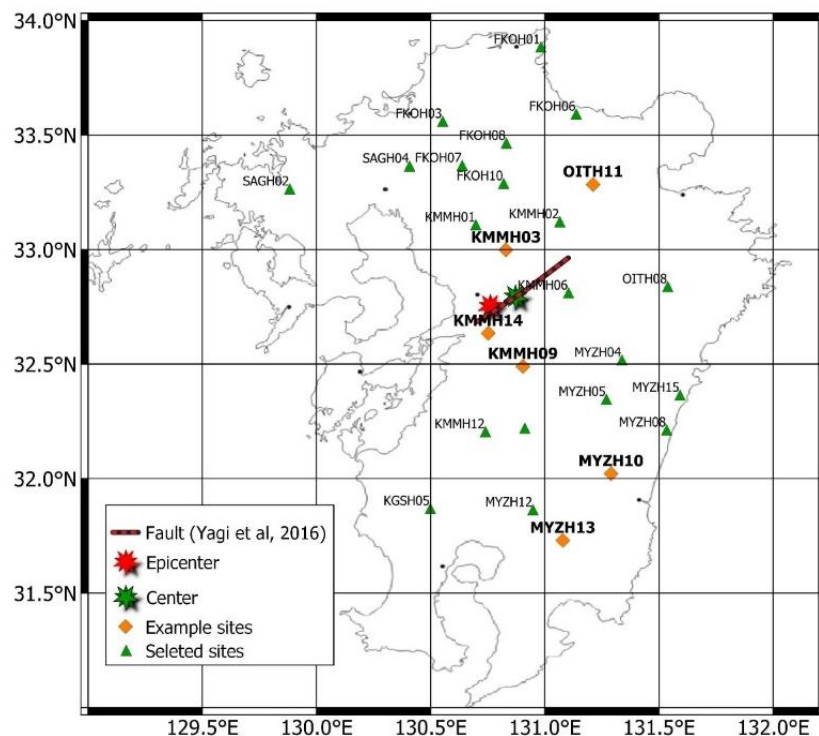


Figure III-9. Selected sites for the prediction of site response for Kumamoto earthquake. The fault was determined by Yagi et al., (2016).

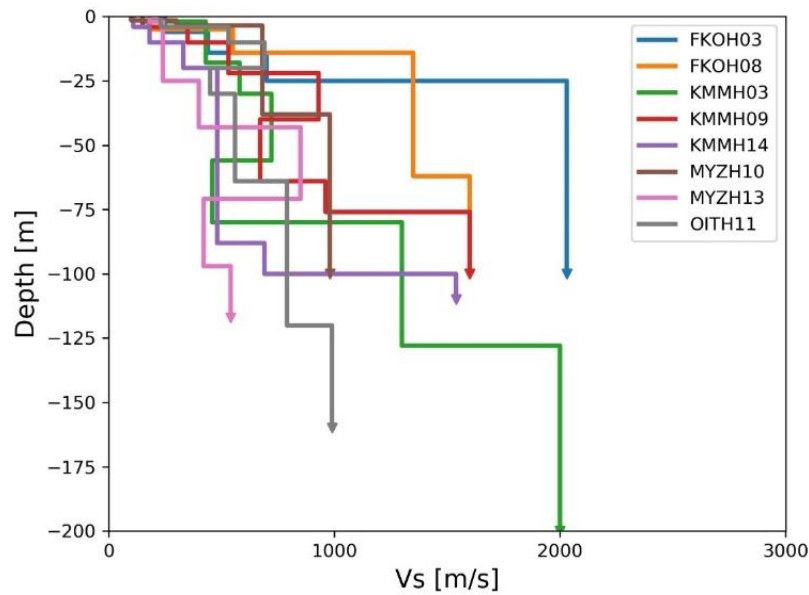


Figure III-10. Vs profile of the stations that are considered in this analysis.

Table III-1. Site data of the representative stations that were selected in this analysis.

Name	Distance to Center [km]	VS <sub>30</sub> [m/s <sup>2</sup> ]	Depth	Prefecture	Site
<b>FKOH03</b>	90.3	497	100	FUKUOKAKEN	UMI
<b>FKOH08</b>	74.7	536	100	FUKUOKAKEN	KOISHIWARA
<b>KMMH03</b>	23.0	421	200	KUMAMOTOKEN	KIKUCHI
<b>KMMH09</b>	33.9	400	100	KUMAMOTOKEN	IZUMI
<b>KMMH14</b>	21.0	248	110	KUMAMOTOKEN	TOYONO
<b>MYZH10</b>	94.4	495	100	MIYAZAKIKEN	KUNITOMI
<b>MYZH13</b>	119.8	251	117	MIYAZAKIKEN	MIYAKONOJOU-S
<b>OITH11</b>	63.0	459	160	OITAKEN	KOKONOE

Because the objective of this section is to evaluate the methodology proposed previously to estimate the site response, the real record at downhole of each site is taken as an input of the simulation. For estimating site effects for future earthquakes, the downhole signal could be also estimated by stochastic approximations as Empirical Green Function method evaluated at downhole. This will be discussed in Chapter VII.

From the downhole record at each site, the  $PGA_{downhole}$  and  $S_{downhole}$  are obtained. Additionally, using the whole data recorded at the site, the methodology of the section III.3 is applied for the computation of the  $f_{sp}$  curves (Table III-2). Note that we computed the  $f_{sp}$  curves without considering the Kumamoto earthquake that will be simulated through our procedure (Figure III-11).

Table III-2. Inputs and site characteristics for Kumamoto earthquake.

Site Name	$PGA_{ref\_downhole} [m/s^2]$	$\sigma$	$PGA_{downhole} [m/s^2]$	$f_{sp}$
<b>FKOH03</b>	1.348E+00	0.049	2.252E-01	0.86
<b>FKOH08</b>	9.008E-01	0.041	2.392E-01	0.79
<b>KMMH03</b>	1.137E+00	0.056	1.447E+00	0.44
<b>KMMH09</b>	4.634E-01	0.036	4.600E-01	0.50
<b>KMMH14</b>	2.111E+00	0.056	1.717E+00	0.55
<b>MYZH10</b>	4.855E+00	0.024	1.766E-01	0.96
<b>MYZH13</b>	1.445E+00	0.043	1.506E-01	0.91
<b>OITH11</b>	7.520E-01	0.065	1.457E+00	0.34

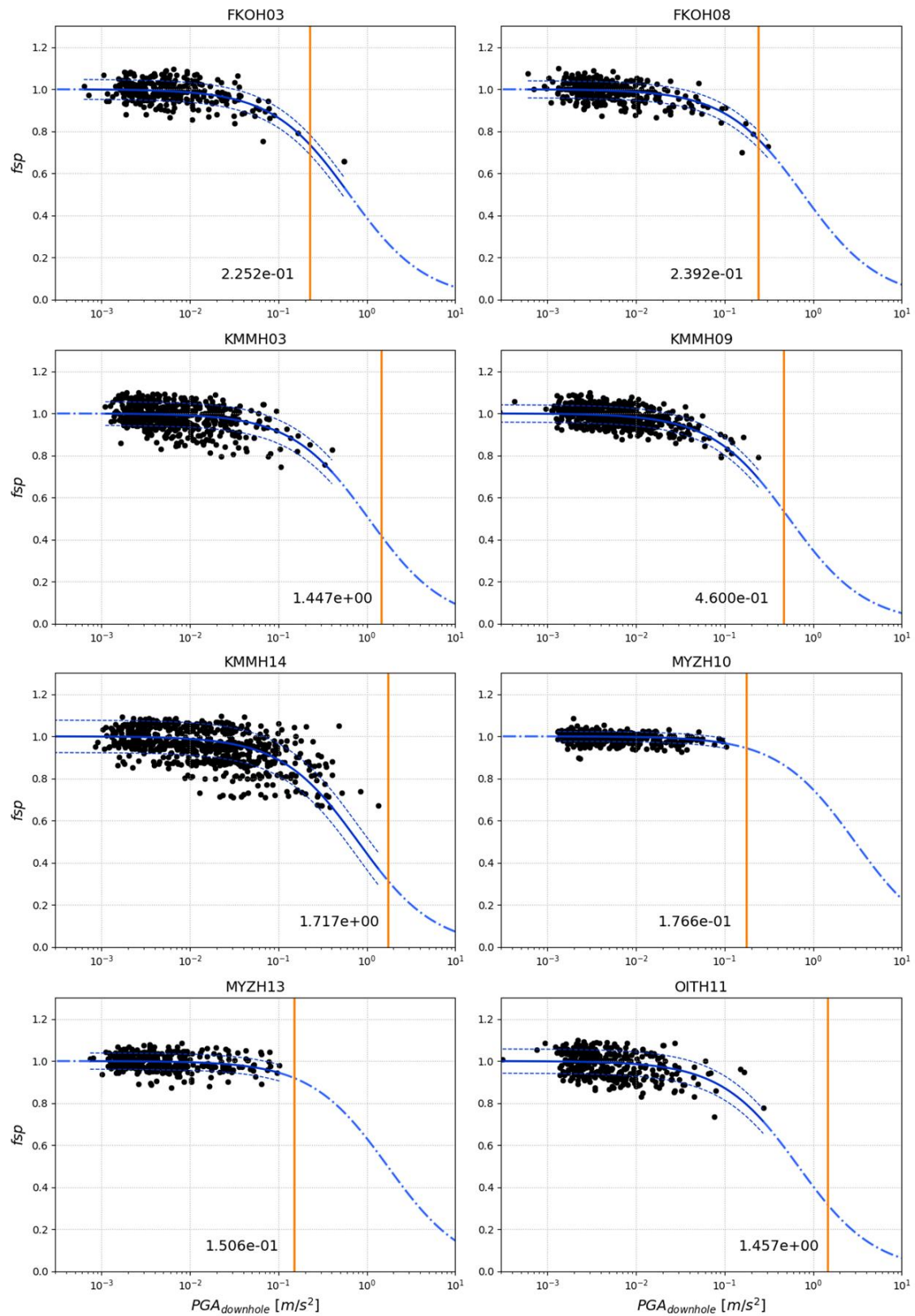


Figure III-11. fsp curves for the example sites for Kumamoto analysis. Orange vertical line represents the registered  $PGA_{downhole}$  generated (at each station) by the 2016 Kumamoto earthquake.

### III.5.3 Estimation of $\widehat{BSR}$

Once the  $f_{sp}$  curve and  $PGA_{downhole}$  are obtained,  $\widehat{f_{sp}}$  is estimated by the Eq. (III-5). The results (Table III-2) are used to shift  $BSR_{linear}$ , estimating the site response for Kumamoto earthquake (Eq. (III-7)). Since this earthquake was recorded by all the considered sites, the observed  $BSR$  can be computed with (Eq. (II-6)). Comparing the observed  $BSR$  from Kumamoto earthquake recordings and the estimated one, we evaluate the performance of the methodology proposed in this section (Figure III-12).

To quantify the changes in the predictions of  $BSR$  (Figure III-12), Eq. (III-3) is used to quantify the misfit ( $\psi$ ) between the observed  $BSR$  and the computed one from the records for this earthquake (Table III-3). This equation was explained in subsection III.3.2. This misfit represents the area between both curves using a logarithmic base.

Table III-3. Comparison between the misfit between the  $BSR$  observed and either  $\widehat{BSR}$  or  $BSR_{linear}$ .

Name	Misfit to observed $BSR$		Misfit $\widehat{BSR}$ / Misfit $BSR_{linear}$
	$\widehat{BSR}$	$BSR_{linear}$	
<b>FKOH03</b>	1.326	2.383	0.56
<b>FKOH08</b>	1.391	1.637	0.85
<b>KMMH03</b>	5.676	6.192	0.92
<b>KMMH09</b>	4.102	5.421	0.76
<b>KMMH14</b>	6.101	5.862	1.04
<b>MYZH10</b>	0.918	0.890	1.03
<b>MYZH13</b>	1.165	1.275	0.91
<b>OITH11</b>	3.034	4.311	0.70

At all sites the application of the estimated shift causes an improvement in the prediction of  $BSR$  compared to  $BSR_{linear}$  (Table III-3). However, the improvement is slightly different in each case, requiring an independent analysis. At FKOH03 and FKOH08,  $\widehat{f_{sp}}$  is computed with an interpolation between observed data (Figure III-11). In the other cases the  $PGA_{downhole}$  of Kumamoto is the highest and  $\widehat{f_{sp}}$  is computed by extrapolating the trend defined by the weaker ground motion, and this can be the source of error in predicting  $\widehat{f_{sp}}$ .

For the cases where  $\widehat{f_{sp}}$  is estimated by interpolation, (i.e. stations FKOH03 and FKOH08), the  $f_{sp}$  corrections improve the fitting of the main peak in comparison with  $BSR_{linear}$  (Figure III-12). Even when, for both cases, the Kumamoto earthquake is close to the limit of  $PGA$  where the  $f_{sp}$  curve is well defined (Figure III-11). However, even if the correction do not change strongly the frequency content of the motion, the improvement is still there.

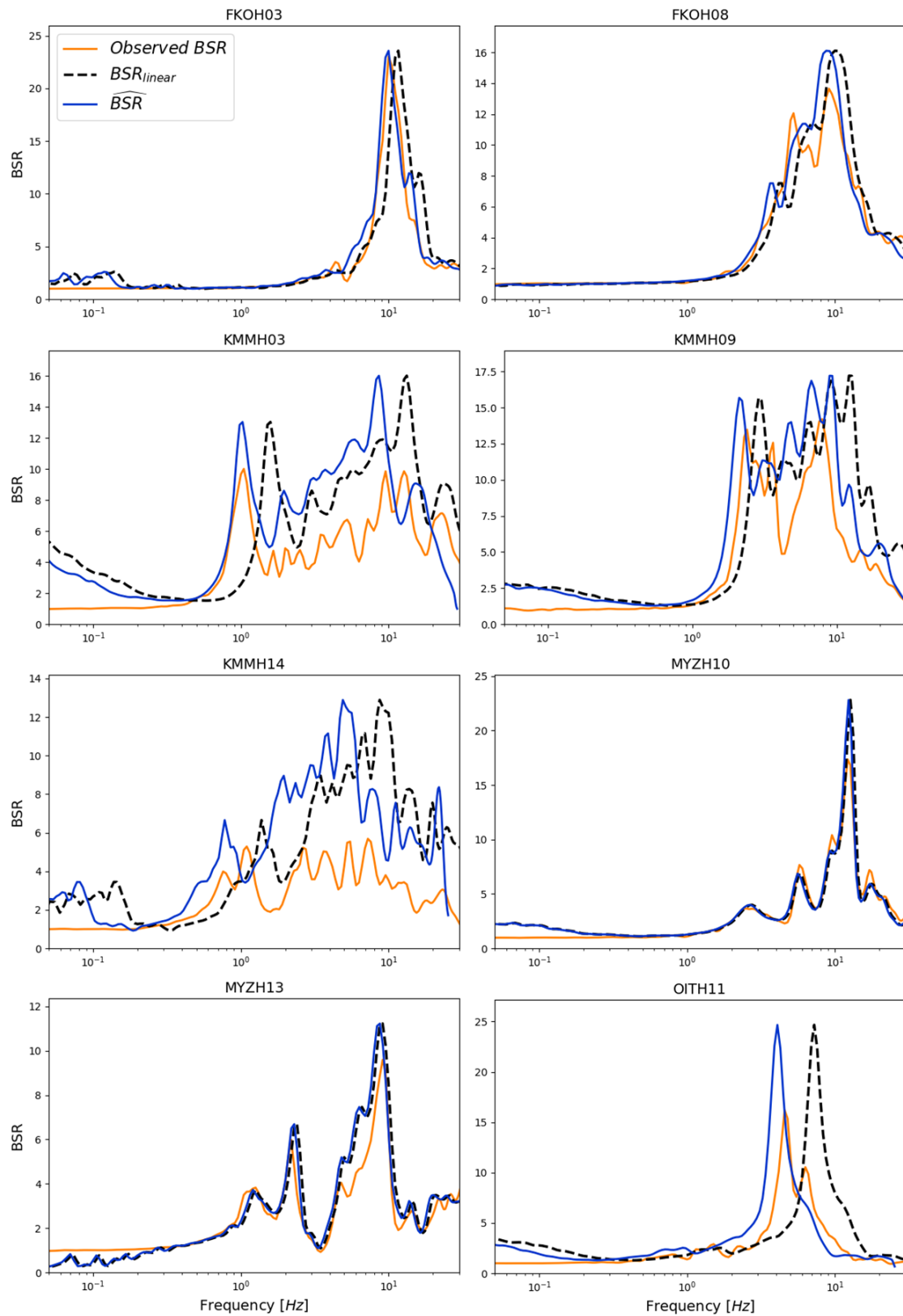


Figure III-12. BSR comparison for several stations, Kumamoto 2016.

At KMMH03, the main peak of the real *BSR*, is well estimated, around 1 Hz, with our methodology (Figure III-12). However, this observed *BSR* does exhibit various frequency peaks on a broad frequency band (mainly two around 1Hz and 10Hz) that are not well recovered in the

predicted BSR. The station is located within a few kilometers of the active fault (Figure III-7). Consequently, it is possibly subject to near-source high-frequency effects. The correction applied is very efficient on the lower frequency of  $\overline{BSR}$  but tends to shift a little too much the higher frequency part ( $> 10z$ ) of the  $\overline{BSR}$ .

For KMMH09, the simulation does not well predict the peaks of the observed BSR and the fundamental resonance peak is too much shifted towards lower frequencies (Figure III-12). The observed BSR at this station exhibits peaks around 3 and 8 Hz. However,  $\overline{BSR}$  for this situation estimates peaks around 2 Hz and 6 Hz. This overestimation can be due to the fact that Kumamoto earthquake is stronger than the previously recorded earthquake at this vertical array (Figure III-11). Furthermore, here the trend of the  $f_{sp}$  points (Figure III-11) is not well matching a hyperbolic function (Eq. (III-5)), making the error more considerable at strong solicitations. But like for the site KMMH0, the application of the frequency correction leads to an improvement of the seismic motion prediction (Table III-3).

In the case of the site KMMH14, the observed BSR curve has a complicated shape in comparison with other sites, presenting a large number of amplification peaks. Additionally, the decreasing of the BSR amplitude is very high in this site. Even with those factors, the estimated BSR is better than  $BSR_{linear}$  alone, fitting the main peaks of the observed BSR (Table III-3).

At MYZ10 and MYZH13 the frequency lag between the linear BSR and the one derived from strong ground motion is very weak, and the associated  $f_{sp}$  curves are flat on a very large PGA window. The soil column under these stations seems to be characterized by a linear behavior. Here, the methodology does thus not bring significant improvement in the prediction of BSR (Figure III-12). But in both cases, the BSR estimation is rather good.

At OITH11 the correction is particularly precise and fits very well the real BSR (Figure III-12). At this station, the BSR has one main peak and a simple shape, and the predictions well estimate the main peak, even when the  $PGA_{downhole}$  for Kumamoto is almost one order of magnitude higher than the strongest previous earthquake recorded by this site.

#### III.5.4 Prediction of the amplitude of the Fourier spectrum at surface

Using the Eq. (III-8), the Fourier spectrum can be computed at the surface. Since BSR is changing, between weak motions and strong predictions, the predicted Fourier spectrum should show an improvement using our approach in comparison with using directly  $BSR_{linear}$  (Figure III-13).

The same kind of analysis, computing the misfit (Eq. (III-3)) is applied (Table III-4). However, the misfit computed on the Fourier spectrum at the surface is not comparable between sites. Indeed, it depends on the shape of the BSR curve. Anyway, this misfit can still give an appreciation of the level of match between the observation and the simulation.

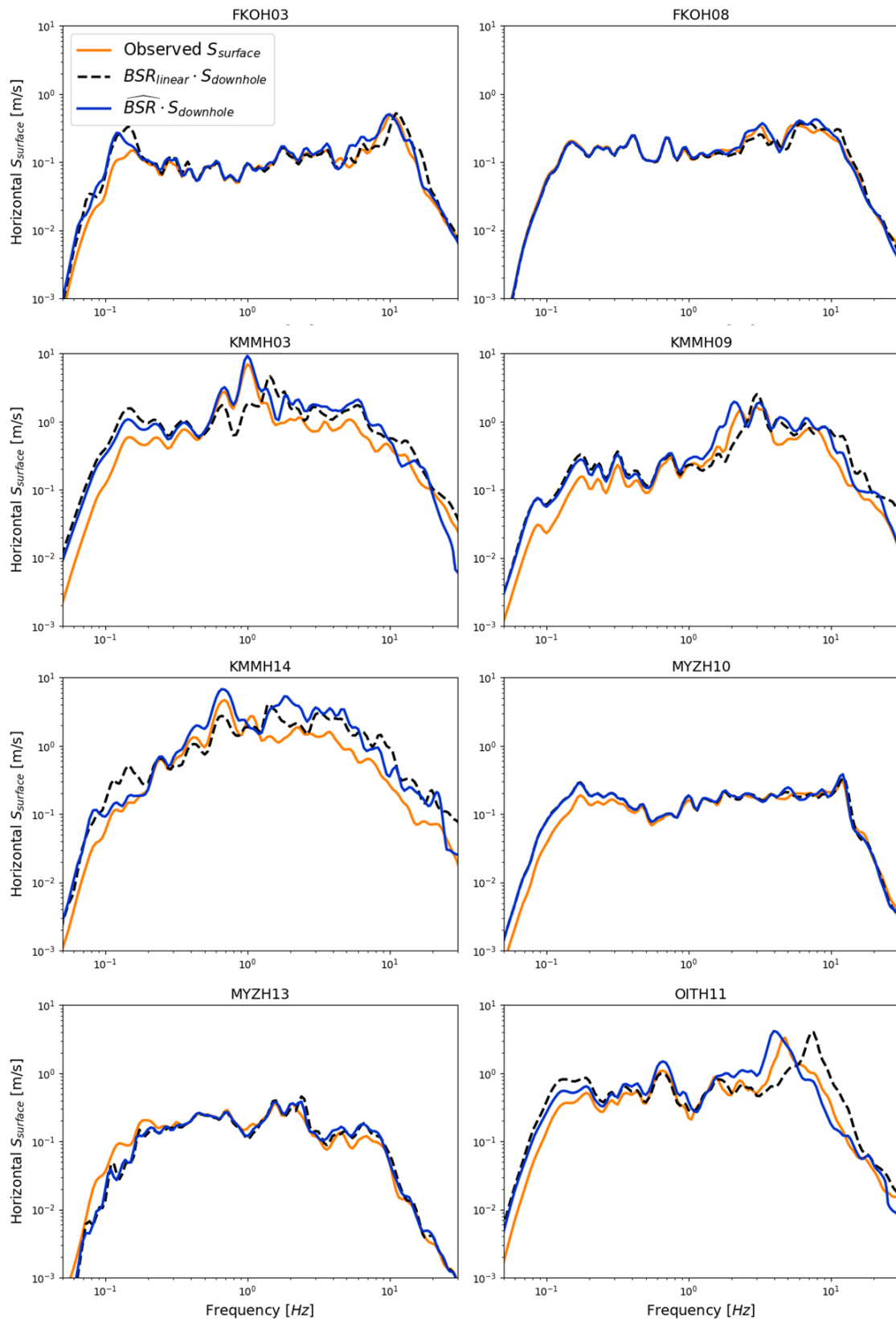


Figure III-13. Fourier spectrum at the surface, Kumamoto 2016.

Table III-4. Comparison of the misfit of the horizontal spectrum at the surface with respect to the observed one.

Name	Misfit to observed $S_{surface}$		Misfit $\widehat{BSR}$ / Misfit $BSR_{linear}$
	$\overline{BSR}$	$BSR_{linear}$	
<b>FKOH03</b>	0.038	0.049	0.77
<b>FKOH08</b>	0.042	0.045	0.91
<b>KMMH03</b>	0.998	1.392	0.72
<b>KMMH09</b>	0.332	0.356	0.93
<b>KMMH14</b>	2.028	1.332	1.52
<b>MYZH10</b>	0.027	0.025	1.08
<b>MYZH13</b>	0.036	0.046	0.77
<b>OITH11</b>	0.577	0.673	0.86

For the sites MYZH10 and MYZH13 the  $BSR$  shift is not significant (Figure III-13), it leads in a very similar amplitude Fourier spectrum than the one produced by the use of  $BSR_{linear}$  alone (Table III-4). However, in all cases, the procedure better predicts the surface motion in comparison with using the linear site response alone.

The excellent fit observed at KMMH03, is due to the fact that the main energy of the spectrum is around 1 Hz, which is the frequency where the  $BSR$  is well defined for this station (Figure III-12).

At KMMH09 and KMMH14 the comparison is more difficult because of the important reduction of the amplitude of  $BSR$  passing from weak to strong ground motion. However, the general shape of the observed spectrum is better predicted by applying the shift site to the  $BSR_{linear}$ . For instance, the main amplification peak is accurately predicted for the site KMMH14 when  $\widehat{f}_{sp}$  is used.

Like for the  $BSR$  estimation, the simulation at OITH11 improves significantly the amplitude Fourier spectrum considering the corrected  $BSR$  in comparison with the prediction using the linear site response. We notice that among the 8 stations presented as examples, OITH11 has the lowest  $PGAref_{downhole}$  ( $7.52 \times 10^{-1} \text{ m/s}^2$ ) meaning it is the most prone to be affected with non-linear effects. In contrast,  $VS_{30}$  of this site is equal to 458.5 m/s, which makes it belong to soil type B in the Eurocode 8 and being considered as hard soil. It indicates  $VS_{30}$  is not the best proxy for non-linear estimation. This analysis will be discussed in the next parts of this document (Chapter IV).

### III.5.5 Time history prediction

From the amplitude Fourier spectrum at the surface we can go back to the in the temporal domain taking into account the same phase that the downhole recording (Brax et al., 2016; Robinson, 1967, 1957). Using Eq. (I-13) the time histories can thus be predicted. However, it requires to do the computation considering North-South and in East-West components separately. To do this, the downhole and surface station should be well aligned. This is unfortunately not always the case (Oth et al., 2011) and this sensor mis-orientation creates an error on the individual time histories computation. However, we expect this error to be small because the orientation of the surface and downhole stations is close. Another source of uncertainty is due to the assumption of the phase equality between the recordings at downhole

and at the surface, since we are using the phase of the downhole to obtain the time history at the surface.

We present the results we obtained at FKOH13, KMMH03, KMMH14 and OITH11 (Figure III-14). For most of the stations, the overall shape (main phase time arrival, duration, frequency content) of the simulated traces is similar to the observed strong ground motions but the amplitudes don't match very well, except for station FKOH03 where the frequency lag is negligible.

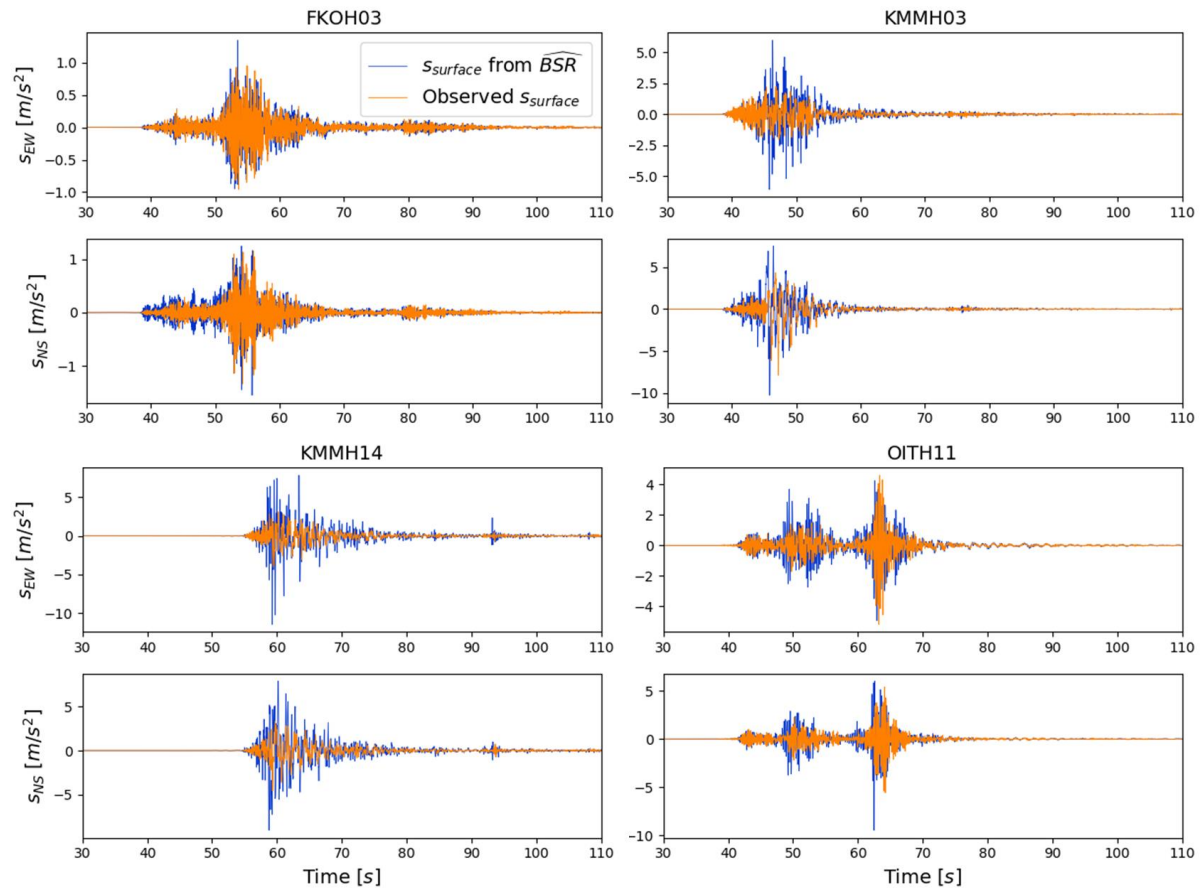


Figure III-14. Temporal signals for three sites evaluated in the earthquake of Kumamoto.

At KMMH03 and KMMH14 the decay of stiffness is more important resulting in a large decrease of the amplification level (Figure III-12). In this case, the *PGA* for the simulation is higher than for the observation (Figure III-14).

At OITH11, the shape and the *PGA* are adequately recovered in both directions (Figure III-14). However, the ground motion has in general higher amplitudes in the simulated trace than the observation.

The Table III-5 shows the *PGA* for all the stations. Since our computation consider here only the frequency lag correction, it is expected that it doesn't well reproduce the *PGA*. Furthermore, the *PGA* is most of the time overestimated but so does also the simulations considering only the linear *BSR*.

Table III-5. PGA of the geometrical average of the horizontal components for the observed event and the simulation using  $\overline{BSR}$  and  $BSR_{linear}$ .

Station	$PGA_{surface}$ observed [ $m/s^2$ ]	$PGA_{surface}$ from $\overline{BSR}$ [ $m/s^2$ ]	$PGA_{surface}$ from $BSR_{linear}$ [ $m/s^2$ ]
FKOH03	1.34	1.60	1.56
FKOH08	1.01	1.57	1.53
KMMH03	7.87	10.27	7.74
KMMH09	2.46	4.89	4.51
KMMH14	6.08	12.93	9.95
MYZH10	0.97	0.93	0.83
MYZH13	0.50	0.65	0.65
OITH11	5.74	9.97	12.31

### III.5.6 Prediction of the response spectra

In earthquake engineering, the seismic solicitation is usually considered through the computation of the elastic response spectra. This spectrum represents the response of a single degree freedom system (SDOF) to a given solicitation. It is derivate from the formula:

$$-s_{surface} = \frac{d^2u}{dt^2} + 2\xi_b f_b \frac{du}{dt} + f_b^2 u \quad (III-9)$$

Where  $s_{surface}$  is the seismic motion,  $\xi_b$  and  $f_b$  are the damping and the resonance frequency of the building respectively. The term  $u$  is the displacement at the top of the building. The period ( $T$ ) is defined as  $T=1/f_b$ . Solving Eq. (III-9) for  $u$ , the maximal acceleration of the building with some resonance period is computed as:

$$Sa(T, \xi) = \max\left(\left| \frac{d^2u(t)}{dt^2} \right| \right) \quad (III-10)$$

Sa is the spectral acceleration of a building characterized with a period  $T$ , and a damping  $\xi$ . Here, the damping of the building is taken equal to 5% to be consistent with what is given in the Eurocode.

The geometrical average between the elastic response spectrum for both horizontal components is shown in Figure III-15. For periods higher than 1s, Sa is very similar between the observation, the approximation (blue line) and the linear solution. This is because BSR is close to one for low frequencies. For larger periods, and especially around the maximum Sa values, the simulation resulting from the linear BSR as well as the one using  $\overline{BSR}$  presents larger acceleration. It is due to the non-consideration of the decrease of the amplification that occurs for strong events.

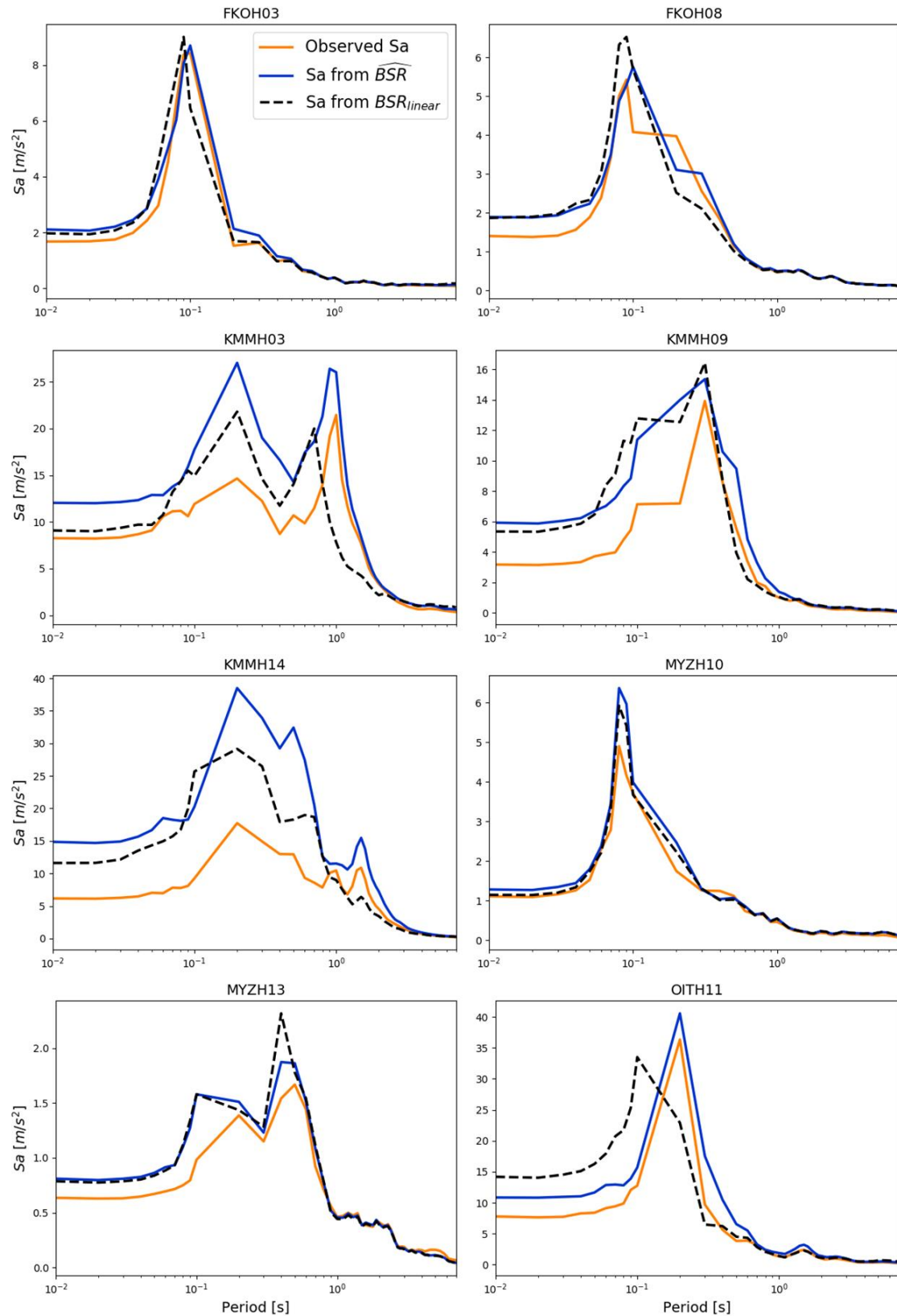


Figure III-15. Geometric average of the elastic response spectra for the horizontal components at the studied sites.

At stations where the frequency lag between the BSR is important (OITH11 and KMMH03 especially), the response spectrum is better fitted using the approximation with  $\widehat{BSR}$  (blue line Figure III-15). For KMMH03 a linear estimation (black line) underestimate  $Sa$  for a period around

1s. On the contrary, using  $\widehat{BSR}$  we improve the prediction. Something similar is obtained for station OITH11, around 0.2 s of period.

In general, using  $\widehat{BSR}$  is a better estimation of the observed response spectra. However, in most of sites the amplitude is higher. This is related to the fact that we didn't take in account the decrease of the amplification that we observe on the real data.

### III.6 Amplification decrease consideration

In section III.1 was shown that the two main effects of the non-linearity on the site response ( $BSR$ ) is a shift to lower frequencies of the amplification peaks, and a decrease of the peaks amplitude. The previous sections of this chapter were dedicated to the study of the frequency shift alone. This section focuses on the study of the decrease of the amplification between weak and strong ground motions.

In a single layered 1D model associated with a Kevin-Vought material with a rigid bedrock, the transfer function is derivate using Eq. (I-20) (see section I.1.2):

$$|TF_{\{0/H\}}(f)| = \frac{1}{\sqrt{\cos^2\left(2\pi fH/V_s\right) + \sinh^2\left(\xi 2\pi fH/V_s\right)}}$$

In this case, the local maximums are reached when the term in the denominator reaches a minimum. It occurs several times for periodic frequencies when the  $\cos$  function equals zero:

$$f^{\{n\}} = \frac{V_s}{2H} (0.5 + n) \quad \text{for } n = 0, 1, 2, \dots$$

Where  $V_s$  is the shear velocity of the material,  $H$  the thickness of the layer, and  $n$  the harmonic number. This amplification peaks depend just on the shear velocity and layer thickness. However, in the case of the amplification, when those peaks are evaluated in the transfer function the amplitude is:

$$|TF_{\{0/H\}}(f^{\{n\}})| = \frac{1}{\sinh\left(\xi\left(\pi/2 + n\pi\right)\right)}$$

The previous equation shows that the amplification value depends on the soil damping and the harmonic number. Since the  $\sinh$  function is a monotonically increasing function, it means that the amplification is lower for higher harmonics than for low harmonics, as showed the Figure I-3. Additionally, the previous equation does not depend on the frequency directly. From this idea, we propose a methodology based on the comparison of the amplitude of the harmonics between  $BSR$  and  $BSR_{linear}$  to compare the effect of the decreasing.

The number and the amplitude of the peaks in  $BSR$  are related to the soil configuration, properties of the soils, and the depth of downhole station (Cadet et al., 2012b). Based on that, we try to compare the effects of the non-linear behavior in the amplification by comparing  $BSR$  against  $BSR_{linear}$  peak amplifications. However, the comparison is between harmonics and not directly frequency to frequency amplification (Cadet et al., 2012a).

Before the harmonic comparison, a shift is applied to  $BSR$  to fit the  $BSR$  harmonics with  $BSR_{linear}$  harmonics. We use an algorithm that shifts  $BSR$  by using the already computed  $f_{sp}$ , and after the subtraction between the shifted  $BSR$  and  $BSR_{linear}$  is computed:

$$\Delta BSR_{ISA}(f) = BSR(f/\sqrt{f_{sp}}) - BSR_{linear}(f) \quad \text{(III-11)}$$

The equation allows to apply the inverse shift to  $BSR$  to fit  $BSR_{linear}$ . This procedure allows the comparison by computing the term  $\Delta BSR_{ISA}$  (change of  $BSR$  with inverse shift applied). The resulting function ( $\Delta BSR_{ISA}$ ) represents the difference between  $BSR$  with respect to the linear soil response for each frequency peak ( $BSR_{linear}$ ). Figure III-16 shows the value of  $\Delta BSR_{ISA}$  for all the ground motions at stations IBRH11 and KSRH10.

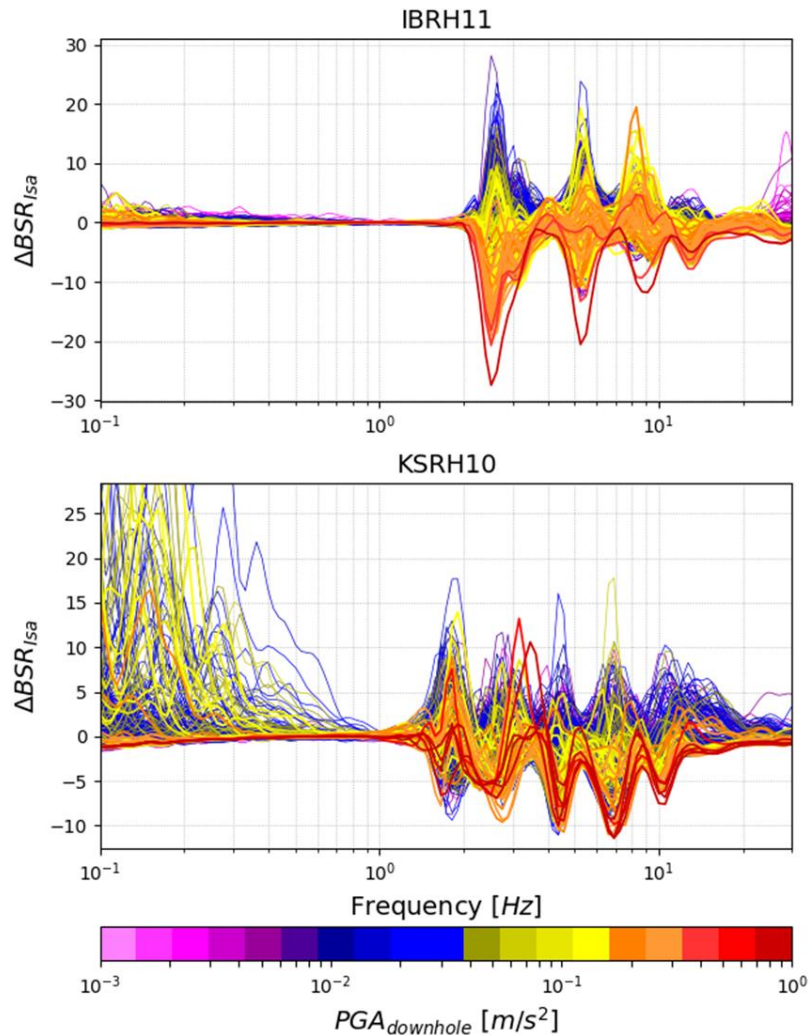


Figure III-16.  $\Delta BSR_{ISA}$  for the station IBRH11 and KSRH10 using all the earthquakes recorded by those stations.

There is a huge variability for the BSR amplitude with respect  $BSR_{linear}$ . Figure III-16 shows that for some cases, especially for weak ground motions, the amplitude is even higher than  $BSR_{linear}$ . Those differences can be related either with sub-surface geometrical 2D effects or non-vertical incidence wave. Also, it could be related with the normal variation of the water table, that could have an impact on the damping of the soil layers.

Figure III-16 shows that the decrease in  $\Delta BSR_{ISA}$  is depending on the intensity of the ground motion, expressed regarding  $PGA_{downhole}$ . Also, the negative peaks of  $\Delta BSR_{ISA}$  are corresponding to the frequency of the amplification peaks in  $BSR_{linear}$  for both stations (Figure III-4).

To analyze the dependency between  $PGA_{downhole}$  and  $\Delta BSR_{ISA}$ , the arithmetic average  $\Delta BSR_{ISA}(f)$  for 10 logarithmic window ranges of  $PGA_{downhole}$  are analyzed (Figure III-17). For weak ground motion, the average of  $\Delta BSR_{ISA}$  is around zero, even if the dispersion is very high, showing a linear behavior as expected. The decrease of amplitude can be seen for strong ground motions.

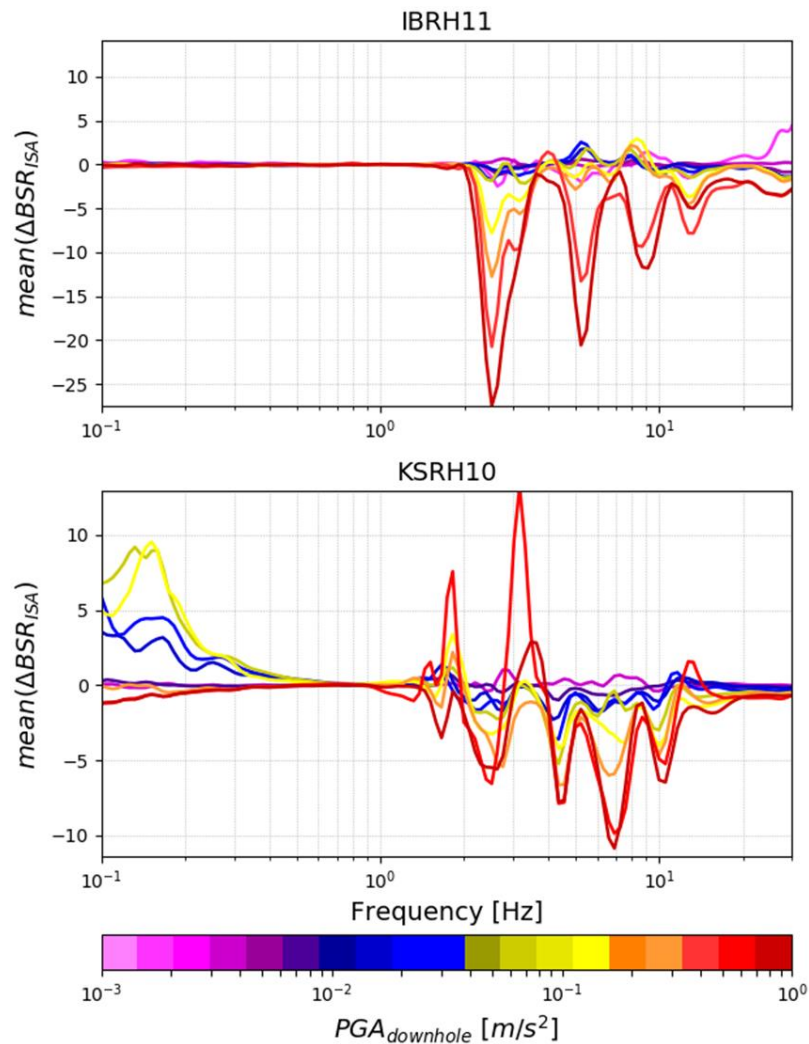


Figure III-17. Average of  $\Delta BSR_{ISA}$  separated by  $PGA_{downhole}$  logarithmic steps.

At high frequencies it is expected that  $\Delta BSR_{ISA}$  has lower values because of the effect of the damping of the soil (e.g. Ktenidou et al., 2014). In Figure III-17, at very high frequencies (around 30Hz)  $\Delta BSR_{ISA}$  is slightly lower for strong events. It indicates that  $\Delta BSR_{ISA}$  is a function also depending on the frequency. The reason could be related to the increase of the damping for strong ground motion.

For low  $PGA_{downhole}$  values the average curves are defined with a large number of data (Figure III-17), but for strong  $PGA_{downhole}$  the curves are defined by few ground motions. Because of this, the analysis of the trend for strong events is complicated, especially for the curve 0.6  $m/s^2$  at KSRH10. However, we can observe that the decrease is higher for strong events.

The dispersion of  $\Delta BSR_{ISA}$  is large for weak and strong events (Figure III-16). Computing the standard deviation for the same 10 logarithmic steps of  $PGA_{downhole}$  in Figure III-17, Figure III-18 shows that the dispersion is always larger around the peaks of  $\Delta BSR_{ISA}$ .

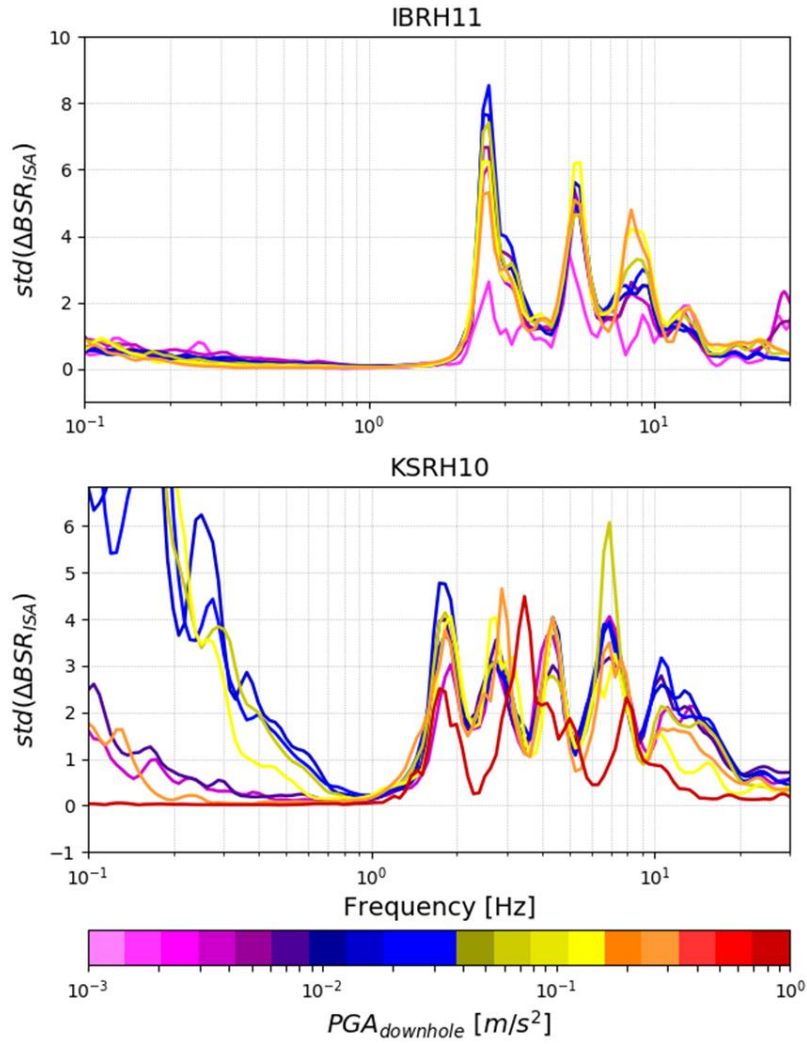


Figure III-18. Standard deviation of  $\Delta BSR_{ISA}$  separated by  $PGA_{downhole}$  logarithmic steps.

$\Delta BSR_{ISA}$  depends on the intensity of the seismic solicitation ( $PGA_{downhole}$ ), on  $BSR_{linear}$ , and on the frequency ( $f$ ). To study  $\Delta BSR_{ISA}$  a polynomial regression is applied to fit the data as a function of those three variables. For a specific site (i.e.: a given  $BSR_{linear}$ ). This surface can be expressed as:

$$\widehat{\Delta BSR}_{ISA} = h(PGA_{downhole}, BSR_{linear}, f) \quad (\text{III-12})$$

Where  $h$  represents a surface that fits the observed data. This function is taken as a polynomial of third grade that can be written as:

$$h(PGA_{downhole}, BSR_{linear}, f) = \sum_{i=0}^3 \sum_{j=0}^{3-i} \sum_{k=0}^{3-i-j} [\theta_{\{i,j,k\}} \cdot x^i \cdot y^j \cdot z^k] \quad (\text{III-13})$$

The terms  $\theta_{\{i,j,k\}}$  are constant parameters that are estimated by the regression process. The terms  $x$ ,  $y$ , and  $z$  are function of the parameters  $PGA_{downhole}$ ,  $BSR_{linear}$ , and  $f$  respectively. Those functions transform the inputs to be between 0 and 1. This normalization is used to improve the performance of regressions by removing the effects of the scale that the parameters have intrinsically (Goodfellow et al., 2016). The functions  $x$ ,  $y$ , and  $z$  are defined as:

$$x = \frac{\lg_{10}(PGA_{downhole}) - \lg_{10}(PGA_{downhole}^{\{min\}})}{\lg_{10}(PGA_{downhole}^{\{max\}}) - \lg_{10}(PGA_{downhole}^{\{min\}})} \quad (\text{III-14})$$

$$y = \frac{BSR_{linear} - BSR_{linear}^{\{min\}}}{BSR_{linear}^{\{max\}} - BSR_{linear}^{\{min\}}}$$

$$z = \frac{\lg_{10}(f) - \lg_{10}(f^{\{min\}})}{\lg_{10}(f^{\{max\}}) - \lg_{10}(f^{\{min\}})}$$

Where  $PGA_{downhole}^{\{min\}}$  and  $PGA_{downhole}^{\{max\}}$  are the horizontal  $PGA$  at downhole of the weakest and the strongest earthquake that were used in the regression respectively.  $BSR_{linear}^{\{min\}}$  and  $BSR_{linear}^{\{max\}}$  are the extreme values of  $BSR_{linear}$  in the frequency window that is analyzed. The frequency window edges are defined by  $f^{\{min\}}$  and  $f^{\{max\}}$ . Here we consider a window going from 0.3 Hz and 30 Hz.

Merging the Eq. (III-14) and Eq. (III-13) it is possible to estimate  $\Delta \widehat{BSR}_{ISA}$  through Eq. (III-12) since  $BSR_{linear}$  is known. The other parameters depend also of the database recorded at the site and are known for estimating  $\Delta BSR_{ISA}$  with a given  $PGA_{downhole}$ .

For all the evaluated sites we found that polynomials of third grade give an adequate match with our dataset. We present on Figure III-19 the resulting function for IBRH11 and KSRH10.

The performance of the regression depends on the considered site (Figure III-19). The surface obtained at IBRH11 fits much better the data at KSRH10. Applying the same methodology to the whole Kik-Net sites we observe that the dispersion is site dependent.

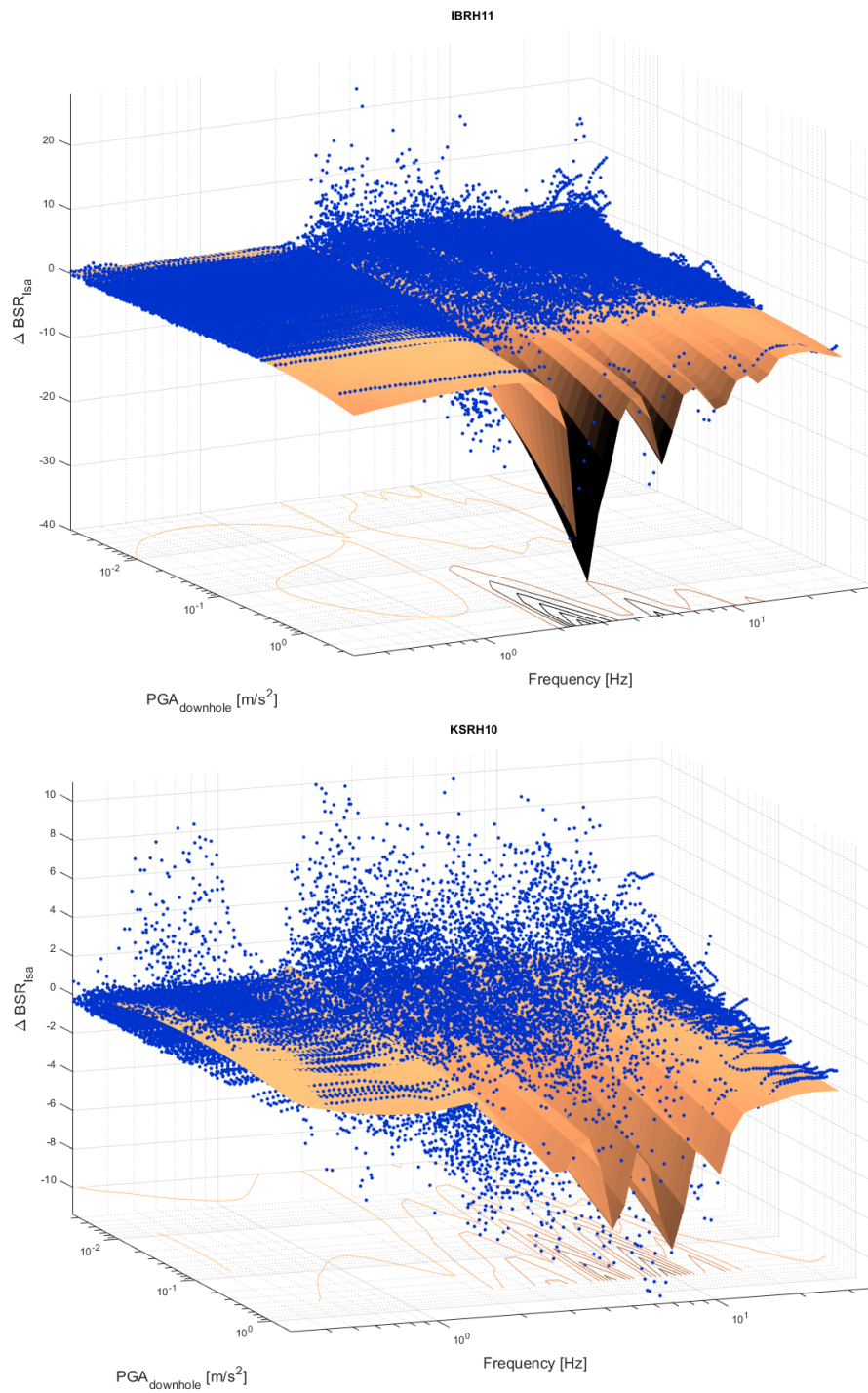


Figure III-19. Interpolated surface  $\Delta \widehat{BSR}_{ISA}$  from  $PGA_{downhole}$ ,  $BSR_{linear}$ , and the frequency. Top site IBRH11, bottom site KSRH10. Blue points represent the real data to be fitted.

The surfaces of the Figure III-19 for the sites IBRH11 and KSRH10 are described by the Eq. (III-12) with the parameters in Table III-6. The general parameters for each site are shown in Table III-7.

Table III-6. Results of the regression for the sites IBRH11 and KSRH10 (Eq. (III-13)).

Site: IBRH11				Site: KSRH10			
i	j	k	$\theta_{\{i,j,k\}}$	i	j	k	$\theta_{\{i,j,k\}}$
0	0	0	0.50316	0	0	0	0.30542
0	1	0	-0.06260	0	1	0	0.32026
0	2	0	-0.40345	0	2	0	-0.15114
0	3	0	0.03833	0	3	0	0.11823
0	0	1	-0.05740	0	0	1	-0.08790
0	1	1	0.36714	0	1	1	-1.06507
0	2	1	0.79034	0	2	1	0.01866
0	0	2	0.17914	0	0	2	0.21305
0	1	2	-0.71398	0	1	2	1.00006
0	0	3	-0.08856	0	0	3	-0.13001
1	0	0	-0.07096	1	0	0	0.09540
1	1	0	0.06202	1	1	0	0.29880
1	2	0	-0.05265	1	2	0	-0.08460
1	0	1	0.04419	1	0	1	-0.17882
1	1	1	0.78278	1	1	1	-0.67487
1	0	2	-0.20104	1	0	2	0.07508
2	0	0	0.17320	2	0	0	-0.09399
2	1	0	-0.88558	2	1	0	-0.00806
2	0	1	0.14400	2	0	1	0.07170
3	0	0	-0.14849	3	0	0	0.01117

Table III-7. Dataset parameters for the sites IBRH11 and KSRH10 (Eq. (III-14)).

Site	$PGA_{downhole}^{\{min\}}$	$PGA_{downhole}^{\{max\}}$	$BSR_{linear}^{\{min\}}$	$BSR_{linear}^{\{max\}}$	$f^{\{min\}}$	$f^{\{max\}}$
IBRH11	1.624E-03	2.678E+00	1.13	37.37	0.30	29.69
KSRH10	2.564E-03	1.304E+00	1.23	18.35	0.30	29.69

### III.7 Predictions of the site effects using both $f_{sp}$ curves and $\Delta BSR_{ISA}$ . Application to 2016 Kumamoto earthquake, Mw 7.1

In this section is presented an application of the empirical prediction methodology of strong ground motion. The  $BSR$  curve for the Kumamoto earthquake is predicted in several sites using  $f_{sp}$  to correct the shift to lower frequencies and  $\Delta BSR_{ISA}$  for the amplification correction.

#### III.7.1 Methodology

To predict  $BSR$  for a new event, the first step consists in computing the  $f_{sp}$  curves (subsection III.3.3) and  $\Delta BSR_{ISA}$  2D function in the site of interest.

Using  $\Delta \widehat{BSR}_{ISA}$  and  $\widehat{f}_{sp}$  the estimated  $BSR$  function for the new ground motion is computed with the help of the following formula:

$$\widehat{BSR}'(f) = BSR_{linear} \left( f \cdot \sqrt{\widehat{f}_{sp}} \right) + \Delta \widehat{BSR}_{ISA} \left( f \cdot \sqrt{\widehat{f}_{sp}} \right) \quad (III-15)$$

The term  $\widehat{BSR}$  is the simulated borehole spectral ratio for the new ground motion.  $\Delta\widehat{BSR}_{ISA}$  is obtained from Eq. (III-12) and  $\widehat{fsp}$  from Eq. (III-5).

### III.7.2 Estimation of $BSR$

Applying this methodology to the Kumamoto (Japan) earthquake (Mw 7.1), the site response is estimated and compared with the real records of this earthquake. Kumamoto earthquake was presented in the subsection (III-15), and the analysis is presented to the same stations in this subsection (Figure III-9).

The record at downhole is the input of the computation. Taking the  $PGA_{downhole}$ , of the horizontal component, the shift of  $BSR_{linear}$  is estimated following the trend of  $fsp$  for the other earthquakes. The resulted  $\widehat{fsp}$  is the same that was computed in the subsection (III-15) and they are presented in the Table III-2 and in the Figure III-11.

To estimate  $\Delta\widehat{BSR}_{ISA}$  the surface function ((III-13)) blindly is estimated at each site. The resulting parameters for the evaluated sites are shown in the Table III-8 and Table III-9.

Table III-8. Results of the regression for Kumamoto earthquake observation (Eq. (III-13)).

Site: FKOH03				Site: FKOH08			
i	j	k	$\theta_{\{i,j,k\}}$	i	j	k	$\theta_{\{i,j,k\}}$
0	0	0	0.25183	0	0	0	0.48470
0	1	0	-0.94130	0	1	0	-0.20936
0	2	0	1.06809	0	2	0	0.01040
0	3	0	-0.13183	0	3	0	-0.07844
0	0	1	-0.14069	0	0	1	0.04382
0	1	1	1.26216	0	1	1	0.44153
0	2	1	-1.07559	0	2	1	0.11200
0	0	2	0.38796	0	0	2	-0.12064
0	1	2	-0.40627	0	1	2	-0.29298
0	0	3	-0.26465	0	0	3	0.06000
1	0	0	0.02835	1	0	0	-0.04478
1	1	0	0.48405	1	1	0	0.43051
1	2	0	-0.19819	1	2	0	0.10780
1	0	1	0.10859	1	0	1	-0.03791
1	1	1	0.25005	1	1	1	-0.59363
1	0	2	-0.15800	1	0	2	0.20778
2	0	0	-0.12629	2	0	0	0.08127
2	1	0	-0.45970	2	1	0	-0.04403
2	0	1	0.00993	2	0	1	-0.12737
3	0	0	0.08536	3	0	0	-0.02391
Site: KMMH03				Site: KMMH09			
i	j	k	$\theta_{\{i,j,k\}}$	i	j	k	$\theta_{\{i,j,k\}}$
0	0	0	0.12902	0	0	0	0.36252
0	1	0	0.00100	0	1	0	-0.13314
0	2	0	0.02053	0	2	0	-0.13533
0	3	0	-0.06331	0	3	0	0.08299
0	0	1	0.02753	0	0	1	-0.05036
0	1	1	-0.04076	0	1	1	0.66622
0	2	1	0.09350	0	2	1	-0.03744

0	0	2	-0.04626	0	0	2	-0.10787
0	1	2	0.00756	0	1	2	-0.37591
0	0	3	0.03141	0	0	3	0.08743
1	0	0	-0.00042	1	0	0	0.03100
1	1	0	0.08722	1	1	0	0.05516
1	2	0	0.05793	1	2	0	0.06107
1	0	1	-0.05969	1	0	1	0.24092
1	1	1	-0.23806	1	1	1	-0.41527
1	0	2	0.04187	1	0	2	0.01245
2	0	0	-0.00197	2	0	0	-0.14448
2	1	0	-0.07729	2	1	0	0.04244
2	0	1	0.07752	2	0	1	-0.16957
3	0	0	-0.01084	3	0	0	0.10869
<b>Site: KMMH14</b>				<b>Site: MYZH10</b>			
<b>i</b>	<b>j</b>	<b>k</b>	<b><math>\theta_{\{i,j,k\}}</math></b>	<b>i</b>	<b>j</b>	<b>k</b>	<b><math>\theta_{\{i,j,k\}}</math></b>
0	0	0	0.11985	0	0	0	0.64761
0	1	0	-0.06299	0	1	0	0.01083
0	2	0	-0.47226	0	2	0	-0.54942
0	3	0	-0.05509	0	3	0	0.03484
0	0	1	-0.02520	0	0	1	0.01888
0	1	1	0.76455	0	1	1	0.22379
0	2	1	0.70355	0	2	1	0.65830
0	0	2	-0.02711	0	0	2	-0.08104
0	1	2	-1.01410	0	1	2	-0.30098
0	0	3	0.23237	0	0	3	0.07306
1	0	0	-0.06305	1	0	0	-0.04722
1	1	0	0.40005	1	1	0	-0.06148
1	2	0	0.00031	1	2	0	-0.31313
1	0	1	-0.28726	1	0	1	0.02011
1	1	1	-0.16695	1	1	1	0.44336
1	0	2	-0.11672	1	0	2	-0.08395
2	0	0	0.15358	2	0	0	0.07835
2	1	0	-0.37662	2	1	0	-0.15855
2	0	1	0.35470	2	0	1	0.07279
3	0	0	-0.11832	3	0	0	-0.05609
<b>Site: MYZH13</b>				<b>Site: OITH11</b>			
<b>i</b>	<b>j</b>	<b>k</b>	<b><math>\theta_{\{i,j,k\}}</math></b>	<b>i</b>	<b>j</b>	<b>k</b>	<b><math>\theta_{\{i,j,k\}}</math></b>
0	0	0	0.15209	0	0	0	0.36052
0	1	0	0.01520	0	1	0	0.08324
0	2	0	-0.30898	0	2	0	-0.08635
0	3	0	-0.13446	0	3	0	0.01288
0	0	1	-0.02180	0	0	1	-0.02722
0	1	1	0.19157	0	1	1	-0.21465
0	2	1	0.63964	0	2	1	0.10107
0	0	2	0.09429	0	0	2	0.05679
0	1	2	-0.40343	0	1	2	0.05030
0	0	3	-0.01554	0	0	3	0.00151
1	0	0	-0.00229	1	0	0	-0.04600

1	1	0	0.09640	1	1	0	-0.15246
1	2	0	0.03431	1	2	0	0.03801
1	0	1	-0.07083	1	0	1	0.05675
1	1	1	-0.16639	1	1	1	0.53352
1	0	2	0.01408	1	0	2	-0.18239
2	0	0	0.03226	2	0	0	0.06896
2	1	0	-0.02298	2	1	0	-0.32786
2	0	1	0.04398	2	0	1	0.10899
3	0	0	-0.03144	3	0	0	-0.05323

Table III-9. Dataset parameters Kumamoto earthquake (Eq. (III-14)).

Site	$PGA_{downhole}^{\{min\}}$	$PGA_{downhole}^{\{max\}}$	$BSR_{linear}^{\{min\}}$	$BSR_{linear}^{\{max\}}$	$f^{\{min\}}$	$f^{\{max\}}$
<b>FKOH03</b>	6.300E-04	5.554E-01	1.00	23.57	3.020E-01	2.969E+01
<b>FKOH08</b>	6.010E-04	3.062E-01	1.00	16.11	3.020E-01	2.969E+01
<b>KMMH03</b>	1.104E-03	4.036E-01	1.52	16.03	3.020E-01	2.969E+01
<b>KMMH09</b>	2.860E-04	2.407E-01	1.29	17.21	3.020E-01	2.969E+01
<b>KMMH14</b>	2.150E-04	1.352E+00	0.92	12.88	3.020E-01	2.969E+01
<b>MYZH10</b>	1.294E-03	1.042E-01	1.11	22.80	3.020E-01	2.969E+01
<b>MYZH13</b>	7.440E-04	1.030E-01	0.98	11.23	3.020E-01	2.969E+01
<b>OITH11</b>	3.110E-04	2.725E-01	1.30	24.67	3.020E-01	2.969E+01

Using  $\Delta BSR_{ISA}$  (Eq. (III-12)) and  $\widehat{f}_{sp}$  (Eq. (III-5)) the site response for Kumamoto earthquake strong ground motion is computed. Applying Eq. (III-15), the new estimation of  $BSR$  ( $\widehat{BSR}'$ ) results in a shift and a decrease of the amplification (Figure III-20). To compare how well does our simulation fit the data at the different stations, Table III-10 compares the misfit (Eq. (III-3)) that is computed between the observation and each prediction.

In comparison with the linear prediction for all the sites,  $\widehat{BSR}'$  is a better approximation than  $BSR_{linear}$  (Table III-10). Even for sites as FKOH03, FKOH08, MYZH10 and MYZH13 where the shift correction is very low, the correction of the amplitude reduction results in a better estimation of  $BSR$ .

In sites showing an important non-linearity (KMMH03 and OITH11) both corrections together result in a significant improvement in comparison with the direct use of  $BSR_{linear}$ . However, for the site KMMH03, the misfit at high frequencies is still present. In the case of the site OITH11 there is an overestimation of the shift and the amplitude of  $BSR$  is underestimated, in particular around 8Hz. However, the procedure generally fits the Kumamoto earthquake recordings at these stations.

At KMMH14 applying the shift correction,  $\widehat{BSR}$  does not estimate adequately the observed  $BSR$  (Figure III-12) but with the approach proposed in this section,  $\widehat{BSR}'$  the prediction is improved (Figure III-20).

Table III-10. Misfit between the approximation of  $BSR$  with the observed one for the Kumamoto earthquake.

Name	Misfit to observed $BSR$		Misfit $\widehat{BSR}' /$ Misfit $BSR_{linear}$	Misfit $\widehat{BSR} /$ Misfit $BSR_{linear}$
	$\widehat{BSR}'$	$BSR_{linear}$		
<b>FKOH03</b>	1.759	2.383	0.74	0.56
<b>FKOH08</b>	1.591	1.637	0.97	0.85
<b>KMMH03</b>	2.045	6.192	0.33	0.92
<b>KMMH09</b>	2.867	5.421	0.53	0.76
<b>KMMH14</b>	3.065	5.862	0.52	1.04
<b>MYZH10</b>	0.607	0.890	0.68	1.03
<b>MYZH13</b>	1.028	1.275	0.81	0.91
<b>OITH11</b>	2.104	4.311	0.49	0.70

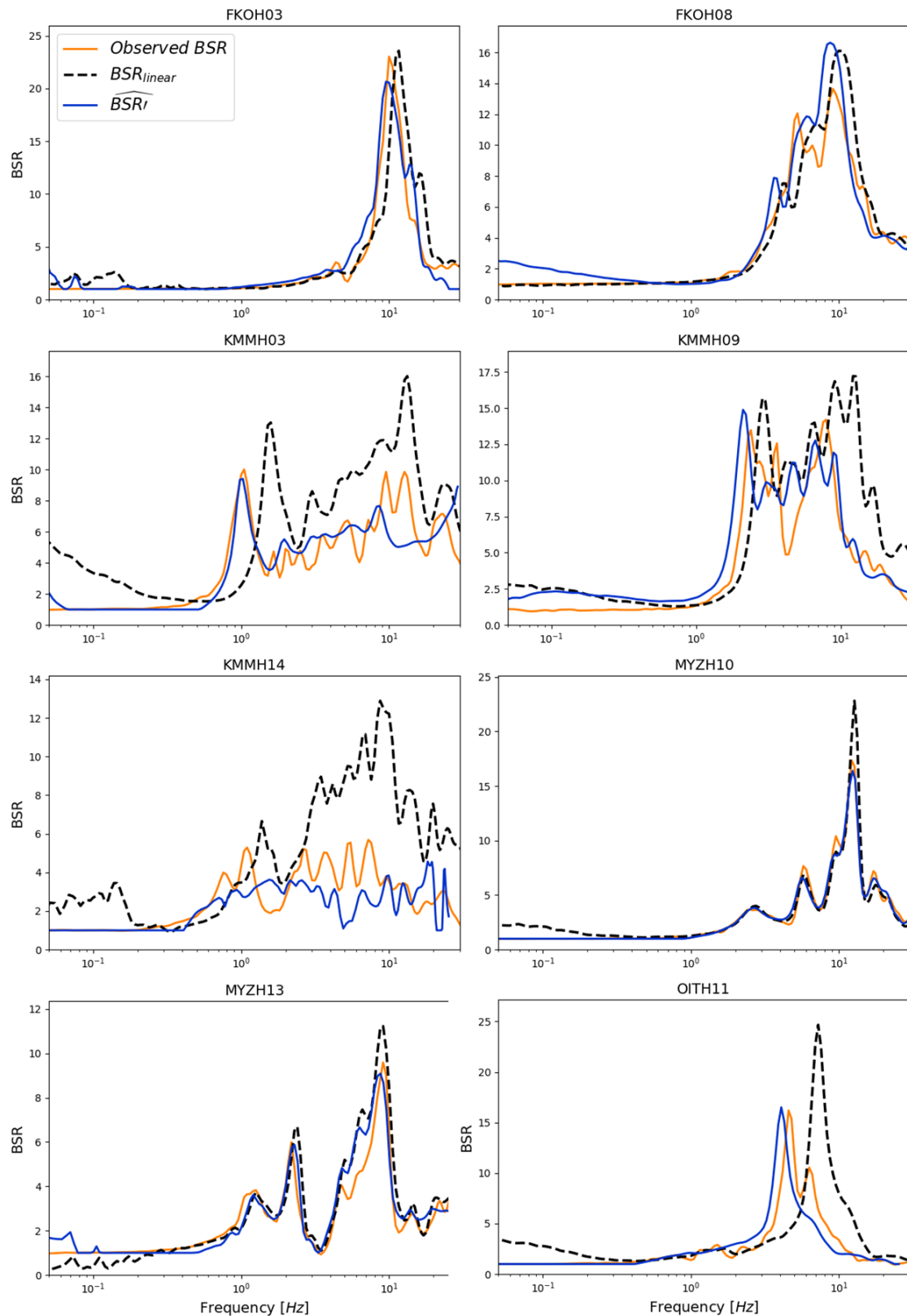


Figure III-20. BSR estimation for Kumamoto earthquake correcting by shift decrease ( $f_{sp}$ ) and amplification reducing  $\Delta BSR_{ISA}$ .

Comparing the results shown in this section with the predictions that just took into account the correction of the frequency shift (section III.5), the estimations for the sites with high non-linearity are improved (Table III-3 and Table III-10). Even if in many cases it still underestimates

the site response amplification level. For instance, at KMMH14 (Figure III-20), the main peak amplitudes are lower than the observed amplification. Additionally, for weak ground motion the variability in the amplitude of  $BSR$  is still too high to ensure a perfect prediction, participating thus to the uncertainty of the evaluation. In particular, we must keep in mind that the amplification correction could result in an underestimation of the real site response leading in a misevaluation of strong ground motion at the surface.

### III.7.3 Prediction of the Fourier spectrum at surface

Once the site response is estimated ( $\widehat{BSR}'$ ), the seismic ground motion at surface is obtained following the same methodology explained in the section III.5 and it's Fourier spectrum can be computed.

The spectra at all the sites, as is expected from the results for BSR, is better predict in comparison with the results obtained by the use of the linear site response (Figure III-21), at least for sites having high non-linear effects. Indeed, the frequency peaks and the amplitudes are better estimated for sites where the decrease of the amplitude and the shift of the site's response were significant (KMMH03, OITH11, or KMMH14). For the stations where the non-linearity is not as significant, it appears that using directly the linear BSR gives already a good estimation of the surface motion (Table III-11).

Table III-11. Comparison of the misfit of the horizontal spectrum (from  $\widehat{BSR}'$ ) at the surface with respect to the observed one.

Name	Misfit to observed $S_{surface}$		Misfit $\widehat{BSR}'$ / Misfit $BSR_{linear}$	Misfit $\widehat{BSR}$ / Misfit $BSR_{linear}$
	$\widehat{BSR}'$	$BSR_{linear}$		
<b>FKOH03</b>	0.049	0.049	1.00	0.77
<b>FKOH08</b>	0.055	0.045	1.22	0.91
<b>KMMH03</b>	0.359	1.392	0.26	0.72
<b>KMMH09</b>	0.280	0.356	0.79	0.93
<b>KMMH14</b>	0.654	1.332	0.49	1.52
<b>MYZH10</b>	0.022	0.025	0.88	1.08
<b>MYZH13</b>	0.046	0.046	1.00	0.77
<b>OITH11</b>	0.379	0.673	0.56	0.86

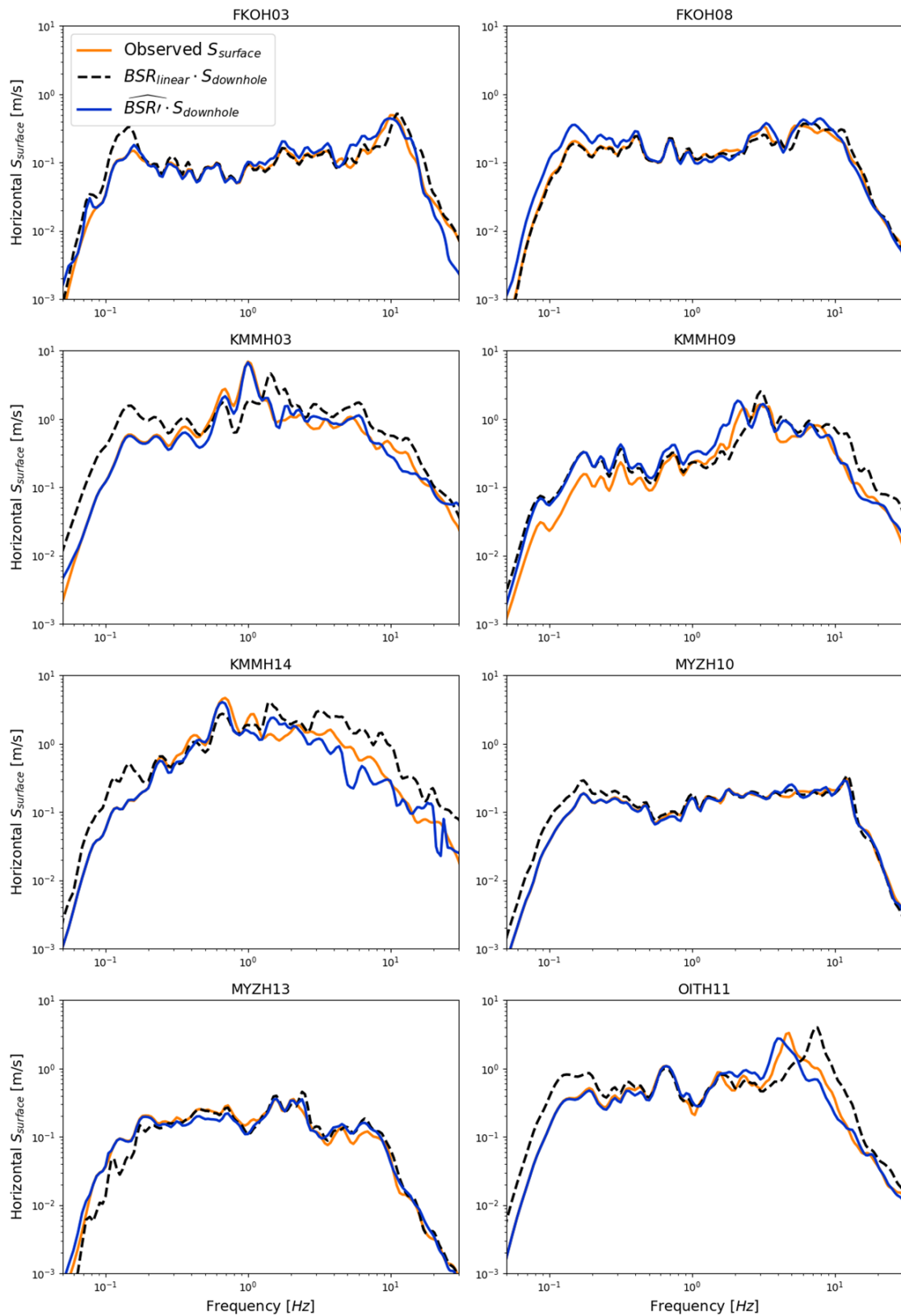


Figure III-21. Horizontal Fourier spectra for the Kumamoto earthquake.

#### III.7.4 Time history prediction

We compute the accelerometric time histories by using the phase of the downhole station. We obtain here an overall better fitting in the amplitude of the signal (Figure III-22) than using  $f_{sp}$

correction. Table III-12 gives the PGA in order to compare the predictions to the real data. Surprisingly, the predicted PGA taking into account the site non-linear behavior is not better than the one considering the linear site response. This is certainly due to the fact that PGA depends on the whole frequency band of the signal. Indeed, the misestimation of PGA is representative of the uncertainties for all frequencies.

Table III-12. PGA comparison between the simulation with linear and non-linear correction (including decrease of the amplification), and observation.

Station	$PGA_{surface}$ observed [ $m/s^2$ ]	$PGA_{surface}$ from $\widehat{BSR}'$ [ $m/s^2$ ]	$PGA_{surface}$ from $BSR_{linear}$ [ $m/s^2$ ]
FKOH03	1.34	1.57	1.56
FKOH08	1.01	1.59	1.53
KMMH03	7.87	6.86	7.74
KMMH09	2.46	3.99	4.51
KMMH14	6.08	4.20	9.95
MYZH10	0.97	0.80	0.83
MYZH13	0.50	0.59	0.65
OITH11	5.74	7.77	12.31

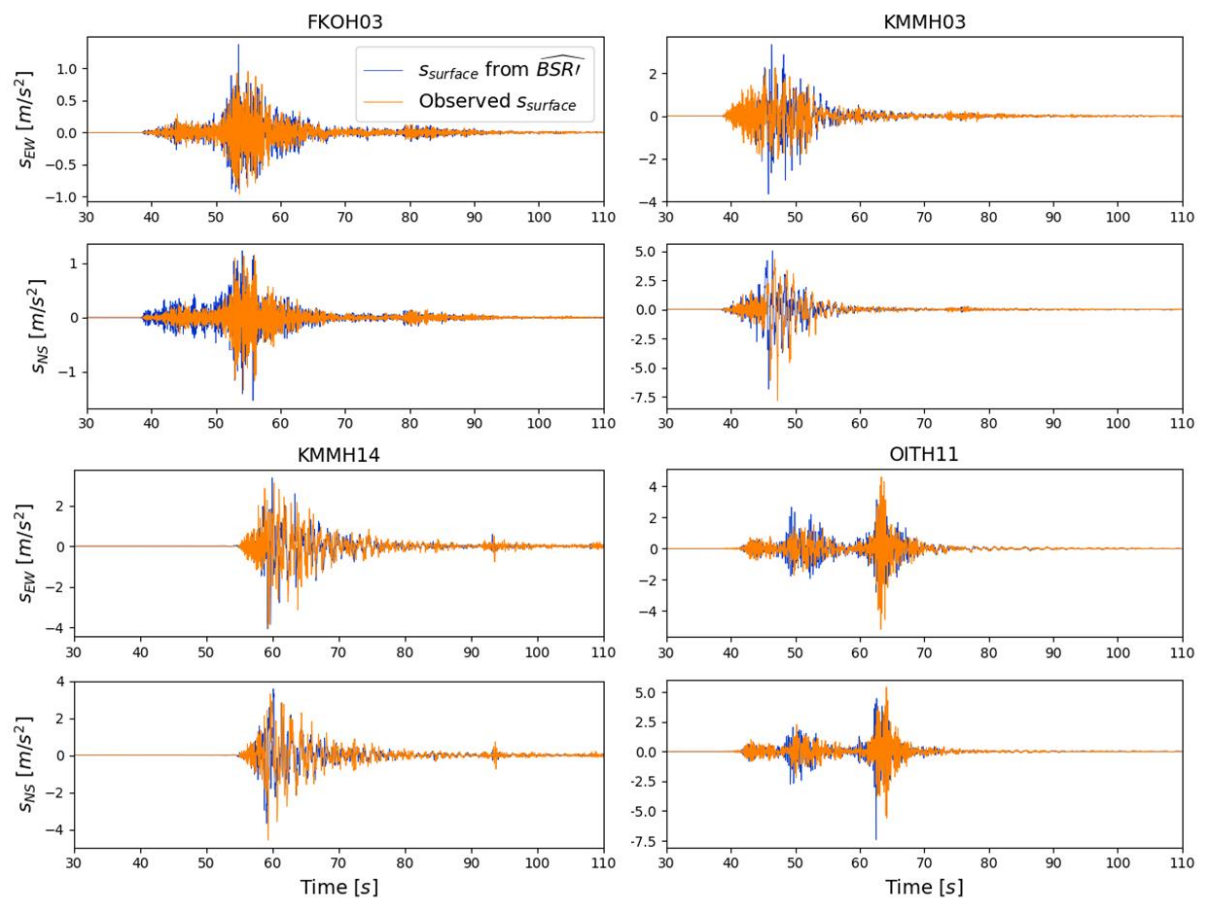


Figure III-22. Time histories of Kumamoto earthquake and the predictions involving a correction by a decrease of the amplification.

### III.7.5 Prediction of the response spectra

Regarding the response spectra, the improvement is especially significant for periods around the main peak (Figure III-23). In some cases, using  $BSR_{linear}$  the pseudo acceleration ( $S_a$ ) is overestimated, especially at sites FKOH08, KMMH14, and MYZH13. At the other sites, the simulation overestimates the low periods.

In general, the response spectra confirm that the procedure detailed here improves the prediction of the seismic ground motion.

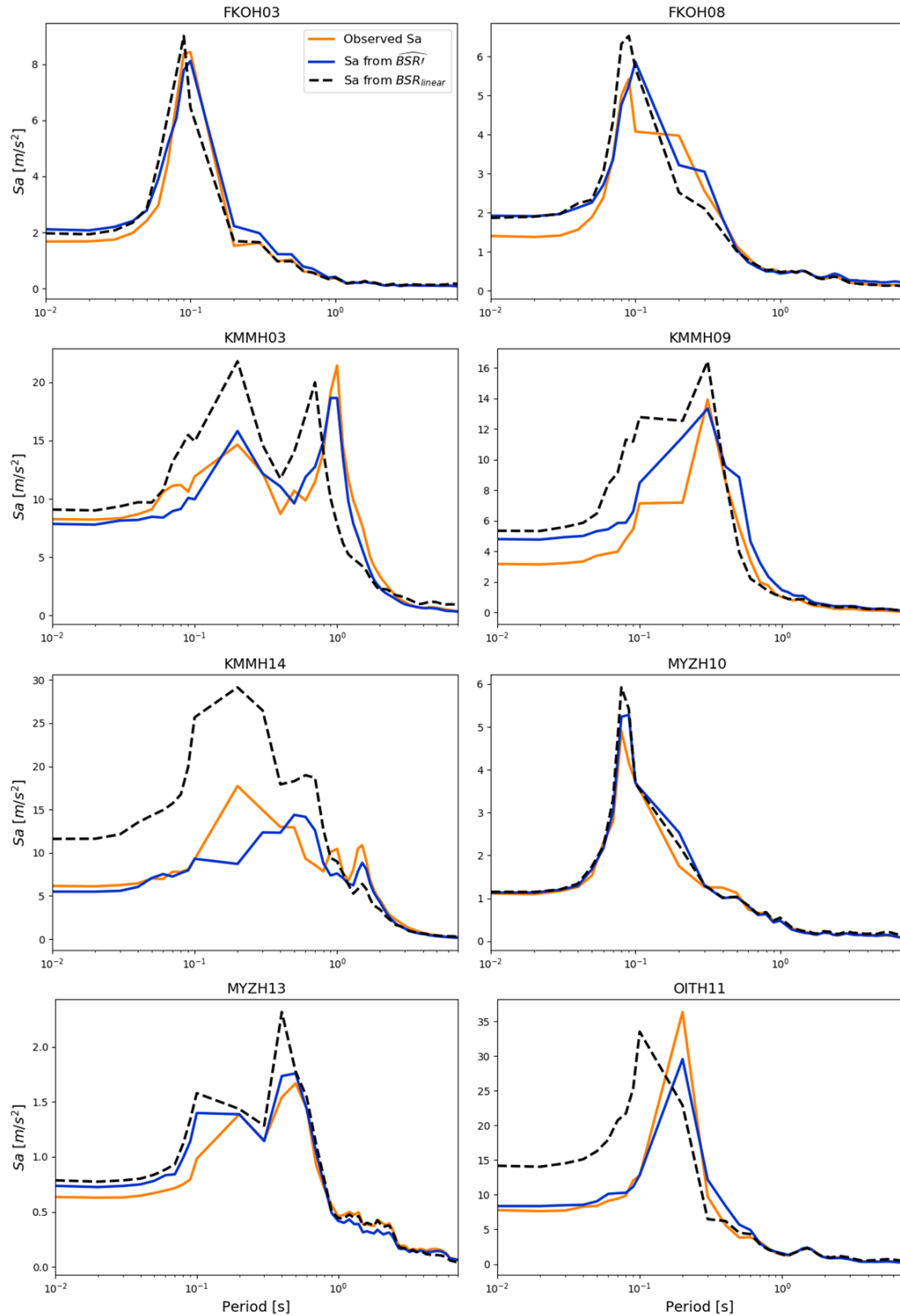


Figure III-23. Response spectra comparison for the approximations and the observed one for Kumamoto earthquake.

### III.8 Conclusion

A methodology to quantify the effects of non-linear soil behavior through the estimation of the frequency shift and the decrease of amplification level in the Borehole Spectral Ratio ( $BSR$ ) is proposed.

The logarithmic shift of  $BSR$ , referred to as the frequency shift parameter ( $fsp$ ), is related with the intensity of the incoming seismic solicitation. Following this observation, we can blindly estimate the non-linear effects for future strong ground motions.

Similarly, we found a relationship between the intensity of the seismic input ground motion and the decrease of the amplification level. The computation of this relation is still a difficult task with a higher dispersion than for the  $fsp$  curves.

For the earthquake of Kumamoto 2016, we estimated the non-linear site response and the Fourier spectrum at the surface, including the non-linear effects. The prediction provided very close results to the observations and improve by 40% the evaluation compared to a linear evaluation.

The trend of the  $fsp$  curves gives a way to quantifies how prone a site is to develop non-linear effects as well as a possible way to quantify the level of non-linearity of the soil under strong earthquakes.

The work herein presented is very promising for the prediction of the non-linear ground motion. However, some limitations can be mentioned, and they are the subject of current work:

- The methodology used to evaluate the decrease of the amplification level must still be more studied and calibrated, since the selection of the surface is complicated to define to find the trend between intensity ( $PGA_{downhole}$ ),  $BSR_{linear}$ , frequency, and a decrease of the amplification ( $\Delta BSR_{isa}$ ).
- To estimate the ground motion at the surface in the time domain, the phase modification due to the site effects must be taken into account. This effect has been studied before, and usually is assumed that adding a minimal phase to spectral ratio amplitude, the effect is considered (Brax et al., 2016). However, since we are using borehole arrays configuration, the applicability of the same assumptions must still be studied.

We relate the non-linearity of the of the soil with the intensity of the ground motion, quantified by the  $PGA_{downhole}$ . However, other intensity parameters could be tested in the future to reduce the dispersion of the  $fsp$  curves.

## Chapter IV Evaluation of $f_{sp}$ on H/V spectral ratio

In this chapter an alternative approach for computing  $f_{sp}$  to avoid the need of a downhole station is described. In the previous chapters, borehole arrays were used to analyze the site effect, however as was mentioned, the downhole station recordings include the downwards waves that are reflecting from the surface. Additionally, setting up a vertical array is difficult, requires larger investments and only few data around the world are existing in comparison with data from surface stations.

We thus worked on a methodology using the already well-known H/V spectral ratio technique. We are analyzing in this chapter the frequency shift of this curve to lower frequencies, going from weak to strong ground motions.

### IV.1 Earthquake H/V spectral ratio technique

The H/V spectral ratio on earthquake recordings is a technique to estimate site transfer function for the empirical site effects evaluation. Originally the technique was proposed by Nogoshi and Igarashi, (1971). This approach consists in the computation of the ratio of the horizontal components Fourier spectrum with the spectrum of the vertical one. We consider here the combination of the horizontal recordings:

$$A_{\{H/V\}}(f) = \frac{\sqrt{EW_{surf}^2 + NS_{surf}^2}}{UD_{surf}} \quad (IV-1)$$

Where EW and NS represent the horizontal Fourier spectra of the components in east-west and in north-south directions respectively. UD is the Fourier spectrum of the vertical component.

If this technique was first used with ambient vibration (Nakamura, 1989) in order to estimate the site effects, it has been applied to earthquakes assuming that the vertical component is not affected by the site effect and can thus be used as a reference (Langston, 1979). Lermo and Chávez-García, (1993) compares the result of the  $A_{\{H/V\}}$  curve with standard spectral ratios from real records and analytic models, concluding that earthquake H/V spectral ratio technique is adequate to evaluate site effects from simple geology and for weak ground motions, especially the first frequency peak of the transfer function ( $f_0$ ). This have been corroborated by other studies (e.g. Duval et al., 2001).

### IV.2 $A_{\{H/V-linear\}}$ curve and fundamental frequency of the site, $f_{0\{H/V\}}$

The earthquake H/V spectral ratio,  $A_{\{H/V\}}(f)$ , is a function that can change between strong ground motions and weak ground motion, mainly due to the effects of the non-linearity (Wen et al., 2006). Those changes will be analyzed in the next section of this chapter. In this section the computation of the H/V spectral ratio from weak ground motion is shown.

A similar methodology to the one presented in the section I.4 for  $BSR_{linear}$  is proposed. Taking in account H/V spectral ratio from weak ground motions, a linear curve for the site is computed (Eq. IV-2).

$$A_{\{H/V-linear\}}(f) = \frac{\sum_{i=1}^n A_{\{H/V\}_{weak(i)}}}{n} \quad (IV-2)$$

The weak ground motions are selected using the recordings having a  $PGA_{downhole}$  between  $10^{-4} m/s^2$  and  $6 \cdot 10^{-3} m/s^2$ . The Figure IV-1 gives two examples for the stations, IBRH11 and KSRH10, already considered in the previous chapter.

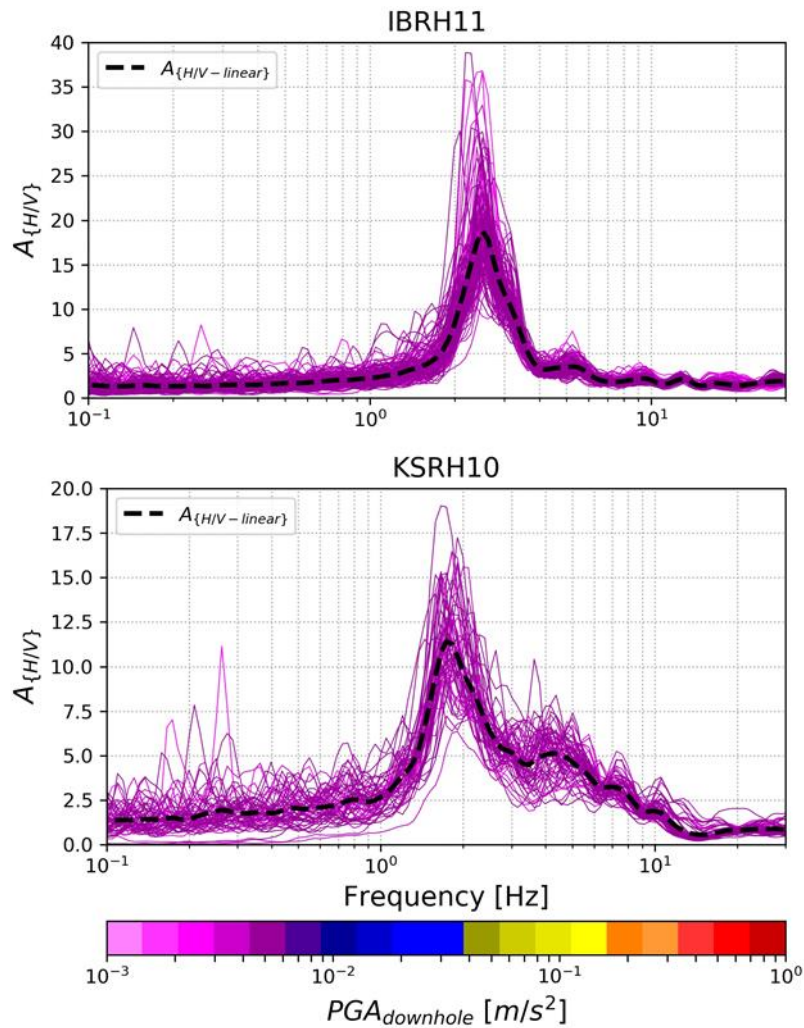


Figure IV-1. H/V spectral ratio curves from weak ground motions and definition of  $A_{\{H/V-linear\}}$ . Sites IBRH11 top, KSRH10 bottom.

Isolating weak ground motion allows to define a unique H/V curve that we supposed to be characteristic of the site linear response (Figure IV-1). The H/V spectral ratio for strong ground motions present a higher variation and different frequency peaks than the weak ground motions.

$A_{\{H/V-linear\}}$  curve (Figure IV-1) presents a more irregular shape, in comparison with  $BSR_{linear}$  (Figure IV-2), with a higher dispersion and less frequency peaks. In general, often the  $A_{\{H/V-linear\}}$  curves present just one clear frequency peak, showing that they are only able to point out the fundamental resonance frequency and mainly detect the main impedance contrast in the soil column (Lermo and Chávez-García, 1993). Also,  $A_{\{H/V\}}$  technique is not affected by downward waves as  $BSR$  is, removing the peaks from this effect.

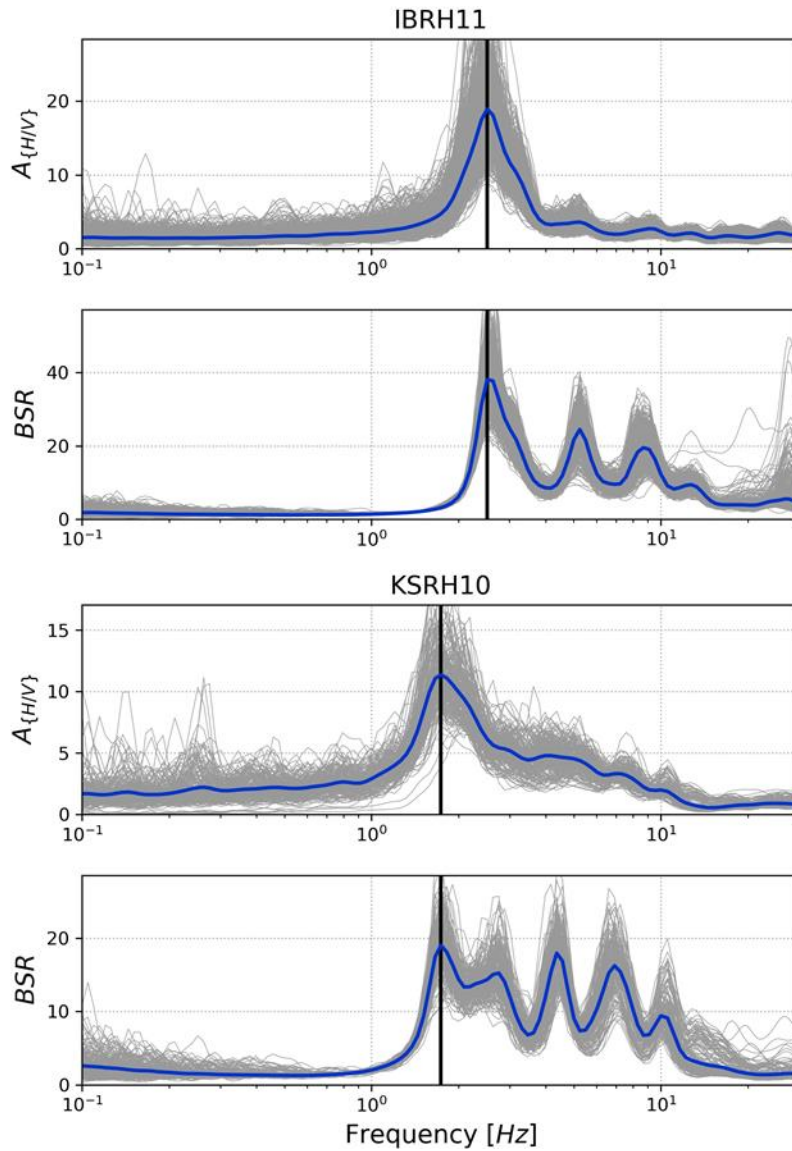


Figure IV-2. Comparison of  $BSR_{linear}$  and  $A_{\{H/V\}-linear}$  (blue lines) for the sites IBRH11 and KSRH10. Gray lines represent the weak ground motions. Black vertical line the fundamental frequency for each curve.

The fundamental resonance peak in  $A_{\{H/V\}-linear}$  and  $BSR_{linear}$  is found approximately at the same frequency (Figure IV-2) : 2.5Hz at IBRH11 and 1.7 Hz at KSRH10. However,  $A_{\{H/V\}}$  present usually several local peaks that make the picking of the first peak complicated. Due to this, the interpretation of H/V spectral ratio must be done carefully (Acerra et al., 2004; Koller et al., 2004). In the work presented here, the recommendations of the SESAME European project (Acerra et al., 2004) are taken to determine the main fundamental frequency peak for  $A_{\{H/V\}}$ , called  $f_{o\{H/V\}}$ . However, SESAME methodology is working with ambient vibration recordings and we follow only part of their recommendations, to adapt them to earthquake H/V spectral ratios.

The algorithm used to automatically detect the fundamental frequency is based on four criteria. The two first concerns the amplitude ( $A_{\{H/V\}}$ ) : it must decrease at least to the half of the peak amplitude, in the frequency windows going from one fourth of the resonance peak to the peak itself ( $f_{o\{H/V\}}$ ) and from the resonance peak to four times the peak.

$$\exists f \in \left[ \frac{f_{o\{H/V\}}}{4}, f_{o\{H/V\}} \right] : A_{\{H/V\}-linear}(f) < 0.5 A_{\{H/V\}-linear}(f_{o\{H/V\}})$$

$$\exists f \in [f_{o_{\{H/V\}}}, 4 \cdot f_{o_{\{H/V\}}}] : A_{\{H/V-linear\}}(f) < 0.5 A_{\{H/V-linear\}}(f_{o_{\{H/V\}}})$$

The third criterion requires that the amplitude of the selected peak is upper than two.

$$A_{\{H/V-linear\}}(f_{o_{\{H/V\}}}) > 2$$

The fourth criterion uses the standard deviation of the amplitude between all the record considered ( $\sigma_{A_{\{H/V\}}}$ ). The criterion establishes that there is a peak on the curve  $A_{\{H/V\}} \pm \sigma_{A_{\{H/V\}}}$  very close to  $f_{o_{\{H/V\}}}$ , specifically between  $[0.95 f_{o_{\{H/V\}}}, 1.05 f_{o_{\{H/V\}}}]$ .

$$\begin{aligned} \exists f \in [0.95 \cdot f_{o_{\{H/V\}}}, 1.05 \cdot f_{o_{\{H/V\}}}] : \frac{d}{df} (A_{\{H/V-linear\}} \pm \sigma_{A_{\{H/V-linear\}}}) \\ = 0 \text{ and } \frac{d^2}{df^2} (A_{\{H/V-linear\}} \pm \sigma_{A_{\{H/V-linear\}}}) < 0 \end{aligned}$$

Because we are using earthquake recordings instead of ambient vibrations, other criteria from SESAME (Acerra et al., 2004) are not used to define  $f_{o_{\{H/V\}}}$ . Analyzing the whole spectral H/V ratio, the peak detected at the lowest frequency and matching three of the four criteria is selected as the fundamental resonance frequency ( $f_{o_{\{H/V\}}}$ ). Comparing this method with the first frequency peak found on the *BSR* curve ( $f_{o_{\{BSR\}}}$ ) for all the database (Figure IV-3), we observe that for most of the stations  $f_{o_{\{H/V\}}}$  and  $f_{o_{\{BSR\}}}$  coincide. For some sites, however, those values are not equal. This mismatch can, in some cases at least, be due to the difficulty of defining the first peak added to the dispersion associated with the  $A_{\{H/V\}}$  curves. For example, at AKTH14 the first peak is too small, and is not detected among the of  $A_{\{H/V\}}$  dispersion (Figure IV-4).

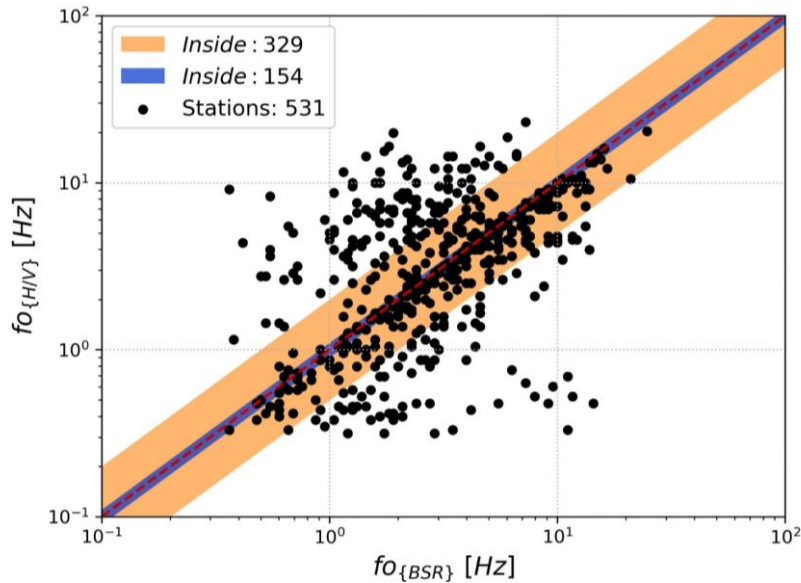


Figure IV-3. Comparison of the first frequency peak ( $f_o$ ) computed from *BSR* and from *H/V* curves. Orange range is  $f_{o_{\{H/V\}}} = [0.5, 2] f_{o_{\{BSR\}}}$ . Blue range represents the range  $f_{o_{\{H/V\}}} = [0.9, 1.1] f_{o_{\{BSR\}}}$ .

Figure IV-3 shows that for some stations  $f_{o_{\{H/V\}}}$  is lower than  $f_{o_{\{BSR\}}}$ . FKSH11 is one example of this observation (Figure IV-4). This difference could occur due to the presence of a strong contrast located somewhere underneath the vertical array. In this case the contrast is not detected by  $BSR_{linear}$ , but it can appear on the H/V spectral ratio. At FKSH11 for example, the downhole station is located at 100 m deep in a layer characterized by a  $V_s$  of 700 m/s, indicating that the bedrock may not have been reached and a sharp velocity contrast may exist deeper. On the contrary, the cases where  $f_{o_{\{H/V\}}}$  is higher than  $f_{o_{\{BSR\}}}$  may be related with a strong contrast

at shallower depth that makes that a deeper contrast is too weak, and the peak disappears in the variability of H/V.

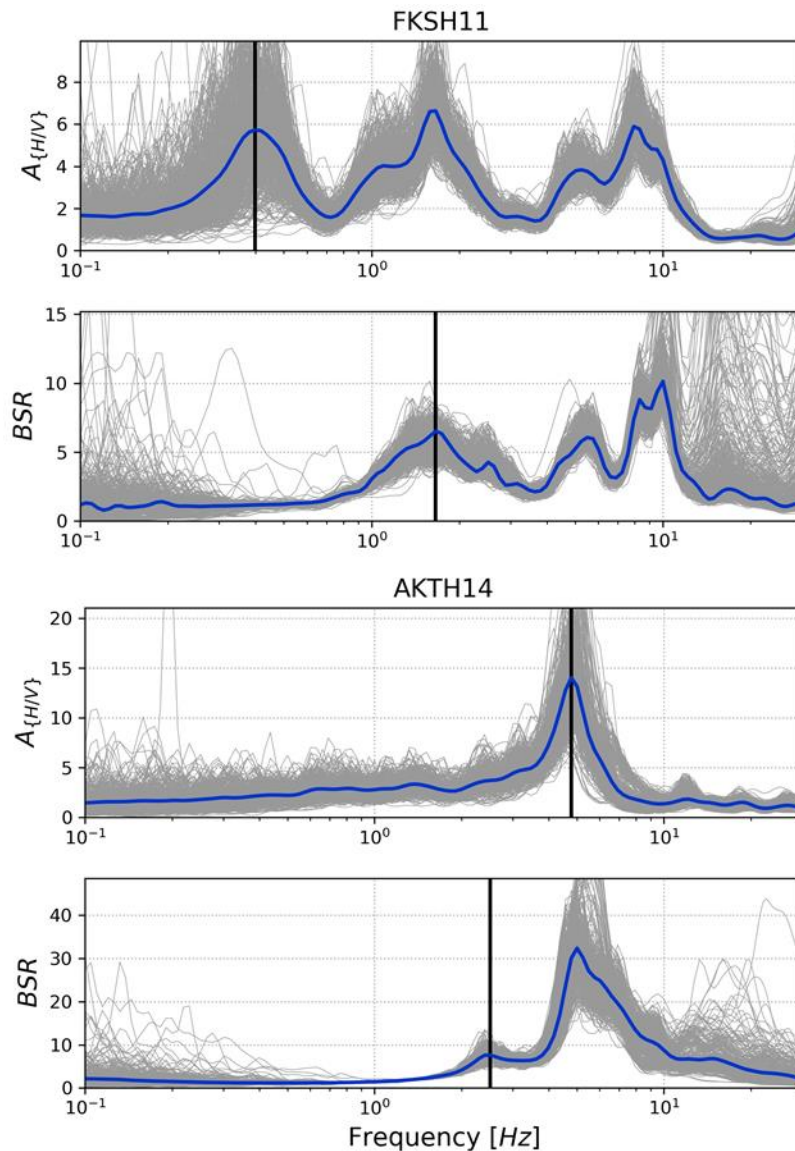


Figure IV-4. Comparison of  $BSR_{linear}$  and  $H/V_{linear}$  (blue lines) for the sites FKSH11 and IBRH15 where  $f_0$  does not coincide. Gray lines represent the weak ground motions. Black vertical line the fundamental frequency for each curve

### IV.3 Effects of the non-linearity on the curve of H/V ratio

Figure IV-5 shows  $A_{H/V}$  for two sites (IBRH11 and KSRH10). We observe a dependency of  $A_{H/V}$  with the intensity of the ground motion, measured by  $PGA_{downhole}$ . This variation in  $A_{H/V}$  is related with the decrease of stiffness in the soil for strong ground motions (Wen et al., 2006). Like  $BSR$  curves, the strong ground motions generate a shift to lower frequencies of the fundamental resonance peak.

Contrary to what we observe on  $BSR$ , the amplitude of  $A_{H/V}$  curves do not show any difference between weak and strong ground motions (Figure IV-5). The strong ground motion can develop both, higher and lower values in the  $A_{H/V}$  curves with respect  $A_{H/V-linear}$ . This high variation of the amplitude in  $A_{H/V}$  has been detected in several previous studies, and this amplitude is not

related with the amplification of the site (e.g. Bonilla et al., 1997). Due to this, the analysis presented herein focuses on the frequency shift phenomenon only.

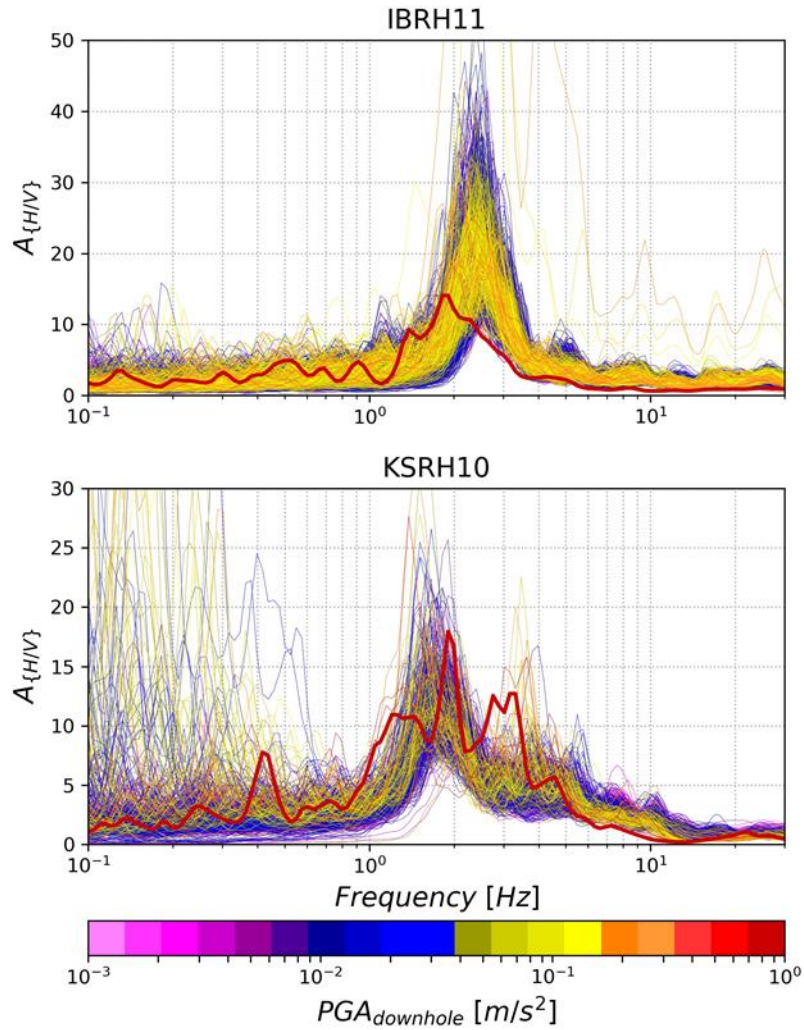


Figure IV-5. HV ratio curve in function of the  $PGA_{downhole}$  for sites IBRH11 and KSRH10.

For analyzing the shift of  $A_{\{H/V\}}$  to lower frequencies, a methodology similar to the one established for  $f_{sp}$  (see section III.3) is proposed. Each  $H/V$  curve from each recorded ground motion is compared with  $H/V_{linear}$  to estimate the shift between both curves. The algorithm for computing  $f_{sp}$  is the same that the one explained in the subsection III.3.2 and detailed in the Eq. (III-3) and (III-4), but in this case, instead of  $BSR$  and  $BSR_{linear}$  curves,  $A_{\{H/V\}}$  and  $A_{\{H/V-linear\}}$  curves are used. It leads to a new definition of  $f_{sp}$ :

$$\psi = \sum_i \left| A_{\{H/V-linear\}} \left( \frac{\bar{f}}{L_S} \right) - A_{\{H/V\}}(\bar{f}) \right| \Delta x$$

$$\Delta x = \log_{10}(f_{i+1}/f_i) \quad \text{and} \quad \bar{f} = 0.5 \cdot (f_{i+1} + f_i)$$

$$f_{sp} = \left( \arg \min_{L_S} \psi \right)^2$$

Applying this equation for all the recorded ground motions at IBRH11 and KSRH10 (Figure IV-6) a  $f_{sp}$  is defined for each event and a  $f_{sp}$  curve can be obtained from a regression among the data. This curve has a higher dispersion in comparison with the one computed from  $BSR$ . This is

linked to the higher dispersion that  $A_{\{H/V-linear\}}$  computation exhibits, making  $f_{sp\{H/V\}}$  definition more difficult.

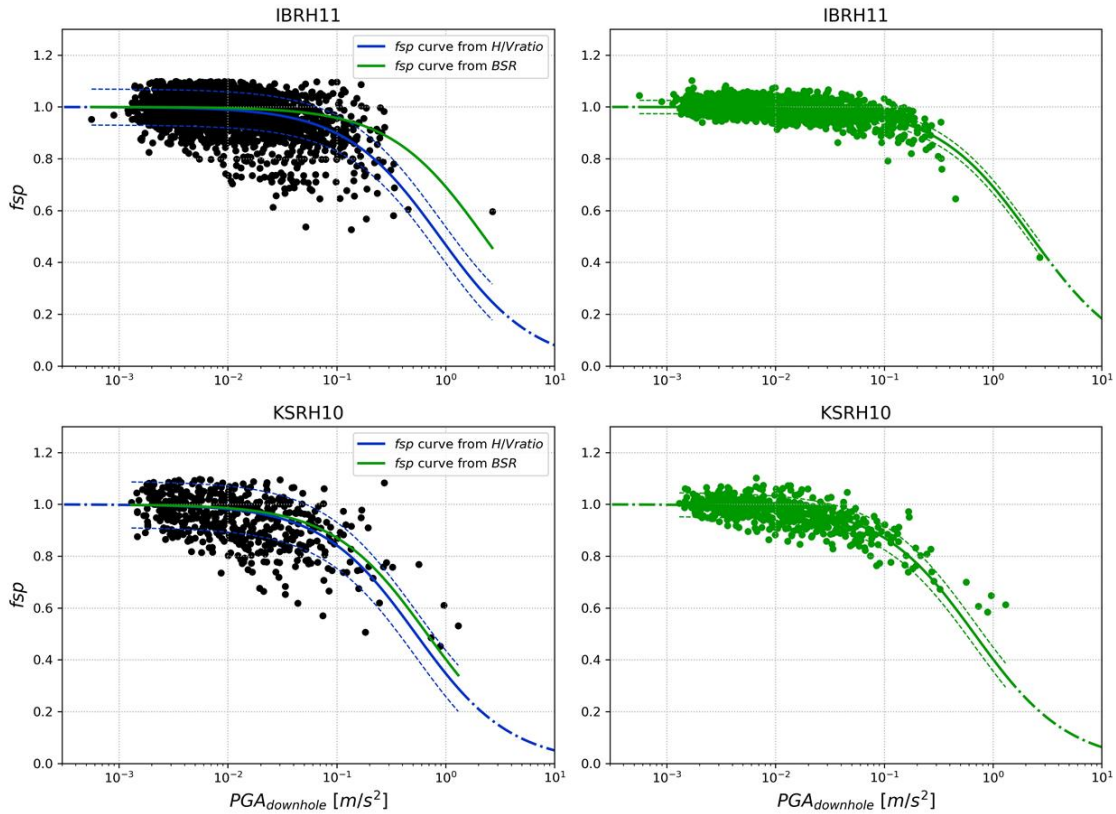


Figure IV-6.  $f_{sp}$  points computed from the shift in the  $A_{\{H/V\}}$  curve (left column) and comparison with  $f_{sp}$  points and curves from  $BSR$  (right column). Sites IBRH11 and KSRH10. Dashed lines represent plus-minus the standard deviation curves.

The  $f_{sp}$  curves derived from  $A_{\{H/V-linear\}}$  show that  $f_{sp}$  decreases when seismic solicitation increases. It indicates, as expected, that strong ground motions generate a shift to lower frequencies in the  $A_{\{H/V\}}$  curves.

#### IV.4 Analysis of $f_{sp}$ curves for all the whole database.

Figure IV-6 shows that the  $f_{sp}$  curves from  $A_{\{H/V-linear\}}$  and  $BSR_{linear}$  are close, even if the dispersion is very different. The data are fitted with a hyperbolic function having a shape depending on one single parameter,  $PGA_{Ref}$ :

$$\widehat{f_{sp}} = \frac{1}{1 + \frac{PGA_{downhole}}{PGA_{Ref_{downhole}}}}$$

In this case,  $PGA_{ref_{downhole}}$  is the  $PGA_{downhole}$  when  $f_{sp}$  takes a value of 0.5. We interpret low  $PGA_{ref_{downhole}}$  as a sign that the associated site is more prone to develop non-linear effects. The parameter is called  $PGA_{ref_{downhole-HV}}$ , if it comes from the  $H/V$  spectral ratio technique, and  $PGA_{ref_{downhole-BSR}}$ , if it comes from  $BSR$  curves (Figure IV-7).

Figure IV-7 shows that there is a good correlation between both  $PGA_{ref}$ , but the dispersion associated is large. This dispersion is due to the complexity of the definition a  $f_{sp}$  curve using  $H/V$  data, as it is observed in the Figure IV-6 for both examples. For some sites, both curves are totally different. Usually they correspond to sites where the  $f_{sp}$  curve is derived from only few data making the computation uncertainty very high.

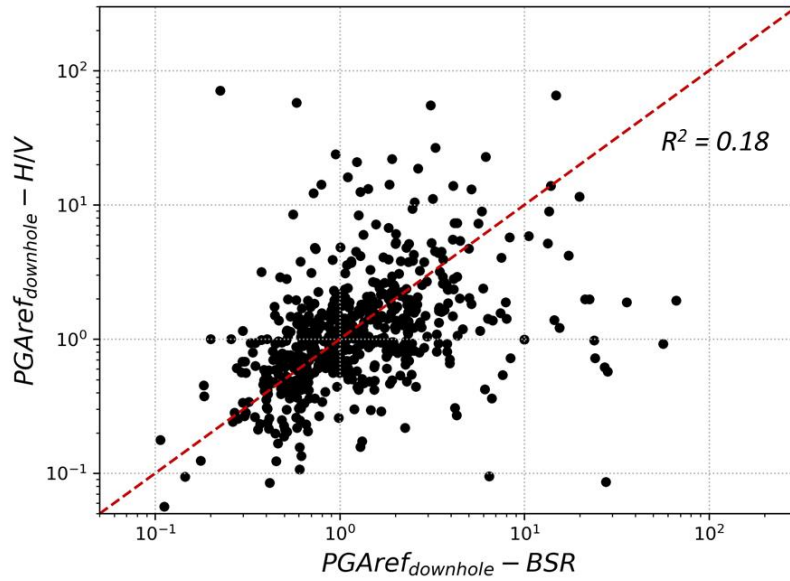


Figure IV-7. Comparison between  $f_{sp}$  curves from  $H/V$  and  $BSR$  data.

$PGAref_{downhole-HV}$  and  $PGAref_{downhole-BSR}$  are quite equivalent for all the station. The observed difference is related with the uncertainty of the estimation of  $f_{sp}$  curves. In a general way, although there is a high variability, we conclude that  $PGAref_{downhole-HV}$  and  $PGAref_{downhole-BSR}$  are equivalent. It means that the shift related with the non-linear effects is equivalent for  $A_{\{H/V\}}$  and the  $BSR$ .

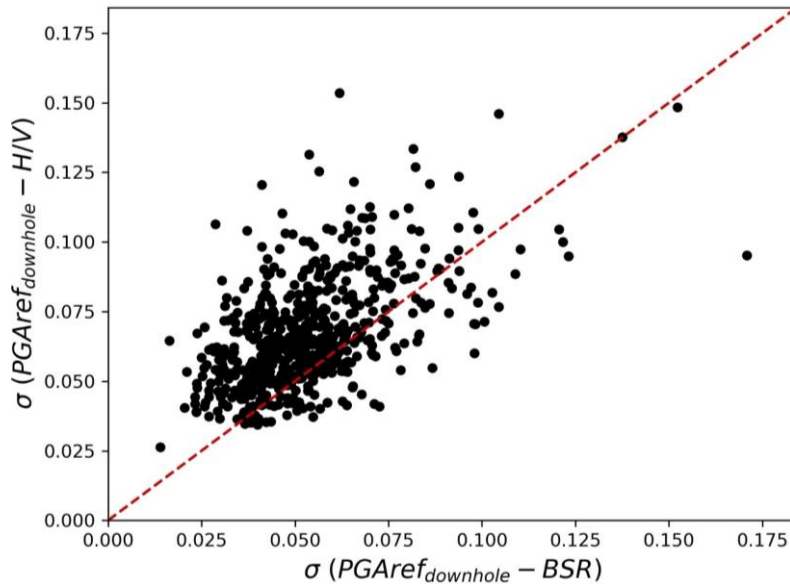


Figure IV-8. Comparison of the dispersion (Eq. (IV-3)) for  $H/V$  and  $BSR$  computation. From 596 site, there are 476 above the 1:1 curve (red dashed line).

To study the dispersion between the  $f_{sp}$  curves, the standard deviation is computed around the prediction error for each point as:

$$\sigma = std(f_{sp} - \widehat{f_{sp}}) \quad (IV-3)$$

Where  $f_{sp}$  is the value computed from the data (Eq. (III-3) and (III-4)) and  $\widehat{f_{sp}}$  is computed following the hyperbolic regression process (Eq. (III-5)). The curves taking into account the

standard deviation is represented by dash lines in the plots (Figure IV-6). For most of the sites  $\sigma$  is lower using *BSR* curves (Figure IV-8). Indeed, among the 596 sites where the definition of a *fsp* curve is considered as feasible, 476 presents a lower standard deviation using *BSR* to define *fsp*. It indicates that the borehole arrays have a better performance than  $A_{(H/V)}$  curves in the evaluation of the influence of the decay of stiffness in the site response.

However, for some sites the definition of the *fsp* curve with *H/V* technique has a similar or even lower dispersion ( $\sigma$ ) than using borehole arrays (*BSR*) (Figure IV-8). In Figure IV-9 are shown eight sites where the *fsp* curve can be identified with *H/V* ratio curves. Those sites do not present any similarity in the  $V_s$  profile (Figure IV-10). Although most of them present high values of shear velocity at shallow layers.

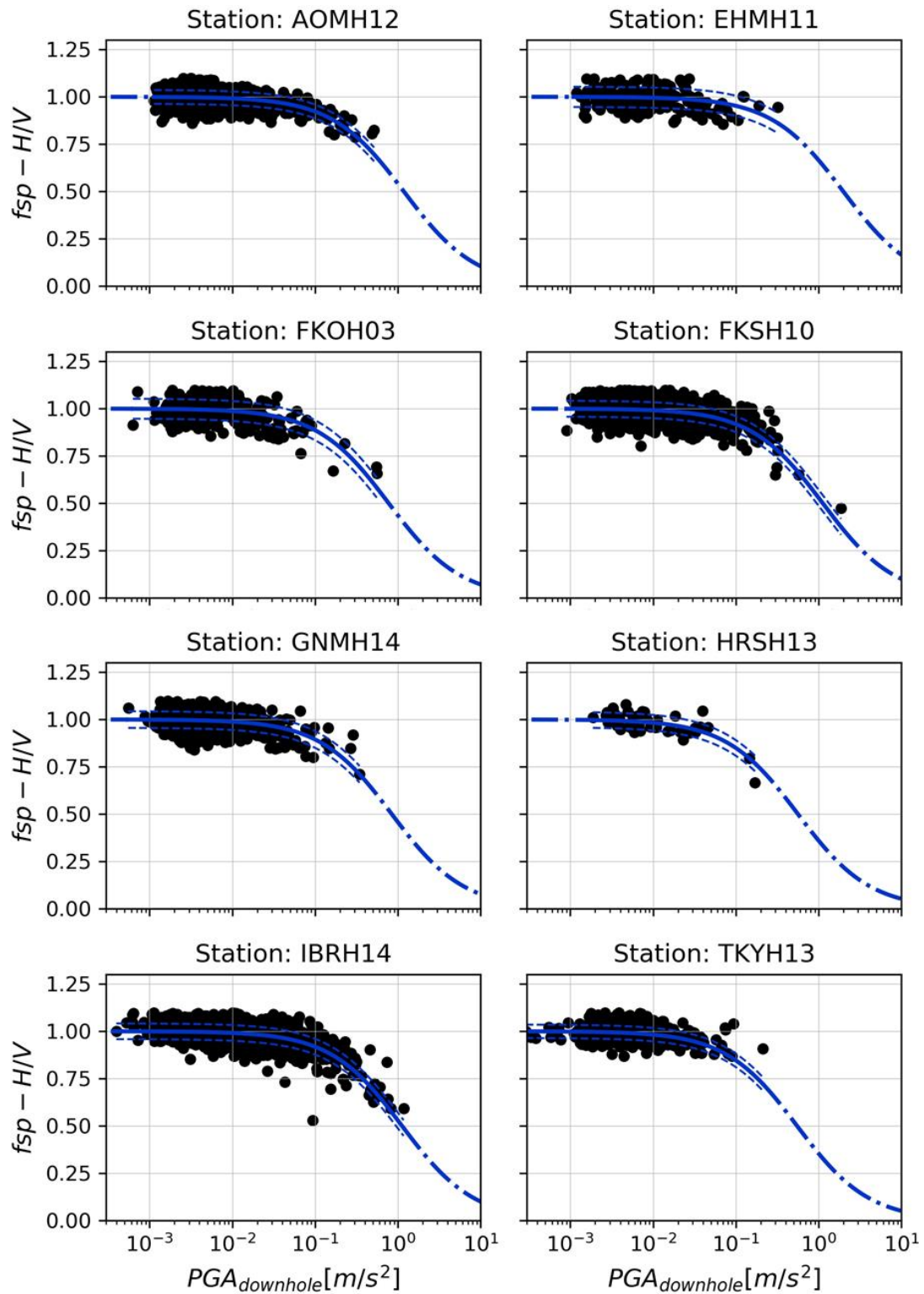


Figure IV-9. Examples of sites where  $f_{sp}$  curves were computed from H/V data and they are well defined.

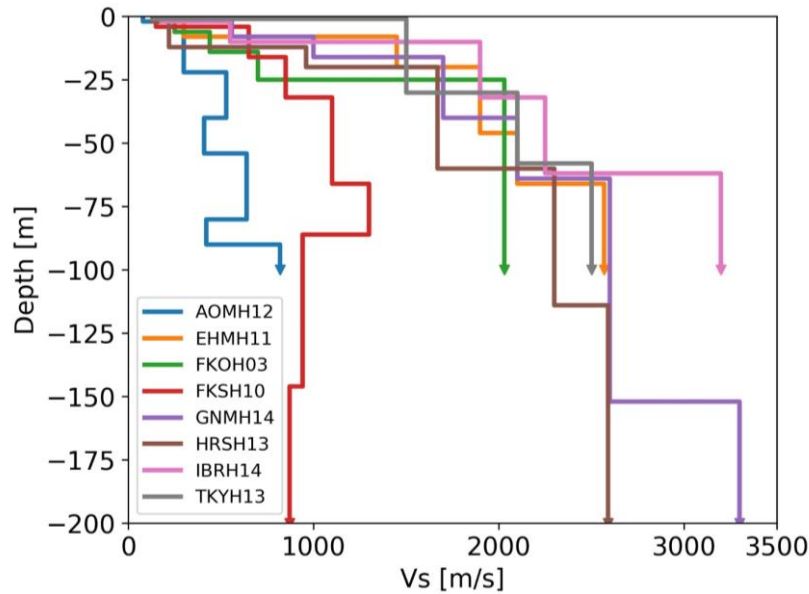


Figure IV-10. Vs profile for some sites where  $f_{sp}$  curve is well defined.

#### IV.5 Summary and discussion

This chapter is focused on the impact of the non-linear soil behavior on the earthquake  $H/V$  spectral ratio ( $A_{\{H/V\}}$ ). The fundamental frequency ( $f_0$ ) derived from those curves is more or less similar than the one obtained with  $BSR$  computation. However, we notice that under the same conditions  $f_0$  can differ for both methodologies, especially when there is a high variability between  $A_{\{H/V\}}$  curves.

When strong ground motions are used,  $A_{\{H/V\}}$  curves present a shift of the resonance peak to lower frequencies, quantified by the  $f_{sp}$  parameter. This shift increases with the intensity of the ground motion, expressed in this chapter in terms of PGA at the downhole sensors.

The analysis of  $A_{\{H/V\}}$  curves shows that their amplitude is not related to the intensity of the shakings. Several studies already established that the amplitude of the  $H/V$  curve shouldn't be considered as an estimation of the level of amplification due to lithological site effects (e.g. Bonilla et al., 1997; Lermo and Chávez-García, 1993)

We compare  $f_{sp}$  derived from the analysis of the  $A_{\{H/V\}}$  curves, with the shift already studied in the Chapter III that is computed using borehole spectral ratios ( $BSR$ ). We find a similar trend of the  $f_{sp}$  curves computed with both methodologies. The main difference is that, in general,  $f_{sp}$  curves from  $H/V$  data have a higher dispersion. From this aspect, it is possible to conclude that  $BSR$  is a more efficient tool to quantify the non-linear effects than the earthquake  $H/V$  approach. However,  $A_{\{H/V\}}$  curves do not require a downhole station, making this methodology more applicable than  $BSR$ .

In general, both kind of analysis are appropriate and, for some sites,  $A_{\{H/V\}}$  also can generate  $f_{sp}$  curves with a low dispersion: around 20% of the stations had a lower dispersion using  $A_{\{H/V\}}$  to compute the  $f_{sp}$  curves than  $BSR$ .

The relationship and the explanation of  $A_{\{H/V\}}$  shift and site characteristics is not clear yet. It is important to determine the condition when derive  $f_{sp}$  curves from  $A_{\{H/V\}}$  is adequate. This could be aborted in future works.

## Chapter V Analysis of the $\widehat{fsp}$ curves using site parameters.

In the previous chapters we established a methodology based on the shift of the borehole spectral ratio (*BSR*) to evaluate the non-linear effects of the soil in the site response. In this chapter, we investigate the relationship of those  $\widehat{fsp}$  curves with other site parameters, the shear velocity profile, and the fundamental resonance frequency. The  $\widehat{fsp}$  curves from different sites are analyzed together, explaining their behavior based on site parameters. This evaluation leads to the first link between linear parameters and non-linear effects, expressed using *fsp*.

### V.1 Description of the $\widehat{fsp}$ curves at the kik-net sites

Following the procedure described in the section III.3, we compute *fsp* for all kik-net database. We have then selected 653 sites where it was possible to compute the *fsp* curves with more than 10 ground motions. From this data set, we focus in this section on the analysis of the dispersion of our results and the correlation between curves and parameters commonly used to describes the sites.

#### V.1.1 Variation of the $\widehat{fsp}$ curves from site to another

As was mentioned in subsection III.3.3 a hyperbolic curve was used to fit the *fsp* points (blue line Figure III-6). Comparing all the stations (Figure V-2), we observe that the kik-net sites present a huge variability between them. The hyperbolic function is characterized by an only parameter (Figure III-7), this parameter,  $PGA_{ref\_downhole}$ , can be interpreted as a measure of how much linear, or non-linear, is one site.

Figure V-1 shows some sites with different *fsp* curve. The sites are sorted from the one the more prone to non-linear effects (i.e. this site is characterized by a low  $PGA_{ref\_downhole}$ ) to the one showing a very high  $PGA_{ref\_downhole}$  making *fsp* almost constant for any value of  $PGA_{downhole}$ . For example, at YMNH12 we didn't observe any frequency shift between  $BSR_{linear}$  and the response derived from higher seismic solicitation, even for the strongest event that was recorded at this station characterized by  $PGA_{downhole}$  of  $0.25 \text{ m/s}^2$ . At other sites, the decrease of *fsp* starts at low  $PGA_{downhole}$ , meaning that even for weak motions, a shift of the frequency peaks is significant. It is the case at HYGH02 where events with  $PGA_{downhole}$  equal to  $0.03 \text{ m/s}^2$  already present a considerable frequency shift, resulting in  $fsp < 0.8$ .

Because we are using  $PGA_{downhole}$  to quantify the intensity of the curves, the parameter which define the hyperbolic curve is called  $PGA_{ref\_downhole}$  in this work. This parameter was already used in the section IV.4 for comparing  $\widehat{fsp}$  curves. The Table V-1 shows the  $PGA_{ref\_downhole}$  for the eight sites of the Figure V-1, represented by orange lines in Figure V-2. The characteristics of other sites found in the Annex C.

Figure V-2 shows that, for the evaluated stations in this figure, 50% of the stations have an *fsp* lower than 0.8 for a  $PGA_{downhole}$  of  $6.60 \times 10^{-1} \text{ m/s}^2$ ; 25% have developed a lower value of *fsp* for a  $PGA_{downhole}$  of  $1.15 \text{ m/s}^2$ ; and 75% for  $PGA_{downhole}$  of  $2.40 \text{ m/s}^2$ . Thus, most of the analyzed KIK-net stations are prone to non-linear soil behavior.

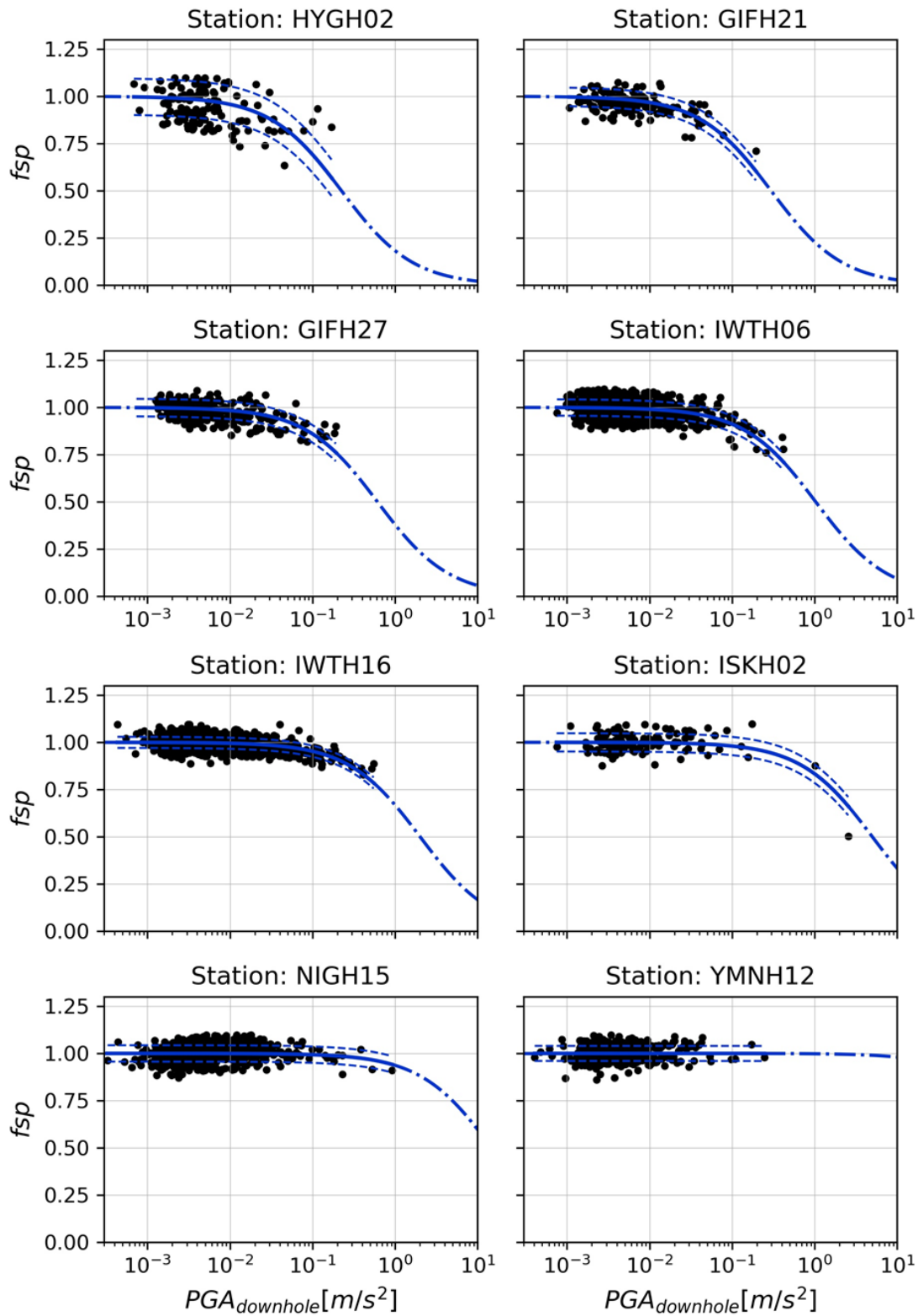


Figure V-1.  $f_{sp}$  curve for several stations that represents the general behavior of the data set. The blue line is the hyperbolic function that is fitted in each case. Dashed lines represent  $\pm\sigma$ , and dashed-dot lines represent the hyperbolic function when it is extrapolated. The characteristic of each site is summarized in Table V-1.

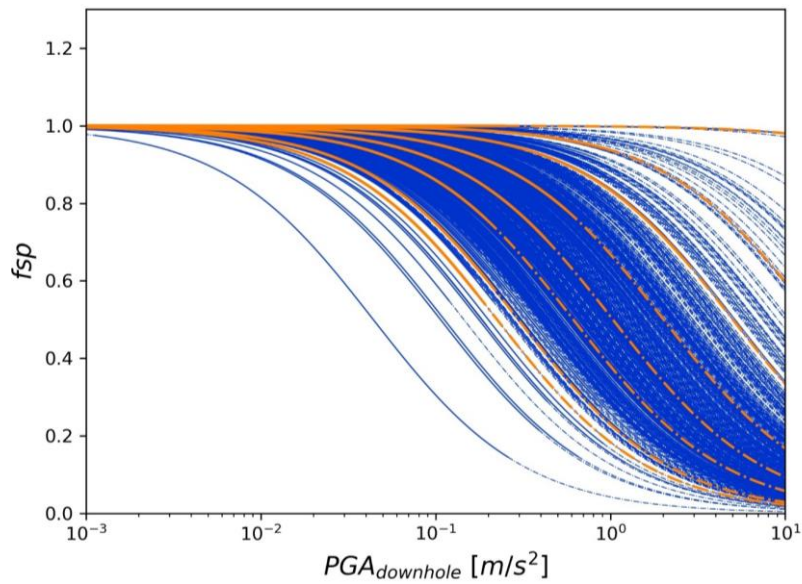


Figure V-2.  $f_{sp}$  curves for 653 sites of the Kik-Net network. Continuous lines indicate that the curves are interpolated using data, dash lines indicate the portion of curves that are extrapolated. Orange lines correspond to data shown in Figure V-1

Table V-1. Site parameters and results of the analysis of  $f_{sp}$  for representative sites (Figure V-1).

Station	$PGA_{ref\_downhole}$ [m/s <sup>2</sup> ]	$\sigma$	Max $PGA_{downhole}$ [m/s <sup>2</sup> ]	Downhole Depth [m]	$V_{s\_borehole}$ [m/s]	$V_{s30}$ [m/s]
HYGH02	2.25E-01	0.0960	1.70E-01	103	1784	612
GIFH21	2.97E-01	0.0490	1.94E-01	200	2200	964
GIFH27	6.13E-01	0.0464	1.92E-01	200	1600	685
IWTH06	1.03E+00	0.0432	4.19E-01	100	750	432
IWTH16	2.01E+00	0.0294	5.51E-01	150	1160	535
ISKH02	5.01E+00	0.0483	2.55E+00	102	530	721
NIGH15	1.49E+01	0.0433	9.15E-01	100	1540	686
YMNH12	$\infty$	0.0398	2.45E-01	148	1350	447

### V.1.2 Description of the standard deviation to quantify the variation of $\widehat{f_{sp}}$ curves at the kik-net sites

Figure V-3 shows that not only the  $f_{sp}$  curve are different for each site also the associated dispersion. Those differences in the dispersion of  $f_{sp}$ , could be related to the dependency of the mechanical behavior of the shallow soil layers to other parameters than the amplitude of the seismic solicitation. For example, the change of the water table level could modify temporarily the  $BSR$  function at certain sites by its effect on the soil shear modulus (Roumelioti et al., 2018).

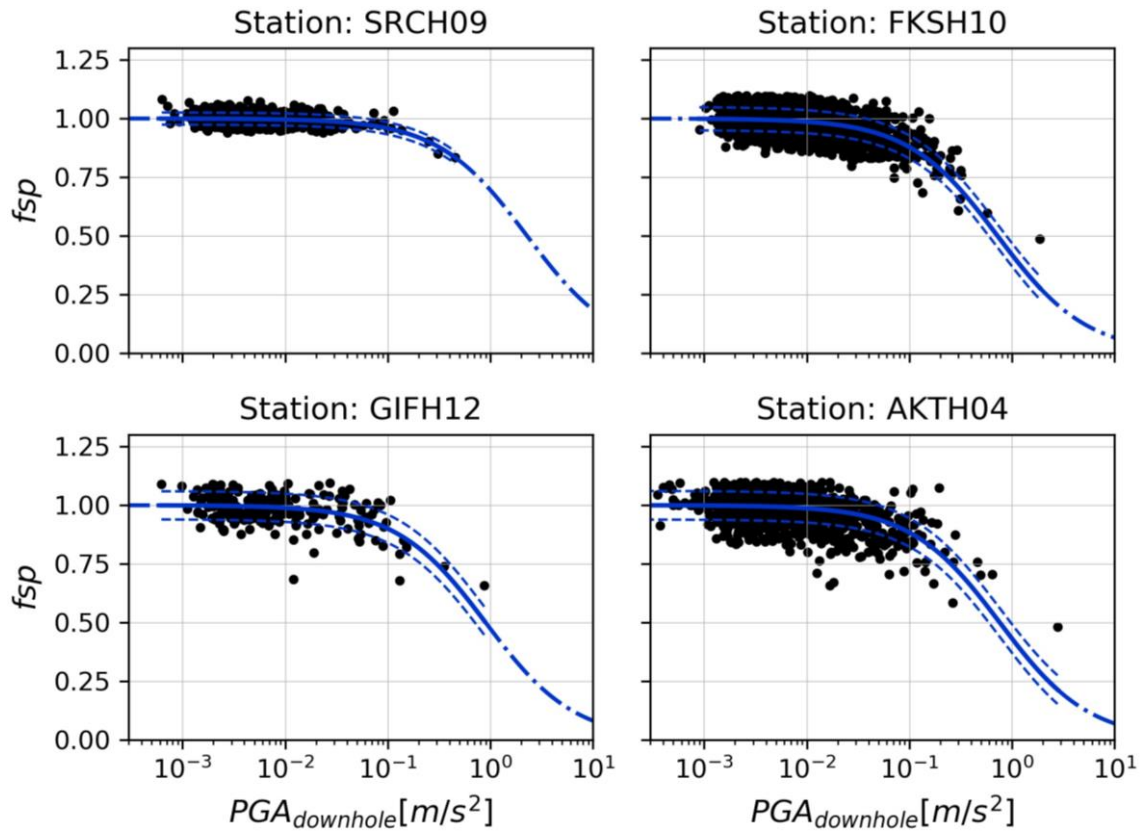


Figure V-3.  $f_{sp}$  curves for sites with different dispersion levels. The characteristic of each site is summary in Table V-2.

To measure the dispersion of the  $f_{sp}$  points around  $\widehat{f_{sp}}$ , we are considering the standard deviation:

$$\sigma = std(f_{sp} - \widehat{f_{sp}})$$

Table V-2 shows this value for the same four station of the Figure V-3, illustrates clearly the increase of dispersion with increasing  $\sigma$ .

Table V-2. Summary of site parameters and results of for some sites with different values.

Station	$PGA_{ref\_downhole}$ [m/s <sup>2</sup> ]	$\sigma$	Max $PGA_{downhole}$ [m/s <sup>2</sup> ]	Downhole Depth [m]	$V_{S_{borehole}}$ [m/s]	$V_{S_{30}}$ [m/s]
SRCH09	1.96E+00	0.0241	5.06E-01	122	780	241
FKSH10	8.21E-01	0.0503	1.95E+00	200	870	487
GIFH12	9.00E-01	0.0600	8.71E-01	106	1500	667
AKTH04	5.84E-01	0.0879	2.75E+00	100	1500	459

Even if the hyperbolic formulation of the regression curve is fitting the distribution of  $f_{sp}$  at most of the sites, following the shape of the modulus reduction curve Duncan and Chang, 1970; Ishihara, 1996, it doesn't match at some sites (Figure V-4) especially at high  $PGA_{downhole}$ .

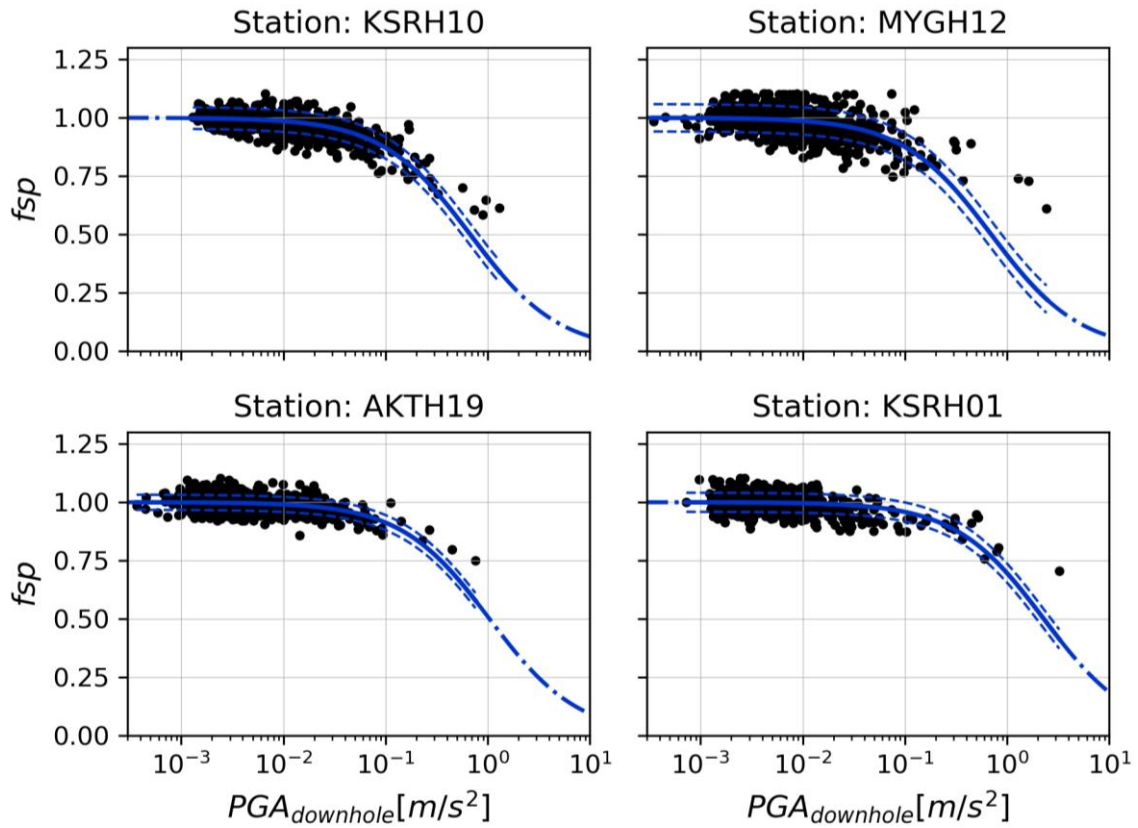


Figure V-4. Station where part of the fitting error is because of the shape limitation of the hyperbolic curve.

Another source of the dispersion is the uncertainty of the  $f_{sp}$  computation. When  $BSR$  curve has multiples peaks and complex shapes, it makes the process of comparison between  $BSR_{linear}$  and  $BSR$  harder. For example, Figure V-5 shows the  $BSR$  of the events recorded at IBRH19. These curves do not have a clear first main peak but are characterized by two or three small peaks depending of the considered event. In this case, the  $f_{sp}$  computation is highly uncertain, producing a high variability in the results (Figure V-5).

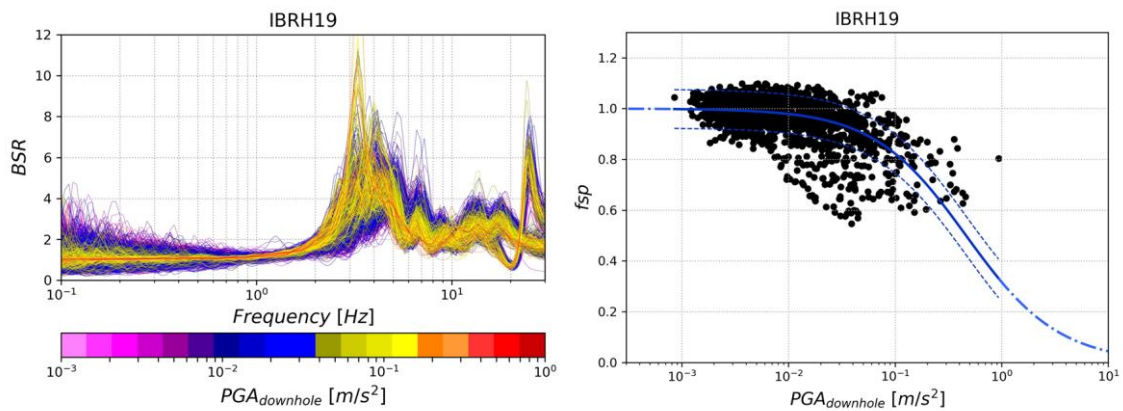


Figure V-5.  $BSR$  curves for the site IBRH19 (left), and resulting  $f_{sp}$  points left. The shape of the  $BSR$  curve around the first peak creates a huge dispersion on the  $f_{sp}$  graphic.

### V.1.3 Selection of a sub-dataset

In order to remove  $\widehat{f_{sp}}$  curves that does not match the observed data, we select the ones associated with low values of  $\sigma$ . To do this, we consider a threshold of 0.06 and retain 462 sites (Figure V-6).

Additionally, we also remove from our analysis, the sites where  $PGA_{ref\_downhole}$  is extraordinarily high  $PGA_{ref\_downhole}$ . Considering a threshold of  $100\text{m/s}^2$ , we finally kept 440 stations .

Using the database (Figure V-6), 50% of the stations have an  $f_{sp}$  lower than 0.8 for a  $PGA_{downhole}$  of  $1.33\text{ m/s}^2$ . 25% have developed a lower value of  $f_{sp}$  for a  $PGA_{downhole}$  of  $8.03 \times 10^{-1}\text{ m/s}^2$ , and 75% for  $PGA_{downhole}$  of  $2.34\text{ m/s}^2$ .

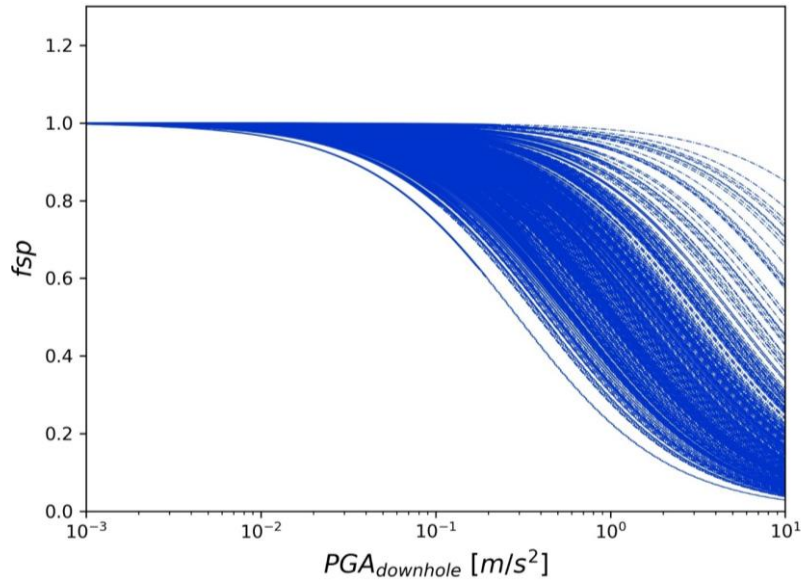


Figure V-6.  $f_{sp}$  curves for 440 sites of the Kik-Net network with  $\sigma < 0.06$  and a  $PGA_{ref\_downhole} < 100\text{ m/s}^2$ . Continuous lines indicate that the curves are interpolated using data, dash lines indicate the portion of curves that are extrapolated.

## V.2 The relationship between $f_{sp}$ curves and site parameters

In this section, we present the relationship between  $PGA_{ref\_downhole}$  and site parameters that mainly were computed from the  $V_s$  profiles, available in the kik-net database.

### V.2.1 Analysis of the average shear wave velocity

The averaged shear wave velocity is widely used in earthquake engineering. This average has the general expression:

$$V_{sh} = \frac{h}{\sum \frac{\Delta z_{\{i\}}}{V_{s_{\{i\}}}}} \quad (\text{V-1})$$

Where  $h$  represents the depth that is considered.  $\Delta z_{\{i\}}$  and  $V_{s_{\{i\}}}$  are the thickness and the shear velocity of each layer included between the surface and the considered depth ( $h$ ). For example,  $V_{s_{30}}$  parameter consists in the time-average shear velocity in the first 30 m of the site. This parameter is widely used to quantify site effects on different building codes. In this section we evaluate if this parameter is related with the non-linear effects that we observe on the KIK-net sites.

Figure V-7 shows the distribution of  $PGA_{ref\_downhole}$  according to  $V_{s_{30}}$ . From this graph, we can see that there is not a direct relationship between  $V_{s_{30}}$  and  $PGA_{ref\_downhole}$ . It confirms that sites with either low or high  $V_{s_{30}}$  could be prone to the non-linearity (see section III.2). The very low  $R^2$  value does not allow to suggest any trend or correlation between both parameters.

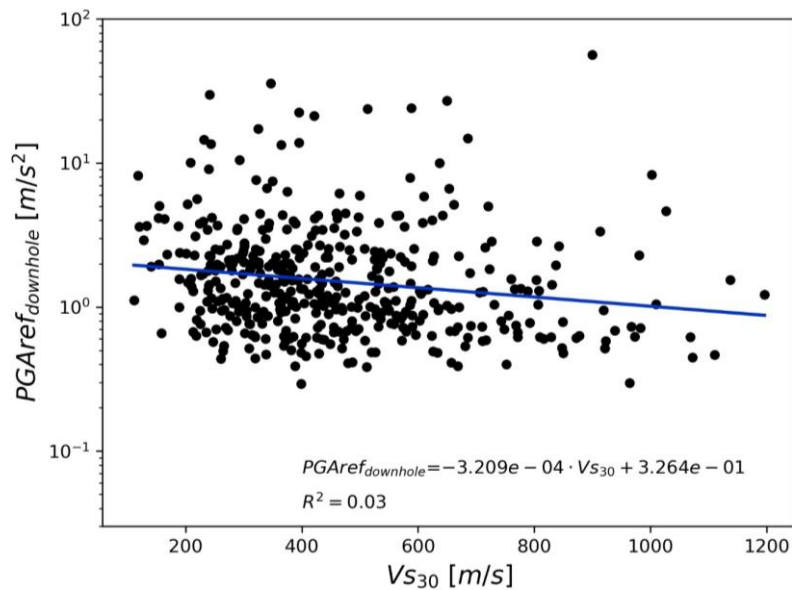


Figure V-7. The relation between  $PGAreferencedownhole$  and  $Vs_{30}$ . Sites with  $\sigma < 0.06$  and enough data to define the curve ( $PGAreferencedownhole < 100 \text{ m/s}^2$ ) were selected (436 sites).

Sites with high  $Vs_{30}$  can have a shallow and thin soft layer lying on a very strong bedrock. This strong contrast of impedance can develop high strain at the base of the soft layer. In a linear model, this configuration produces very important high frequency amplifications. This can also explain why these sites are prone to develop non-linear effects. In contrast, sites with a low mean shear wave velocity but without major contrasts can be resistant to non-linear effects.

For example, GIFH21 (Figure V-8), characterized with a  $Vs_{30}$  of  $964 \text{ m/s}$ , can be classified as a rock or a stiff soil. However, in the  $\widehat{f}_{sp}$  curve for this site (Figure V-8 right) we can observe that several ground motions presented a significant shift. The  $PGAreferencedownhole$  is equal to  $0.30 \text{ m/s}^2$ , meaning that this site is one of the most prone sites to develop non-linear effects (Figure V-2).

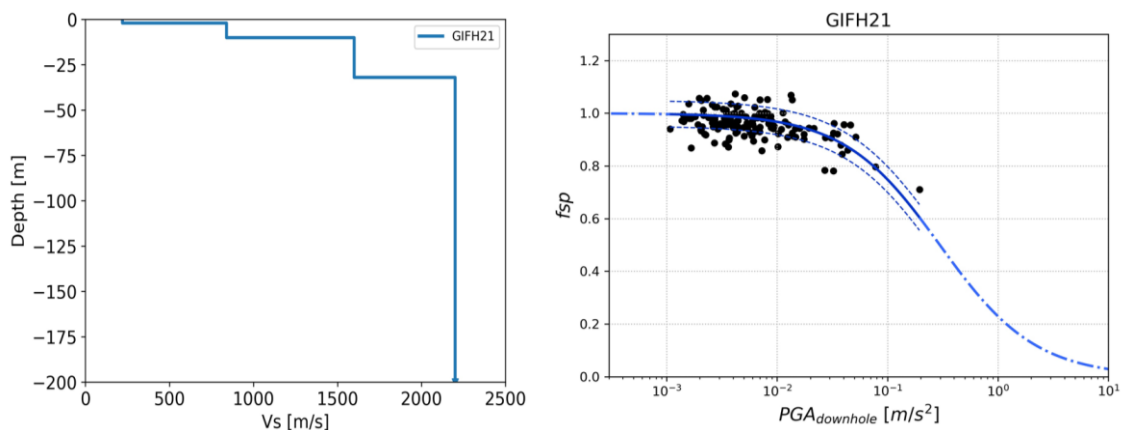


Figure V-8. Shear velocity profile (left) and  $f_{sp}$  curve (right) for the site GIFH21.

If other depths are used to evaluate the average of shear velocity (Eq. (V-1)) instead of 30 m, the correlation keeps being low (Figure V-9). It means that the shear velocity average cannot explain the  $f_{sp}$  curves. However, Figure V-9 shows that adding more information about deeper layers can improve a bit the correlation. This result is not initially evident since the non-linearity is an effect that is expected to occur at shallow layers. This dependence can be explained by the effect of the contrast, as was mentioned, before, but moreover it could be due to the downhole recordings we are using. Both ideas will be analyzed in the next two sections of this chapter.

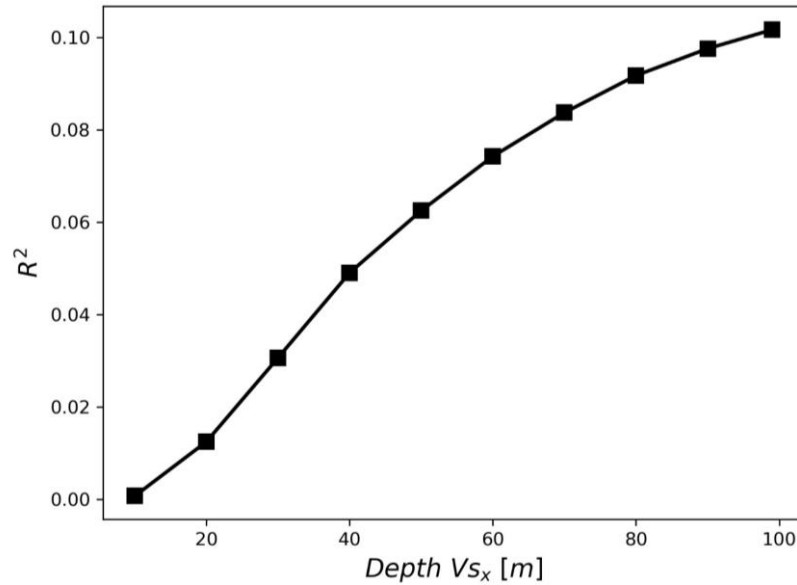


Figure V-9. The coefficient of determination between  $PGAref_{downhole}$  and average shear velocity using different depth ( $V_{s_x}$ ).

### V.2.2 Influence of the impedance contrast on $f_{sp}$ curves

In the previous subsection was mentioned that the contrast between soil layer, also called impedance contrast, could have an important influence on the  $f_{sp}$  curves. To evaluate this relation, we define a parameter that characterizes the impedance contrast. We use a velocity contrast, because we do not have density soil information existing in a soil column. This parameter compares the surface layers with the deep ones, by using  $V_{s30}$  and the average of deeper layers. This coefficient ( $\vartheta$ ) is defined as:

$$\vartheta = \frac{V_{s30}}{V_{s30 \text{ to } 50}} \quad (V-2)$$

Where  $\Delta z_{(j)}$  and  $V_{s(j)}$  are the thickness and the shear velocity of each layer. The coefficient of the Eq. (V-2) is dividing the average velocity of the first 30 m of soil by the average between 30 to 50 m. This coefficient is close to one in the case of weak velocity contrast underneath the site. If the value is much higher than one, it indicates that there is a strong contrast somewhere in the soil column.

The correlation between this parameter and  $PGAref_{downhole}$  shows a  $R^2$  of 0.13. It means that this coefficient could be more effective to explaining the  $\widehat{f_{sp}}$  curve than using  $V_{s_h}$  alone, even until 100m.

Figure V-10 shows that there is a slight proportional trend between  $PGAref_{downhole}$  and  $\vartheta$ . It indicates that for higher impedances, the sites have a lower  $PGAref_{downhole}$ . However, the correlation is still too weak to draw any clear conclusions.

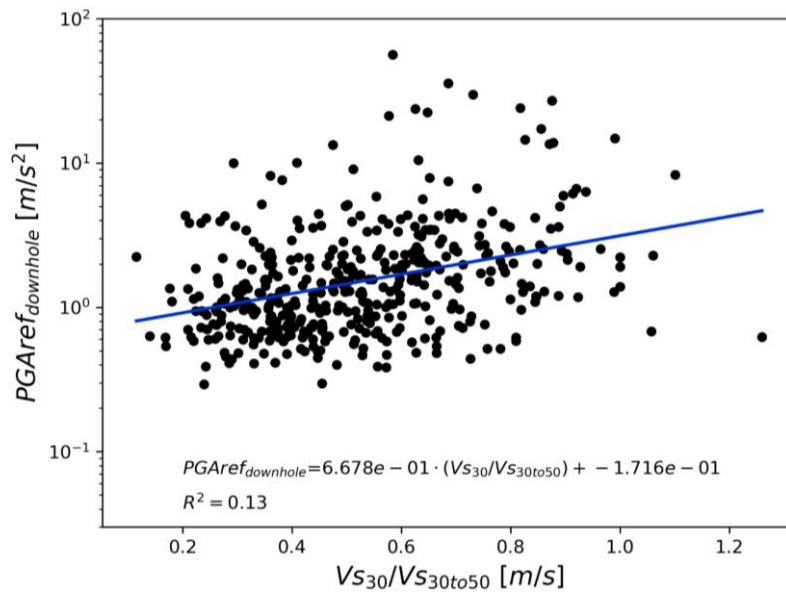


Figure V-10. Effect of the contrast between soil layers on  $PGAREf_{downhole}$ .

### V.2.3 Influence of the downhole device on the $f_{sp}$ curves

The correlation between the bedrock rigidity on which the downhole sensor is set up and the depth with  $f_{sp}$  is investigated in this section.

Until now in this study, the  $PGA_{downhole}$  has been considered for the computation of  $f_{sp}$  curves, corresponding to the peak acceleration recorded during the earthquake at the downhole station (see section III.3.3). However, because of the difference of rigidity of the bedrock they are installed on, same  $PGA_{downhole}$  won't lead in the same deformation in the soil layers above it, even if the velocity profile in the shallow layers is equivalent. Thus, for the same soft soil profile we may have different  $f_{sp}$  (and subsequently different  $PGAREf$ ) for the same  $PGA_{downhole}$  depending on the  $V_s$  of the medium below the bottom station

Figure V-11 compares the  $V_s$  around the downhole station with  $PGAREf_{downhole}$ . The coefficient of determination ( $R^2$ ) is equivalent to the one considering the velocity profile in the 80 first meters. From this, we conclude that considering the velocity condition underneath the downhole sensor is as important as taking into account the  $V_s$  profile of the site.

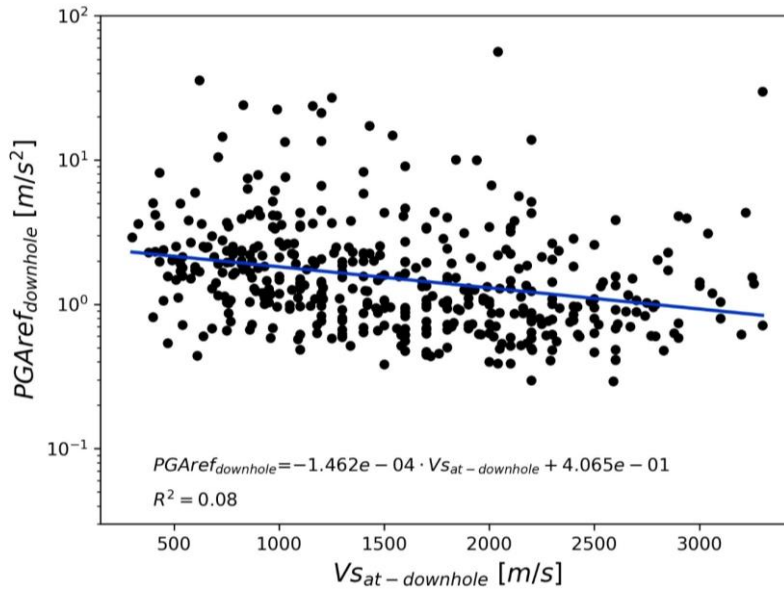


Figure V-11. The relationship between  $PGAreferencedownhole$  and shear velocity at downhole  $VS_{at-downhole}$ , where the device is located.

Figure V-12 shows that the depth of the downhole station is also not related with  $PGAreferencedownhole$ , making this parameter not discriminant for the analysis of  $f_{sp}$ .

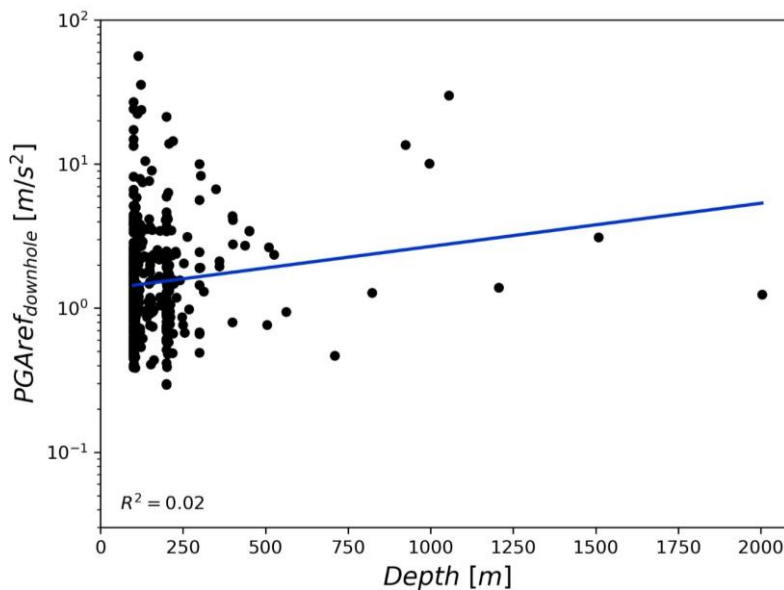


Figure V-12. Depth of the downhole stations against  $PGAreferencedownhole$ .

#### V.2.4 Relationship between the fundamental frequency, determined by the H/V ratio, and $f_{sp}$ curves.

The fundamental peak of the  $HV$  curve (section IV.2) is depending on several parameters of the soil, like the depth of the strong velocity contrast and the rigidity of the soil (Bonneyoy-Claudet et al., 2006). Because of this, the relationship between this parameter and the disposition to non-linear effects is analyzed (Figure V-13).

There is a very weak relationship between  $f_{o(H/V)}$  and  $PGAreferencedownhole$  (Figure V-13) since  $R^2$  is rather low (0.07). It indicates that  $f_{o(H/V)}$  alone cannot explain the proneness of a site to develop non-linear effects.

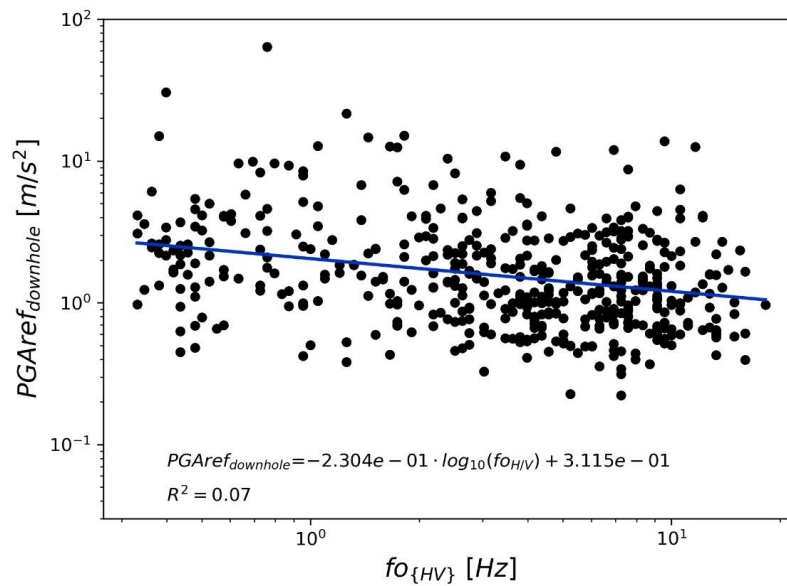


Figure V-13. Relation between  $PGA_{ref\_downhole}$  and the fundamental frequency defined by H/V spectral ratio computation ( $f_{o_{HV}}$ ).

### V.3 $f_{sp}$ with different intensity parameters

The section III.4 shows that  $f_{sp}$  is related with the rigidity of the entire soil column and it could be compared to the modulus reduction curves. To make the comparison easier, it is necessary to look for the relationship between  $f_{sp}$  with a strain estimator. Since the strain in the soil column is unknown, several proxies are explored in this section.

#### V.3.1 Parameter: $PGA_{surface}$

As was mentioned initially, the  $PGA_{downhole}$  was chosen as a proxy of the seismic solicitation. In this subsection, the  $f_{sp}$  curves are presented using  $PGA_{surface}$  instead, keeping the methodology of computation similar. Here, the limit of PGAs that are considered to compute  $BSR_{linear}$  is taken from  $3 \cdot 10^{-4} m/s^2$  to  $5 \cdot 10^{-2} m/s^2$ . In general, we observe that the variability of BSR considering  $PGA_{surface}$  (Figure V-14) is very similar to the use of  $PGA_{downhole}$ .

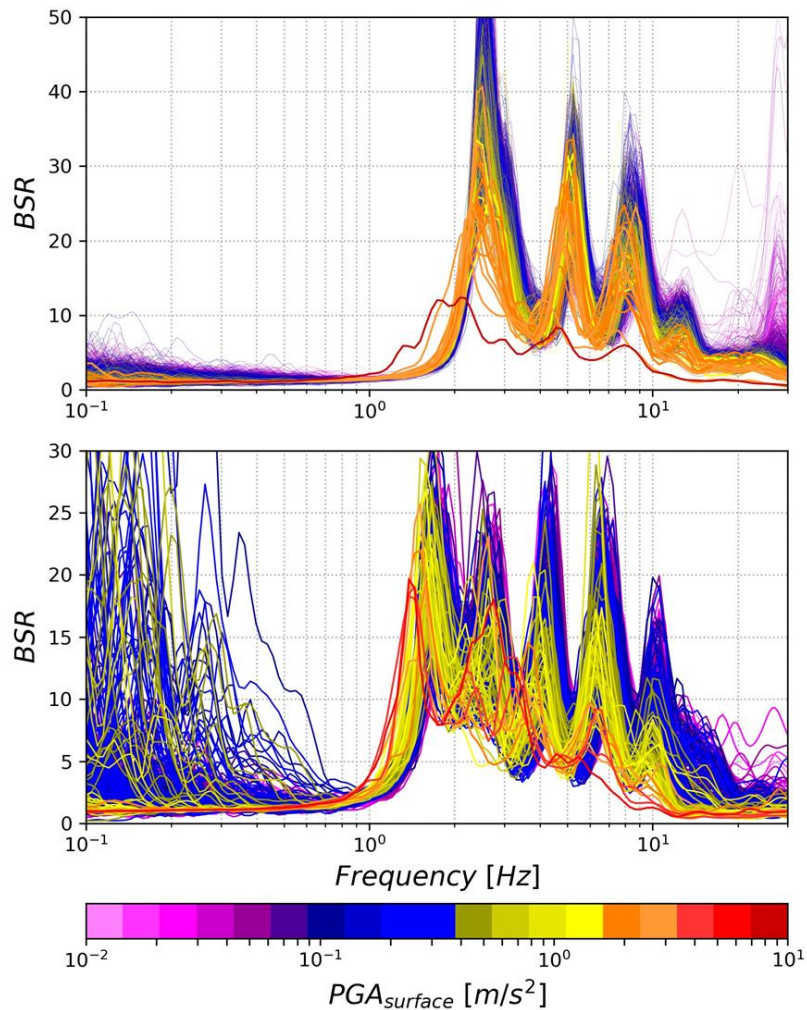


Figure V-14. BSR curves with respect to  $PGA_{surface}$  at two sites. IBRH11 top and KSRSH10 bottom.

Computing the  $f_{sp}$  for the entire database (Figure V-15), a wide range of  $PGA_{ref_{surface}}$  is found.  $PGA_{ref_{downhole}}$  and  $PGA_{ref_{surface}}$  are certainly related but the relationship is not straightforward as shown in Figure V-16. The  $R^2$  value characterizing the correlation between both parameters indicates that even if they are related, they are not totally equivalent.

The dispersion between  $PGA_{ref_{downhole}}$  and  $PGA_{ref_{surface}}$  is related to the downward waves. Indeed, the station at downhole can record strong amplitudes or not with respect to the signal at the surface. This depends notably on the depth of the station and the stiffness of each site (Bonilla et al., 2002), which are not unique for all the sites.

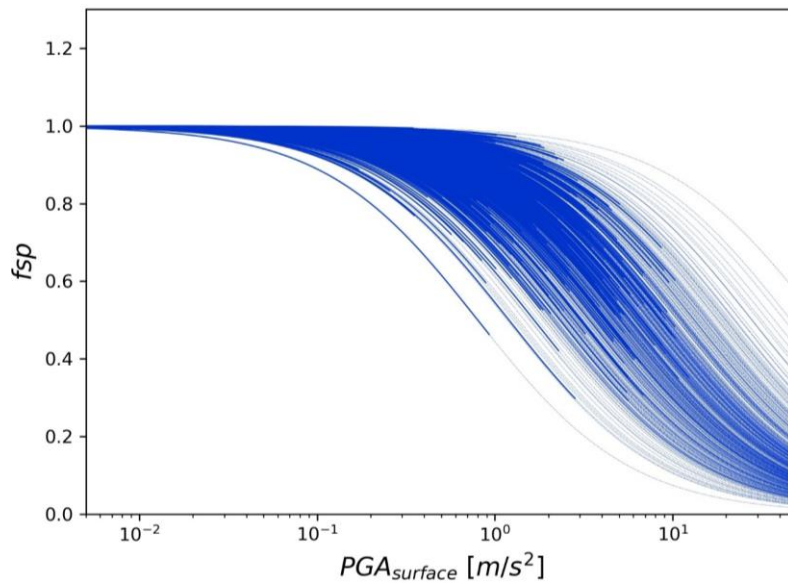


Figure V-15.  $f_{sp}$  curves in terms of  $PGA_{surface}$ .

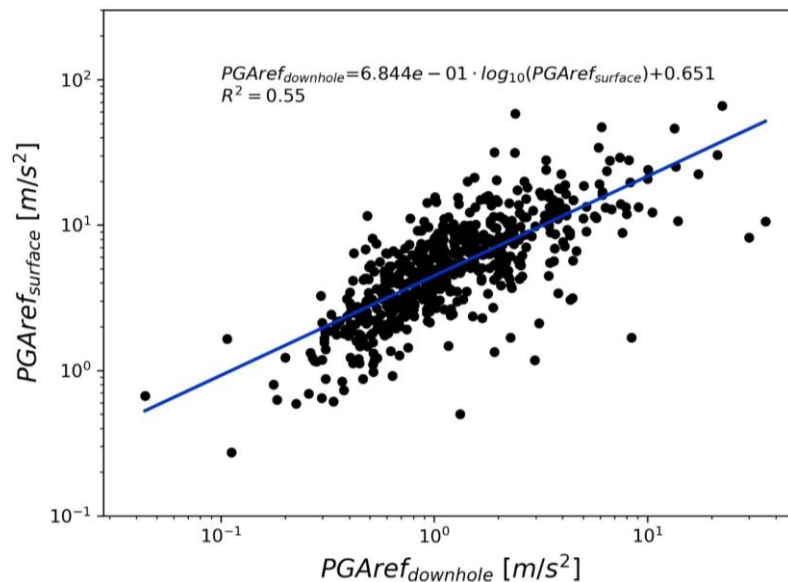


Figure V-16. Comparison between  $PGAref_{surface}$  and  $PGAref_{downhole}$  for all sites.

To compare both intensity parameters, the dispersions of the  $f_{sp}$  curves are compared (Eq. (IV-3)). Figure V-17 shows that the dispersion is almost independent of the considered parameter. For both of them, in most of the stations, more or less the same  $\sigma$  is obtained. However, determining  $PGAref$  considering the PGA at the surface is a little bit more efficient, reducing the dispersion in comparison to  $PGAref_{downhole}$ . Indeed, over the 587 sites taken into account, 400 has a lower  $\sigma$  for  $PGAref_{surface}$ . Those correspond to the points under the 1:1 curve in Figure V-17 (red dashed line).

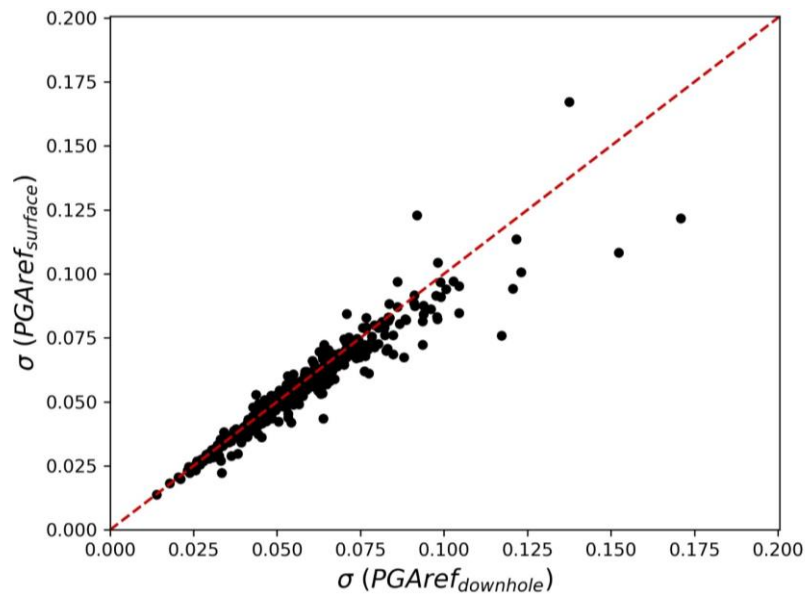


Figure V-17. Comparison of the dispersion for all sites either  $PGAREf_{surface}$  or  $PGAREf_{downhole}$  is used in the computation of the  $f_{sp}$  curves. Red dashed line represents the 1:1 curve.

In general, predicting  $PGAREf_{surface}$  from site parameters results in a very high dispersion and in a unclear relationship between the parameters (Figure V-18 and Figure V-19). Even if the results seem to indicate that the  $f_{sp}$  curves are easier to be explained than in terms of the  $PGAREf_{downhole}$ , the difference is not very clear. For example, the parameter  $f_{0\{H/V\}}$  has a better correlation with  $PGAREf_{downhole}$  (Figure V-13) than with  $PGAREf_{surface}$  (Figure V-19).

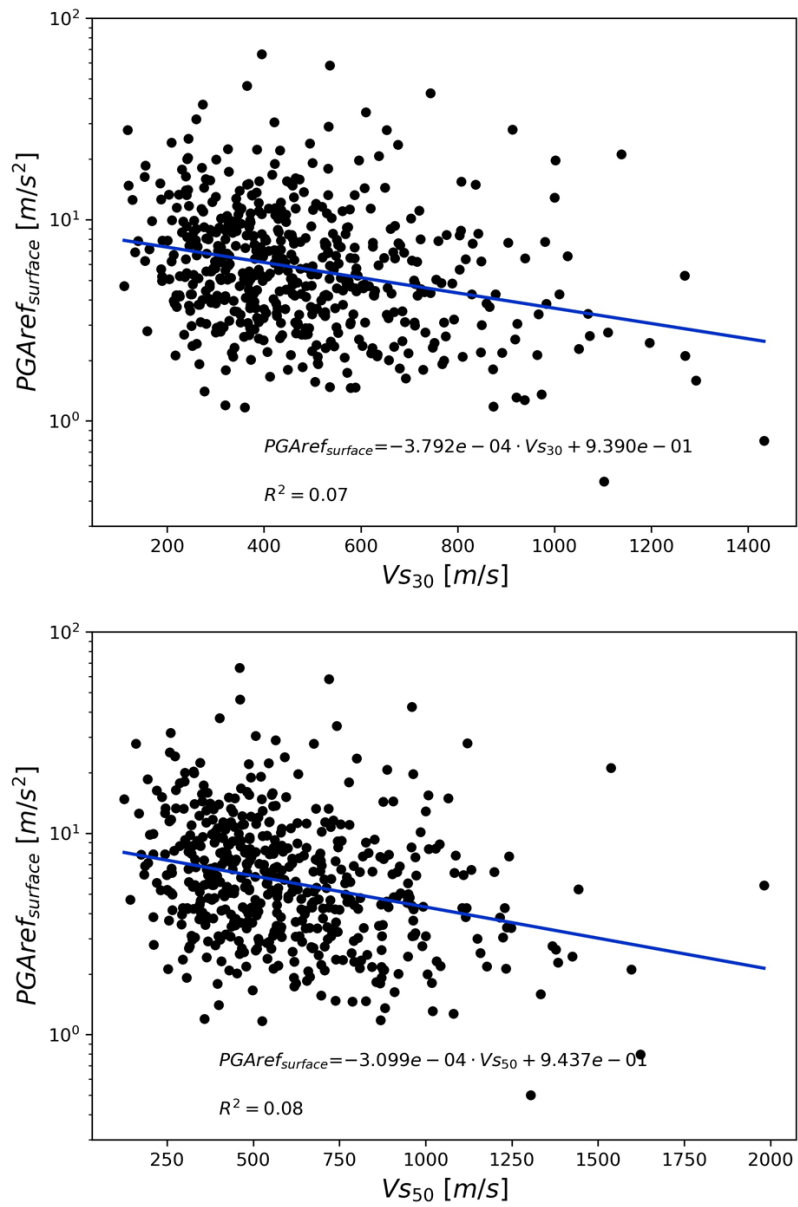


Figure V-18. Comparison of the site parameters  $V_{S30}$  and  $V_{S50}$ , with  $PGA_{ref\_surface}$ .

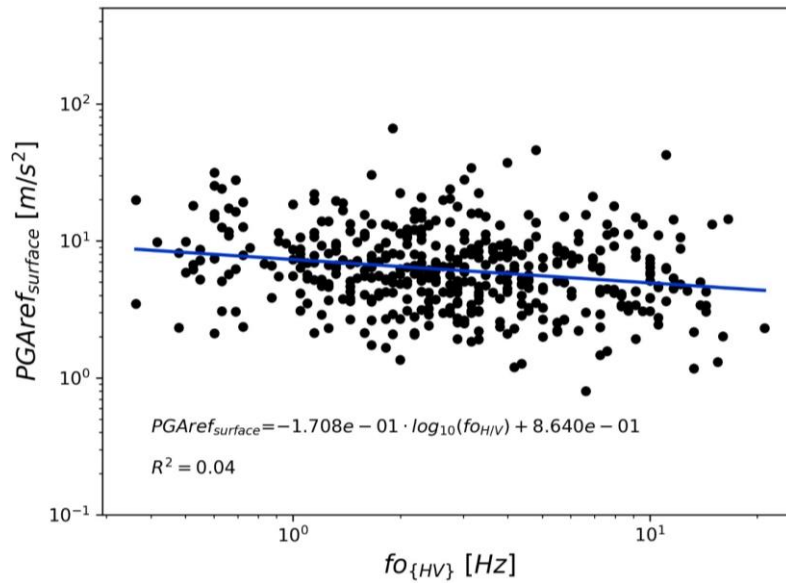


Figure V-19. Comparison between  $PGAref_{surface}$  with  $fo_{(HV)}$ .

### V.3.2 $PGV_{surface}/Vs_{30}$

One proxy of the strain, already used in the section III.4, was proposed by Chandra et al., (2016); Idriss,(2011). It is defined as the ratio of  $PGV_{surface}$  and  $Vs_{30}$  (Eq. (III-6)). Replacing this parameter in all the process of  $f_{sp}$  computation, a new definition of  $f_{sp}$  curve is achieved for all the sites (Figure V-20).

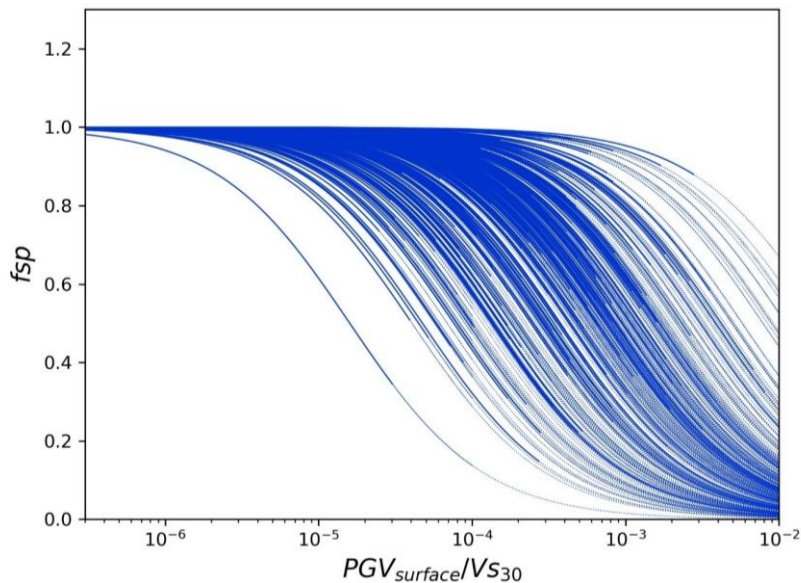


Figure V-20. Curves  $f_{sp}$  in function of  $PGV/Vs_{30}$ . Sites with a  $\sigma < 0.06$  and with enough data to define the  $f_{sp}$  curve (325 sites accomplish the criteria).

The range of values of  $\hat{\gamma}_r$  (the reference parameter to define the  $f_{sp}$  curves in terms of  $PGV/Vs_{30}$ ), starts from the order of  $10^{-5}$  to almost  $6 \times 10^1$ . Comparing with  $PGAref_{downhole}$ , that was used previously (Chapter II), both terms are related (Figure V-21).

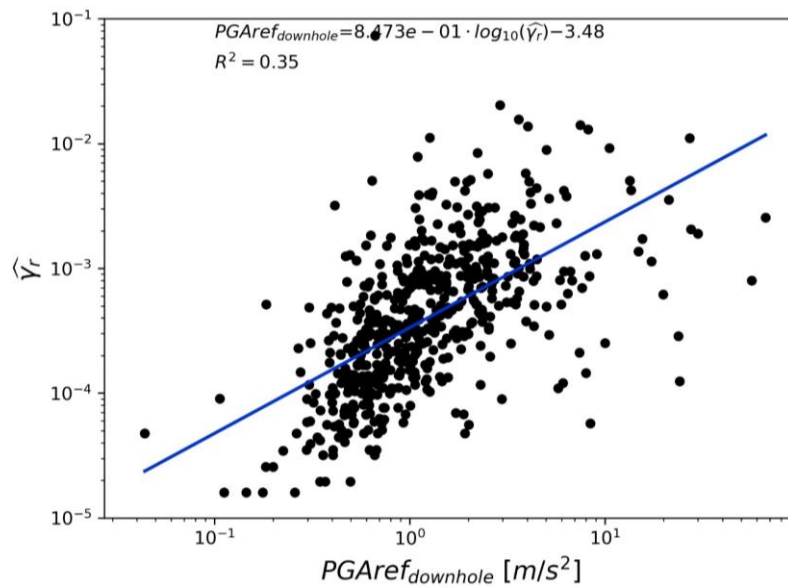


Figure V-21. Comparison between  $PGAreferdownhole$  and  $\hat{\gamma}_r$  for all sites.

But, even if there seem to be a relation between  $\hat{\gamma}_r$  and  $PGAreferdownhole$ , these two parameters are not totally equivalent ( $R^2=0.35$ ). Comparing the performance of the  $f_{sp}$  curves (Figure V-22), 116 sites from 567 sites (where both  $f_{sp}$  curves are well defined) have a lower  $\sigma$  value by using  $\hat{\gamma}_r$ . It could indicate that finally  $PGAreferdownhole$  is a better proxy of the solicitation for the  $f_{sp}$  curve computation.

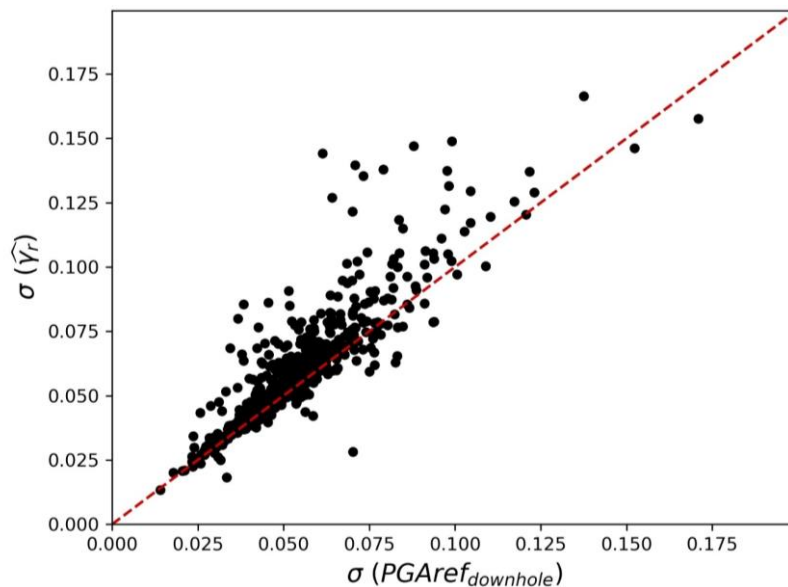


Figure V-22. Comparison of the dispersion for all sites with  $\hat{\gamma}_r$  and  $PGAreferdownhole$  in the computation of the  $f_{sp}$  curves. Red dashed line represents the 1:1 curve.

Even if  $\hat{\gamma}_r$  is function of  $V_{S30}$ , the relation between  $\hat{\gamma}_r$  and  $V_{S30}$  is not so straightforward since  $\hat{\gamma}_r$  is obtained from a regression process. We consider thus these parameters as independent and plot  $\hat{\gamma}_r$  in function of  $V_{S30}$  and  $V_{S50}$  (Figure V-23). We find a better correlation between these parameters than the one found previously. It may prove that  $PGV_{surface}/V_{S30}$  is a good proxy of the strain, as was already proposed by Chandra et al., (2016); Idriss, (2011). It implies also that the prediction of the  $f_{sp}$  curves in function of  $PGV_{surface}/V_{S30}$  could be achieved more accurately

by considering the shear profile of the site. It finally makes the comparison between stations more adequate.

The sites with high values of shear velocity generally have a lower  $\hat{\gamma}_r$  (Figure V-23 and Figure V-24). This can be explained, at least partly, by the fact that the higher  $V_{S30}$  is, the smaller  $PGV_{surface}/V_{S30}$  is. But it cannot explain totally the relationship, because the range of  $V_{S30}$ , less than one order of magnitude, is lower than the range of  $\hat{\gamma}_r$ , more than two orders of magnitude. A similar result is obtained with  $V_{S50}$ .

Although the Figure V-23 shows a relationship between  $V_{S30}$  and  $\hat{\gamma}_r$ , the link between  $V_{S30}$  and the effects of the soil non-linear behavior is not totally proven. In terms of  $V_{S50}$ , the correlation is higher than with  $V_{S30}$ . This improvement indicates that the correlation between  $\hat{\gamma}_r$  and shear velocity profile is not just explained by the presence of  $V_{S30}$  in the proxy of the strain, since  $V_{S50}$  generates even a higher correlation (Figure V-24).

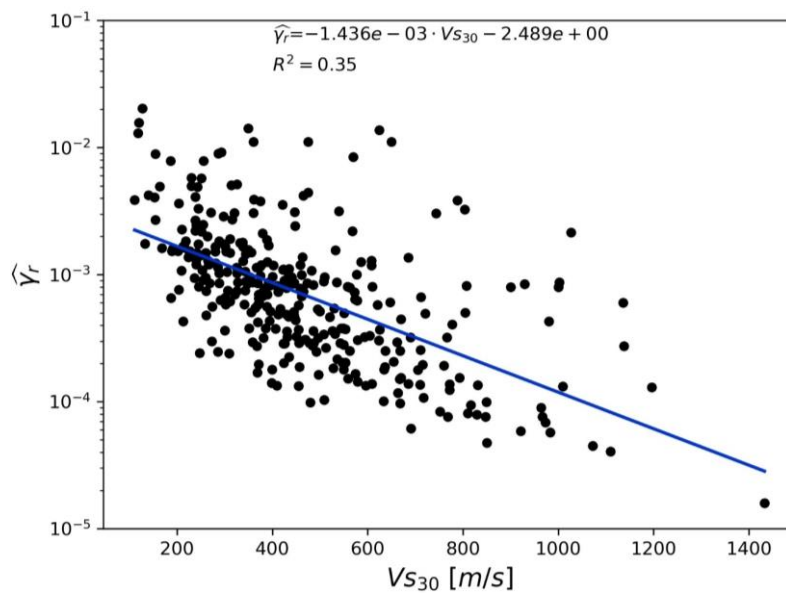


Figure V-23. Comparison of the site parameters  $V_{S30}$  with  $\hat{\gamma}_r$  (325 sites).

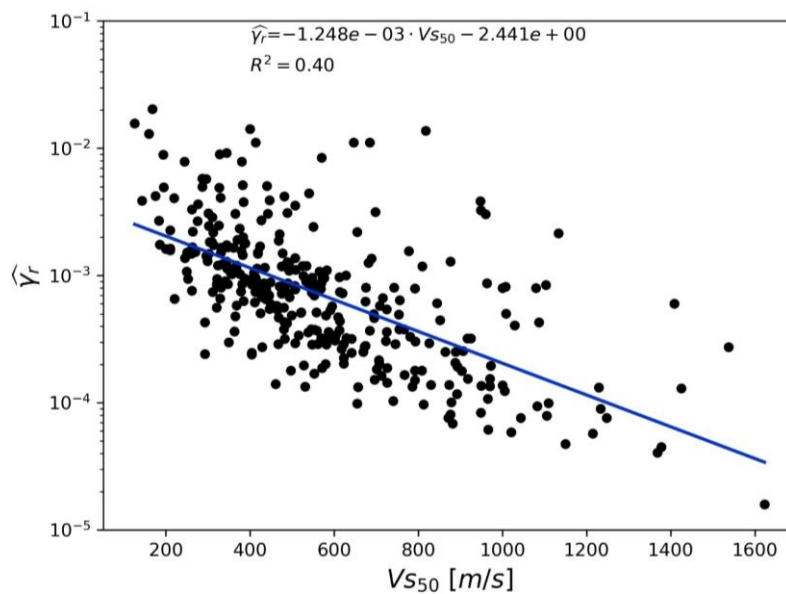


Figure V-24. Comparison of the site parameters  $V_{S50}$  with  $\hat{\gamma}_r$  (325 sites).

Studying the parameter  $f_{O_{\{H/V\}}}$  a similar result is obtained (Figure V-25). This parameter presents an inverse relationship with  $f_{sp}$  curves, meaning that sites with high  $f_{O_{\{H/V\}}}$  are more prone to have non-linear effects. However, the dispersion between both parameters is too large to be totally affirmative.

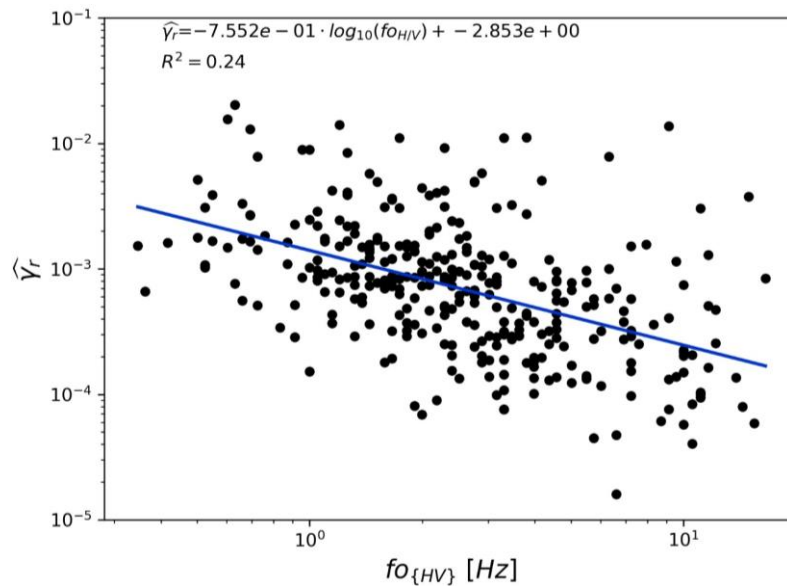


Figure V-25. Comparison of  $\hat{\gamma}_r$  with  $f_{O_{\{H/V\}}}$ .

#### V.4 Summary and discussion

The  $f_{sp}$  curves, described by a simple hyperbolic function, for all the database were analyzed in detail considering different parameters.

From this analysis, was obtained that there is not a direct relationship between these curves, in terms of  $PGA_{surface}$  or  $PGA_{downhole}$ , and the average of shear velocity using different depths. This result could be related with the site effects that are different for each station.

Other works have found that mean  $V_s$  alone is not able to well predict site effects, although it is an important parameter in the definition of site effects (e.g. Luzi et al., 2011). About the non-linear effects,  $V_{s30}$  can be an important parameter to predict the non-linear effects. We find that evaluating  $\hat{f}_{sp}$  using  $PGV_{surface}/V_{s30}$  shows a strong dependency on  $V_{s30}$ . This improvement, in comparison with  $PGAs$  analysis, can be related with the relationship between  $PGV_{surface}/V_{s30}$  and the global strain that affect the soil columns under seismic solicitation (Chandra et al., 2016; Idriss, 2011). The relationship between non-linear effects and  $V_{s30}$  has already been described in previous studies. Indeed, Régnier et al., (2016b) shows the same dependence between  $V_{s30}$  and non-linear effects, although this analysis defines the non-linearity in a different way than in this study.

In general, the relationship between the  $\hat{f}_{sp}$  curves and the site parameters shows that hard sites (high  $V_s$  profile or sites with high  $f_{O_{\{H/V\}}}$ ) are more prone to develop a shift during weak ground motions. However, the trend is not clear, even considering  $PGV_{surface}/V_{s30ref}$ , and it must be still improved in future works.

Given a site, the use of either  $PGA_{downhole}$  or  $PGA_{surface}$  to determine the  $\hat{f}_{sp}$  curves, reduces a little the uncertainty ( $\sigma$ ) comparatively to the use of  $PGV_{surface}/V_{s30ref}$ . But  $PGA_{downhole}$  and  $PGA_{surface}$  are not equivalent in the definition of the  $\hat{f}_{sp}$  curves (Figure V-16). This is probably

due to the downward waves recorded at the downhole sensor. However, both parameters have a high correlation in the results and a similar performance (Figure V-17).

There are some limitations in our analysis that must be mentioned. Indeed, the hyperbolic function that is used for describing the  $f_{sp}$  is adequate for most of the sites. However, at some sites, the trend indicates that this function is not adequate to explain the data distribution, especially for strong ground motions (Figure V-4).

Another limitation is that we intentionally removed from the analysis the stations that does not show non-linear effects (characterized by a flat  $f_{sp}$  curve). The analysis of these stations, and the reason why they did not develop those effect must be taking into account in future works.

Finally, the analysis of this chapter is based on the shear velocity profiles. However, several studies already noticed that those  $V_s$  profiles are not all accurate, especially for shallow layers. This bias could have an important impact in the results of our analysis.

# Chapter VI Ground motion prediction using an Empirical Green's Function method constrained by a global database

In this chapter, we present a new methodology for predicting synthetic accelerograms based on an Empirical Green's Function (EGF method) approach and a global database of source time functions.

EGF methods have been widely used because they enable to reproduce temporal signals taking into account path and site effects realistically. The general idea of this approach is to take advantage of real signals of small earthquakes to produce realistic ground motions coming from a more significant earthquake from a similar source region.

In this chapter, we combine the procedure proposed by Kohrs-Sansorny et al., (2005) with the analysis of the source duration of global earthquakes presented in Courboux et al., (2016) based on the SCARDEC database (Vallée et al., 2011).

In the first section a background about source models and basic concepts of seismology are presented, and then, the new EGF method is explained. We then apply the method to the recordings of the Pedernales Earthquake, (M7.8 April 2016) in the city of Quito. Finally, we apply the method to a hypothetical M8.5 earthquake coming from the subduction zone.

## VI.1 Source model ( $\omega^2$ -model)

The seismic moment ( $M_o$ ) is a measure of the seismic energy released during an earthquake. This term is an estimation of the work done for the earthquake to generate the slip ( $D$ ) (Eq. (V-1)). Vvedenskaya, (1956) introduced this term and after it was measured by empirical data from long period components of the seismograms (Aki, 1966; Bullen et al., 1985).

$$M_o = \mu \cdot A \cdot D \quad (\text{VI-1})$$

Where  $\mu$  is the rupture strength of the material against the movement at the fault, in terms of stress.  $A$  is the area activated during the earthquake on the fault, and  $D$  is the average displacement, better known as slip.  $M_o$  is widely used in seismology because it is a parameter that depends directly of the source of the earthquake. It never saturates (as it can be the case for magnitude measurements that are based on ground motion amplitude). The moment magnitude scale depends directly on the seismic moment (Eq. (V-1)) and is defined as (Hanks and Kanamori, 1979; Kanamori, 1977):

$$M_w = \frac{2}{3} (\log_{10}(M_o [Nm]) - 9.05) \quad (\text{VI-2})$$

Another interesting measure to study the source is the stress drop ( $\Delta\sigma = \sigma_o - \sigma_f$ ). The stress drop is the difference between the stress on the fault before and after the earthquake. This can be estimated by several ways, but in general, it is founded as:

$$\Delta\sigma \propto \mu \frac{D}{L_c}$$

Where the stress drop ( $\Delta\sigma$ ) is proportional to the strength of the material ( $\mu$ ) and the slip ( $D$ ), and inversely proportional to a measure of a characteristic length of the fault ( $L_c$ ). Even, for most of the models of the geometric faults, the stress drop is expressed as (Kanamori and Anderson, 1975):

$$\Delta\sigma = a \cdot \mu \frac{D}{L_c} \quad (\text{VI-3})$$

Where  $a$  is a constant that depends of the shape of the fault. As example, in case the fault is assumed as circular and growing with a constant velocity, the stress drop can be computed from the radius of the fault (Eshelby, 1957; Madariaga, 1976). For a strike slip (shear fault), the stress drop depends of the width ( $w$ ) of the fault (Knopoff, 1958). Both examples are shown in the next equation, and they confirm the general shape of the Eq. (VI-3).

$$\Delta\sigma = \frac{7}{16} \mu \cdot D \cdot \pi / r \leftrightarrow \text{Circular fault}$$

$$\Delta\sigma = \frac{2}{\pi} \mu \cdot D / w \leftrightarrow \text{Shear fault}$$

Aki, (1967) derivates a source model, called  $\omega^2$ -model, from a theoretical spectrum for a step pulse in the source (in velocity terms). In this case, the general spectrum of the source in terms of displacement ( $STF^{(u)}$ ) is summered in the Eq. (VI-4) (Aki, 1967; Brune, 1971, 1970).

$$STF^{(u)}(f) = C \cdot M_0 / \left(1 + \left(f/f_c\right)^2\right) \quad (\text{VI-4})$$

Where  $C$  is a constant that considers the radiation pattern, the spatial division of the energy, and the conditions of the source media.  $C$  parameter is obtained generally with an average between a suitable range of azimuths. Several functions have been proposed for this terms, depending on the kind of waves and fault that is studied (e.g. Boore and Boatwright, 1984; Satoh, 2002).

$M_0$  in Eq. (VI-4) represents seismic moment and determines the amplitude of the spectrum especially at low frequencies. The term  $f_c$  is the corner frequency and it defines the frequency after which the spectrum falls with a slope of  $f^2$ . In case the spectrogram is analyzed in terms of the angular frequency ( $\omega=2\pi f$ ), the spectrum still falls with a slope of  $\omega^2$ . From this particularity the model takes his name,  $\omega^2$ -model.

The corner frequency ( $f_c$ ) is another parameter that can be determined for an earthquake. This parameter is related with the duration of the rupture process and, depending on some assumptions on the rupture velocity and the type of fault, with the spatial size of the fault (e.g. Brune, 1971, 1970; Dong and Papageorgiou, 2003; Madariaga, 1976).

$$f_c = k \cdot \beta_s / L_c \quad (\text{VI-5})$$

Where  $k$  is a constant that depends of the kind of rupture, the azimuth, and the kind of waves,  $\beta_s$  is the shear velocity of the material around the source, and  $L_c$  is a characteristic length of the fault that is a measure of the spatial size of the fault.

In summary, the relaxation of stress, expressed in the stress drop ( $\Delta\sigma$ ), and the release of energy, represented by the seismic moment ( $M_0$ ), are related. Additionally, the duration of the fault can

be integrated to this relationship, in the  $\omega^2$ -model by the corner frequency  $f_c$ . It is important to note that the Eq. (VI-3) and (VI-5) (for  $\Delta\sigma$  and  $f_c$ ) are valid for a large list of numerical models.

Aki, (1967) developed an analysis assuming a sequence of similarities between earthquake to create a scale between them. Starting from the equations developed in the previous section, a relationship that depends on one parameter was proposed.

As expected, there is a relationship between the spatial size of the fault (related with time duration- $f_c$ ), the stress drop, and the energy that is released during an earthquake. Using Eq. (V-1) in (VI-3) we can find:

$$\Delta\sigma = a \frac{M_o}{A} \cdot \frac{1}{L_c}$$

Assuming that the area of the fault ( $A$ ) is proportional to the square of the characteristic length ( $A=b \cdot L_c^2$ ), the previous expression can be reduced (Aki, 1967). Using (VI-5) we obtain:

$$\Delta\sigma = d \frac{M_o \cdot f_c^3}{(k \cdot \beta_s)^3} \quad (\text{VI-6})$$

Where  $d$  is a constant that depends on the shape of the fault; and  $k$  is another constant that depends on the kind of rupture, the azimuth, and the kind of waves. Those parameters together with  $\beta_s$  (the shear velocity of the material around the fault) are constant values for earthquakes with a similar focal mechanics and around the same zone.

## VI.2 Effects of $M_o$ , $f_c$ and $\Delta\sigma$ in the spectrum of an earthquake following the $\omega^2$ -model

If the earthquake follows the  $\omega^2$ -model, the parameters  $f_c$ ,  $M_o$ , and by the Eq. (VI-6)  $\Delta\sigma$  can be determined by an analysis of the Fourier amplitude spectrum. The spectra from  $\omega^2$ -model (Eq. (VI-4)), is plotted for several cases as an example on Figure VI-1. A general case is presented with  $\beta_s=3600$  m/s (Boore, 2005),  $C=2.37 \cdot 10^{-19}$  (Boore, 2005), and a circular fault for S-waves is assumed, implying  $k=0.26$  (Eq. (VI-5)) (Kaneko and Shearer, 2014), and  $d=7/16$  (Eq. (VI-6)) (Eshelby, 1957).

The shape of the Eq. (VI-4) implies that the spectra of the displacement (top Figure VI-1), starts with a plateau until the corner frequency, represented by vertical lines in Figure VI-1. After this value, the spectrum falls with a slope of  $f^2$ . In the previous chapters, the spectra analysis was done in terms of the acceleration. To pass from the spectra of displacement to acceleration from the Fourier transform properties the next equation is obtained:

$$|F(s)| = |4\pi^2 f^2 \cdot F(u)|$$

Where  $F$  refers to the Fourier transform function (Eq. (I-11)),  $s$  to the acceleration of the ground motion, and  $u$  to the displacement of the shaking. This spectrum of the accelerogram is presented in the Figure VI-1 bottom. Following the  $\omega^2$ -model, the spectrum grows from low frequencies until the corner frequency with a slope of  $f^2$ . After this frequency the spectrum takes a shape of a plateau for falling after in higher frequencies (Figure VI-1). In case the spectrogram is analyzed in terms of the angular frequency ( $\omega=2\pi f$ ), the spectrum still grows with a slope of  $\omega^2$ . From this proposition, the model takes his name,  $\omega^2$ -model.

Figure VI-1 is showing a comparison between four earthquakes with two different magnitudes ( $M_o$ ) and two different stress drops ( $\Delta\sigma$ ). Clearly, for displacement and acceleration, the low

frequency content (before  $f_c$ ) is controlled by the seismic moment. At higher frequencies, the stress drop and the seismic moment affect the spectrum. With high values of  $\Delta\sigma$  the spectrum at high frequencies increases. Also, higher values of  $M_o$  generate higher values in the spectrum.

In terms of the corner frequency ( $f_c$ ) the spectrogram will be shifted to lower frequencies with a lower  $f_c$ , if we look in the displacement spectra (Figure VI-1). In the opposite case, the spectrum is shifted to higher frequencies in terms of the displacement. In terms of acceleration, an increasing of  $f_c$  generates a shift to higher frequencies in the spectrogram and an increasing. However, at low frequencies the spectrum depends of the seismic moment and the spectra always lie on the same line at low frequencies if  $M_o$  is constant.

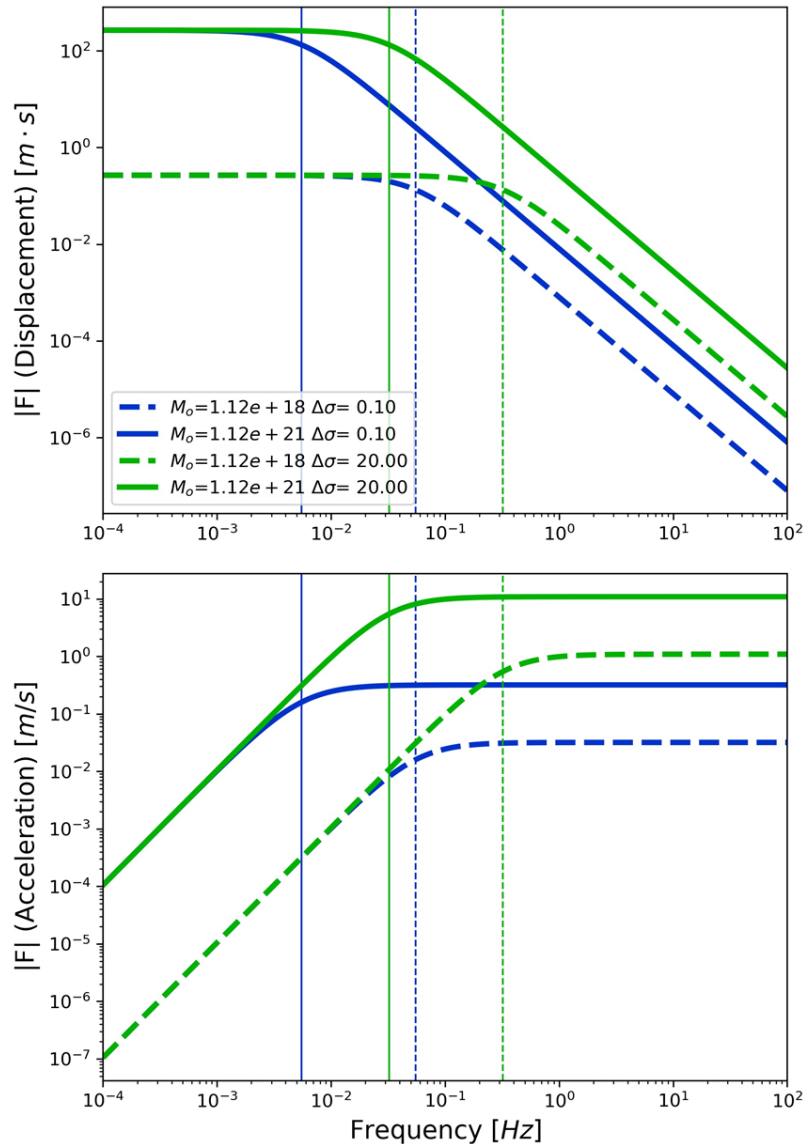


Figure VI-1. Theoretical sketch of spectra from the  $\omega^{-2}$  spectral model (Brune, 1971; Adaptation Modified from figure 2 of Boore, 2003, Figure 2) for displacement (top) and for acceleration (bottom). The green lines correspond to  $\Delta\sigma=20\text{MPa}$  (200 bar) and blue lines to  $\Delta\sigma=0.1\text{MPa}$  (1 bar). The continuous lines correspond to  $M_o=1.12\times 10^{21}$  Nm ( $M_w=8$ ) and dashed lines to  $M_o=1.12\times 10^{18}$  Nm ( $M_w=6$ ). The other parameters of source and radiation are the same for all the cases. Vertical lines represent the values of  $f_c$  for each case. It is clear that, following this model, the stress drop value has a great impact on the level of high frequencies.

Using the general shape of the spectrum (Figure VI-1) it is possible to determine the corner frequency ( $f_c$ ). On the acceleration spectra of real signals, the determination of  $f_c$  is often not an easy task. It consists in picking the frequency where the spectrum stops growing with a slope of  $f^2$  and the plateau starts (Figure VI-2, bottom). On displacement spectra,  $f_c$  is the intersection between the low frequency plateau and the  $f^2$  slope (Figure VI-2, top).

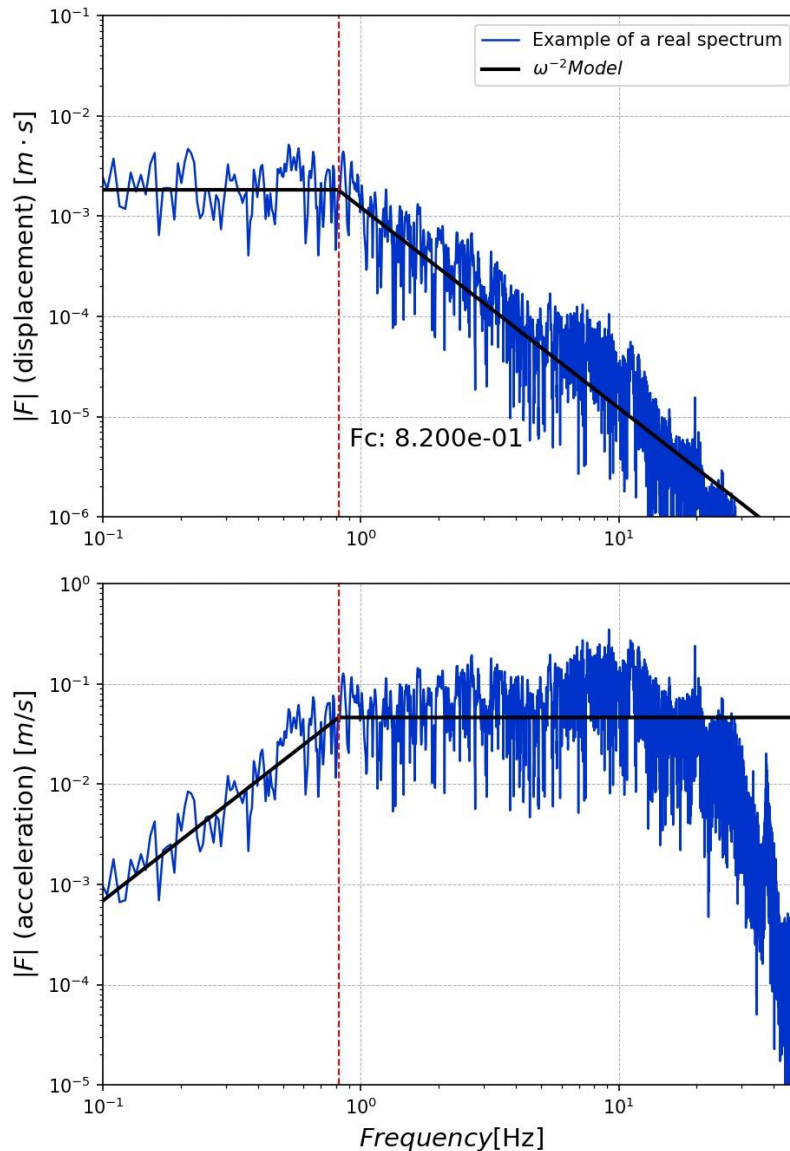


Figure VI-2. General shape of a spectrogram for a ground motion that follows the  $\omega^{-2}$ -model. (black lines)

Both figures show that real spectra are different than the theoretical  $\omega^{-2}$ -model (Figure VI-2). There are many reasons for that: first the signals contain the influence of the source, but also of the path effects and the site effects. However, those terms affect mainly the high frequencies and at low frequencies the spectrum looks more like the model of source (Figure VI-2). If the earthquake is large enough, determination of the corner frequency should not be so much affected by those effects. This is not the case for small events, which corner frequencies  $f_c$  may be biased or even hidden by attenuation (e.g. Dujardin et al., 2016b).

$M_0$  constrains low frequency content of the spectra before  $f_c$  (Figure VI-2).  $M_0$  then can be obtained by analyses on low frequency band (Aki, 1966; Bullen et al., 1985) on the spectra or directly on the time domain signals. If we use Eq. (VI-6) for determining the stress drop, we need

simply to find the  $f_c$  value and  $M_o$ . Since the factor  $f_c$  is raised to the power 3 in the equation, its determination is of major importance in the value obtained for the stress drop and its variability (Cotton et al., 2013). There are many debates to state if whether or not Eq. (VI-6) gives a real estimation of the stress drop. Many authors now call this value “stress parameter” (Archuleta and Ji, 2016 for example). In the following work, nevertheless we will keep the term of stress-drop because it does not change anything in our approach.

$M_o$  constrains low frequency content of the spectra before  $f_c$  (Figure VI-2). It implies that  $M_o$  can be founded by analysis of low frequency band (Aki, 1966; Bullen et al., 1985). The stress drop can be estimated by the Eq. (VI-6). The procedure of this section is one of the ways to determine those parameters thorough an analysis on the spectra. However, there is other methods also valid, and in some case more complex and precise especially to determine the seismic moment and the stress drop (e.g. Godano et al., 2015; Kanamori and Rivera, 2008; Kikuchi and Kanamori, 1991; Vallée et al., 2011).

The stress drop can be estimated by the Eq. (VI-6). The procedure of this section is one of the ways to determine those parameters thorough an analysis on the spectra. However, there are other methods also valid, and in some case more complex and precise especially to determine the seismic moment and the stress drop (e.g. Godano et al., 2015; Kanamori and Rivera, 2008; Kikuchi and Kanamori, 1991; Vallée et al., 2011).

### VI.3 Empirical Green’s function method

The method of Green’s functions allows solving a linear system for any input. The method solves the system for Dirac’s delta as input. The answer to this impulse is known as the Green’s function, and the answer of the system to any input can be computed as the convolution between the Green’s function and the input function (Green, 1828).

When this methodology is applied to seismology, the accelerogram at any point of the earth is obtained as the convolution between the function of releasing of energy in the source (the source time function, *STF*) and the Green’s function. However, a real Green’s function is not possible to compute in a seismologic problem, since it requires an analytic solution of the system, very difficult to obtain because of the lack of knowledge and the complexity of the medium. Although, a numerical Green function can be approached though the modelling of seismic wave propagation in a heterogeneous medium. Thanks to the development of super computers, this approach is now efficient in the regions of the world where the underground medium is well known (i.e. Maufroy et al., 2016). However, they are often limited to rather low frequencies due to the poor knowledge of structure velocities.

Hartzell, (1978) was the first to propose an approximation using signals from earthquakes as Empirical Green’s function (*EGF*). A small event that occurred close to the event to simulate, with the same focal mechanism is used to represent the propagation and site effects with the assumption that the details of its STF is negligible compared to STF of the larger event to be simulated. Then a difference of magnitude of one or two is necessary between the small event taken as EGF and the target one (Courboux, 2010).

The EGF method has the great advantage to account for the wave path in a complex medium: The simulations include the azimuth-dependent propagation effects at regional scale and account for the local 3D site effects under the assumption of linearity. Since the pioneering work on Hartzell, (1978), it has been widely used by many researchers and engineers to produce realistic ground motions (i.e. Causse et al., 2009; Dujardin et al., 2016a; Frankel, 1995; Honoré

et al., 2011; Irikura, 1986; Kurahashi and Irikura, 2011; Salichon et al., 2010) using simple source models or more complex ones that takes into account the rupture extension.

The methodology we propose is based on the work of Kohrs-Sansorny et al., (2005). This methodology or similar ones have been used in different contexts and gave reliable results (Alessandro and Boatwright, 2006; Alfonso-Naya et al., 2012; Honoré et al., 2011; Salichon et al., 2010). They are based on a stochastic definition of the source following a special scheme of summation, and the use of EGF.

The method is easy to use and reliable because very few parameters are necessary. We propose in this chapter a way to constrain these parameters and their variability.

A seismogram at any point can be expressed as Eq (VI-7).

$$S(f) = STF(f) \cdot P(f) \cdot TF(f) \quad (\text{VI-7})$$

Where  $S$ ,  $STF$ ,  $P$ , and  $TF$  are respectively the Fourier Transform of the components of the source, the path, and the site effects respectively. The term associated with the source ( $STF$ ) determines the energy that is release and the initial frequency content of the earthquake.

Following the method of *EGF* presented by Kohrs-Sansorny et al., (2005), the model of source ( $STF$ ) is chosen supposing that the earthquakes are following the  $\omega^2$ -model (Eq. (VI-4)). Expressing this model in terms of the spectrum of the acceleration, Eq. (VI-4) becomes:

$$STF(f) = 4\pi^2 f^2 \cdot C \cdot M_o \left/ \left( 1 + \left( f/f_c \right)^2 \right) \right. \quad (\text{VI-8})$$

If the system is linear, then for a strong motion coming from the same location than a weak ground motion, the path effects ( $P$ ) and site effects ( $TF$ ) are the same. Then:

$$R = S_{strong} / S_{weak} = STF_{strong} / STF_{weak} \quad (\text{VI-9})$$

This means that with a linear assumption, the scale between a weak and strong ground motion ( $R$ ) can be estimated by the scale between the sources. When the ratio of two earthquakes ( $R$ ) is evaluated on the  $\omega^2$ -model, and supposing a similar radiation pattern ( $C$  is constant in Eq. (VI-8)), Eq. (VI-8) in the Eq. (VI-9) produces (Joyner and Boore, 1986):

$$R = \frac{M_o}{m_o} \cdot \frac{1 + \left( f/f_c \right)^2}{1 + \left( f/F_c \right)^2} \quad (\text{VI-10})$$

Where  $M_o$  and  $m_o$  are the seismic moments of the earthquake that is estimated (strong event) and the earthquake that will be used as *EGF* (weak event), respectively.  $F_c$  is the corner frequency of the target earthquake and  $f_c$  is the corner frequency of the small earthquake, used as *EGF*.

With the previous conditions, the general shape of the scale between two earthquakes ( $R$ ) is shown in the Figure VI-3 (Eq. (VI-10)). At low frequencies,  $R$  depends exclusively of the scale of the seismic moment between both earthquakes. At higher frequencies the stress drops ratio between both earthquakes (represented by the ratio of the corner frequencies  $f_c$  and  $F_c$  in this figure) is influencing also the shape of  $R$ .

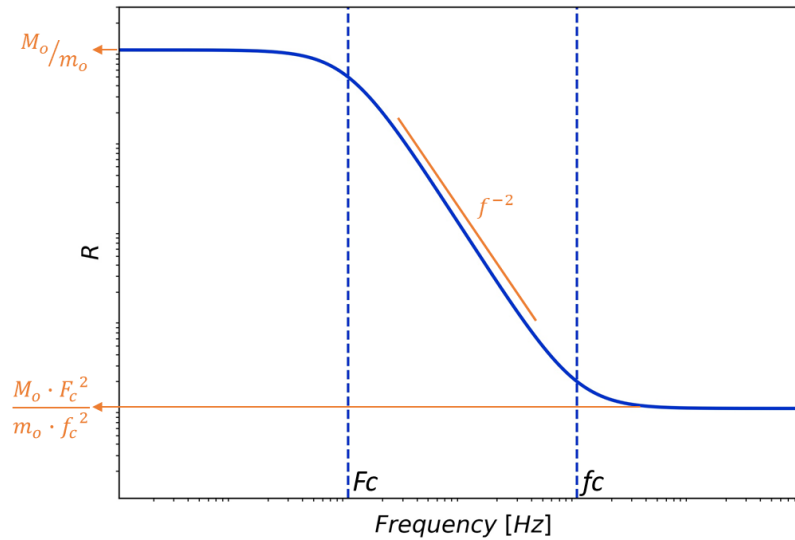


Figure VI-3. General shape of the scale function ( $R$ , Eq. (VI-10)). The axes are in  $\log_{10}$  scale.  $F_c$  and  $f_c$  represent respectively the corner frequencies of the strong event and the weak event.  $M_o/m_o$  is the ratio between the seismic moments of the strong and weak event.

Eq. (VI-10) represents the ratio of a theoretical case. However, to recreate a realistic result, the variability of the release of energy in the source must be considered. Joyner and Boore, (1986) proposed to sum lags of time to represent the spatial and random release of energy during the source. These random delays are generated in a way that in the frequency domain the Eq. (VI-10) is in average satisfied.

Several methods are proposed to generate those delays. Wennerberg, (1990) proposes a method where the time delays are generated by groups in a two-stage method. This way of generation allows obtaining realistic and different histories that can be associated with the real ones. This method avoids the convergence when a large number of random summations is done. Because of this reason, this EGF method is applicable in the simulation of stronger events, obtaining yet a large range of different possible faults. With this model of two-step generation, the ratio  $R$  (Eq. (VI-10)) is generated with a previous step in the time domain. A time function ( $r$ ) is defined as:

$$r^{(i)} = \kappa \sum_{d=0}^{\eta_c} \left[ \sum_{c=0}^{\eta_d} \delta(t - t_c - t_d) \right] \quad (\text{VI-11})$$

$r^{(i)}$  is composed by scaled points that are also composed by a summation of impulses that are distributed in time randomly. The index  $i$  represents the index of the simulation, and the factor  $\kappa$  is a coefficient of scaling.  $\delta$  refers to the Dirac's delta function, where  $t_c$  and  $t_d$  are random delays in time.  $\eta_d$  and  $\eta_c$  are the numbers of pulses in which are divided the signal.

The Dirac's function ( $\delta$ ) in the Eq. (VI-11) cannot be defined, and a discrete approximation is necessary, since all the process is done in a discrete analysis. The function  $\delta$  is approximated as:

$$\delta(t - t_c - t_d) \approx \frac{1}{\Delta t} \cdot \hat{\delta} \left( \text{int} \left( \frac{t - t_c - t_d}{\Delta t} \right), 0 \right) \quad (\text{VI-12})$$

The term  $\Delta t$  represents the step of time that stores the accelerogram. In other words, it is the inverse of the sample frequency that is used ( $\Delta t = 1/f_{\text{sample}}$ ). This term is necessary because in the Eq. (VI-11) the Dirac's function cannot be defined, and a discrete approximation is done with the

Kronecker delta ( $\hat{\delta}$ ). So to guarantee that the energy of  $r^{ij}$  won't be affected, the normalization  $1/\Delta t$  must be added. The function *int* is a truncation process to remove the decimals of the number in the interior.

As was mention, the method of EGF that is used (Kohrs-Sansorny et al., 2005; Wennerberg, 1990) makes the equality in the Eq. (VI-10) to be accomplished in average for all the simulation. To achieve this, the scale ( $\kappa$ ), the number of delays ( $\eta_c$  and  $\eta_d$ ), and the distributions of probability for  $t_c$  and  $t_d$  are fitted.  $\eta_d$  and  $\eta_c$  are defined as:

$$\eta = \eta_d \cdot \eta_c \text{ where: } \eta = \left(\frac{f_c}{F_c}\right)^4 \quad (\text{VI-13})$$

Eq. (VI-13) guarantees that there are enough impulses to estimate the signal in high frequencies, but also that there is not too much to make that the simulations trend to be unrealistic and identical between them. The coefficient  $\kappa$  is obtained to scale the number of used points ( $\eta$ ) with the scale function that is searched (Eq. (VI-10)):

$$\kappa = \frac{M_o}{m_o \cdot \eta} \quad (\text{VI-14})$$

The delay times  $t_c$  and  $t_d$  are distributed with a density probability function that makes that in average the Fourier transform amplitude of  $r^{ij}$  will be equal to the expected scale ( $R$ : Eq. (VI-10)).

For computing this density probability for the time lags, several functions have been used. Some studies have used simple probability density (e.g. Joyner and Boore, 1986; Wennerberg, 1990) that can be applied but generates no realistic predictions in time or in the frequency domain, as was noted by the authors. In this study, we follow the approximation of Ordaz et al., (1995) that guarantees that in average the spectra of the generated scales ( $r$ ) satisfying the Eq. (VI-10) for all the frequencies.

However, this method (Ordaz et al., 1995) uses a single-step summation, and this produces that the summation converges. Because this, neither different possibilities are reproduced nor realistic time accelerograms are constructed. In Kohrs-Sansorny et al., (2005) both methodologies are mixed reproducing time delays with density of probability of Ordaz et al., (1995), and using the two-step summation of Wennerberg, (1990). In this case, the general density of probability for the time delays is (Kohrs-Sansorny et al., (2005):

$$\rho = \int_{-\infty}^{\infty} \frac{\sqrt{1 + \left(\frac{2}{1 + (F_2/F_1)^2}\right) \cdot (f/F_1)^2}}{1 + (f/F_2)^2} \cdot e^{i2\pi f t} df \quad (\text{VI-15})$$

Where for  $\rho_c$ , the density function of  $t_c$ , the values  $F_1$  and  $F_2$  are  $F_d$  and  $F_c$  respectively. For  $\rho_d$ , the density function of  $t_d$ , the values  $F_1$  and  $F_2$  are  $F_d$  and  $F_c$ .  $F_c$  and  $f_c$  being the corner frequencies of the strong earthquake and the weak earthquake respectively.  $F_d$  is defined as:

$$F_d = \eta_c^{1/4} \cdot F_c \quad (\text{VI-16})$$

Generating the time delays  $t_c$  and  $t_d$  with adequate distributions; defined in Eq. (VI-13), (VI-15), and (VI-16); allows us to find the ratio between the spectra from weak and strong ground motions (Eq. (VI-9)).

$$S_{strong}(f) = S_{weak}(f) \cdot \hat{R}^{ij}(f) \quad (\text{VI-17})$$

Where  $S_{strong}$  is the amplitude spectrum (FAS) of the signal at the surface of the target signal.  $S_{weak}$  the amplitude of the Fourier spectrum of the weak record (EGF).  $\hat{R}^{(i)}$  is the Fourier transform of the summation of the impulses defined in the Eq (VI-11). The Eq. (VI-17) in time domain view represents a convolution defined as:

$$S_{strong}^{(i)}(t) = EGF(t) * r_i(t) \quad (VI-18)$$

Where  $S_{strong}^{(i)}$  is one of the possibilities of the accelerogram of the target earthquake,  $EGF$  is the accelerogram used from the weak ground motion, and  $r_i$  is the scale founded with the Eq. (VI-11).

### VI.3.1 Criteria to use EGF method

As it was mentioned before, the EGF method has several assumptions, especially to find the scale function ( $r$ ) between the weak (EGF) and the strong earthquake. Those assumptions imply that the method is restricted to be applied if the next points are accomplish (Honoré-Foundotos, 2013):

- The EGF and the target event has the same location. Ideally, the EGF source involves the same zone than the target event, since the future earthquake source is assumed to be around the hypocenter of the EGF. If the site of prediction is located far enough the differences in the locations can be neglected.
- The EGF have the same focal mechanism than the target event.
- The EGF have an adequate signal to noise ratio. Since the EGF will be scaled, if this one has a high level of noise it will produce an amplification of the noisy effects, producing a not realistic prediction.

### VI.4 Relationship between corner frequency, seismic moment and stress drop

In summary, the methodology explained in the previous section Kohrs-Sansorny et al., (2005) estimates the ground motions as a function of a weak ground motion  $EGF$  and the earthquake that is estimated. The input parameters that are necessary are the seismic moment and the corner frequencies of both the small and the target event.

Concerning the small event used as EGF, it is easy from classical seismological methods to compute its seismic moment. Its corner frequency  $f_c$  will be determined as precisely as possible on the signal of different stations, ideally placed in different azimuths to avoid a possible directivity effect of the rupture process. This determination is maybe the part of the work that needs the higher attention.

Concerning the target earthquake, there are several propositions to estimate the seismic moment, of a future earthquake that could occur in some region. These methods involve historical analysis and seismic risk hazard.

Estimating the corner frequency of the target event is a more difficult task since it involves estimating the rupture process and the stress drop of an earthquake that hasn't occurred yet. In this section we propose a method to fit the  $F_c$  value of the target event and its variability

Integrating some of the equations that have been explained in this chapter, we can see that the corner frequency ( $f_c$ ), the stress drop ( $\Delta\sigma$  in Eq. (VI-6)), and the spatial size of the fault ( $L_c$  in Eq. (VI-5)) are related between them. Many studies have been done to find a relationship between those parameters with the seismic moment ( $M_o$ ) (e.g. Hanks, 1977; Scholz, 1982).

Allmann and Shearer, (2009) gathered the determination of the corner frequencies  $f_c$  from many authors on earthquakes around the world. Figure VI-4 shows the relationship between  $f_c$  and the seismic moment. From this figure, we can see clearly that  $f_c$  and  $m_o$  are related. Additionally, under constant stress drop, the relationship  $M_o$  and  $f_c$  follows approximately a logarithmic line proportional to  $f_c^{-3}$ , as is predicted in Eq. (VI-6).

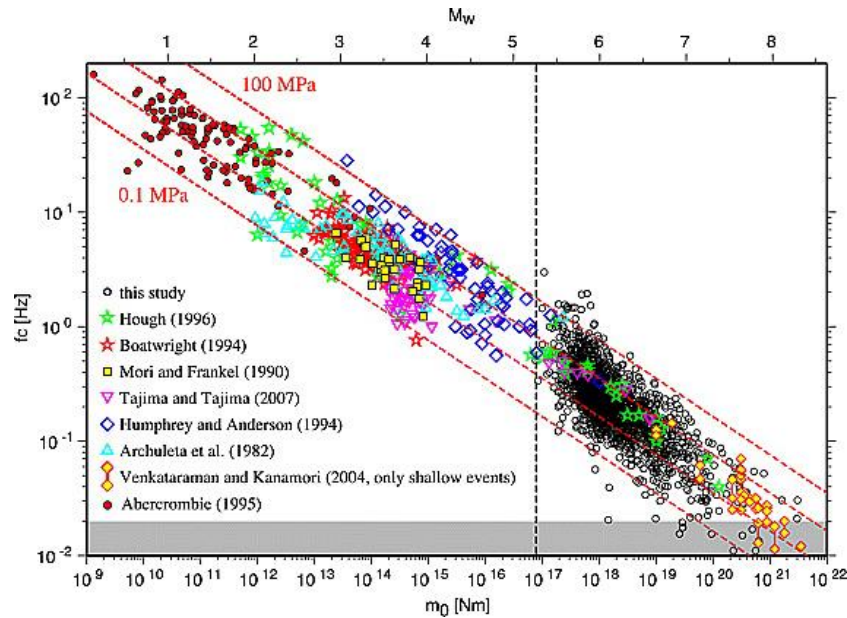


Figure VI-4. Relationship between the seismic moment and the equivalent radius of the fault for several earthquakes. Extracted figure from Allmann and Shearer, (2009).

The variability of the stress drop has been studied since  $\Delta\sigma$  is an important parameter in the prediction of the earthquakes high frequencies for several methods, as Ground Motion Prediction Equations (GMPE) and *EGF* (through  $f_c$ ). Chouet et al., (1978) showed that the average value of the stress drop ( $\Delta\sigma$ ) depends of the region where the earthquake occurs but that its variability is constant.

The variability of  $\Delta\sigma$  has been studied in many regions and cases (e.g. Allmann and Shearer, 2009; Oth et al., 2010; Shearer et al., 2006) and it is approximately constant, independent of the seismic moment and the size of the earthquake. In Cotton et al., (2013) the variability of the stress drop was studied by two methods. They found that the variability of the stress drop that is obtained by analysis of the *PGA* is lower by three to four times the variability obtained by spectrum analysis. Maybe this result can be explained by the uncertainty in the process of picking the corner frequency in a spectra analysis.

Following those studies, using the database of SCARDEC (Vallée et al., 2011) Courboulex et al., (2016) determine the total duration of the rupture ( $T$ ) directly of the *STF* from 2892 events between 1992 to 2014. SCARDEC database is a global database of source time functions together with parameters as the seismic moment, depth and focal mechanism. It analyzes earthquake with a seismic magnitude above  $M_w$  5.8 (Vallée and Douet, 2016).

The total duration of the rupture is related to the corner frequency ( $f_c$ ) of an earthquake (Brune, 1971, 1970; Madariaga, 1976). In general, the relationship between both parameters is expressed as (VI-19).

$$f_c = q/T \quad (\text{VI-19})$$

Where  $T$  is the total rupture duration, and  $q$  is a value that changes depending on the type of fault (Appendix B Godano et al., 2015). For a rectangular fault, that generates an  $stf$  with a trapezoidal shape,  $q$  has the value of 0.803 (Haskell, 1964). If the fault takes another kind of geometry,  $q$  value changes. Other models even make the parameter  $q$  different for P and S waves, but in general, the range of  $q$  varies from 0.3 to 1.0 (Figure VI-5).

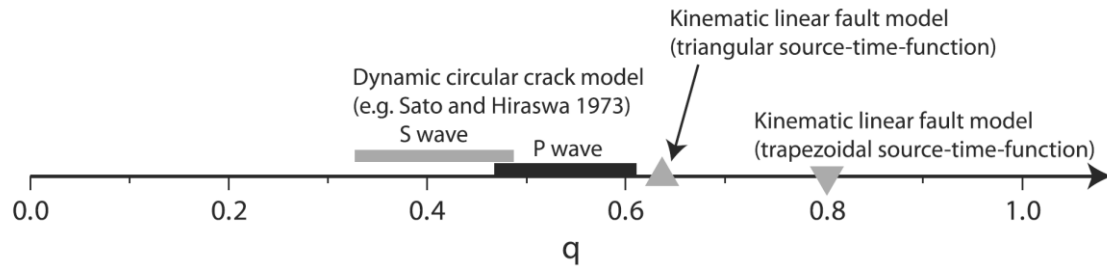


Figure VI-5. Estimation of the  $q$  parameter for different fault rupture models (Godano et al., 2015, Figure B3).

Courboux et al., (2016) proposed a relationship between the seismic moment and the total rupture duration ( $T$ ) of the source (Figure VI-6). This relationship is equivalent to the Figure VI-4, but it is determining the duration by an analysis of STF and not through the corner frequency determination. This reduces the uncertainty in the definition of the stress drop.

The database was separated into two groups: earthquakes that occurred in a subduction zone context and the others (not subduction) groups. This 2 groups comes from the fact that the duration of the Source process, for an equivalent magnitude, is larger in subduction context (i.e. the stress drop is lower) than in other regions (e.g. Allmann and Shearer, 2009; Bilek and Lay, 1999; Chounet et al., 2018), as is clear in the Figure VI-6.

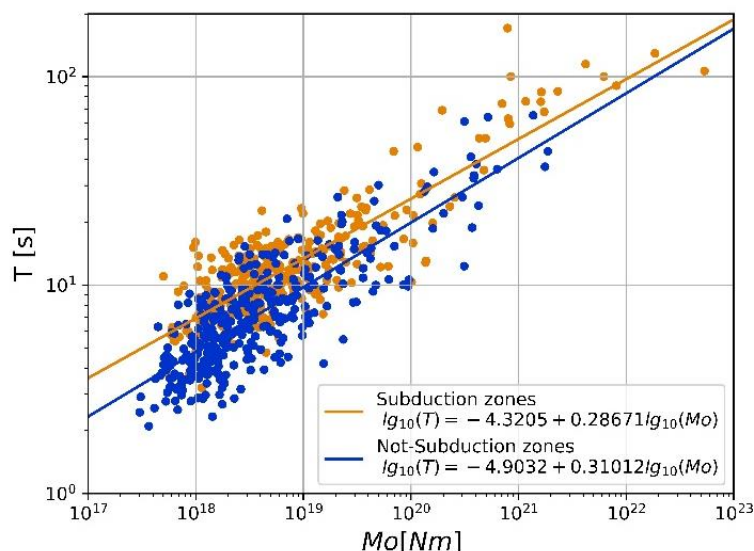


Figure VI-6. STF duration obtained from the analysis of global earthquakes Courboux et al., (2016). The relationship between Duration of the rupture ( $T$ ) and seismic moment ( $M_0$ ).

As in the case of  $f_c$  (Figure VI-4) there is an uncertainty of  $T$  associated with the stress drop (Figure VI-6). This variability is following a log-normal distribution (Courboux et al., 2016). The log-normal distribution has a mean equal to the proposed linear regression in Figure VI-6. It means that the parameter  $\mu$  of the distribution is computed with the Equation (VI-20).

$$\mu = \ln(T) - \frac{\sigma_{\ln}^2}{2} \quad (\text{VI-20})$$

Where  $\sigma_{\ln}$  is the lognormal standard deviation of the distribution, proposed as 0.32 for subduction events and 0.34 for other kind of events (Courboulex et al., 2016).

Using the distribution of  $T$  (Equation (VI-20)) and introducing the Equation (VI-19), we can estimate the corner frequency of the earthquake with the seismic magnitude. It allows us to use the empirical Green's function method just fixing the magnitude of the earthquake that we want to estimate.

To manage the variability of  $T$  and with the spatial release of energy, we make several simulations, each one with new values of inputs. This process is repeated a large number of times in order to explore the space of possible results. Figure VI-7 shows the implemented algorithm to develop the procedure described before (we choose the language Python).

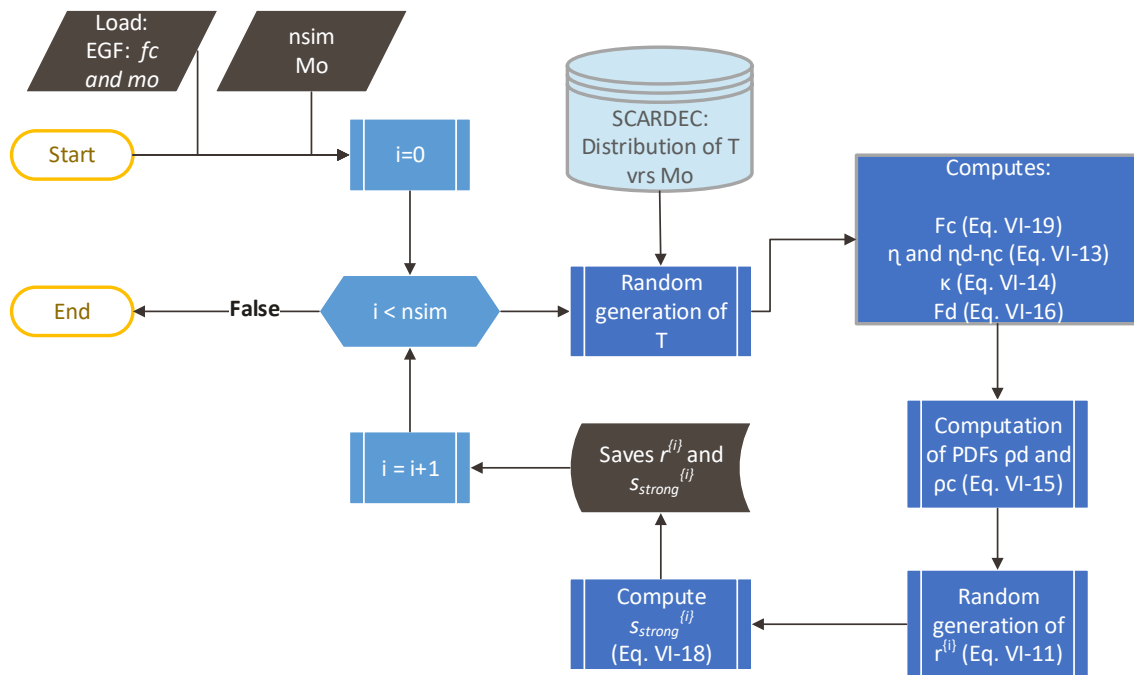


Figure VI-7. Scheme of the algorithm developed for ground motion simulation. The inputs are the corner frequency  $f_c$  and the seismic moment  $m_o$  of the small event used as EGF, the EGF traces and the moment of the target earthquake ( $M_o$ ).  $nsim$  represents the number of simulations.

### VI.5 Sensitivity analysis of EGF method facing a stochastic duration of the fault

When  $f_c$  is not a fixed value, it implies a variation in the answer of the EGF method. In this section, the variability between the results is discussed because the variation of  $f_c$  is studied. We analyze those changes studying the scale function  $R$ , since it is in average the spectrum where all the simulation  $r^{(i)}$  converges.

From the Eq. (VI-10) is obtained the scaling function ( $R$ ) that will modify the weak ground motion (EGF) to become the simulated one. The previous section showed that the corner frequency can be related with the rupture duration ( $T$ ) by the Eq. (VI-19). In terms  $T$ , by mixing Eq. (VI-17) and Eq. (VI-19), the scale that the EGF method assess is written as:

$$R(f) = \frac{M_o}{m_o} \cdot q^2 \frac{1 + \left(f/f_c\right)^2}{q^2 + T^2 f^2} \quad (\text{VI-21})$$

The parameter  $q$  depends on the kind of fault, explained in the subsection 2.  $M_o$  and  $m_o$  are the seismic moments of the strong and weak earthquake respectively. The value of  $f_c$  is the corner frequency of the *EGF*. All the previous parameters are constant in the model proposed in this chapter. The term  $T$  is modeled as a stochastic variable with a lognormal distribution that is explained in the subsection 2.

First, to understand how  $R(f)$  changes for different values of  $T$ , we start analyzing low frequencies in the function  $R(f)$ . In this case,  $R(f)$  is independent of the value of  $T$ . It is proven by evaluating the Eq. (VI-21) at low frequencies:

$$\lim_{f \rightarrow 0} R = \frac{M_o}{m_o}$$

The scaling function  $R(f)$  at low frequencies depends only on the seismic moment ratio. It means that the predicted earthquake at low frequencies is not affected neither by the variation of the fault duration  $T$  nor by the  $q$  value. This trend appears before  $f$  takes the value of almost zero. Indeed, it is just necessary that  $f$  approximates to  $0.5 q/T$ .

At high frequencies  $R(f)$  also trends to a fixed value:

$$\lim_{f \rightarrow \infty} R = \frac{M_o}{m_o} \cdot \left(q / (T \cdot f_c)\right)^2$$

This means that high frequencies of the predicted earthquake will be affected by the changes in  $T$  and the selected value of  $q$ . Additionally,  $R$  trends to a constant value for high frequencies. The definition of high frequencies is marked approximately for  $f$  approximates to  $2f_c$ .

In a graphical analysis (Figure VI-8) it is easy to see that the low frequencies are not affected by the variation of  $T$ . The result on other frequencies is inverse to  $T^2$ , and the effect becomes stronger with higher frequencies.  $R$  and  $q$  have an increasing relationship, being more important for higher frequencies. A high value of  $q$  produces an increase at middle and high frequencies of  $R$  (Figure VI-8). Also, we can observe that higher values of  $f_c$  produce a reduction in the  $R$  function, again the effect becomes more important on high frequency bands.

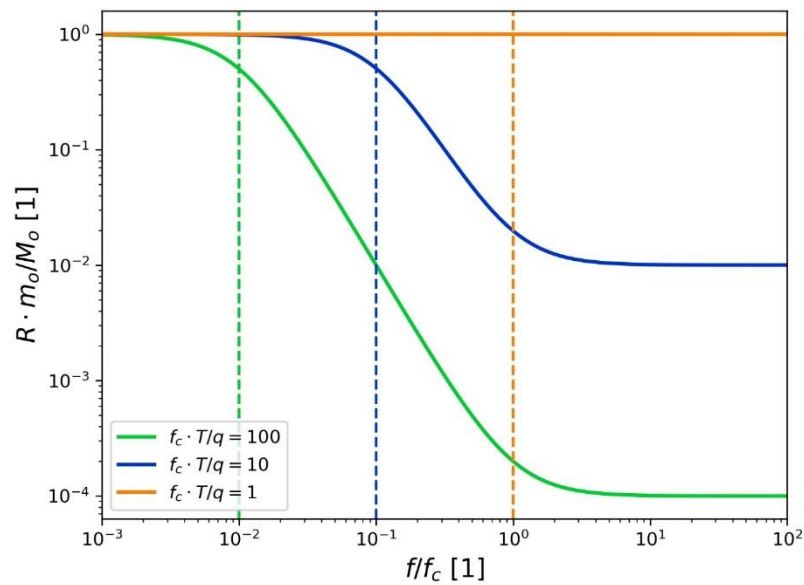


Figure VI-8. Variation of the scale function ( $R$ ) in function of the corner frequencies. The term  $f_c$  is picked from the EGF,  $F_c$  is estimated as  $F_c = q/T$ .

#### VI.6 Case of the Pedernales Mw 7.8 (Ecuador) Earthquake ok 16 April 2016

The methodology described before (Figure VI-7), is applied for the earthquake that occurred along the coast of Ecuador in the zone of Pedernales on 16<sup>th</sup> April 2016 at 23:58 UTC. The earthquake occurred on the interpolate interface of the subduction between the Nazca plate and the northern Andean plate, at shallow depth. During the last century, several strong earthquakes (around 9 events with  $M_w > 7$ ) have occurred in this zone (e.g. Kanamori and McNally, 1982; Nocquet et al., 2017).

Generally all the country of Ecuador has a large seismic hazard (Beauval et al., 2013; Kelleher, 1972). Because many large cities exist in Ecuador with buildings that generally were not constructed following a seismic code, it is a country of high seismic risk. Several studies have been developed to analyze the zone and to improve the hazard assessment (e.g. Bonilla et al., 1992) like for example the REMAKE program that is a French-Ecuadorian cooperation in seismic research. In this context, the earthquake catalogs for Ecuadorian zone have been updated to find the recurrence of the earthquakes in function of  $M_w$  (e.g. Beauval et al., 2013; Yepes et al., 2016).

In Beauval et al., (2018) an Ecuadorian catalog is used together with other global catalogs to compute a hazard map for all Ecuador. In this study, after establishing the seismic moment of the earthquake by the catalogs, GMPE are used to estimate the  $PGA$  for the different zones. The GMPEs are selected depending of the zone and kind of earthquake that is studied. For the zone of the subduction interface, that corresponds to the Pedernales Earthquake, in Beauval et al., 2018 the average of three GMPEs (Abrahamson et al., 2016; Montalva et al., 2017; Zhao et al., 2006) was used to estimate the uncertainty in the ground motion prediction.

In our study we are proposing an alternative to GMPEs using an EGF method explained in the chapter before. As example, in this case we will develop the prediction for the Pedernales Earthquake. This earthquake has a seismic moment of  $7.054 \times 10^{20} \text{Nm}$  ( $M_w = 7.8$ ). The epicenter of the earthquake is at latitude  $0.348^\circ$  and longitude  $-79.972^\circ$ , but the fault is scattered for a large zone of around 100 km (Figure VI-9).

The simulations presented herein are realized for the city of Quito. This city, that counts around 2'800,000 inhabitants, is located on the Andes Cordillera lying on a piggy back basin caused by a reverse fault. In this city strong site effects in different zones have been detected (Chatelain et al., 1996; Guéguen et al., 2000; Laurendeau et al., 2017). This allows us to test the *EGF* method under different circumstances. Additionally, the Quito city is located far enough of the fault to be able to apply the *EGF* method (Figure VI-9).

We use the records of the permanent accelerometric network in Quito (RENAC-Quito) in 14 stations where Pedernales earthquake was well recorded (Figure VI-9). These stations are operated by the Instituto geofísico de la Escuela Politécnica Nacional (IGEPN). The records from these stations are adequate in general for analysis at frequencies lower than 10 Hz. This is mainly due to the noise generated by the city and the fact that the accelerometers are not sensitive to week motions (Cauzzi and Clinton, 2013; Laurendeau et al., 2017).

To develop the *EGF* method, we select six earthquakes as good candidates for *EGF*. The criteria were:

- Proximity to the source of the Pedernales earthquake (Figure VI-9).
- Same focal mechanism than the Pedernales Earthquake
- Adequate seismic moment (at least 1 order of magnitude smaller than the mainshock)
- Good signal to noise ratio (S/N larger than 3 for frequencies between 0.1Hz and 15 Hz)
- When the earthquakes were large enough we used the Scardec solution (Vallée and Douet, 2016) to check that the STF was simple. Indeed, a complex source with many pulses could introduce spurious complexity in the simulated waveforms.

The selected earthquakes characteristics are summarized in Table VI-1. All of them are aftershocks produced around the mainshock in the next days after the Pedernales earthquake (Figure VI-9).

Table VI-1. Characteristics of the *EGF* used in this study (USGS global catalog)

Name	Mw	Source time (UTC)			Location		
		Date	Hour	Latitude [°]	Longitude [°]	Depth [km]	
<b>2016041707</b>	5.8	17/04/2016	7:14	-0.385	-80.201	24.0	
<b>2016041709</b>	5.6	17/04/2016	9:23	-0.234	-80.694	10.0	
<b>2016041922</b>	5.7	19/04/2016	22:22	0.578	-80.025	15.4	
<b>2016042203A</b>	6.0	22/04/2016	3:03	-0.292	-80.504	10.0	
<b>2016042203B</b>	5.9	22/04/2016	3:25	-0.281	-80.504	10.3	
<b>2016042301</b>	5.7	23/04/2016	1:24	0.613	-80.252	10.0	

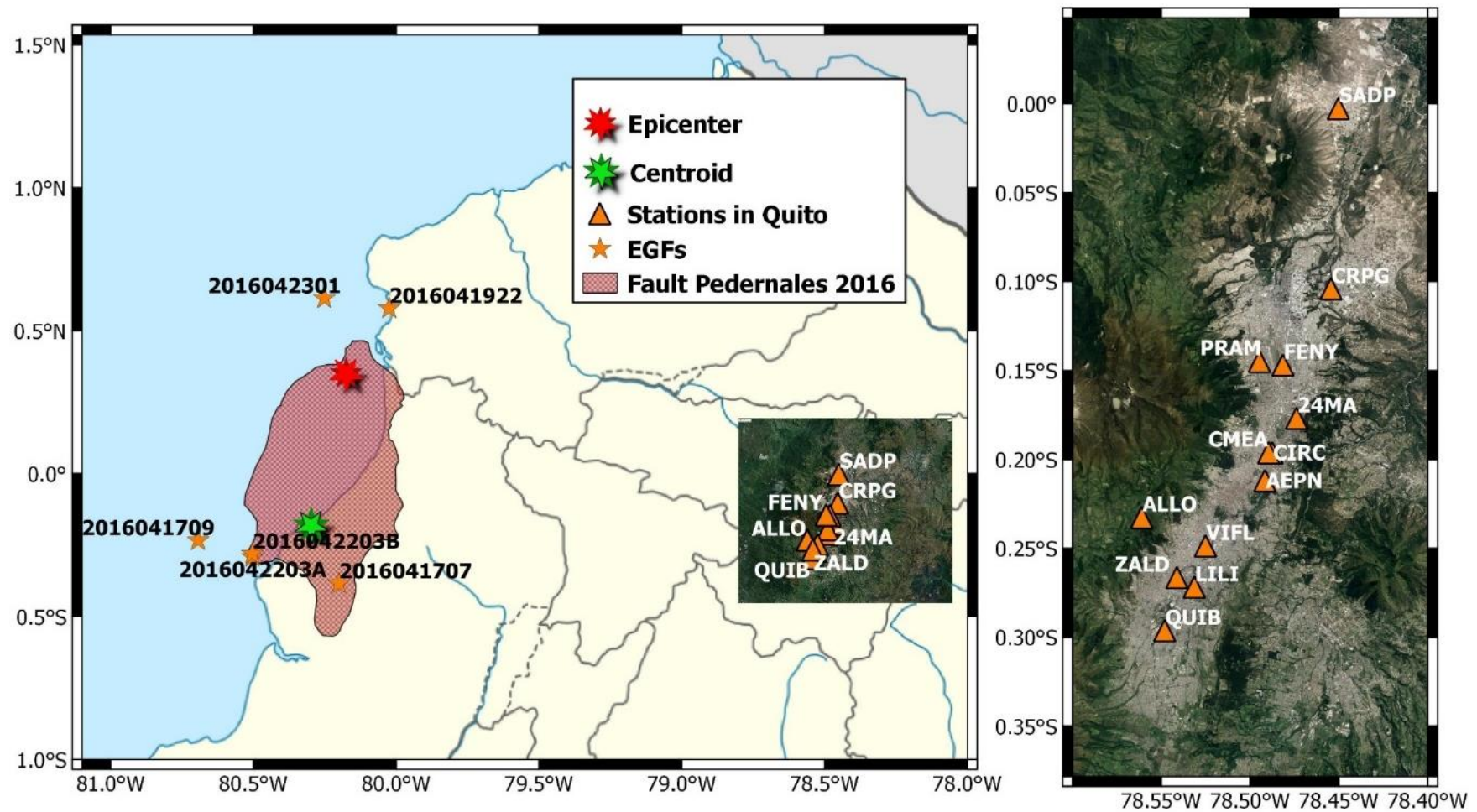


Figure VI-9. Left: Epicenters of the Pedernales earthquake, Mw7.8 (red star) and the 6 aftershocks (orange stars) used as EGF in this study. The main fault zone activated during the earthquake (dashed red area represent the area where the slip is larger than 1m) is extracted from Nocquet et al., (2017). The green star represents the centroid, where the maximum of energy was released. The accelerometric stations of the RENAC–QUITO networks are represented by orange squares. Right: Zoom on the Quito basin. Stations and topography.

### VI.6.1 Signal processing and distance correction

To isolate the waves coming from the earthquakes, removing the vibrations from other sources different than the earthquake, a signal process is applied. This process is similar to the one applied to the Kik-Net database and explained in the section II.2. In summary, this signal process consists in:

- The linear trend was removed
- The mean was removed
- The signal is cut by a Hanning window with a width of 4s, 2s before the first arrival of the P-waves and 2s after the coda we defined.
- A butter (also call Butterworth) bandpass filter at 0.1 Hz and 15 Hz of order 3

Then, an extra correction related with the distance is applied. This correction is applied to the amplitude of the signal to be equivalent to an earthquake that is located at the same distance than the Pedernales earthquake. This correction is related to the geometrical attenuation of the wave.

For the case of Pedernales, the general distance of the source to Quito, where the prediction is realized, is around 200 km. For these distances, the geometrical attenuation corresponds to multiple reflected and refracted S-waves. At this distances, beyond 130 km, the attenuation can be modeled with a power coefficient of 0.5 (Atkinson and Mereu, 1992). Based on this, and neglecting the anelastic attenuation ( $Q(f)$ ), we use as a correction by the distance the Equation (VI-22):

$$EGF(t) = \sqrt{R_{EGF}/R_{Objective}} \cdot EGF'(t) \quad (VI-22)$$

Where  $EGF$  is the final record that is used,  $EGF'$  is the processed record without any distance correction, and  $R_{EGF}$  and  $R_{Objective}$  are the distances from the site to the source of the EGF and to the Earthquake objective respectively.

To define the distance between the stations to the mainshock, a point on the slip inversion of Nocquet et al. (2017) was selected where most of the energy was released (centroid on Figure VI-9). Since the distances from the earthquake to the stations were much larger than the depth, we did not take in account the depth in the correction by distance. The distances between the centroid of Pedernales's earthquake and the stations are shown in Table VI-2.

### VI.6.2 Determination of the corner frequency for each EGF

In the  $\omega^2$ -model the spectrum in acceleration and in displacement can be fitted to simple shapes (see Figure VI-1). We analyzed manually for each EGF the Fourier spectrum in acceleration and in displacement to find the corner frequency ( $f_c$ ) (Figure VI-10). The procedure was explained in more details in the section VI.2.

Table VI-2. Position of the stations (source: Instituto Geofísico) and distance to the centroid of the Pedernales earthquake (80.2981W, 0.1830S, green point Figure VI-9).

Name	Distance [km]	Position	
		Longitude [°]	Latitude [°]
<b>24MA</b>	203.6	-78.47380	-0.17688
<b>AEPN</b>	201.6	-78.49165	-0.21199
<b>ALLO</b>	193.8	-78.56099	-0.23273
<b>CIRC</b>	202.0	-78.48755	-0.19630
<b>CMEA</b>	201.8	-78.48950	-0.19620
<b>CRPG</b>	205.7	-78.45439	-0.10411
<b>FENY</b>	202.7	-78.48150	-0.14700
<b>LILI</b>	197.1	-78.53140	-0.27190
<b>PRAM</b>	201.2	-78.49470	-0.14490
<b>QUIB</b>	195.3	-78.54809	-0.29639
<b>SADP</b>	206.2	-78.45023	-0.00255
<b>VIFL</b>	197.8	-78.52511	-0.24870
<b>ZALD</b>	196.0	-78.54121	-0.26652

It's important to note that just in this part of the analysis of looking  $f_c$ , the signals were not filtered at low frequencies. We applied just lowpass filter (butter 3<sup>rd</sup> order, 10Hz) to reduce the effect of the noise and clarify the results, but at low frequencies the wave was not manipulated. We think that a low frequency cut-off exists on these stations at 20sec, as if it is not mentioned anywhere. Due to this, for some cases high noisy at low frequencies can be observed still, for example the station QUIB (Figure VI-10). This noisy at low frequencies produces a strange raising that is not expected by the  $\omega^2$ -model. However, this raising for most of the cases was before  $f_c$ , allowing us to compute  $f_c$  in each case using the analysis described in the section VI.2.

In the  $\omega^2$ -model the spectrum in acceleration and in displacement can be fitted to simple shapes (see Figure VI-1). We analyzed by eye analysis for each EGF the Fourier spectrum in acceleration and in displacement to find the corner frequency ( $f_c$ ). In general, this analysis finds  $f_c$  as the frequency where the spectrum of the displacement pass from being plane to decay with a slope of -2 in log scale (right column Figure VI-10). In the spectrum of acceleration,  $f_c$  is the point where the spectrum passes to be plane when before was raising with a slope of 2, in log scale (left column of Figure VI-10). The procedure was explained in more detail in the section VI.2.

It's important to note that just in this part of the analysis of looking  $f_c$ , the signals were not filtered at low frequencies. We applied just lowpass filter (butter 3<sup>rd</sup> order, 10Hz) to reduce the effect of the noise and clarify the results, but at low frequencies the wave wasn't manipulated. Due to this, for some cases high noisy at low frequencies can be observed still, for example the station QUIB (Figure VI-10). This noisy at low frequencies produces a strange raising that is not expected by the  $\omega^2$ -model. However, this raising for most of the cases was before  $f_c$ , allowing us to compute  $f_c$  in each case using the analysis described in the section VI.2.

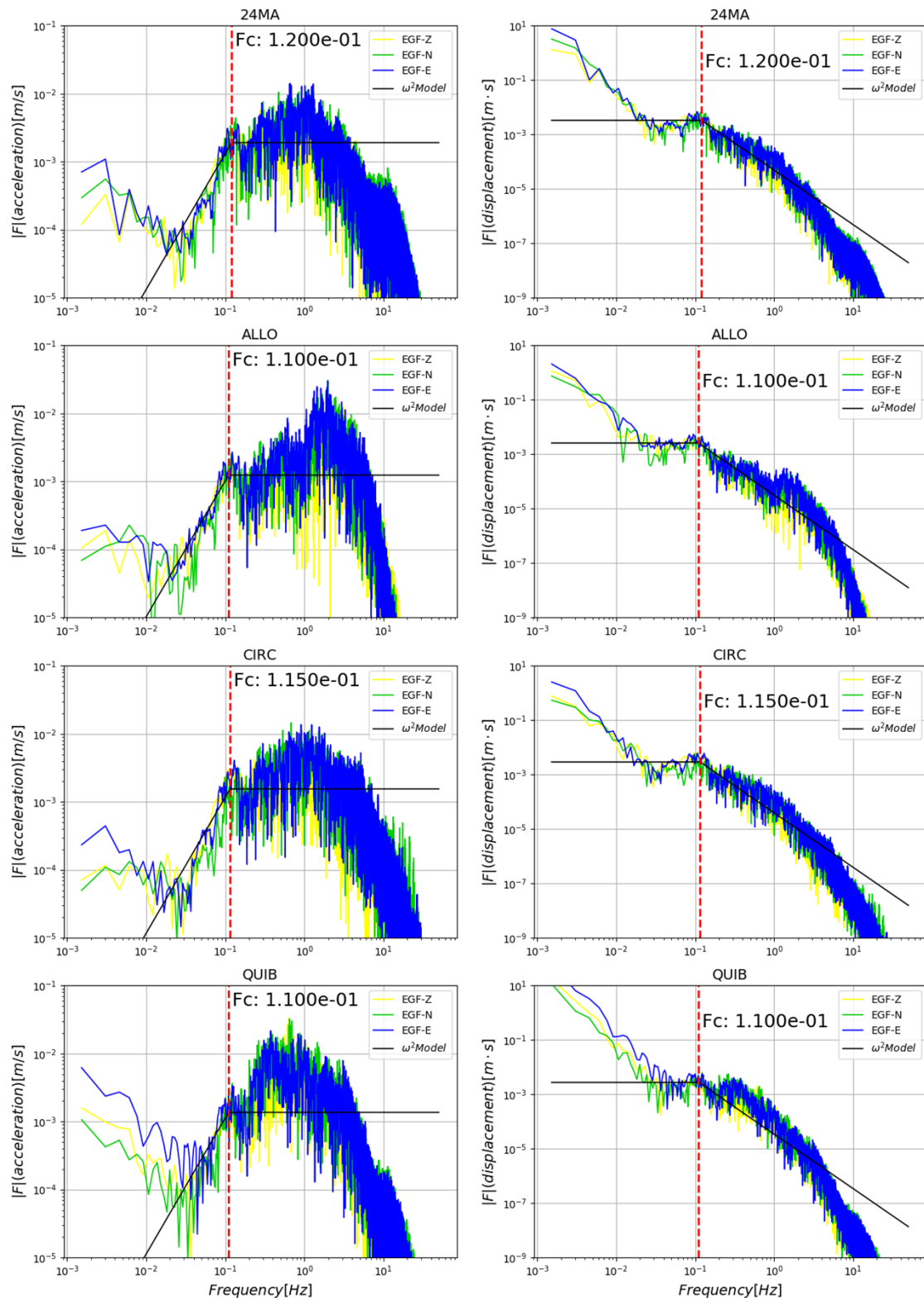


Figure VI-10. Example of corner frequency ( $f_c$ ) determination for the EGF 201604192200 at four stations. Left column: accelerogram analysis. Right column: Displacement analysis. The black line is the general schematic shape of the  $\omega^2$  model.

In the  $\omega^2$  model, the corner frequency ( $f_c$ ) is related to the source of the earthquakes, especially with the stress drop of the fault and the azimuth with respect to the station (Brune, 1970). Because all sites are located approximately with the same azimuth with respect the fault,  $f_c$  must

be equal for all the sites when the same earthquake is evaluated. After computing in each site  $f_c$ , we compare the results at all the stations that were evaluated (Figure VI-11). We removed stations from this analysis where  $f_c$  was too difficult to be defined. Based on this analysis, we choose as corner frequency the average values between all sites.

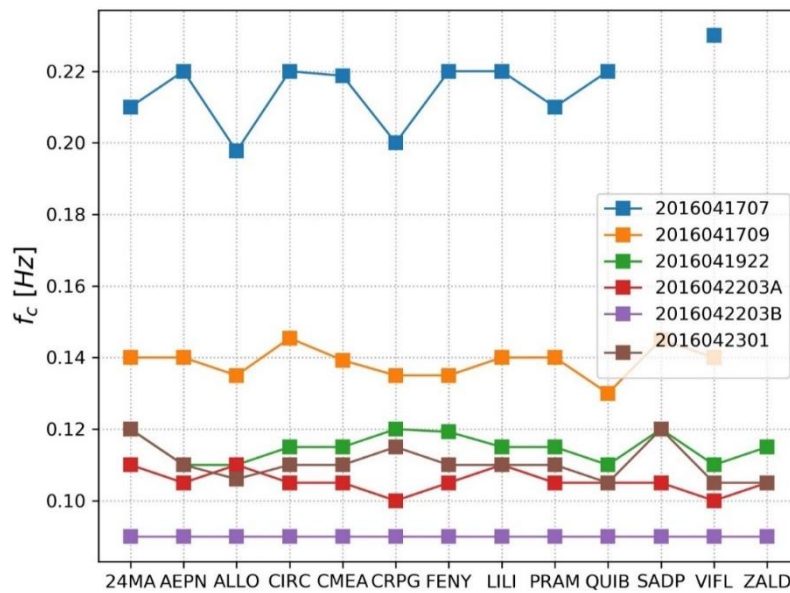


Figure VI-11. Corner frequency ( $f_c$ ) of each EGF for the stations where the determination was possible.

The final  $f_c$  was chosen for each EGF as the average for all the sites (Table VI-3). The value of the seismic moment was taken from USGS global catalog of earthquakes.

Table VI-3. Corner frequency and  $M_o$  (from USGS) for the 6 earthquakes selected as EGF.

EGF	$M_o$ [Nm]	$f_c$ [Hz]
<b>2016041707</b>	6.795E+17	2.16E-01
<b>2016041709</b>	2.782E+17	1.38E-01
<b>2016041922</b>	3.698E+17	1.15E-01
<b>2016042203A</b>	1.122E+18	1.06E-01
<b>2016042203B</b>	9.976E+17	9.00E-02
<b>2016042301</b>	3.881E+17	1.10E-01

### VI.6.3 Comparison in a blind test simulation

500 simulations were run for each EGF. For each station, we simulate strong ground motions with the same seismic moment and the location than Pedernales Earthquake, 16<sup>th</sup> April 2016.

To generate the scale for each EGF, we generate random values of the source duration, which is distributed with a lognormal density function (Eq. (VI-20)) and characterized by the seismic moment of the Pedernales Earthquake. From this, the corner frequency is obtained using Eq. (VI-19) with a  $q$  value of 0.803 that is characteristic of a linear fault with a trapezoidal STF (Godano et al., 2015; Haskell, 1964), as is approximately the Pedernales case.

In Figure VI-12, the histogram of the fault duration  $T$  selected for the EGF 2016041922 is shown. For the other earthquakes, although different realizations were generated, the histograms are very similar since the duration of the fault just depend on the target earthquake, which is the

same in all the simulations. Looking at the frequencies around low durations in Figure VI-12, it is evident that the random variable was truncated. As was explained before, it is done to avoid that the corner frequency of the strong earthquake could be larger than the corner frequency of the EGF.

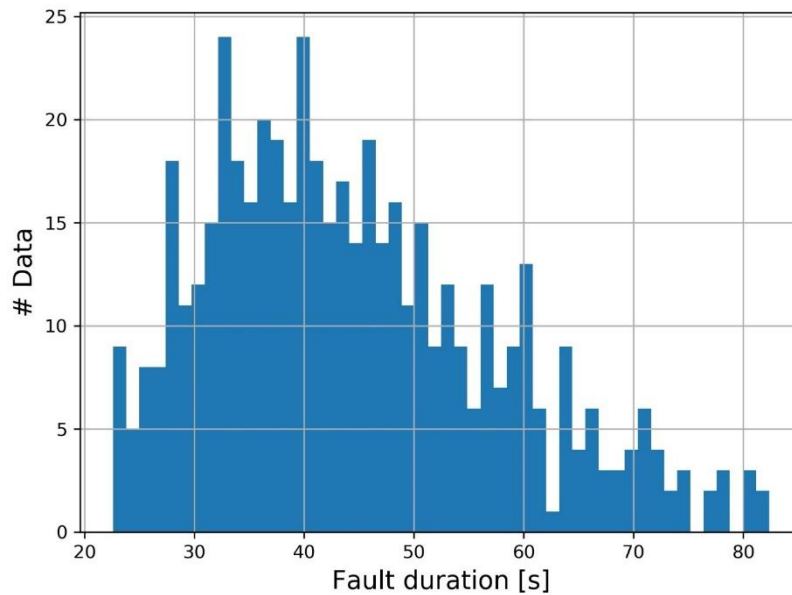


Figure VI-12. Histogram of the simulated rupture times for the Pedernales Earthquake. 500 simulation were done for each case, the case for the EGF 2016041922 is shown.

The first step in the creation of synthetic ground motion is to generate the scales between weak ground motion to estimate the strong one ( $r^{(i)}$ , Eq. (VI-11)). For example, one  $r^{(i)}$  is showed for each EGF in Figure VI-13. The  $r$  functions are discrete, and they are different between each other. This enables a large variability in the shape of the synthetic ground motions. The difference in the number of steps is due to the number of impulses, which is different in each case (Eq. (VI-13)), depending on  $f_c$ . Also, it is important to note that they are not symmetric and some of them doesn't produce a clear unique pick. This is related with the two-step generation method used in this study (Kohrs-Sansorny et al., 2005; Wennerberg, 1990).

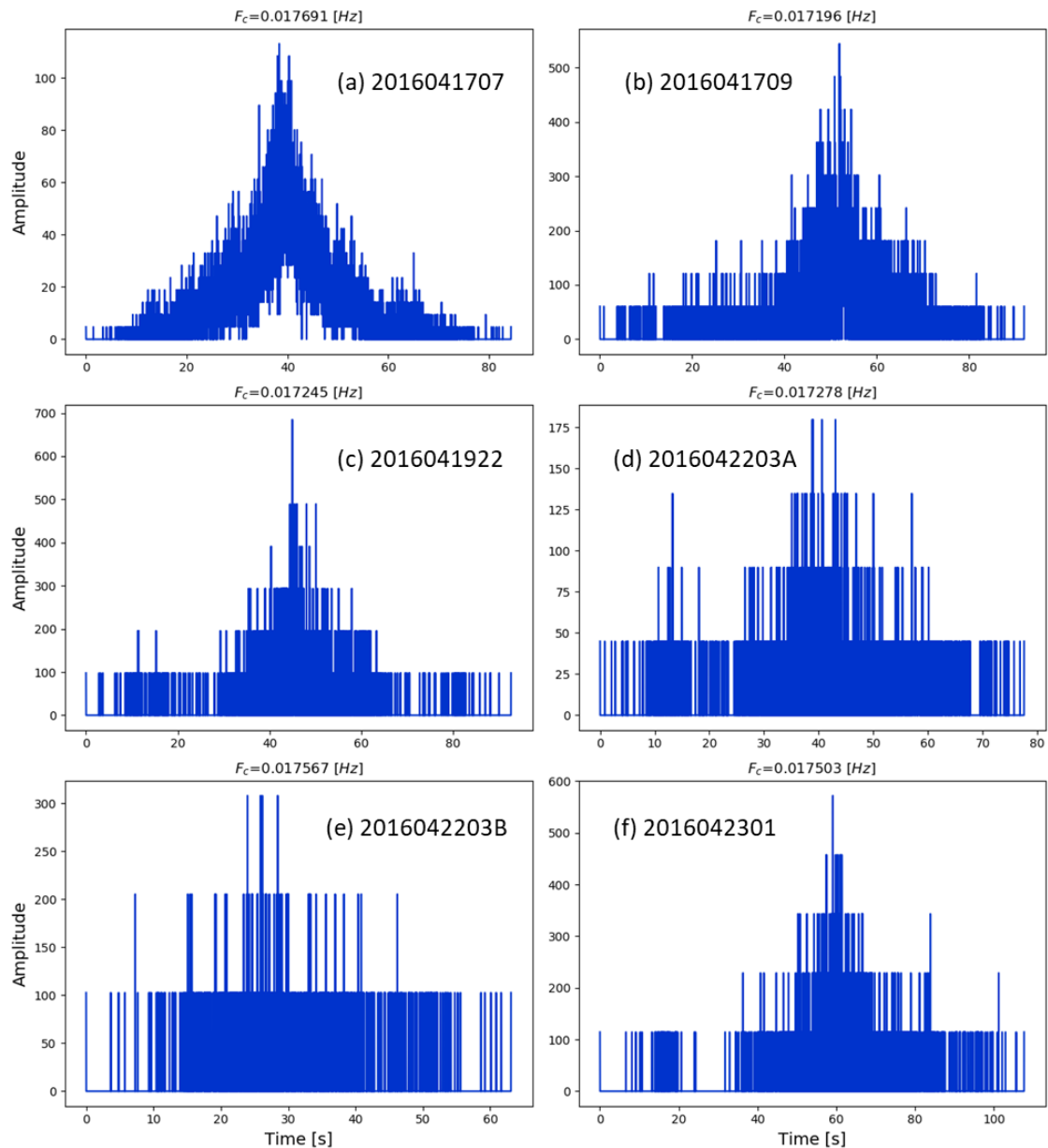


Figure VI-13. Example of  $r^{(i)}$  for the six different EGF. The corner frequency for all the cases corresponds approximately to the corner frequency expected for Pedernales earthquake ( $F_c=0.01769$  Hz).

Figure VI-14 shows six cases from the realizations done for the EGF 2016042301. Between those  $r$  functions, there is a considerable variability related with the amplitude and with the duration. For the simulation with  $F_c=9.9 \times 10^{-3}$  Hz, the duration is until 200s approximately, whereas, for the simulation with  $F_c=3.1 \times 10^{-3}$  Hz, the duration is around 35s. In terms of amplitude, there is also a clear difference between cases, being the amplitude higher if  $F_c$  is higher.

The fact that the amplitude of the  $STF$  becomes higher and the time shorter means that in some simulation the energy is released faster. It could produce a very different ground motion on the surface and produce a different impact on the hazard. This is one of the reasons the method proposed in this document gives an advantage considering the variability of the corner frequency for the objective earthquake.

In terms of stress drop ( $\Delta\sigma$ ), since it is related with  $F_c$  (Eq. (VI-6)) the relationship previously mentioned remains equal. Higher stress drop means that the energy is released in a shorter window of time (less duration) producing higher values on the amplitude of  $r$ .

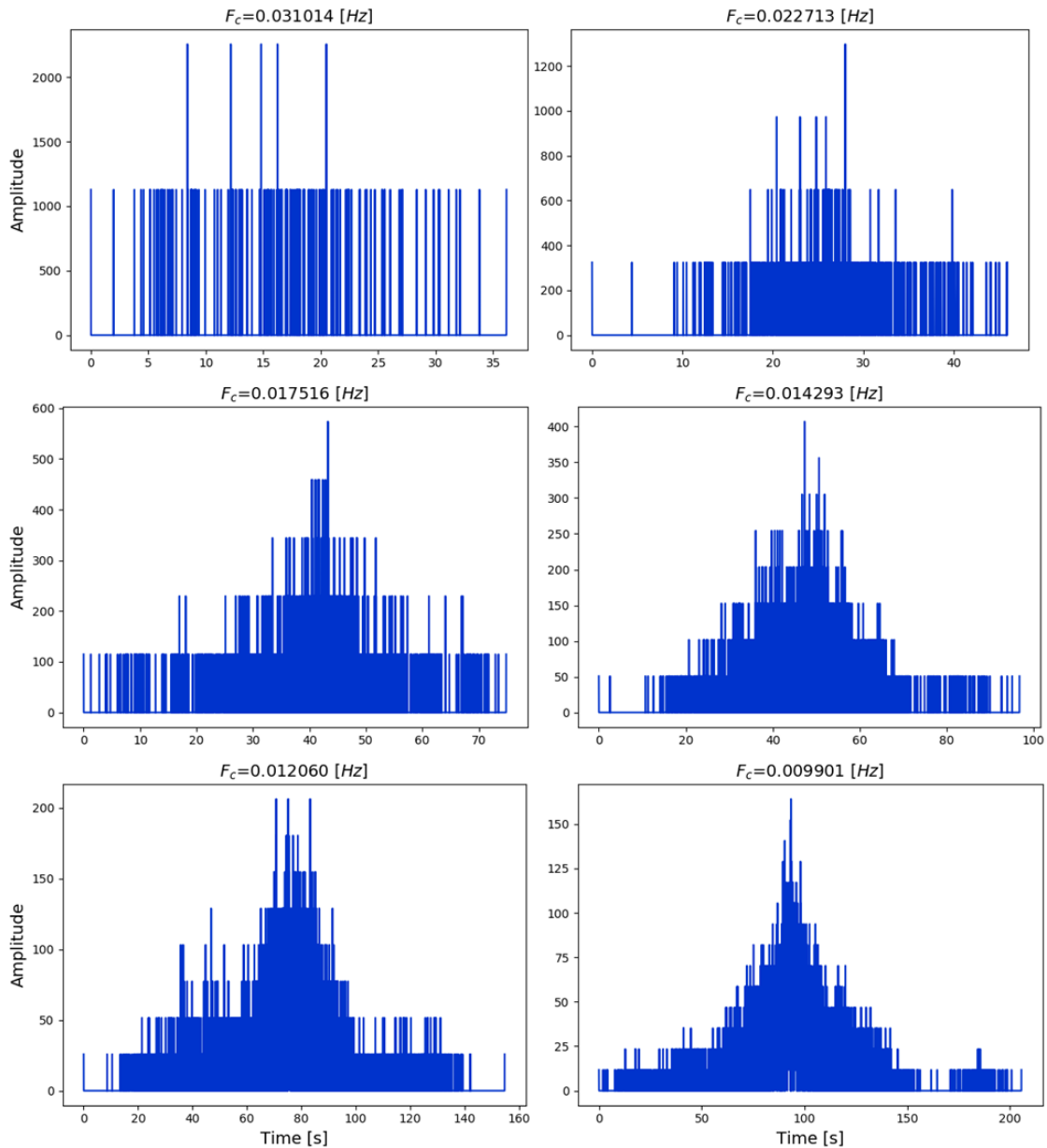


Figure VI-14. Six realizations of  $r^{ij}$  for the case 2016042301 with different values of  $F_c$ .

Figure VI-15 compares four realizations with approximately a constant value of  $F_c$  (same  $\Delta\sigma$ ) and the same EGF. In this case the variability associated between simulations is related with the source variability of an earthquake, which is represented by the lag times in the Eq. (VI-11). This variability doesn't change the number of points that built  $r$ , which depends of the ratio of the corner frequencies (Eq. (VI-13)). It implies that the changes are just in the distribution of those points and that represents a change in the duration, that goes from 60 s to 120 s in the examples (Figure VI-15); however, it represents a low change in the general amplitude of  $r^{ij}$ .

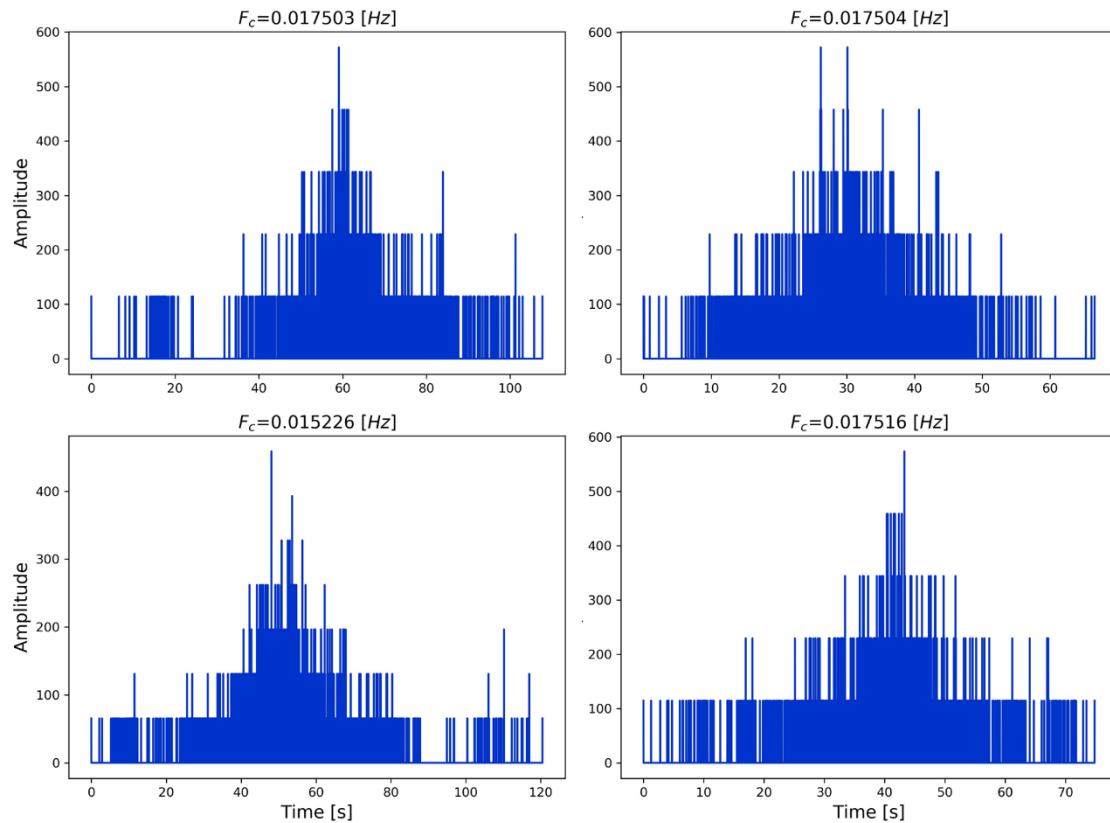


Figure VI-15. Four realization of  $r^{(i)}$  for the EGF 2016042301 and with  $F_c$  similar.

The variability that is found in the EGF method comes from three sources: the spatial variability, the corner frequency or stress drop variability, and the uncertainty of select an adequate EGF.

The next step in the EGF method is to compute the scale between the EGF and the strong ground motion. In the Eq. (VI-10), the theoretical spectrum of the scale is given, and it would be the result using the  $\omega^2$ -model. When this theoretical function is compared with the spectrum of the  $r^{(i)}$  computed by the methodology explained herein (Eq. (VI-11)), we find a good agreement (Figure VI-16). Looking at large frequencies there is a small misfit, but it is related to the number of points that are used to define  $STF$  (Eq. (VI-13)). However, if more points are used, it will result in a convergence with simulations very similar between them (Ordaz et al., 1995).

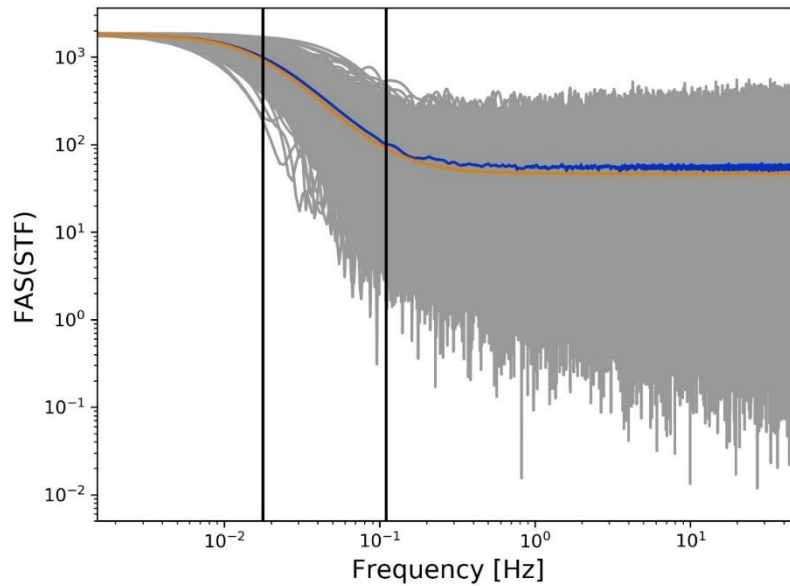


Figure VI-16. The theoretical spectrum of the STF (Eq. (VI-10)) here represented by an orange line and the spectrum of the STF computed using Eq. (VI-11) for all the simulation by gray lines. The arithmetic average between all the simulations is shown by a blue line very close to the orange one.  $F_c$  average and  $f_c$  for the EGF are represented by vertical black lines, EGF 2016042301.

By convolving the function  $r^{(i)}$  with the records for each EGF (Eq. (VI-18)) we obtain an synthetic signals corresponding to a MW 7.8 earthquake that would occur at the same place than the Pedernales Earthquake. For the same EGF, the model produces different alternatives for ground motion. On Figure VI-17 are shown some cases that were produced using the different  $r$  functions. The shaking intensity and the duration are different for each realization.

In general, the simulation with larger  $F_c$  values produces a larger PGA (Figure VI-17) because the energy is release in a shorter range of time (Figure VI-14). However, this relationship presents a variability related to nature of the scale function and the EGF method that is used. The Figure VI-18 shows the PGA in function of the corner frequency. The general trend marks an inverse relationship between  $F_c$  and PGA. It is explained because higher  $F_c$ , associated with higher stress drop, implies that the same energy is released in a shorter time window producing a higher shaking concentrated in a shorter time.

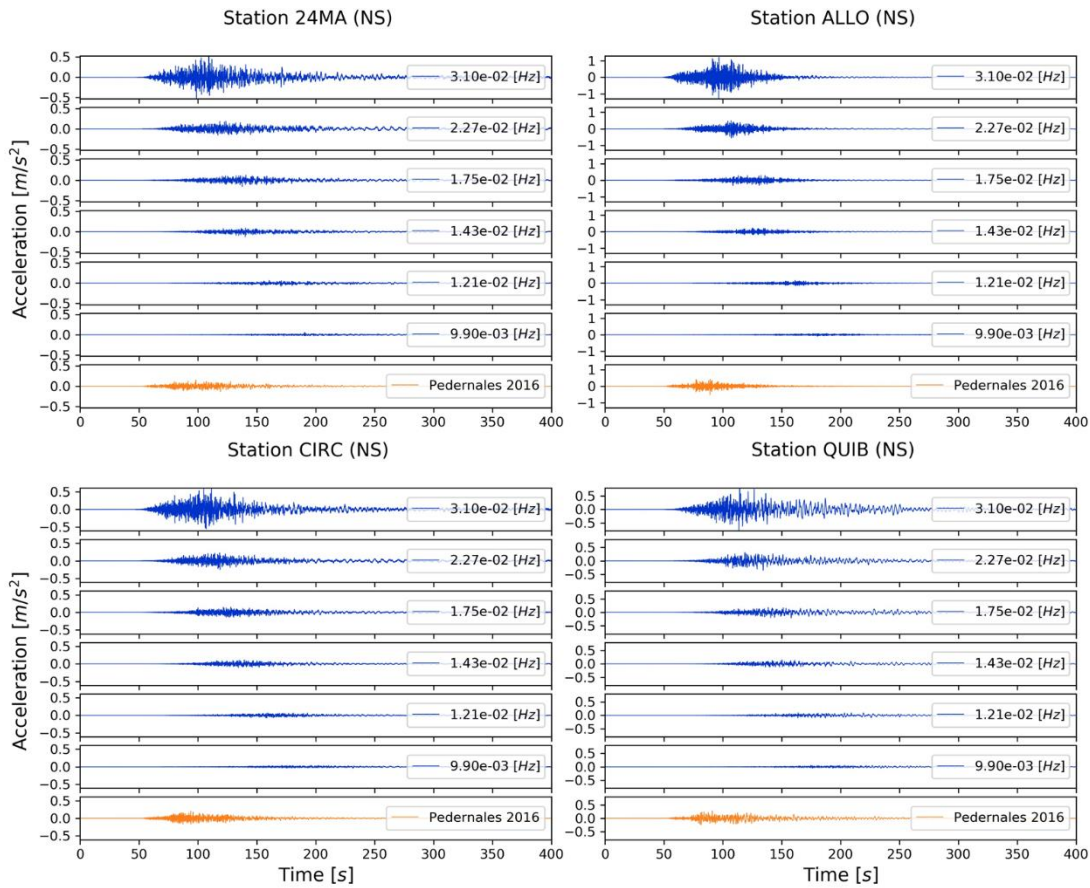


Figure VI-17. Synthetic accelerograms of the Pedernales earthquake at four station (north-south component), using 20162301 EGF. The  $F_c$  value is indicated on the right side for each trace. The real Pedernales recording is reproduced at the bottom.

The Figure VI-18 shows that for the same  $F_c$  and the same EGF, there is still a variability in the  $PGA$  (market with the orange line with the sub index a.). This variability is associated with the source variability of the earthquake, modulated by time lags in the EGF method that we are using. This variability is much lower than the variability coming from the stress drop (marked as variation c. in Figure VI-18) represented by the changes in  $F_c$ .

The third source of variability comes from the selection of the  $EGF$ , and in the Figure VI-18 it is shown how the  $PGA$  is different between them (variability marked as b.), especially different for the EGF 2016041707 and 2016041709. In comparison, the  $PGA$  sensitivity is more important to the variation of  $F_c$  and the selection of the EGF than to the spatial variability.

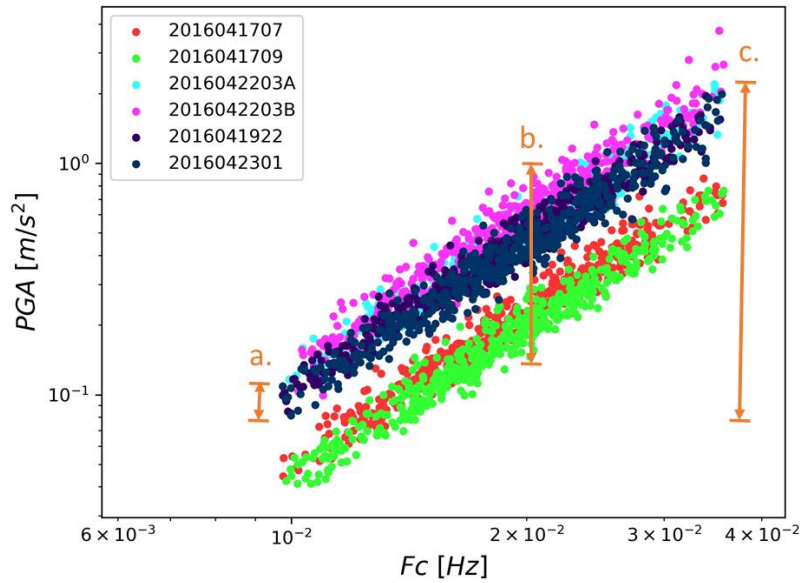


Figure VI-18. PGA from the synthetic signal against  $F_c$ . The variations are divided in: A. source variability, B. uncertainty related with the EGF selection, and C.  $F_c$ -stress drop variability. The data are the realizations for the site ALLO in the north-south direction with 500 simulation for each one of the six EGF.

#### VI.6.3.1 Analysis of the simulations of Pedernales with congruent results

To separate the results and develop a better analysis, the four EGF that present a similar trend and dispersion of PGA (Figure VI-18) are separated from the other two. In this subsection the EGF 2016042203A, 2016042203B, 2016041922, and 2016042301 are analyzed together.

With the results that are obtained, that consist in 500 traces for each one of the three components in 13 station, an analysis to represent the variability of the synthetic seismograms is developed. We compute the logarithmic mean and standard deviation of the Fourier spectra that is presented respectively with continues and dashed lines in the Figure VI-19. We show four sites, but other sites are presented in Annex D. The statistics of the results show that in general, the prediction estimates the shape and the amplitude of the Fourier Spectrum of the Pedernales Earthquake. It is important to note that Pedernales case is just one of the possible cases of rupture with the same parameters (Position and seismic moment). It is not unusual that the average and the Pedernales case are different. However, we expect that the Pedernales case is in the range of confidence of the L

At low frequencies ( $f < 0.1$  Hz) and at high frequencies ( $f > 10$  Hz) the estimations can't be taken into account because the signal to noise ratio of the records is too low. The analysis presented here use a frequency window between 0.1Hz to 10 Hz, that is the frequency range where the filtering process does not affect the spectrum.

For most of the station, with those EGF (Figure VI-18), the predictions are adequate since Pedernales case is situated in the limits of standard deviation. We success predicting the shape and the magnitude of the spectra of the strong motions that we aim to produce.

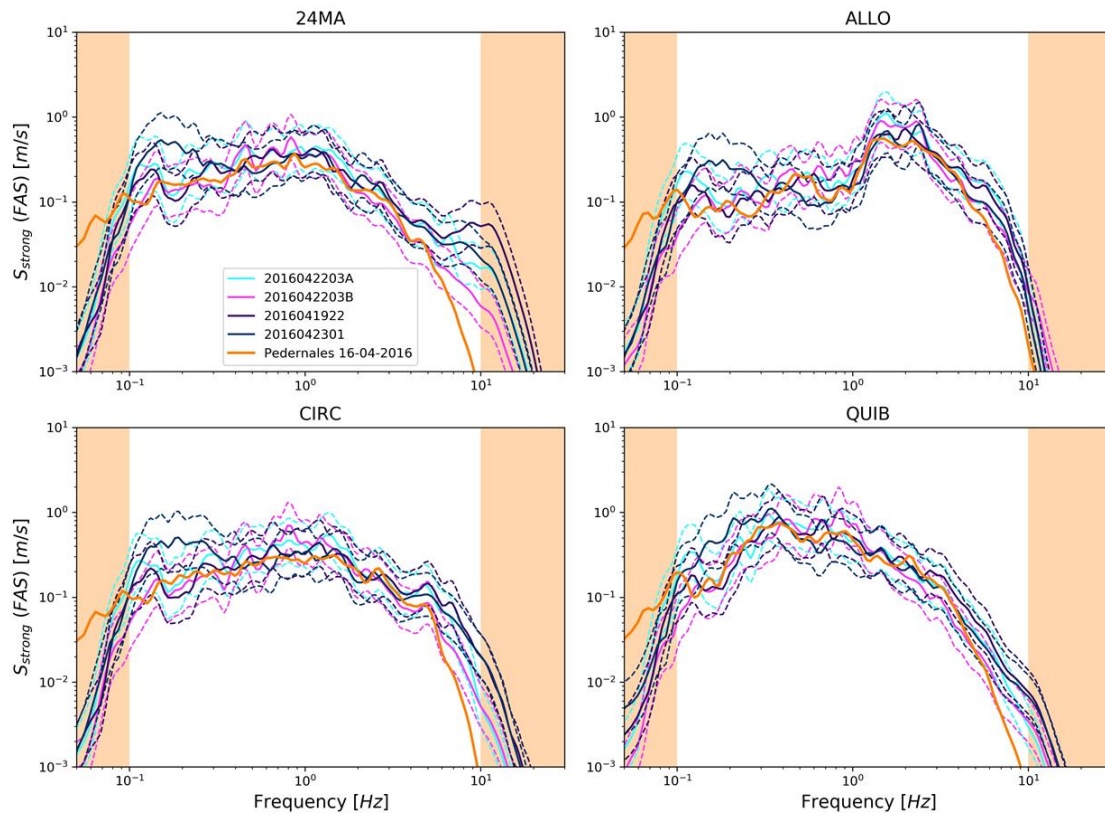


Figure VI-19. Mean for the estimated spectra for four EGF with similar results and their error margin. Four representative sites are selected (based on Laurendeau et al., 2017): 24MA is a site with low site amplification, ALLO is a site located in the mountains, QUIB is a site located at the south of Quito, CIRC is a site at the north of Quito. Red area after 10Hz and before 0.1Hz means that the analysis is not adequate on this zone. Lines represent the average for each EGF between all the simulation and dashed lines represent the average either multiplied or divided by the log standard deviation.

The synthetic signal obtained by the EGF method could produce a different impact on buildings. To estimate the influence of the earthquake on structures, we compute the elastic response spectra with a damping of 5% (Figure VI-20). We observe that the main peak in the response spectra is around a period of 0.5 s, and all the EGF success in predicting the period where the peak occurs. The amplitude of the response spectra at the main peak is predicted with a higher variability between all EGF with respect the valleys in high periods and at very low periods. The Pedernales amplitude is around the mean for all EGF. We consider adequate the simulation because for most of the estimation, the Pedernales case is between the range of one standard deviation.

In Figure VI-20 we can detect a second peak, between a period of 2.5 to 3.0 s, for QUIB situated at the south of Quito. All EGF in QUIB shows a similar peak around a period of 2.8 s. This second peak at the south of Quito, was also detected by Laurendeau et al., (2017) using spectral ratios. It shows that the EGF method can include site effect in their prediction adequately.

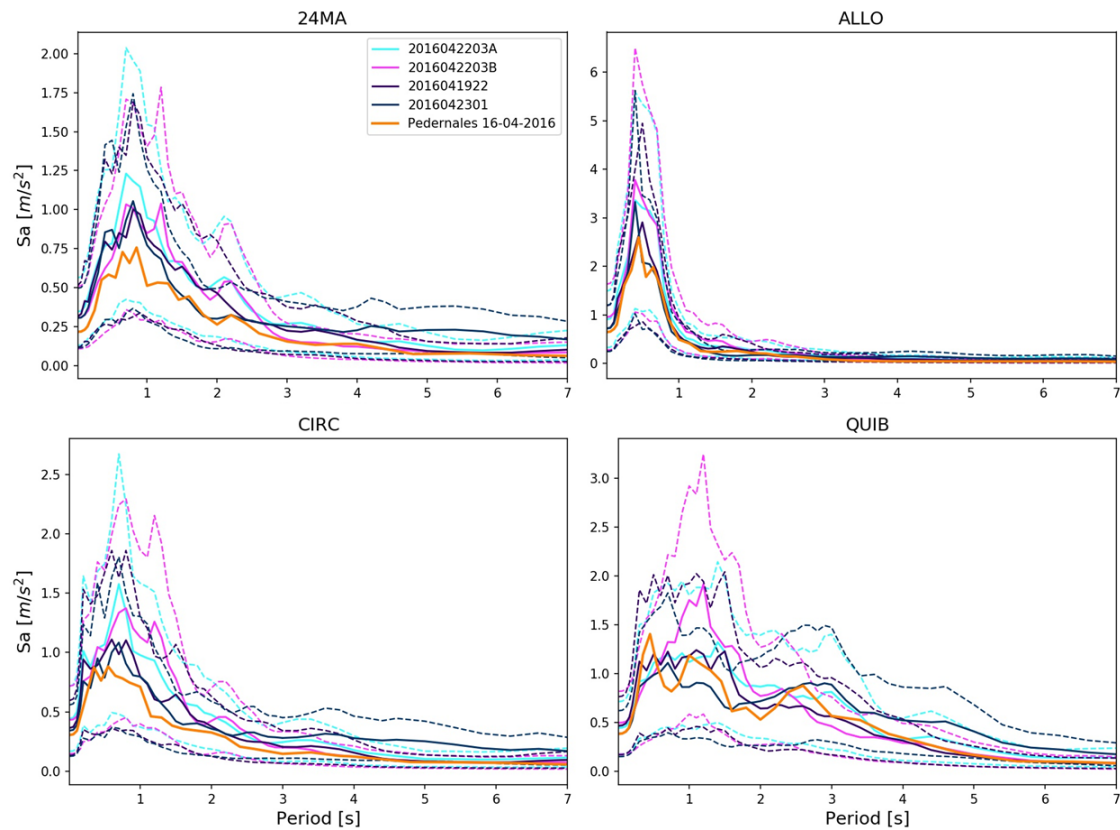


Figure VI-20. Statistics for the response spectra in a structure with 5% of damping for all the EGF. Four representative sites are selected. Continues lines represent the average for each EGF between all the simulation and dashed lines represent the average either multiplied or divided by the log standard deviation.

The four EGFs also predict correctly the registered PGA for Pedernales case (Figure VI-21). In this figure, we compare the results with an adequate and more recent GMPE for earthquakes coming from forearc part of subduction zones Abrahamson et al., (2016).

The Abrahamson GMPE were computed with the Pedernales seismic moment ( $7.054 \times 10^{20}$  Nm) for the forearc case with a general  $v_{S30}$  for all the sites of 300 m/s, the average value for Quito city (TRX Consulting CA, 2011). Also, a central value of epistemic uncertainty is used for this GMPE. The Abrahamson GMPE has been found to be the more adequate for the prediction of this earthquake in a wider range of frequency by Beauval et al., (2017).

Although GMPE also predicts for most of the sites the PGA between the range of standard deviation (Figure VI-21), this range is larger for GMPE than for the individual prediction of the EGF. Additionally, Figure VI-21 shows that the EGF method is not producing extreme values of PGA and the predictions are similar than GMPE.

We observe that the sites where the GMPE is overestimating the PGA, the EGF method is closer. In fact, those overestimated sites outside of the range, between 200 to 207 km (24MA, PRAM, AEPN, CMEA, FENY, CRPG, SADP and CIRC), are close between each other located at the north of Quito (see Figure VI-9). We know that the assumption of a general  $V_{S30}$  for all Quito is not adequate, since Quito present several kinds of soils around on its zone. The uncertainty on  $V_{S30}$  makes complicate to compare GMPE predictions and EGF predictions, however, it is possible to say that the general behavior is better followed by the EGF method.

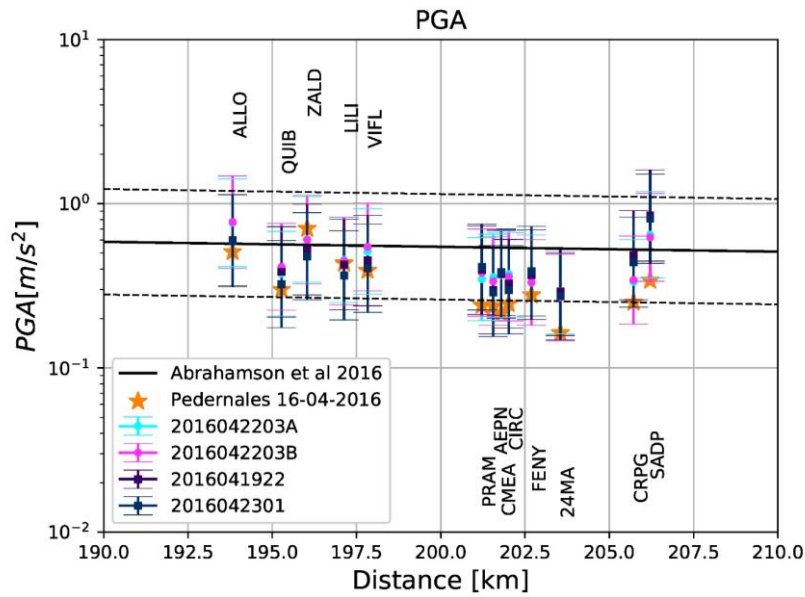


Figure VI-21. PGA estimation for Pedernales Earthquake using GMPE Abrahamson et al., (2016) and EGF method.

To analyse the main peak in the response spectra, that in most of the sites occurs around 0.6s, we analyze the  $S_a$  vs. distance plot (Figure VI-22). We observe that for all the sites, the EGF method predicts in the range of error the Pedernales case. Using the GMPE, it predicts most of the cases in its error range too, except for the site ALLO. From Figure VI-21, we assume that the GMPE parameters were rather well estimated since the PGA was well predicted for this site. Consequently, in this case, we relate the underestimation of ALLO peak with site effects, maybe with topographic effects since the site is in a mountainous region.

Something similar we could say for the sites between 200 to 205 km that were not well estimated in PGA by the GMPE (Figure VI-21). If another  $V_{S30}$  is implemented in the GMPE, it would improve the estimations of PGA, but it would change also the prediction at 0.6s, making it lower too. It means that GMPE is not able to estimate the response spectra for all the periods at the same time.

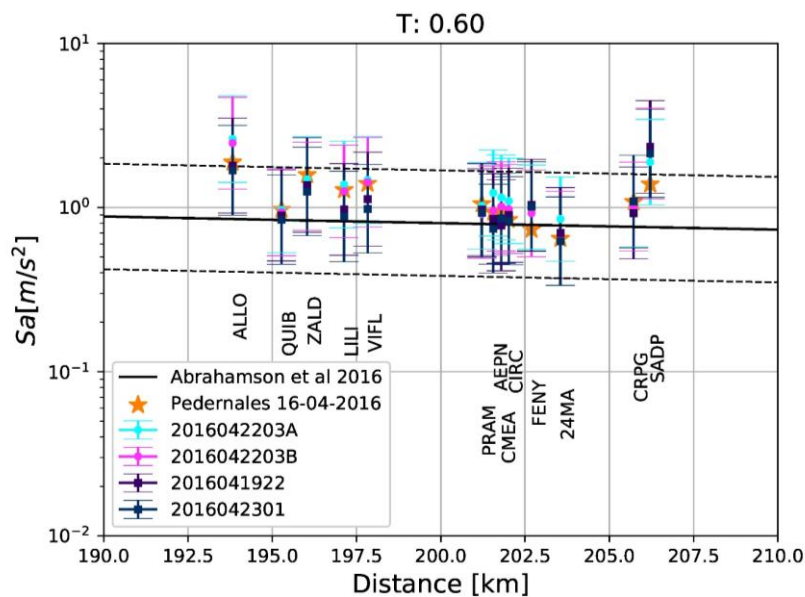


Figure VI-22. Response spectra at 0.6 s, from GMPE (Abrahamson et al., 2016) and EGF method.

When we look at the second peak around a period of 2.8 s (Figure VI-20), that has been related to site effects at the south of Quito (Laurendeau et al., 2017), the sites of the south are really better predicted with the EGF method than with GMPE (Figure VI-23). The sites at the south of Quito, located between 195 to 200 km (ZALD, QUIB, VIFL, and LILI see Figure VI-9), are in the normal range of prediction for the four EGF. At the contrary, it is not possible to predict the second peak using GMPE. This is due to the shape on the spectra proposed by GMPEs is inadequate, with just in main peak, and the fact that  $VS_{30}$  cannot account for low frequency site effects.

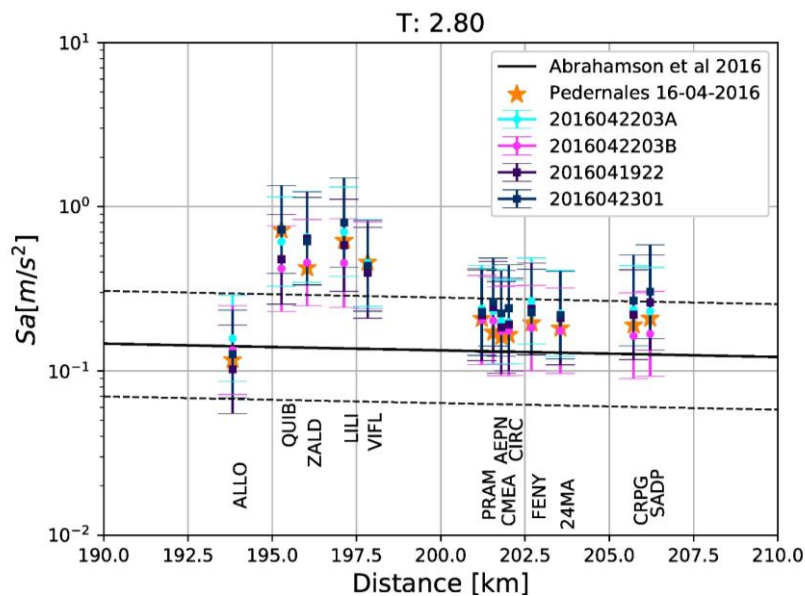


Figure VI-23. Response spectra at 2.8 s, comparing GMPE Abrahamson et al., 2016, and EGF method and real signal. Continuous line and markers represent the mean of the estimation. Dashed and error lines represent the logarithmic standard deviation added and removed.

This impediment of the GMPEs to predict particularities in the response spectra, because they use a general shape, is shown compared with the prediction for the EGF 2016042203A (Figure VI-24). For example, in the site QUIB, where a strong site effect makes to appear a second peak in the response spectra at a period around 3s, the GMPE doesn't fit the response of the Pedernales earthquake. For sites with one peak, but with a particular shape as the site ALLO, the GMPEs cannot estimate the main peak of the response spectrum inside its limits of confidence. In the case that no strong site effects are acting, as the case of the site 24MA or CIRC, the GMPE is adequate for most of the periods. However, in those sites, the EGF has also a good performance in the prediction of the Pedernales earthquake.

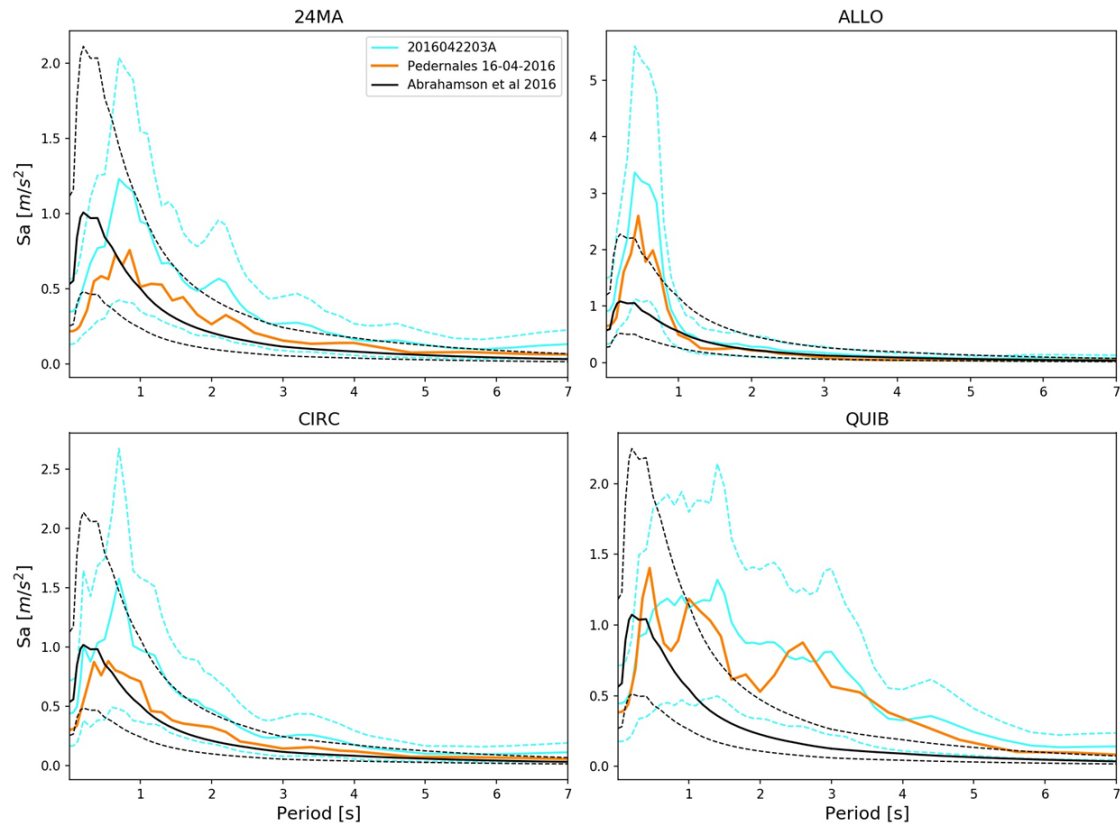


Figure VI-24. Comparison of GMPE response spectra (Abrahamson et al., 2016) with the prediction from the EGF 2016042203A and the Pedernales Earthquake 2016.

The general shape of the GMPE is not related to the bad choice of  $V_{S30}$  (Figure VI-25). Using a low  $V_{S30}$  of 200 m/s will improve the prediction at large periods, but it would overestimate the response spectra at low periods. Using a high  $V_{S30}$  the result would be inverse. However, in any case, the second peak around 2.8 s at the site QUIB would not be represented by GMPE.

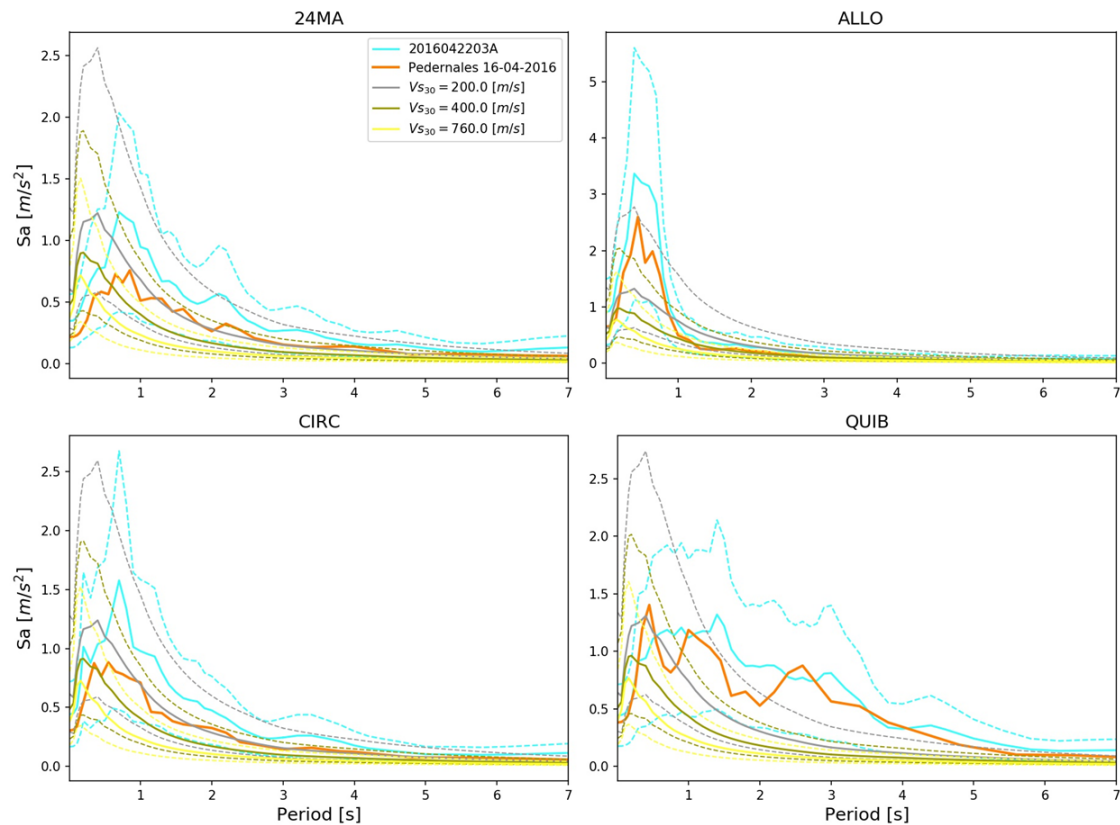


Figure VI-25. Effect of using different  $V_{s30}$  values in the GMPE prediction.  $V_{s30}$  is chosen in consideration to the variability of Quito Beauval et al., (2017).

### VI.6.3.2 Analysis of the Pedernales simulations for EGF 2016041707 and 2016041709

We can see in Figure VI-18 that EGF 2016041707 and 2016041709 underestimates the PGA with respect to the other EGF. In this subsection, both results are analyzed and compared with Pedernales earthquake.

Figure VI-26 shows the mean with the standard deviation for both EGF. In the case of 2016041707, the differences with respect to Pedernales earthquake is almost constant for all the frequencies and sites. It could indicate that the seismic moment for this EGF is overestimated. However, even in this case, we can see that the shape of the average accelerogram is followed by the estimation.

The synthetic waves obtained from the EGF 2016041709 has a higher energy at low frequencies, around 0.1 Hz (Figure VI-26). This phenomenon occurs at any site, so we conclude that it is not due to a site effect but rather to a specific source effect or to wave propagation that may be affected by a particular local effect around the source.

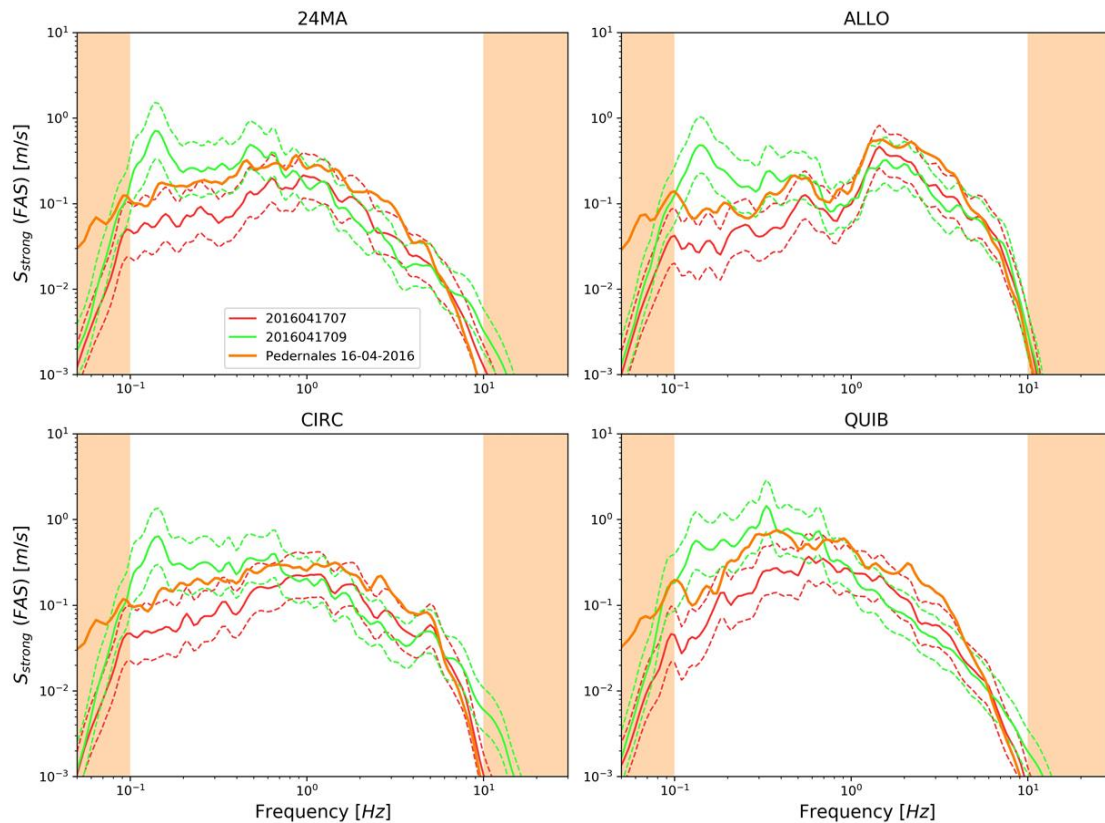


Figure VI-26. Mean for the estimated spectra for the EGF in comparison with Pedernales earthquake and other EGF. Red area after 10Hz and before 0.1Hz means that the analysis is not adequate on this zone. Lines represent the average for each EGF between all the simulation and dashed lines represent the average either multiplied or divided by the log standard deviation.

In terms of the response spectra using the EGF 2016041707 (Figure VI-27), we obtain that the prediction underestimates the Pedernales earthquake for all the periods. However, the shape of the response spectrum for Pedernales is kept in all the site using this EGF.

In the case of the EGF 2016041709, the response spectra that is predicted does not fit in most of the station the Pedernales earthquake (Figure VI-27). Additionally, this response spectrum has a very particular shape in comparison with other EGF and Pedernales. For example, at high periods this earthquake produces high  $S_a$  values. Those higher values at high period can be explained by the bulb that we find in the spectra for this earthquake, around 0.1-0.2 Hz in all the sites (Figure VI-26).

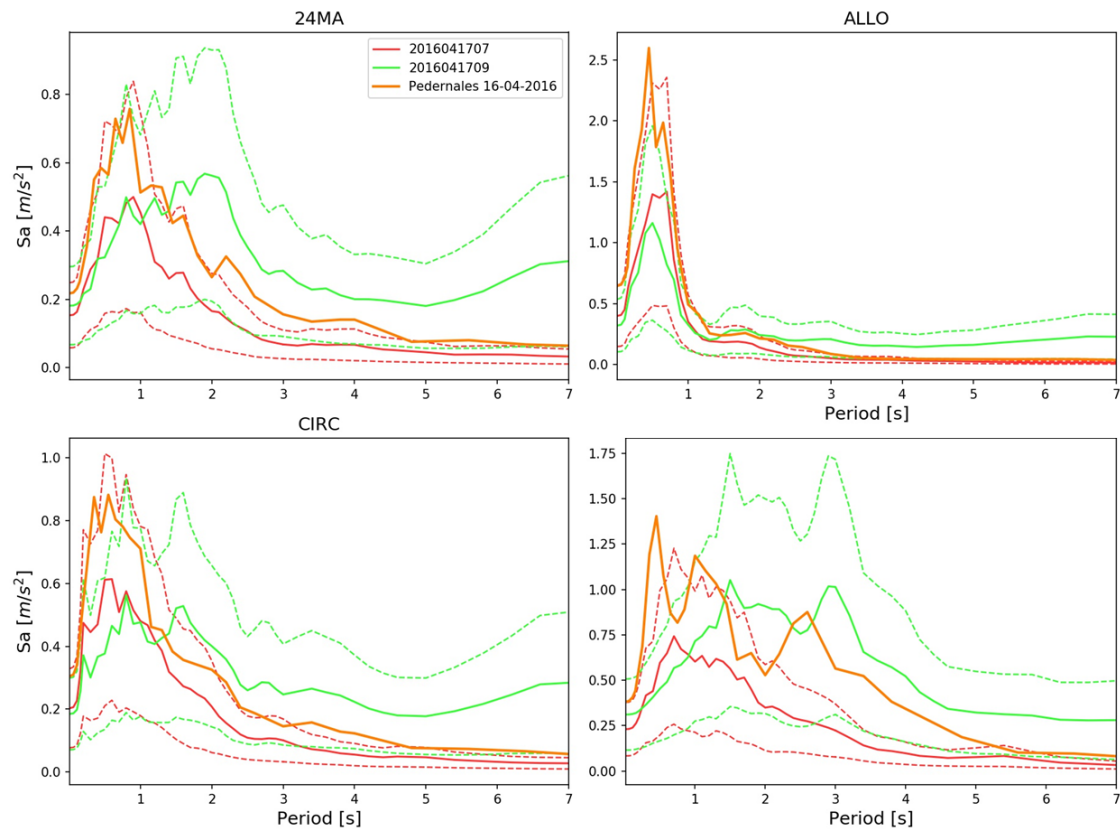


Figure VI-27. Mean and standard deviation for the response spectra for the EGFs that div. A structure with 5% of damping is taken. Four representative sites are selected. Continues lines represent the average for each EGF between all the simulation and dashed lines represent the average  $\pm$  std.

In the site ZALD the signals from both EGF have not been recorded adequately, so this site was removed from the analysis for both EGF. In the case of the EGF 2016041707, for all the periods and in all the sites (Figure VI-28, Figure VI-29, and Figure VI-30) the prediction is underestimating the Pedernales case. However, the general order in  $S_a$  or PGA of the sites is predicted by this EGF.

The prediction of the EGF 2016041709 is not similar neither Pedernales case nor other EGF predictions. In this case, the PGA and low periods the peak is Response spectra is underestimated (Figure VI-28 and Figure VI-29), but at high periods are overestimated (Figure VI-30).

At high periods the stations at south (QUIB, LILI, VIFL) are predicted to have a higher pseudo acceleration than the other sites (Figure VI-30). It shows that the EGF method is still well predicting strong site effects for those sites with respect the others. Also, from this we interpreted that the misfit from the EGF predictions is related with the source or path effects, and not with the site effects.

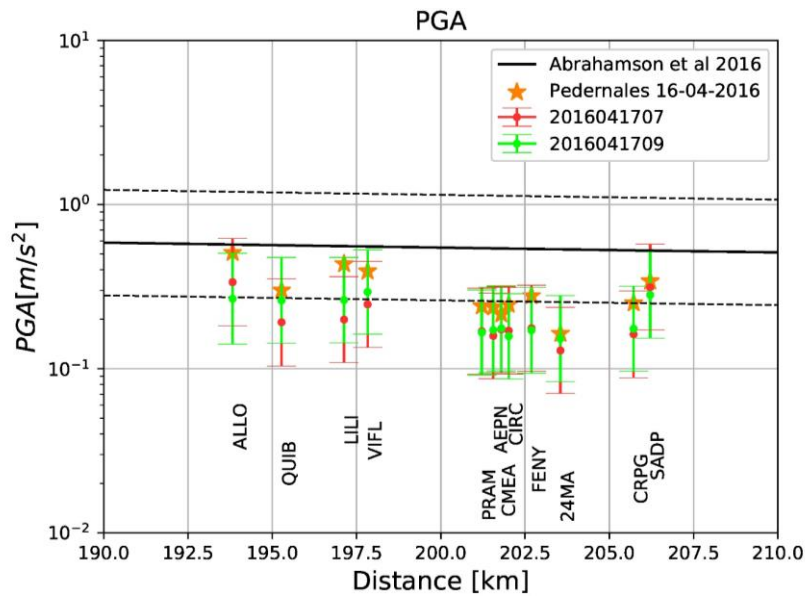


Figure VI-28. PGA estimation comparing GMPE Abrahamson et al., 2016 and EGF results with a different value than Pedernales earthquake. Continuous lines and markers represent the mean of the estimation. Dashed and error lines represent the logarithmic standard deviation added and removed.

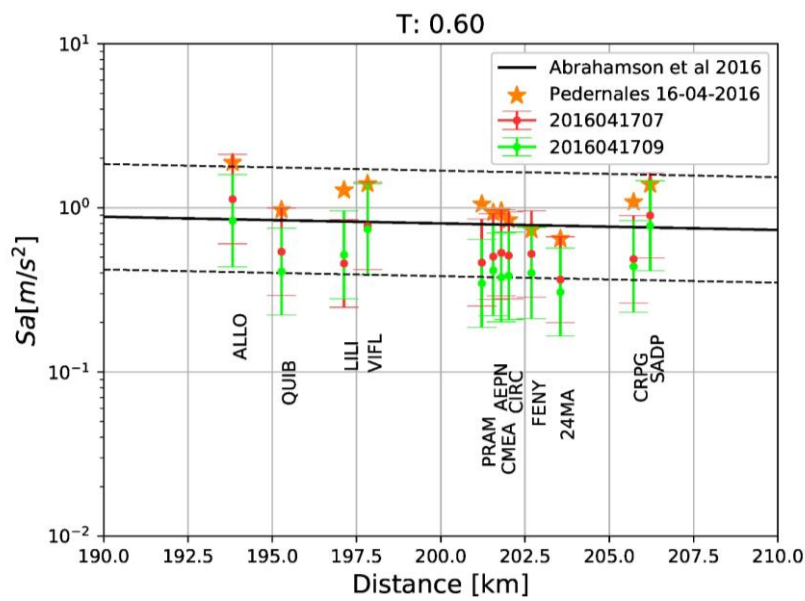


Figure VI-29. Response spectra at 0.6 s, comparing GMPE (Abrahamson et al., 2016) and EGF method for cases where the prediction of the spectra wasn't adequate. Continue line and markers represents the mean of the estimation. Dashed and error lines represent the logarithmic standard deviation added and removed.

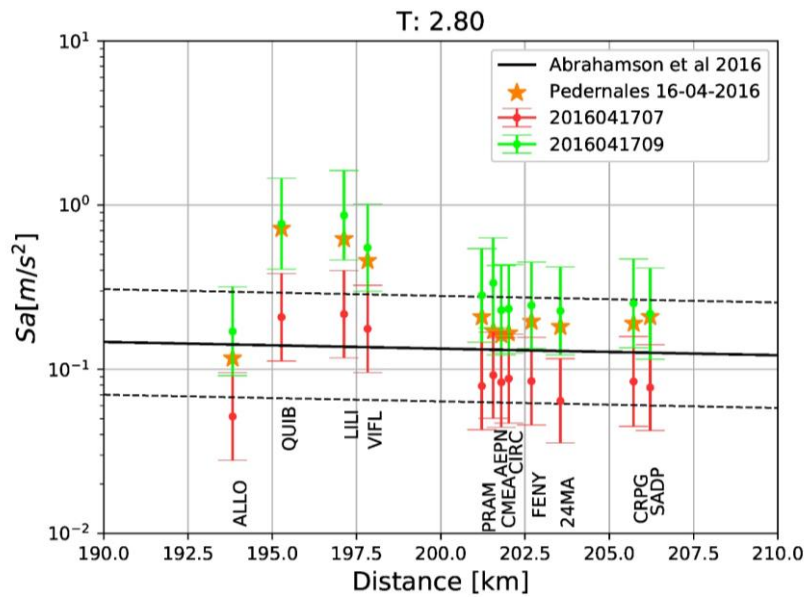


Figure VI-30. Response spectra at 2.8 s, comparing GMPE Abrahamson et al., 2016 and EGF results. Continue line and markers represents the mean of the estimation. Dashed and error lines represent the logarithmic standard deviation added and removed.

For the EGF 2016041707, we make the hypothesis that the seismic moment or the depth of this earthquake was not correctly determined, which implies that the scale obtained by the EGF method is too low to predict the Pedernales earthquake. Due to this, a high seismic moment could explain why for all the results in this EGF (Figure VI-26, Figure VI-27, Figure VI-28, Figure VI-29, and Figure VI-30), the Pedernales case is underestimated and the prediction is low in comparison with the other EGF predictions.

In the case of the EGF 2016041709, it doesn't predict neither the shape nor the amplitude of the spectra or response spectra. These differences indicate that the EGF doesn't accomplish all the hypothesis of having a similar fault and path than the Pedernales Earthquake. When we look at the location of this EGF (Figure VI-9), this EGF is at the west of other studied EGF and of the Pedernales earthquake. The epicenter of this earthquake is located very close to the trench between the Nazca and the northern Andes Plate. This proximity and the shallow depth of the earthquake could indicate that regional backarc-forearc effects are affecting this EGF, and this is an important aspect that must be taken in account (e.g. Abrahamson et al., 2015; Kishida et al., 2013; Vacareanu et al., 2015)). If this is the case, 2016041709 earthquakes are not a good EGF to predict the Pedernales earthquake.

But certainly, 2016041709 can be important for a future large earthquake that occurs in the subduction interface up to a shallow depth and that ruptures the interplate interface up to the trench, as it was the case for the large 2011 Tohoku event in Japan (Bletery et al., 2014). In this case, a strong ground motion could produce strong shaking for building with high resonance periods.

### VI.7 Simulation of a Mw8.5 earthquake in Quito.

Using the same methodology, a new subduction earthquake in the same zone than Pedernales earthquake is simulated. We placed the centroid at the at the same point than the Pederbales event, but with a larger value of Mw 8.5. Since this earthquake has not occurred in the reality, we cannot compare the prediction with real records as it was the case in the previous subsection. However, based in historical earthquakes coming from the same fault than

Pedernales earthquake (interface between the Nazca and the northern Andes Plate), it is interesting to evaluate the effect on Quito of Mw 8.5 earthquake coming from the same zone.

In the past, earthquakes around Mw 8.5 have occurred around this zone. For example, the Mw 8.2 in 1979 and Mw 8.8 1906 (Kanamori and McNally, 1982). Nocquet et al., (2017) proposed that the Pedernales earthquake could be the beginning of a new super cycle on this zone and future earthquake with similar magnitudes or higher could be expected.

The results of the simulation of the Pedernales earthquake (section VI.6) shows that four of the EGF are adequate to simulate the earthquake. To simulate a Mw 8.5 earthquake, we use the 4 adequate EGF that occurred at north and at south: 2016041922, 2016042203A, 2016042203B, and 2016042301.

The same signal processing than for Pedernales simulation is applied (subsection VI.6.1). The new M8.5 earthquake is created in the same place (Table VI-2), implying that the same correction by distance is applied. The corner frequencies of the EGF were obtained with the procedure that was showed in the subsection VI.6.2 and summarized in Table VI-3.

Because the Mw 8.5 earthquake (seismic moment of  $6.30957 \times 10^{21}$  Nm) is higher than for Pedernales case, the expected corner frequency of the strong earthquake is lower (Figure VI-6). Because of this reason,  $r$  for Mw 8.5 case is built with a bigger number of points (Eq. (VI-13)) making that it looks more continue than in the Pedernales case (Figure VI-31).

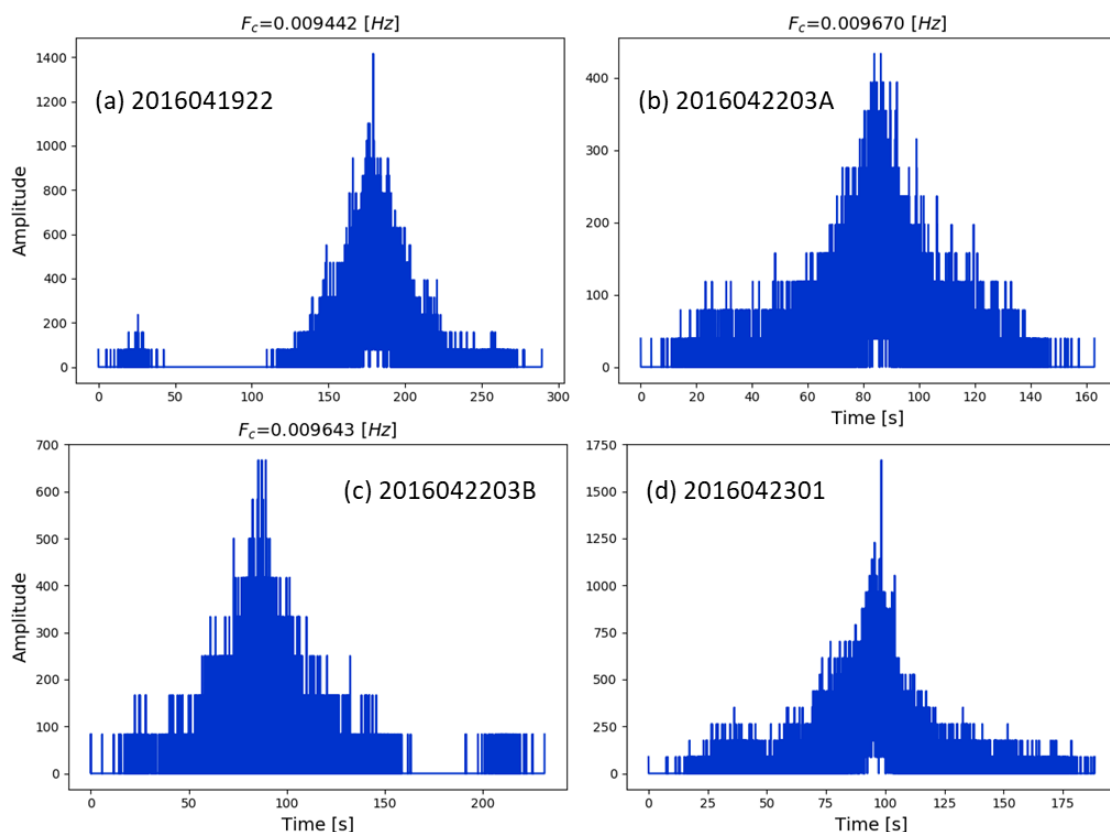


Figure VI-31. Examples of  $STF$  for  $F_c$  around the average expected for a Mw 8.5 earthquake ( $M_o=6.30957 \times 10^{21}$  Nm).

To compare the effect of the variation on  $F_c$ , the  $r$  functions from the same EGF are compared (Figure VI-32).  $r$  has different shapes indicating that the method proposed works well preventing that  $r$  converges to one only shape. In the case where  $F_c$  is equal to 0.006 Hz ( $T=133$  s) the shape

of  $r$  is not regular and it presents more than one peak, even for this case that the number of points is around 100000 (Eq. (VI-13)).

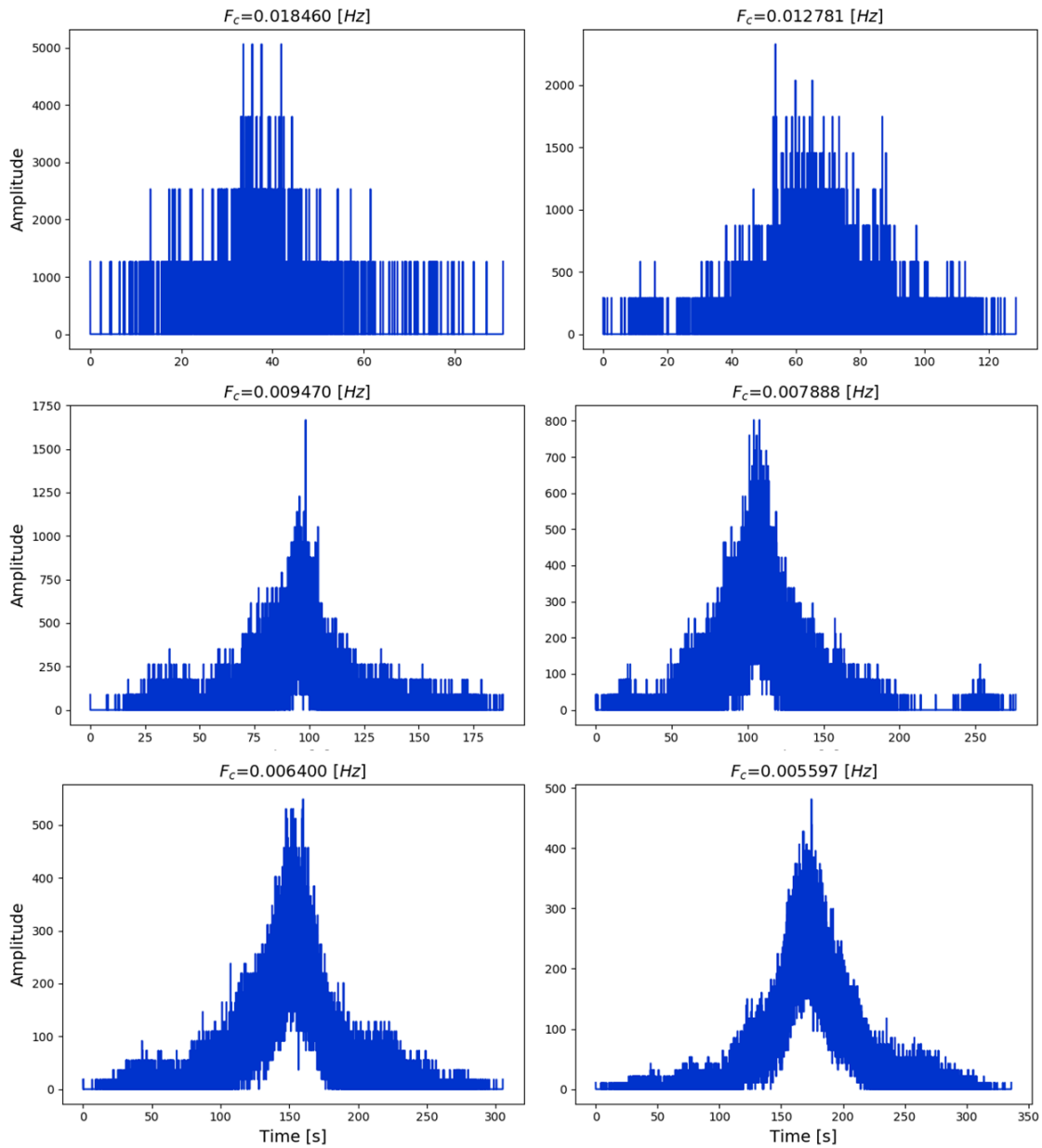


Figure VI-32. Comparison between STF from the EGF 2016042301. The STF were selected to represent the range of variation of the STF.

The EGF method can produce time domain signals. Figure VI-33 presents examples of predicted signals with a different range of  $F_c$  for the EGF 2016042301. The time signals have a large range of a duration and amplitude of the shaking.

Analyzing the spectrum of all the simulation and for all the EGF, we obtain that with different EGF is obtained similar shapes and amplitude on the spectrum (Figure VI-34). The site effects are important causing a variability between the sites in different frequencies. Like the previous subsection, four sites were selected to represent the site condition on Quito.

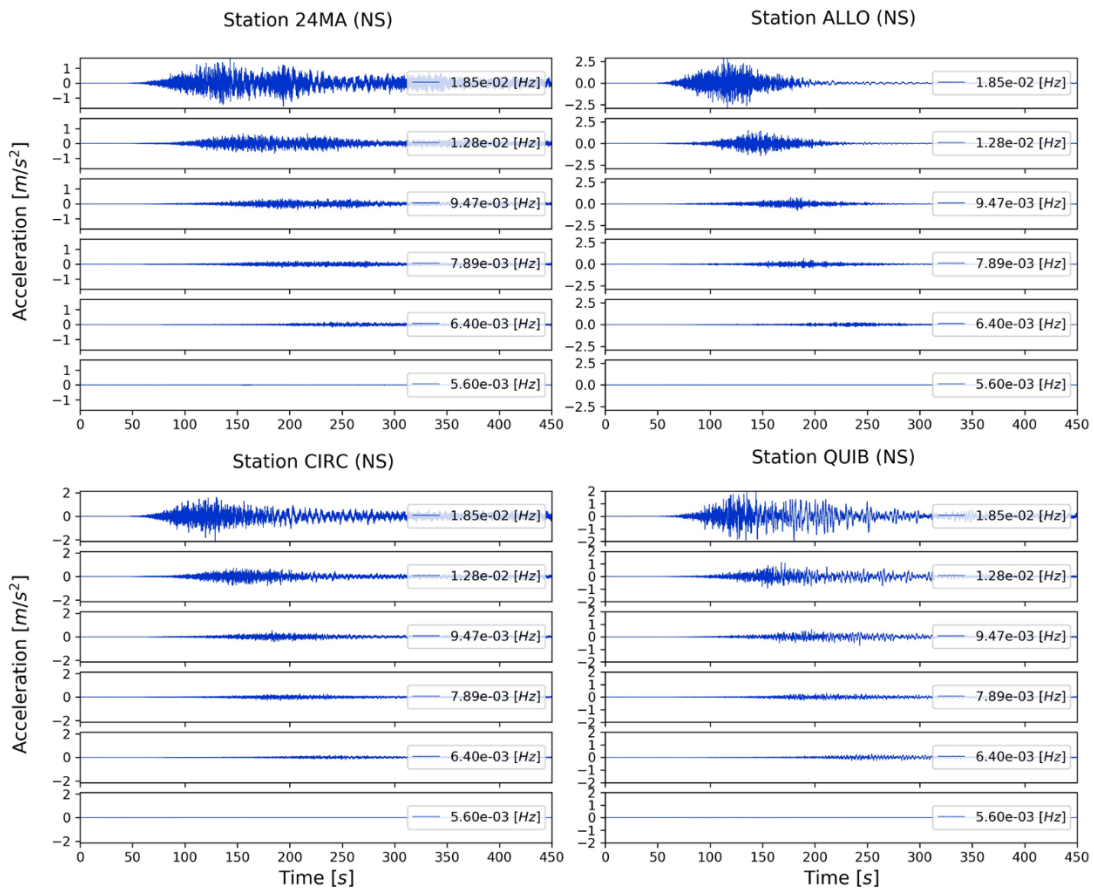


Figure VI-33. Temporal simulation in north-south direction for an earthquake Mw 8.5 using EGF 2016042301.

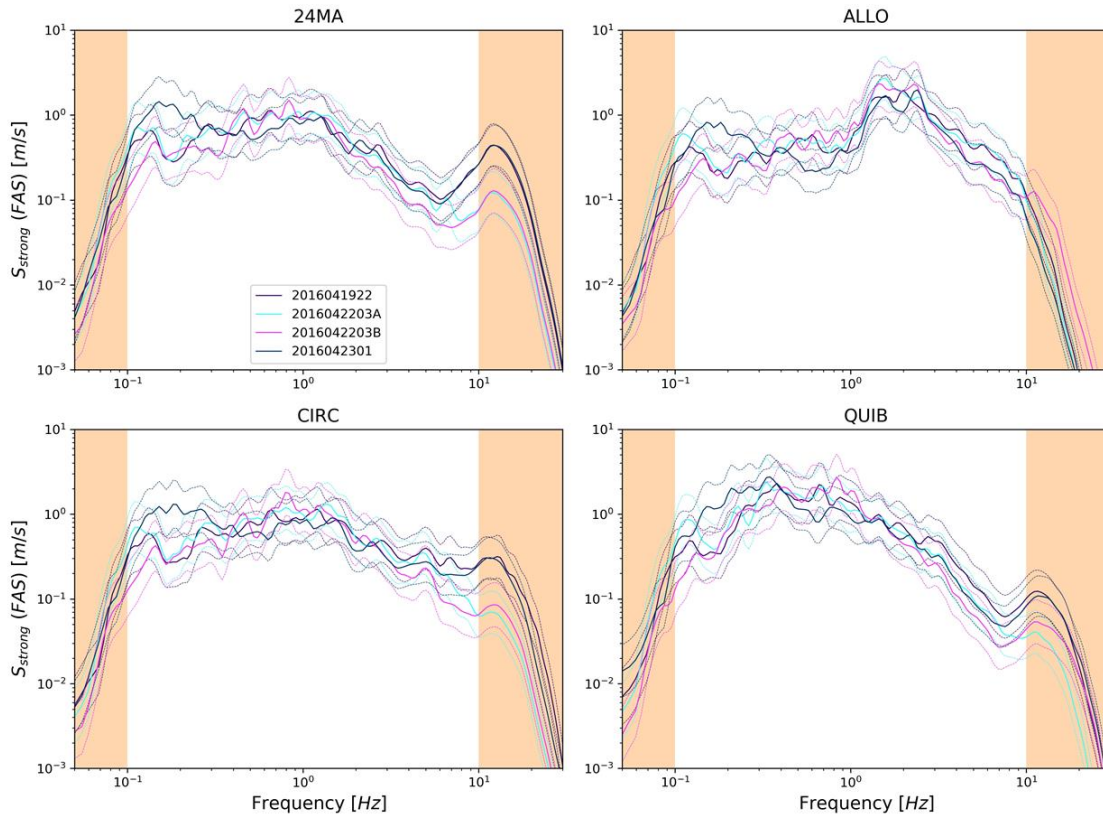


Figure VI-34. Prediction of the spectrogram for 1000 simulation of Mw 8.5 earthquake. The average of the horizontal with the standard deviation is included. Representative sites were selected for Quito. 24MA is a site with low site amplification, ALLO is a site located in the mountains, QUIB is a site located at the south of Quito, CIRC is a site at the north of Quito.

The response spectra are analyzed (Figure VI-35). It shows that the shape of the spectrum is very similar than for the Pedernales earthquake (Figure VI-20), but the amplitude is higher in the case of Mw 8.5. Especially in the period where the peaks occur,  $S_a$  is from 2 to 3 times higher than Pedernales. For example, a building in the mountains (represented by ALLO station) and with a period around 0.5 s will experiment a strong horizontal shaking around 1g.

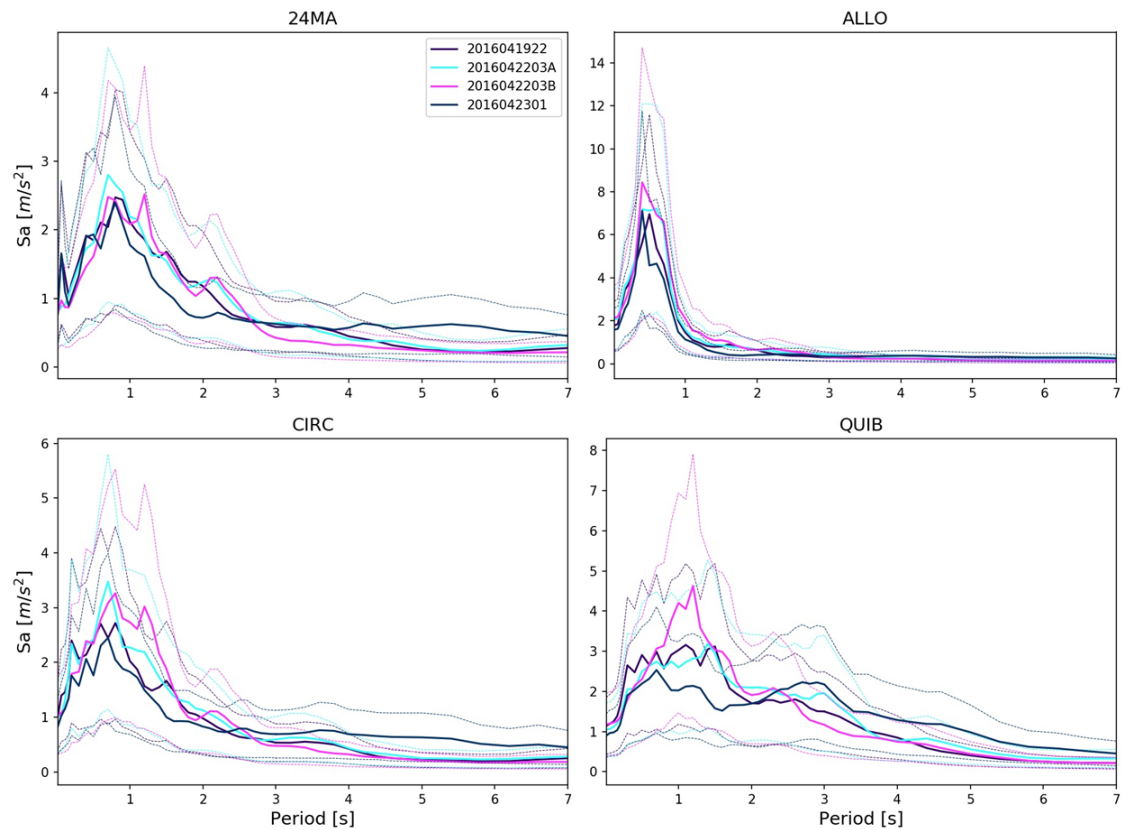


Figure VI-35. Horizontal response spectra (5% damping) for sites that are representative of the site conditions in Quito. Mw 8.5 earthquake.

The response spectra are presented for three periods for all the stations. Like in the previous section (Figure VI-21, Figure VI-22, and Figure VI-23), the PGA, the  $S_a$  at 0.6s, and  $S_a$  at 2.8 s are shown. The first one (PGA) indicates the intensity of shaking at the ground. We selected the peak at 0.6 s because around this period in most of the stations is the main peak. The period at 2.8 s is a period where the sites located at south develop site effects.

In the case of PGA, the shaking that is predicted is higher than the predicted by the GMPE (Abrahamson et al., 2016). In the sites ALLO and SADP, the average of the predictions from the EGF method is higher than the GMPE with one standard deviation. In other sites, the prediction is around this border.

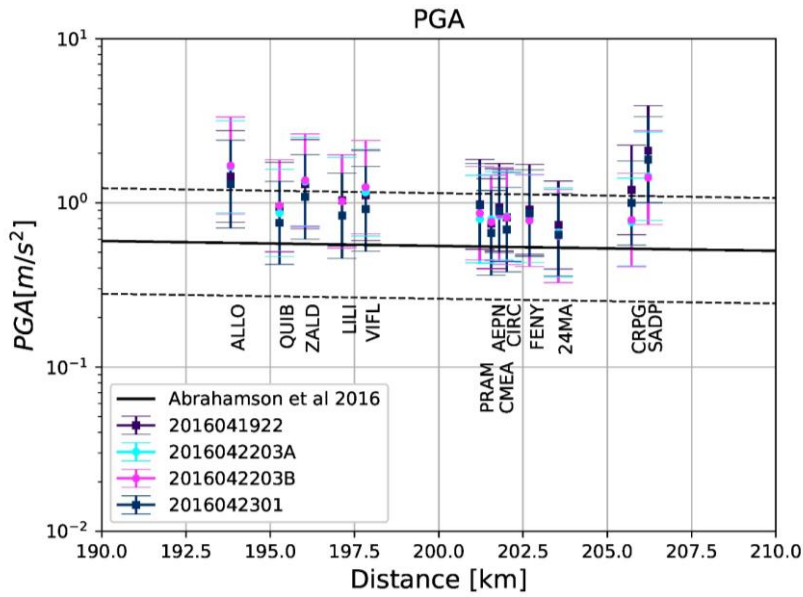


Figure VI-36. PGA estimation for M8.5 earthquake comparing GMPE (Abrahamson et al., 2015) and EGF method. Continue line represents the mean estimation and dashed lines represents the logarithmic standard deviation that was added and removed.

The main peak for all the sites is around 0.6 s (Figure VI-35). Plotting this period for all the sites we obtain that the predicted pseudo acceleration is higher than expected by GMPE (Figure VI-37). At this period the stronger shaking must be felt by sites ALLO and SADP. The site with the lowest pseudo peak acceleration is in the site 24MA. It is because this site does not present high site effects in his response (Laurendeau et al., 2017), remarking that in the other sites it is important to consider the site effects.

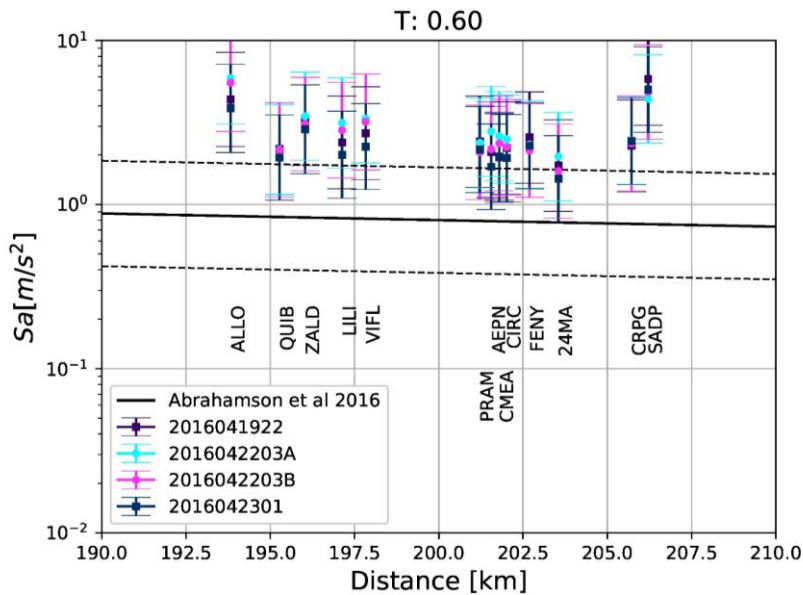


Figure VI-37. Response spectra at 0.6 s, comparing GMPE (Abrahamson et al., 2015) and EGF method.

Additionally, the response spectrum at 2.8 s is analyzed (Figure VI-38) because around this period the sites at the south of Quito have a second peak. This second peak is related to site effects Laurendeau et al., 2017. In this case, like for Pedernales (Figure VI-23), sites at the south of Quito present a higher amplification on this period (QUIB, ZALD, LILI, and VIFL).

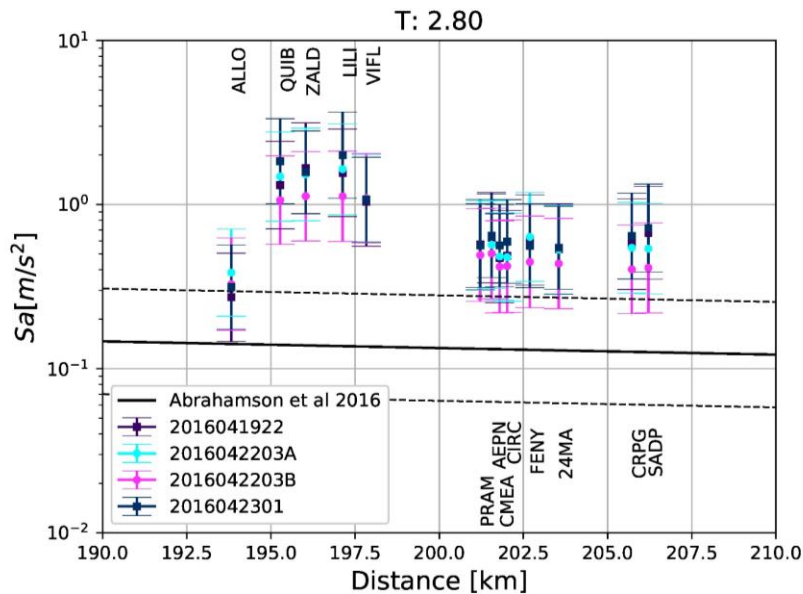


Figure VI-38. Response spectra at 2.8 s, comparing GMPE (Abrahamson et al., 2015) and EGF method.

The results show that a Mw 8.5 earthquake coming from the same fault than Pedernales earthquake can produce a strong shaking on Quito. For constructions with a resonance period of 0.6s, the shaking could reach around  $5 \text{ m/s}^2$  (Figure VI-37). Around periods of 2.8s (Figure VI-38) the buildings will suffer a shaking lower than  $1 \text{ m/s}^2$ , except the ones located at the south of Quito. In this case, the shaking has a pseudo acceleration upper than  $1 \text{ m/s}^2$  for a period 2.8 s.

Those results show that a future Mw 8.5 earthquake could produce strong effects in Quito, especially for high buildings with periods around 2.8s located at the south of Quito.

### VI.8 Summary and discussion

The methodology here presented, makes a step forward to make more applicable the EGF method. In comparison with the previous methodology on what is based our proposition (Kohrs-Sansorny et al., 2005) the methodology proposed herein presents a methodology to estimate of the corner frequency (and then the stress drop) of a future earthquake based on a global database of STF, the SCARDEC database. Here, we use the relationship presented before between corner frequency, fault duration and magnitude (Courboulex et al., 2016) to estimate the corner frequency. We include the variability associated with this estimation on the results through a random process that allows us to obtain a result in terms of mean values and variability.

We first apply the methodology to the earthquake of Pedernales Ecuador to compare if the estimations are adequate for this case. We evaluate six different EGF to reproduce the earthquake, finding that four of them make appropriated estimations. These results from the Figure VI-21, the Figure VI-22, and the Figure VI-23 show that EGF method can include characteristics as the site effects and path effects. This reduces the variability of the estimation and makes more realistic the prediction.

In comparison with the GMPE method, EGF has a quite lower uncertainty on the result, and similar results that are congruent. This shows that the methodology explained in this document is not producing extreme or unrealistic predictions. We showed that for sites with strong site effects the error in the prediction is reduced in comparison with GMPE.

However, as it was shown, when not adequate EGF are selected, or their parameters are no correct, the approximation could produce different estimations (Figure VI-28, Figure VI-29, and Figure VI-30). This was the case of two of the six EGF evaluated. In one case (2016041707) there is a high odd that the used seismic moment is too high in comparison with the real. However, this case success in reproducing the shape of the spectra of the Pedernales Earthquake. Also, it predicts approximately the order in which sites the earthquake will be stronger than the others. The misfit of EGF is almost constant for all the frequencies and sites, what can be explained if the seismic magnitude was too low in comparison with the real one.

In the case of the EGF 2016041709, the hypocenter of this is very close to the trench fault. It could involve a different source and path effects than the Pedernales earthquake suffered. Due to this, the estimation of this EGF is different in shape and amplitude.

We mark the importance of the good selection of the EGF in this methodology. We see that if the EGF are adequate, the method can better estimate the ground motion with a lower uncertainty than other methods, like GMPE and moreover it enables to obtain synthetic accelerograms. Since the EGF must accomplish several criteria to be adequate, the selection process must be careful. The source and the path effects of the EGF must be similar than the earthquake that will be estimated. We suggest using several EGF for a similar estimation, validating the EGF that produces similar predictions.

EGF method supposes that the future source is located around the EGF source. However, large earthquakes occur on large faults (about 500 km estimated for the 1906 earthquake in Ecuador from Kanamori and McNally, 1982). Those difference should be taken in account specifically for the prediction of very strong earthquakes. One way of including this effect is to use together more than one EGF in one prediction and to take into account the rupture propagation.

The EGF approach supposes that the response of the soils is linear. In the previous chapter of this thesis, I have shown that the site effects can be different for weak and strong ground motions. This produces an impediment to correctly predict strong ground motions on sites where the non-linear effects of the soil can produce strong changes in the final shaking. These effects must be studied to be included in the method.

## Chapter VII First attempt to the integration of non-linear site effects on the Empirical Green Function methodology using borehole arrays

In the previous chapter the empirical Green's function method was detailed and used to predict the Pedernales earthquake. However, one of the hypotheses of this methodology relies on the linearity of the system. This is unfortunately not realistic for strong ground motions since the site response has a non-linear behavior, as was shown in the section V.1. In this chapter a methodology for integrating the non-linear effects into the empirical Green's function approach is shown. The methodology is based in the *fsp* curves and is an extension of the methodology presented in Chapter III.

### VII.1 Methodology of integration of non-linear effects by *fsp* curves and the EGF method.

The ground motion can be separated in three parts as was shown in the Eq. (VI-7).

$$S(f) = STF(f) \cdot P(f) \cdot TF(f)$$

The terms *STF* and *P* represent the source and the path effects of the ground motion respectively. The variable *TF* represents the site effects and corresponds to the transfer function of the site. In the case that the analysis is done at a site with a linear site response, the term *TF* should not be different between a weak and a strong event (with epicenters located at the same position). It allows to apply the EGF methodology of the Chapter VI.

We are working here with data recorded by borehole arrays. In this case, the prediction of a strong ground motion at the downhole station follows the formula:

$$S_{downhole}(f) = STF_{strong}(f) \cdot P(f) \cdot D(f) \quad (VII-1)$$

Where *D* represents the downward waves reflected at the free surface. The methodology that is proposed suppose that this waves depend of the site parameters and they remain the same for weak and strong ground motions. This can be considered adequate if the stations are deep enough (Bonilla et al., 2002) or if the site has a high damping enable us to neglect the downward waves. The methodology of EGF in the Chapter VI can be thus used for evaluating downhole records. In the *EGF* method the scale between *STF* (Eq. (VI-10)) is expressed as:

$$R(f) = \frac{STF_{strong}(f)}{STF_{weak}(f)}$$

Where *R* is the Fourier spectrum of the *r* function defined in the Eq. (VI-11). As explained in section VI.3, several realizations,  $r^{(j)}$ , are produced and the average is computed to define *R*. Including the function  $r^{(j)}$  and translating the Eq (VII-1) in the time domain, we obtain:

$$s_{downhole}^{\{j\}}(t) = r^{\{i\}}(t) * EGF_{downhole}(t) \quad (VII-2)$$

Where  $r^{ij}$  is one realization of the time source (Eq. (VI-11)), and  $EGF_{downhole}$  is the record of a weaker ground motion at the downhole station, used as  $EGF$ . The selected  $EGF$  must fulfil the hypothesis on which the methodology is based (see section VI.3). For example, the  $EGF$  epicenter must be localized close to the one of the strong earthquake, the focal mechanism must be similar, and any other characteristic to guarantee that the wave travel path is similar. Additionally, we have to ensure that the source time function is matching the  $\omega^2$ -model (Eq. (VI-10)).

For the surface record, the site effects are computed using the Borehole Spectral Ratio ( $BSR$ ) function. To include this function, widely studied in the previous chapters, in the prediction of a strong ground motion at surface, we start from the definition:

$$BSR(f) = S_{surface}(f) / S_{downhole}(f)$$

As was shown in the Chapter I, the site effects depend on the rigidity of the soil, and they are changing in function of the seismic solicitation intensity (Figure III-2). Because  $BSR$  is not constant function with respect to the ground motion intensity, the assumption to develop the  $EGF$  method (Eq. (VI-9)) is not verified anymore at the surface sensors. However, if the downward waves do not depend on the ground motion intensity, the downhole record can be predicted by the  $EGF$  method (Eq. (VII-2)) and the surface one with the convolution:

$$S_{surface}^{\{i\}}(f) = S_{downhole}^{\{i\}}(f) \cdot \widehat{BSR}(f) \quad (\text{VII-3})$$

The estimation of  $BSR$ , represented by the term  $\widehat{BSR}$  (Eq. (III-7)) is obtained by the estimation of  $f_{sp}$  with the procedure that is explained in the section III.5. The term  $S_{downhole}^{\{i\}}$  is the spectrum of a realization  $S_{downhole}^{\{i\}}$  computed with the  $EGF$  method (Eq. (VII-2)).

## VII.1 Ground motion prediction of an aftershock (Mw 7.9) of the 2011 Tohoku earthquake

To try out the proposed methodology, we select an earthquake for which the  $f_{sp}$  and the  $EGF$  methodologies can be applied at the same time. It requires that the earthquake is strong enough to generate appreciable non-linear effects in a site that is far enough to apply the  $EGF$  method. Many strong earthquakes have generated strong non-linear effects in Japan, but those are located too close for being modeled by the simple  $EGF$  method described in Chapter VI. For example, from the 2011 Tōhoku earthquake Mw 9.0 recordings we observed strong decreases of  $f_{sp}$  values on several sites, but the extension of this earthquake was too large in comparison with the distance to the stations for considering this earthquake as a punctual source, which is a supposition  $EGF$  method requires.

We select then the strongest aftershock of Tōhoku, Mw 7.9, that occurred at 06:15 (UTC) on 11<sup>th</sup> March 2011, just half hour after the mainshock and, together with the mainshock, they produced several casualties in Japan. The source depth was found to be equal to 42.6 km. This earthquake generated a strong shaking at FKSH10 for which we could observe a decrease of  $f_{sp}$ .

### VII.1.1 Application of the $EGF$ method with linear site effects

We will first validate that the  $EGF$  method is able to reproduce the ground motion at FKSH10. To assure this, we apply the method at two sites where the site effect should be linear, meaning that the  $EGF$  method works alone. One point is the station TCGH17 located at a distance of 41 km from FKSH10 (Figure VII-1). This site has a  $V_{s30}$  of 1433 m/s, so it is considered as a rock station. The second point that this section evaluates is the downhole station of the site FKSH10.

This site has a  $V_{S30}$  of 487 m/s but the borehole station is located at 200 m of depth where a shear velocity of 870 m/s is reported.

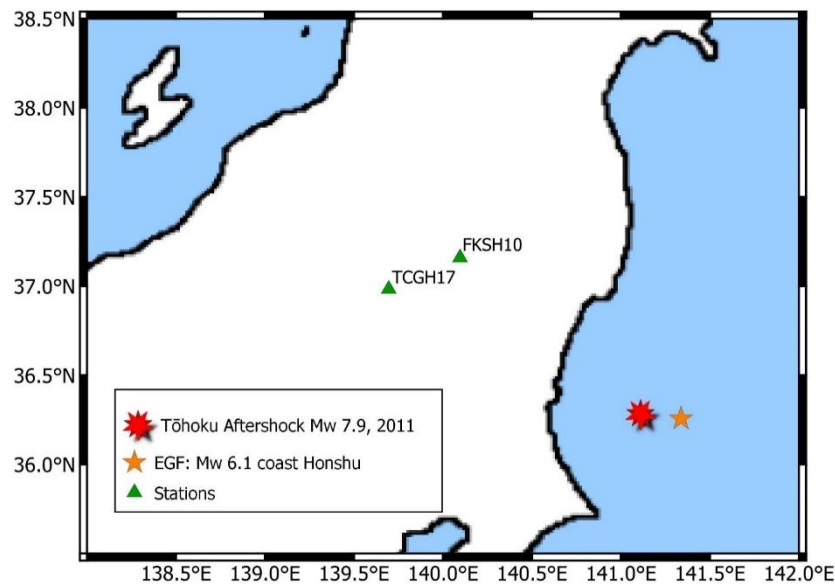


Figure VII-1. Location of the Aftershock and the EGF that we use to recreate the earthquake. The station FKSH10 presented non-linear effects for this earthquake, and the station TCGH17 is a rock reference site where we validate the method.

Figure VII-2 shows the soil profile of both stations. The site at FKSH10 shows a  $V_s$  almost constant with depth, except for the shallowest 15 meters. In the case of TCGH17 the profile exhibits hard materials starting from the surface. This site has layers with  $V_s > 2000$  m/s just after 15 m. It supports the assumption that this site has a linear behavior.

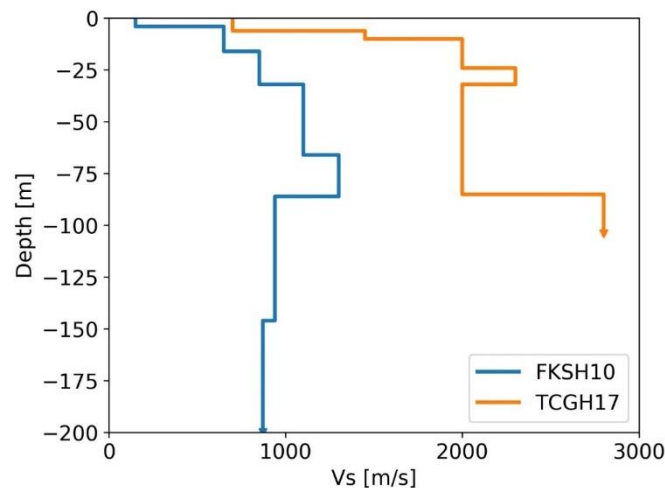


Figure VII-2. Shear velocity profile of the station that are analyzed on this chapter.

To use the EGF method, we select an earthquake that occurred around the same location, same focal depth and with similar focal mechanism than the considered Tohoku aftershock. We choose an earthquake around the Honshu coast with Mw equal to 6.1 (Figure VII-1). The earthquake occurred on 15<sup>th</sup> September 2011 at 08:00 (UTC).

The distances from the station to the epicenter of the mainshock are given in the Table VII-1.

Table VII-1. Station and distances to the epicenter of Tohoku aftershock, 2011 Mw 7.9.

Name	Distance [km]	Position	
		Longitude [°]	Latitude [°]
FKSH10	133.0	140.093	37.1616
TCGH17	148.6	139.6922	36.9853

The parameters considered for the EGF computation are gathered in the Table VII-2. Taking into account that the Tohoku aftershock is located in a subduction zone, we define the distribution of the duration of fault with the subduction database presented in Courboux et al., (2016) (Figure VI-6). Additionally, because the purpose of this simulation is to test the integration of the two methodologies presented in this document, the EGF method of the Chapter VI and *fsp*, we select the corner frequency of the EGF as 0.12 Hz to fit the result at TCGH17.

Table VII-2. Parameters consider the EGF simulation of Tohoku aftershock starting from  $M_w$  6.1 earthquake.

Corner frequency of the EGF [Hz]	0.12
Magnitude Moment target event [Nm]	8.49E+20
Magnitude Moment EGF [Nm]	2.86E+18
Number of simulations	500
q parameter	0.803

Applying the same procedure of the EGF method for the surface of the site TCGH17, we obtain a good fitting between the recorded and the predicted ground motion (Figure VII-3). It demonstrates that we are able to simulate accurately this earthquake at a station close to FKSH10 with linear condition. The method generates some discrepancies at high frequencies with the mean value, but in general, the observed Tohoku ground motion is always between the error range given by the standard deviation of our simulation.

Figure VII-4 shows the prediction of the downhole seismic movement using as *EGF* the record at the same sensor. The fitting is good, although there are some differences for frequencies higher than 20 Hz. This result shows again that the linearity hypothesis is alright.

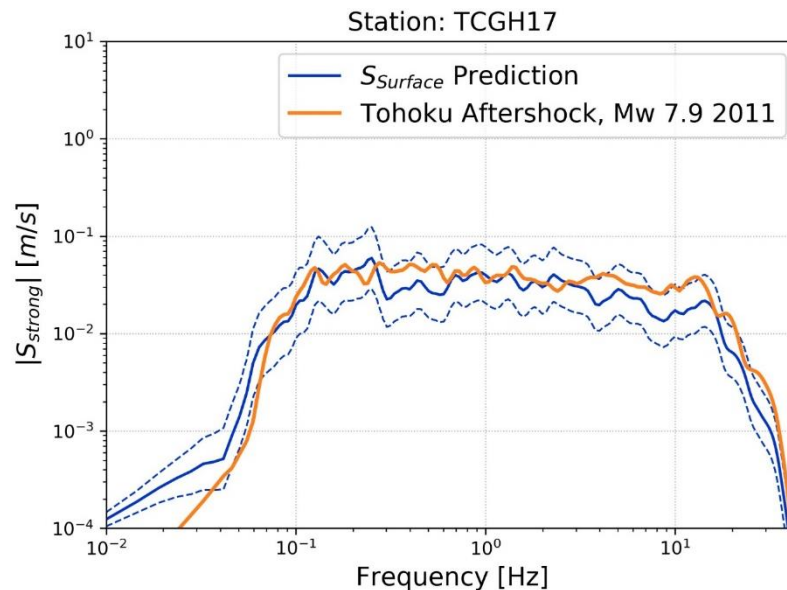


Figure VII-3. Prediction at surface of the shaking of the Tohoku aftershock Mw 7.9, 2011. Station TGH17 on rock.

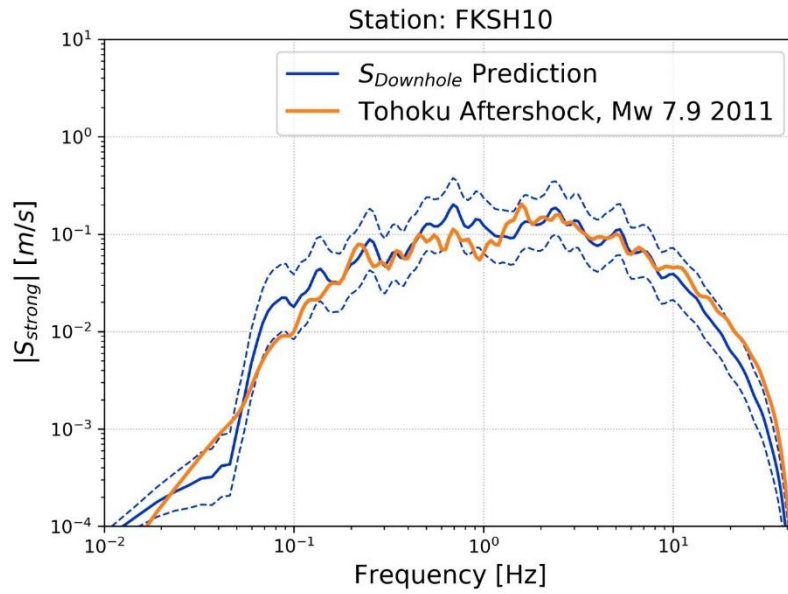


Figure VII-4. Prediction of shaking due to the Tohoku earthquake Mw 7.9 at the downhole station in the site FKSH10.

#### VII.1.2 Comparison of the EGF simulation of the surface strong ground motion at FKSH10 with or without including non-linear effects

To estimate the site effects, we selected the average of the  $PGA_{downhole}$  between all the simulations at the downhole station of FKSH10. This procedure results in a  $PGA_{downhole}$  of  $0.26 \text{ m/s}^2$ . Using this value,  $f_{sp}$  is derived from the regression curve defined for the station (Figure VII-5).

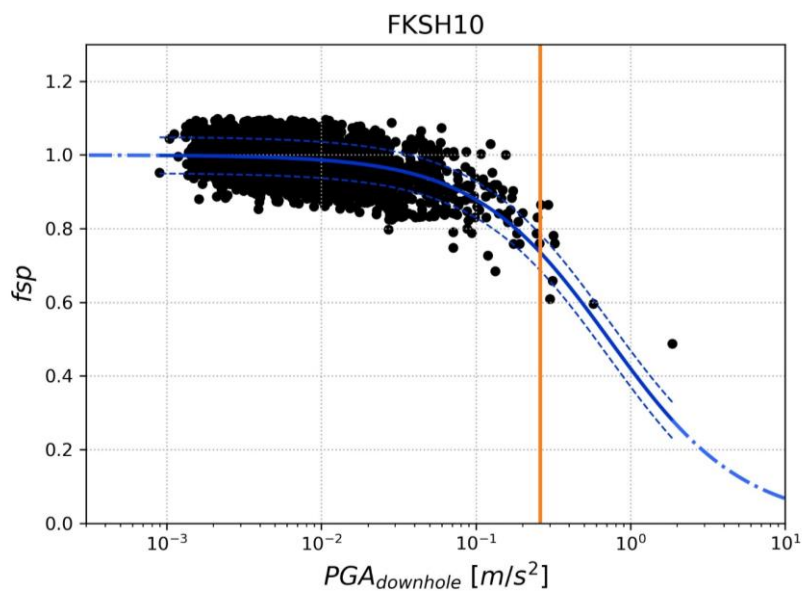


Figure VII-5.  $f_{sp}$  curve for FKSH10. Orange vertical line represent the average  $PGA_{downhole}$  that was obtained from the time historic simulations at downhole.

The  $f_{sp}$  for the considered seismic solicitation is equal to 0.73. Using Eq. (III-7), we estimate the site effects by finding  $\widehat{BSR}$  for Tohoku earthquake, Mw 7.9. Figure VII-6 show the comparison between the real BSR for this earthquake and  $BSR_{linear}$ . We can see that the non-linear effects for this case are not very strong. However, the implementation of the  $f_{sp}$  curve in the EGF method allows to well predict the resonance of the soil for this earthquake.

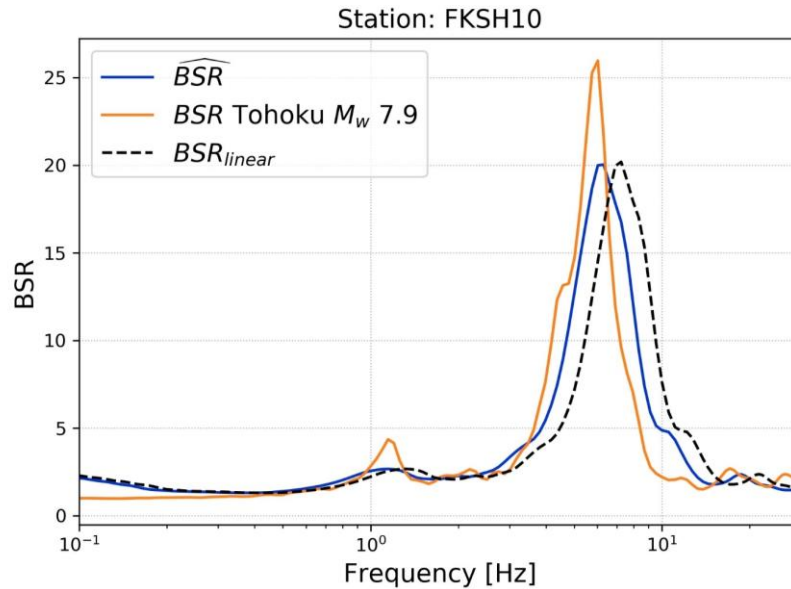


Figure VII-6. BSR site effect estimation using the correction of  $f_{sp}$  (blue line) and the linear site response (black dashed line). The orange line represents the Tohoku aftershock.

We apply the Eq. (VII-3) to propagate the shaking from downhole to surface. In Figure VII-7 we compare the motion computed with this methodology (blue line), and the real record of Tohoku aftershock (orange line). Additionally, the figure shows in green line the result of evaluating the EGF method directly at the surface. We can observe that the improvement of using  $f_{sp}$  lays around the central frequency peak, at around 6 Hz. In this case, the non-linear effects are not as evident as in the case of Kumamoto earthquake (see section III.5), but they still generate a frequency shift to lower frequencies. Our methodology better predicts this.

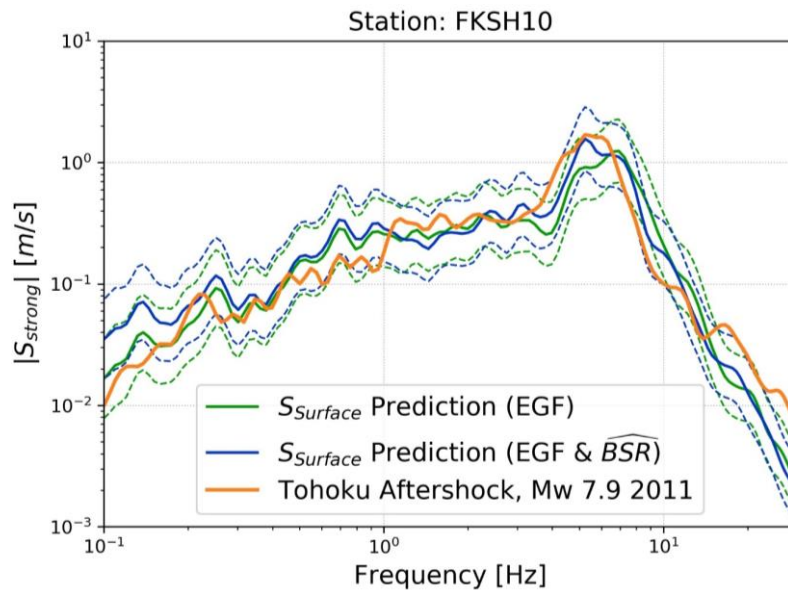


Figure VII-7 Comparison of the spectra at surface generating by EGF method with non-linear corrections (blue line), conventional EGF method (green line) and the real record that we are recreating (orange line).

Using the same methodology of comparison than for Kumamoto earthquake, Table VII-3 shows the misfit for the site effects ( $BSR$ ), and for the seismic motion at the surface ( $S_{surface}$ ). For both cases, the improvement is clear enough. Because the  $BSR$  function is very simple with a unique peak, and because  $\widehat{BSR}$  clearly estimates better this peak (Figure VII-6), the simulation misfit is 67% improved comparatively to the one from the direct linear approximation.

Table VII-3. Comparison of the misfit obtained with each approximation.

Misfit to observed $BSR$			Misfit to observed $S_{surface}$		
$\widehat{BSR}$	$BSR_{linear}$	Ratio	$EGF$	$EGF+fsp$	Ratio
4.771	7.122	0.670	0.207	0.271	0.764

Considering the phase of the downhole simulated recording, we obtain the time histories of the ground motion at the surface. It allows us to compute the response spectra (Figure VII-8). The EGF method without any correction does not predict the central peak of the response spectra (green line). But including the non-linear effects makes the main peak be inside the standard deviation. The lower amplitude of the response spectrum at low periods is related to the fact that the EGF method underestimates in general for all the stations the high frequencies (Figure VII-3, Figure VII-4, and Figure VII-6).

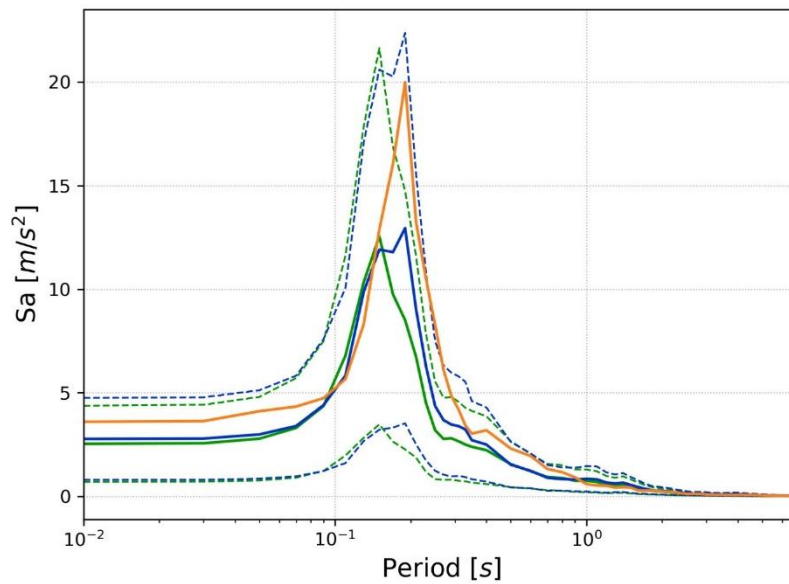


Figure VII-8. Geometrical average of the horizontal response spectra for the shaking at surface. Dashed lines represent the response spectra  $\pm$  the standard deviation.

## VII.2 Conclusion and discussion

We attempt to integrate the effects of the soil non-linear behavior on the strong ground motion in the EGF simulation process. This method consists first in simulating the event at a close rock reference site. In this case, we use the downhole station, and after we convolve the result with a modified borehole transfer function taking in account the non-linear effects.

This new methodology offers the same advantage that the EGF method, offering accelerometric signals, and also includes the non-linear effect. We applied the methodology for an aftershock of the Tohoku earthquake with Mw 7.9. We improve the ground motion prediction at the surface and the response spectra.

However, this method is limited here to some earthquakes only because we have to fulfil the hypothesis of the EGF methodology that we are using as well as the one of the *fsp* technique. Indeed, the reason why we did not analyze another station or earthquake where the non-linear effects are more evident, is because other earthquakes have a magnitude too large to be considered as a punctual source, or stations are too close from the fault, generating complex effects from the source. The Tohoku aftershock was the best case we found to apply both the EGF approach and the *fsp* correction of the site transfer function.

These conditions make the methodology too restrictive, and in future works, a new method to simulate close events must be join to the *fsp* analysis. The consideration of closer earthquakes than  $\sim 150$ km in the methodology could be reached with other EGF methods, that can recreate the finite fault complexity (e.g. Yagi and Fukahata, 2011), or by other numerical simulation of the source. These alternatives should be studied in future works.

## Conclusions

Among the methods to evaluate strong ground motions, we decided to concentrate our efforts on empirical approaches. While numerical approaches require the knowledge of the characteristics of medium traveled by the seismic waves, empirical approaches overpass this limitation. The empirical green function considers that the source to site travel path is similar for weak and strong earthquakes. In particular, this method considers lithological site effects as perfectly linear. While this can be true for rock material, the non-linear behavior of softer materials associated with the large deformation that can be developed close to the surface will invalidate this hypothesis. Indeed, the seismic site response change between strong ground motions compare to weak ones. The aim of this work was to fill in this gap and to propose a solution to integrate the non-linear soil behavior empirically to empirical green function.

We evaluate the non-linear soil behavior effects on the site response. The two main and more usual effects are a decrease of the shear modulus (link to the stiffness of the soil) and an increase of the attenuation. From simple analytical models, we know that the resonance frequencies depend exclusively on the stiffness and the layering of the soil if the waves propagate in 1-D direction with vertical incidence in a linear viscoelastic soil model. Any change on the stiffness would produce a change of the resonance frequencies. Therefore, we propose a new parameter ( $f_{sp}$ ) that quantifies the changes of stiffness by observing the logarithmic shift of the frequency peaks in the transfer function. We first test this parameter on numerical simulations and found that  $f_{sp}$  succeed in fitting the decrease of stiffness in the Equivalent Linear Method perfectly. For more complex models the parameter fits the general stiffness reduction of the soil column.

$f_{sp}$  supposes that the soil column keeps the same stiffness during all the ground motion since the parameter is calculated from the spectra computed with the whole recorded ground motions. This supposition is equal to the hypothesis of the *EQL* method, but it may not be adequate for real ground motions that temporarily generate high strain (Kaklamanos et al., 2013).

The borehole spectra ratio (*BSR*) is a tool to estimate empirically the site effects. We use *BSR* to compare the site response for many events recorded by the Japanese accelerometric database, Kik-Net. The intensity of the ground motion generates a modification on the borehole transfer functions between weak and strong ground motions. These changes are related to the non-linear soil behavior of the soil layers. For strong ground motions, the *BSR* curve presents a shift of the frequency peaks to lower frequencies and a reduction of the amplitude.

We use the parameter  $f_{sp}$  computed from *BSR* to quantify the effects of the non-linear soil behavior on site response during a strong ground motion. We find a non-linear correlation between  $f_{sp}$  with parameters of the ground motion intensity (*PGA* and *PGV*).

The curves provided by this non-linear regression is site-dependent but for all sites follows a hyperbolic curve ( $\widehat{f_{sp}}$  curve). This correlation gives a way to (1) quantify how likely a site is prone to develop non-linear soil behavior. (2) estimate the non-linear soil behavior effects on site response for future strong ground motions.

Additionally, when using a proxy of strain as ground motion intensity parameter, the hyperbolic curve fits roughly the modulus reduction curves from the shallow layers. It gives us a possible way to estimate the modulus reduction curve directly from the records of seismic ground

motions. A wide comparison between the performance of this technique and the laboratory tests should be studied in future works. Additionally, in future works must be analyzed if this curve is adequate as a parameter of numerical models as the Equivalent linear method.

Looking at all sites, the relationship between  $\widehat{fsp}$  curves and site parameters show that sites with a high  $V_{s30}$  are more prone to develop a shift of the resonance frequencies during weaker ground motions meaning that the site is more prone to non-linear soil behavior.

To check the applicability of this approach to earthquake recordings on only one seismic station at the surface, we calculate  $fsp$  from earthquake  $H/V$  spectral ratio. The curves between  $fsp$  and ground motion intensity parameter are similar to the ones obtained with  $BSR$ . The main difference is that the  $\widehat{fsp}$  curves from  $H/V$  spectral ratio have a higher dispersion. Because of this, we find that  $BSR$  is a more efficient tool to quantify the non-linear soil behavior than the earthquake  $H/V$  spectral ratio. However, in general, both kinds of analysis is appropriate, and, for some sites even, the  $H/V$  spectral ratio approach shows a lower dispersion. The  $fsp$  parameter could also be calculated on other techniques to estimate the site response based on an outcrop reference sites, as the rock reference spectral ratio.

Applying  $fsp$  to the earthquake  $H/V$  spectral ratio, the curves between  $fsp$  and intensity are similar than the one obtained with  $BSR$  computation. The main difference is that the  $fsp$  curves from  $H/V$  spectral ratio have a higher dispersion. Because of this, we find that  $BSR$  is a more efficient tool to quantify the non-linear effects than the earthquake  $H/V$  spectral ratio. However, in general, both kinds of analysis is appropriate, and, for some sites even, the  $H/V$  spectral ratio approach shows a lower dispersion. Other techniques based in reference sites, as the rock reference spectral ratio, could be also analyzed with the  $fsp$  parameter. This application should be part of future works associated with  $fsp$  parameter.

We find that for some site a low performance in the  $fsp$  curves, in most of the cases due to the high dispersion of the  $fsp$  points. Differentiate for which sites the  $fsp$  technique could be applied and for which sites should not it is an important task that should be aborted in future works.

Looking at the results in all the stations,  $fsp$  highlights the importance of implementing the non-linear soil behavior in the seismic hazard assessment. More than 50 % of the sites show that the site response is considerable affected for ground motions with a  $PGA$  at surface upper than  $1m/s^2$ .

The non-linear effects can result in either an increase or a decrease of the amplification, depending of the frequency or period that is analyzed. That is why, several approximations as GMPEs and linear numerical models should consider those effects.

We found a relationship between the intensity of the seismic input and the decrease of the amplification level in the  $BSR$  curves. Even this procedure has a high uncertainty, including in the prediction of future site response the analysis of the decrease of  $BSR$ , it improves the ground motion prediction. However, it is not possible yet to conclude physical properties of the site from this analysis. The improvement of the derivation of those curves and the estimation of site parameters as the damping should be part of future works.

We also use empirical data to predict the source and path effects of an earthquake. We use the well know methodology of empirical Green's functions, specifically the one proposed by Kohrs-Sansorny et al., (2005). This methodology consists in scaling a weak ground motion, using his

information about the source and the green function of the traveled media to obtain a strong event.

We give a step forward to this EGF methodology by the implementation of the estimation of the corner frequency (that is one of the main parameters of the methodology) of a future earthquake. This prediction is based on a global database SCARDEC.

We applied the methodology to the 2016 Pedernales earthquake, Ecuador, to compare if the estimations are adequate for this case. The results show that our EGF method recreates characteristics, like the site effects and path effects, adequately. We have to keep in mind though that the system remains linear. In comparison with the GMPE method, EGF has a quite lower uncertainty on the result. Indeed, we show that for sites with strong site effects the error in the prediction is reduced in comparison with GMPE because the GMPE suppose a generalized shape of the response spectra, that is not accomplish in some sites.

We propose a first attempt to integrate the non-linear effects in the EGF method. To achieve this, we use a borehole array from kik-Net database, and we simulate the downhole station with the EGF method. Then, we convolve the obtained ground motion with the borehole transfer function taking into account the non-linear effects. We approximate the borehole transfer function by our methodology, applying the *fsp* to *BSR*. We obtain the first result that, although it does not bring significant changes, shows an encouraging improvement in the prediction.

We should apply our approach to a stronger event where the non-linear effects are more evident, but the limitations of the *EGF* method we use here did not allow to do so. This method is, indeed, limited to earthquakes that are far enough to consider the source like a punctual point source. However, we present the general methodology that could be implemented to other EGF method or procedure to estimate an earthquake in a closer place with low non-linear effects. The introduction of the *fsp* correction in other methods to simulate the rock ground motion, as stochastic method (SMSIM), should be analyzed in future works.

## Bibliography

- Abrahamson, N., Gregor, N., Addo, K., 2016. BC Hydro Ground Motion Prediction Equations for Subduction Earthquakes. *Earthq. Spectra* 32, 23–44. <https://doi.org/10.1193/051712EQS188MR>
- Acerra, C., Aguacil, G., Anastasiadis, A., Atakan, K., Azzara, R., Bard, P.-Y., Basili, R., Bertrand, E., Bettig, B., Blarel, F., 2004. Guidelines for the implementation of the H/V spectral ratio technique on ambient vibrations measurements, processing and interpretation.
- Aguirre, J., Irikura, K., 1997. Nonlinearity, liquefaction, and velocity variation of soft soil layers in Port Island, Kobe, during the Hyogo-ken Nanbu earthquake. *Bull. Seismol. Soc. Am.* 87, 1244–1258.
- Aki, K., 1993. Local site effects on weak and strong ground motion. *Tectonophysics, New horizons in strong motion: Seismic studies and engineering practice* 218, 93–111. [https://doi.org/10.1016/0040-1951\(93\)90262-I](https://doi.org/10.1016/0040-1951(93)90262-I)
- Aki, K., 1967. Scaling law of seismic spectrum. *J. Geophys. Res.* 72, 1217–1231.
- Aki, K., 1966. Generation and propagation of G waves from the Niigata Earthquake of June 16, 1964. Part 2. Estimation of earthquake movement, released energy, and stress-strain drop from the G wave spectrum. *Bull Earthq Res Inst* 44, 73–88.
- Alessandro, C.D., Boatwright, J., 2006. A Stochastic Estimate of Ground Motion at Oceano, California, for the M 6.5 22 December 2003 San Simeon Earthquake, Derived from Aftershock Recordings. *Bull. Seismol. Soc. Am.* 96, 1437–1447. <https://doi.org/10.1785/0120040183>
- Alfonso-Naya, V., Courboux, F., Bonilla, L., Ruiz, M., Vallée, M., Yépes, H., 2012. A large earthquake in Quito (Ecuador): Ground motion simulations and site effects. Presented at the 15th World Conf. on Earthquake Engineering.
- Allmann, B.P., Shearer, P.M., 2009. Global variations of stress drop for moderate to large earthquakes. *J. Geophys. Res. Solid Earth* 114. <https://doi.org/10.1029/2008JB005821>
- Anderson, J., Bodin, P., Brune, J., Prince, J., Singh, S., Quaas, R., Onate, M., 1986. Strong ground motion from the Michoacan, Mexico, earthquake. *Science* 233, 1043–1049.
- Aoi, S., Kunugi, T., Fujiwara, H., 2004. Strong-Motion seismograph network operated by NIED: K-NET AND KiK-net. *J. Jpn. Assoc. Earthq. Eng.* 4, 65–74. [https://doi.org/10.5610/jaee.4.3\\_65](https://doi.org/10.5610/jaee.4.3_65)
- Archuleta, R.J., Ji, C., 2016. Moment rate scaling for earthquakes  $3.3 \leq M \leq 5.3$  with implications for stress drop. *Geophys. Res. Lett.* 43, 12,004–12,011. <https://doi.org/10.1002/2016GL071433>
- Archuleta, R.J., Seale, S.H., Sangas, P.V., Baker, L.M., Swain, S.T., 1992. Garner Valley downhole array of accelerometers: Instrumentation and preliminary data analysis. *Bull. Seismol. Soc. Am.* 82, 1592–1621.
- Asano, K., Iwata, T., 2016. Source rupture processes of the foreshock and mainshock in the 2016 Kumamoto earthquake sequence estimated from the kinematic waveform inversion of strong motion data. *Earth Planets Space* 68, 147. <https://doi.org/10.1186/s40623-016-0519-9>

- ASTM, D., 2003. Standard test methods for the determination of the modulus and damping properties of soils using the cyclic triaxial apparatus.
- Atkinson, G.M., Mereu, R.F., 1992. The shape of ground motion attenuation curves in southeastern Canada. *Bull. Seismol. Soc. Am.* 82, 2014–2031.
- Beauval, C., Marinière, J., Laurendeau, A., Singaicho, J.-C., Viracucha, C., Vallée, M., Maufroy, E., Mercerat, D., Yepes, H., Ruiz, M., Alvarado, A., 2017. Comparison of Observed Ground-Motion Attenuation for the 16 April 2016 Mw 7.8 Ecuador Megathrust Earthquake and Its Two Largest Aftershocks with Existing Ground-Motion Prediction Equations. *Seismol. Res. Lett.* 88, 287–299. <https://doi.org/10.1785/0220160150>
- Beauval, C., Marinière, J., Yepes, H., Audin, L., Nocquet, J., Alvarado, A., Baize, S., Aguilar, J., Singaicho, J., Jomard, H., 2018. A New Seismic Hazard Model for Ecuador. *Bull. Seismol. Soc. Am.* 108, 1443–1464.
- Beauval, C., Yepes, H., Palacios, P., Segovia, M., Alvarado, A., Font, Y., Aguilar, J., Troncoso, L., Vaca, S., 2013. An earthquake catalog for seismic hazard assessment in Ecuador. *Bull. Seismol. Soc. Am.* 103, 773–786.
- Beresnev, I.A., Wen, K.-L., 1996. Nonlinear soil response—A reality? *Bull. Seismol. Soc. Am.* 86, 1964–1978.
- Beresnev, I.A., Wen, K.-L., Yeh, Y.T., 1994. Source, path and site effects on dominant frequency and spatial variation of strong ground motion recorded by smart1 and smart2 arrays in Taiwan. *Earthq. Eng. Struct. Dyn.* 23, 583–597. <https://doi.org/10.1002/eqe.4290230602>
- Bilek, S.L., Lay, T., 1999. Rigidity variations with depth along interplate megathrust faults in subduction zones. *Nature* 400, 443.
- Bletery, Q., Sladen, A., Delouis, B., Vallée, M., Nocquet, J., Rolland, L., Jiang, J., 2014. A detailed source model for the Mw9.0 Tohoku-Oki earthquake reconciling geodesy, seismology, and tsunami records. *J. Geophys. Res. Solid Earth* 119, 7636–7653.
- Bonilla, L., Ruiz, M., Yepes, H., 1992. Evaluation of seismic hazard in Ecuador. Presented at the Simposio Internacional sobre Prevención de Desastres Sísmicos= International Symposium on Earthquake Disaster Prevention, México. Centro Nacional de Prevención de Desastres (CENAPRED); Japón. Agencia de Cooperación Internacional (JICA); NU. Centro para el Desarrollo Regional (UNCRD), pp. 118–25.
- Bonilla, L.F., 2000. Computation of linear and nonlinear site response for near field ground motion. PhD Thesis.
- Bonilla, L.F., Archuleta, R.J., Lavallée, D., 2005. Hysteretic and Dilatant Behavior of Cohesionless Soils and Their Effects on Nonlinear Site Response: Field Data Observations and Modeling. *Bull. Seismol. Soc. Am.* 95, 2373–2395. <https://doi.org/10.1785/0120040128>
- Bonilla, L.F., Guéguen, P., Lopez-Caballero, F., Mercerat, E.D., Gélis, C., 2017. Prediction of nonlinear site response using downhole array data and numerical modeling: The Belleplaine (Guadeloupe) case study. *Phys. Chem. Earth Parts ABC, Advance in seismic site response: usual practices and innovative methods* 98, 107–118. <https://doi.org/10.1016/j.pce.2017.02.017>

Bonilla, L.F., Steidl, J.H., Gariel, J.-C., Archuleta, R.J., 2002. Borehole Response Studies at the Garner Valley Downhole Array, Southern California. *Bull. Seismol. Soc. Am.* 92, 3165–3179. <https://doi.org/10.1785/0120010235>

Bonilla, L.F., Steidl, J.H., Lindley, G.T., Tumarkin, A.G., Archuleta, R.J., 1997. Site amplification in the San Fernando Valley, California: variability of site-effect estimation using the S-wave, coda, and H/V methods. *Bull. Seismol. Soc. Am.* 87, 710–730.

Bonilla, L.F., Tsuda, K., Pulido, N., Régnier, J., Laurendeau, A., 2011. Nonlinear site response evidence of K-NET and KiK-net records from the 2011 off the Pacific coast of Tohoku Earthquake. *Earth Planets Space* 63, 50.

Bonnefoy-Claudet, S., Cotton, F., Bard, P.-Y., Cornou, C., Ohrnberger, M., Wathélet, M., 2006. Robustness of the H/V ratio peak frequency to estimate 1D resonance frequency. Presented at the Proceedings of the 3rd International Symposium on the Effects of Surface Geology on Seismic Motion, p. 10.

Boore, D.M., 2005. On Pads and Filters: Processing Strong-Motion Data. *Bull. Seismol. Soc. Am.* 95, 745–750. <https://doi.org/10.1785/0120040160>

Boore, D.M., 2003. Simulation of ground motion using the stochastic method. *Pure Appl. Geophys.* 160, 635–676.

Boore, D.M., Boatwright, J., 1984. Average body-wave radiation coefficients. *Bull. Seismol. Soc. Am.* 74, 1615–1621.

Borcherdt, R.D., 1970. Effects of local geology on ground motion near San Francisco Bay. *Bull. Seismol. Soc. Am.* 60, 29–61.

Brax, M., Causse, M., Bard, P.-Y., 2016. Ground motion prediction in Beirut: a multi-step procedure coupling empirical Green's functions, ground motion prediction equations and instrumental transfer functions. *Bull. Earthq. Eng.* 14, 3317–3341. <https://doi.org/10.1007/s10518-016-0004-7>

Brune, J., 1971. Correction (to Brune, 1970). *J Geophys Res* 76, 5002.

Brune, J.N., 1970. Tectonic stress and the spectra of seismic shear waves from earthquakes. *J. Geophys. Res.* 75, 4997–5009.

Bullen, K. E., Bullen, Keith Edward, Bolt, B.A., 1985. *An Introduction to the Theory of Seismology*. Cambridge University Press.

Cadet, H., Bard, P.-Y., Duval, A.-M., Bertrand, E., 2012a. Site effect assessment using KiK-net data: part 2—site amplification prediction equation based on  $f_0$  and  $V_{sz}$ . *Bull. Earthq. Eng.* 10, 451–489.

Cadet, H., Bard, P.-Y., Rodriguez-Marek, A., 2012b. Site effect assessment using KiK-net data: Part 1. A simple correction procedure for surface/downhole spectral ratios. *Bull. Earthq. Eng.* 10, 421–448. <https://doi.org/10.1007/s10518-011-9283-1>

Causse, M., Chaljub, E., Cotton, F., Cornou, C., Bard, P.-Y., 2009. New approach for coupling  $k-2$  and empirical Green's functions: application to the blind prediction of broad-band ground motion in the Grenoble basin. *Geophys. J. Int.* 179, 1627–1644.

- Cauzzi, C., Clinton, J., 2013. A High- and Low-Noise Model for High-Quality Strong-Motion Accelerometer Stations. *Earthq. Spectra* 29, 85–102. <https://doi.org/10.1193/1.4000107>
- Chabot, S., Glinsky, N., Mercerat, E.D., Bonilla Hidalgo, L.F., 2018. A high-order discontinuous Galerkin method for 1D wave propagation in a nonlinear heterogeneous medium. *J. Comput. Phys.* 355, 191–213. <https://doi.org/10.1016/j.jcp.2017.11.013>
- Chandra, J., Guéguen, P., Bonilla, L.F., 2016. PGA-PGV/Vs considered as a stress–strain proxy for predicting nonlinear soil response. *Soil Dyn. Earthq. Eng.* 85, 146–160. <https://doi.org/10.1016/j.soildyn.2016.03.020>
- Chandra, J., Guéguen, P., Steidl, J.H., Bonilla, L.F., 2015. In situ assessment of the  $G$ – $\gamma$  curve for characterizing the nonlinear response of soil: Application to the Garner Valley downhole array and the wildlife liquefaction array. *Bull. Seismol. Soc. Am.* 105, 993–1010.
- Chatelain, J.-L., Guillier, B., Yepes, H., Fernandez, J., Valverde, J., Tucker, B., Hoeffler, G., Kaneko, F., Souris, M., Dupérier, E., 1996. Projet pilote de scénario sismique à Quito (Équateur): méthode et résultats. *Bull IFEA* 25, 553–588.
- Chouet, B., Aki, K., Tsujiura, M., 1978. Regional variation of the scaling law of earthquake source spectra. *Bull. Seismol. Soc. Am.* 68, 49–79.
- Chounet, A., Vallée, M., Causse, M., Courboux, F., 2018. Global catalog of earthquake rupture velocities shows anticorrelation between stress drop and rupture velocity. *Tectonophysics* 733, 148–158.
- Cotton, F., Archuleta, R., Causse, M., 2013. What is Sigma of the Stress Drop? *Seismol. Res. Lett.* 84, 42–48. <https://doi.org/10.1785/0220120087>
- Courboux, F., 2010. Small earthquakes to understand and predict large ones (Habilitation à diriger des recherches). Université Nice Sophia Antipolis.
- Courboux, F., Vallée, M., Causse, M., Chounet, A., 2016. Stress-Drop Variability of Shallow Earthquakes Extracted from a Global Database of Source Time Functions. *Seismol. Res. Lett.* 87, 912–918. <https://doi.org/10.1785/0220150283>
- Cruz-Atienza, V., 2006. Rupture dynamique des faille non-planaires en différences finies. PhD Thesis Univ. Nice Sophia Fr.
- Darragh, R.B., Shakal, A.F., 1991. The site response of two rock and soil station pairs to strong and weak ground motion. *Bull. Seismol. Soc. Am.* 81, 1885–1899.
- Dikmen, Ü., 2009. Statistical correlations of shear wave velocity and penetration resistance for soils. *J. Geophys. Eng.* 6, 61.
- Dobry, R., Vucetic, M., 1987. Dynamic properties and seismic response of soft clay deposits.
- Dong, G., Papageorgiou, A.S., 2003. On a new class of kinematic models: symmetrical and asymmetrical circular and elliptical cracks. *Phys. Earth Planet. Inter., The quantitative prediction of strong-motion and the physics of earthquake sources* 137, 129–151. [https://doi.org/10.1016/S0031-9201\(03\)00012-8](https://doi.org/10.1016/S0031-9201(03)00012-8)
- Douglas, J., 2011. Ground-motion prediction equations 1964–2010. Pacific Earthquake Engineering Research Center Berkeley, CA.

Dufour, N., Payeur, J.-B., Bertrand, E., Mercerat, E.D., Régnier, J., Vancaenenbroeck, V., 2018. Installation of a borehole vertical array in the Var Valley, Nice, France. Presented at the 16th European Conference on Earthquake Engineering, Thessaloniki.

Dujardin, A., Causse, M., Courboux, F., Traversa, P., 2016a. Simulation of the basin effects in the Po Plain during the Emilia-Romagna seismic sequence (2012) using empirical Green's functions. *Pure Appl. Geophys.* 173, 1993–2010.

Dujardin, A., Courboux, F., Causse, M., Traversa, P., 2016b. Influence of Source, Path, and Site Effects on the Magnitude Dependence of Ground-Motion Decay with Distance. *Seismol. Res. Lett.* 87, 138–148. <https://doi.org/10.1785/0220150185>

Duncan, J., Chang, C., 1970. Nonlinear analysis of stress and strain in soils. *ASCE J Soil Mech Found* 96, 1629–1653.

Duval, A., Bard, P.-Y., Lebrun, B., Lacave-Lache, C., Riepl, J., Hatzfeld, D., 2001. H/v technique for site response analysis. Synthesis of data from various surveys. *Boll. Geofis. Teor. Ed Appl.* 42, 267–280.

Earle, P.S., Shearer, P.M., 1994. Characterization of global seismograms using an automatic-picking algorithm. *Bull. Seismol. Soc. Am.* 84, 366–376.

Eshelby, J.D., 1957. The determination of the elastic field of an ellipsoidal inclusion, and related problems. *Proc R Soc Lond A* 241, 376–396.

Field, E.H., Jacob, K.H., 1995. A comparison and test of various site-response estimation techniques, including three that are not reference-site dependent. *Bull. Seismol. Soc. Am.* 85, 1127–1143.

Field, E.H., Johnson, P.A., Beresnev, I.A., Zeng, Y., 1997. Nonlinear ground-motion amplification by sediments during the 1994 Northridge earthquake. *Nature* 390, 599–602. <https://doi.org/10.1038/37586>

Finn, L., D, W., Lee, K.W., Martin, G.R., 1977. An effective stress model for liquefaction. *Electron. Lett.* 103.

Fleur, S.S., Bertrand, E., Courboux, F., Lépinay, B.M. de, Deschamps, A., Hough, S., Cultrera, G., Boisson, D., Prépetit, C., 2016. Site Effects in Port-au-Prince (Haiti) from the Analysis of Spectral Ratio and Numerical Simulations. *Bull. Seismol. Soc. Am.* <https://doi.org/10.1785/0120150238>

Fourier, J., 1822. *Theorie analytique de la chaleur*, par M. Fourier. Chez Firmin Didot, père et fils.

Frankel, A., 1995. Simulating strong motions of large earthquakes using recordings of small earthquakes: the Loma Prieta mainshock as a test case. *Bull. Seismol. Soc. Am.* 85, 1144–1160.

Gatti, F., Carvalho Paludo, L.D., Svay, A., Lopez-Caballero, F.-, Cottureau, R., Clouteau, D., 2017. Investigation of the earthquake ground motion coherence in heterogeneous non-linear soil deposits. *Procedia Eng., X International Conference on Structural Dynamics, EURODDYN 2017* 199, 2354–2359. <https://doi.org/10.1016/j.proeng.2017.09.232>

Ghayoomi Majid, Suprunenko Ganna, Mirshekari Morteza, 2017. Cyclic Triaxial Test to Measure Strain-Dependent Shear Modulus of Unsaturated Sand. *Int. J. Geomech.* 17, 04017043. [https://doi.org/10.1061/\(ASCE\)GM.1943-5622.0000917](https://doi.org/10.1061/(ASCE)GM.1943-5622.0000917)

- Glaser, S., Baise, L., 2000. System identification estimation of soil properties at the Lotung site - ScienceDirect. *Soil Dyn. Earthq. Eng.* 19, 521–531. [https://doi.org/10.1016/S0267-7261\(00\)00026-9](https://doi.org/10.1016/S0267-7261(00)00026-9)
- Godano, M., Bernard, P., Dublanchet, P., 2015. Bayesian inversion of seismic spectral ratio for source scaling: Application to a persistent multiplet in the western Corinth rift. *J. Geophys. Res. Solid Earth* 120, 2015JB012217. <https://doi.org/10.1002/2015JB012217>
- Goodfellow, I., Bengio, Y., Courville, A., Bengio, Y., 2016. *Deep learning*. MIT press Cambridge.
- Goto, H., Hata, Y., Yoshimi, M., Yoshida, N., 2017. Nonlinear Site Response at KiK-net KMMH16 (Mashiki) and Heavily Damaged Sites during the 2016 Mw 7.1 Kumamoto Earthquake, Japan Nonlinear Site Response at KiK-net KMMH16 (Mashiki) and Heavily Damaged Sites. *Bull. Seismol. Soc. Am.* 107, 1802–1816. <https://doi.org/10.1785/0120160312>
- Green, G., 1828. *An essay on the application of mathematical analysis to the theories of electricity and magnetism*. Wezäta-Melins Aktiebolag.
- Guéguen, P., Chatelain, J.-L., Guillier, B., Yepes, H., 2000. An indication of the soil topmost layer response in Quito (Ecuador) using noise H/V spectral ratio. *Soil Dyn. Earthq. Eng.* 19, 127–133.
- Gueguen, P., Langlais, M., Foray, P., Rousseau, C., Maury, J., 2011. A Natural Seismic Isolating System: The Buried Mangrove Effects. *Bull. Seismol. Soc. Am.* 101, 1073–1080. <https://doi.org/10.1785/0120100129>
- Hanks, T.C., 1977. Earthquake stress drops, ambient tectonic stresses and stresses that drive plate motions, in: *Stress in the Earth*. Springer, pp. 441–458.
- Hanks, T.C., Kanamori, H., 1979. A moment magnitude scale. *J. Geophys. Res. Solid Earth* 84, 2348–2350. <https://doi.org/10.1029/JB084iB05p02348>
- Hardin, B.O., Blandford, G.E., 1989. Elasticity of Particulate Materials. *J. Geotech. Eng.* 115, 788–805. [https://doi.org/10.1061/\(ASCE\)0733-9410\(1989\)115:6\(788\)](https://doi.org/10.1061/(ASCE)0733-9410(1989)115:6(788))
- Hartzell, S.H., 1978. Earthquake aftershocks as Green's functions. *Geophys. Res. Lett.* 5, 1–4.
- Haskell, N.A., 1964. Total energy and energy spectral density of elastic wave radiation from propagating faults. *Bull. Seismol. Soc. Am.* 54, 1811–1841.
- Honoré, L., Courboux, F., Souriau, A., 2011. Ground motion simulations of a major historical earthquake (1660) in the French Pyrenees using recent moderate size earthquakes. *Geophys. J. Int.* 187, 1001–1018.
- Honoré-Foundotos, L., 2013. *Generation of broadband synthetic accelerograms : contribution to seismic hazard assessment by validation of blind approaches (Theses)*. Université Nice Sophia Antipolis.
- Hujeux, J., 1985. Une loi de comportement pour le chargement cyclique des sols. *Génie Parasismique* 287–302.
- Idriss, I., 2011. Use of Vs30 to represent local site conditions. Presented at the Proceedings of the 4th IASPEI/IAEE international symposium. Effects of source geology on seismic motion, August, pp. 23–26.

- Idriss, I.M., Seed, H.B., 1968. An analysis of ground motions during the 1957 San Francisco earthquake. *Bull. Seismol. Soc. Am.* 58, 2013–2032.
- Irikura, K., 1986. Prediction of strong acceleration motion using empirical Green's function. Presented at the Proc. 7th Japan Earthq. Eng. Symp, pp. 151–156.
- IRIS, 2011. How Often Do Earthquakes Occur?- Incorporated Research Institutions for Seismology [WWW Document]. Often Earthq. Occur. URL [https://www.iris.edu/hq/inclass/factsheet/how\\_often\\_do\\_earthquakes\\_occur](https://www.iris.edu/hq/inclass/factsheet/how_often_do_earthquakes_occur) (accessed 10.1.18).
- Ishibashi, I., Zhang, X., 1993. Unified dynamic shear moduli and damping ratios of sand and clay. *SOILS Found.* 33, 182–191. <https://doi.org/10.3208/sandf1972.33.182>
- Ishihara, K., 1996. *Soil Behaviour in Earthquake Geotechnics*. Clarenton Press, Oxford.
- Iwan, W.D., 1967. On a Class of Models for the Yielding Behavior of Continuous and Composite Systems. *J. Appl. Mech.* 34, 612–617. <https://doi.org/10.1115/1.3607751>
- Iwasaki, T., Tatsuoka, F., Takagi, Y., 1978. Shear moduli of sands under cyclic torsional shear loading. *Soils Found.* 18, 39–56.
- Joyner, W.B., Boore, D.M., 1986. On Simulating Large Earthquakes by Green's–Function Addition of Smaller Earthquakes. *Earthq. Source Mech.* 269–274.
- Kaklamanos, J., Bradley, B.A., Thompson, E.M., Baise, L.G., 2013. Critical Parameters Affecting Bias and Variability in Site-Response Analyses Using KiK-net Downhole Array Data Critical Parameters Affecting Bias and Variability in Site-Response Analyses. *Bull. Seismol. Soc. Am.* 103, 1733–1749. <https://doi.org/10.1785/0120120166>
- Kanamori, H., 1977. The energy release in great earthquakes. *J. Geophys. Res.* 82, 2981–2987. <https://doi.org/10.1029/JB082i020p02981>
- Kanamori, H., Anderson, D.L., 1975. Theoretical basis of some empirical relations in seismology. *Bull. Seismol. Soc. Am.* 65, 1073–1095.
- Kanamori, H., McNally, K.C., 1982. Variable rupture mode of the subduction zone along the Ecuador-Colombia coast. *Bull. Seismol. Soc. Am.* 72, 1241–1253.
- Kanamori, H., Rivera, L., 2008. Source inversion of Wphase: speeding up seismic tsunami warning. *Geophys. J. Int.* 175, 222–238.
- Kaneko, Y., Shearer, P.M., 2014. Seismic source spectra and estimated stress drop derived from cohesive-zone models of circular subshear rupture. *Geophys. J. Int.* 197, 1002–1015. <https://doi.org/10.1093/gji/ggu030>
- Kelleher, J.A., 1972. Rupture zones of large South American earthquakes and some predictions. *J. Geophys. Res.* 77, 2087–2103. <https://doi.org/10.1029/JB077i011p02087>
- Kikuchi, M., Kanamori, H., 1991. Inversion of complex body waves—III. *Bull. Seismol. Soc. Am.* 81, 2335–2350.
- Kishida, T., Stewart, J.P., Graves, R.W., Midorikawa, S., Miura, H., Bozorgnia, Y., Campbell, K.W., 2013. Comparison of ground motion attributes from 2011 Tohoku-oki mainshock and two subsequent events 10, 1–7.
- Knopoff, L., 1958. Energy release in earthquakes. *Geophys. J. Int.* 1, 44–52.

- Kohrs-Sansorny, C., Courboux, F., Bour, M., Deschamps, A., 2005. A Two-Stage Method for Ground-Motion Simulation Using Stochastic Summation of Small Earthquakes. *Bull. Seismol. Soc. Am.* 95, 1387–1400. <https://doi.org/10.1785/0120040211>
- Kokusho, T., 1980. Cyclic triaxial test of dynamic soil properties for wide strain range. *SOILS Found.* 20, 45–60. [https://doi.org/10.3208/sandf1972.20.2\\_45](https://doi.org/10.3208/sandf1972.20.2_45)
- Koller, M., Chatelain, J., Guiller, B., Duval, A., Atakan, K., Lacave, C., Bard, P., SESAME participants, 2004. Practical user guideline and software for the implementation of the H/V ratio technique on ambient vibrations: Measuring conditions, processing method and results interpretation. *Earthq. Eng. Vanc. BC Can.* 1–6 Aug Pap.
- Kondner, R.L., 1963. A hyperbolic stress-strain formulation for sands. Presented at the Proc. 2nd Pan Am. Conf. on Soil Mech. and Found. Eng., Brazil, 1963, pp. 289–324.
- Konno, K., Ohmachi, T., 1998. Ground-motion characteristics estimated from spectral ratio between horizontal and vertical components of microtremor. *Bull. Seismol. Soc. Am.* 88, 228–241.
- Kramer, L., 1996. *Geotechnical earthquake engineering*. Prentice-Hall International Series.
- Kramer, S.L., 1996. Appendix B.6: Damping, in: *Geotechnical Earthquake Engineering*. Prentice-Hall, New Jersey.
- Ktenidou, O., Cotton, F., Abrahamson, N.A., Anderson, J.G., 2014. Taxonomy of  $\kappa$ : A review of definitions and estimation approaches targeted to applications. *Seismol. Res. Lett.* 85, 135–146.
- Ktenidou, O.-J., Roumelioti, Z., Abrahamson, N., Cotton, F., Pitilakis, K., Hollender, F., 2018. Understanding single-station ground motion variability and uncertainty ( $\sigma$ ): lessons learnt from EUROSEISTEST. *Bull. Earthq. Eng.* 16, 2311–2336. <https://doi.org/10.1007/s10518-017-0098-6>
- Kuo, C.-H., Wen, K.-L., Lin, C.-M., Hsiao, N.-C., Chen, D.-Y., 2018. Site amplifications and the effect on local magnitude determination at stations of the surface–downhole network in Taiwan. *Soil Dyn. Earthq. Eng.* 104, 106–116. <https://doi.org/10.1016/j.soildyn.2017.10.003>
- Kurahashi, S., Irikura, K., 2011. Source model for generating strong ground motions during the 2011 off the Pacific coast of Tohoku Earthquake. *Earth Planets Space* 63, 11.
- Kurtulus, C., Sertcelik, F., Canbay, M.M., Sertcelik, I., 2010. Estimation of Atterberg limits and bulk mass density of an expansive soil from P-wave velocity measurements. *Bull. Eng. Geol. Environ.* 69, 153–154.
- Langston, C.A., 1979. Structure under Mount Rainier, Washington, inferred from teleseismic body waves. *J. Geophys. Res. Solid Earth* 84, 4749–4762. <https://doi.org/10.1029/JB084iB09p04749>
- Laurendeau, A., Courboux, F., Bonilla, L.F., Alvarado, A., Naya, V.A., Guéguen, P., Mercerat, E.D., Singaicho, J.C., Bertrand, E., Perrault, M., Barros, J.G., Ruiz, M., 2017. Low-Frequency Seismic Amplification in the Quito Basin (Ecuador) Revealed by Accelerometric Recordings of the RENAC Network. *Bull. Seismol. Soc. Am.* 107, 2917–2926. <https://doi.org/10.1785/0120170134>

Lavallee, D., Bonilla, L., Archuleta, R., 2003. Hysteresis model for nonlinear soil under irregular cyclic loadings: introducing the generalized Masing rules. *J Geotech Geoenviron Eng.*

LeBrun, B., Hatzfeld, D., Bard, P.Y., 2001. Site Effect Study in Urban Area: Experimental Results in Grenoble (France). *Pure Appl. Geophys.* 158, 2543–2557. <https://doi.org/10.1007/PL00001185>

Lermo, J., Chávez-García, F.J., 1993. Site effect evaluation using spectral ratios with only one station. *Bull. Seismol. Soc. Am.* 83, 1574–1594.

Lopez-Caballero, F., Modaressi-Farahmand-Razavi, A., 2010. Assessment of variability and uncertainties effects on the seismic response of a liquefiable soil profile. *Soil Dyn. Earthq. Eng.* 30, 600–613. <https://doi.org/10.1016/j.soildyn.2010.02.002>

Lopez-Caballero, F., Modaressi-Farahmand-Razavi, A., Modaressi, H., 2007. Nonlinear numerical method for earthquake site response analysis I — elastoplastic cyclic model and parameter identification strategy. *Bull. Earthq. Eng.* 5, 303–323. <https://doi.org/10.1007/s10518-007-9032-7>

Lussou, P., Bard, P.-Y., Modaressi, H., Gariel, J.-C., 2000. Quantification of soil non-linearity based on simulation. *Soil Dyn. Earthq. Eng.* 20, 509–516. [https://doi.org/10.1016/S0267-7261\(00\)00100-7](https://doi.org/10.1016/S0267-7261(00)00100-7)

Luzi, L., Puglia, R., Pacor, F., Gallipoli, M.R., Bindi, D., Mucciarelli, M., 2011. Proposal for a soil classification based on parameters alternative or complementary to  $V_s$ ,30. *Bull. Earthq. Eng.* 9, 1877–1898. <https://doi.org/10.1007/s10518-011-9274-2>

Madariaga, R., 1976. Dynamics of an expanding circular fault. *Bull. Seismol. Soc. Am.* 66, 639–666.

Masing, G., 1926. Eigenspannumyen und verfeshungung beim messing. Presented at the Proc. Inter. Congress for Applied Mechanics, pp. 332–335.

Maufroy, E., Chaljub, E., Hollender, F., Bard, P.-Y., Kristek, J., Moczo, P., De Martin, F., Theodoulidis, N., Manakou, M., Guyonnet-Benaize, C., 2016. 3D numerical simulation and ground motion prediction: Verification, validation and beyond—Lessons from the E2VP project. *Soil Dyn. Earthq. Eng.* 91, 53–71.

Maufroy, E., Cruz-Atienza, V.M., Cotton, F., Gaffet, S., 2015. Frequency-Scaled Curvature as a Proxy for Topographic Site-Effect Amplification and Ground-Motion Variability Frequency-Scaled Curvature as a Proxy for Topographic Amplification. *Bull. Seismol. Soc. Am.* 105, 354–367. <https://doi.org/10.1785/0120140089>

Mellal, A., 1997. Analyse des effets du comportement non linéaire des sols sur le mouvement sismique.

Mellal, A., Modaressi, H., 1998. A simplified numerical approach for nonlinear dynamic analysis of multilayered media. Presented at the 11th European Conf. on Earthquake Eng.

Menq, F., 2003. Dynamic properties of sandy and gravelly soils.

Modaressi, H., Foerster, E., 2000. CyberQuake. User's Man. BRGM Fr.

- Mogami, T., Kubo, K., 1953. The behavior of soil during vibration procedure. Presented at the Proceedings of the 3rd International Conference on Soil Mechanical and Foundation. Zurich:[sn], pp. 152–153.
- Montalva, G.A., Bastías, N., Rodriguez-Marek, A., 2017. Ground-motion prediction equation for the Chilean subduction zone. *Bull. Seismol. Soc. Am.* 107, 901–911.
- Montoya Noguera, S., 2016. Evaluation et réduction des risques sismiques liés à la liquéfaction : modélisation numérique de leurs effets dans l'ISS. Paris Saclay.
- Montoya-Noguera, S., Lopez-Caballero, F., 2018. Modeling added spatial variability due to soil improvement: Coupling FEM with binary random fields for seismic risk analysis. *Soil Dyn. Earthq. Eng.* 104, 174–185.
- Nakata, N., Snieder, R., 2012. Estimating near-surface shear wave velocities in Japan by applying seismic interferometry to KiK-net data. *J. Geophys. Res. Solid Earth* 117. <https://doi.org/10.1029/2011JB008595>
- Nocquet, J.-M., Jarrin, P., Vallée, M., Mothes, P.A., Grandin, R., Rolandone, F., Delouis, B., Yepes, H., Font, Y., Fuentes, D., Régnier, M., Laurendeau, A., Cisneros, D., Hernandez, S., Sladen, A., Singaicho, J.-C., Mora, H., Gomez, J., Montes, L., Charvis, P., 2017. Supercycle at the Ecuadorian subduction zone revealed after the 2016 Pedernales earthquake. *Nat. Geosci.* 10, 145–149. <https://doi.org/10.1038/ngeo2864>
- Nogoshi, M., Igarashi, T., 1971. On the amplitude characteristics of microtremor, Part II. *J. Seismol. Soc. Jpn.* 24, 26–40.
- Noguchi, S., Sasatani, T., 2008. Quantification of degree of nonlinear site response. Presented at the 14th world conference on earthquake engineering, Beijing, Paper, p. 0049.
- Okada, Y., Kasahara, K., Hori, S., Obara, K., Sekiguchi, S., Fujiwara, H., Yamamoto, A., 2004. Recent progress of seismic observation networks in Japan —Hi-net, F-net, K-NET and KiK-net—. *Earth Planets Space* 56, xv–xxviii. <https://doi.org/10.1186/BF03353076>
- Ordaz, M., Arboleda, J., Singh, S.K., 1995. A scheme of random summation of an empirical Green's function to estimate ground motions from future large earthquakes. *Bull. Seismol. Soc. Am.* 85, 1635–1647.
- Oth, A., Bindi, D., Parolai, S., Giacomo, D.D., 2010. Earthquake scaling characteristics and the scale-(in)dependence of seismic energy-to-moment ratio: Insights from KiK-net data in Japan. *Geophys. Res. Lett.* 37. <https://doi.org/10.1029/2010GL044572>
- Oth, A., Parolai, S., Bindi, D., 2011. Spectral Analysis of K-NET and KiK-net Data in Japan, Part I: Database Compilation and Peculiarities. *Bull. Seismol. Soc. Am.* 101, 652–666. <https://doi.org/10.1785/0120100134>
- Pavlenko, O.V., Irikura, K., 2003. Estimation of Nonlinear Time-dependent Soil Behavior in Strong Ground Motion Based on Vertical Array Data. *Pure Appl. Geophys.* 160, 2365–2379. <https://doi.org/10.1007/s00024-003-2398-9>
- Péquegnat, C., Guéguen, P., Hatzfeld, D., Langlais, M., 2008. The French accelerometric network (RAP) and national data centre (RAP-NDC). *Seismol. Res. Lett.* 79, 79–89.

Pyke, R.M., 1979. NONLINEAR SOIL MODELS FOR IRREGULAR CYCLIC LOADINGS. *J. Geotech. Geoenvironmental Eng.* 105.

Régnier, J., Bonilla, L.-F., Bard, P.-Y., Bertrand, E., Hollender, F., Kawase, H., Sicilia, D., Arduino, P., Amorosi, A., Asimaki, D., Boldini, D., Chen, L., Chiaradonna, A., DeMartin, F., Ebrille, M., Elgamal, A., Falcone, G., Foerster, E., Foti, S., Garini, E., Gazetas, G., Gélis, C., Ghofrani, A., Giannakou, A., Gingery, J.R., Glinsky, N., Harmon, J., Hashash, Y., Iai, S., Jeremić, B., Kramer, S., Kontoe, S., Kristek, J., Lanzo, G., Lernia, A. di, Lopez-Caballero, F., Marot, M., McAllister, G., Mercerat, E.D., Moczo, P., Montoya-Noguera, S., Musgrove, M., Nieto-Ferro, A., Pagliaroli, A., Pisanò, F., Richterova, A., Sajana, S., d'Avila, M.P.S., Shi, J., Silvestri, F., Taiebat, M., Tropeano, G., Verrucci, L., Watanabe, K., 2016a. International Benchmark on Numerical Simulations for 1D, Nonlinear Site Response (PRENOLIN): Verification Phase Based on Canonical Cases. *Bull. Seismol. Soc. Am.* 106, 2112–2135. <https://doi.org/10.1785/0120150284>

Régnier, J., Bonilla, L.-F., Bard, P.-Y., Bertrand, E., Hollender, F., Kawase, H., Sicilia, D., Arduino, P., Amorosi, A., Asimaki, D., Boldini, D., Chen, L., Chiaradonna, A., DeMartin, F., Elgamal, A., Falcone, G., Foerster, E., Foti, S., Garini, E., Gazetas, G., Gélis, C., Ghofrani, A., Giannakou, A., Gingery, J., Glinsky, N., Harmon, J., Hashash, Y., Iai, S., Kramer, S., Kontoe, S., Kristek, J., Lanzo, G., Lernia, A. di, Lopez-Caballero, F., Marot, M., McAllister, G., Mercerat, E.D., Moczo, P., Montoya-Noguera, S., Musgrove, M., Nieto-Ferro, A., Pagliaroli, A., Passeri, F., Richterova, A., Sajana, S., d'Avila, M.P.S., Shi, J., Silvestri, F., Taiebat, M., Tropeano, G., Vandeputte, D., Verrucci, L., 2018. PRENOLIN: International Benchmark on 1D Nonlinear Site-Response Analysis—Validation Phase Exercise. *Bull. Seismol. Soc. Am.* 108, 876–900. <https://doi.org/10.1785/0120170210>

Régnier, J., Bonilla, L.F., Bertrand, E., Semblat, J.-F., 2014. Influence of the VS Profiles beyond 30 m Depth on Linear Site Effects: Assessment from the KiK-net Data. *Bull. Seismol. Soc. Am.* 104, 2337–2348. <https://doi.org/10.1785/0120140018>

Régnier, J., Cadet, H., Bard, P.-Y., 2016b. Empirical Quantification of the Impact of Nonlinear Soil Behavior on Site Response. *Bull. Seismol. Soc. Am.* 106, 1710–1719. <https://doi.org/10.1785/0120150199>

Régnier, J., Cadet, H., Bonilla, L.F., Bertrand, E., Semblat, J.-F., 2013. Assessing Nonlinear Behavior of Soils in Seismic Site Response: Statistical Analysis on KiK-net Strong-Motion Data. *Bull. Seismol. Soc. Am.* 103, 1750–1770. <https://doi.org/10.1785/0120120240>

Robinson, E., 1967. Predictive decomposition of time series with application to seismic exploration. *GEOPHYSICS* 32, 418–484. <https://doi.org/10.1190/1.1439873>

Robinson, E., 1957. Predictive decomposition of seismic traces. *GEOPHYSICS* 22, 767–778. <https://doi.org/10.1190/1.1438415>

Roscoe, K.H., Schofield, A.N., Thurairajah, A., 1963. Yielding of Clays in States Wetter than Critical. *Géotechnique* 13, 211–240. <https://doi.org/10.1680/geot.1963.13.3.211>

Roumelioti, Z., Hollender, F., Gueguen, P., 2018. Shear wave velocity variations at the Corssa (Central Greece) vertical array. Presented at the 16th European conference in earthquake engineering, Thessaloniki, Greece.

- Salichon, J., Kohrs-Sansornny, C., Bertrand, E., Courboux, F., 2010. A Mw 6.3 earthquake scenario in the city of Nice (southeast France): ground motion simulations. *J. Seismol.* 14, 523–541.
- Satoh, T., 2002. Empirical Frequency-Dependent Radiation Pattern of the 1998 Miyagiken-Nanbu Earthquake in Japan. *Bull. Seismol. Soc. Am.* 92, 1032–1039. <https://doi.org/10.1785/0120010153>
- Sawazaki, K., Sato, H., Nakahara, H., Nishimura, T., 2009. Time-lapse changes of seismic velocity in the shallow ground caused by strong ground motion shock of the 2000 Western-Tottori earthquake, Japan, as revealed from coda deconvolution analysis. *Bull. Seismol. Soc. Am.* 99, 352–366.
- Sawazaki, K., Sato, H., Nakahara, H., Nishimura, T., 2006. Temporal change in site response caused by earthquake strong motion as revealed from coda spectral ratio measurement. *Geophys. Res. Lett.* 33. <https://doi.org/10.1029/2006GL027938>
- Schnabel, P.B., 1972. SHAKE: A computer program for earthquake response analysis of horizontally layered sites. EERC Rep. 72-12 Univ. Calif. Berkeley.
- Scholz, C.H., 1982. Scaling laws for large earthquakes: consequences for physical models. *Bull. Seismol. Soc. Am.* 72, 1–14.
- Seed, H.B., Idriss, I.M., 1971. Simplified procedure for evaluating soil liquefaction potential. *J. Soil Mech. Found. Div.*
- Seed, H.B., Idriss, I.M., 1970. Soil moduli and damping factors for dynamic response analyses.
- Seed, H.B., Wong, R.T., Idriss, I., Tokimatsu, K., 1986. Moduli and damping factors for dynamic analyses of cohesionless soils. *J. Geotech. Eng.* 112, 1016–1032.
- Shearer, P.M., Orcutt, J.A., 1987. Surface and near-surface effects on seismic waves—theory and borehole seismometer results. *Bull. Seismol. Soc. Am.* 77, 1168–1196.
- Shearer, P.M., Prieto, G.A., Hauksson, E., 2006. Comprehensive analysis of earthquake source spectra in southern California. *J. Geophys. Res. Solid Earth* 111. <https://doi.org/10.1029/2005JB003979>
- Singh, S., Mena, E. a, Castro, R., 1988. Some aspects of source characteristics of the 19 September 1985 Michoacan earthquake and ground motion amplification in and near Mexico City from strong motion data. *Bull. Seismol. Soc. Am.* 78, 451–477.
- Sjögreen, B., Petersson, N., 2011. A Fourth Order Accurate Finite Difference Scheme for the Elastic Wave Equation in Second Order Formulation. *J. Sci. Comput.* 52, 1–32. <https://doi.org/10.1007/s10915-011-9531-1>
- Steidl, J.H., Tumarkin, A.G., Archuleta, R.J., 1996. What is a reference site? *Bull. Seismol. Soc. Am.* 86, 1733–1748.
- Theodoulidis, N., Hollender, F., Mariscal, A., Moiriat, D., Bard, P., Konidakis, A., Cushing, M., Konstantinidou, K., Roumelioti, Z., 2018. The ARGONET (Greece) seismic observatory: An accelerometric vertical array and its data. *Seismol. Res. Lett.* 89, 1555–1565.

- Thompson, E.M., Baise, L.G., Kayen, R.E., Guzina, B.B., 2009. Impediments to Predicting Site Response: Seismic Property Estimation and Modeling Simplifications. *Bull. Seismol. Soc. Am.* 99, 2927–2949. <https://doi.org/10.1785/0120080224>
- Tonni, L., Simonini, P., 2013. Shear wave velocity as function of cone penetration test measurements in sand and silt mixtures. *Eng. Geol.* 163, 55–67. <https://doi.org/10.1016/j.enggeo.2013.06.005>
- TRX Consulting CA, 2011. Estudio de Caracterización de Ruta con Métodos Geofísicos no Invasivos.
- Vacareanu, R., Radulian, M., Iancovici, M., Pavel, F., Neagu, C., 2015. Fore-Arc and Back-Arc Ground Motion Prediction Model for Vrancea Intermediate Depth Seismic Source. *J. Earthq. Eng.* 19, 535–562. <https://doi.org/10.1080/13632469.2014.990653>
- Vallée, M., Charléty, J., Ferreira, A.M.G., Delouis, B., Vergoz, J., 2011. SCARDEC: a new technique for the rapid determination of seismic moment magnitude, focal mechanism and source time functions for large earthquakes using body-wave deconvolution. *Geophys. J. Int.* 184, 338–358. <https://doi.org/10.1111/j.1365-246X.2010.04836.x>
- Vallée, M., Douet, V., 2016. A new database of source time functions (STFs) extracted from the SCARDEC method. *Phys. Earth Planet. Inter.* 257, 149–157.
- Vucetic, M., Dobry, R., 1991. Effect of Soil Plasticity on Cyclic Response. *J. Geotech. Eng.* 117, 89–107. [https://doi.org/10.1061/\(ASCE\)0733-9410\(1991\)117:1\(89\)](https://doi.org/10.1061/(ASCE)0733-9410(1991)117:1(89))
- Vvedenskaya, A., 1956. The determination of displacement fields by means of dislocation theory. *Izv. Akad. Nauk SSSR* 227–284.
- Weiler, W.A., 1988. Small strain shear modulus of clay. *Earthq. Eng. Soil Dyn. Recent Adv. Ground-Motion Eval.* 331–345.
- Wen, K.-L., Chang, T.-M., Lin, C.-M., Chiang, H.-J., 2006. Identification of nonlinear site response using the H/V spectral ratio method. *Terr. Atmospheric Ocean. Sci.* 17, 533.
- Wennerberg, L., 1990. Stochastic summation of empirical Green's functions. *Bull. Seismol. Soc. Am.* 80, 1418–1432.
- Winkler, K.W., Plona, T.J., 1982. Technique for measuring ultrasonic velocity and attenuation spectra in rocks under pressure. *J. Geophys. Res. Solid Earth* 87, 10776–10780. <https://doi.org/10.1029/JB087iB13p10776>
- Yagi, Y., Fukahata, Y., 2011. Rupture process of the 2011 Tohoku-oki earthquake and absolute elastic strain release. *Geophys. Res. Lett.* 38. <https://doi.org/10.1029/2011GL048701>
- Yagi, Y., Okuwaki, R., Enescu, B., Kasahara, A., Miyakawa, A., Otsubo, M., 2016. Rupture process of the 2016 Kumamoto earthquake in relation to the thermal structure around Aso volcano. *Earth Planets Space* 68, 118. <https://doi.org/10.1186/s40623-016-0492-3>
- Yepes, H., Audin, L., Alvarado, A., Beauval, C., Aguilar, J., Font, Y., Cotton, F., 2016. A new view for the geodynamics of Ecuador: Implication in seismogenic source definition and seismic hazard assessment. *Tectonics* 35, 1249–1279.
- Zeghal, M., Elgamal, A., 1994. Analysis of Site Liquefaction Using Earthquake Records. *J. Geotech. Eng.* 120, 996–1017. [https://doi.org/10.1061/\(ASCE\)0733-9410\(1994\)120:6\(996\)](https://doi.org/10.1061/(ASCE)0733-9410(1994)120:6(996))

Zeghal, M., Elgamal, A., Tang, H., 1995. Lotung Downhole Array. II: Evaluation of Soil Nonlinear Properties | Journal of Geotechnical Engineering | Vol 121, No 4. J. Geotech. Eng. 121. [https://doi.org/10.1061/\(ASCE\)0733-9410\(1995\)121:4\(363\)](https://doi.org/10.1061/(ASCE)0733-9410(1995)121:4(363))

Zekkos, D., Athanasopoulos-Zekkos, A., Hubler, J., Fei, X., Zehtab, K.H., Marr, W.A., 2018. Development of a Large-Size Cyclic Direct Simple Shear Device for Characterization of Ground Materials with Oversized Particles. Geotech. Test. J. 41, 263–279. <https://doi.org/10.1520/GTJ20160271>

Zhao, J.X., Zhang, J., Asano, A., Ohno, Y., Oouchi, T., Takahashi, T., Ogawa, H., Irikura, K., Thio, H.K., Somerville, P.G., 2006. Attenuation relations of strong ground motion in Japan using site classification based on predominant period. Bull. Seismol. Soc. Am. 96, 898–913.

## Annex A. Derivation of the equation for 1D wave in a viscoelastic media

### Linear elastic soil with damping lying on a rigid rock

All the realistic soils present an important property that dissipates energy. This dissipation of energy is associated with the pore water viscosity, interparticle friction, and particles rearrangement. This phenomenon is introduced into the strain-stress relationship, making the response stress of the material proportional to the rate of strain. An element with only this characteristic is known as a damper. A damper together to the spring, for who the stress is proportional to the strain and dominated by the Hooke's law (Eq. (I-2)), build configurations that model the stress-strain relationship, also call constitutive model.

In seismology is widely used the configuration of Voigt-Kelvin. A material with this constitutive model has a short memory damping, with reversible strains. In this constitutive model the stress that a material produces facing an imposed strain, is dominated by the strain amplitude and the rate that this strain is applied (Eq. (I-14)).

$$\tau = G \frac{\partial u}{\partial z} + \eta \frac{\partial \left( \frac{\partial u}{\partial z} \right)}{\partial t} \quad (\text{A-1})$$

Where  $\eta$  and  $G$  represent the viscosity and stiffness of the material. The strain is the derivate of the displacement with respect  $z$  ( $\partial u / \partial z$ ). This model can't be used to model permanent strains since it tends to zero after the load is gone. Another limitation is that in this case the failure of the material never would occur.

Introducing the constitutive model of Voigt-Kelvin (Eq. (I-14)) instead of the Hooke's law (Eq. (I-2)) in the motion equation (Eq. (I-1)), a new solution can be founded, with a new differential equation that domain the problem:

$$\rho \frac{\partial^2 u}{\partial t^2} = G \frac{\partial^2 u}{\partial z^2} + \eta \frac{\partial^3 u}{\partial z^2 \partial t} \quad (\text{A-2})$$

The Eq. (I-15) is a linear partial differential equation, it implies that like the previous case, this problem can be solved through a transfer function.

For computing the transfer function, first we use the general function for the solution of the Eq. (I-15):

$$u(z, t) = w(z) \cdot e^{i2\pi f t} \quad (\text{A-3})$$

Where  $f$  is the frequency of the input wave and  $w$  is a special function that will be defined. Rewriting the Eq. (I-15) with the new definition of  $u(z, t)$  is obtained:

$$-4\pi^2 f^2 \rho \cdot w(z) = \frac{\partial^2 w}{\partial z^2} (G + 2\pi f \eta i)$$

The previous equation is an ordinary linear differential equation, it means it has just one independent variable ( $z$ ). The previous kind of equation has a general solution for  $w(x)$  defined as:

$$w(z) = C e^{ik^* z} + D e^{-ik^* z}$$

Where  $k^*$  is constant that must be defined with the problem context. Introducing the general solution of  $w$ :

$$-4\pi^2 f^2 \rho \cdot (C e^{ik^*z} + D e^{-ik^*z}) = -k^{*2} (C e^{ik^*z} + D e^{-ik^*z}) (G + 2\pi f \eta i)$$

From we obtain that:

$$k^{*2} = \frac{4\pi^2 f^2 \rho}{(G + 2\pi f \eta i)} \quad (\text{A-4})$$

Were  $k^*$  is usually called the wave number. In the damped layer model, this number is complex. Integrating the previous definition in the Eq. (A-3):

$$u(z, t) = (C e^{ik^*z} + D e^{-ik^*z}) \cdot e^{i2\pi f t} \quad (\text{A-5})$$

Where C and D are constants that guarantee the boundary conditions,  $k^*$  is the wave number (Eq. (I-17)). The Eq. (I-16) is the general solution for a layer under a cyclic excitation with constant frequency ( $f$ ).

Using the Eq. (I-14) and the free boundary condition at the surface (Eq. (I-5)), the previous function arrives to:

$$0 = G(C e^{ik^*0} + D e^{-ik^*0}) \cdot e^{i2\pi f t} + \eta(C e^{ik^*0} + D e^{-ik^*0}) \cdot 2\pi f i \cdot e^{i2\pi f t}$$

$$0 = (C + D) \cdot (G + 2\pi f i \eta) e^{i2\pi f t}$$

From the previous equation is found that  $C=D$ , because the other terms can't be zero. Updating the function solution and reducing it with the Euler formula we obtain:

$$u(z, t) = 2C \cdot \cos(k^*z) \cdot e^{i2\pi f t}$$

With the previous definition of  $u(z, t)$  is possible to define the transfer function for any input with any frequency as:

$$TF_{\{0/H\}}(f) = \frac{u(0, t)}{u(H, t)} = \frac{2c \cdot \cos(k^* \cdot 0) \cdot e^{i2\pi f t}}{2c \cdot \cos(k^* \cdot H) \cdot e^{i2\pi f t}}$$

$$TF_{\{0/H\}}(f) = \frac{1}{\cos\left(2\pi f H \sqrt{\frac{\rho}{(G + 2\pi f \eta i)}}\right)}$$

Here a new term is introduced:  $\xi$  is the damping coefficient of the material and is defined as:

$$\xi = \frac{\pi f \eta}{V_s^2 \rho} \quad (\text{A-6})$$

Using the damping coefficient ( $\xi$ ) and introducing the definition of the stiffness in terms of shear velocity ( $G=V_s^2\rho$ ), it reduces the  $TF$  equation to:

$$TF_{\{0/H\}}(f) = \frac{1}{\cos\left(\frac{2\pi f H}{V_s} \sqrt{\frac{1}{(1 + 2\xi i)}}\right)} \quad (\text{A-7})$$

The Eq. (I-19) is the formal definition of the transfer function for a damped layer on a total rigid bedrock. However, through some assumptions, the function can be reduced more.

The value  $\xi$  has a dependence on the frequency (Eq. (I-18)). However, many studies have shown that  $\xi$  is almost constant for any frequency S. L. Kramer, 1996, then  $\xi$  is widely considered as a

constant parameter of the soil, with a normal range between 0 to 0.4. Considering that the damping ratio is low, then is possible to assume that:

$$1 \approx 1 - \xi^2$$

and it results that:

$$\sqrt{(1 + 2\xi i)} \approx 1 + \xi i$$

$$TF_{\{0/H\}}(f) = \frac{1}{\cos\left(\frac{2\pi f H}{V_s(1 + \xi i)}\right)}$$

Very similar to the first assumption, because the damping coefficient is low enough, we can assume also that:

$$1 \approx 1 + \xi^2$$

Reducing the transfer function to:

$$\frac{1}{(1 + \xi i)} \approx 1 - \xi i$$

$$TF_{\{0/H\}}(f) = \frac{1}{\cos\left(\frac{2\pi f H \cdot (1 - \xi i)}{V_s}\right)} \quad (\text{A-8})$$

To analyze the amplification with the transfer function, we evaluate the absolute value of  $TF$ . To develop this, the  $\cos$  function is separated from the identity  $\cos(a + bi) = \cos(a) \cosh(b) - i \sin(a) \sinh(b)$ , after making an algebraic develop and including the Euler formula, we arrive to:

$$|\cos(a + bi)| = \sqrt{\cos^2(a) + \sinh^2(b)} \quad (\text{A-9})$$

Applying the previous equation in the transfer function the absolute value of  $TF$  is:

$$|TF_{\{0/H\}}(f)| = \frac{1}{\left| \cos\left(\frac{2\pi f H \cdot (1 - \xi i)}{V_s}\right) \right|}$$

$$|TF_{\{0/H\}}(f)| = \frac{1}{\sqrt{\cos^2\left(\frac{2\pi f H}{V_s}\right) + \sinh^2\left(\xi \frac{2\pi f H}{V_s}\right)}} \quad (\text{A-10})$$

In this case, the transfer function with damping (Eq. (I-20)) makes a difference with respect to the zero-damping case (Eq. (I-8)). The resonance frequencies don't go to infinite since the denominator is never zero if the term inside of the hyperbolic sine is neither zero ( $\xi > 0$ ). However, the frequencies with maximal amplification are defined by the same Eq. (I-9) then the no damped case:

$$f^{\{n\}} = \frac{V_s}{2H} (0.5 + n) \quad \text{for } n = 0, 1, 2, \dots$$

In sake of the simplicity and to make the analysis easier, usually the amplitude of the transfer function (Eq. (I-20)) is reduced with an additional assumption.

$$\sinh^2(x) \approx x^2$$

Reducing the absolute value of the transfer function to:

$$|TF_{\{0/H\}}(f)| = \frac{1}{\sqrt{\cos^2\left(\frac{2\pi fH}{V_s}\right) + \left(\xi \frac{2\pi fH}{V_s}\right)^2}}$$

However, this assumption is not accomplished totally when the term  $\xi \frac{2\pi fH}{V_s}$  is high (Figure 0-1), for example in the evaluation of  $TF$  for high frequencies.

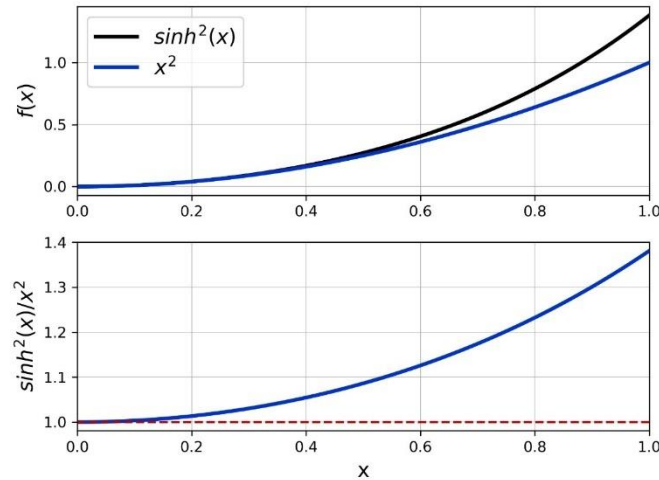


Figure 0-1. Comparison of  $\sinh^2(x)$  and  $x^2$  functions.

## Undamped layer on total rigid bedrock

To understand the soil response when it's facing propagation of seismic waves first here is presented a simple unidimensional model. It consists in one layer of soil lying on a total rigid rock.

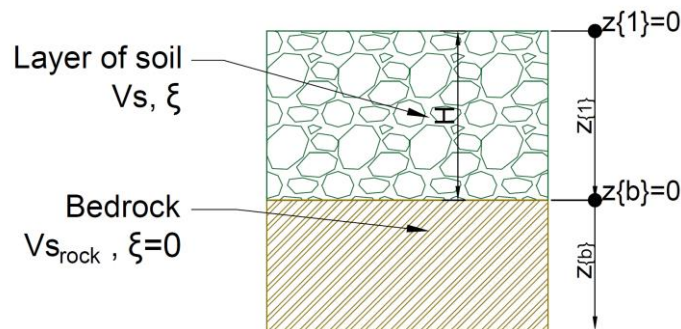


Figure A-2. Soil overlying a bedrock.  $H$  and  $V_s$  represent the thickness and the shear velocity of the soil.

In the previous figure,  $H$  represents the thickness of the soil layer,  $V_s$  is the shear wave velocity, who quantifies the rigidity of the material, and  $\xi$  represents the ratio damping of the soil. To analyze the propagation of a wave in this model, we can start from the motion equation that is required to be accomplished at any place of the model by the dynamic equilibrium (second Newton's law). The motion equation (Eq. (I-1)) for a differential element is express as:

$$\rho \frac{\partial^2 u}{\partial t^2} = \frac{\partial \tau}{\partial z} \quad (\text{A-11})$$

Where  $u$  represents the lateral displacement,  $t$  is the time,  $\rho$  is the density,  $z$  is the depth, and  $\tau$  represents the shear stress. Since we will evaluate first a model in one dimension, the equation just considers lateral displacement and shear stress traveling in the unique dimension.

If the material is modulated with no damping ( $\xi=0$ ) and as a spring, it means that the relationship between stress and strains is constant and the material can be model through the Hooke's law (Eq. (2)).

$$\tau = G \frac{\partial u}{\partial z} \quad (\text{A-12})$$

Where  $G$  represents the shear modulus. Introducing this relationship (Eq. (I-2)) to the motion equation (Eq. (I-1)), we can relate the stress and the strain (Eq. (I-3)):

$$\frac{\partial^2 u}{\partial t^2} = V_s^2 \frac{\partial^2 u}{\partial z^2} \quad (\text{A-13})$$

Where  $V_s$  is the shear velocity defined as:

$$V_s = \sqrt{G/\rho} \quad (\text{A-14})$$

The motion equation can be solved by transforming the equation to new variables. The solution, called d'Alembert's Solution, start proposing two new parametric variables as:

$$\varphi_1 = V_s t - z$$

$$\varphi_2 = V_s t + z$$

In terms of those both variables, the motion equation (Eq. (I-3)) is expressed as:

$$\frac{\partial^2 u}{\partial \varphi_1 \cdot \partial \varphi_2} = 0$$

This differential equation is well known as a hyperbolic differential equation. To find the solution  $u$ , the equation is integrated two times, one with respect  $\varphi_1$  and another respect  $\varphi_2$ . Solving that the general solution for  $u$  is expressed as:

$$u(z, t) = f(\varphi_1) + g(\varphi_2) = h(V_s t - z) + g(V_s t + z)$$

It means that the solution will consist in two parts ( $h$  and  $g$  functions). Physically,  $f$  and  $g$  are describing two functions one for describing the upwards waves and the downwards waves. Because the wave equation is a periodic function and the Eq. (I-3) is linear from (Eq. (A-15)), since it is describing two periodic functions.

$$u(z, t) = A \cdot \sin(\alpha(V_s t - z)) + B \cdot \sin(\alpha(V_s t + z)) \quad (\text{A-15})$$

Where  $A$ ,  $B$ , and  $\alpha$  are constants that will be defined with the condition of each problem. Note that in the previous equation solution, both periodic functions have the same angular frequency ( $\alpha V_s / 2\pi$ ). It is because here the problem is constrained and just a periodic wave with a unique frequency is considered. However, the solution for an input wave with many frequencies will result from the summation of the solutions for waves with individual frequencies. This is called superposition principle, characteristic of any linear system as the linear partial differential equation (Eq. (I-3)).

To define the constants  $A$ ,  $B$  and  $\alpha$ , the boundary conditions must be defined. At the surface ( $z=0$ , see Figure I-1) the shear stress can't be developed, it implies that at the surface the Eq. (I-5):

$$\tau(z = 0) = 0 \quad \text{then} \quad \frac{\partial u}{\partial z}(z = 0, t) = 0 \quad (\text{A-16})$$

Replacing Eq. (A-15) in Eq. (I-5):

$$0 = -A\alpha \cdot \cos(\alpha V_s t) + B\alpha \cdot \cos(\alpha V_s t)$$

$$0 = (B - A)\alpha \cdot \cos(\alpha V_s t)$$

The previous expression only can be satisfied if  $A=B$ , since  $\alpha$  can't be zero because it will result in a zero-constant solution. Updating the Eq. (A-15) with the new parameters:

$$u(z, t) = A(\sin(\alpha V_s t + \alpha z) + \sin(\alpha V_s t - \alpha z))$$

Rewriting the previous equation using trigonometric identities, we obtain:

$$u(z, t) = 2A \cdot \sin(\alpha V_s t) \cos(\alpha z) \quad (\text{A-17})$$

At the bedrock, like at surface, a stress is imposed. This stress is in function of the input wave that is chosen for the problem. To obtain a general solution in this explanation, a basic periodic function is taken (Eq. (I-6)). As was mention it allows to find the solution for more complex inputs.

$$\frac{\partial u}{\partial z} G = \tau(z = -H) = \tau_o \cdot \sin(2\pi f t) \quad (\text{A-18})$$

Where  $\tau_o$  is the stress wave amplitude, and  $f$  is the frequency associated with the wave. Making the derivate of Eq. (A-17), is obtained:

$$\frac{\partial u}{\partial z} = -2A\alpha \cdot \sin(\alpha V_s t) \sin(\alpha z)$$

Introducing the previous expression in the boundary condition at the bedrock (Eq. (I-6)), we can reduce to:

$$\begin{aligned} \tau_o \cdot \sin(2\pi f t) &= -2A\alpha G \cdot \sin(\alpha V_s t) \sin(\alpha H) \\ \left( \frac{\tau_o}{-2\alpha G \cdot \sin(\alpha H)} \right) \cdot \sin(2\pi f t) &= A \cdot \sin(\alpha V_s t) \end{aligned}$$

In the previous equation, the only variable is the time. Because the time is in both sides evaluated by the  $\sin$  function, the equality just can be accomplished for any time if:

$$\alpha = 2\pi f / V_s$$

It will let the solution equation as:

$$u(z, t) = 2A \cdot \sin(2\pi f t) \cos(2\pi f z / V_s) \quad (\text{A-19})$$

In some cases, the previous equation is presented in function of the angular frequency ( $\omega=2\pi f$ ) and the wave number ( $k= \omega/V_s$ ). directing to:

$$u(z, t) = 2A \cdot \sin(\omega t) \cos(kz)$$

The transfer function is the ratio of the amplitude between the two periodic functions that describe the wave on two points. In this case, we evaluate the surface and the bottom of the layer. The ratio will be defined as:

$$\begin{aligned} TF_{\{0/H\}}(f) &= \frac{u(0, t)}{u(H, t)} = \frac{2A \cdot \sin(2\pi f t) \cos(2\pi f 0 / V_s)}{2A \cdot \sin(2\pi f t) \cos(2\pi f H / V_s)} \\ TF_{\{0/H\}}(f) &= \frac{1}{\cos(2\pi f H / V_s)} \quad (\text{A-20}) \end{aligned}$$

The Eq. (I-8) shows that the amplification given by the site is different and depending on the frequencies. Also, Eq. (I-8) predicts that for some frequencies the amplification will trend to

infinite because for some frequencies the denominator trend to zero. It occurs when the term inside the *cos* function, is equal to  $\pi(0.5 + n)$  where *n* is any entire number (e.g. 0, 1, 2, ...).

$$0 = \cos\left(\frac{2\pi fH}{V_s}\right)$$

$$f^{\{n\}} = \frac{V_s}{2H} (0.5 + n) \quad \text{for } n = 0, 1, 2, \dots \tag{A-21}$$

Where  $f^{\{n\}}$  is the *n*th frequency peak that is amplified by the site. This phenomenon occurs because the input wave enters into constructive interference with the downwards waves, what is called resonance. This together with the hypothesis that the bedrock is infinite rigid and that the soil is undamped, meaning that the energy can't escape of the model, makes that the amplification for those frequencies trend to infinite.

### Solution for many layers of viscoelastic soil lying in an elastic bedrock

In this subsection, the changes in the wave due to the pass from one media to other is studied. First, the bedrock in this model is not infinitely rigid, producing that part of the energy in the downwards waves pass to the bedrock, and another part returns to the layers of soil. This effect makes that part of the energy can leave the model, changing the solution in comparison with the found solutions of previous subsections. Additionally, a more realistic case involves several layers of soil. It will change the iteration of how the waves move in the system because of the effects of media interfaces.

For solving this system, we must define a new coordinate system for each layer of soil and the bedrock (Figure A-3). Where zero is the upper point of each the layer, and  $H_{\{m\}}$  the bottom point of each layer.

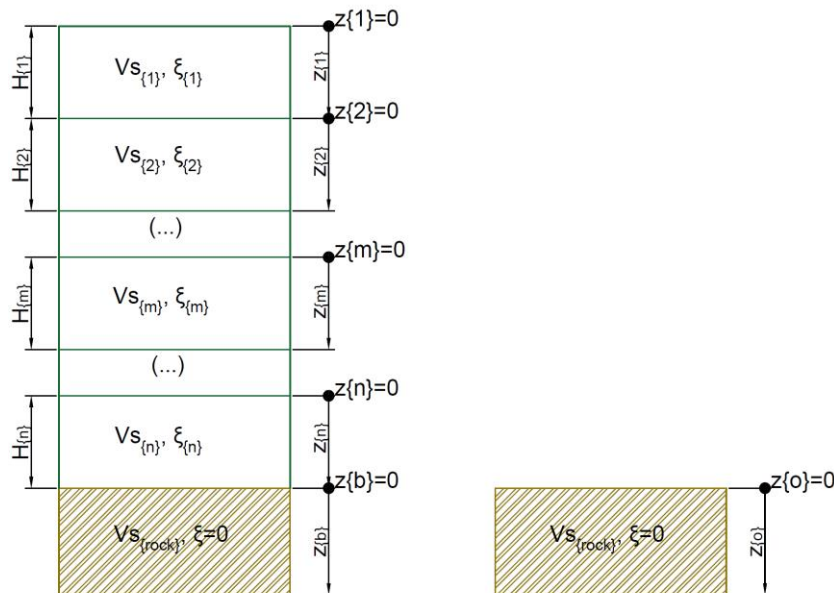


Figure A-3. Model of one damped layer lying on an elastic bedrock. Each layer has a local coordinates system.

The soil layers are damped in this model and they are controlled by the Eq. (I-15). The bedrock domain will be controlled by the no damping case (Eq. (I-3)). Because both equation that domain the problem are linear, the methodology to solve this problem will follow the same procedure as

the previous models. A transfer function will be defined, for after being used to transfer the input wave to one point of interest.

In this case, more equation must be found, one by layer. However, the general solution for all the layer has the shape of the Eq. (I-16), because is solved for a harmonic input:

$$\begin{aligned}
 u_{\{1\}}(z_{\{1\}}, t) &= (A_{\{1\}}e^{ik_{\{1\}}^*z_{\{1\}}} + B_{\{1\}}e^{-ik_{\{1\}}^*z_{\{1\}}}) \cdot e^{i2\pi ft} \\
 u_{\{2\}}(z_{\{2\}}, t) &= (A_{\{2\}}e^{ik_{\{2\}}^*z_{\{2\}}} + B_{\{2\}}e^{-ik_{\{2\}}^*z_{\{2\}}}) \cdot e^{i2\pi ft} \\
 &\dots \\
 u_{\{m\}}(z_{\{m\}}, t) &= (A_{\{m\}}e^{ik_{\{m\}}^*z_{\{m\}}} + B_{\{m\}}e^{-ik_{\{m\}}^*z_{\{m\}}}) \cdot e^{i2\pi ft} \\
 &\dots \\
 u_{\{b\}}(z_{\{b\}}, t) &= (A_{\{b\}}e^{ik_{\{b\}}^*z_{\{b\}}} + B_{\{b\}}e^{-ik_{\{b\}}^*z_{\{b\}}}) \cdot e^{i2\pi ft}
 \end{aligned} \tag{A-22}$$

Where  $k_{\{m\}}^*$  is the wave number (Eq. (I-17)) and  $A_{\{m\}}$  and  $B_{\{m\}}$  are constants to be defined with the problem conditions. The other terms are explained in Figure I-4. Those equations for each layer must accomplish the wave equation (Eq. (I-1)). The boundary conditions are the same (Eq. (I-5) and Eq. (I-6)), meaning that at the surface the shear stress can't be developed. Making the same analysis in the first layer than for the monolayer case; from the free boundary condition (Eq. (I-5)) and the Eq. (I-14) for the first layer is obtained:

$$A_{\{1\}} = B_{\{1\}} \tag{A-23}$$

The definition of an incoming wave is defined differently in this situation since the bedrock has a finite elasticity. At the bedrock interface ( $u_{\{b\}}(0, t)$ ), the movement, in this case, is produced by the upwards waves ( $A_{\{b\}}e^{ik_{\{b\}}^*z_{\{b\}}}$  term), coming directly from the earthquake, and also by the downwards waves ( $B_{\{b\}}e^{-ik_{\{b\}}^*z_{\{b\}}}$  term) that are returning from upper soil layers. To solve this situation, it is widely used as input of the model just the upwards waves incoming directly from the earthquake. This point of view means that the input wave corresponds to the movement that will be felt by an outcrop where the soil layer doesn't exist. In this movement will be defined as:

$$u_{\{o\}}(0, t) = 2A_{\{b\}} \cdot e^{i2\pi ft} \tag{A-24}$$

Where  $u_{\{o\}}$  is the displacement in the outcrop (Figure I-4). The term  $2A_{\{b\}}$  comes from imposing the conditions of free surface to general displacement formula.

For all the other layers, all the interfaces must satisfy continuity in stress and displacement. From this statement the Eq. (I-22) is obtained.

$$\begin{aligned}
 u_{\{m\}}(0, t) &= u_{\{m-1\}}(H_{m-1}, t) \\
 \tau_{\{m\}}(0, t) &= \tau_{\{m-1\}}(H_{m-1}, t)
 \end{aligned} \tag{A-25}$$

Introducing the previous conditions (Eq. (I-22)) in an interface between two layers (Eq. (I-21)), a new expression is obtained, first using the continuity in displacement:

$$\begin{aligned}
 (A_{\{m\}}e^0 + B_{\{m\}}e^{-0}) \cdot e^{i2\pi ft} &= (A_{\{m-1\}}e^{ik_{\{m-1\}}^*H_{\{m-1\}}} + B_{\{m-1\}}e^{-ik_{\{m-1\}}^*H_{\{m-1\}}}) \cdot e^{i2\pi ft} \\
 A_{\{m\}} + B_{\{m\}} &= A_{\{m-1\}}e^{ik_{\{m-1\}}^*H_{\{m-1\}}} + B_{\{m-1\}}e^{-ik_{\{m-1\}}^*H_{\{m-1\}}}
 \end{aligned}$$

After defining the stress on each point (Eq. (I-14)):

$$\tau_{\{m\}} = G_{\{m\}} \frac{\partial u_{\{m\}}}{\partial z_{\{m\}}} + \eta_m \frac{\partial^2 u_{\{m\}}}{\partial z_{\{m\}} \partial t}$$

$$\frac{\partial u_{\{m\}}}{\partial z_{\{m\}}} = (A_{\{m\}} e^{ik_{\{m\}}^* z_{\{m\}}} - B_{\{m\}} e^{-ik_{\{m\}}^* z_{\{m\}}}) \cdot e^{i2\pi f t} ik_{\{m\}}^*$$

$$\frac{\partial^2 u_{\{m\}}}{\partial z_{\{m\}} \partial t} = -(A_{\{m\}} e^{ik_{\{m\}}^* z_{\{m\}}} - B_{\{m\}} e^{-ik_{\{m\}}^* z_{\{m\}}}) \cdot e^{i2\pi f t} 2\pi f k_{\{m\}}^*$$

Including the previous equations, the continuity in stress (Eq. (I-22)) leads to:

$$\begin{aligned} & (G_{\{m\}} \cdot i - \eta_m \cdot 2\pi f) k_{\{m\}}^* (A_{\{m\}} - B_{\{m\}}) \\ &= (G_{\{m-1\}} \cdot i - \eta_{m-1} \cdot 2\pi f) k_{\{m-1\}}^* (A_{\{m-1\}} e^{ik_{\{m-1\}}^* H_{\{m-1\}}} \\ & \quad - B_{\{m-1\}} e^{-ik_{\{m-1\}}^* H_{\{m-1\}}}) \\ A_{\{m\}} - B_{\{m\}} &= \frac{(G_{\{m-1\}} \cdot i - \eta_{m-1} \cdot 2\pi f) k_{\{m-1\}}^*}{(G_{\{m\}} \cdot i - \eta_m \cdot 2\pi f) k_{\{m\}}^*} (A_{\{m-1\}} e^{ik_{\{m-1\}}^* H_{\{m-1\}}} \\ & \quad - B_{\{m-1\}} e^{-ik_{\{m-1\}}^* H_{\{m-1\}}}) \end{aligned}$$

Resuming with the Eq. (I-18) for including the damping coefficient in the previous equation:

$$\begin{aligned} Gi - \eta \cdot 2\pi f &= Gi - 2\xi V_s^2 \rho \\ G(i - 2\xi) &= Gi(1 + 2\xi i) \\ A_{\{m\}} - B_{\{m\}} &= \frac{G_{\{m-1\}} i (1 + 2\xi_{\{m-1\}} i) k_{\{m-1\}}^*}{G_{\{m\}} i (1 + 2\xi_{\{m\}} i) k_{\{m\}}^*} (A_{\{m-1\}} e^{ik_{\{m-1\}}^* H_{\{m-1\}}} - B_{\{m-1\}} e^{-ik_{\{m-1\}}^* H_{\{m-1\}}}) \end{aligned}$$

For reducing terms, a new variable is defined to characterize the interface between two layers. The impedance is defined as the ratio between the apparent stiffness of the top layer over the stiffness of the bottom layer (Eq. (I-24)).

$$\alpha_{\{m-1\}}^* = \frac{G_{\{m-1\}} (1 + 2\xi_{\{m-1\}} i) k_{\{m-1\}}^*}{G_{\{m\}} (1 + 2\xi_{\{m\}} i) k_{\{m\}}^*} \quad (\text{A-26})$$

Leading to:

$$A_{\{m\}} - B_{\{m\}} = \alpha_{\{m-1\}}^* (A_{\{m-1\}} e^{ik_{\{m-1\}}^* H_{\{m-1\}}} - B_{\{m-1\}} e^{-ik_{\{m-1\}}^* H_{\{m-1\}}})$$

Mixing the previous equations of stress continuity with the displacement continuity, the coefficients of each layer could be found since the coefficient of the immediately upper layer as:

$$\begin{aligned} & A_{\{m\}} \\ &= \left( A_{\{m-1\}} e^{ik_{\{m-1\}}^* H_{\{m-1\}}} (1 + \alpha_{\{m-1\}}^*) + B_{\{m-1\}} e^{-ik_{\{m-1\}}^* H_{\{m-1\}}} (1 - \alpha_{\{m-1\}}^*) \right) / 2 \\ & B_{\{m\}} \\ &= \left( A_{\{m-1\}} e^{ik_{\{m-1\}}^* H_{\{m-1\}}} (1 - \alpha_{\{m-1\}}^*) + B_{\{m-1\}} e^{-ik_{\{m-1\}}^* H_{\{m-1\}}} (1 + \alpha_{\{m-1\}}^*) \right) / 2 \end{aligned} \quad (\text{A-27})$$

The previous equations are very useful for computing the transfer function. For example, to find the transfer function between the input wave (Eq. (A-24)) to the top in the surface of the soil layers (Eq. (A-23)):

$$TF_{\{0/outcrop\}}(f) = \frac{u_{\{1\}}(0, t)}{u_{\{0\}}(0, t)} = \frac{2A_{\{1\}} \cdot e^{i2\pi f t}}{2A_{\{b\}} \cdot e^{i2\pi f t}}$$

Including the Eq. (I-23) in the previous one:

$$TF_{\{0/outcrop\}}(f) = 2 \cdot A_{\{1\}} / \left( A_{\{n\}} e^{ik_{\{n\}}^* H_{\{n\}}} (1 + \alpha_{\{n\}}^*) + B_{\{n\}} e^{-ik_{\{n\}}^* H_{\{n\}}} (1 - \alpha_{\{n\}}^*) \right) \quad (\text{A-28})$$

Transforming the previous equation again with Eq. (I-23):

$$TF_{\{0/outcrop\}}(f) = 4 \cdot A_{\{1\}} / \left( \begin{array}{l} A_{\{n-1\}} e^{i(k_{\{n\}}^* H_{\{n\}} + k_{\{n-1\}}^* H_{\{n-1\}})} (1 + \alpha_{\{n\}}^*) (1 + \alpha_{\{n-1\}}^*) + \\ B_{\{n-1\}} e^{i(k_{\{n\}}^* H_{\{n\}} - k_{\{n-1\}}^* H_{\{n-1\}})} (1 + \alpha_{\{n\}}^*) (1 - \alpha_{\{n-1\}}^*) + \\ A_{\{n-1\}} e^{i(-k_{\{n\}}^* H_{\{n\}} + k_{\{n-1\}}^* H_{\{n-1\}})} (1 - \alpha_{\{n\}}^*) (1 - \alpha_{\{n-1\}}^*) + \\ B_{\{n-1\}} e^{i(-k_{\{n\}}^* H_{\{n\}} - k_{\{n-1\}}^* H_{\{n-1\}})} (1 - \alpha_{\{n\}}^*) (1 + \alpha_{\{n-1\}}^*) \end{array} \right)$$

Recurrently the terms  $A_{\{m\}}$  and  $B_{\{m\}}$  could be replaced with the Eq. (I-23) by their predecessor  $A_{\{m-1\}}$  and  $B_{\{m-1\}}$  until the first layer. The final formula is expanding, and it will arrive at the general solution:

$$TF_{\{0/outcrop\}}(f) = A_{\{1\}} / \left( \begin{array}{l} A_{\{1\}} \cdot a(k_{\{n\}}^* H_{\{n\}}, \dots, k_{\{1\}}^* H_{\{1\}}, \alpha_{\{n-1\}}^*, \dots, \alpha_{\{1\}}^*) + \\ B_{\{1\}} \cdot b(k_{\{n\}}^* H_{\{n\}}, \dots, k_{\{1\}}^* H_{\{1\}}, \alpha_{\{n-1\}}^*, \dots, \alpha_{\{1\}}^*) \end{array} \right)$$

Where  $a$  and  $b$  are functions depending on the layer configuration and soil parameters. The params  $A_{\{1\}}$  and  $B_{\{1\}}$  are equals (Eq. (A-23)) reducing the previous equation to:

$$TF_{\{0/outcrop\}}(f) = 1/c(k_{\{n\}}^* H_{\{n\}}, \dots, k_{\{1\}}^* H_{\{1\}}, \alpha_{\{n-1\}}^*, \dots, \alpha_{\{1\}}^*)$$

Since  $c=a+b$ ,  $c$  is a function of the layer configuration and soil parameters too. The wave number of each layer ( $k_{\{m\}}^*$ ) can be also defined in terms of the damping and shear velocity replacing the Eq. (I-18) and Eq. (I-4) in the Eq. (I-17):

$$k_{\{m\}}^* = \frac{2\pi f}{V_{s\{m\}}} \sqrt{\frac{1}{1 + 2\xi_{\{m\}} i}}$$

Because the damping for all layers is small enough, it implies that the same condition to pass from the Eq. (I-19) to the Eq. (A-8) are accomplished in all the layers. It allows rewriting the term affected by the square root in the wave number as:

$$k_{\{m\}}^* \approx \frac{2\pi f}{V_{s\{m\}}} (1 - \xi_{\{m\}} i) \quad (\text{A-29})$$

It implies that the absolute value of the transfer function between the outcrop and the surface of the soil is defined as:

$$\left| TF_{\{0/outcrop\}}(f) \right| = 1 / |c(k_{\{n\}}^* H_{\{n\}}, \dots, k_{\{1\}}^* H_{\{1\}}, \alpha_{\{n-1\}}^*, \dots, \alpha_{\{1\}}^*)| \quad (\text{A-30})$$

Where  $c$  is the combination of exponential functions obtained from recurrently replace the Eq. (I-23) to define the Eq. (I-25). The wave number ( $k_{\{m\}}$ ) is defined in the Eq. (I-27), the thickness of each layer ( $H_{\{m\}}$ ) depends on each case, and the impedance ( $\alpha_{\{m\}}$ ) for each layer is defined in the Eq. (I-24).

Using the same procedure, but this time involving the downwards waves, the transfer function between any layer interface and the surface can be found as:

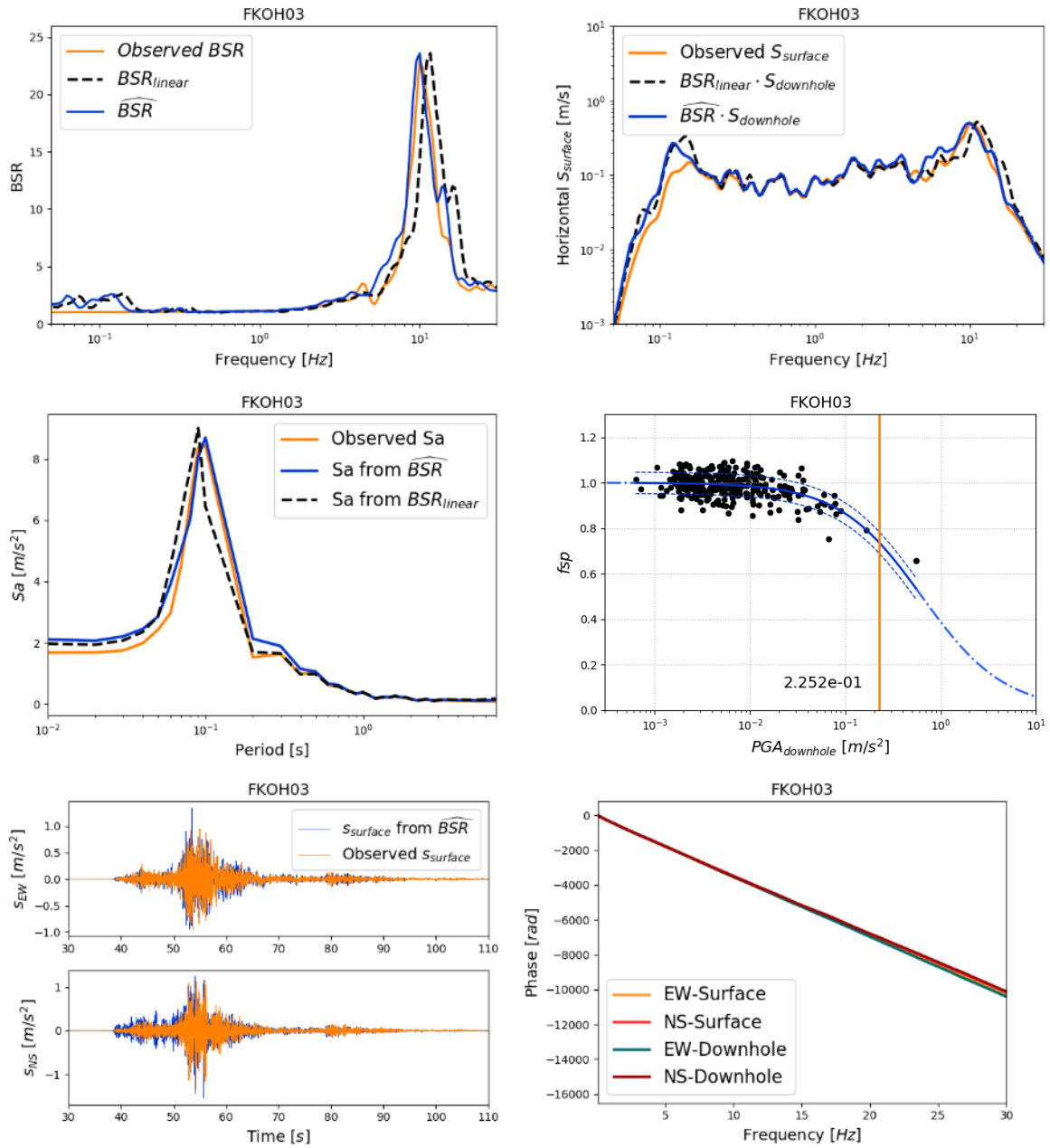
$$TF_{\{0/H\}}(f) = \frac{u_{\{1\}}(0, t)}{u_{\{m\}}(0, t)} = \frac{2A_{\{1\}} \cdot e^{i2\pi ft}}{(A_{\{m\}} + B_{\{m\}}) \cdot e^{i2\pi ft}}$$

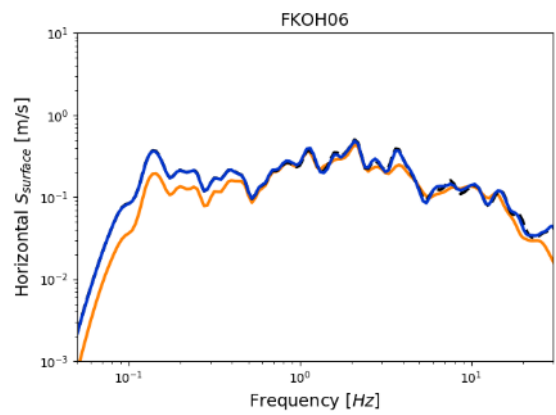
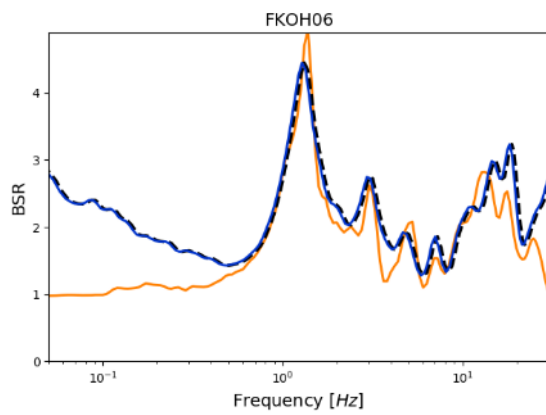
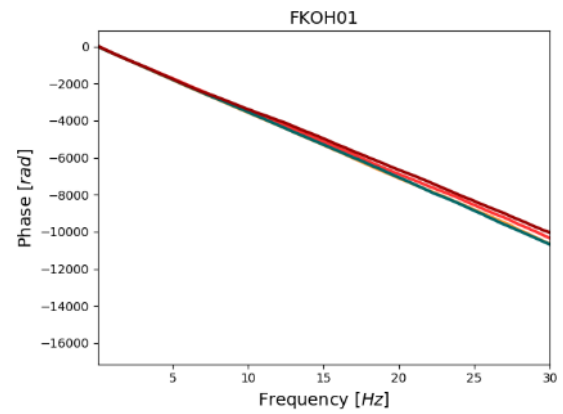
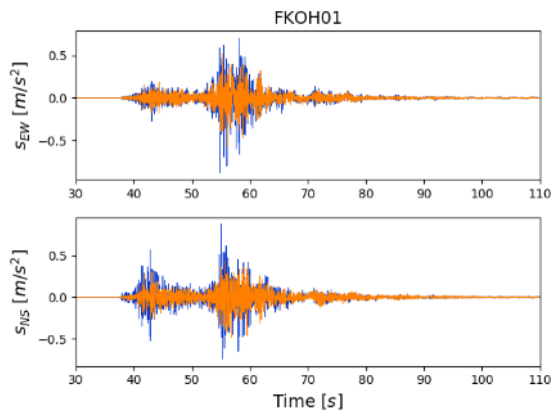
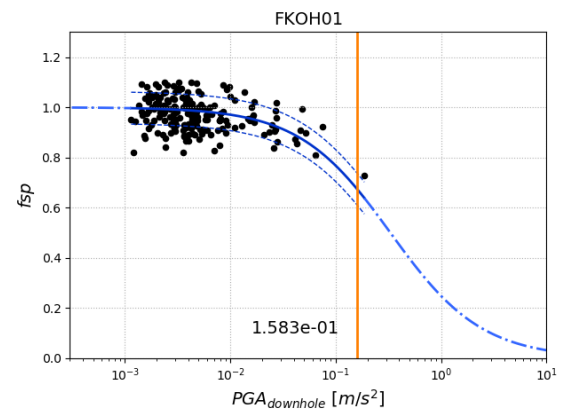
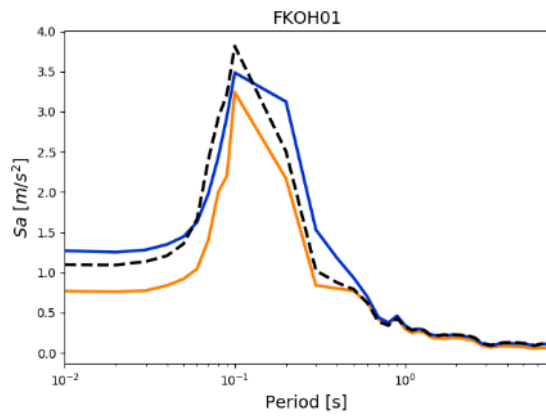
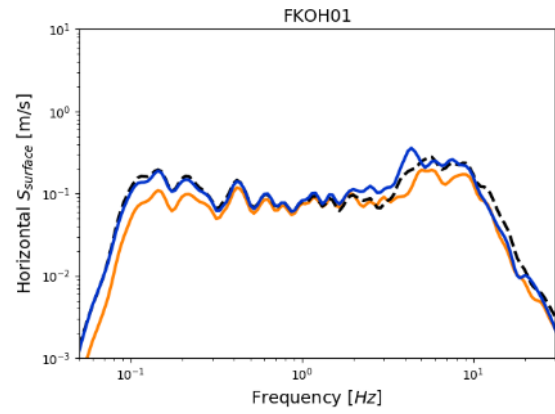
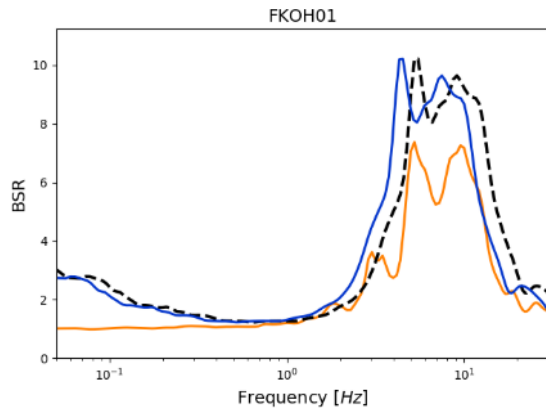
Replacing recurrently the Eq. (I-23) to move from  $A_{\{m\}}$  and  $B_{\{m\}}$  to  $A_{\{1\}}$  and  $B_{\{1\}}$ , and computing the absolute value of the transfer function:

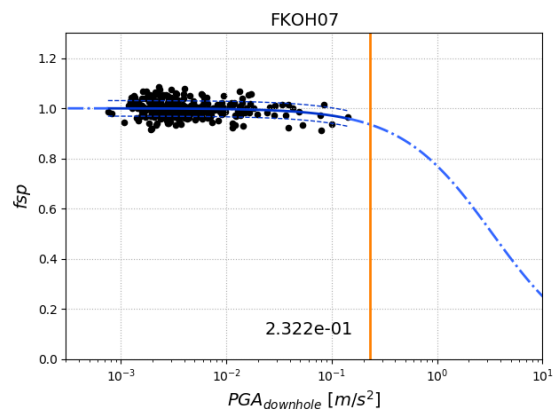
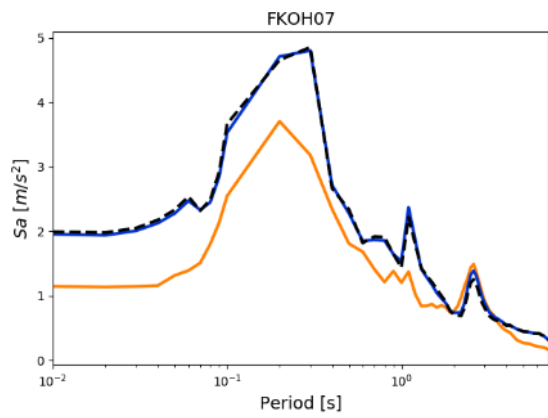
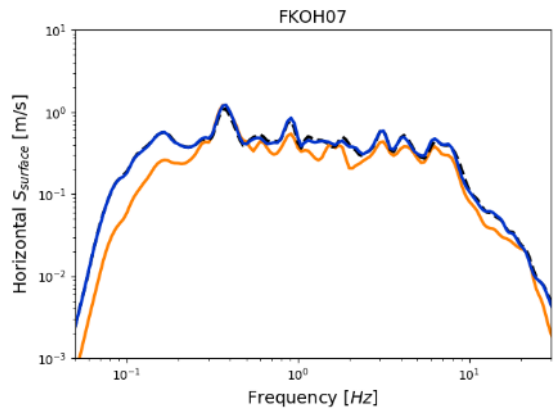
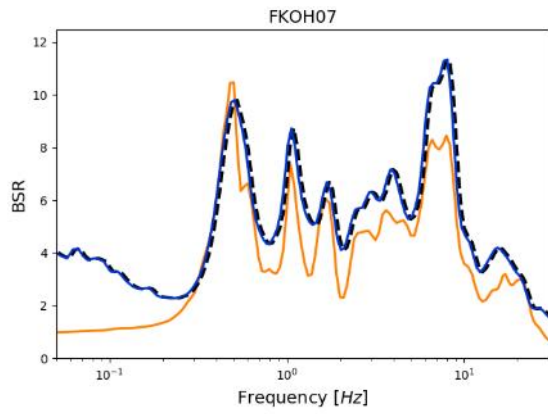
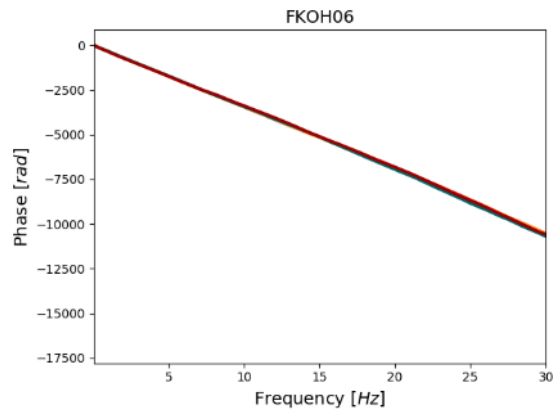
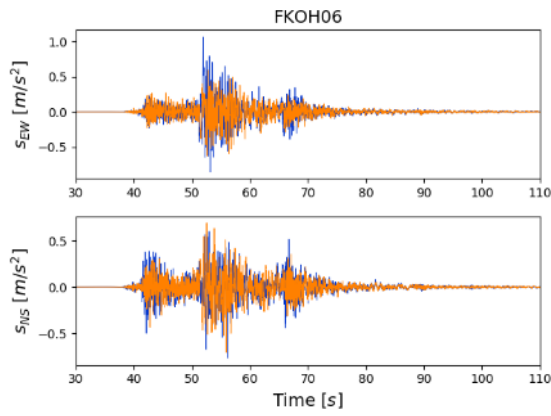
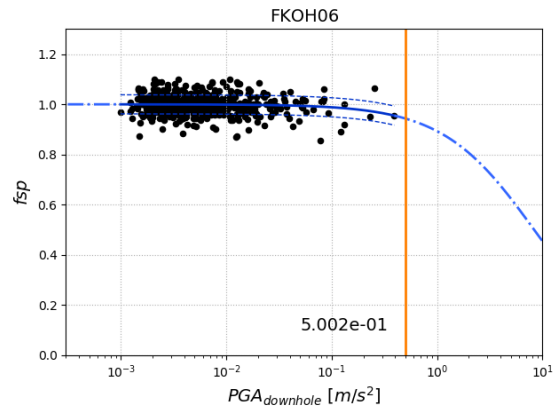
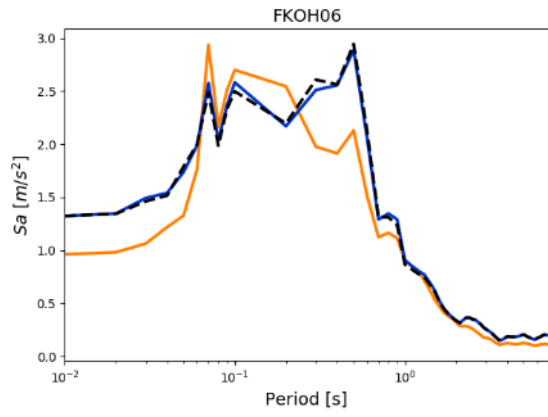
$$|TF_{\{0/H\}}(f)| = \left| \frac{1}{d(k_{\{m\}}^* H_{\{m\}}, \dots, k_{\{1\}}^* H_{\{1\}}, \alpha_{\{m-1\}}^*, \dots, \alpha_{\{1\}}^*)} \right| \quad (\text{A-31})$$

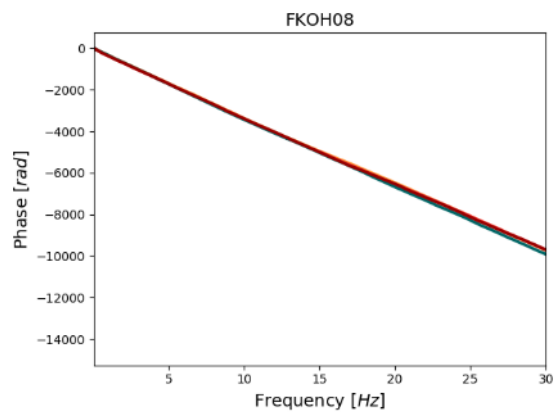
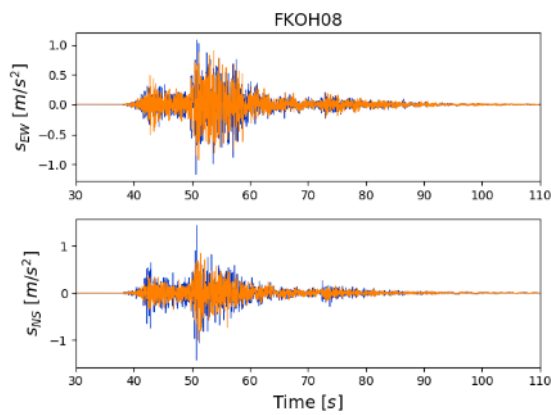
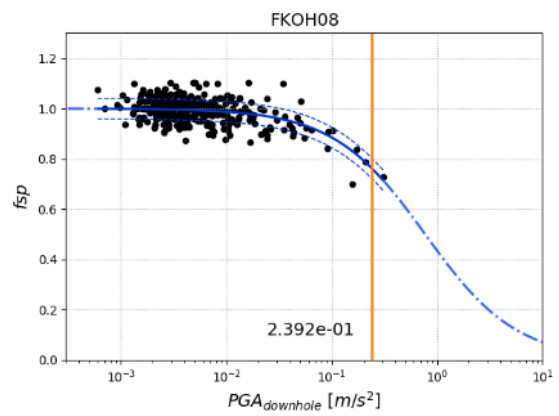
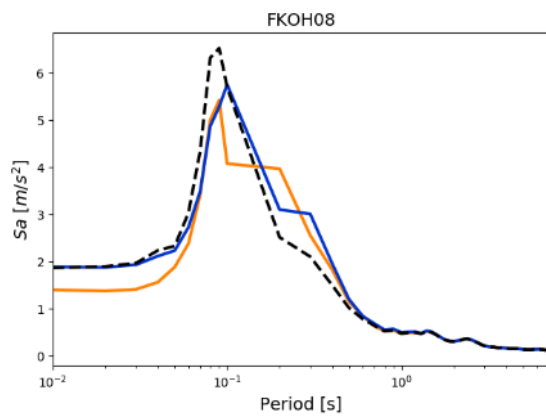
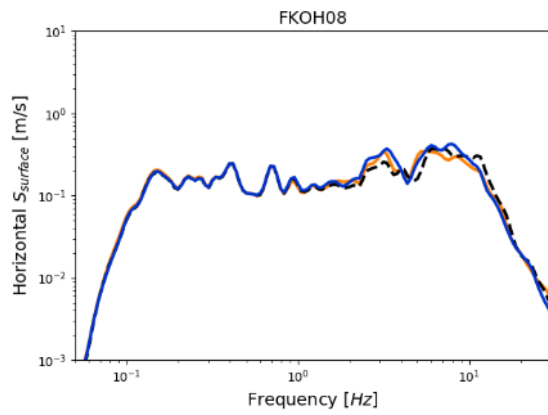
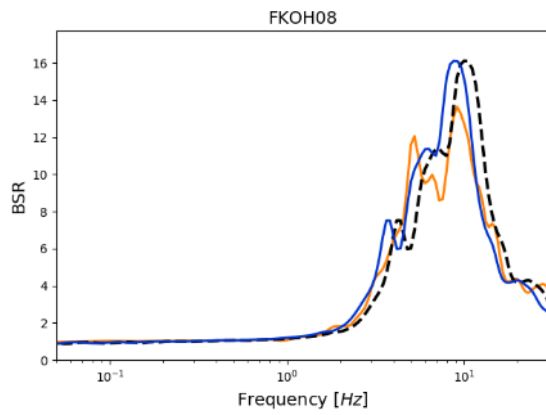
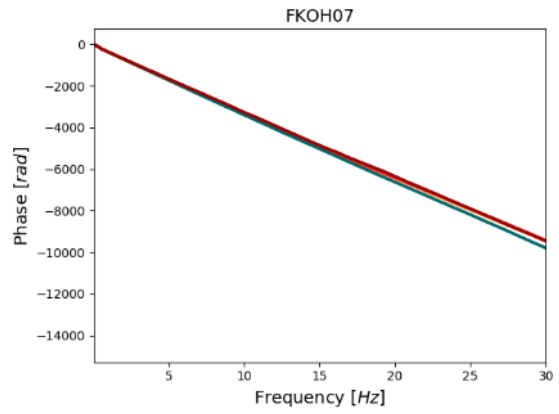
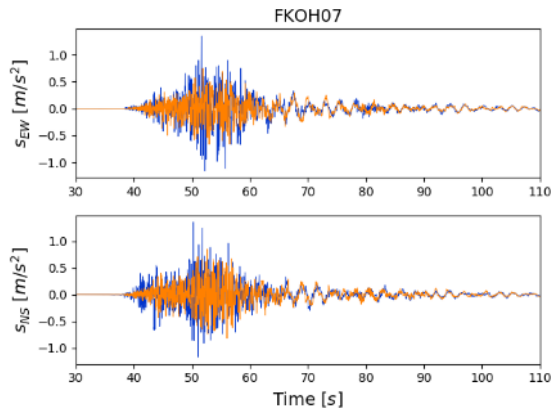
Where like the Eq. (I-26),  $d$  is a combination of exponential functions, but in this case is different since it involves just the parameters of the layers upper than the layer  $m$ . Additionally, it involves the downwards waves.

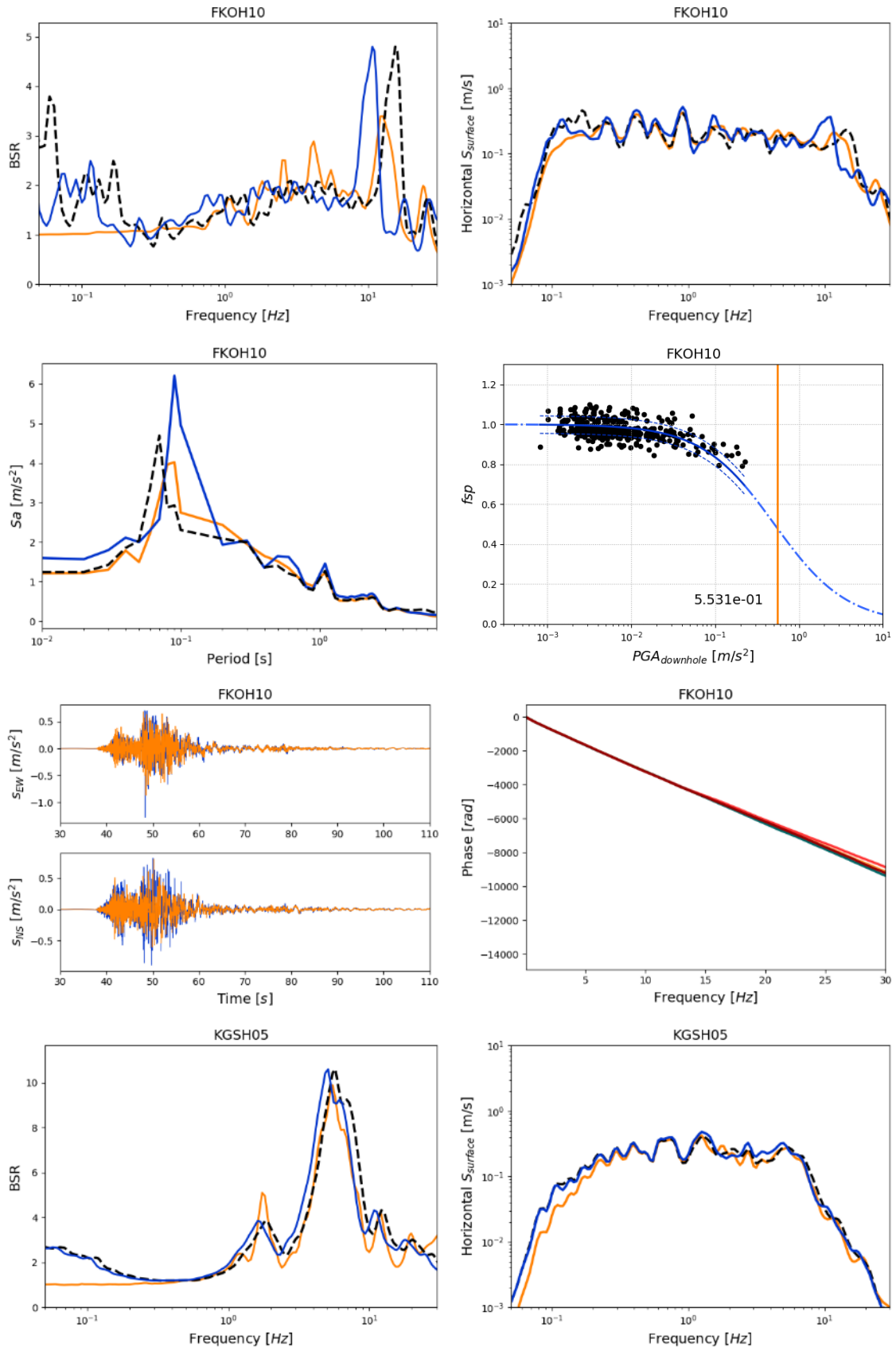
# Annex B. Results of the Kumamoto simulation

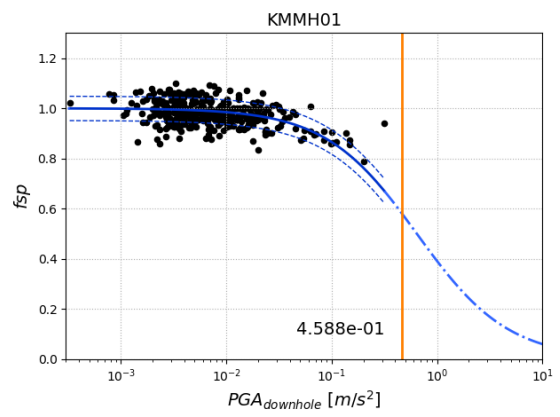
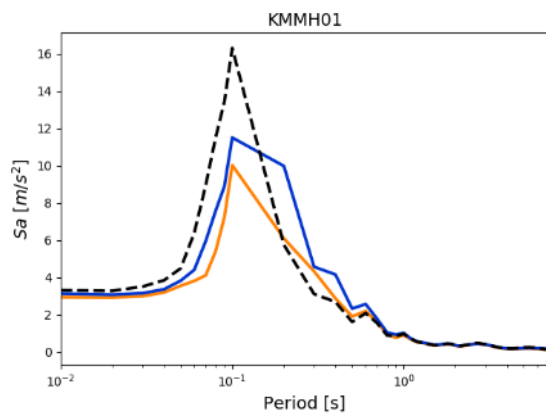
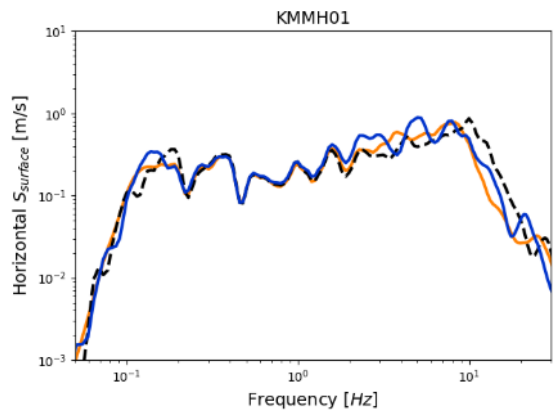
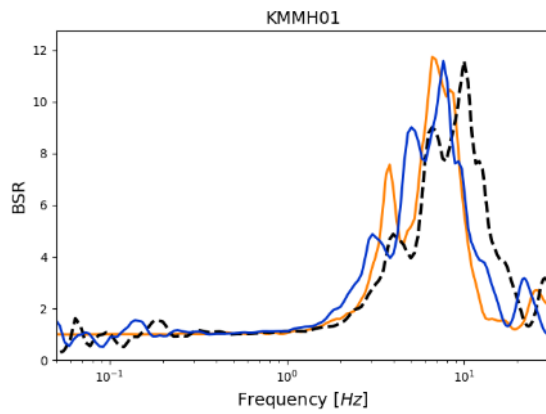
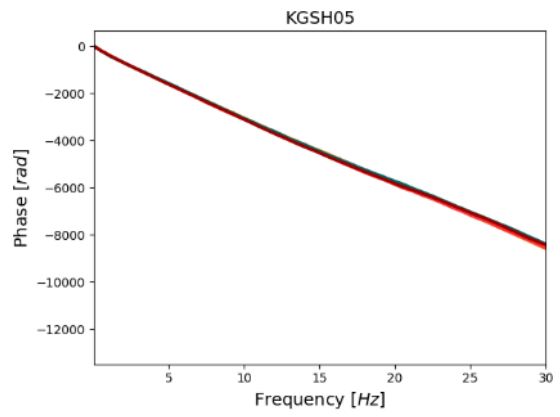
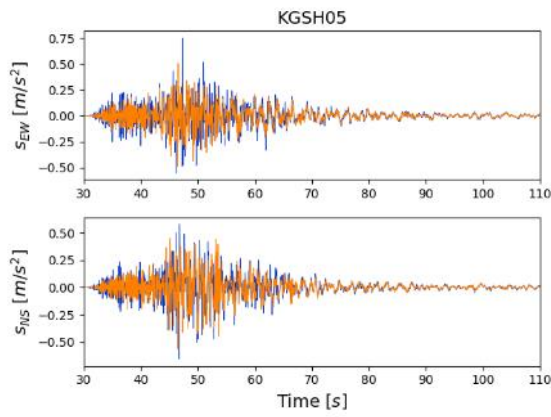
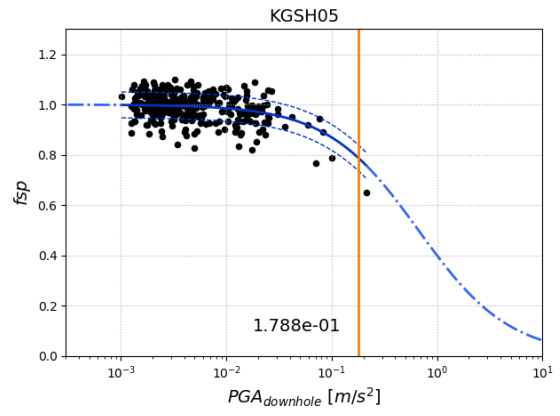
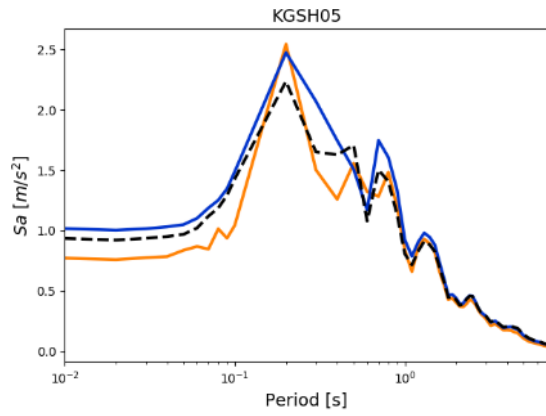


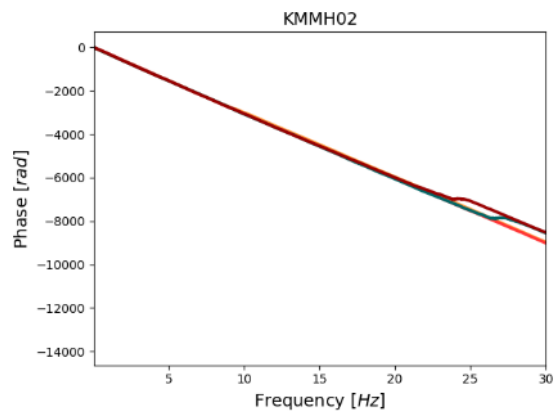
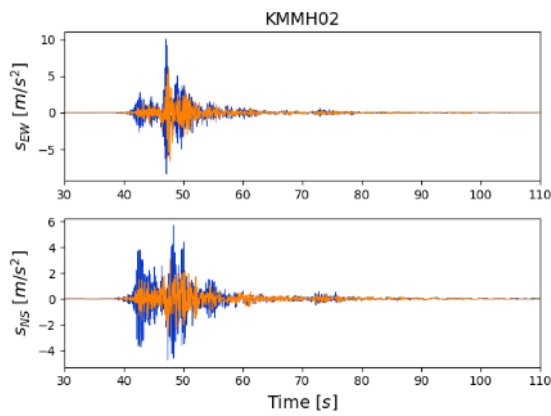
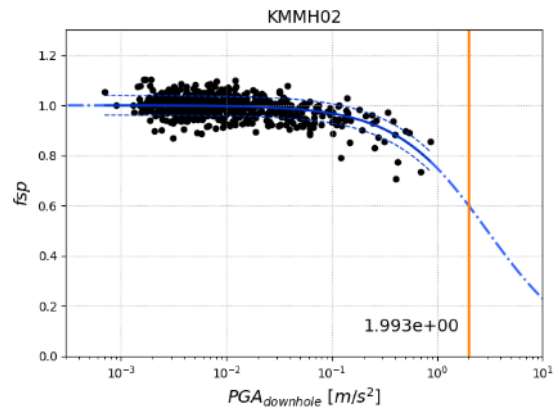
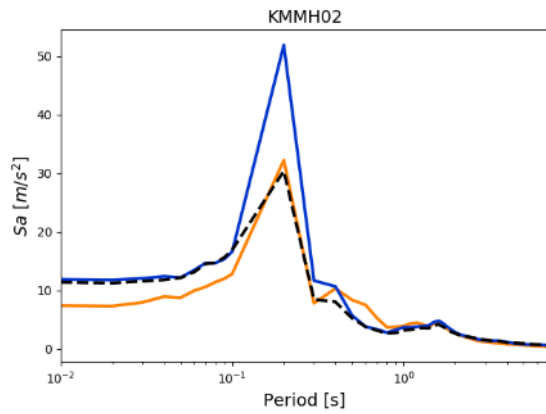
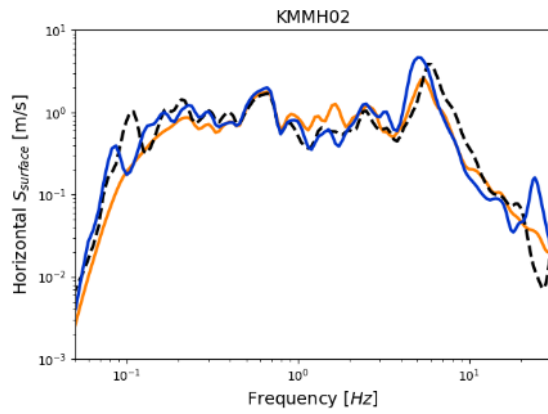
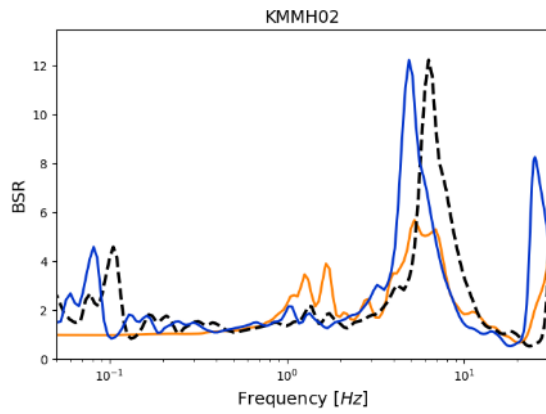
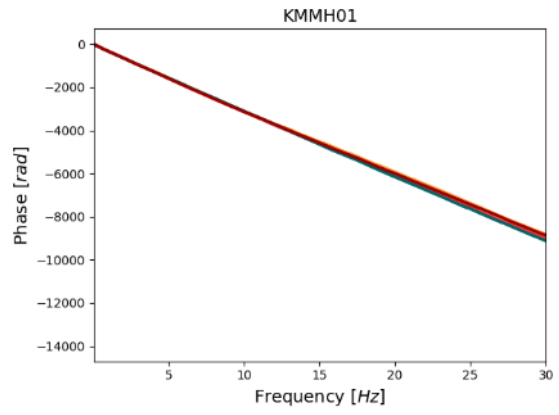
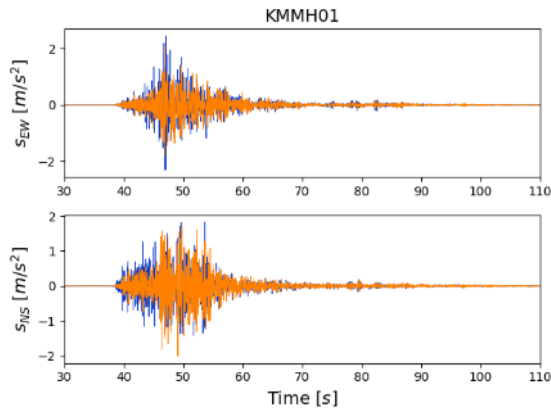


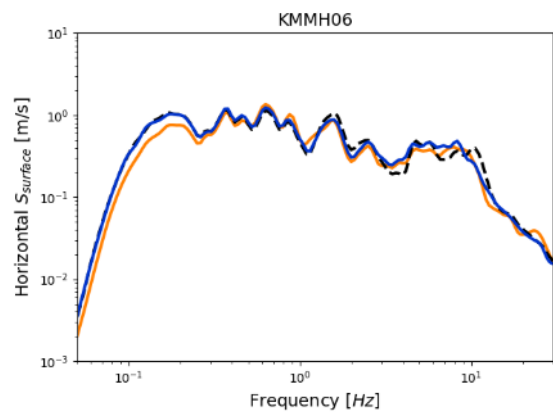
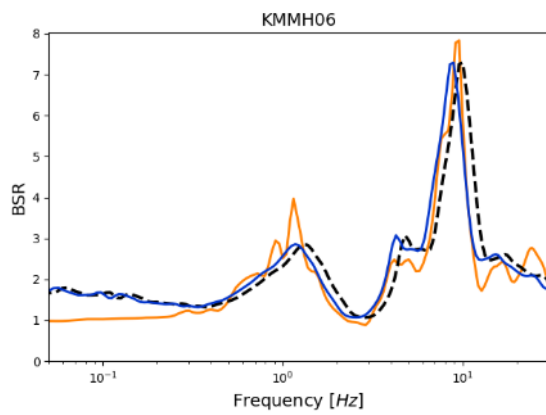
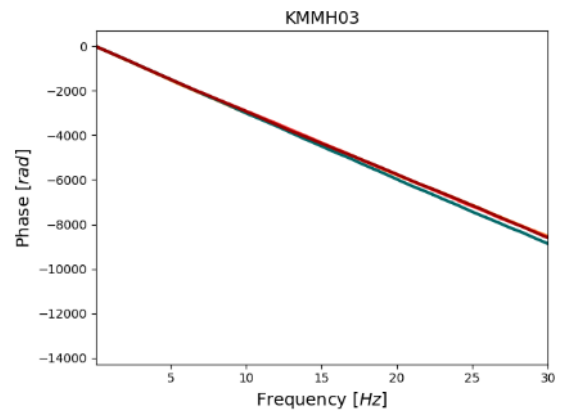
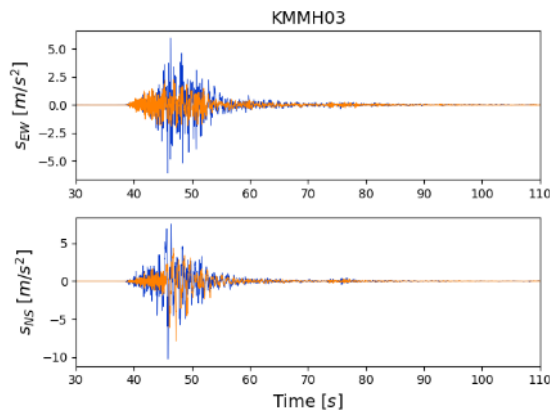
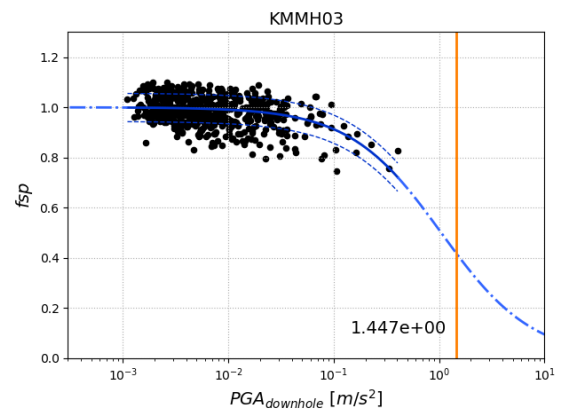
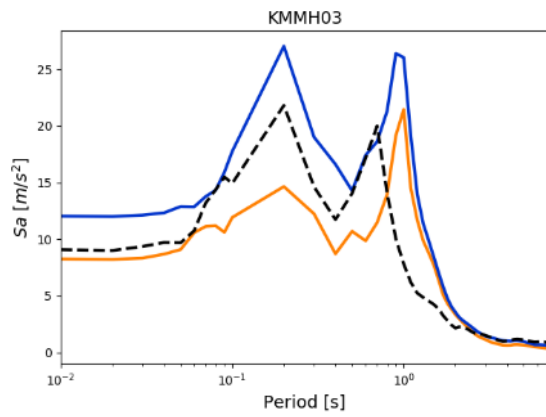
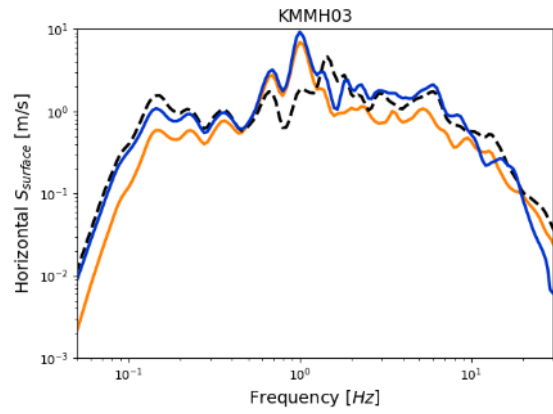
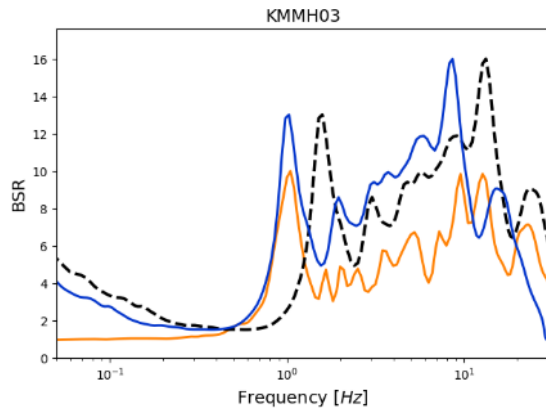


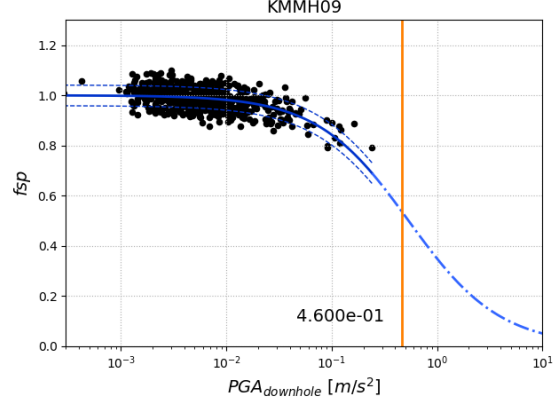
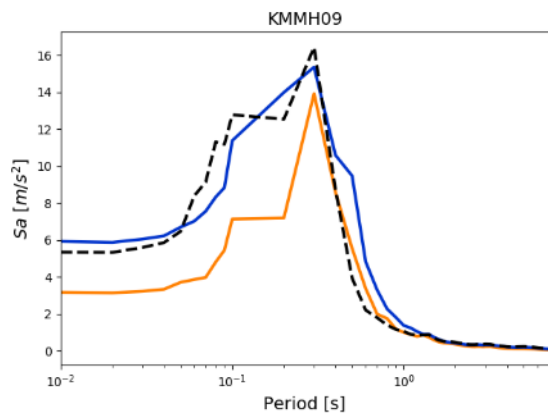
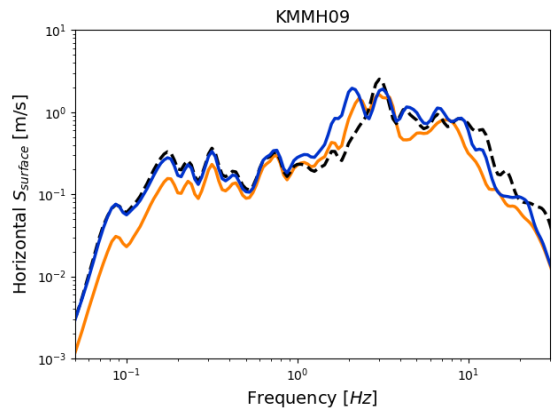
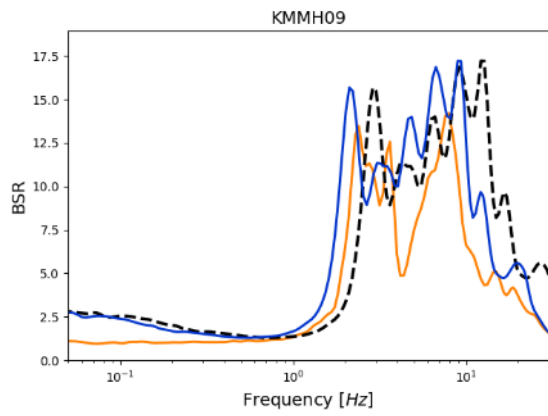
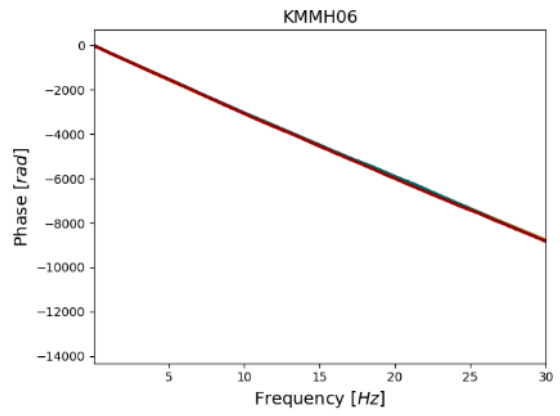
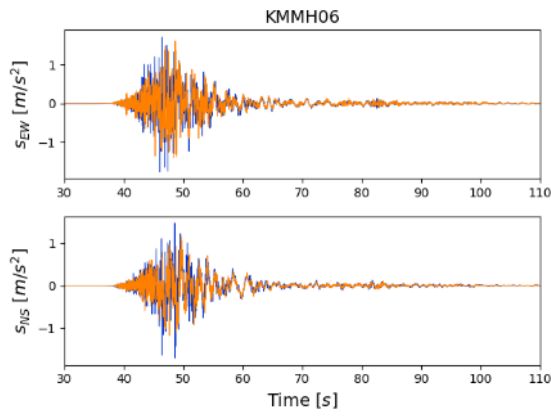
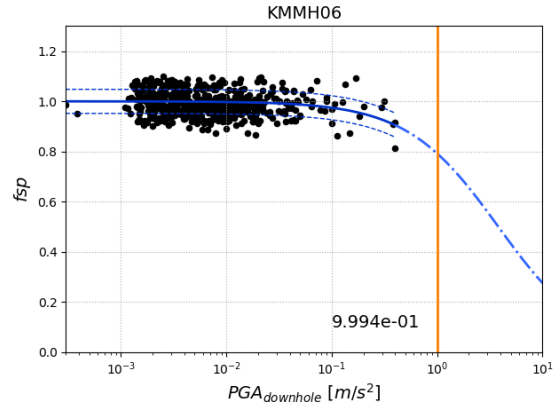
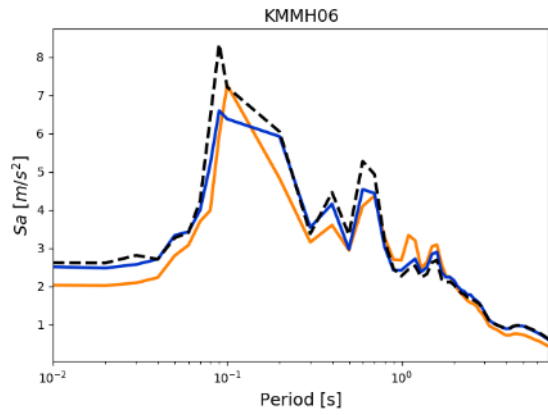


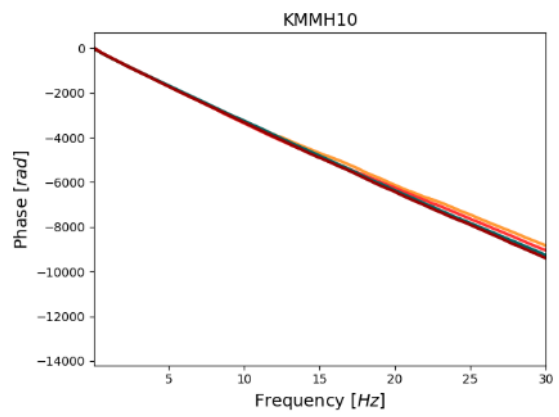
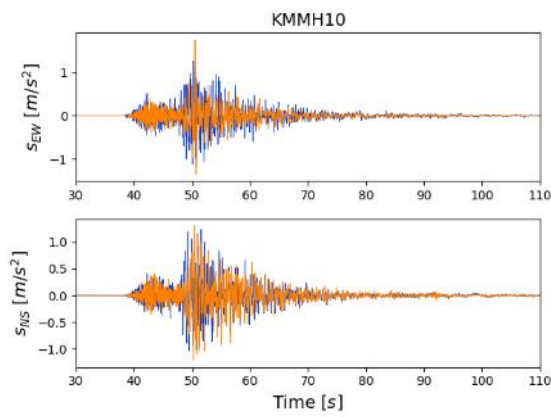
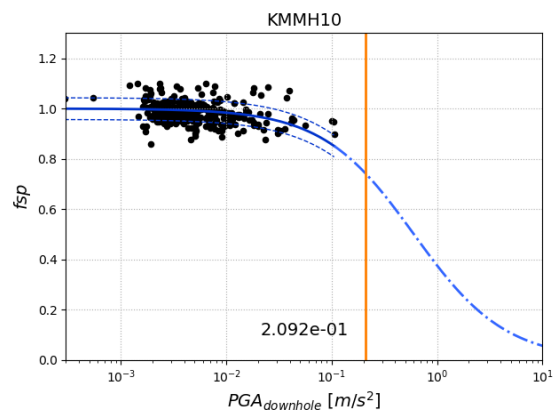
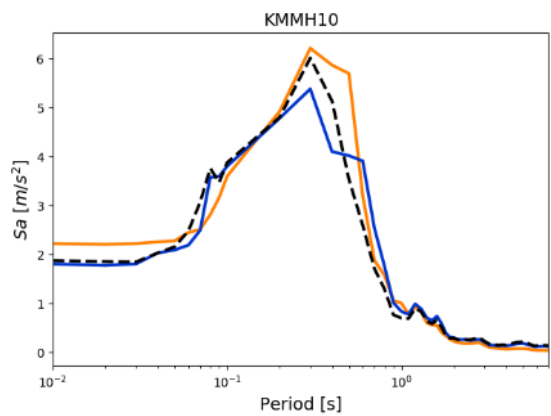
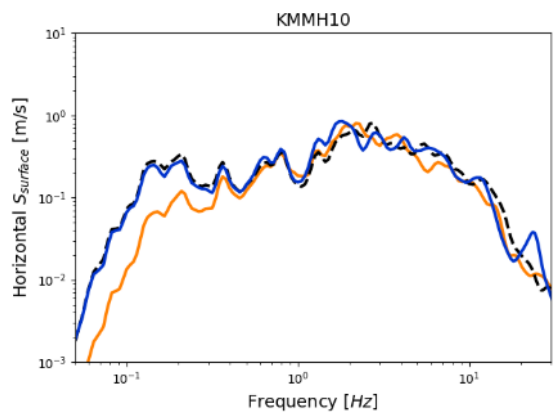
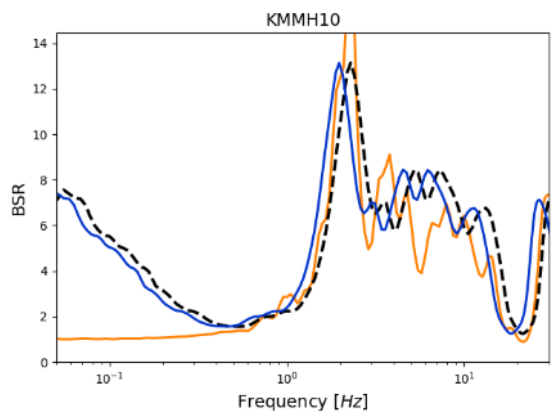
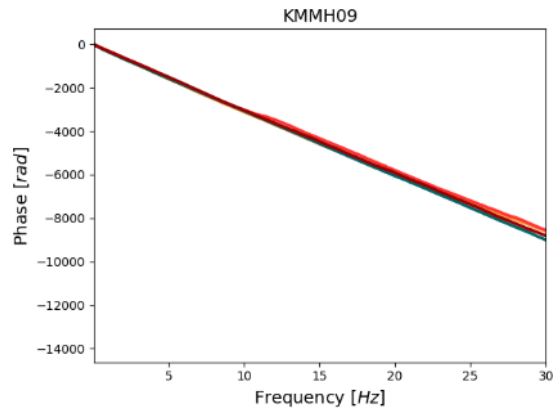
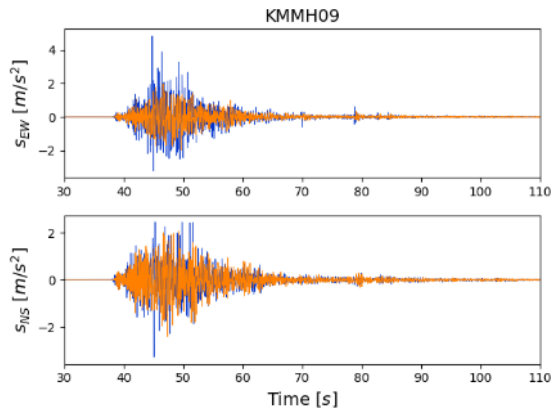


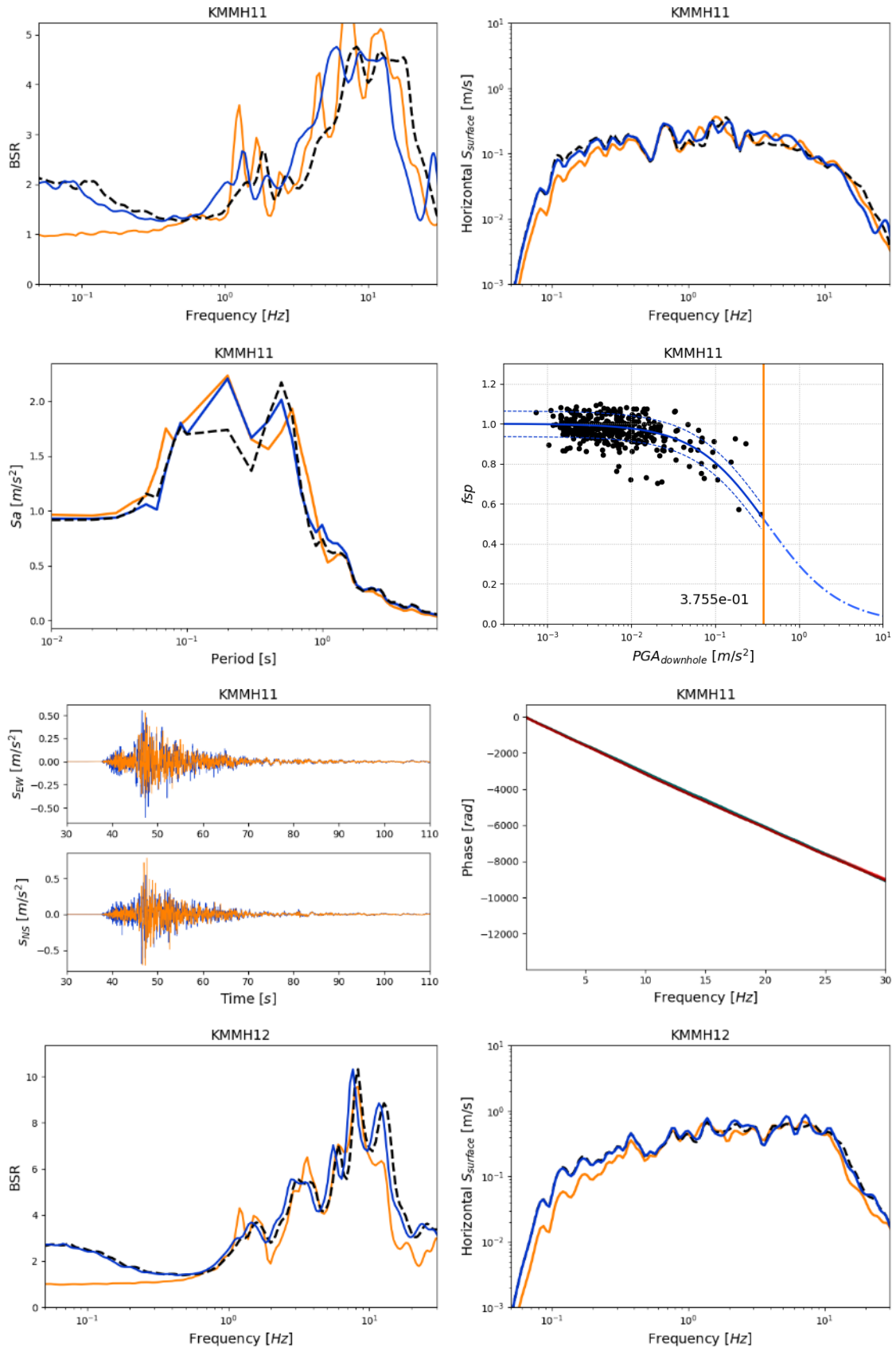


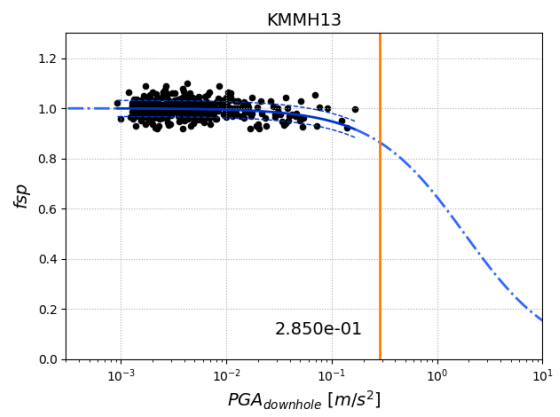
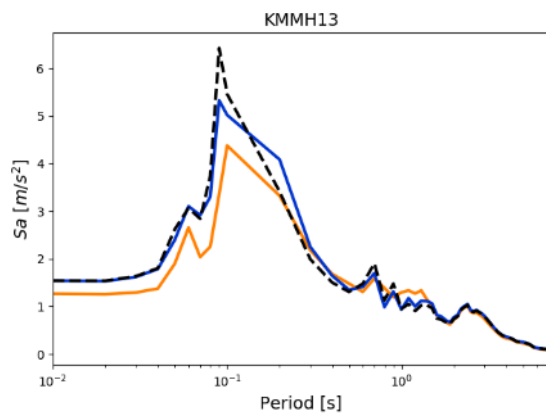
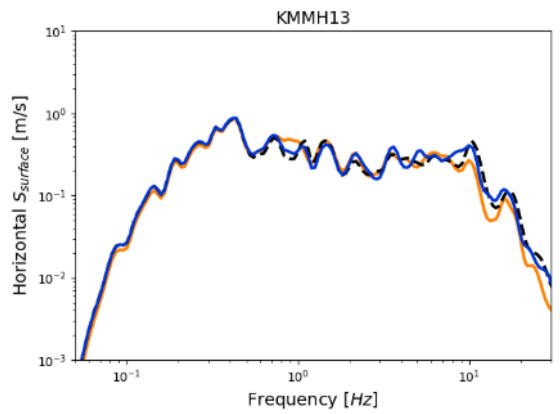
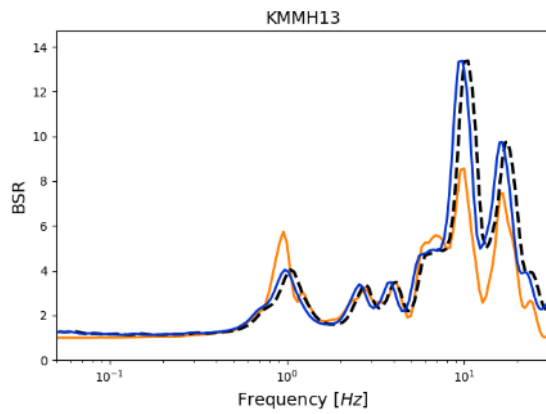
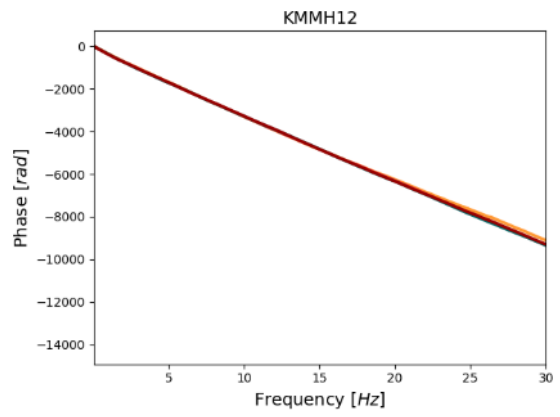
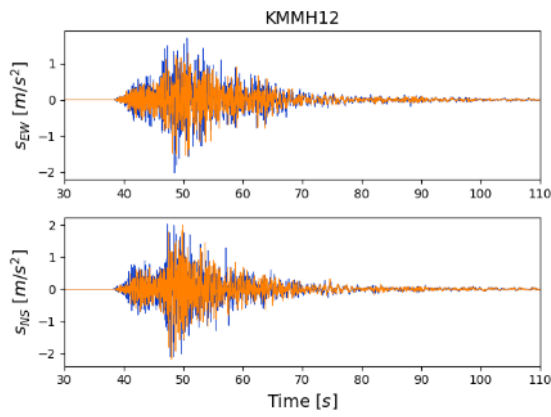
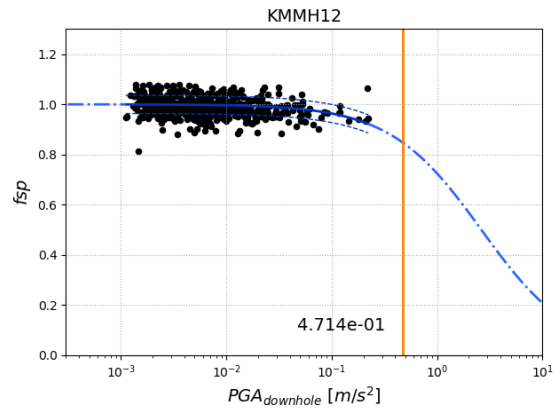
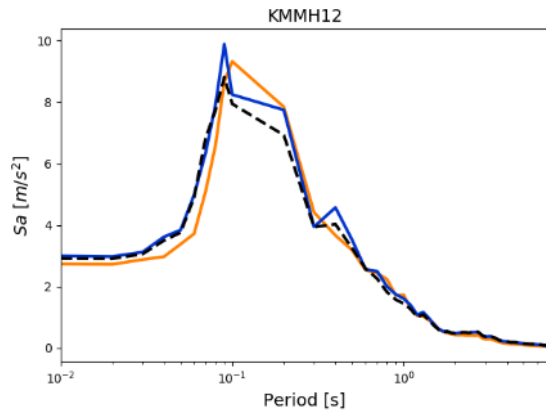


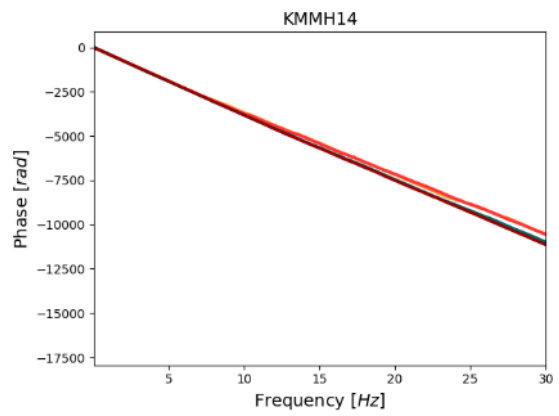
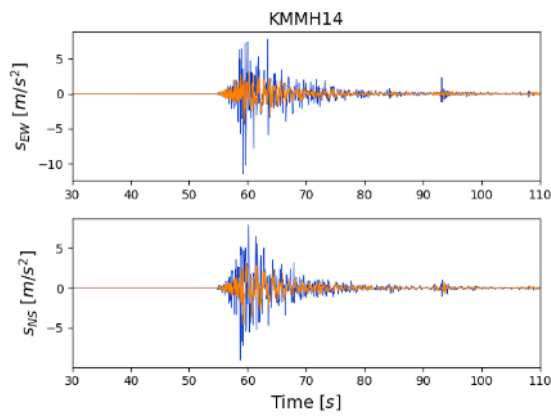
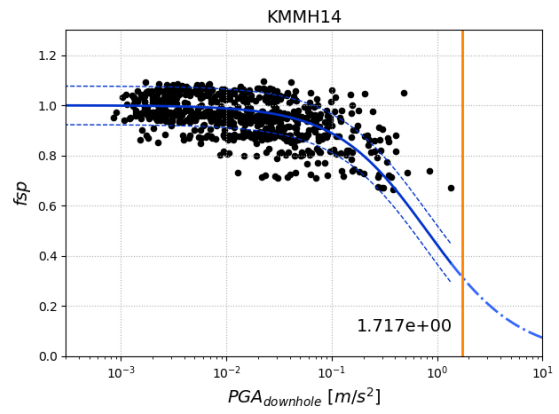
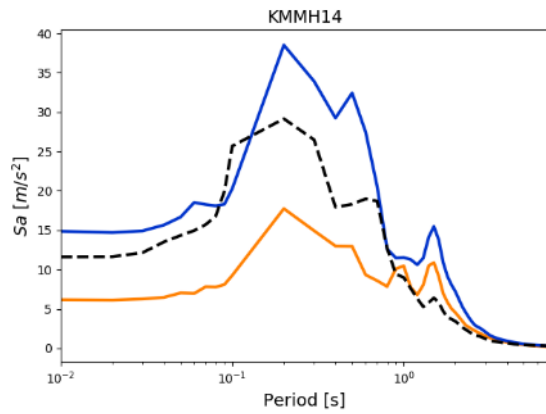
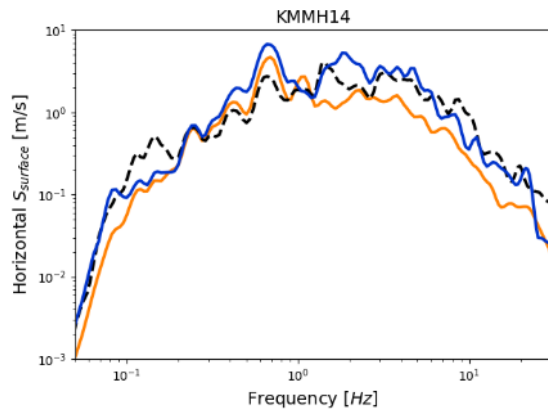
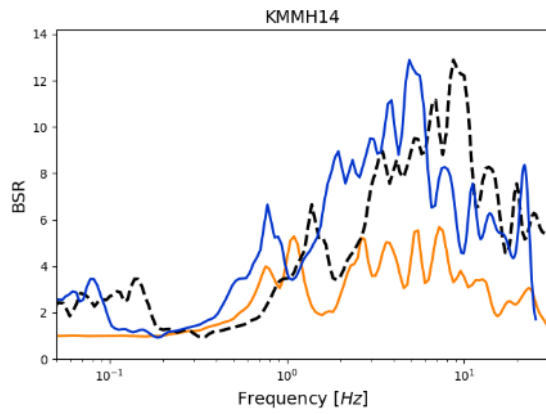
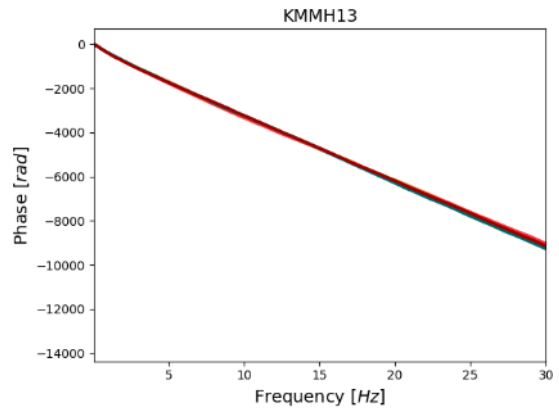
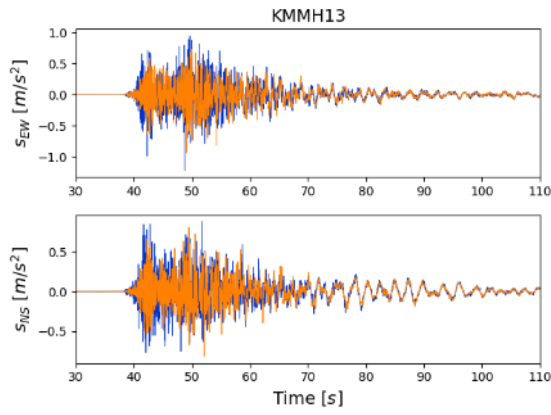


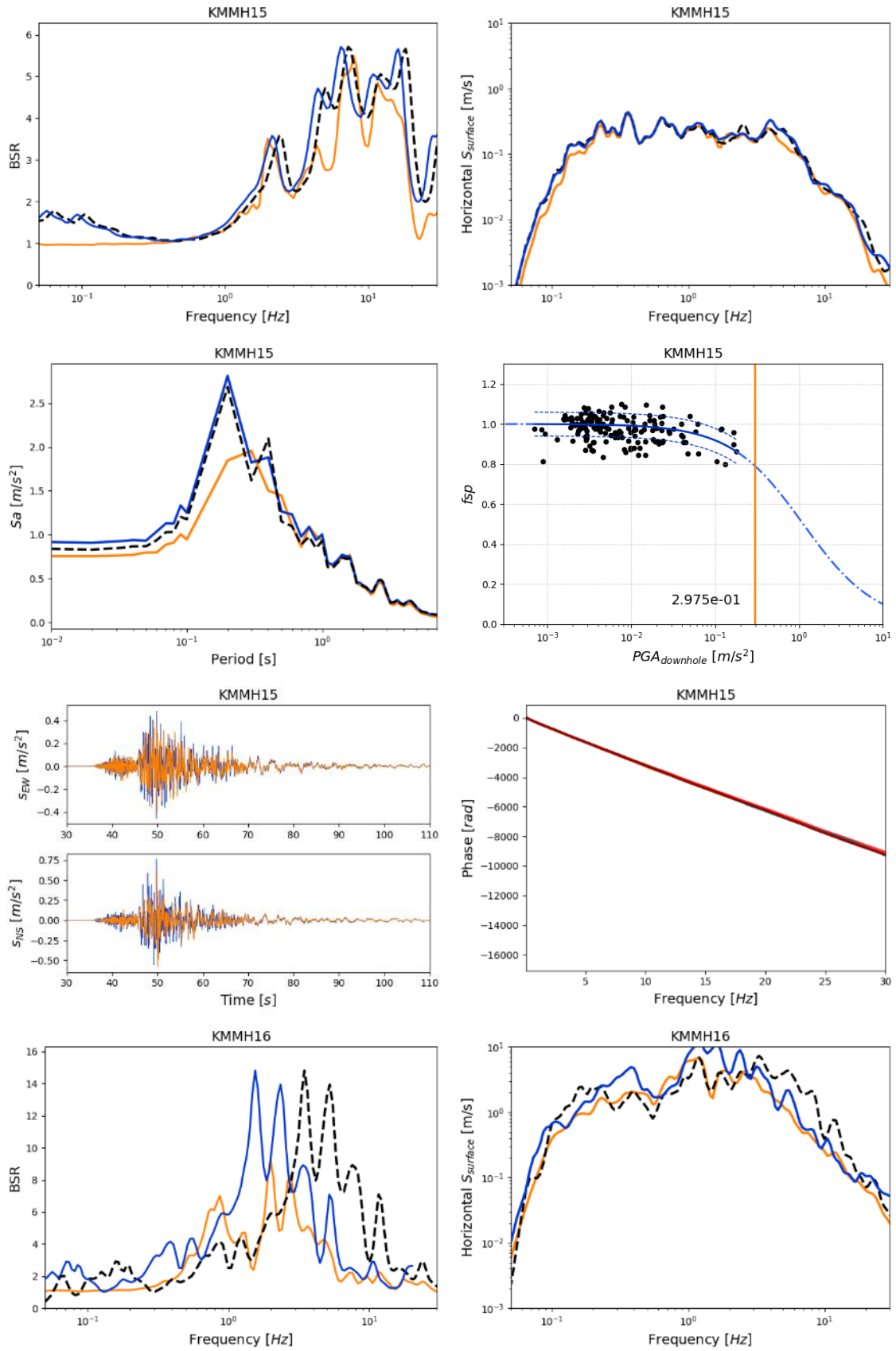


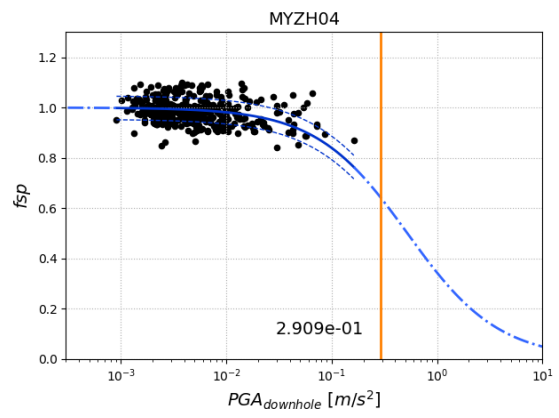
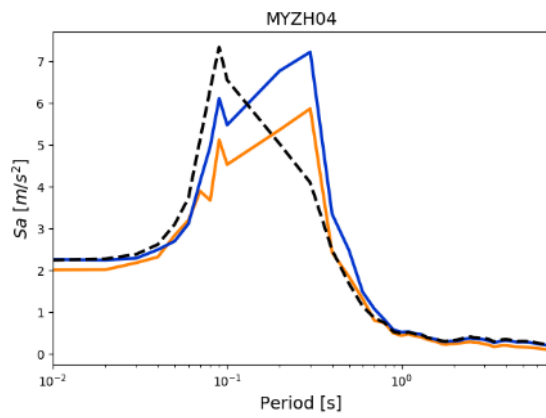
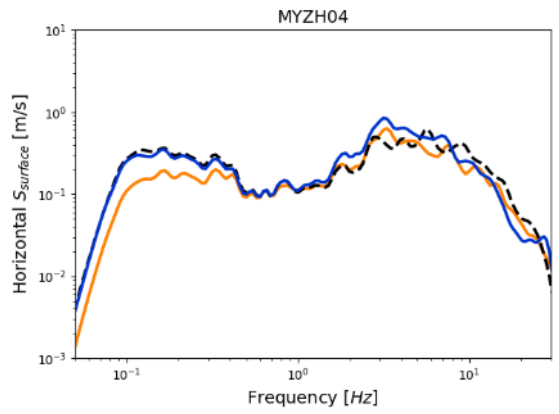
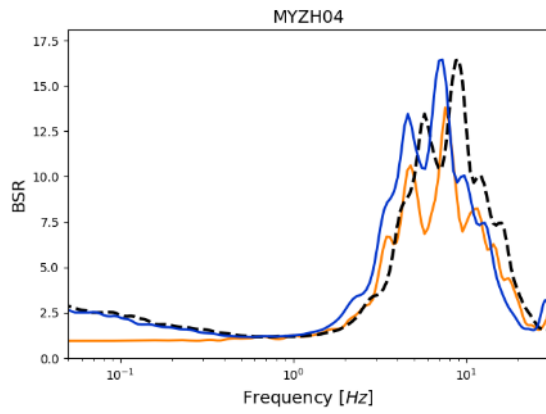
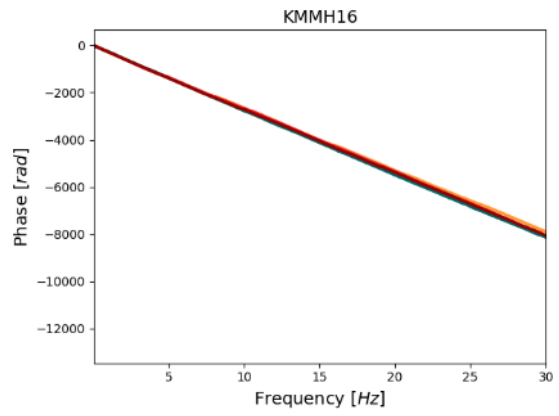
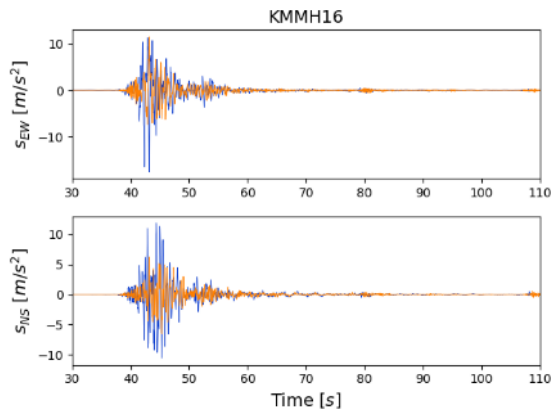
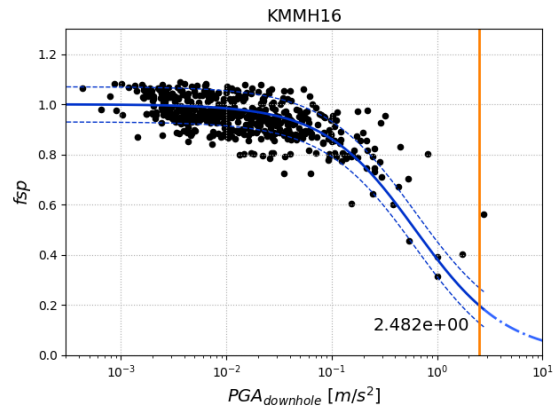
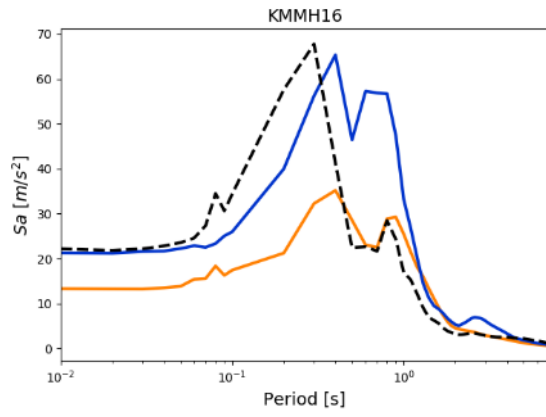


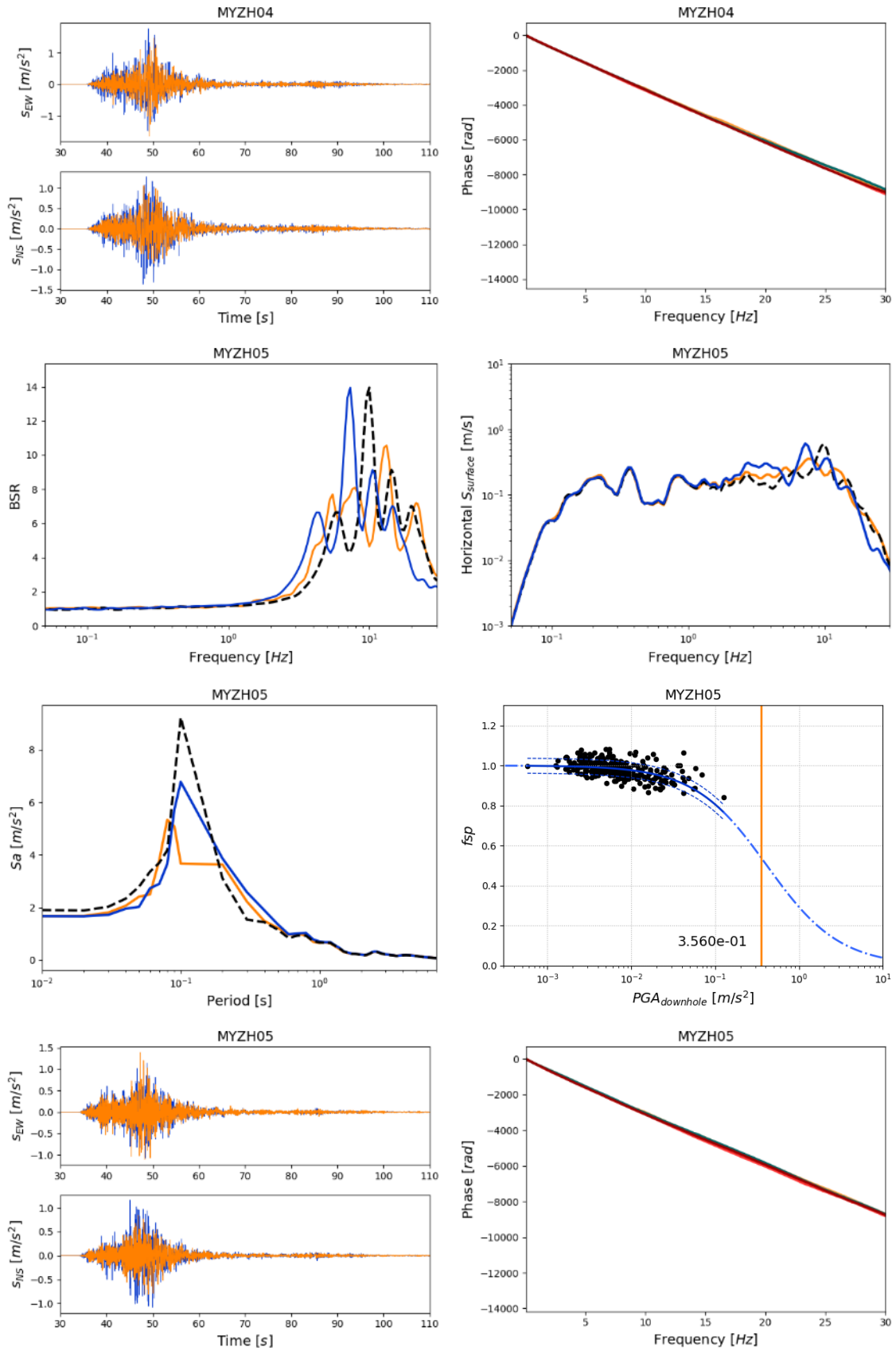


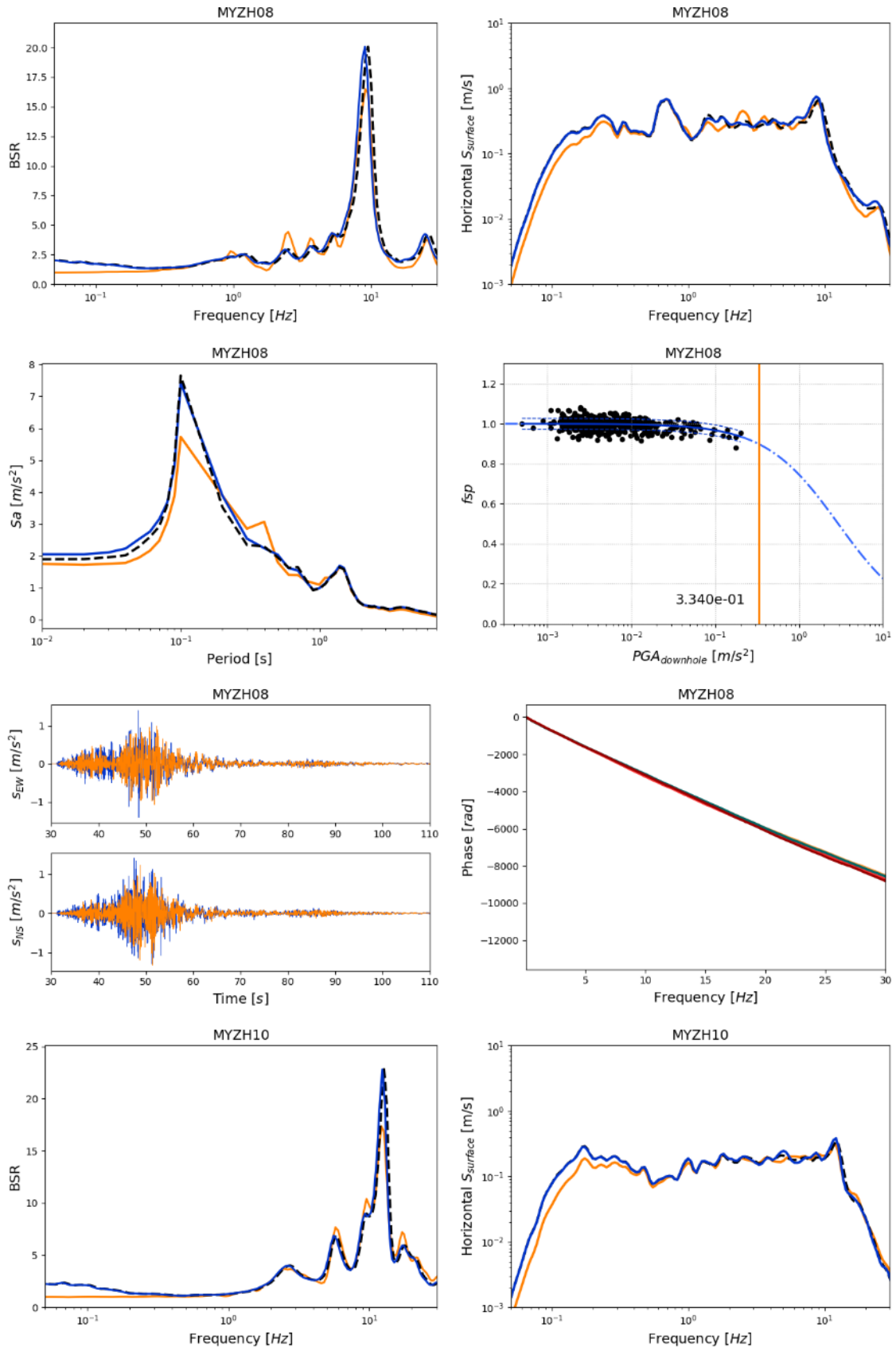


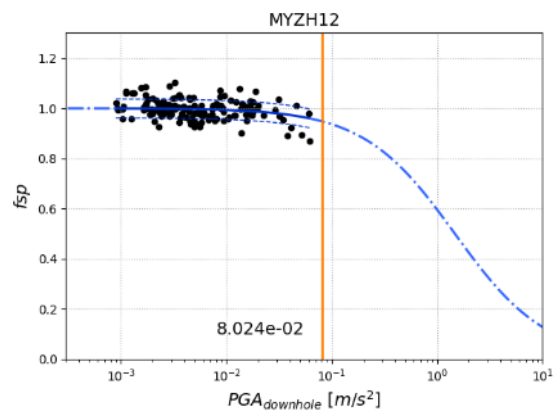
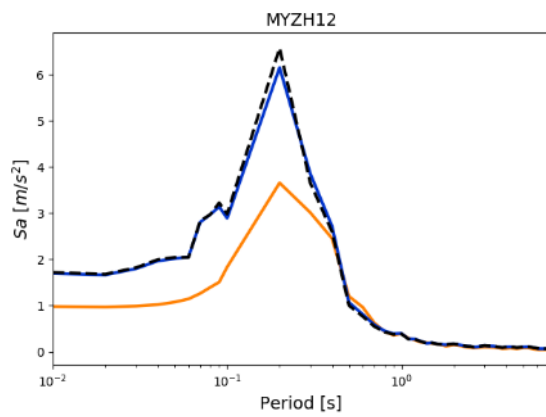
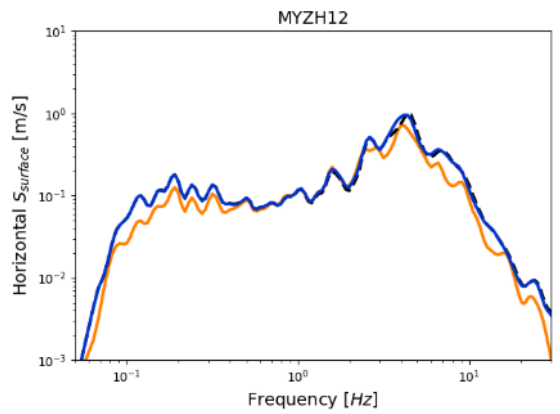
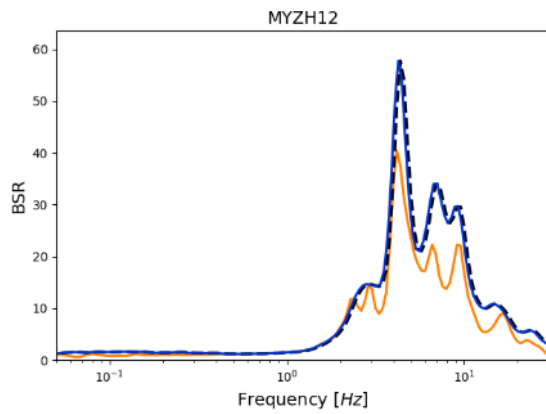
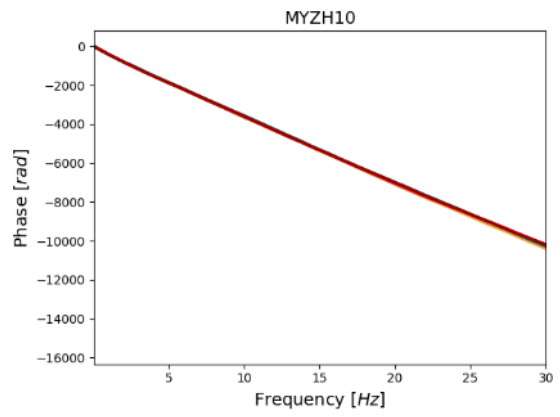
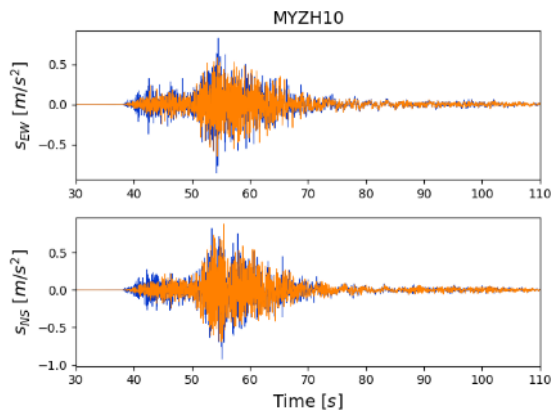
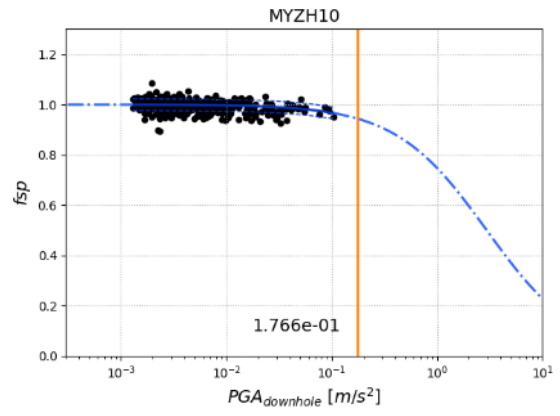
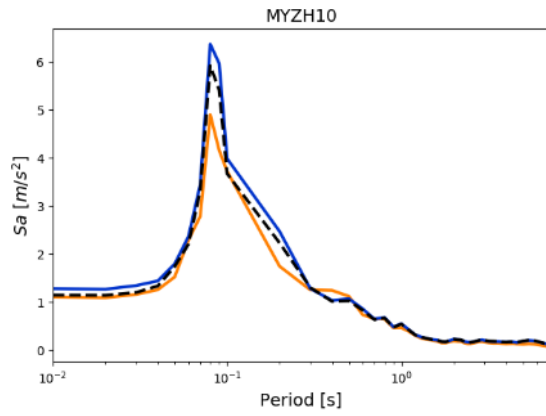


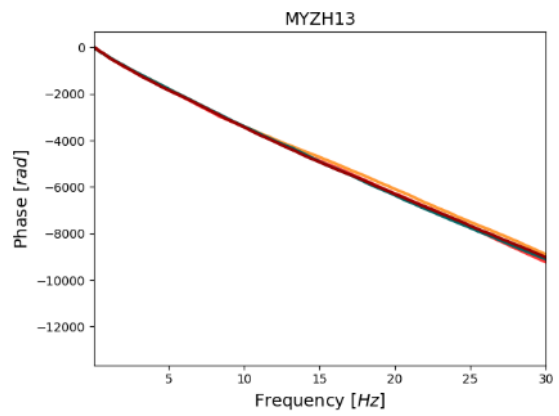
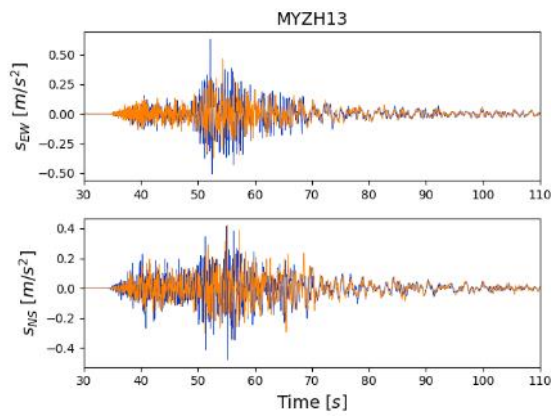
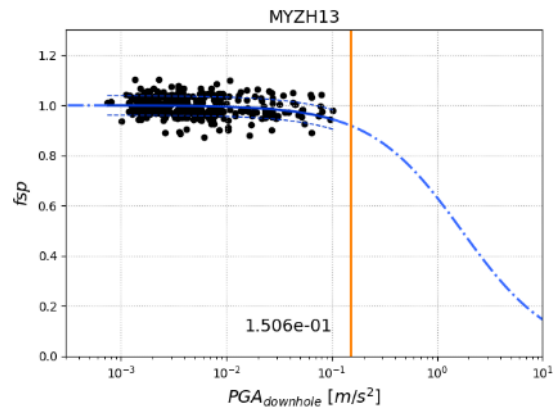
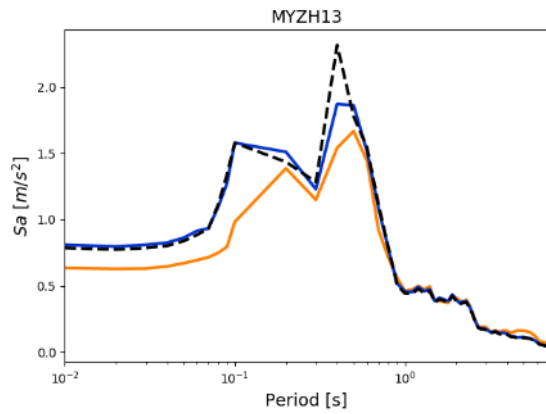
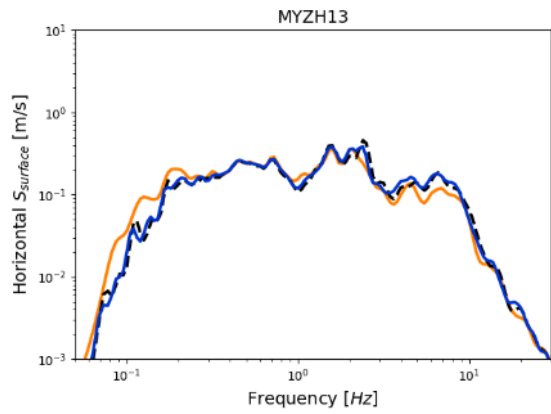
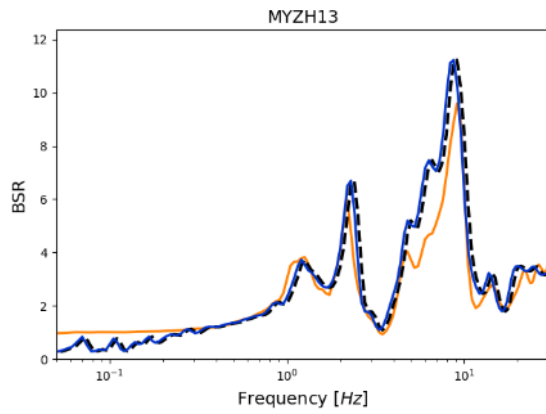
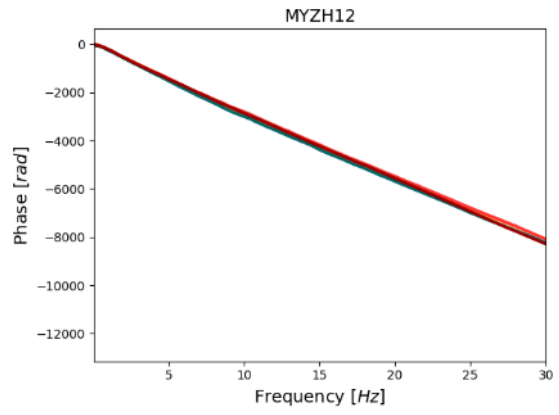
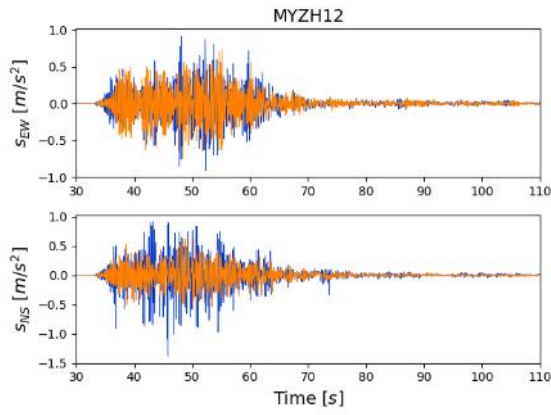


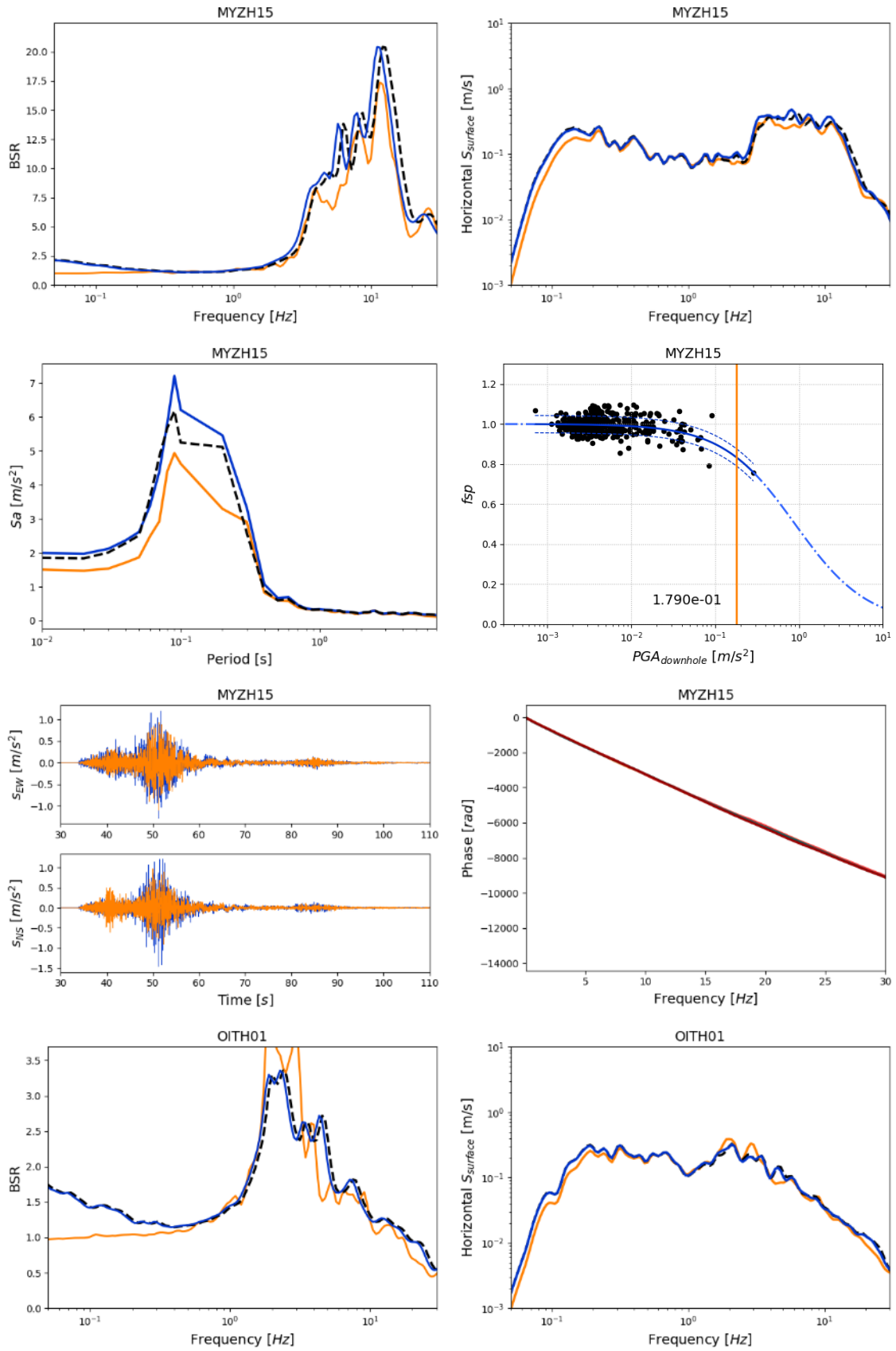


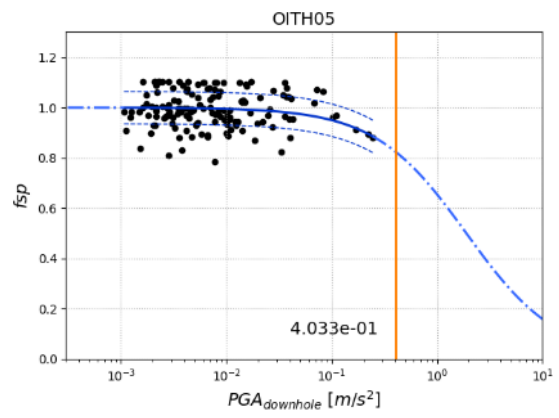
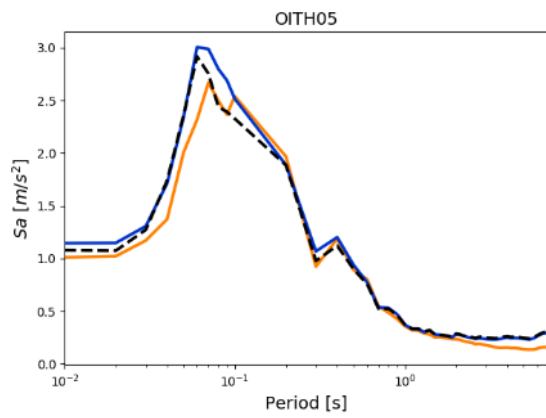
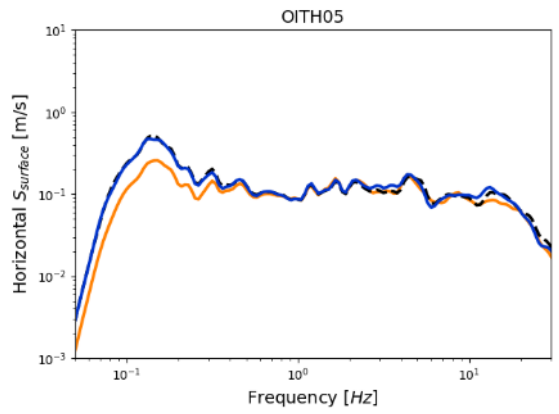
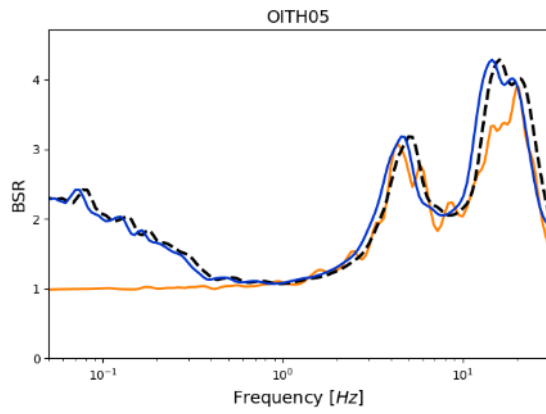
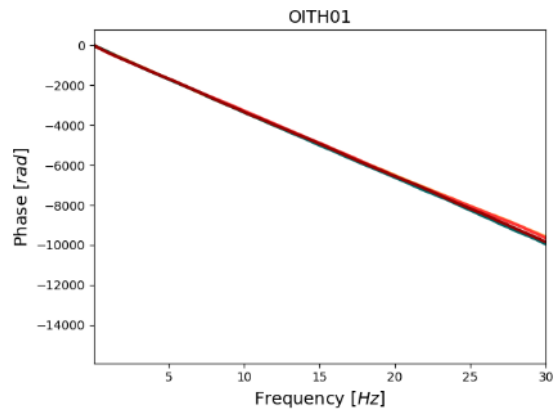
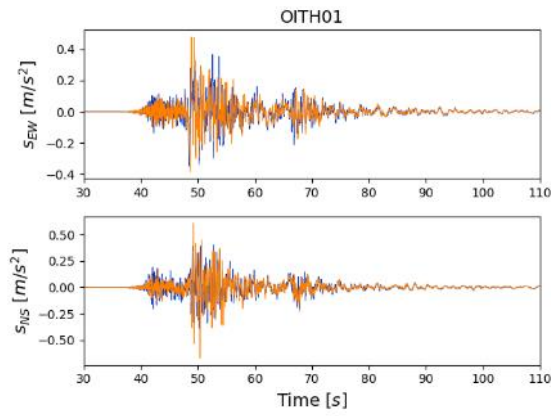
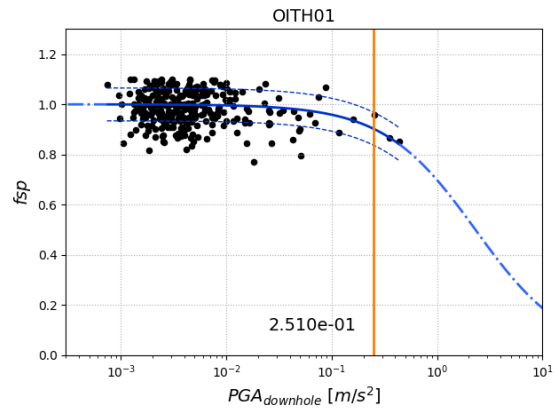
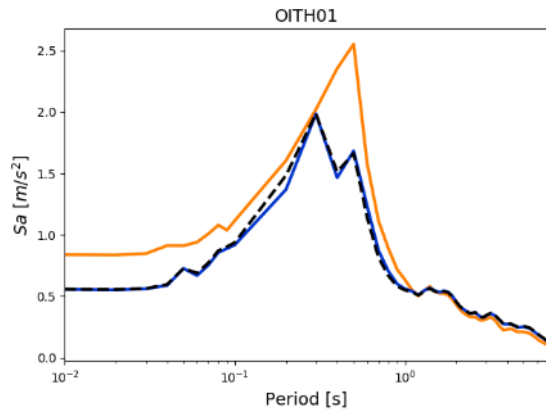


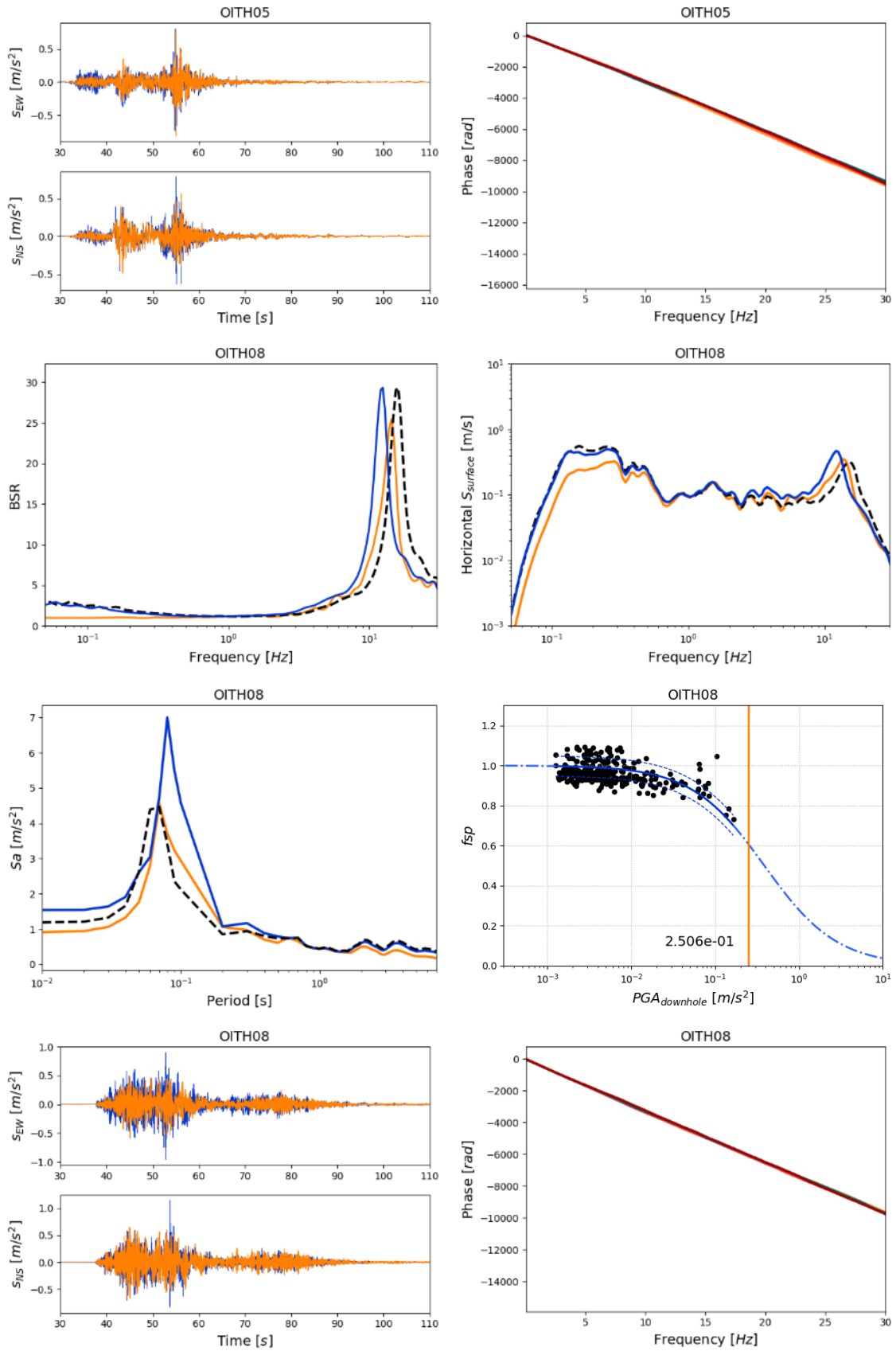


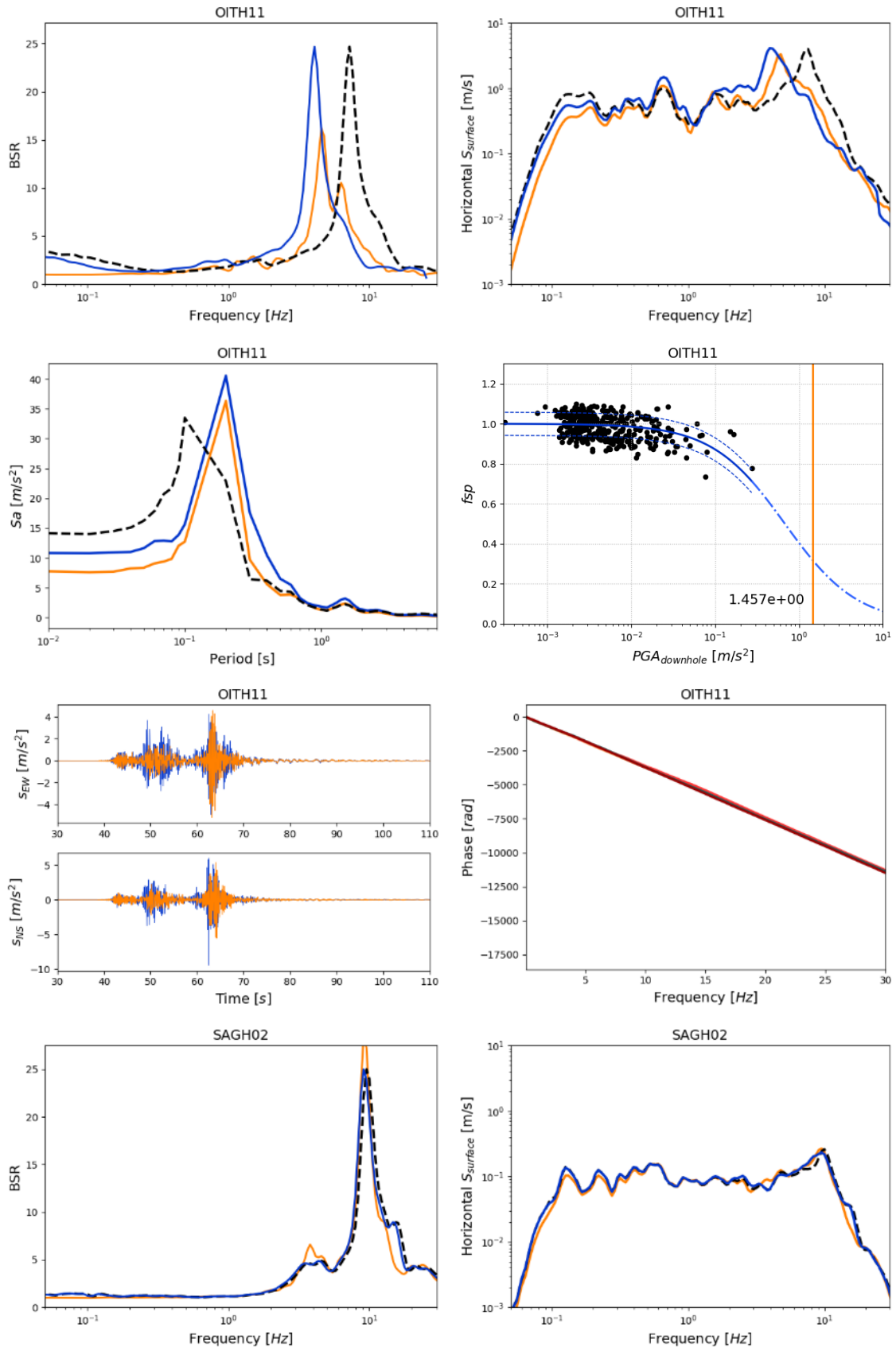


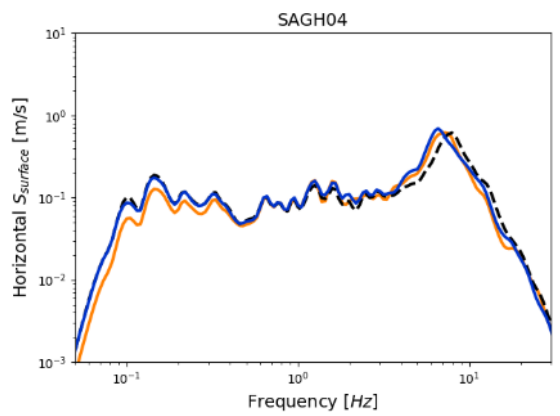
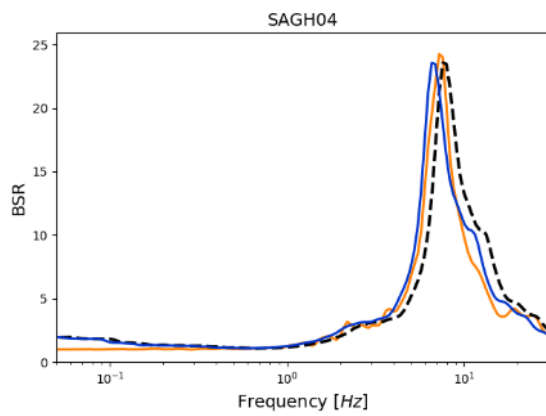
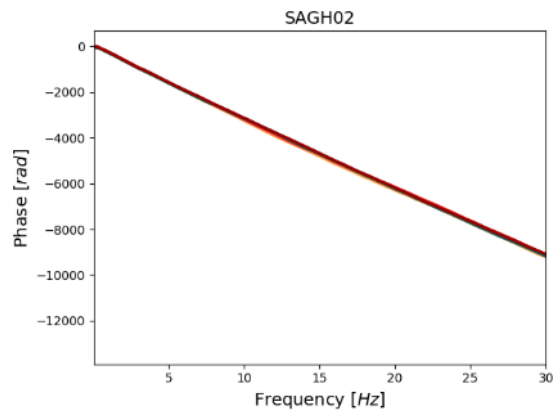
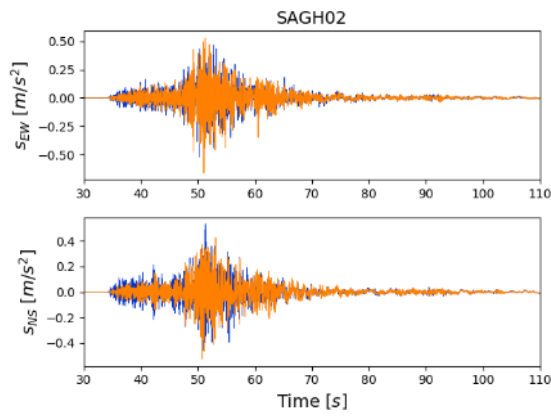
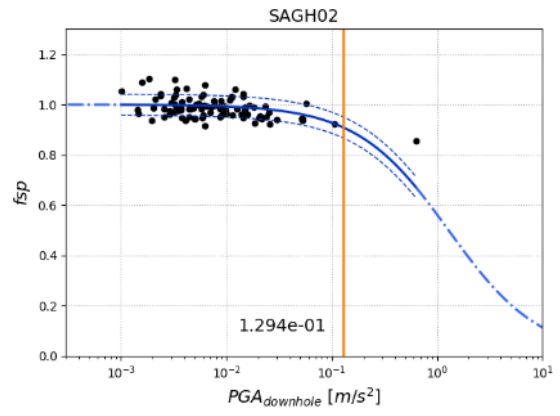
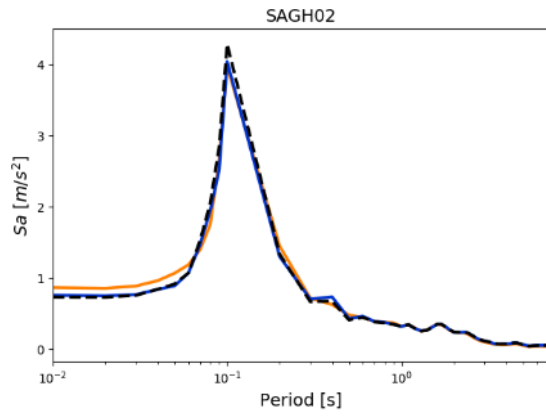


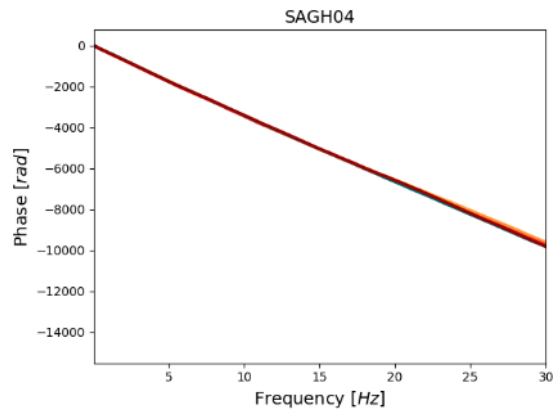
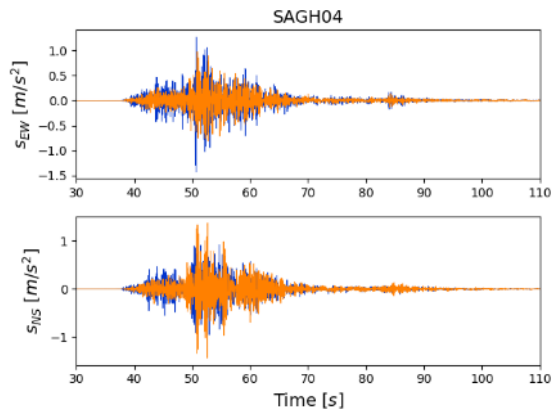
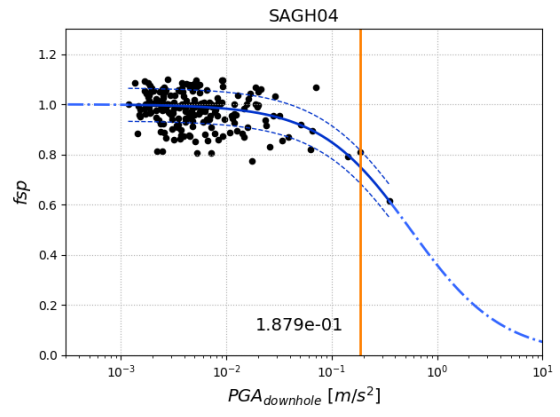
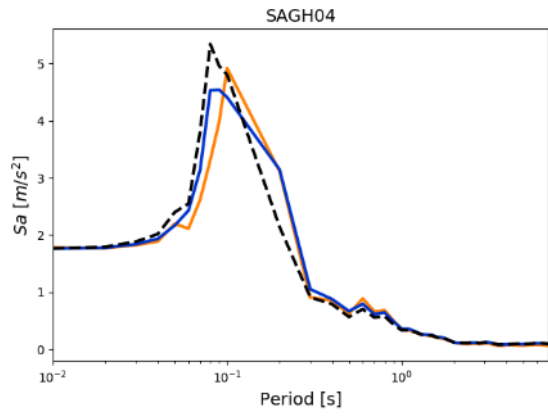












## Annex C. Fsp curves

In this annex the general data from stations with  $\sigma$  lower than 0.06 are shown.

Station	$PGA_{ref\ downhole}$ [m/s <sup>2</sup> ]	$\sigma$	#data	max $PGA_{downhole}$ [m/s <sup>2</sup> ]	Depth Downhole [m]	Vs30 [m/s]
ABSH05	4.02E+00	0.0507	86	1.51E-01	106	624
ABSH06	2.52E+00	0.0471	377	3.78E-01	100	251
ABSH08	1.01E+00	0.0577	172	2.54E-01	105	517
ABSH09	1.57E+00	0.0519	289	3.54E-01	157	394
ABSH11	5.39E-01	0.059	369	2.54E-01	122	266
ABSH12	7.22E-01	0.0459	486	3.51E-01	120	269
ABSH13	1.90E+00	0.0498	517	7.16E-01	105	464
ABSH14	1.37E+00	0.0546	362	3.74E-01	103	352
ABSH15	6.16E+00	0.0332	465	4.37E-01	100	465
AICH04	3.00E+01	0.0445	156	3.40E-01	1055	241
AICH05	2.79E+00	0.0412	292	4.56E-01	401	301
AICH06	5.64E+00	0.0423	137	8.24E-01	300	219
AICH07	4.33E+00	0.0582	286	1.84E-01	201	428
AICH09	2.13E+00	0.0391	268	1.67E-01	360	274
AICH12	4.09E+00	0.0327	227	1.35E+00	401	163
AICH14	1.39E+01	0.0437	82	3.71E-01	207	395
AICH15	6.84E-01	0.0413	252	1.27E-01	120	663
AICH16	9.18E-01	0.0239	341	1.39E-01	101	364
AICH17	6.43E-01	0.0411	256	3.44E-01	101	314
AICH19	1.46E+00	0.0598	209	1.06E-01	100	587
AICH20	7.39E-01	0.0535	199	1.41E-01	100	691
AICH21	1.44E+00	0.0401	197	2.25E-01	100	355
AKTH01	4.47E+00	0.0379	803	4.38E-01	100	475
AKTH03	2.53E+00	0.0348	753	2.91E-01	103	320
AKTH06	3.55E+00	0.0523	950	6.12E-01	100	455
AKTH07	2.02E+00	0.025	586	1.86E-01	105	350
AKTH09	4.42E-01	0.055	592	7.94E-01	101	320
AKTH10	9.30E-01	0.0498	382	2.31E-01	100	334
AKTH11	6.72E+00	0.041	65	1.61E-01	350	340
AKTH12	2.51E+00	0.0426	367	2.30E-01	100	389
AKTH13	2.40E+00	0.0583	451	2.60E-01	100	536
AKTH15	1.13E+00	0.0599	592	2.33E-01	100	498
AKTH16	1.14E+00	0.0436	1147	9.77E-01	154	375
AKTH17	2.18E+00	0.0534	1122	5.51E-01	177	289
AKTH18	2.69E+00	0.0439	937	7.64E-01	100	431
AKTH19	1.04E+00	0.0323	945	7.58E-01	180	288
AOMH01	6.60E-01	0.0411	647	3.37E-01	100	302

Station	$PGA_{ref\_downhole}$ [m/s <sup>2</sup> ]	$\sigma$	#data	max $PGA_{downhole}$ [m/s <sup>2</sup> ]	Depth Downhole [m]	Vs30 [m/s]
AOMH02	6.09E-01	0.0548	55	4.64E-02	200	872
AOMH05	1.31E+00	0.0379	1092	3.54E-01	312	238
AOMH06	1.46E+00	0.0406	966	3.32E-01	100	434
AOMH07	5.85E-01	0.0432	275	3.31E-01	109	572
AOMH08	2.35E+00	0.0366	381	1.85E-01	160	298
AOMH09	4.38E-01	0.0375	201	9.33E-02	162	261
AOMH11	2.20E+00	0.0451	932	2.39E-01	100	539
AOMH12	2.00E+00	0.0345	1295	5.16E-01	100	281
AOMH13	1.99E+00	0.0298	1579	5.43E-01	150	154
AOMH14	1.07E+00	0.0358	293	1.70E-01	100	361
AOMH15	2.06E+00	0.0547	455	2.46E-01	100	578
AOMH16	7.62E-01	0.027	1490	4.63E-01	150	226
AOMH17	2.01E+00	0.0364	1332	9.64E-01	114	378
AOMH18	6.27E-01	0.0501	549	4.24E-01	100	369
CHBH06	3.45E+00	0.0205	653	4.12E-01	180	238
CHBH14	2.35E+00	0.0426	645	6.42E-01	525	201
CHBH16	1.25E+00	0.0439	373	1.16E-01	2003	361
CHBH17	1.28E+00	0.0469	600	2.33E-01	822	526
CHBH20	3.48E+00	0.0546	458	1.82E-01	306	1909
EHHM01	7.97E-01	0.0581	212	3.45E-01	100	743
EHHM04	3.69E+00	0.0372	179	1.51E+00	200	254
EHHM05	9.63E-01	0.0579	191	1.06E+00	134	362
EHHM06	5.88E-01	0.0442	193	3.47E-01	200	717
EHHM08	1.02E+00	0.0427	182	6.88E-01	100	364
EHHM09	9.59E-01	0.039	149	3.95E-01	150	267
EHHM10	6.33E-01	0.0378	181	1.65E-01	100	318
FKIH01	2.58E+00	0.0412	157	6.98E-01	100	716
FKIH02	1.54E+00	0.034	64	7.15E-02	100	343
FKIH03	1.57E+00	0.0577	78	2.21E-01	200	760
FKIH04	2.06E+00	0.0485	159	2.87E-01	200	300
FKIH05	3.63E+00	0.0257	132	3.15E-01	122	187
FKIH07	1.86E+00	0.0572	196	3.35E-01	104	384
FKOH03	7.04E-01	0.0468	333	5.55E-01	100	497
FKOH04	1.35E+00	0.0454	121	3.22E-01	100	260
FKOH05	1.34E+00	0.0495	133	2.57E-01	100	777
FKOH06	8.32E+00	0.038	560	5.00E-01	303	1002
FKOH07	2.73E+00	0.0309	311	2.32E-01	437	271
FKOH08	8.25E-01	0.0407	367	3.06E-01	100	536
FKOH10	5.17E-01	0.0467	505	5.53E-01	200	921
FKSH02	2.54E+00	0.0426	456	9.24E-01	100	508

Station	$PGA_{ref}^{downhole}$ [m/s <sup>2</sup> ]	$\sigma$	#data	max $PGA_{downhole}$ [m/s <sup>2</sup> ]	Depth Downhole [m]	Vs30 [m/s]
FKSH03	7.48E+00	0.0428	1226	5.99E-01	127	350
FKSH04	9.80E-01	0.0431	651	3.64E-01	268	246
FKSH05	6.39E-01	0.0541	627	5.38E-01	105	596
FKSH08	8.77E-01	0.044	1373	1.22E+00	105	563
FKSH10	7.24E-01	0.0492	2715	1.86E+00	200	487
FKSH11	1.41E+00	0.0361	1930	1.99E+00	115	240
FKSH12	5.56E-01	0.0433	2592	1.07E+00	105	449
FKSH13	1.11E+00	0.0412	347	1.60E-01	105	562
FKSH14	1.09E+00	0.0412	2062	1.37E+00	147	237
FKSH15	1.54E+00	0.0421	325	2.25E-01	100	804
FKSH16	1.45E+00	0.0433	804	9.95E-01	300	532
FKSH17	1.06E+00	0.0252	1962	9.19E-01	100	544
FKSH19	1.19E+00	0.0295	2392	3.70E+00	100	338
GIFH04	6.05E-01	0.0545	128	2.09E-01	100	380
GIFH05	9.47E-01	0.0524	81	1.04E-01	100	262
GIFH07	9.12E-01	0.0477	197	3.09E-01	100	424
GIFH08	1.09E+00	0.0568	258	4.24E-01	100	385
GIFH09	3.10E+00	0.0576	219	1.86E-01	1508	216
GIFH10	3.94E+00	0.0424	161	1.96E-01	100	385
GIFH14	1.07E+00	0.0474	178	9.65E-01	100	627
GIFH15	1.17E+00	0.0457	280	2.27E-01	104	369
GIFH16	1.43E+00	0.0525	227	3.55E-01	100	831
GIFH17	4.77E-01	0.0528	136	1.05E-01	100	429
GIFH18	7.70E-01	0.0565	321	1.96E-01	107	553
GIFH20	6.18E-01	0.0526	382	3.06E-01	128	810
GIFH21	2.97E-01	0.049	145	1.94E-01	200	964
GIFH22	1.04E+00	0.0513	124	3.77E-01	100	807
GIFH23	1.10E+00	0.0517	191	2.34E-01	100	588
GIFH25	5.15E-01	0.0579	170	1.77E-01	102	469
GIFH26	1.28E+00	0.0343	191	3.13E-01	100	425
GIFH27	6.13E-01	0.0464	273	1.92E-01	200	685
GIFH28	4.36E+00	0.055	265	2.32E-01	400	367
GNMH08	1.19E+00	0.038	569	2.36E-01	150	339
GNMH09	6.30E-01	0.0366	626	2.03E-01	110	624
GNMH10	3.89E-01	0.0388	234	9.11E-02	100	668
GNMH11	2.13E+01	0.0337	852	3.23E-01	200	421
GNMH12	6.15E-01	0.043	740	2.82E-01	102	407
GNMH13	8.51E-01	0.046	522	1.71E-01	204	323
GNMH14	7.16E-01	0.0494	907	3.44E-01	200	983
HDKH01	1.99E+00	0.0439	552	6.16E-01	100	368

Station	$PGA_{ref\_downhole}$ [m/s <sup>2</sup> ]	$\sigma$	#data	max $PGA_{downhole}$ [m/s <sup>2</sup> ]	Depth Downhole [m]	Vs30 [m/s]
HDKH02	2.27E+00	0.0307	356	6.63E-01	110	444
HDKH03	8.68E-01	0.037	483	2.22E-01	106	341
HDKH04	6.68E-01	0.0498	566	1.02E+00	220	235
HDKH05	1.33E+00	0.0387	459	3.97E-01	100	766
HDKH07	4.50E+00	0.0464	813	8.79E-01	101	459
HRSH03	4.15E-01	0.055	164	4.93E-01	200	487
HRSH06	1.79E+00	0.0305	139	6.47E-01	100	279
HRSH07	1.40E+00	0.0312	346	8.93E-01	102	461
HRSH10	4.95E-01	0.0418	203	3.55E-01	100	265
HRSH11	1.72E+00	0.0339	168	1.87E-01	100	689
HRSH13	2.93E-01	0.0444	46	1.70E-01	200	399
HRSH14	1.78E+00	0.0458	174	3.19E-01	100	550
HRSH16	7.28E-01	0.0424	112	1.67E-01	100	455
HRSH18	1.33E+00	0.0347	165	2.76E-01	100	402
HYGH03	5.85E-01	0.0554	140	2.61E-01	100	509
HYGH04	5.99E-01	0.0548	192	2.02E-01	100	472
HYGH05	3.84E+00	0.0332	70	2.51E-01	100	533
HYGH08	1.47E+00	0.0444	272	2.41E-01	110	285
HYGH09	1.34E+01	0.0588	221	3.60E-01	100	364
HYGH10	3.80E+00	0.0337	207	2.94E-01	100	224
HYGH11	1.17E+00	0.0552	124	8.86E-02	200	271
HYGH13	5.03E-01	0.048	79	1.35E-01	100	381
HYMH01	2.25E+01	0.0541	153	8.11E-02	112	395
HYMH02	4.20E+00	0.0469	227	8.45E-02	101	498
HYMH03	8.03E-01	0.0526	69	4.22E-02	100	603
IBRH10	8.31E+00	0.0279	1870	9.94E-01	900	144
IBRH11	2.25E+00	0.0258	2581	2.68E+00	103	242
IBRH12	1.00E+00	0.0468	2477	1.52E+00	200	486
IBRH13	1.43E+00	0.0511	2340	2.69E+00	100	335
IBRH14	6.20E-01	0.0456	2063	1.17E+00	100	829
IBRH15	1.08E+00	0.039	2478	1.46E+00	107	450
IBRH16	4.91E-01	0.0579	2444	1.30E+00	300	626
IBRH17	2.65E+00	0.0236	1896	1.26E+00	510	301
IBRH18	7.63E-01	0.0468	2056	1.60E+00	504	559
IBRH20	1.36E+01	0.0383	1073	9.52E-01	923	244
IBUH01	1.23E+00	0.0355	580	5.47E-01	101	307
IBUH03	1.12E+00	0.0534	302	5.65E-01	153	111
IBUH04	1.26E+00	0.0383	92	1.17E-01	102	352
IBUH05	1.66E+00	0.043	611	2.67E+00	177	379
IBUH06	9.43E-01	0.0355	344	2.24E-01	562	304

Station	$PGA_{ref\_downhole}$ [m/s <sup>2</sup> ]	$\sigma$	#data	max $PGA_{downhole}$ [m/s <sup>2</sup> ]	Depth Downhole [m]	Vs30 [m/s]
IBUH07	2.49E+00	0.0348	339	8.92E-01	200	259
IKRH02	2.91E+00	0.0287	329	3.67E-01	127	128
IKRH03	2.05E+00	0.0334	543	3.75E-01	252	326
ISKH02	5.01E+00	0.0483	135	2.55E+00	102	721
ISKH03	2.00E+00	0.0433	313	2.84E-01	207	311
ISKH04	1.20E+00	0.0565	214	7.89E-01	116	444
ISKH05	5.34E-01	0.0515	149	3.93E-01	105	681
ISKH06	5.96E+00	0.0379	254	5.62E-01	200	500
ISKH08	7.20E-01	0.0473	79	7.89E-02	100	427
ISKH09	9.80E-01	0.0547	228	4.68E-01	106	636
IWTH01	5.94E-01	0.046	1197	4.88E-01	200	438
IWTH02	1.01E+00	0.0309	1309	4.52E-01	102	390
IWTH04	1.10E+00	0.0284	2127	1.61E+00	106	456
IWTH05	1.56E+00	0.0321	1791	1.79E+00	100	429
IWTH06	1.03E+00	0.0432	1071	4.19E-01	100	432
IWTH07	2.19E+00	0.0423	1290	7.44E-01	120	396
IWTH08	8.64E-01	0.0237	983	5.94E-01	100	305
IWTH09	7.32E-01	0.0446	1453	1.26E+00	100	967
IWTH10	9.94E-01	0.0409	1018	2.40E-01	100	496
IWTH11	1.92E+00	0.0299	1221	3.76E-01	300	343
IWTH12	1.74E+00	0.04	1309	8.24E-01	100	368
IWTH14	6.04E-01	0.0537	1416	9.11E-01	100	816
IWTH15	2.98E+00	0.0307	2110	1.19E+00	122	338
IWTH16	2.01E+00	0.0294	1731	5.51E-01	150	535
IWTH19	2.49E+00	0.0419	1731	9.58E-01	101	482
IWTH20	3.51E+00	0.0302	1824	2.08E+00	156	289
IWTH23	5.83E-01	0.0581	2068	1.52E+00	103	923
IWTH24	2.14E+00	0.0437	2163	2.45E+00	150	486
IWTH27	9.96E-01	0.0451	2319	1.67E+00	100	670
IWTH28	3.13E+00	0.0429	991	1.26E+00	263	417
KGSH01	1.29E+00	0.0594	243	1.55E-01	202	603
KGSH03	1.22E+00	0.0597	340	5.62E-01	100	1196
KGSH04	2.14E+00	0.0412	180	2.88E-01	100	280
KGSH05	6.80E-01	0.0518	335	2.12E-01	107	477
KGSH06	6.70E-01	0.0571	164	3.17E-01	203	455
KGSH07	1.91E+00	0.0542	242	6.49E-01	302	260
KGSH08	2.83E+01	0.0404	199	1.84E-01	150	nan
KGSH09	1.57E+00	0.0331	166	7.36E-01	100	409
KGSH11	1.24E+00	0.0442	118	5.44E-02	200	430
KGSH13	4.09E+00	0.0306	50	9.91E-02	101	300

Station	$PGA_{ref\ downhole}$ [m/s <sup>2</sup> ]	$\sigma$	#data	max $PGA_{downhole}$ [m/s <sup>2</sup> ]	Depth Downhole [m]	Vs30 [m/s]
KGWH01	1.10E+00	0.0551	184	2.60E-01	117	255
KGWH04	4.57E-01	0.0598	59	1.56E-01	105	407
KKWH02	9.73E-01	0.0528	83	7.42E-02	112	657
KKWH08	7.62E-01	0.0232	479	4.48E-01	100	311
KKWH10	4.46E+00	0.0538	70	1.60E-01	105	328
KKWH11	1.96E+00	0.014	65	7.55E-02	105	243
KKWH13	2.22E+00	0.0521	141	1.34E-01	168	356
KKWH14	9.20E-01	0.0598	288	2.61E-01	150	538
KKWH15	1.87E+00	0.0456	100	6.97E-02	148	529
KMMH01	7.21E-01	0.0483	363	4.59E-01	100	575
KMMH02	3.61E+00	0.0398	633	1.99E+00	124	577
KMMH03	1.06E+00	0.0563	571	1.45E+00	200	421
KMMH04	3.61E+00	0.0293	231	3.28E-01	127	120
KMMH05	3.93E+00	0.0374	228	6.52E-01	100	230
KMMH06	4.33E+00	0.0479	570	9.99E-01	111	568
KMMH08	2.44E+00	0.0534	193	1.78E-01	103	525
KMMH09	5.58E-01	0.0418	583	4.60E-01	100	400
KMMH10	6.79E-01	0.0435	320	2.09E-01	300	463
KMMH12	2.71E+00	0.0365	624	4.71E-01	123	410
KMMH13	2.37E+00	0.0322	421	2.85E-01	177	403
KMMH17	2.86E+00	0.0489	96	1.39E-01	100	727
KNGH18	8.36E-01	0.0437	873	3.16E-01	100	388
KNGH19	1.04E+00	0.0591	539	3.47E-01	100	731
KNGH20	6.93E-01	0.0419	621	3.28E-01	106	273
KNGH21	7.75E-01	0.0479	676	3.26E-01	210	792
KOCH01	8.02E-01	0.0541	116	1.33E-01	200	359
KOCH03	7.26E-01	0.0548	192	3.06E-01	100	668
KOCH07	6.21E-01	0.0564	154	2.74E-01	104	385
KOCH08	1.29E+00	0.0402	149	1.20E-01	100	608
KSRH01	2.29E+00	0.0408	644	3.24E+00	106	215
KSRH02	8.19E-01	0.0577	774	1.71E+00	105	219
KSRH04	1.57E+00	0.0593	695	1.71E+00	240	189
KSRH07	1.48E+00	0.0479	938	2.74E+00	222	204
KSRH08	2.71E+01	0.0478	695	6.14E-01	100	650
KSRH09	1.71E+00	0.0493	916	1.62E+00	100	230
KSRH10	6.74E-01	0.0462	555	1.30E+00	255	213
KYTH01	9.07E+00	0.0328	168	8.16E-01	155	240
KYTH03	1.00E+01	0.0449	152	7.31E-02	300	637
KYTH04	6.21E-01	0.0583	201	2.89E-01	100	1069
KYTH05	3.67E+00	0.0312	89	7.01E-01	150	133

Station	$PGA_{ref}^{downhole}$ [m/s <sup>2</sup> ]	$\sigma$	#data	max $PGA_{downhole}$ [m/s <sup>2</sup> ]	Depth Downhole [m]	Vs30 [m/s]
MIEH01	3.56E+00	0.0562	386	7.56E-01	140	342
MIEH02	3.41E+00	0.0556	212	7.70E-01	200	423
MIEH03	5.98E-01	0.0547	241	3.42E-01	100	435
MIEH05	7.33E-01	0.0598	255	5.11E-01	100	590
MIEH07	1.32E+00	0.0532	136	2.37E-01	207	617
MIEH08	1.05E+00	0.0438	162	3.51E-01	150	1010
MIEH10	4.11E+00	0.039	308	3.65E+00	197	422
MYGH01	1.39E+00	0.0413	606	5.27E-01	1206	210
MYGH02	4.82E-01	0.0587	730	1.39E+00	203	399
MYGH04	4.81E-01	0.0469	2277	2.04E+00	100	850
MYGH06	2.55E+00	0.0509	2353	2.06E+00	100	593
MYGH08	5.17E+00	0.0269	2804	2.09E+00	100	203
MYGH09	1.82E+00	0.0434	2232	1.58E+00	100	358
MYGH10	1.96E+00	0.0492	2788	2.22E+00	205	348
MYGH12	6.99E-01	0.0585	763	2.43E+00	102	748
MYGH13	8.36E-01	0.0383	727	3.46E-01	100	571
MYZH01	1.06E+00	0.0474	149	1.45E-01	103	547
MYZH02	9.50E-01	0.0573	156	1.51E-01	210	919
MYZH04	7.14E-01	0.0461	453	2.91E-01	100	484
MYZH05	4.48E-01	0.0393	294	3.56E-01	100	1072
MYZH07	6.31E-01	0.0584	193	9.79E-02	100	878
MYZH08	3.47E+00	0.027	560	3.34E-01	214	374
MYZH09	6.25E-01	0.0486	133	1.13E-01	100	973
MYZH10	3.35E+00	0.0232	453	1.77E-01	100	495
MYZH11	8.67E-01	0.0372	139	1.61E-01	212	510
MYZH12	9.99E-01	0.0372	143	8.02E-02	101	319
MYZH13	1.79E+00	0.0385	365	1.51E-01	117	251
MYZH14	7.68E-01	0.0393	65	1.08E-01	201	331
MYZH15	8.96E-01	0.0433	370	2.86E-01	200	446
MYZH16	5.20E-01	0.0514	359	3.46E-01	100	847
NARH07	6.80E-01	0.0552	64	1.78E-01	100	655
NGNH09	6.70E-01	0.0395	101	4.14E-02	100	771
NGNH11	5.80E-01	0.0423	430	2.07E-01	206	372
NGNH13	2.38E+01	0.0576	353	2.66E-01	124	513
NGNH16	8.69E-01	0.0511	432	1.00E-01	247	276
NGNH17	8.86E-01	0.0367	275	7.34E-02	100	609
NGNH18	1.98E+00	0.047	431	1.21E+00	100	379
NGNH19	3.19E+00	0.0381	509	1.64E-01	115	473
NGNH20	1.84E+00	0.036	328	5.17E-01	100	530
NGNH21	1.19E+00	0.0449	438	1.96E-01	180	508

Station	$PGA_{ref\_downhole}$ [m/s <sup>2</sup> ]	$\sigma$	#data	max $PGA_{downhole}$ [m/s <sup>2</sup> ]	Depth Downhole [m]	Vs30 [m/s]
NGNH22	6.86E-01	0.0505	332	1.73E-01	100	939
NGNH28	7.91E+00	0.0546	383	1.13E+00	120	587
NGNH29	2.62E+00	0.0481	510	1.11E+00	110	465
NGNH30	1.48E+00	0.0505	413	2.14E-01	101	457
NGNH31	4.86E-01	0.0566	368	3.23E-01	218	527
NGNH32	5.17E-01	0.041	121	1.98E-01	100	310
NGNH33	3.44E+00	0.0442	218	2.99E-01	106	435
NGNH35	3.84E-01	0.055	176	1.00E-01	105	512
NGNH37	4.68E-01	0.0486	220	4.59E-02	709	338
NGNH54	5.16E+00	0.0477	215	3.27E-01	104	661
NGSH01	1.34E+00	0.0506	109	2.39E-01	207	398
NGSH02	4.33E+00	0.0508	44	1.44E-01	112	642
NGSH03	9.52E-01	0.0533	217	1.87E-01	200	634
NGSH04	4.82E-01	0.032	83	1.34E-01	100	633
NGSH05	1.29E+00	0.0497	107	3.81E-01	200	381
NIGH03	1.51E+00	0.0411	370	1.62E-01	221	251
NIGH04	2.51E+00	0.0431	741	3.21E-01	100	392
NIGH05	4.17E+00	0.0317	571	3.84E-01	147	245
NIGH07	8.78E-01	0.0414	579	3.81E-01	106	528
NIGH08	2.46E+00	0.0568	806	2.95E-01	300	327
NIGH10	6.65E+00	0.0599	782	6.40E-01	100	653
NIGH11	6.34E+00	0.0523	976	3.51E+00	205	375
NIGH12	2.35E+00	0.0405	743	2.93E+00	110	553
NIGH13	4.13E+00	0.039	407	9.84E-01	100	461
NIGH15	1.49E+01	0.0433	716	9.15E-01	100	686
NIGH16	2.13E+00	0.0589	140	2.38E-01	100	525
NIGH17	1.54E+00	0.0538	379	5.59E-01	150	383
NIGH18	1.83E+00	0.0519	352	3.41E-01	110	311
NIGH19	2.09E+00	0.0373	393	7.18E-01	100	625
NMRH01	1.02E+00	0.0535	662	3.03E-01	110	438
NMRH03	2.38E+00	0.028	928	7.34E-01	228	190
NMRH04	2.33E+00	0.0364	818	1.53E+00	216	168
NMRH05	1.57E+00	0.031	817	1.40E+00	220	209
OITH02	1.56E+00	0.0576	149	1.72E-01	100	533
OITH03	8.01E-01	0.0593	146	1.64E-01	400	486
OITH04	1.18E+00	0.0567	213	1.84E-01	230	459
OITH06	1.28E+00	0.051	194	1.74E-01	103	712
OITH07	1.98E+00	0.0432	145	1.39E-01	101	276
OITH08	4.11E-01	0.0502	363	2.51E-01	101	657
OITH10	1.95E+00	0.0596	246	2.21E-01	100	837

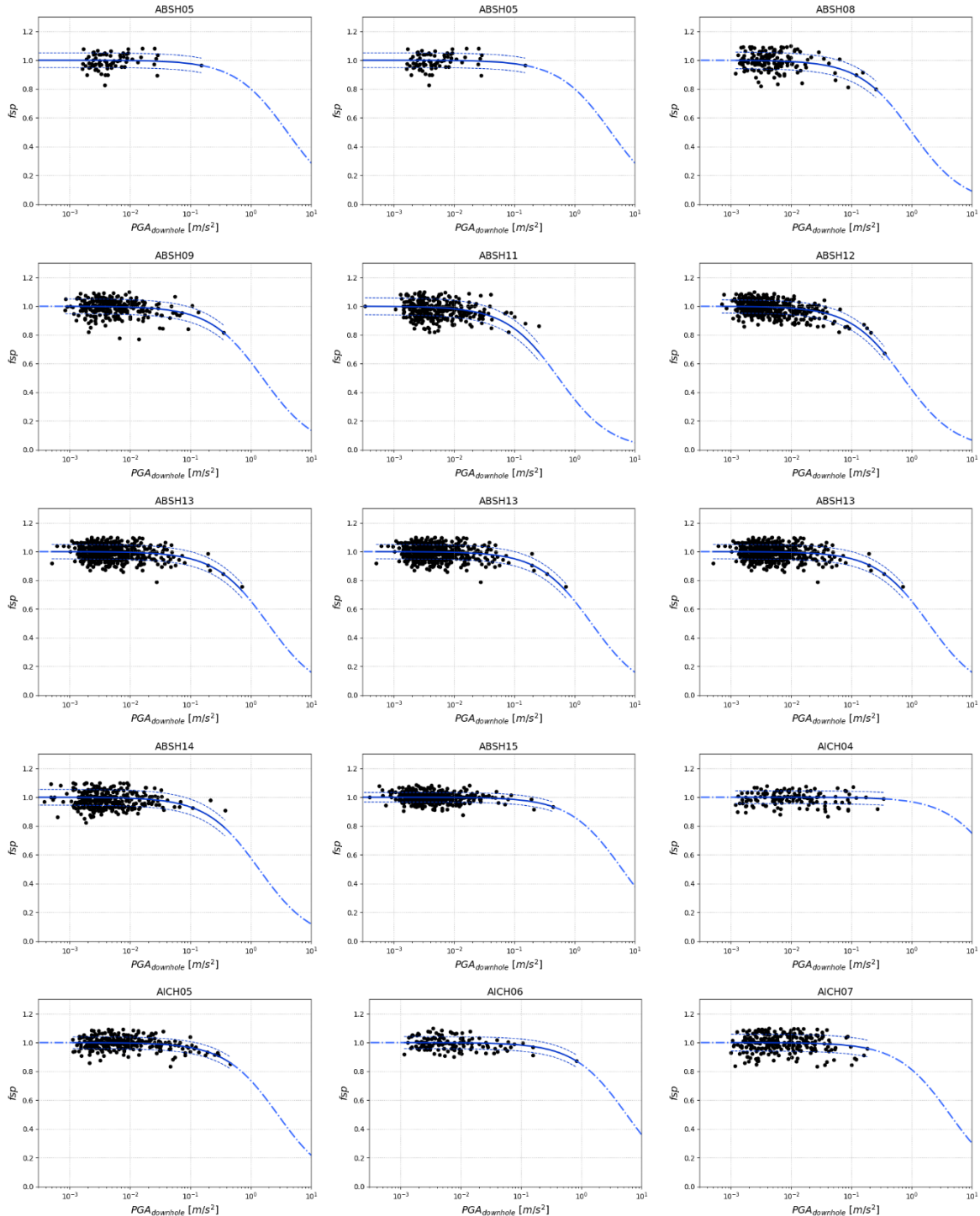
Station	$PGA_{ref\ downhole}$ [m/s <sup>2</sup> ]	$\sigma$	#data	max $PGA_{downhole}$ [m/s <sup>2</sup> ]	Depth Downhole [m]	Vs30 [m/s]
OITH11	9.61E-01	0.0576	392	1.46E+00	160	459
OKYH01	1.43E+00	0.0428	139	3.59E-01	201	241
OKYH05	3.86E+00	0.048	182	4.92E-01	100	608
OKYH06	9.55E-01	0.0496	153	2.04E-01	100	550
OKYH11	7.30E-01	0.0585	174	3.20E-01	200	532
OKYH14	7.32E-01	0.043	188	1.15E+00	100	710
OSMH01	1.79E+00	0.0308	389	1.31E-01	150	239
OSMH02	1.95E+00	0.0525	566	4.41E-01	360	325
RMIH01	1.69E+00	0.0515	57	7.68E-02	100	298
RMIH02	5.03E+00	0.0287	65	3.42E-01	107	155
RMIH05	6.33E-01	0.0377	99	6.58E-01	105	218
SAGH01	2.29E+00	0.0377	144	4.50E-01	200	980
SAGH02	1.38E+00	0.0411	92	6.31E-01	102	558
SAGH03	1.09E+00	0.0399	118	4.85E-01	103	434
SBSH03	1.45E+01	0.0164	133	7.91E-02	220	231
SBSH05	1.15E+00	0.0274	121	7.00E-02	100	264
SBSH06	1.75E+00	0.0337	166	1.36E-01	130	447
SBSH07	1.66E+00	0.034	244	1.98E-01	100	226
SBSH08	1.73E+01	0.0239	166	1.85E-01	100	325
SBSH10	2.65E+00	0.0372	101	3.63E-01	100	842
SIGH01	4.30E+00	0.0422	178	1.08E-01	100	563
SIGH03	1.54E+00	0.0546	193	1.52E-01	200	393
SITH05	2.26E+00	0.0375	915	3.86E-01	100	670
SITH06	1.50E+00	0.042	1285	6.81E-01	200	369
SITH07	1.27E+00	0.0411	985	3.12E-01	102	705
SITH08	1.64E+00	0.0431	806	4.17E-01	100	521
SITH09	3.35E+00	0.059	622	3.98E-01	122	913
SITH10	1.09E+00	0.0338	926	4.49E-01	102	542
SITH11	9.37E-01	0.0451	981	2.70E-01	102	372
SMNH03	1.69E+00	0.0566	217	8.35E-01	101	435
SMNH06	8.00E-01	0.0536	84	1.83E-01	201	288
SMNH12	8.76E-01	0.0509	186	6.71E-01	101	590
SMNH13	1.02E+00	0.0547	97	1.25E-01	100	650
SMNH14	1.23E+00	0.0566	104	3.50E-01	100	605
SMNH16	7.03E-01	0.0211	98	2.63E-01	100	252
SOYH02	8.19E+00	0.0179	46	1.04E-01	100	118
SOYH06	1.05E+01	0.0371	57	1.80E-01	135	293
SOYH08	2.30E+00	0.0592	55	4.86E-02	100	533
SOYH09	1.15E+00	0.0392	66	7.64E-02	100	244
SOYH10	2.42E+01	0.057	109	8.12E-02	100	588

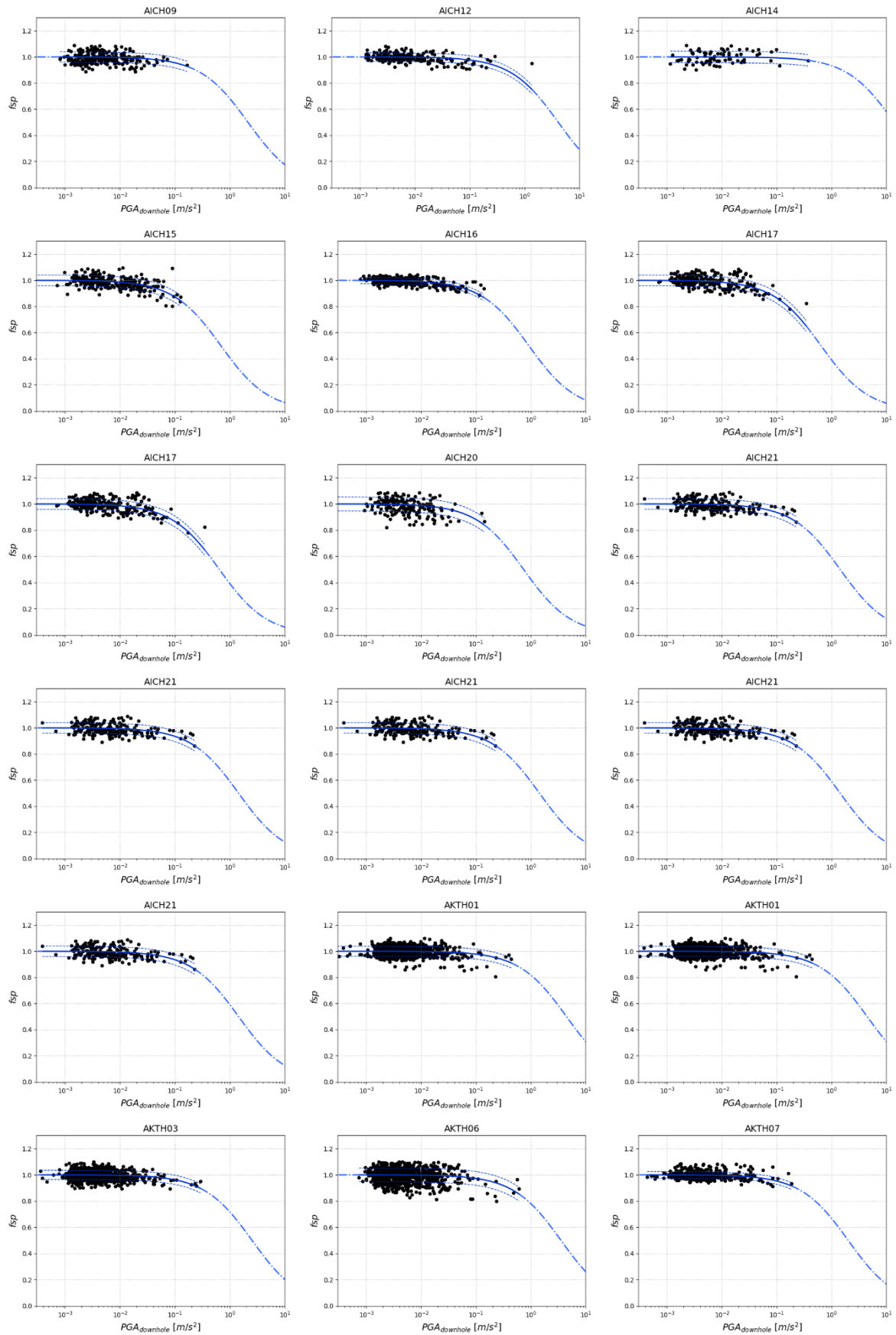
Station	$PGA_{ref\_downhole}$ [m/s <sup>2</sup> ]	$\sigma$	#data	max $PGA_{downhole}$ [m/s <sup>2</sup> ]	Depth Downhole [m]	Vs30 [m/s]
SRCH06	7.63E+00	0.0496	121	2.04E-01	147	321
SRCH07	2.27E+00	0.0336	216	1.76E-01	200	316
SRCH08	3.58E+01	0.0321	263	3.17E-01	122	347
SRCH09	2.28E+00	0.0258	567	4.52E-01	122	241
SRCH10	4.64E+00	0.0517	341	2.64E-01	200	1027
SZOH25	3.45E+00	0.0297	155	1.51E-01	450	332
SZOH26	3.43E+00	0.0435	61	5.28E-01	450	289
SZOH28	1.01E+01	0.0444	130	8.75E-01	996	208
SZOH29	4.86E-01	0.0522	94	2.34E-01	102	520
SZOH32	6.78E-01	0.0563	253	2.14E-01	103	579
SZOH34	1.34E+00	0.0498	402	4.78E-01	118	430
SZOH35	6.60E-01	0.0588	441	5.73E-01	300	158
SZOH38	1.92E+00	0.0568	637	8.32E-01	200	588
SZOH39	1.60E+00	0.0533	485	1.29E+00	103	377
SZOH40	6.82E-01	0.0482	292	3.63E-01	207	493
SZOH41	5.89E+00	0.0536	214	6.86E-01	109	610
SZOH42	4.14E+00	0.0551	727	1.31E+00	203	153
SZOH53	1.29E+00	0.0586	117	2.24E-01	100	808
TCGH08	1.84E+00	0.0565	746	3.90E-01	203	723
TCGH09	9.94E-01	0.0423	1834	6.77E-01	103	468
TCGH10	2.31E+00	0.0358	2802	2.04E+00	132	371
TCGH11	8.82E-01	0.0551	1234	7.27E-01	200	329
TCGH12	3.83E+00	0.0236	2762	1.91E+00	120	344
TCGH13	8.69E-01	0.0535	2171	1.42E+00	140	574
TCGH14	7.90E-01	0.0363	1571	4.15E-01	100	849
TCGH15	1.90E+00	0.0365	523	8.80E-01	300	423
TCGH16	1.29E+00	0.0499	2645	1.83E+00	112	213
TKCH01	2.21E+00	0.0507	613	9.45E-01	122	445
TKCH02	2.21E+00	0.0506	504	8.00E-01	103	441
TKCH03	6.88E-01	0.0586	750	7.39E-01	200	372
TKCH04	2.53E+00	0.0314	684	8.21E-01	172	446
TKCH05	6.00E-01	0.0536	702	1.27E+00	100	337
TKCH06	2.47E+00	0.0301	602	9.07E-01	227	299
TKCH07	1.91E+00	0.0419	705	1.70E+00	100	140
TKCH08	2.04E+00	0.027	786	1.32E+00	100	353
TKCH10	2.86E+00	0.048	365	3.76E-01	100	804
TKCH11	1.51E+00	0.0311	568	7.72E-01	100	459
TKSH03	3.90E-01	0.0572	113	1.03E-01	201	389
TKSH04	1.26E+00	0.0444	120	1.05E-01	100	475
TKSH06	9.44E-01	0.0489	109	1.96E-01	157	470

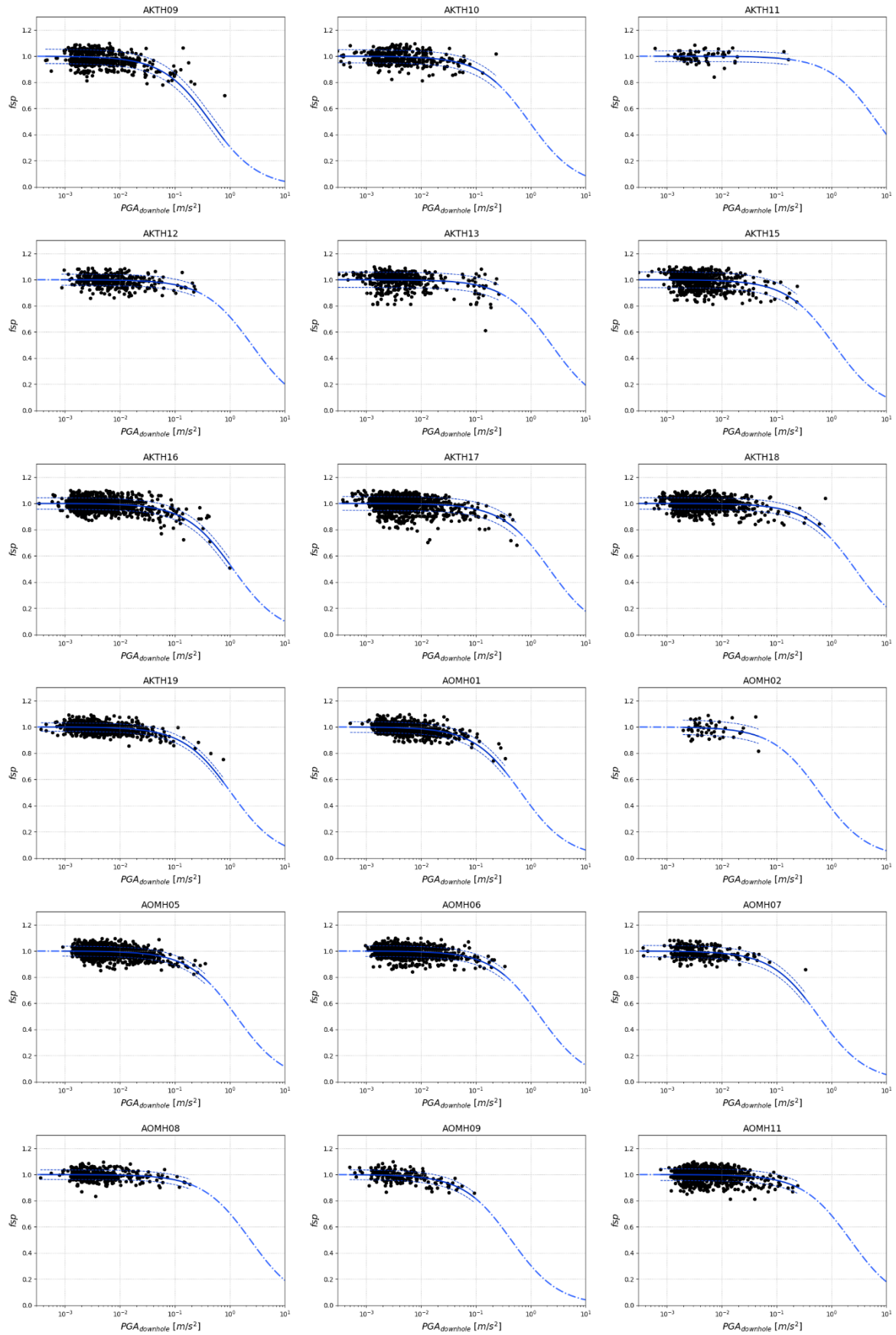
Station	$PGA_{ref}^{downhole}$ [m/s <sup>2</sup> ]	$\sigma$	#data	max $PGA_{downhole}$ [m/s <sup>2</sup> ]	Depth Downhole [m]	Vs30 [m/s]
TKYH12	1.48E+00	0.0345	820	3.33E-01	147	326
TKYH13	4.65E-01	0.0423	700	2.12E-01	100	1110
TTRH03	9.97E-01	0.0424	141	7.58E-01	200	189
TTRH04	1.98E+00	0.0489	195	9.01E-01	207	254
TTRH05	4.07E-01	0.0433	50	9.43E-02	152	479
TTRH06	1.03E+00	0.0484	88	2.25E-01	100	587
TTRH07	3.80E+00	0.0465	134	8.22E-01	100	389
TYMH01	1.04E+00	0.0548	148	2.23E-01	200	383
TYMH02	1.06E+00	0.0307	64	1.35E-01	212	281
TYMH05	2.26E+00	0.0459	140	3.51E-01	144	628
TYMH06	2.22E+00	0.0565	191	3.78E-01	200	570
TYMH07	6.17E-01	0.0538	161	1.66E-01	100	426
WKYH02	5.38E-01	0.0577	121	1.58E-01	100	369
WKYH04	9.41E-01	0.0558	124	4.14E-01	100	550
WKYH06	4.00E-01	0.0481	122	1.42E-01	100	752
WKYH08	1.42E+00	0.0519	196	1.86E-01	112	344
YMGH05	7.54E-01	0.0523	53	4.53E-01	200	432
YMGH09	1.07E+00	0.053	135	1.82E-01	100	303
YMGH10	9.70E-01	0.0436	75	2.19E-01	200	526
YMGH11	5.83E-01	0.0412	104	2.07E-01	200	711
YMGH12	1.54E+00	0.0386	77	1.18E-01	102	1138
YMGH13	1.06E+00	0.0456	72	1.12E-01	200	404
YMGH14	6.18E-01	0.0261	91	7.76E-02	100	320
YMGH15	1.35E+00	0.0507	168	3.14E-01	110	549
YMGH16	8.74E-01	0.0532	167	1.82E-01	106	756
YMGH17	9.43E-01	0.0344	181	2.52E-01	100	225
YMNH09	7.44E-01	0.0536	273	3.70E-01	158	768
YMNH10	6.21E-01	0.0409	397	1.56E-01	107	771
YMNH11	9.56E-01	0.0366	717	3.21E-01	200	295
YMNH13	1.29E+00	0.0574	284	2.12E-01	204	788
YMNH14	7.65E-01	0.0541	495	3.85E-01	250	309
YMNH15	9.34E-01	0.0457	499	3.97E-01	116	579
YMTH01	1.72E+00	0.0321	1024	1.05E+00	207	328
YMTH02	2.77E+00	0.031	1881	5.98E-01	150	Nan
YMTH03	5.66E+01	0.0303	618	2.20E-01	114	900
YMTH04	5.74E-01	0.0572	1339	5.27E-01	100	248
YMTH06	1.12E+00	0.029	915	5.74E-01	145	261
YMTH07	1.67E+00	0.0429	1657	7.91E-01	200	372
YMTH09	9.30E-01	0.0368	363	1.59E-01	200	291
YMTH11	1.23E+00	0.0539	779	2.97E-01	109	412

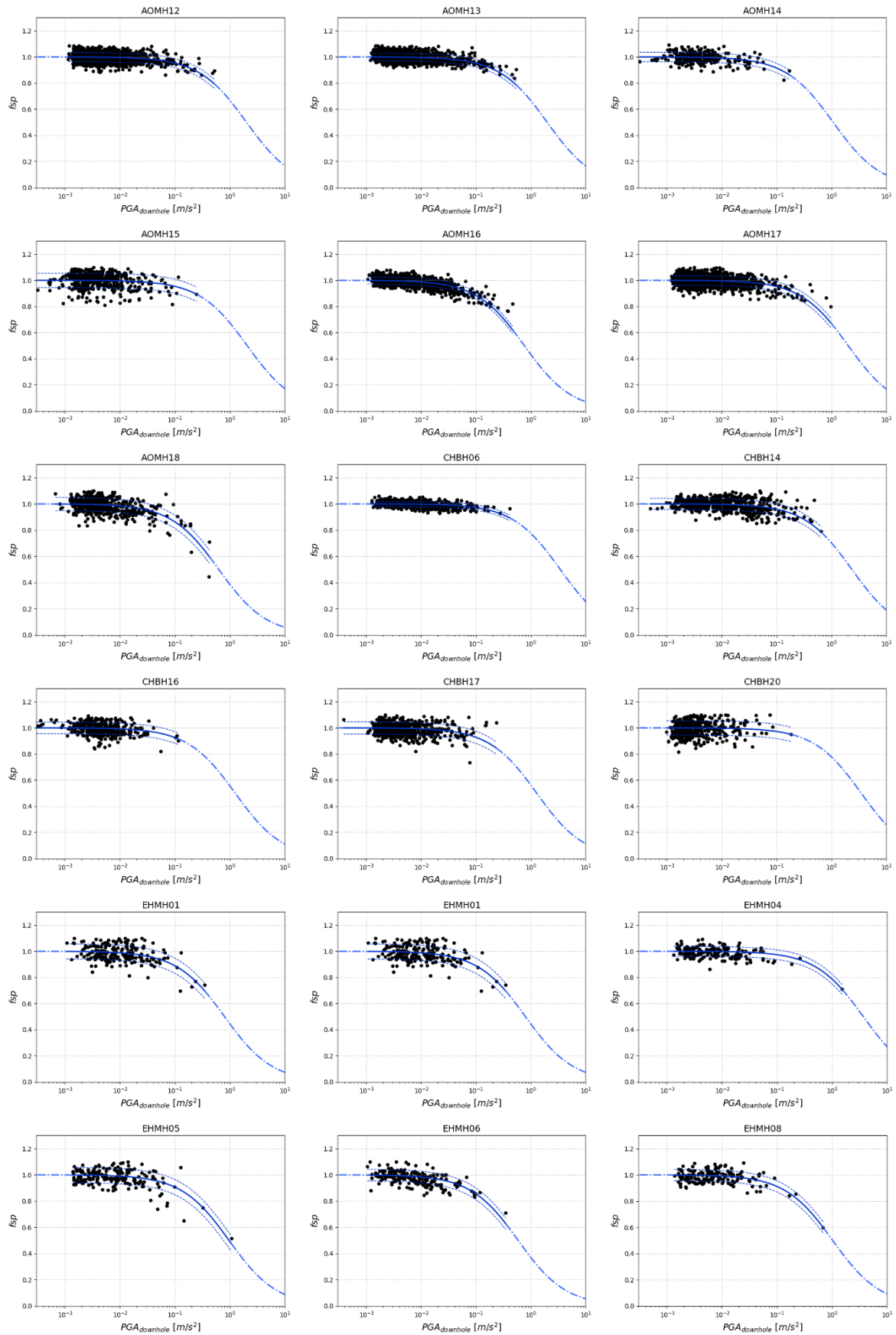
Station	$PGA_{ref\_downhole}$ [m/s <sup>2</sup> ]	$\sigma$	#data	max $PGA_{downhole}$ [m/s <sup>2</sup> ]	Depth Downhole [m]	Vs30 [m/s]
YMTH12	1.61E+00	0.0514	1035	3.09E-01	203	367
YMTH14	1.82E+00	0.0437	1371	1.75E+00	103	311
YMTH15	1.11E+00	0.0264	856	2.56E-01	100	286

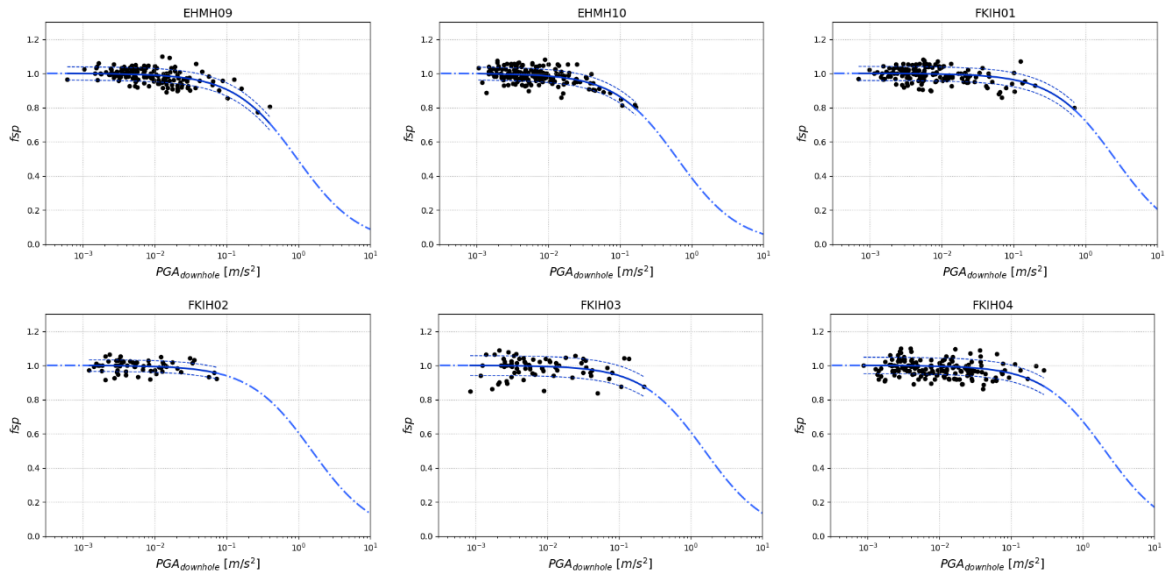
As example, the first 75 sites are shown. The data from other sites can be obtained by request to the authors (e.g. [david.castro@cerema.fr](mailto:david.castro@cerema.fr) or [da.castro790@uniandes.edu.co](mailto:da.castro790@uniandes.edu.co))











## Annex D. Results for Quito simulation with EGF method

